

**STE THRUST CHAMBER TECHNOLOGY
MAIN INJECTOR TECHNOLOGY PROGRAM
AND
NOZZLE ADVANCED DEVELOPMENT PROGRAM (ADP)
FINAL REPORT**

CONTRACT NAS8-37490

**Prepared for
George C. Marshall Space Flight Center
National Aeronautics and Space Administration
Marshall Space Flight Center, AL 35812**

**Prepared by
United Technologies Corporation
Pratt & Whitney
P.O. Box 109600, West Palm Beach, FL 33410-9600**

(NASA-CR-193919) STE THRUST
CHAMBER TECHNOLOGY: MAIN INJECTOR
TECHNOLOGY PROGRAM AND NOZZLE
ADVANCED DEVELOPMENT PROGRAM (ADP)
Final Report (United Technologies
Corp.) 411 p

N94-25019

Unclass

G3/20 0206788



**UNITED
TECHNOLOGIES
PRATT & WHITNEY**

CONTENTS

Section		Page
1.0	INTRODUCTION AND SUMMARY	1-1
1.1	MAIN INJECTOR PROGRAM	1-1
1.2	NOZZLE DEVELOPMENT ADP	1-2
2.0	40K SUBSCALE TASK	2-1
2.1	40K SUBSCALE INJECTOR	2-1
2.1.1	40K Subscale Injector Design	2-1
2.1.2	40K Subscale Injector Design History	2-10
2.1.3	Subscale Injector Fabrication History	2-14
2.2	IGNITER	2-45
2.2.1	Hypergolic Igniter Design	2-45
2.2.2	Torch Igniter Design History	2-46
2.2.3	Torch Igniter Fabrication History	2-51
2.3	CALORIMETER COMBUSTION CHAMBER	2-54
2.3.1	Calorimeter Combustion Chamber Design	2-54
2.3.2	Calorimeter Combustion Chamber Design History	2-70
2.3.3	Calorimeter Combustion Chamber Fabrication History	2-72
2.4	TRANSITION SPOOLPIECE	2-98
2.4.1	Transition Spoolpiece Design	2-98
2.4.2	Transition Spoolpiece Fabrication History	2-99
2.5	40K SUBSCALE TESTING	2-101
2.5.1	Test Setup	2-101
2.5.2	Instrumentation	2-101
2.5.3	Test Program Discussion	2-105
2.5.4	Analysis of Test Results	2-118
3.0	LARGE-SCALE TASK	3-1
3.1	LARGE-SCALE INJECTOR	3-1
3.1.1	Large-Scale Injector Design	3-1
3.1.2	Large-Scale Injector Design History	3-6
3.1.3	Large-Scale Injector Fabrication History	3-10
3.1.4	Large-Scale Injector Instrumentation	3-26
3.2	THRUST MOUNT DESIGN AND FABRICATION HISTORY	3-29
3.3	ACOUSTIC LINER	3-34
3.3.1	Acoustic Liner Design History	3-34
3.3.2	Acoustic Liner Fabrication Plans	3-40
3.4	TEST SUMMARY	3-43

4.0	NOZZLE SKIRT FABRICATION TRIALS	4-1
4.1	NOZZLE SKIRT FABRICATION TRIALS — PHASE I	4-5
4.1.1	Tubular Concepts	4-5
4.1.2	Sheetmetal Concepts	4-68
4.2	NOZZLE FABRICATION TRIALS — PHASE II	4-106
4.2.1	40K Subscale Nozzle Sample	4-106
4.2.2	Single-Tube Samples	4-110
4.2.3	Cylindrical Samples	4-119
4.2.4	40K MTD Nozzle Samples	4-128
5.0	SUBSCALE NOZZLE TASK	5-1
5.1	SUBSCALE NOZZLE FABRICATION AND TEST SUPPORT	5-1
5.1.1	Design and Analysis	5-3
5.1.2	Manufacturing and Assembly	5-54
5.1.3	Integration and Test	5-67
5.1.4	Subscale Injector Performance Enhancement	5-71
	APPENDIX A HEAT TRANSFER MODELS	A-1

LIST OF ILLUSTRATIONS

Figure		Page
2.1.1-1	Subscale Injector Design	2-3
2.1.1-2	Tangential LOX Entry Swirl Concept	2-4
2.1.1-3	Subscale Injector Element Pattern	2-5
2.1.1-4	Subscale Injector Element Assembly	2-6
2.1.1-5	Mass Distributions of Scarfed and Unscarfed Elements	2-7
2.1.1-6	Water Flow of Typical Inner Element (100 psid)	2-8
2.1.1-7	Water Flow of Typical Outer Row Element (100 psid)	2-8
2.1.1-8	Film Cooling Holes	2-9
2.1.2-1	Subscale Injector Cross-Section	2-12
2.1.2-2	Outer Row Element Concept	2-12
2.1.2-3	Vibratory Response of Subscale Element With Likely Combustion Excitation Frequencies	2-13
2.1.2-4	Injector Faceplate Seal Installation	2-13
2.1.2-5	Outer Row Injector Element Replaceable Film Cooling Orifice	2-14
2.1.3-1	Sample Integral Element Interpropellant Plate	2-16
2.1.3-2	Subscale Injector Integral Element Flow Fixture	2-17
2.1.3-3	Photograph of Subscale Injector Integral Element Flow Fixture	2-18
2.1.3-4	Sample Injector Element Water Flow at 100 psid	2-19
2.1.3-5	EDM Electrode for Sample Subscale Interpropellant Plate	2-22
2.1.3-6	Subscale Interpropellant Plate	2-23
2.1.3-7	Subscale Interpropellant Plate Acceptance Flow Results	2-23
2.1.3-8	Weibull Plot of Element Effective Flow Areas	2-24
2.1.3-9	Typical Fuel Sleeve Braze Sample	2-26

2.1.3-10	Fuel Sleeve Braze Sample (Right) With Concentricity Tool	2-27
2.1.3-11	Redesigned Braze Concentricity Tools	2-27
2.1.3-12	Injector Electron Beam Weld Sample	2-28
2.1.3-13	Injector Electron Beam Weld Sample Section Photomicrograph	2-29
2.1.3-14	Injector Assembly Before Installation Interpropellant Plate	2-30
2.1.3-15	Subscale Injector LOX Side	2-30
2.1.3-16	Subscale Injector Fuel Side	2-31
2.1.3-17	Subscale Injector Assembly — LOX Side Exploded View	2-33
2.1.3-18	Subscale Injector Assembly — LOX Side Closeup	2-34
2.1.3-19	Subscale Injector Assembly — Fuel Side Exploded View	2-35
2.1.3-20	Subscale Injector Assembly — Fuel Side Closeup	2-36
2.1.3-21	Subscale Injector Assembly — Fuel Side Closeup With Faceplate	2-37
2.1.3-22	Typical Stresscoat Crack Pattern (Inside Radius of Elbow)	2-38
2.1.3-23	Subscale Injector Mounted on Water Flow Stand	2-40
2.1.3-24	LOX Circuit Water Flow Spray Pattern	2-41
2.1.3-25	Cracked Outer Row Oxidizer Element	2-43
2.1.3-26	Cross-Section of Element Wall Showing Area of Recast	2-44
2.2.1-1	Subscale Hypergolic Igniter	2-46
2.2.2-1	Torch Igniter Cross-Section	2-48
2.2.2-2	Torch Igniter Orifice Setup	2-49
2.2.2-3	NANMAC High-Response Igniter Thermocouple	2-50
2.2.2-4	Torch Igniter Thermocouple	2-51
2.2.3-1	Torch Igniter Spark Plug — Shown Firing	2-53
2.2.3-2	Completed Torch Igniter	2-53
2.3.1-1	Subscale Calorimeter Combustion Chamber Design	2-55

2.3.1-2	Maximum Hot Wall to Backside Wall Temperature Difference Versus Cycles to Failure	2-56
2.3.1-3	Low-Cycle Fatigue NASA Z	2-57
2.3.1-4	Effect of LOX Droplet Mass Mean Diameter on Subscale Chamber Characteristic Velocity Efficiency	2-62
2.3.1-5	Supercritical Combustion Model	2-62
2.3.1-6	Predicted LOX Drop Diameter Distribution for the Subscale Combustion Chamber . .	2-63
2.3.1-7	Subcritical Vaporization at High Pressure	2-63
2.3.1-8	Subcritical-Supercritical Burning Model Pressure Dependence of Normalized Combustion and/or Vaporization Time Typified by Kerosene Droplet in Air	2-64
2.3.1-9	Experimental Effect of Pressure on Burning Rate Observed Time Required to Complete Combustion (Normalized by $P=1$ Atm) as a Function of Pressure for Normal Decane in Air	2-65
2.3.1-10	Stability Limits and Estimated n,t Zone for the Subscale Combustor	2-65
2.3.1-11	Schematic of Calorimeter Combustion Chamber Contour	2-66
2.3.1-12	Calorimeter Thrust Chamber Predicted Combustion Wall Heat Flux Profile	2-66
2.3.1-13	Calorimeter Thrust Chamber Burnout Heat Flux	2-67
2.3.1-14	Subscale Combustor Static Pressures	2-68
2.3.1-15	Combustor Wall Heat Flux	2-69
2.3.1-16	Combustor Wall Heat Flux for Two Propellants	2-69
2.3.2-1	Initial Subscale Combustor Assembly	2-71
2.3.2-2	Forward Passages Coolant Feed	2-72
2.3.3-1	Aluminum Liner Throat Machining Sample	2-74
2.3.3-2	Aluminum Liner Machining Sample During Machining	2-75
2.3.3-3	NASA Z Acoustic Liner Machining Sample	2-76
2.3.3-4	NASA Z Liner Throat Sample During Machining	2-77
2.3.3-5	Machining of the First NASA Z Calorimeter Chamber Liner	2-79
2.3.3-6	First NASA Z Liner Showing Land Damage	2-80

2.3.3-7	Chamber Liner — Waxed and Prepared for Silver and Plugs	2-84
2.3.3-8	Electroformed Nickel to NASA Z Bond Sample	2-85
2.3.3-9	Nickel Deposition Process	2-86
2.3.3-10	Chamber Liner Prepared for Nickel Deposition	2-87
2.3.3-11	Nickel Stresses Due to Chamber Pressure and Coolant Pressure	2-87
2.3.3-12	Nickel (59,300 Y.S.) Thickness Required for Calorimeter	2-88
2.3.3-13	Subscale Chamber With Wax-Filled Grooves Mounted in EF Fixture	2-88
2.3.3-14	Subscale Chamber With Nickel Jacket and Port Tabs Installed	2-89
2.3.3-15	Subscale Chamber With Mounting Flange Installed	2-89
2.3.3-16	Subscale Chamber Following External Contour Machining	2-92
2.3.3-17	Flange-Chamber Interface — Current and Previous Designs	2-93
2.3.3-18	Nickel Flash at Port Entrances	2-94
2.3.3-19	Subscale Chamber Water Flow Results	2-94
2.3.3-20	Welding of Discharge Tubes on Subscale Chamber	2-95
2.3.3-21	Completed Subscale Chamber Showing Inlet Tubes	2-96
2.3.3-22	Completed Subscale Chamber Showing Outlet Tubes	2-97
2.4.1-1	Transition Spoolpiece — P&W Injector to NASA Chamber	2-98
2.4.1-2	Transition Spoolpiece Installed in Rig	2-99
2.4.2-1	Braze Sample Assembly for Transition Spoolpiece	2-101
2.5.2-1	Subscale Injector Instrumentation	2-103
2.5.2-2	Combustor High-Frequency Pressure Transducer	2-104
2.5.2-3	Subscale Chamber Pressure Tap Anti-Icing Scheme	2-105
2.5.3-1	Subscale Test Rig	2-116
2.5.3-2	Subscale Rig Test Firing — Test No. P242-007	2-117
2.5.3-3	Typical Chamber Pressure Traces	2-118

2.5.4-1	Streamtube Model of Propellant Distribution	2-123
2.5.4-2	Correlation of Performance Data Using Statistical Regression Model	2-124
2.5.4-3	Performance Data Correlation With Striation Effects	2-124
2.5.4-4	Experimented Versus Calculated c^* Efficiency	2-125
2.5.4-5	Experimental Wall Heat Flux in Subscale Thrust Chamber	2-127
2.5.4-6	Performance Debit Relative to Amount of Wall Cooling	2-128
2.5.4-7	Performance Benefits of Scarfing	2-128
2.5.4-8	Comparison With SSME Subscale Data	2-129
2.5.4-9	Swirl Element Versus Shear Element Heat Flux	2-129
3.1.1-1	Large-Scale Injector Cross-Section	3-3
3.1.1-2	Low-Cost Faceplate Attachment Scheme	3-4
3.1.1-3	Large-Scale Injector Igniter Insert	3-5
3.1.1-4	Bomb Installation for Combustion Stability Testing	3-6
3.1.2-1	Early Full-Scale Injector Cross-Section	3-8
3.1.2-2	Early Full-Scale Injector Fuel Sleeve Options	3-9
3.1.2-3	Redesign of Injector Housing and Interpropellant Plate	3-9
3.1.3-1	Large-Scale Interpropellant Plate After Rough EDM	3-13
3.1.3-2	Rough EDMing Electrode	3-14
3.1.3-3	Large-Scale Interpropellant Plate After Gundrilling	3-15
3.1.3-4	Locations of Damaged Fuel Elements (Looking Up at Fuel Side)	3-16
3.1.3-5	Segment of Electrode for "Gang" EDMing LOX Entry Slots	3-17
3.1.3-6	Waterflow Setup for the Large-Scale Interpropellant Plate	3-18
3.1.3-7	Interpropellant Plate Being Installed in Housing	3-22
3.1.3-8	Large-Scale Injector After EB Weld of Fuel Manifold	3-23
3.1.3-9	Cross-Sections of Previous and Final Facenut Designs	3-24

3.1.3-10	LOX Cavity Proof Pressure Test Method	3-25
3.1.4-1	Large-Scale Injector Instrumentation	3-28
3.1.4-2	Large-Scale Injector Aspirated Probe	3-29
3.2-1	Original Large-Scale Thrust Mount Design	3-30
3.2-2	Original Large-Scale Thrust Mount on Rig	3-31
3.2-3	Large-Scale Thrust Mount Configuration	3-31
3.2-4	Large-Scale Thrust Mount on Rig	3-32
3.2-5	Large-Scale Injector Thrust Mount	3-33
3.3.1-6	Subscale and Full-Scale Acoustic Liners	3-36
3.3.1-7	Subscale and Full-Scale Acoustic Liner Predicted Performance	3-37
3.3.1-8	Full-Scale Acoustic Liner Predicted Acoustic Performance	3-37
3.3.1-9	Effect of Purges on Acoustic Liner at Rated Power	3-39
3.3.2-1	Subscale Combustion Chamber Acoustic Liner	3-41
3.3.2-2	Subscale Acoustic Cavity	3-41
3.3.2-3	Subscale Acoustic Liner Construction	3-42
3.3.2-4	Large-Scale Acoustic Liner Spoolpiece	3-43
4-1	Fabrication Technologies Selected for Nozzle Skirt	4-3
4-2	Nozzle Skirt Fabrication Trials	4-4
4.1.1-1	Round-Tube Specimen Tooling	4-12
4.1.1-2	Square-Tube Specimen Tooling	4-13
4.1.1-3	Diffusion Bonded/Inflation Formed Inconel 625 Sample Using Round Tubes	4-14
4.1.1-4	Diffusion Bonded/Inflation Formed Inconel 625 Round Tubes in an HIP Furnace (Left: 2100°F and 5000 psi; Right: 2100°F and 17,000 psi)	4-15
4.1.1-5	Diffusion Bonded/Inflation Formed Haynes 230 Preformed Square Tubes in a HIP Furnace at 2100°F and 17,000 psi With No Tube-to-Tube Bonds	4-16
4.1.1-6	Diffusion Bonded/Inflation Formed Inconel 625 Round Tubes in an HIP Furnace at 2100°F and 3000 psi With Tooling Bags	4-17

4.1.1-7	Diffusion Bonded/Inflation Formed Inconel 625 Round Tubes in an HIP Furnace at 2100°F and 1000 psi	4-18
4.1.1-8	Preformed Square Inconel 625 Tubes Inflation Formed/Diffusion Bonded in a Hot Isostatic Press Furnace at 7000 psi and 2100°F With Tubes Unmasked To Form Tube-to-Tube Bonds	4-19
4.1.1-9	Preformed Square Inconel 625 Tubes Inflation Formed/Diffusion Bonded in a Hot Isostatic Press Furnace at 3000 psi and 2100°F With Tubes Unmasked To Form Tube-to-Tube Bonds	4-19
4.1.1-10	Preformed Square Inconel 625 Tubes Inflation Formed/Diffusion Bonded in a Hot Isostatic Press Furnace at 500 psi and 2100°F With Tubes Masked To Prevent Tube-to-Tube Bonds, and With Contamination Present Due to Masking	4-20
4.1.1-11	Preformed Square Haynes 230 Tubes Inflation Formed/Diffusion Bonded in a Hot Isostatic Press Furnace at 3000 psi and 2100°F; Microcracking Occurred in Outside Corner Radii Due to High Material Strain and Strain Rate	4-20
4.1.1-12	Preformed Square Haynes 230 Tubes Inflation Formed/Diffusion Bonded in a Hot Isostatic Press Furnace at 3000 psi and 2100°F; Microcracking Occurred in Outside Corner Radii Due to High Material Strain and Strain Rate	4-21
4.1.1-13	Preformed Square Inconel 625 Tubes Inflation Formed/Diffusion Bonded in a Hot Isostatic Press Furnace at 7000 psi and 2100°F Showing Microcracks on Inside Corner Radii Due to Oxide Formation from a Nonvacuum Environment	4-22
4.1.1-14	Preformed Square Inconel 625 Tubes Inflation Formed/Diffusion Bonded in a Hot Isostatic Press Furnace at 7000 psi and 2100°F Showing Tube-to-Tube and Tube-to-Jacket Bonds	4-23
4.1.1-15	Preformed Square Inconel 625 Tubes Inflation Formed/Diffusion Bonded in a Hot Isostatic Press Furnace at 7000 psi and 2100°F Showing Carbides Present in Base Metal and at Bond Locations	4-24
4.1.1-16	Inconel 625 Tubes Inflation Formed/Diffusion Bonded in a Hot Isostatic Press Furnace at 17,000 psi and 2100°F Showing Oxides and Oxygen-Stabilized Carbides	4-25
4.1.1-17	Inconel 625 Tubes Inflation Formed/Diffusion Bonded in a Hot Isostatic Press Furnace at 17,000 psi and 2100°F Showing a Network of Concentrated, Continuous Carbides	4-26
4.1.1-18	Preformed Square Inconel 625 Tubes Inflation Formed/Diffusion Bonded in a Hot Isostatic Press Furnace at 7000 psi and 2100°F Showing Fine Grains at Bond Location and in Tube Parent Material	4-27
4.1.1-19	Preformed Square Inconel 625 Tubes Inflation Formed/Diffusion Bonded With a Subsequent Heat Treat at 2150°F for 2 Hours With a Fast Cooldown Showing No Reduction in Carbides After Heat Treatment	4-28

4.1.1-20	Preformed Square Haynes 230 Tubes Inflation Formed/Diffusion Bonded in a Hot Isostatic Press Furnace at 3000 psi and 2100°F Showing Tube Outer Walls Cracked Due to High Strain in Forming Process	4-29
4.1.1-21	Preformed Square Haynes 230 Tubes Inflation Formed/Diffusion Bonded in a Hot Isostatic Press Furnace at 3000 psi and 2100°F Showing Carbides at Bond Lines . . .	4-30
4.1.1-22	Inconel 625 Tubes Sheetmetal Nickel Plated and Diffusion Bonded at 5000 psi and 1900°F for 6 Hours	4-31
4.1.1-23	Inconel 625 Tubes Sheetmetal Cleaned With Descaling Solution and Diffusion Bonded at 5000 psi and 1900°F for 6 Hours	4-32
4.1.1-24	Inconel 625 Tubes Sheetmetal Cleaned With Chemical Milling Solution and Diffusion Bonded at 5000 psi and 1900°F for 6 Hours	4-33
4.1.1-25	Inconel 625 Tubes Sheetmetal Diffusion Bonded at 5000 psi and 1900°F for 6 Hours, Then Heated at 2150°F To Simulate the Secondary Braze Cycle	4-34
4.1.1-26	Air-Sprayed HVOF	4-37
4.1.1-27	Inert Chamber HVOF Spray	4-38
4.1.1-28	Air-Sprayed Arc-Wire	4-38
4.1.1-29	Inert Chamber Arc-Wire	4-39
4.1.1-30	Inert HVOF Spray Heat Treated at 2000°F for 1 Hour (400×)	4-39
4.1.1-31	Inert Plasma Sprayed Inconel 625 (400×)	4-40
4.1.1-32	Inert Wire Heat Treated at 2000°F for 1 Hour in Vacuum (50×)	4-40
4.1.1-33	Inert Wire Heat Treated at 2000°F for 1 Hour in Vacuum (50×)	4-41
4.1.1-34	INCO 625 Tubes Brazed With NB-10 (Ni-11P)	4-48
4.1.1-35	INCO 625 Tubes Brazed With NB-30 (Ni-19Cr-10Si)	4-49
4.1.1-36	Haynes 230 Tubes Brazed With NB-150 (Ni-15Cr-3.5B)	4-50
4.1.1-37	Inconel Tubes With AMS 4782 Braze Alloy Plasma Sprayed 0.009 Inch Thick	4-51
4.1.1-38	Inconel Tubes With AMS 4782 Braze Alloy Plasma Sprayed 0.009 Inch Thick	4-52
4.1.1-39	Brazing Ranges for Nozzle Braze Alloy Candidates	4-53
4.1.1-40	Phase Diagram for Gold-Silicon Eutectic	4-53

4.1.1-41	Preformed Square Inconel Tubes Brazed With AMS 4782 (Ni-19Cr-10Si) at 2150°F in Vacuum, Then Rebrazed With AMS 4787	4-54
4.1.1-42	Step Braze Sample — Tubes and Jacket Were Plasma and Brazed With AMS 4779 (Ni-3.5Si-1.8B), Then a Second Braze of Alloy AMS 4787 (82Au-18Ni) Was Applied and the Sample Brazed in a Lower Temperature Cycle	4-55
4.1.1-43	Step Braze Sample — Tubes and Jacket Were Plasma and Brazed With AMDRY 300 (Ni-19Cr-9.5Mn-9.5Si), Then a Second Braze of Alloy AMS 4787 (82Au-18Ni) Was Applied and the Sample Brazed in a Lower Temperature Cycle	4-55
4.1.1-44	Fabrication Sample Design for the Step Braze Trials	4-56
4.1.1-45	Round Inconel 625 Tubes Brazed With AMS 4782 (Ni-19Cr-10Si) in Hydrogen Showing No Porosity and Excellent Braze Coverage	4-57
4.1.1-46	Preformed Square Inconel 625 Tubes Brazed With AMS 4782 (Ni-19Cr-10Si) in a Vacuum Environment Showing No Porosity and Excellent Braze Coverage	4-58
4.1.1-47	Inconel 625 Tubes Brazed With AMDRY 300 (Ni-19Cr-9.5Mn-9.5Si) in a Vacuum Environment Showing Excellent Gap Coverage	4-59
4.1.1-48	Inconel 625 Tubes Brazed With AMDRY 300 (Ni-19Cr-9.5Mn-9.5Si) in a Hydrogen Environment Showing Excellent Braze Coverage	4-60
4.1.1-49	Inconel 625 Tubes Brazed With AMDRY 300 (Ni-19Cr-9.5Mn-9.5Si) in a Vacuum Environment Showing Excellent Braze Coverage	4-61
4.1.1-50	Fabrication Sample Design for the Plasma Spray Braze Application Method	4-62
4.1.1-51	Preformed Square Haynes 230 Tubes Brazed at 2175°F With AMS 4782 (Ni-19Cr-10Si) Applied to the Sheetmetal Using Plasma Spray Method	4-63
4.1.1-52	Brazed Tube Sample — Sheetmetal Jacket was Plasma Sprayed With AMS 4782 (Ni-19Cr-10Si)	4-64
4.1.1-53	Braze Sample Bend Tester	4-65
4.1.1-54	Braze Sample Undergoing Bend Testing	4-66
4.1.1-55	Braze Sample Undergoing Bend Testing	4-67
4.1.2-1	Explosion Form Die With Removable/Replaceable Convolute Forms	4-71
4.1.2-2	Explosion Formed Inconel 625 Sample	4-72
4.1.2-3	Explosive Fabricators, Inc Nozzle Proposed Preform Blank	4-73
4.1.2-4	Explosive Fabricators, Inc Nozzle Die Concept	4-73

4.1.2-5	Inconel 625 Panel Explosion Formed With No Cracks	4-74
4.1.2-6	Inconel 625 Panel Preformed Using a Brake Press and Explosion Formed to the Final Geometry	4-74
4.1.2-7	Inconel 625 Panel Showing Typical Failure Due to the Explosion Forming Process . .	4-75
4.1.2-8	Inconel 625 Panel Showing Typical Failure Due to the Explosion Forming Process . .	4-75
4.1.2-9	Random Cross-Sections Taken through an Explosion Formed Inconel 625 Panel	4-76
4.1.2-10	Inconel 625 Panel Explosion Formed and Laser Welded	4-77
4.1.2-11	Inconel 625 Panel Explosion Formed and Laser Welded	4-78
4.1.2-12	Explosion Formed/Laser Welded Sample	4-79
4.1.2-13	Explosion Formed/Laser Welded Sample	4-79
4.1.2-14	Explosion Formed/Laser Welded Double-Convolute Sample	4-80
4.1.2-15	Explosion Formed/Laser Welded Double-Convolute Sample	4-80
4.1.2-16	Haynes 230 Laser Welded/Inflation Formed Test Specimen (6-inch × 12-inch)	4-83
4.1.2-17	Photomicrographs of Haynes 230 Laser Welds Before and After Inflation Forming Showing Tearing Caused by the Forming Process	4-84
4.1.2-18	Photomicrograph of Laser Weld Rupture Caused by Inflation Forming Process (Material = Haynes 230)	4-85
4.1.2-19	Haynes 230 Laser Welded/Inflation Formed Sample Showing Rupture at Bifurcation Point	4-86
4.1.2-20	Laser Welded/Inflation Formed Haynes 230 Sample No. 2	4-87
4.1.2-21	Laser Welded/Inflation Formed Haynes 230 Cross-Section Sample No. 2	4-88
4.1.2-22	Laser Welded/Inflation Formed Inconel 625	4-89
4.1.2-23	Laser Welded/Inflation Formed Inconel 625 Cross-Section Sample No. 1 (40×)	4-90
4.1.2-24	Cross-Section Through Laser Welded/Inflation Formed Inconel 625 Sample No. 2 (32×)	4-90
4.1.2-25	Laser Welded/Inflation Formed "Low-Cycle Fatigue" Inconel 625	4-91
4.1.2-26	Laser Welded/Inflation Formed "Low-Cycle Fatigue" Inconel 625	4-92
4.1.2-27	Laser Welded/Inflation Formed 347 Series Stainless Steel	4-93

4.1.2-28	Laser Welded/Inflation Formed 347 Series Stainless Steel	4-94
4.1.2-29	Laser Welded/Inflation Formed 347 SST Sheetmetal Sample	4-95
4.1.2-30	Laser Welded/Inflation Formed 347 SST Sheetmetal Sample	4-96
4.1.2-31	Diffusion Bonded/Inflation Formed Haynes 230 Sample	4-99
4.1.2-32	Diffusion Bonded/Inflation Formed Inconel 625 Sample Showing Diffusion Bond at 1800°F for 6 Hours	4-100
4.1.2-33	Diffusion Bonded/Inflation Formed Inconel 625 Sample Showing Failure at Diffusion Bond Location	4-101
4.1.2-34	Diffusion Bonded/Inflation Formed Inconel 625 Sample Showing Metal Thinning and No Diffusion Bonding	4-102
4.1.2-35	Diffusion Bonded/Inflation Formed Inconel 625 Sample Showing Fracture Due to Thinning	4-103
4.1.2-36	Diffusion Bonded/Inflation Formed Sheetmetal Sample Showing Typical Failure in Weld Perimeter Location	4-104
4.1.2-37	Diffusion Bonded/Inflation Formed Sheetmetal Sample Showing Typical Failure Near Bond Location	4-104
4.1.2-38	Diffusion Bonded/Inflation Formed Sheetmetal Sample Showing No Diffusion Bonding	4-105
4.2.1-1	Phase II Tooling and Nozzle Assembly for the Brazed Tube Process and the Inflation Formed/Diffusion Bonded Tubes in a Conventional Furnace	4-108
4.2.1-2	Phase II Tooling and Nozzle Assembly for the Inflation Formed/Diffusion Bonded Tubes in a Hot Isostatic Press Furnace	4-109
4.2.1-3	Nozzle Cost Comparison for Various Fabrication Options	4-109
4.2.1-4	Cylindrical Sample Design for Inflation Formed/Brazing Process Parameter Optimization	4-110
4.2.1-5	Single-Tube Inflation Forming Sample Design	4-110
4.2.2-1	Single-Tube Sample — Blocks	4-113
4.2.2-2	Single-Tube Sample Assembly	4-114
4.2.2-3	Transverse Cross-Section Taken Through Single Tube AMS5581 Sample No. 2	4-115
4.2.2-4	Sections Taken Through Defective Tubing	4-116

4.2.2-5	Sections Through the Round, Unprocessed, As-Received AMS 5581 Tubing	4-117
4.2.2-6	Transverse Cross-Section Taken Through Sample No. 3	4-118
4.2.3-1	Cylindrical IF/Braze Mandrel	4-121
4.2.3-2	Inflation Formed/Brazed and Diffusion Bonded Cylindrical Samples	4-122
4.2.3-3	Cylindrical Sample Bag-Braze Design	4-122
4.2.3-4	Cylindrical Sample Hardware — Outer Jacket, Tubes, Inner Vacuum Bag, and Weldment Cover	4-123
4.2.3-5	Cylindrical Sample Hardware — Outer Jacket, Tubes, Inner Vacuum Bag, and Weldment Cover	4-124
4.2.3-6	Cylindrical Bag-Braze Nozzle Sample Assembly	4-125
4.2.3-7	Cylindrical Bag-Braze Sample Assembly	4-126
4.2.3-8	Cylindrical Bag-Braze Sample Assembly	4-127
4.2.4-1	40K MTD Structural Jacket	4-129
4.2.4-2	Spin Chucks for 40K MTD Outer Jacket and Vacuum Bag	4-130
4.2.4-3	Quarter-Scale Bag-Braze Sample Tool Design	4-131
4.2.4-4	Quarter-Scale Nozzle Tube Sample	4-132
5.1-1	Subscale Thrust Chamber Assembly	5-2
5.1.1-1	Subscale Nozzle Film Cooling Simulates Full-Scale Design	5-10
5.1.1-2	Subscale Nozzle Static Pressure Field	5-11
5.1.1-3	Film Coolant Injector Flow into Main Stream of Hot Gas Flow	5-11
5.1.1-4	Subscale Nozzle Temperature Contours	5-12
5.1.1-5	Chamber Rework Section at Port 72	5-12
5.1.1-6	Chamber Rework Section at Port 71	5-13
5.1.1-7	Subscale Thrust Chamber Assembly	5-13
5.1.1-8	Film Coolant Injector Configuration	5-14
5.1.1-9	Subsonic Cavity Configuration	5-14

5.1.1-10	Flow Velocity Contours in Subsonic Cavity for Highest Inlet Pressure Case — Square Post Design	5-15
5.1.1-11	Flow Velocity Field at Subsonic Cavity Exit Plane for Highest Inlet Pressure Case — Square Post Design	5-16
5.1.1-12	Flow Velocity Contours in Subsonic Cavity for Lowest Inlet Pressure Case — Rounded Post Design	5-17
5.1.1-13	Flow Velocity Field at Subsonic Cavity Exit Plane for Lowest Inlet Pressure Case — Rounded Post Design	5-18
5.1.1-14	Flow Velocity Contours in Subsonic Cavity for Highest Inlet Pressure Case — Rounded Post Design	5-19
5.1.1-15	Flow Velocity Field at Subsonic Cavity Exit Plane for Highest Inlet Pressure Case — Rounded Post Design	5-20
5.1.1-16	Flow Velocity Contours in Subsonic Cavity for Lowest Inlet Pressure Case — Rounded Post/Milled Slot Design	5-21
5.1.1-17	Flow Velocity Field at Subsonic Cavity Exit Plane for Lowest Inlet Pressure Case — Rounded Post/Milled Slot Design	5-22
5.1.1-18	Flow Velocity Contours in Subsonic Cavity for Highest Inlet Pressure Case — Rounded Post/Milled Slot Design	5-23
5.1.1-19	Flow Velocity Field at Subsonic Cavity Exit Plane for Highest Inlet Pressure Case — Rounded Post/Milled Slot Design	5-24
5.1.1-20	Nozzle Assembly Critical Life Locations	5-25
5.1.1-21	Analysis of Secondary Coolant Cavity — Design Solution: Porous Stainless Steel Filter	5-26
5.1.1-22	CFD Flow Model of Secondary Cavity Flow Interaction	5-27
5.1.1-23	Core/Secondary Coolant Flow Interaction — Nozzle Temperature Contours	5-28
5.1.1-24	Core/Secondary Coolant Flow Interaction — Temperature Contours Indicate Entrainment of Core Gases	5-29
5.1.1-25	Core/Secondary Coolant Flow Interaction — Velocity Vectors/H ₂ Mass Fraction Contours Show Vortex Mixing	5-30
5.1.1-26	Core/Secondary Coolant Flow Interaction — Pressure Contours Indicate a Step-Induced Shock	5-31
5.1.1-27	Secondary Cavity Design Using Porous Stainless Steel for Flow Distribution	5-32

5.1.1-28	CFD Flow Model of Secondary Cavity Flow Interaction	5-33
5.1.1-29	Comparison of Old and News Subsonic Slot — New Conditions Result in Substantial Improvement in Film Effectiveness	5-34
5.1.1-30	Comparison of Old and News Subsonic Slot — New Conditions Indicate Dramatic Improvement in Film Cooling	5-35
5.1.1-31	Comparison of Old and News Subsonic Slot — Penalty for High Mass Flow Rate is Increased Shock Strength	5-36
5.1.1-32	Subscale Core/Film Coolant Interaction — New Conditions Produce Less Mixing of Secondary Film	5-37
5.1.1-33	Subscale Core/Film Coolant Interaction — Secondary Film Layer Provides Adequate Cooling for Injector Ring	5-38
5.1.1-34	Subscale Core/Film Coolant Interaction — Normal and Tangential Injection Produce Complex Shock and Expansion	5-39
5.1.1-35	Subscale Core/Film Coolant Interaction — Integrity of Primary Jet Maintained	5-40
5.1.1-36	Subscale Core/Film Coolant Interaction — Primary Film Layer Provides Adequate Cooling for Nozzle Skirt	5-41
5.1.1-37	Subscale Core/Film Coolant Interaction — Nozzle Geometry and Film Injection Produce Shock Losses	5-42
5.1.1-38	Subscale Three-Dimensional Primary Injector Analysis — Surface Pressures Indicate Uniform Exit Profiles	5-43
5.1.1-39	Subscale Three-Dimensional Primary Injector Analysis — Exit Mach Contours Indicate Uniform Profile	5-44
5.1.1-40	Subscale Nozzle Flow Rig	5-45
5.1.1-41	Subscale Nozzle Flow Rig	5-45
5.1.1-42	Subscale Nozzle Flow Rig	5-46
5.1.1-43	Ramp Design for Secondary Cavity Flow Distribution	5-46
5.1.1-44	Subscale Nozzle Flow Rig — Air Data: Ramp Versus Porous Metal Designs	5-47
5.1.1-45	Secondary Cavity Design Using Porous Stainless Steel for Flow Distribution	5-47
5.1.1-46	Subscale Nozzle Flow Rig	5-48
5.1.1-47	Secondary Cavity Flow Rig	5-48

5.1.1-48	Gage Total Pressure Distributions At The Slot Exit	5-50
5.1.1-49	Gage Total Pressure Distributions At The Slot Exit	5-50
5.1.1-50	Gage Total Pressure Distributions At The Slot Exit	5-51
5.1.1-51	Pressure Distributions At Pressure Taps and Slot Exit	5-51
5.1.1-52	Pressure Distributions At Pressure Taps and Slot Exit	5-52
5.1.1-53	Pressure Distributions At Pressure Taps and Slot Exit	5-52
5.1.1-54	Nozzle Liner Installed On VTL For Rough Machining	5-53
5.1.2-1	Chamber Rework Fixture	5-56
5.1.2-2	Subscale Nozzle Shipping and Handling Fixture	5-57
5.1.2-3	Injector Ring EB Weld Fixture	5-58
5.1.2-4	Subscale Calorimeter Combustion Chamber	5-59
5.1.2-5	Calorimeter Nozzle Manifold Assembly Before EB Tier Weld	5-60
5.1.2-6	Calorimeter Nozzle Liner Raw Material Prepared for EB Welding	5-61
5.1.2-7	Calorimeter Nozzle and Manifold Assembly in EB Weld Chamber	5-62
5.1.2-8	Fully Machined Calorimeter Nozzle Assembly	5-63
5.1.2-9	Fully Machined Calorimeter Nozzle Assembly	5-64
5.1.2-10	Calorimeter Nozzle Coolant Passages and Instrumentation Holes	5-65
5.1.2-11	Calorimeter Nozzle Forward Flange	5-66
5.1.3-1	Test Instrumentation Plan	5-70
5.1.3-2	Test Instrumentation Plan	5-71

LIST OF TABLES

Tables		Page
2.3.1-1	Subscale Combustor Factors of Safety	2-54
2.3.1-2	Subscale Injection Element Dimensions	2-57
2.3.1-3	Calorimeter Subscale Combustion Chamber Contour	2-59
2.3.1-4	O/F Biasing Experimental Data	2-60
2.3.1-5	O/F Biasing Analytical Results	2-61
2.5.3-1	Early Phase 1 Test Matrix	2-106
2.5.3-2	Early Phase 2 Test Matrix	2-107
2.5.3-3	Early Phase 3 Test Matrix	2-107
2.5.3-4	Early Phase 4 Test Matrix	2-108
2.5.3-5	Early Phase 5 Test Matrix	2-108
2.5.3-6	Final Subscale Test Matrix	2-110
2.5.3-7	Preliminary Subscale Test Results	2-114
2.5.4-1	Predicted Streamtube Flow Splits	2-121
3.1.4-1	Large-Scale Injector Instrumentation List	3-27
3.3.1-1	Acoustic Liner Design Parameters	3-35
4.1.1-1	Inconel 625 — 25 Samples	4-7
4.1.1-2	Haynes 230 — 13 Samples	4-7
4.1.1-3	Haynes 188 — 12 Samples	4-7
4.1.1-4	Average Room Temperature Tensile Properties for Vacuum Plasma Sprayed Inconel 625 Tubes	4-36
4.1.1-5	Tensile Properties of Inert Wire Sprayed Inconel 625 Heat Treated at 2000°F for One Hour in Vacuum	4-36
4.1.1-6	List of Braze Alloys Being Evaluated in Segment 1	4-41
4.1.1-7	Parameters to be Investigated in Segment 2	4-42

4.1.1-8	AMS 4782 Braze Trials	4-43
4.1.1-9	Amdry 300 Braze Trials	4-43
4.1.1-10	AMS 4779 Braze Trials	4-43
4.1.1-11	Braze Alloys Tension/Compression Cracking	4-46
4.2.1-1	Nozzle Skirt Fabrication Options — Producibility Rankings and Costs	4-107
4.2.2-1	Operating Conditions Used In Forming Experiments	4-111
5.1-1	Subscale Nozzle Configuration Comparison	5-2
5.1.1-2	Comparison of Old and New Secondary Slot Model Geometry and Inflow Conditions	5-8
5.1.1-3	Subscale Core/Film Coolant Interaction — Imposed Boundary Values for High-Flow Case	5-9
5.1.3-1	Preliminary Nozzle Characterization Test Matrix – Taguchi DOX Technique	5-68
5.1.3-2	Test Instrumentation Locations	5-69

SECTION 1.0 INTRODUCTION AND SUMMARY

This report documents the Space Transportation Main Engine (STME) Main Injector Technology and Nozzle Advanced Development Programs (ADP) under NASA Marshall Space Flight Center (NASA-MSFC) Contract NAS8-37490.

1.1 MAIN INJECTOR PROGRAM

The purpose of the STME Main Injector Program was to enhance the technology base for the large-scale main injector-combustor system of oxygen-hydrogen booster engines in the areas of combustion efficiency, chamber heating rates, and combustion stability. The initial task of the Main Injector Program, focused on analysis and theoretical predictions using existing models, was complemented by the design, fabrication, and test at MSFC of a subscale calorimetric, 40,000-pound thrust class, axisymmetric thrust chamber operating at approximately 2,250 psi and a 7:1 expansion ratio. Test results were used to further define combustion stability bounds, combustion efficiency, and heating rates using a large injector scale similar to the Pratt & Whitney (P&W) STME main injector design configuration, including the tangential entry swirl coaxial injection elements. The subscale combustion data was used to verify and refine analytical modeling simulation and extend the database range to guide the design of the large-scale system main injector. The subscale injector design incorporated fuel and oxidizer flow area control features which could be varied; this allowed testing of several design points so that the STME conditions could be bracketed. The subscale injector design also incorporated high-reliability and low-cost fabrication techniques such as a one-piece electrical discharged machined (EDMed) interpropellant plate. Both subscale and large-scale injectors incorporated outer row injector elements with scarfed tip features to allow evaluation of reduced heating rates to the combustion chamber.

The Main Injector Program was to culminate in testing of a large-scale high-pressure 580,000-pound class thrust chamber-injector. This large-scale testing was to include attempted destabilization by detonation of bomb devices in the chamber. The large-scale injector did not incorporate the fuel and oxidizer area variability features of the subscale, but it did include the low cost fabrication concept of a one-piece EDMed interpropellant plate. The large-scale injector tests were to provide the necessary combustion technology required at the higher pressure and colder fuel temperatures of the P&W STME configuration.

The STME Main Injector Program was originally the Space Transportation Booster Engine (STBE) Main Injector Program, and was to be a tripropellant program, burning oxygen, methane, and hydrogen. However, before the initial design of the subscale injector was completed, the contract was modified in August 1989 and the methane was dropped and the STBE became the bipropellant STME, burning oxygen and hydrogen. All program tasks remained essentially the same.

Originally, in the STBE phase, the P&W large-scale injector design used an acoustic liner spoolpiece combustion stability aid in the chamber. However, when efforts concentrated on hydrogen fueled engines, it was decided, with NASA concurrence, that the acoustic liner could be dropped. The subscale combustion chamber was redesigned to remove the acoustic liner feature. An acoustic liner spool piece for the large scale injector program was designed prior to dropping methane, however, P&W procured raw material for risk mitigation should an instability issue arise. The acoustic liner was designed to allow addition to the baseline test configuration between the injector and the chamber in place of the NASA-supplied instrumentation ring.

The tasks performed under this contact for the injector were as follows:

- Section 1.0 — Analysis of combustion stability, performance, and chamber heating rates

- Section 2.0 — 40K Subscale Task: Design, analysis, fabrication, and test of a 40K subscale injector, igniter, calorimeter combustion chamber, and transition spoolpiece
- Section 3.0 — Large Scale Injector Task: Design, fabrication, and test of a large scale (580K) injector including a thrust mount assembly and acoustic liner.

The efforts in section 2.0 were completed, however, the hardware designed and fabricated in Section 3.0 was not tested when in, October 1992, program funding was reduced and a stop work order was received from NASA-MSFC. In August 1993, direction was received to stop work on the program with submittal of this final report, and shipment of specified materials to NASA-MSFC.

1.2 NOZZLE DEVELOPMENT ADP

The Nozzle ADP consisted of two tasks: a nozzle skirt fabrication task and a subscale nozzle task. These tasks were selected to assess the two areas of highest technical risk — nozzle skirt low-cost fabrication and nozzle skirt film/convective dump cooling — identified at Government/industry STME cycle selection activity in July 1990. These efforts are detailed in the following sections:

- Section 4.0 — Nozzle Fabrication Demonstration:
 - Phase I — Sample fabrication trials of key nozzle skirt concepts
 - Phase II — Sample fabrication trials to support large scale nozzle
- Section 5.0 — Subscale Nozzle Fabrication and Test Support: Design, analysis, fabrication, and test of a 40K pound thrust size nozzle.

The fabrication task (Section 4.0) provided demonstration of key nozzle skirt fabrication technologies in support of the STME Phase B Preliminary Design. This portion of the program consisted of a subscale sample investigation (Phase I) and a large-scale size scaleup evaluation (Phase II). Phase I investigated the feasibility and producibility of various materials, geometries, and fabrication methods for nozzle skirt tubular concepts and sheetmetal concepts. Following the completion of Phase I, methods were selected for continued evaluation in the Phase II portion of the program based on each method's reliability, cost, durability, weight, and performance. The Phase II portion was to assess the large-scale related process capabilities and sensitivities by performing fabrication trials to support the selection of a fabrication method.

Section 5.0 involved the design, fabrication, and test of a large calorimeter nozzle configuration. The task was to evaluate film cooling and the optimum flow splits between primary film/convective cooling and secondary (subsonic) cooling, along with the effects of various film injector geometries. The nozzle was designed to be used with the 40K subscale injector and main chamber in the previously described sections.

SECTION 2.0 40K SUBSCALE TASK

2.1 40K SUBSCALE INJECTOR

2.1.1 40K Subscale Injector Design

Figure 2.1.1-1 shows a cross-section of the subscale injector design. Hydrogen fuel enters through a INCO 625 Greyloc flange and passes into the INCO 718 manifold. This manifold is EB welded at two locations to the INCO 718 injector housing. The fuel passes through twelve 0.500-inch diameter crossover slots into the fuel cavity, from which it is fed into the combustion chamber through the INCO 718 fuel sleeves and the 347 stainless steel porous faceplate. LOX enters through two 1.5-inch schedule 80, 321 stainless steel pipes. From there it travels into the LOX elements through tangential entry slots and into the combustion chamber. Each of the 62 LOX injectors are tangential-entry, swirl-coaxial elements which produce a hollow-cone spray with an average drop size of 15 to 20 microns at normal operating conditions. The tangential entry swirl concept is shown in Figure 2.1.1-2.

The view of the injector face in Figure 2.1.1-3 shows the injector element pattern. Twenty six of the sixty two elements form a circular outer row, while the remaining thirty six elements fall into a hex pattern in the infield. The igniter comes through the very center of the injector.

The subscale (as well as the large scale) injector features a one-piece electrodischarge machined (EDMed) interpropellant plate with integral LOX elements. This plate has a significant advantage over other interpropellant plate designs with brazed or welded elements because there is no weld or braze joint to provide a possible leak path between oxidizer and fuel. Therefore, the one-piece design is not only significantly more reliable, but it also eliminates the extensive and costly inspection required for a prime reliable braze or weld joint. Another cost advantage can be seen in the EDM process, which allows all or many of the elements to be machined at once ("gang EDM").

A part of the planned subscale testing involved biasing the mixture ratio. By reducing mixture ratio of the outer injector elements, the combustor wall heat flux can be reduced and durability enhanced. It was also desired to run various injector geometries (fuel and LOX flow areas) so that the injector geometry could be optimized for the highest performance. Therefore flexibility features were incorporated into the design of the injector elements, so that the injector elements could be run with various fuel and LOX flow areas. A closeup of an element with its flexibility features can be found in Figure 2.1.1-4.

The subscale injector elements feature removable facenuts on each element allowing the fuel flow metering areas to be varied. The fuel flow area (and thus the O/F ratio) for the entire injector may be changed, or the O/F ratio may be biased for chamber wall compatibility by using facenuts with different annulus sizes on the outer row. The facenuts are secured with purple Loctite, a low-strength thread-locking compound. The facenut changeout can be accomplished through the chamber throat without removing the injector.

Because there was no previous experience with Loctite at cryogenic temperatures, tests were performed on the Loctite to make sure that it retained its thread locking abilities when subjected to very cold temperatures. Tests performed with liquid nitrogen show that the Loctite performed extremely well at cryogenic temperatures, actually strengthening without suffering embrittlement problems, then returning to room temperature properties when its temperature was allowed to return to ambient.

The LOX flow areas may also be varied by internal plugs which screw up into the LOX post to block off a portion of the tangential entry slots as shown in Figure 2.1.1-4. The plugs are installed from the face of the

injector so they can be installed or removed on the test stand without need for removing the injector. The LOX flow metering plugs are held in place by Spiralock self locking threads on the LOX post.

Other features which enhance combustion chamber wall durability, in addition to O/F biasing, are incorporated into the design of the subscale injector. The LOX elements on the outer row are scarfed (cut at a 45-degree angle relative to the injector centerline, such that the shortest side of the injector exit is closest to the chamber centerline and flush with the injector faceplate, as shown in Figure 2.1.1-5) to shift the spray cone and prevent impingement of LOX on the combustor wall. Figures 2.1.1-6 and 2.1.1-7 show water flows of an inner element and an outer row scarfed element respectively. The effect of the scarf on the spray cone angle can be seen clearly. Note that not only does the scarf shift the spray cone towards the center of the plate, but the scarf also shifts the majority of the mass flow towards the injector center. Pattern tests of the spray cone of this element design conducted in other programs have shown that two-thirds of the LOX flow is directed toward the injector centerline. With a normal element the mass is distributed evenly so only one half of the mass goes toward the center of the combustor. The mass distributions of a scarfed and an unscarfed element are shown in Figure 2.1.1-5. Tests show that this distribution is invariant over a range of flow rates and velocities representative of chamber conditions. Thus, scarfing skews the LOX toward the chamber center, which lowers the O/F mixture ratio near the wall.

The injector as originally built also featured film cooling to further enhance wall compatibility. Fifty two film cooling holes (two per outer row element) were drilled into the porous faceplate just outside of the outer row of elements as shown in Figure 2.1.1-8. During the testing at MSFC, these film cooling orifices were welded shut in order to deactivate the film cooling feature.

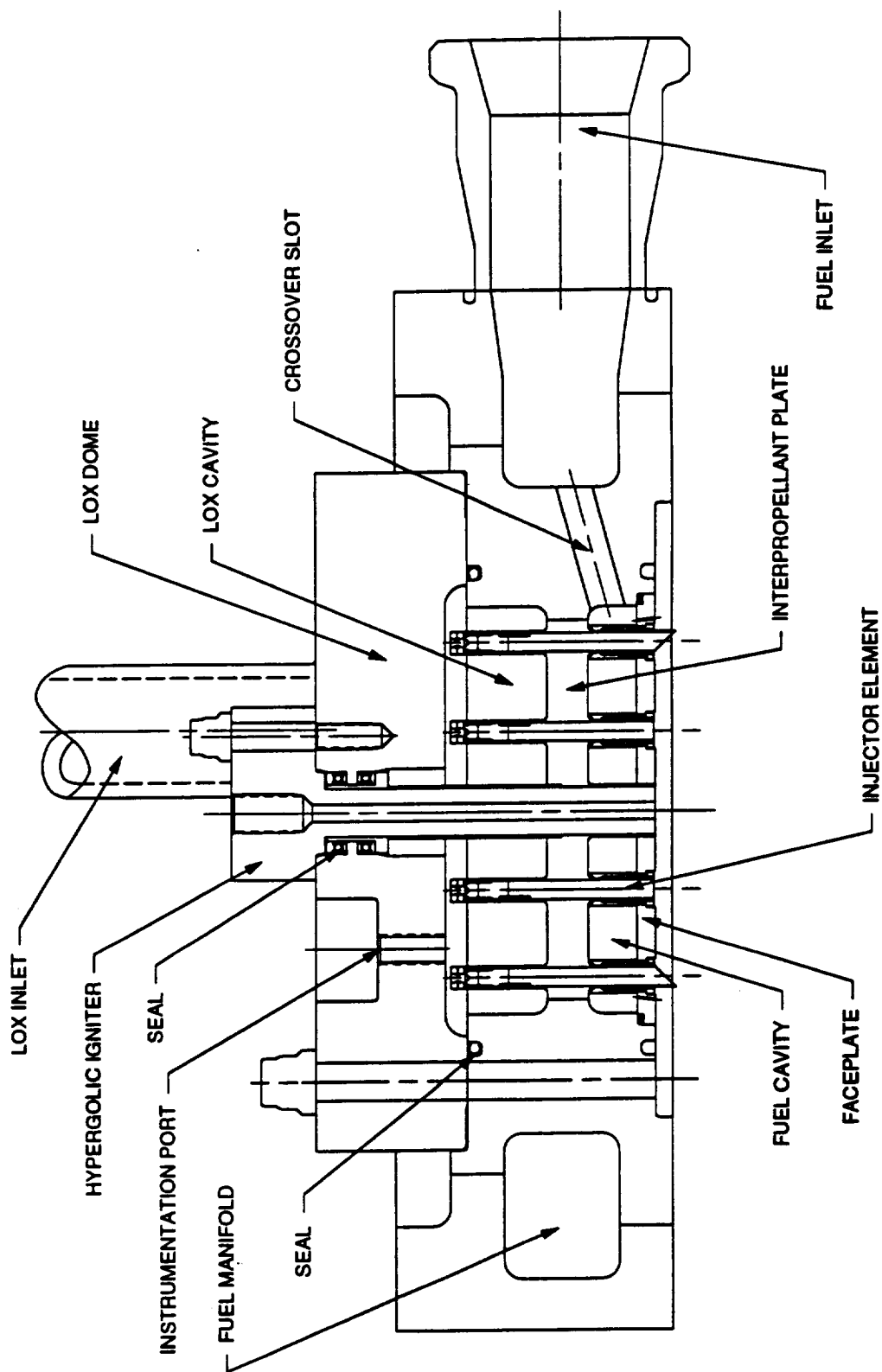


Figure 2.1.1-1. Subscale Injector Design

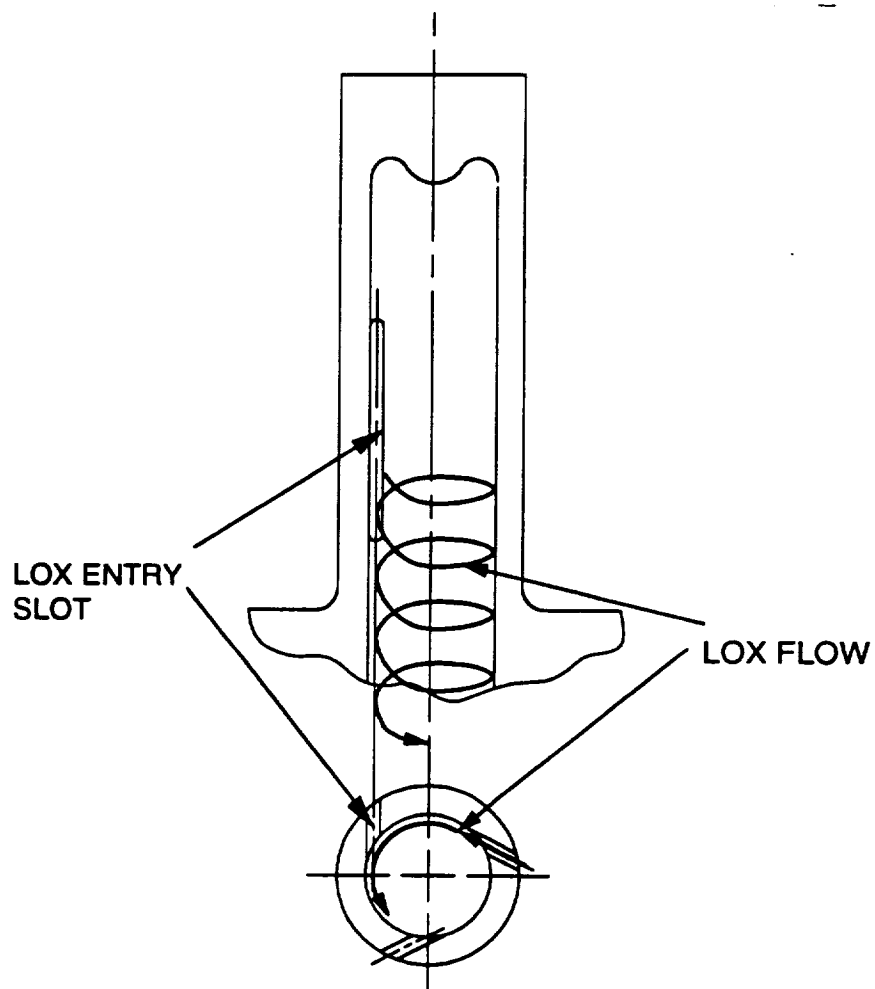


Figure 2.1.1-2. Tangential LOX Entry Swirl Concept

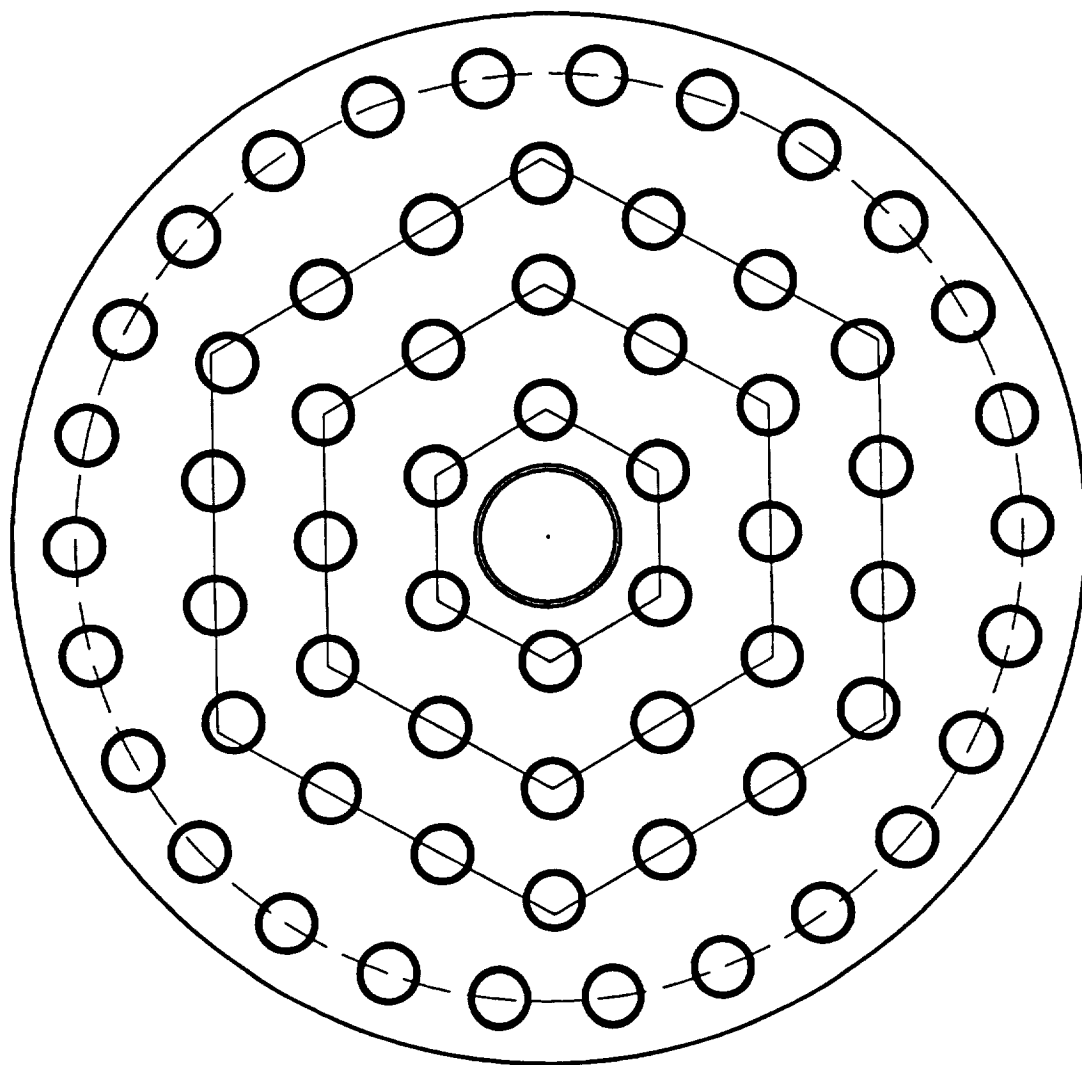


Figure 2.1.1-3. Subscale Injector Element Pattern

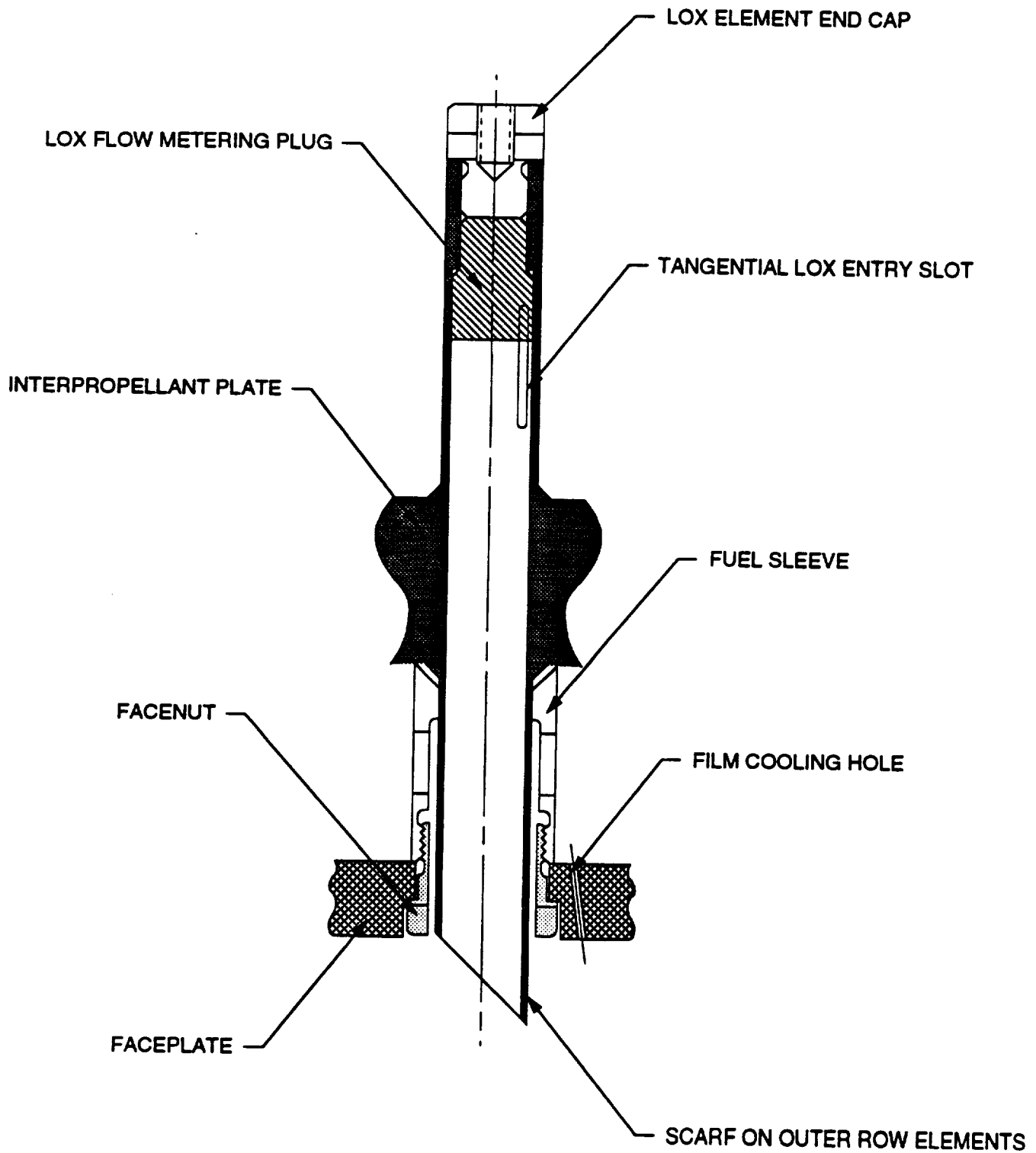


Figure 2.1.1-4. Subscale Injector Element Assembly

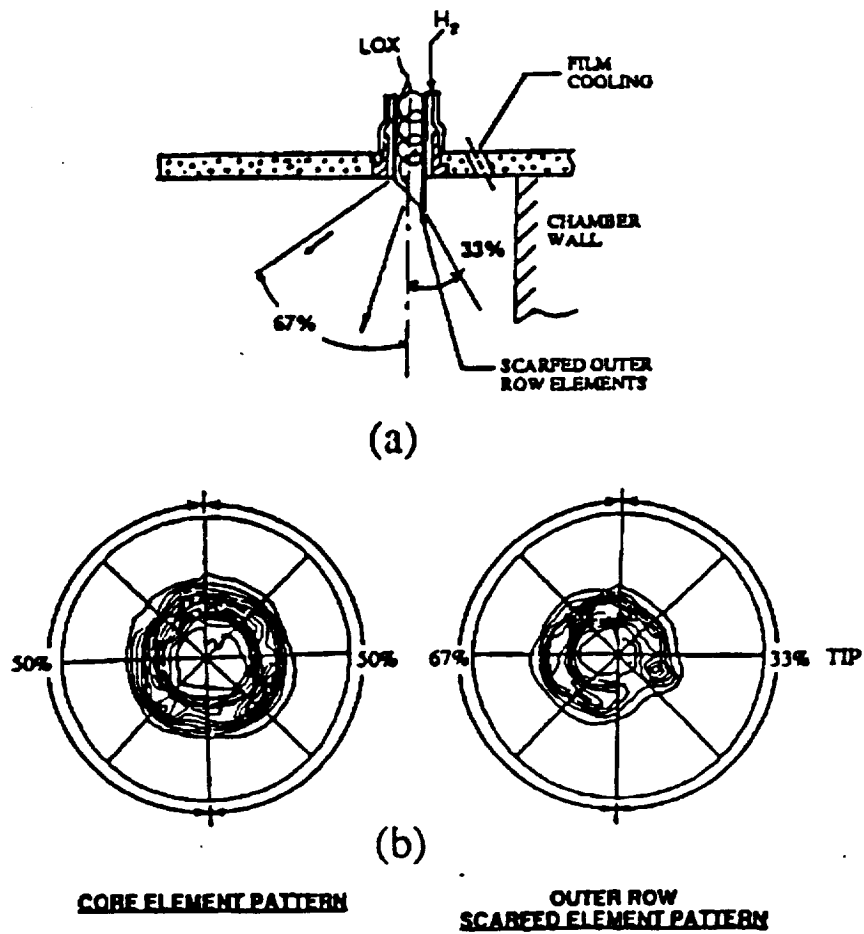
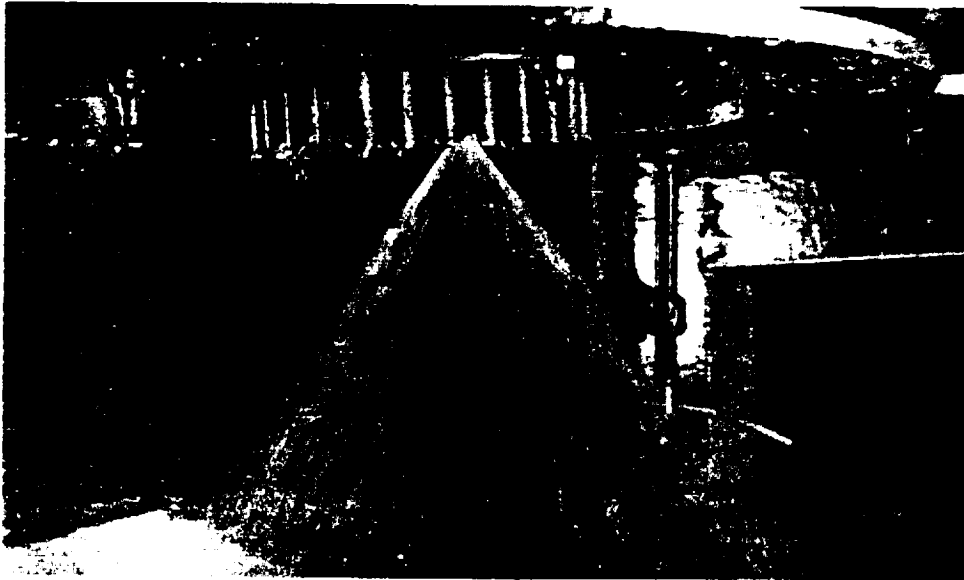
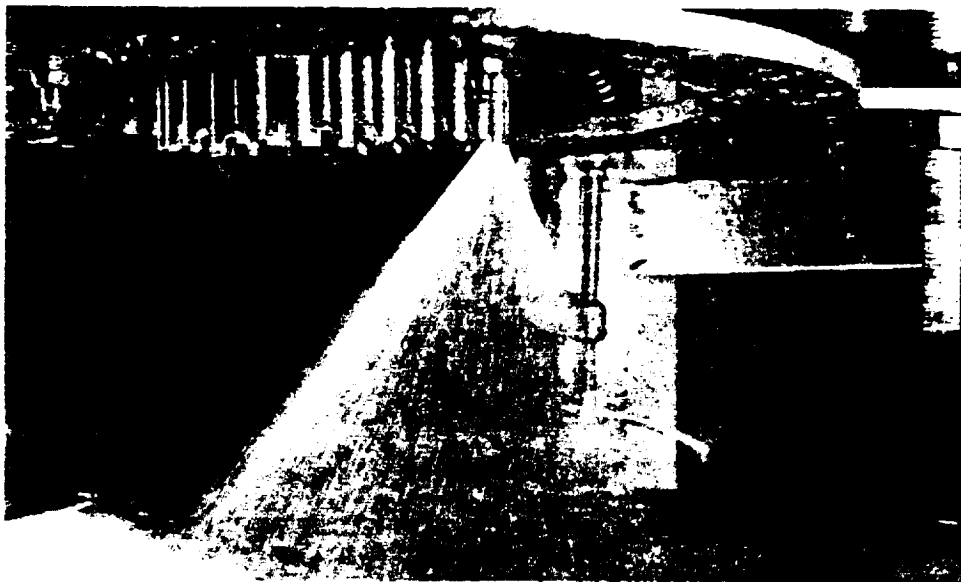


Figure 2.1.1-5. Mass Distributions of Scarfed and Unscarfed Elements



FE300082-3

Figure 2.1.1-6. Water Flow of Typical Inner Element (100 psid)



FE300082-4

Figure 2.1.1-7. Water Flow of Typical Outer Row Element (100 psid)

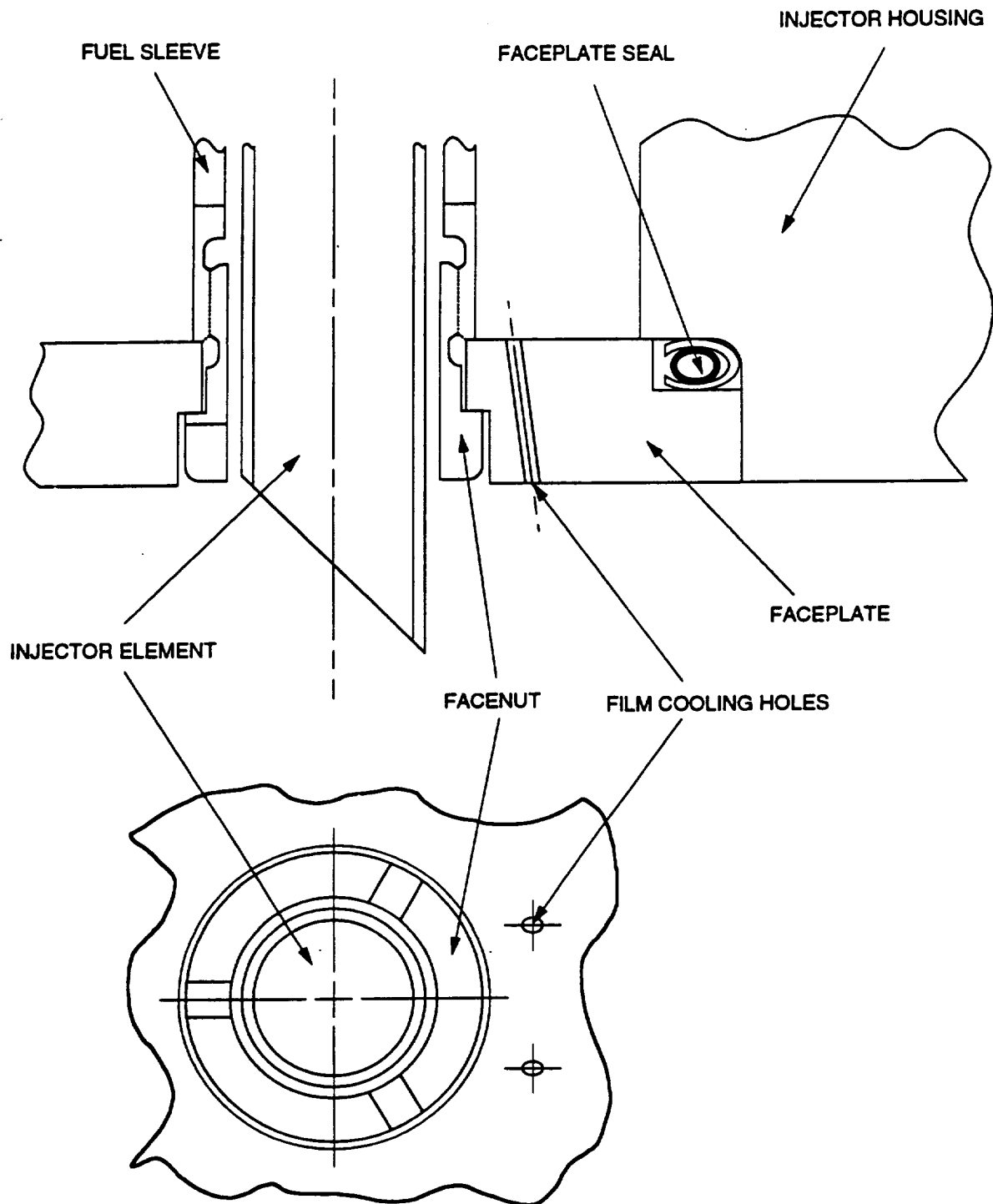


Figure 2.1.1-8. Film Cooling Holes

2.1.2 40K Subscale Injector Design History

Although originally conceived as a tripropellant engine burning oxygen, methane, and hydrogen, by the time of the initial subscale injector design the STBE had become a bipropellant engine burning LOX and methane. The initial design did not have the fuel and LOX area flexibility features of the final design, nor did it have a one-piece, EDMed interpropellant plate with integral LOX elements. Instead it had the standard, well-proven design of fixed area elements brazed into a separate interpropellant plate.

Figure 2.1.2-1 shows a cross section of the initial subscale injector design, which was designed to burn methane. The propellant flowpath is similar to the current design. Methane enters through a 316 stainless steel flange and passes into the INCO 718 manifold. This manifold is EB welded at two locations to the INCO 718 injector housing. The fuel passes through twelve 0.500-inch diameter crossover slots into the fuel cavity, from which it is fed into the combustion chamber through the Haynes 230 nickel alloy fuel elements and the 347 stainless steel porous faceplate. LOX enters through two 1.5-inch schedule 80, 347 stainless steel pipes. From there it travels into the LOX elements through tangential entry slots and into the combustion chamber.

Assembly of the injector would have included three braze cycles. The first would join the LOX elements to the fuel elements, using a gold-nickel-palladium alloy at 2150°F maximum. The second cycle would braze the element assemblies to the interpropellant plate, using a lower melting temperature gold-nickel-palladium alloy at 1975°F maximum. Both sides of this braze would then be accessible for visual inspection and a helium mass spectrometer leak check. The final braze would then be gold-nickel alloy at 1845°F maximum to join the faceplate to the elements.

INCO 718 was chosen as the material for injector housing excellent strength, availability, good weldability, and brazeability. A-286 was also a candidate, but to have complete inspectability of the interpropellant plate braze joint, three braze cycles had to be used. This meant that the housing had to be exposed to a 1975°F braze cycle. There was a concern that A-286 could suffer significant grain size growth with a corresponding reduction in properties, so INCO 718 was chosen. Although hydrogen embrittlement was not a concern at this time (since methane was to be used as the fuel), it was desired to have the flexibility to run hydrogen if required in the future. If hydrogen were to be used at some time in the future, the fully debited INCO 718 mechanical properties used in this design could still meet structural safety margins at the design operating pressures.

To enhance chamber wall compatibility, the outer row of elements featured removable fuel elements so that the O/F ratio could be biased by using fuel elements with different annulus sizes. Figure 2.1.2-2 shows the fuel element which would be screwed onto a brazed, threaded ring on the LOX element. The sleeve would be secured either with the use of a thread-locking compound (i.e., Loctite) or by staking at the injector faceplate. It was intended that the fuel element change out be accomplished without removing the injector; however, the injector was designed to be removed from the test stand without dismounting the entire rig and breaking down the coolant lines to the combustion chamber.

To further enhance chamber wall compatibility, the LOX elements were also scarfed to shift the spray cone and prevent impingement of LOX on the combustor wall.

In December 1988 P&W completed an alternate injector design. The new design, which was essentially the current design, incorporated fuel and LOX area flexibility features to allow testing of several different design points as well as mixture ratio biasing. These features, the facenuts and LOX flow metering plugs, are described under the current subscale injector design. The new injector design also incorporated the low-cost, one-piece interpropellant plate with integral elements, which is also described under the current design. At first the original injector design was kept as the baseline while the new design was only pursued as an alternate. But before fabrication of the injector began, the original baseline injector design was dropped and the new design became the baseline.

The new design would allow testing of three planned injector operating configurations: The STBE Unique burning LOX and methane at a chamber pressure (P_c) of 3000 psi, the STBE Derivative burning LOX and methane at a P_c of 2250 psi, and the STME Unique burning LOX and hydrogen at a P_c of 2250 psi. Outer row mixture ratio biasing at each of these configurations was also planned. The facenut is, which determine fuel annulus gap, and the LOX flow metering plug lengths, which determine LOX slot length, were define for all planned injector geometries.

A vibratory analysis of the injector elements was done to confirm the analytical model prediction that the vibratory modes of the elements do not coincide with the combustion excitation frequencies. The sample subscale interpropellant plate, which has elements identical to those of the actual interpropellant plate used in the subscale injector, was clamped down to simulate the stiffness of the injector assembly, and an element was mechanically excited. An accelerometer mounted onto the element measured the element acceleration forces and frequencies. This procedure was repeated for several elements. The results show that no element modes existed within 10 percent of any likely combustion excitation frequency at Rated Power Level (RPL). Figure 2.1.2-3 shows a plot of magnitude versus frequency for a typical element and gives the likely combustion excitation frequencies.

During a review of the injector fabrication, a potential tolerance stack-up problem between the housing and faceplate was found. With the variable geometry design, the faceplate was not welded into the injector, but secured by the fuel facenuts. There was a possible stack-up problem on the assembly of the injector details that would have allowed a gap between the faceplate and injector housing. This gap would have allowed fuel to leak around the faceplate resulting in less fuel going to the elements, driving up the mixture ratio. To correct this problem, the recess in the faceplate was machined to accept a seal that would assure that there would be a positive seal at the edge of the faceplate so that all fuel is directed to the elements and through the porous face. This modification is shown in Figure 2.1.2-4.

A concept for allowing film cooling in the subscale rig was developed. This would have allowed test demonstration of different levels of film cooling as well as elimination of film cooling. Replaceable orifices were located adjacent to each outer row injector element as shown in Figure 2.1.2-5. The orifices were trapped under the replaceable fuel sleeves and could be changed without removal of the injector from the combustor.

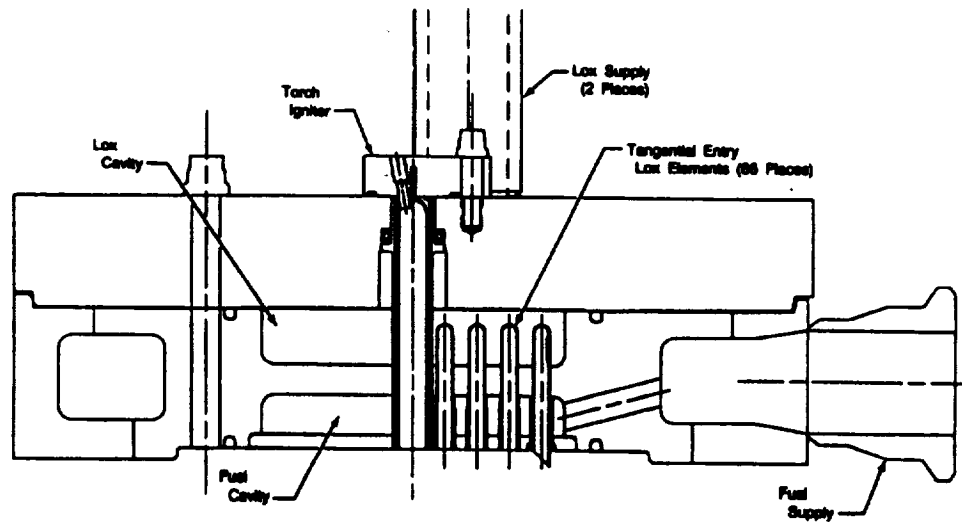


Figure 2.1.2-1. Subscale Injector Cross-Section

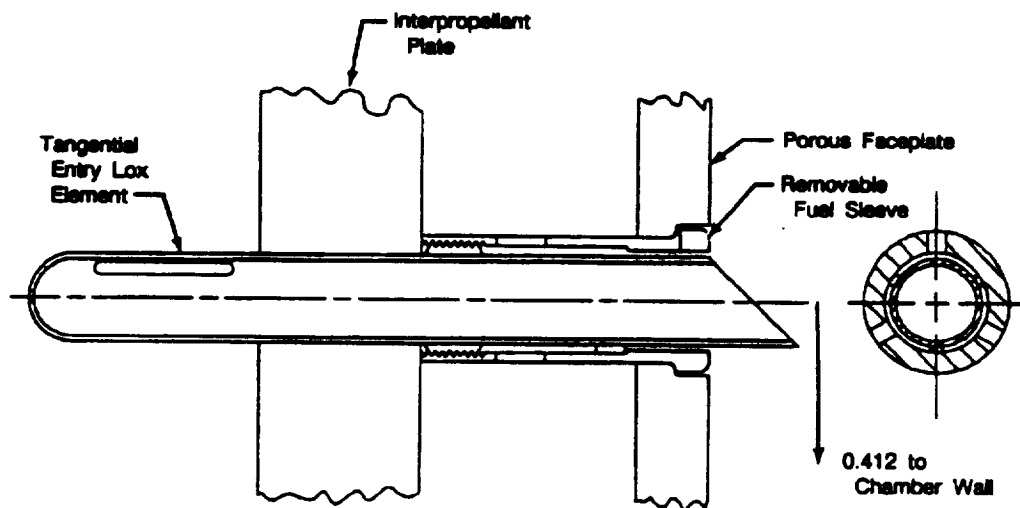


Figure 2.1.2-2. Outer Row Element Concept

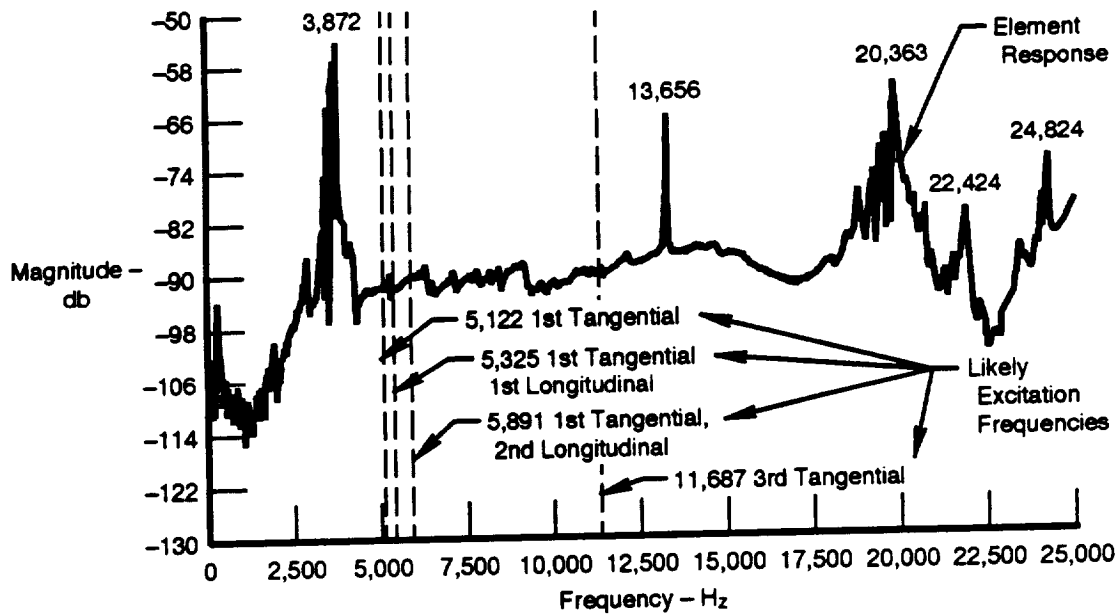


Figure 2.1.2-3. Vibratory Response of Subscale Element With Likely Combustion Excitation Frequencies

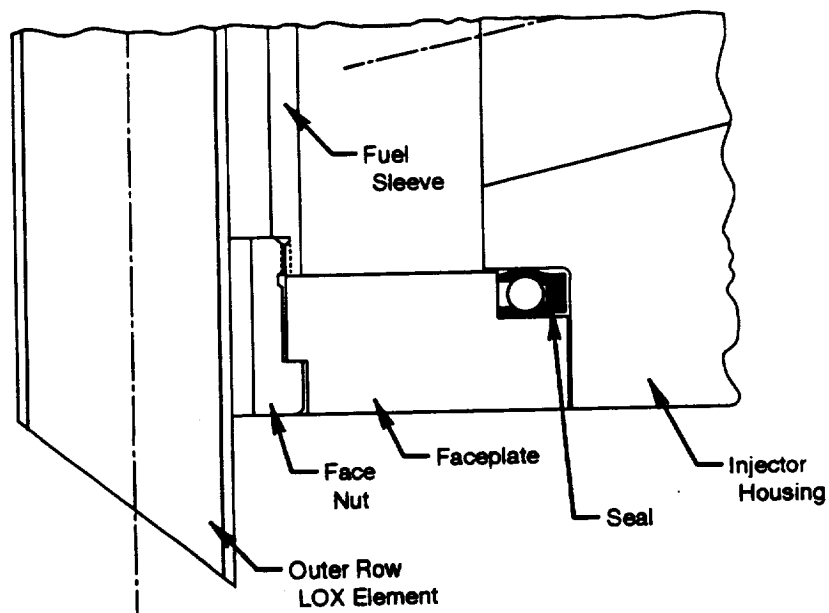


Figure 2.1.2-4. Injector Faceplate Seal Installation

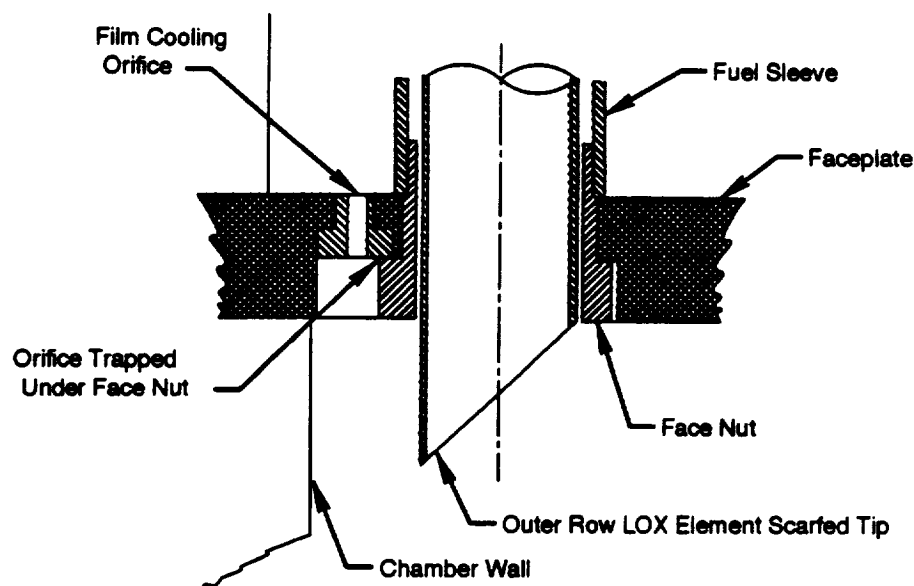


Figure 2.1.2-5. Outer Row Injector Element Replaceable Film Cooling Orifice

2.1.3 Subscale Injector Fabrication History

2.1.3.1 Interpropellant Plate Sample

A sample of the integral element interpropellant plate was fabricated by the interpropellant plate vendor and is shown in Figure 2.1.3-1. This sample was a small wedge section of the injector plate consisting of 14 elements. The sample was used to develop and verify the process for creating the elements and for removal of the recast layer and was also water flow calibrated at P&W to verify that the manufacturing technique produced elements with acceptable effective flow areas and spray cone angles. Tests were also made to verify the effectiveness of the LOX flow metering plugs.

A flow fixture for flowing individual elements of the integral element interpropellant plate was designed and fabricated. This fixture, shown in Figures 2.1.3-2 and 2.1.3-3 allowed water flow calibration of each element to determine the effective flow area and the element-to-element area variation. These results provided a verification that the design goal has been met and a confidence in the repeatability of the manufacturing process. Water flow testing was conducted on the machining sample of the interpropellant plate before releasing the actual interpropellant plate for final fabrication.

The water flow testing of the sample interpropellant plate was conducted on P&W's E-26 pump-fed injector water flow test stand. A photo of an element flowing with 100 psi differential pressure is shown in Figure 2.1.3-4. The water flows indicated that the effective flow areas of the elements were slightly lower than expected. Furthermore, all of the inner elements flowed lower than the outer row of elements. The actual ACds of the outer elements ranged from 95 to 99 percent of nominal, which is within the desired tolerance of plus or minus 5 percent of nominal. The actual ACds of the inner elements, however, were only 91 to 94 percent of nominal. This pattern remained the same when the interpropellant plate was flowed on different days and when the LOX flow restricting plugs were installed in the elements.

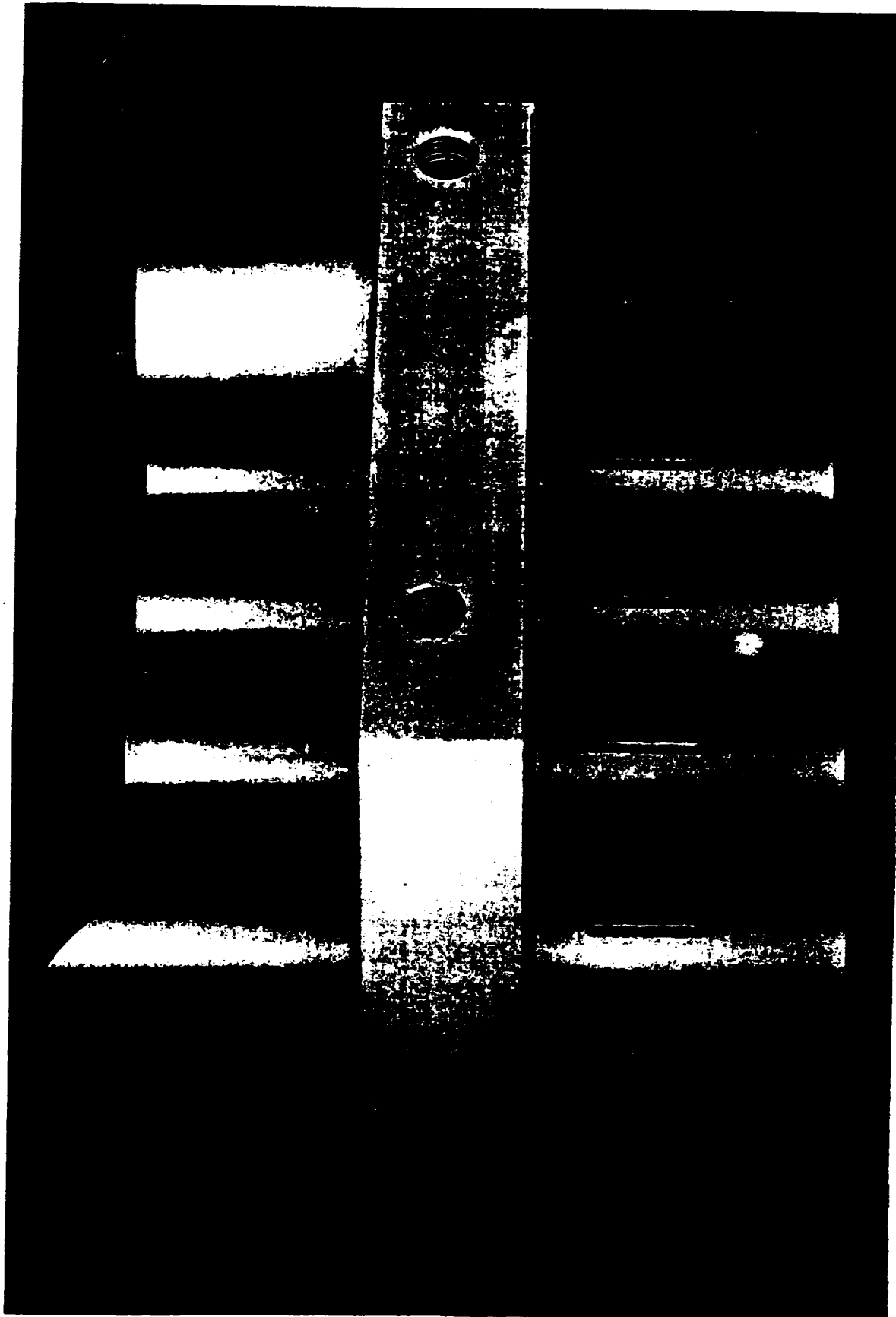
The length and width of each LOX entry slot was carefully inspected to determine if variations in slot dimensions caused the difference in effective flow areas between the outer row of elements and the inner elements. The inspection results showed that the actual physical areas of the slots of all the elements were below nominal, and that the slots on the inner elements were slightly smaller than the slots on the outer row elements.

Sixty-seven percent of the inner element slots were shorter than allowed by the blueprint, while only 56 percent of the outer element slots were too short. More significantly, the outer element slots were wider than the inner element slots. The average width of the outer element slots was almost 0.0006 inch greater than the average width of the inner element slots, a significant difference. This inspection of the slots also revealed that many slots, especially inner element slots, were slightly wider at the top than at the bottom.

Since the dimensions of all of the slots were below nominal, the slots were reworked to nominal. The reworked elements of the sample interpropellant plate were water flow tested again. The inner elements that had been fully reworked flowed very close to the nominal flowrate. There was still a difference between the flowrates of the outer row elements and the inner elements because the outer element slots were larger before rework and were inadvertently reworked to larger than nominal size.

The cause of the inner element slots being smaller than the outer row element slots was EDM electrode wear. The electrodes were changed infrequently, allowing them to wear down from slot to slot. The solution to the wear problem will be to monitor the electrodes for wear and change them frequently.

The sample interpropellant plate was sent to the chemical milling vendor for EDM recast layer removal. The vendor chemical milled the LOX side of the sample to determine if the chemical milling process can hold the tolerances required. Because the tolerances for the fuel sleeve braze had to be held tighter than could be achieved with chemical milling the complex shape of the interpropellant plate, it was decided to mechanically remove the recast layer on the fuel side of the elements using a "hollow hone" to achieve the required tolerances. The tolerances achieved with chemical milling were acceptable everywhere else on the part, except for the LOX entry slots. The recast layer was not removed from the LOX entry slots because no acceptable method was found to remove the recast in the slots and still maintain the tight tolerances required in the slots. The presence of recast in the slots does not significantly affect part life.



FE 200033

Figure 2.1.3-1. Sample Integral Element Interpellant Plate

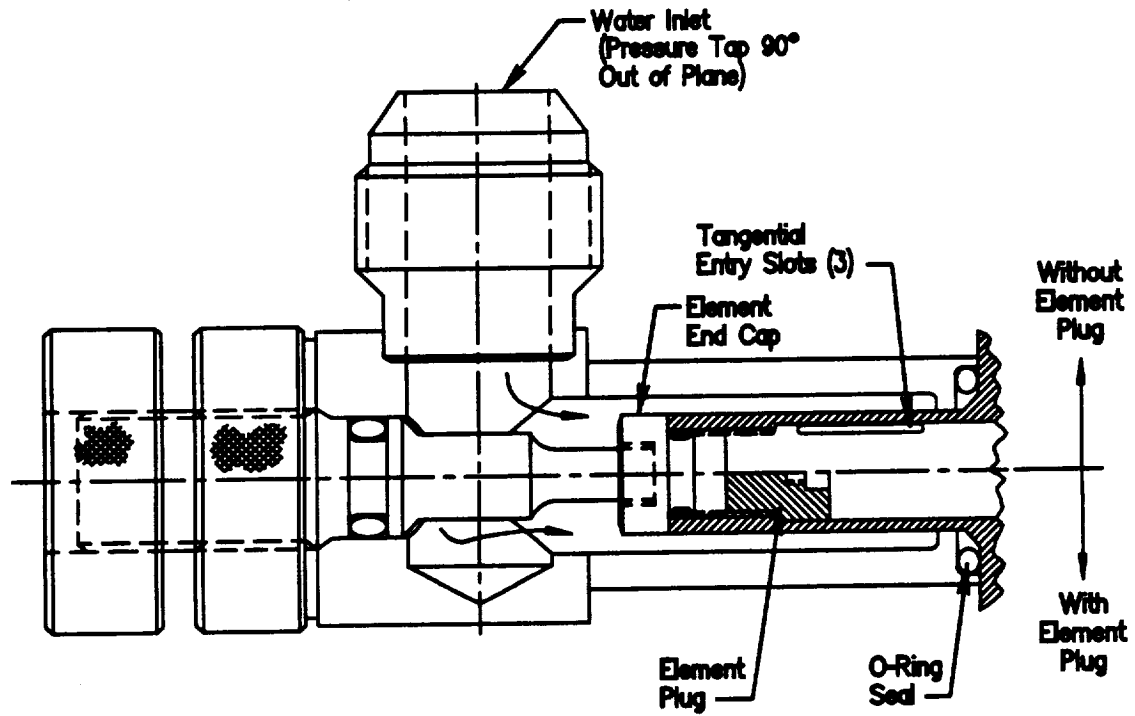


Figure 2.1.3-2. Subscale Injector Integral Element Flow Fixture

FE298070

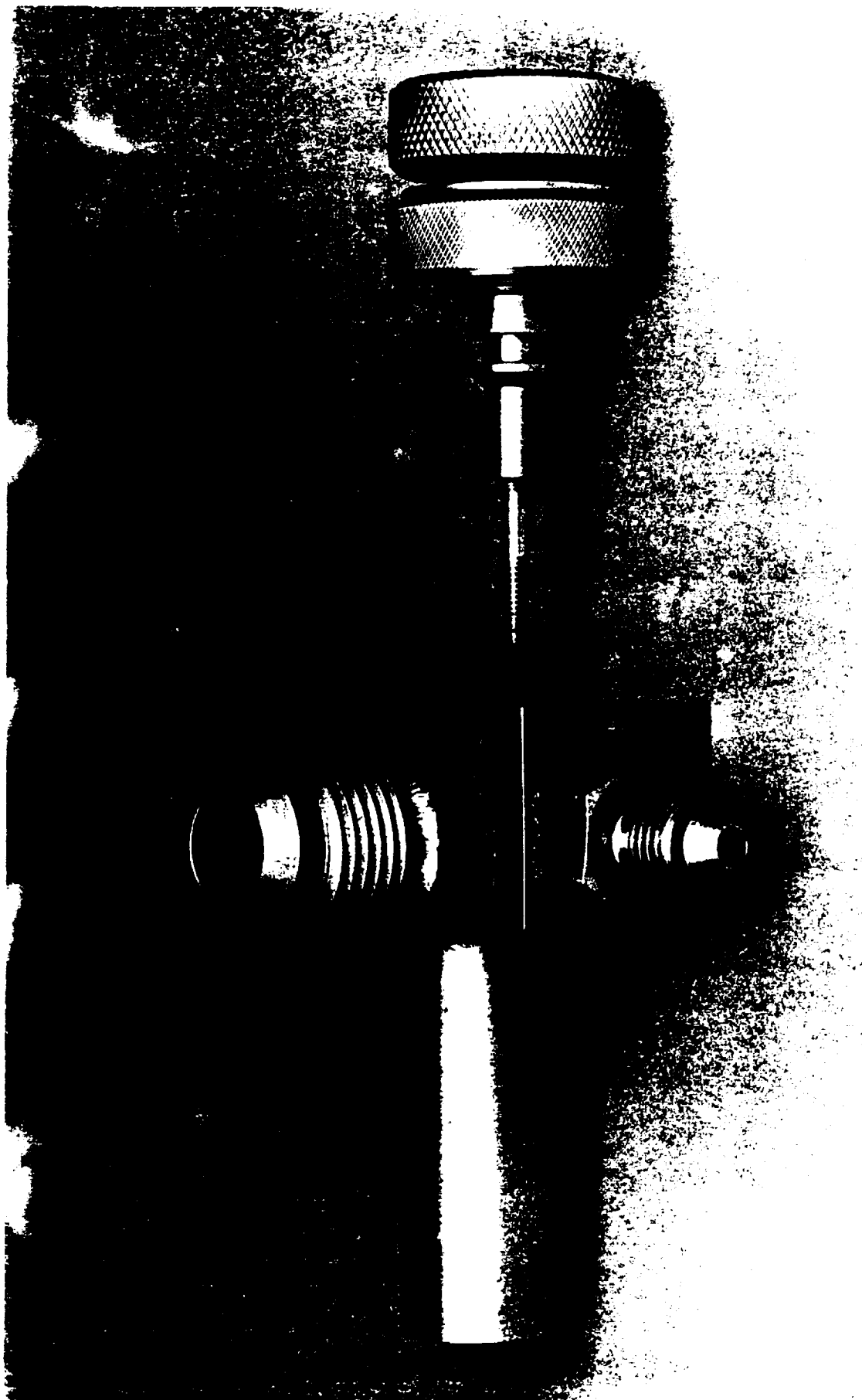
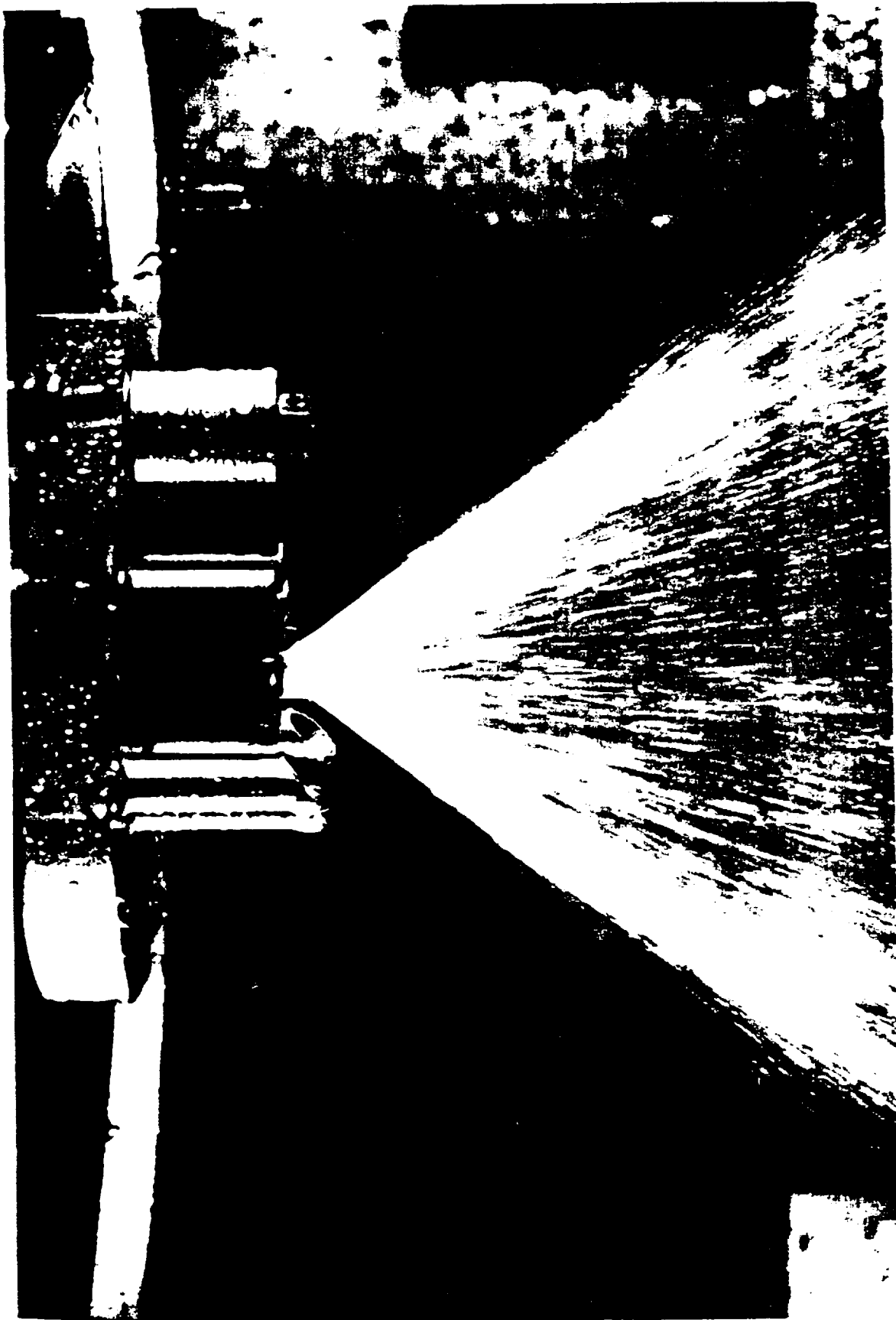


Figure 2.1.3-3. Photograph of Subscale Injector Integral Element Flow Fixture



FE000204-11

Figure 2.1.3-4. Sample Injector Element Water Flow at 100 psid

2.1.3.2 Interpropellant Plate

The interpropellant plate with its integral LOX elements was machined in one piece from a pancake forging. First the OD and ID of the plate were rough turned. Next the element inside diameters were installed. It was the vendor's original intention to drill and then ream the element IDs. However, when the pilot holes were drilled, the drill walked, and the holes were not straight. The holes were then EDMed straight and reamed to final size to remove the recast layer. Afterwards the Spirallock threads were tapped into the top of the LOX side. Next an EDM electrode like the one shown in Figure 2.1.3-5 was machined. This electrode rough EDMed all 62 ODs to within 0.010 inch per side of the finished dimension at once. The process of EDMing many features at once is referred to at P&W as "gang" EDMing. After rough EDMing, the element ODs were inspected to ensure that they were in the correct positions. Using this inspection data, a finishing electrode was fabricated to gang EDM all 62 element ODs to within 0.002" per side of the finished dimension. The remaining excess material was removed when the recast layer was removed. Just as with the sample, The recast on the fuel sides of the LOX elements was removed with a hollow hone, while the recast layer everywhere else was removed by chemical milling. The recast layer on the element IDs was removed when they were reamed to final size. Finally, the tangential LOX entry slots were EDMed into the elements. The recast layer was not removed from the LOX entry slots.

The LOX entry slots were installed with a tool developed by the vendor, which EDMed all three slots into a single element at once. This tool located off the OD of the LOX side of the element and had three arms, each holding an electrode, which moved down into position to install the slots.

After the interpropellant plate with integral LOX elements, shown in Figure 2.1.3-6, was completed, it was water flow tested at P&W. Water flow testing confirmed that 59 of the 62 elements flowed within the desired 5 percent of the target value. The other three elements were within 6 percent of the target value and were not concentrated at any one location on the plate and therefore did not have a significant effect on combustor wall compatibility or injector performance. A chart of effective flow area as a percentage of nominal for each element is shown in Figure 2.1.3-7. As can be seen, there is no pattern of difference between the outer row elements (1 through 26) and the inner elements (27 through 62) like there was on the sample interpropellant plate. The average of the effective flow areas was below the target value due to conservatism in the manufacture of the slots. The supplier targeted the process to maximum material condition (the reworkable side of the tolerance band), which resulted in the target area of the slot being slightly below the design target value. This condition is easily correctable, but was of no consequence. All of the elements flowed within 5 percent of the mean, with the majority (about 57 of 62) flowing within approximately 2 percent of the mean. Figure 2.1.3-8 shows a Weibull plot of the element effective flow areas. Note that the standard deviation was only 0.00025 in². The implied 6-sigma (99.73 percent) process capability for this first part was already well within the design requirements and would improve significantly with the production of more parts, i.e., the learning curve effect.

Figures 2.1.1-6 and 2.1.1-7 show water flows of an inner element and an outer row scarfed element respectively. The effect of the scarf on the spray cone angle can be seen clearly. Note that not only does the scarf shift the spray cone towards the center of the plate, but the scarf also shifts the majority of the mass flow towards the injector center. Pattern tests of the spray cone of this element design conducted in other programs have shown that two-thirds of the LOX flow is directed toward the injector centerline. This feature has proven to enhance injector-chamber wall compatibility.

After the elements were water flow tested to verify proper effective flow area, The LOX element end bolts were sized to fit individual elements. These bolts were to be ground to size so that when a LOX flow metering plug is installed, it will be at the proper position when it seats against the bolts. This was done by setting the position of a gage LOX metering plug, whose length is held to a tolerance of ± 0.0001 inch, so that the element achieves the correct water flow rate. The LOX element end bolt was then be ground to fit, and then later installed and tack welded in place. This same procedure was repeated for each element, and as a result, the LOX

flow metering plugs could be installed randomly across the interpropellant plate. This installation procedure for the LOX element end bolts took place before the interpropellant plate was welded into the injector housing.

FE801832

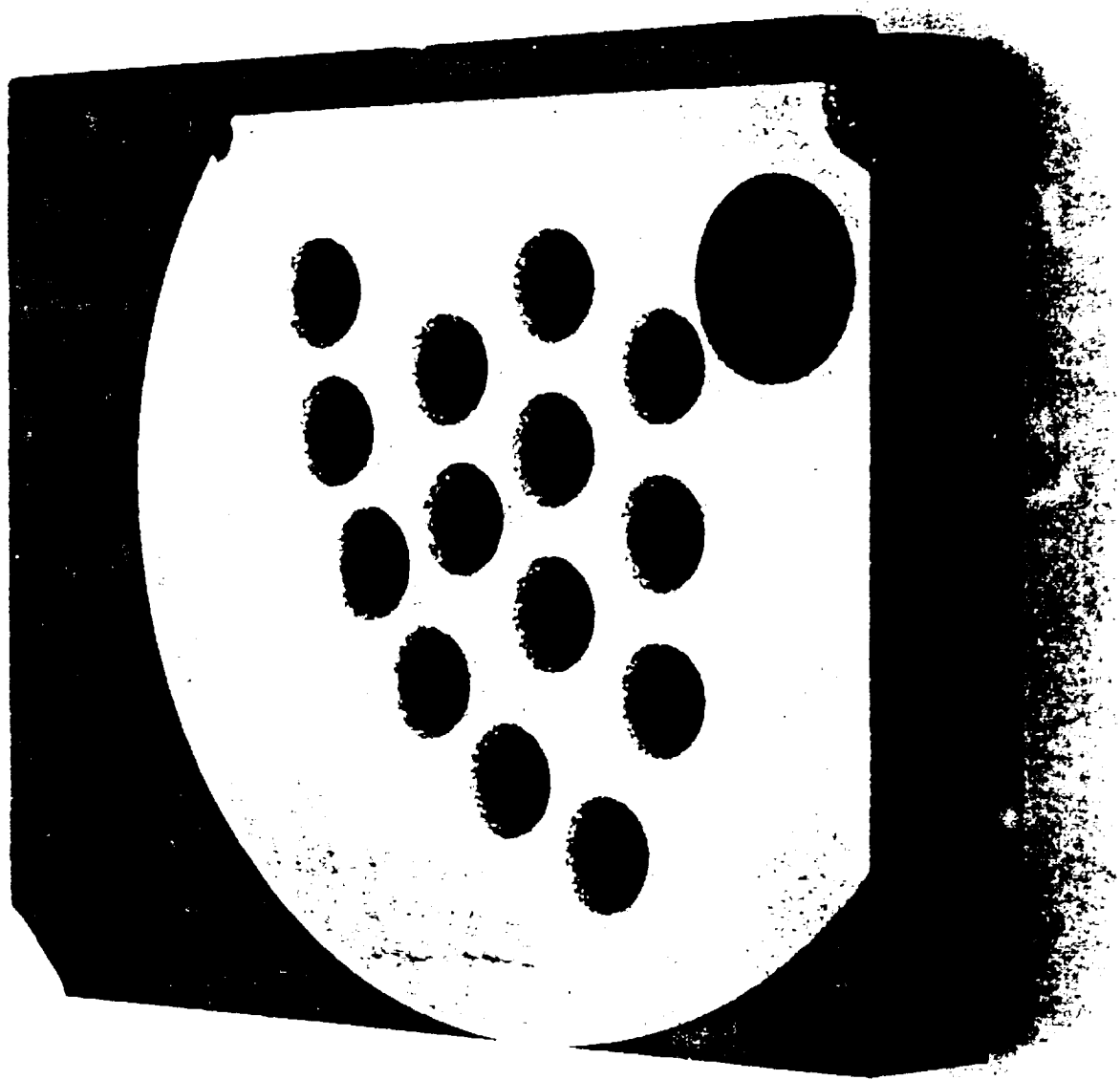
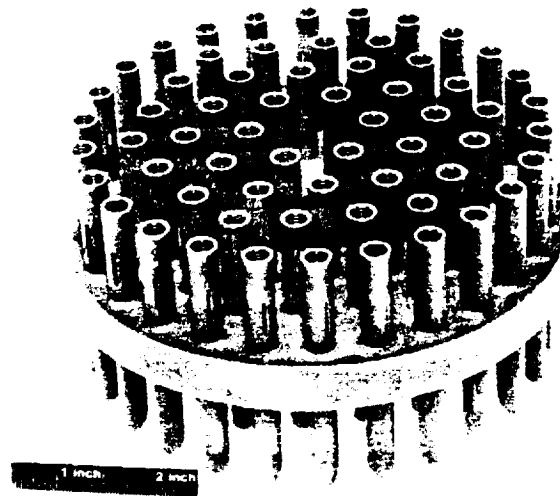


Figure 2.1.3-5. EDM Electrode for Sample Subscale Interpropellant Plate



FE015893

Figure 2.1.3-6. Subscale Interpropellant Plate

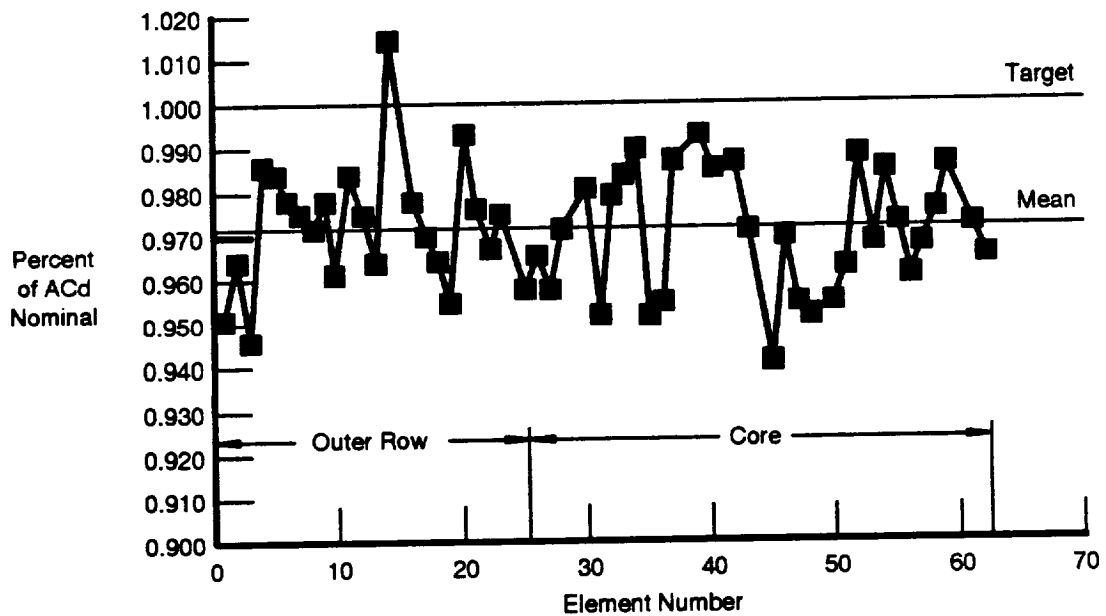


Figure 2.1.3-7. Subscale Interpropellant Plate Acceptance Flow Results

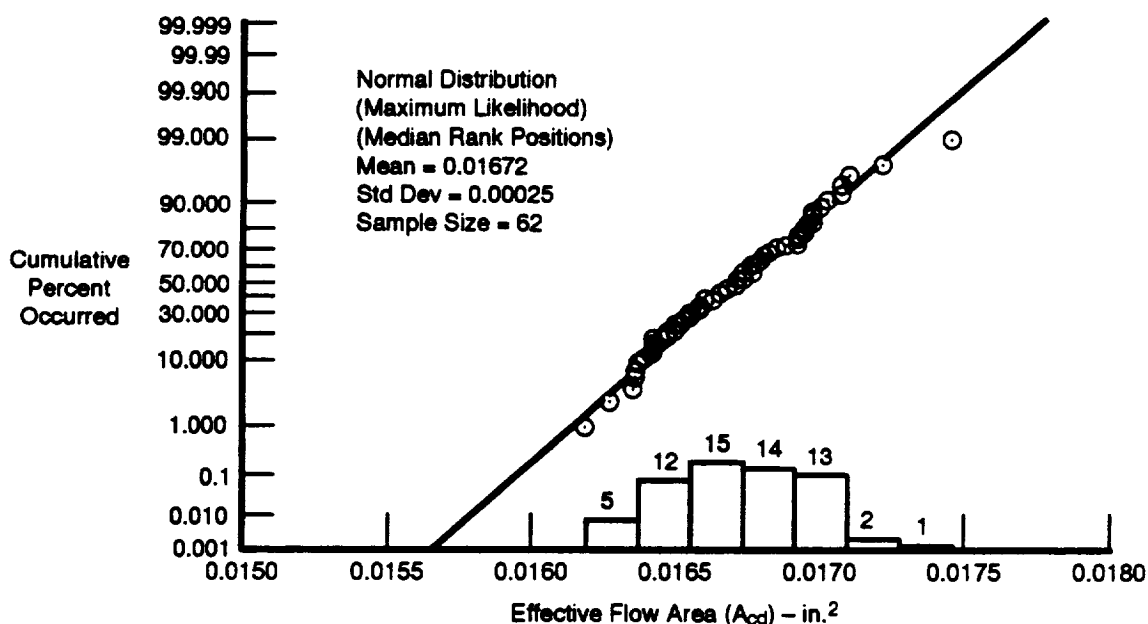


Figure 2.1.3-8. Weibull Plot of Element Effective Flow Areas

2.1.3.3 Injector Details

The fuel manifold outer ring and the injector housing were conventionally machined from INCO 718 pancake forgings at P&W. The igniter sleeve was conventionally machined from Haynes 230 rod at P&W. The remaining injector details, such as the faceplate, interpropellant plate, facenuts, LOX flow metering plugs, LOX element end caps, fuel sleeves, LOX dome, lifting eye, and fuel and LOX inlet flanges and piping were purchased from various outside vendors.

The faceplate was made from 1/4-inch thick 347 stainless steel porous plate. This porous plate was made by sintering together sheets of wire mesh. The plate had a flowrate of 190 SCFM/ft² per minute at 2 psig. The interpropellant plate, LOX dome, LOX flow metering plugs, fuel sleeves and lifting eye were all made from INCO 718. The facenuts were made from Haynes 230, While the fuel inlet flange was made from INCO 625. The LOX inlet piping and flange were made from stainless steel.

The LOX dome was sent to TS 116 test stand at NASA-MSFC for the field welding of the LOX inlet piping. This was done so that the entire rig could be assembled at P&W and delivered to TS 116 ready for quick mounting. The LOX dome was mounted onto a fixture which simulated the injector and correctly positioned the LOX dome. The LOX inlet piping was then fitted, trimmed, and welded into place. The LOX dome was then returned to the vendor for final machining and inspection. Having the LOX inlet piping already welded on also facilitated the proof pressure testing and water flow testing of the injector assembly.

2.1.3.4 Injector Fabrication

Five braze samples, as shown in Figure 2.1.3-9, were processed to simulate a fuel sleeve brazed onto an element. All were made from INCO 718 and brazed with a gold-nickel braze with the same materials, fits, and processes that were used on the actual part. A photograph of one of the samples, along with its braze concentricity tool, is shown in Figure 2.1.3-10. Since the brazes in the actual injector were to be verified with a load test, these samples were used not only to prove that the brazing method produced a strong joint but also to show that the load test verification will not harm a sound, good quality braze joint. The first sample was subjected to a uniaxial load of 150 lb. The braze joints in the actual injector will only experience a load of less

than 89 lb. This first sample was pull tested to 150 lb four additional times and then cut up to check the braze coverage. It was found to have 100 percent coverage with excellent wetting on both sides of the joint.

The next four braze samples were X-ray inspected and no voids were indicated. The samples were then pull tested to 150 lb five times and X-rayed again. No indications of braze failure were found. One of these samples was then subjected to an increasing uniaxial load until failure. The sample failed at a load of 1740 lb. However, the failure occurred at the threads of the fuel sleeve rather than the braze joint. Another sample was subjected to a cyclic load of 150 lb at a rate of 80 to 100 cycles per minute. The sample survived 50,000 cycles without failure.

The fuel sleeve was kept concentric to the LOX post by using a simple tool which is shown with the sample in Figure 2.1.3-10. This tool is inserted into the annulus between the fuel sleeve and the LOX post before brazing. During the braze cycle, the tool holds the fuel sleeve concentric to the LOX element. The tool is removed after the braze cycle. With each of the five samples, some diffusion bonding occurred between the concentricity tool and the LOX element because of contact between the tool, which was made of INCO 718, and the nickel plating added to the LOX element for enhancement of braze alloy wetting. The LOX element had been nickel plated along its entire length in order to avoid having to mask off parts of the element. Removing the tool was difficult and resulted in significant galling of the LOX element. To solve this problem, the LOX element will be nickel plated only in the area of the braze joint. The braze concentricity tool was redesigned by making it shorter and rounding off the sharp edges to prevent it from contacting the nickel plating. Another braze sample was run with the redesigned braze concentricity tool. The braze itself was of good quality, but the tool again bonded to the LOX element. A cut up of the sample showed that some excess braze alloy flowed up to and in between the concentricity tool and the LOX element, joining them. The cut up also showed that some diffusion bonding occurred between the tool and the LOX element.

Additional braze samples, simulating the fuel sleeve to LOX element braze, were run with a redesigned braze concentricity tool to solve the problem of the tool bonding to the LOX element. The samples and tools were INCO 718, and a gold-nickel braze alloy was used. Three samples were run and none of them showed any bonding between the new braze tools and the LOX elements. The redesigned braze concentricity tool is shown in Figure 2.1.3-11. A recess was added to the inside diameter of the tool to decrease the area of contact between the tool and the LOX element.

Electron beam (EB) weld samples were run simulating the fuel manifold outer ring to injector housing welds and the interpropellant plate to injector housing weld. The first set consisted of flat bars of INCO 718 to establish initial weld schedules. The final EB weld samples were identical in size and geometric shape, in the area of the welds, to the actual injector and were made of INCO 718 with the same heat treat as planned for the injector. The weld joints were X-ray inspected and no voids or cracks were found. A slice along the diameter was cut out of the welded sample and is shown in Figure 2.1.3-12. All the welds were of high quality; however, in one area of one of the fuel manifold-to-injector housing welds there was slight microcracking. Figure 2.1.3-13 shows a photomicrograph of this area. The maximum crack length was only 0.020 in. This microcracking is not uncommon in INCO 718, especially with the AMS 5664 heat treat, and is not considered significant. The stresses in the welds were low, and a crack length of up to 0.130 in. would be acceptable for a life of 100 cycles. The microcracking occurred only in a weld on which two passes had to be made because on the first pass the power level on the EB welder was not set correctly and the weld did not fully penetrate the metal. The welds which were done correctly on the first pass showed no microcracking.

The lifting eye and fuel inlet flange were first welded to the fuel manifold outer ring, which then was EB welded to the injector housing. Next the interpropellant plate was also EB welded to the housing. All welds passed fluorescent-penetrant and X-ray inspections. Figure 2.1.3-14 shows the interpropellant plate and the injector after the fuel manifold was welded to the housing and before the welding of the interpropellant plate to the housing. Before the interpropellant plate was installed in the injector assembly, it was nickel plated in preparation of the fuel sleeve braze.

Next, the fuel sleeves were successfully brazed to the LOX elements, and there were no problems with the braze concentricity tools bonding to the elements. During the same braze cycle, the igniter sleeve was brazed to the interpropellant plate, and the injector was solution heat treated and stress relieved. All 62 fuel sleeve braze joints passed a 150-pound load test, and the igniter sleeve braze joint passed a 100 psid leak check. The injector was then precipitation hardened and the LOX dome and combustion chamber interface surfaces, the seal grooves, and the faceplate recess were finish machined. The bolt holes and instrumentation holes installed, and all sealing surfaces were lapped.

Delays in the completion of the injector occurred due to rework of the igniter sleeve to repair handling damage. A large dent was found in top OD of the igniter sleeve. This dent would have prevented the igniter from fitting down into the sleeve and LOX dome-igniter sleeve seals from sealing on this diameter. Therefore, the igniter sleeve was repair by cutting off the damaged section, rough machining a new top for the igniter sleeve, welding it on, and then machining it to final dimensions. Following the repair, the braze of the igniter sleeve to the interpropellant plate was leak tested to assure the rework of the igniter sleeve did not adversely affect the braze joint. A protective cover was made for the igniter sleeve to prevent further handling damage.

Figure 2.1.3-15 shows the LOX side of the completed injector and Figure 2.1.3-16 shows the fuel side of the injector. The rubber ring was attached to the fuel side face to protect the scarfed tips of the outer row elements during manufacturing and was removed before injector assembly.

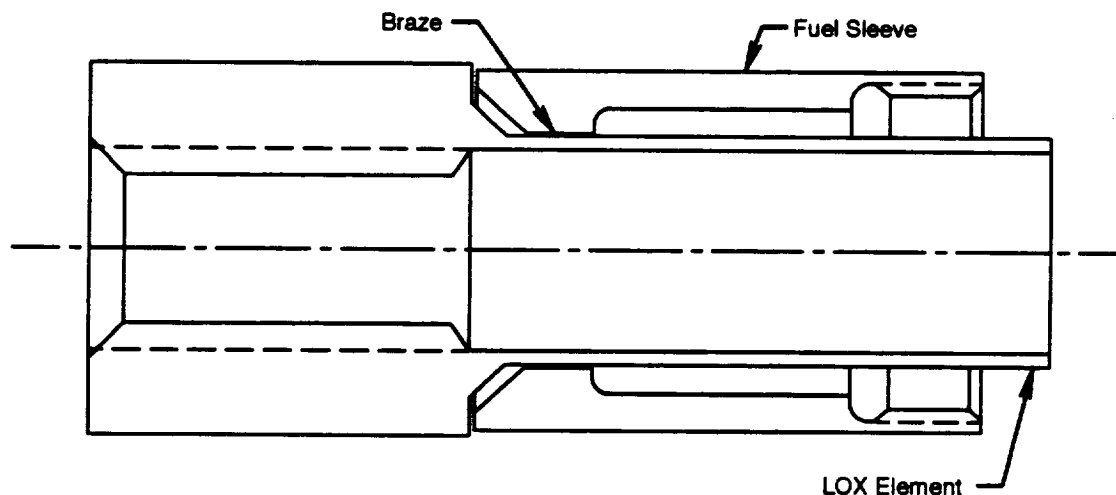


Figure 2.1.3-9. Typical Fuel Sleeve Braze Sample



FE001752

Figure 2.1.3-10. Fuel Sleeve Braze Sample (Right) With Concentricity Tool

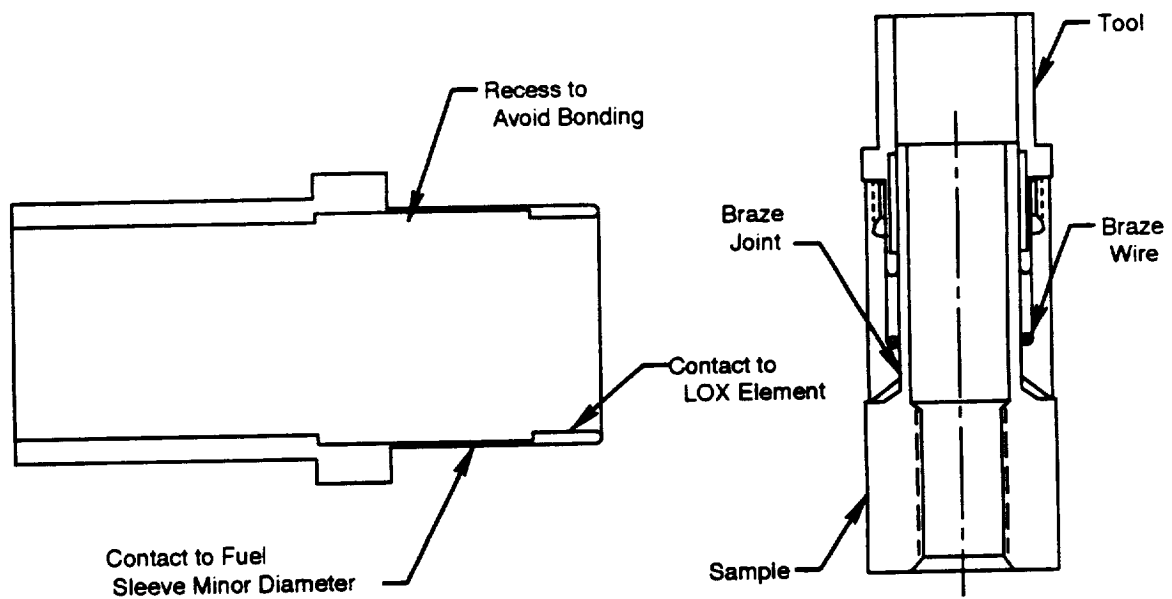
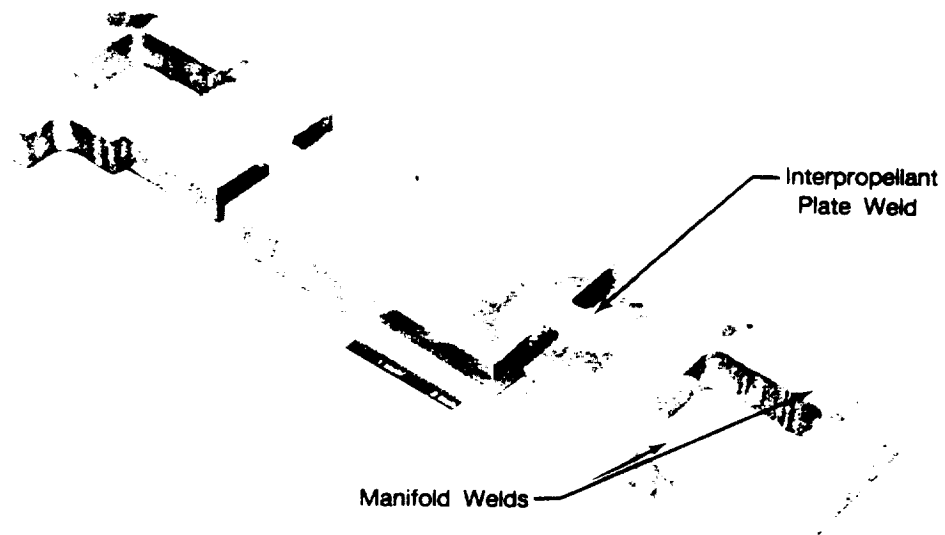
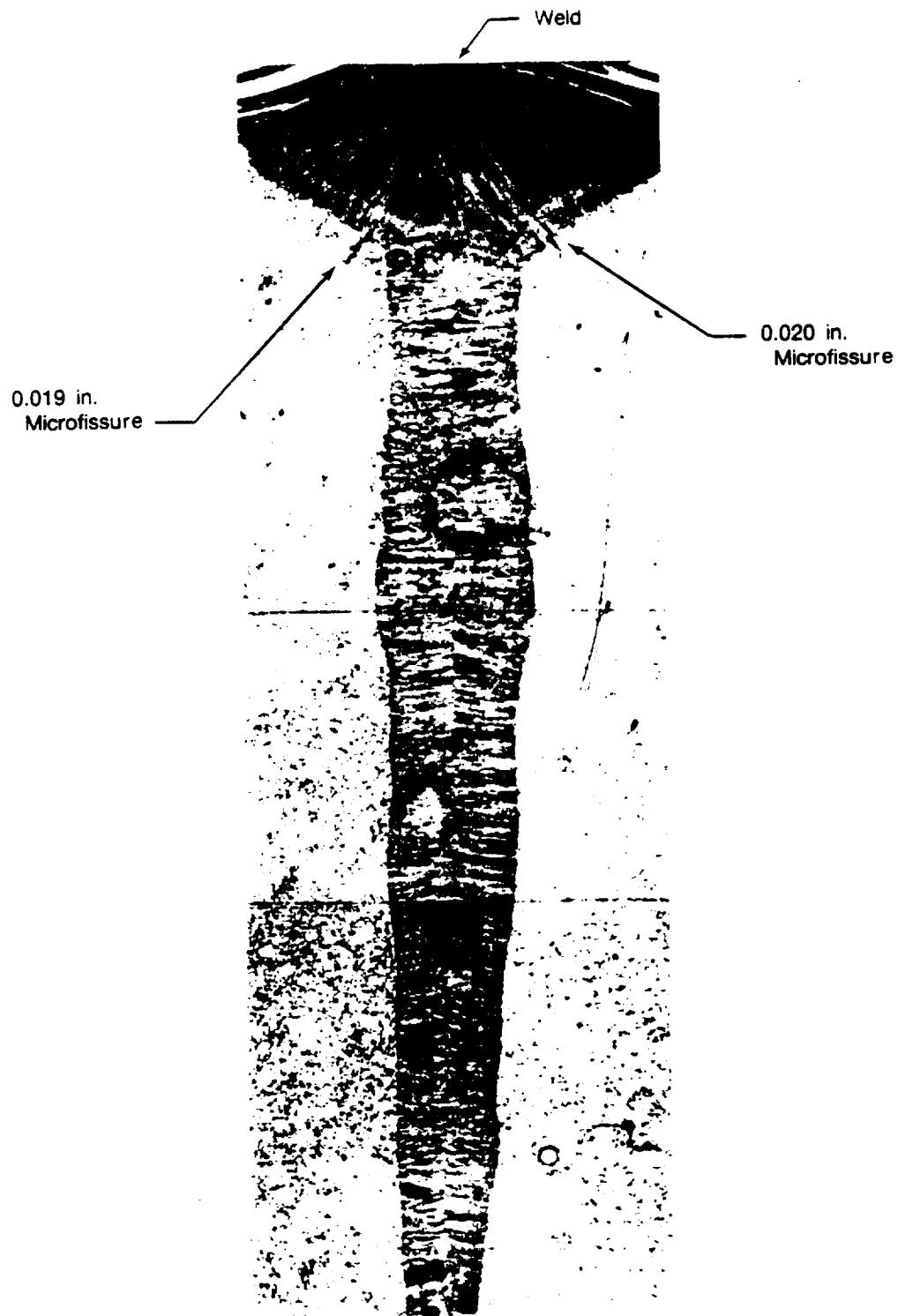


Figure 2.1.3-11. Redesigned Braze Concentricity Tools



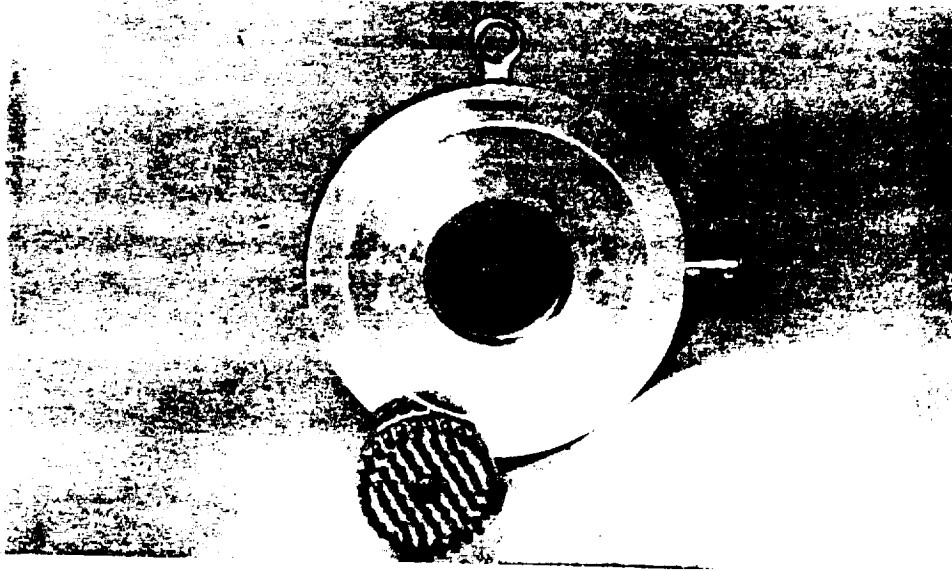
FD368164

Figure 2.1.3-12. Injector Electron Beam Weld Sample



FD369408

Figure 2.1.3-13. Injector Electron Beam Weld Sample Section Photomicrograph



FE505898

Figure 2.1.3-14. Injector Assembly Before Installation Interpropellant Plate

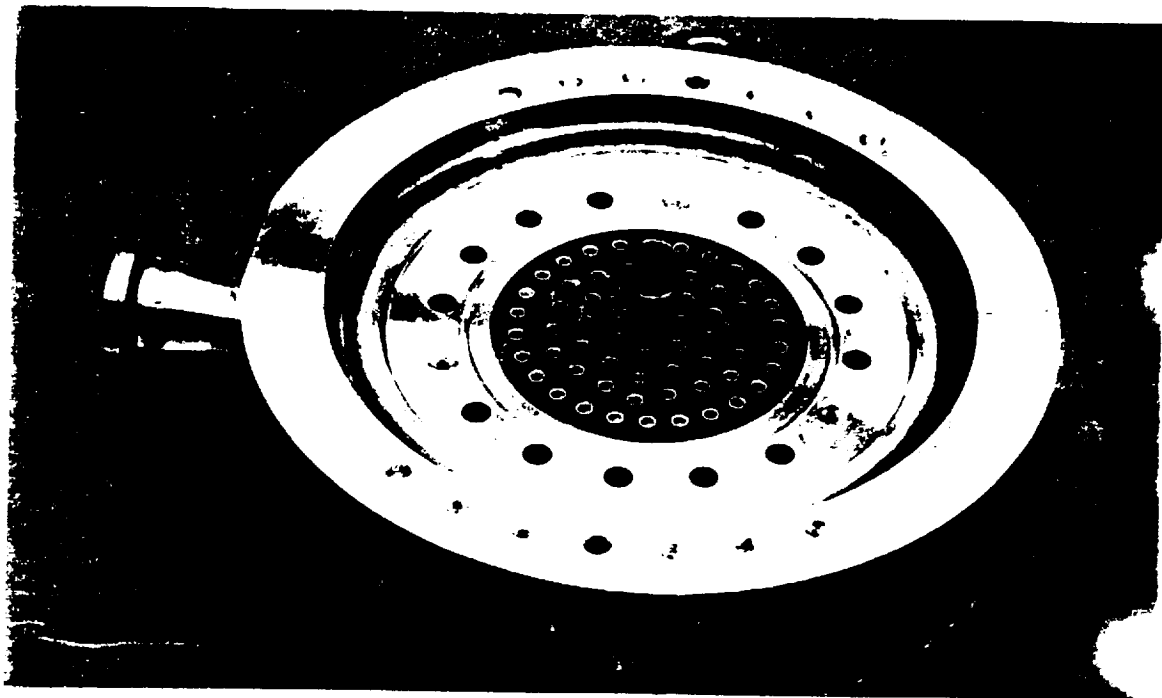


Figure 2.1.3-15. Subscale Injector LOX Side

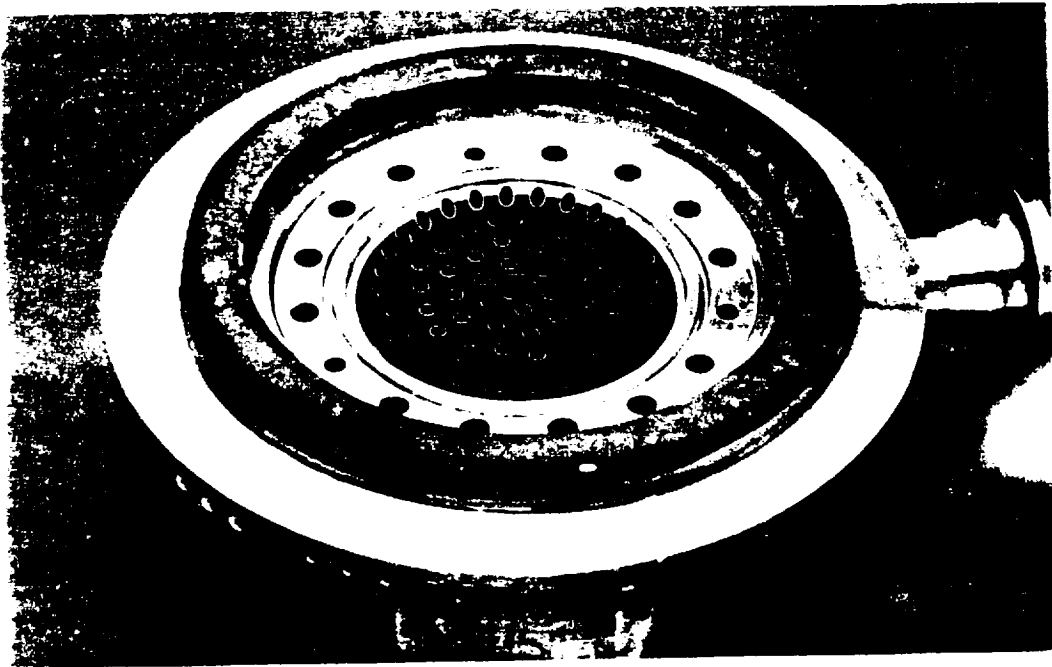


Figure 2.1.3-16. Subscale Injector Fuel Side

2.1.3.5 Injector Assembly

A proof pressure test plate was made to bolt onto the injector at the chamber interface to seal the injector face off so that the injector could be proof pressure tested. A tool was designed and built to install and remove the facenuts through the combustion chamber so that the injector did not have to be taken off the test stand for changeout of the facenuts. A tool was also made to allow changeout of the LOX flow metering plugs, through the combustion chamber, as well as a tool to allow the changeout of the replaceable film cooling orifices.

After the injector was completed it was assembled to the LOX dome and pressure test tooling to check fits, check out the assembly tooling, and perform the proof pressure test. Figure 2.1.3-17 shows the disassembled injector from the LOX side, while Figure 2.1.3-18 shows a closeup of the LOX side with some of the LOX element end caps installed. Figure 2.1.3-19 shows the disassembled injector from the fuel side, while Figure 2.1.3-20 shows a closeup of the fuel side with the faceplate seal installed. Figure 2.1.3-21 shows a closeup of the fuel side with the faceplate, the film cooling orifices, and some of the facenuts installed. The faceplate used in this initial fit-check assembly used replaceable film cooling orifices.

A problem occurred during the attempt to install the facenuts, which secure the faceplate, into the fuel sleeves. When the facenuts were screwed in, the threads began to bind, making them difficult to install. It was thought that there might be some debris in the very fine threads (40/inch) of the fuel sleeves such as braze alloy or stopoff from the braze concentricity tool. A simple tool was quickly made to clean the threads. After the threads were cleaned, the facenuts installed more easily, and the assembly of the injector was completed for proof pressure testing.

During disassembly of the injector following proof test, it was found that six facenuts could not be removed due to apparent thread galling. The tool designed to allow removal and installation of the facenuts with the

injector installed onto the chamber was broken in the attempt to remove these facenuts, and a stronger tool was fabricated to allow for the application of higher torque for removal. The removal was accomplished with this tool, and damage to the facenut threads was noted confirming that thread galling had occurred. The thread damage appears to be confined primarily to the facenuts because these were fabricated from a softer material (Haynes 230) than the fuel sleeves (INCO 718).

It appeared that the binding of the facenuts may have been due to a small shrinkage of the fuel sleeves during the precipitation heat treat of the Inconel 718 material. Some fuel sleeves also appear to be out of round. This condition was probably also caused by distortion during the precipitation heat treat. To correct this situation, a thread chasing tool was designed and made. This tool, unlike the first, actually cut the threads to the correct size rather than just cleaning out debris. Due to the successful removal of the other 56 facenuts, it was not expected that a significant amount of material will need to be removed to provide the proper thread fit to the facenuts. The threads of all 62 fuel sleeves were chased.

The use of Loctite thread locking compound on the facenuts also facilitated the installation and removal of the facenuts. The Loctite acts as an anti-gallant and no other lubricant or anti-gallant is required. There have been no instances of facenuts binding since the fuel sleeve threads were chased with the new tool and Loctite was used during assembly. Loctite on the facenut threads is required by the injector build drawing, but was not used on the initial fit check since, at that time, the facenuts did not need to be locked in place.

While the injector facenut problem was being resolved, several modifications were made to the configuration change tooling. The three tabs which slide into the slots on the head of the facenut were replaced with stronger material following the failure during the facenut removal attempt. While this tool was being repaired, it was also modified to hold the facenut more securely. The LOX flow metering plug installation/removal tool was also modified to be sturdier and to have a replaceable tip. The film cooling orifice installation/removal tool was reworked to correct interference with the faceplate.

For the proof pressure test of the injector assembly, the proof pressure test plate was installed on the injector at the combustion chamber interface and the injector was coated with Stresscoat brittle lacquer, which cracks at 650 to 700 microstrain. The injector was scheduled to be pressurized to 3000 psig (1.2× maximum design operating pressure of 2500 psi) with water in increments of 500 psig. However, at 1500 psig, cracks in the Stresscoat began to appear on the LOX inlet elbows at the outside of the bend. At 2000 psig a clear pattern of cracks had appeared in the Stresscoat on both the outer and inner surfaces of the elbows indicating higher than expected stresses (about 20 ksi versus 8.5 ksi) in the hoop direction. At this point testing was suspended, photographs of the crack patterns in the Stresscoat were taken, and strain gages were applied to the higher stress areas indicated by the Stresscoat pattern. Figure 2.1.3-22 shows a typical Stresscoat crack pattern.

After the strain gages were installed, proof testing resumed. The injector was pressurized in 500 psig increments to 1500 psig and in 250 psig increments to 3000 psig. At 3000 psig the hoop stresses on the outer radius of the bends of the two LOX inlet elbows were 33,885 psi and 31,001 psi. Both exceeded the 29,200 psi room temperature minimum yield strength of the 321 stainless steel from which the elbows were made. Also at 3000 psig, the strain rate became nonlinear indicating the elbow had been yielded during the pressure test. The strain offset corresponded to 4105 psi, and analysis indicated it will not be detrimental to the performance of the elbow.

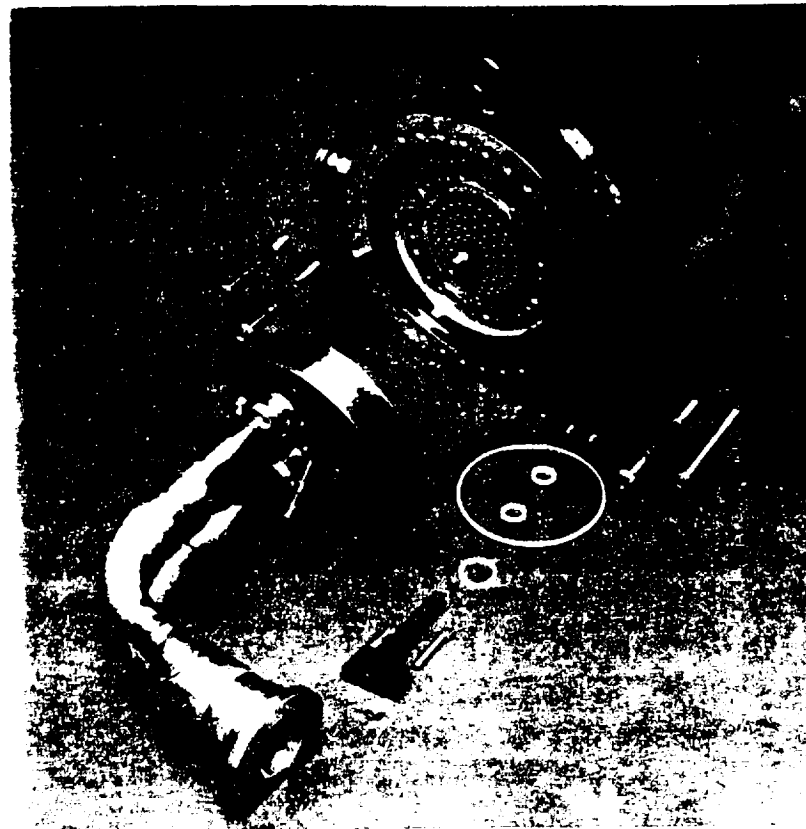
The cause of the higher-than-expected stress in the LOX inlet elbows was attributed to thinning of the wall during the process of bending straight pipe into elbows. Wall thinning was not accounted for in the design of the injector which required that the elbow be made from schedule 80 pipe.

Since the proof testing showed that the LOX inlet elbows were capable of withstanding over 2524 psig (the largest LOX inlet pressure in the test matrix) at room temperature and since 321 stainless steel gains considerable

strength at the cryogenic operating temperatures, the decision was made not to replace the elbows. At liquid oxygen temperatures, the yield strength of 321 stainless increases to over 50,000 psi, resulting in a safety factor to yield of nearly 2.0. Therefore, it was decided that the higher-than-expected stresses in the LOX inlet elbows would not affect the performance or life of the injector with the planned test matrix and that the elbows did not need to be replaced.

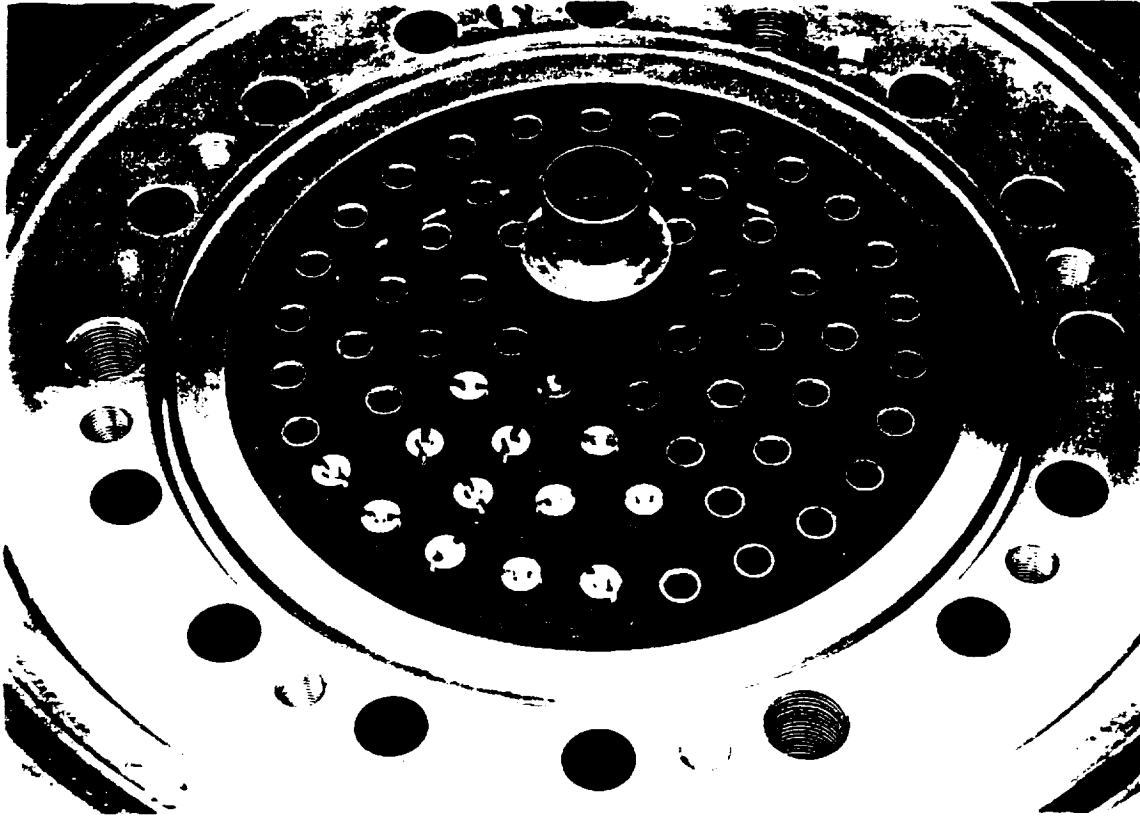
The injector assembly was leak checked both before and after the proof pressure test with helium and no leaks were found.

Several problems were encountered with instrumentation attached to the faceplate. The thermocouples for sensing faceplate metal temperature and the hypotubing for reading combustion chamber pressure were required to be brazed to the faceplate, but to maintain the LOX compatible clean condition, the instrumentation required brazing onto the faceplate before the faceplate was installed onto the injector. This required the instrumentation to be routed through small holes in the fuel cavity behind the faceplate. The small hypotubing and thermocouple wires (0.062-inch diameter) were broken several times during the initial installation attempts. A modification was made to the pressure sensing lines to reduce their diameter to 0.040 inch and installation was successfully accomplished. During the water flow testing, one of the thermocouple leads was broken, requiring replacement. Reassembly was accomplished without incident and the leads were secured to the outside of the fuel manifold to lessen the chance of breakage at the entrance to the injector.



FE808822

Figure 2.1.3-17. Subscale Injector Assembly — LOX Side Exploded View



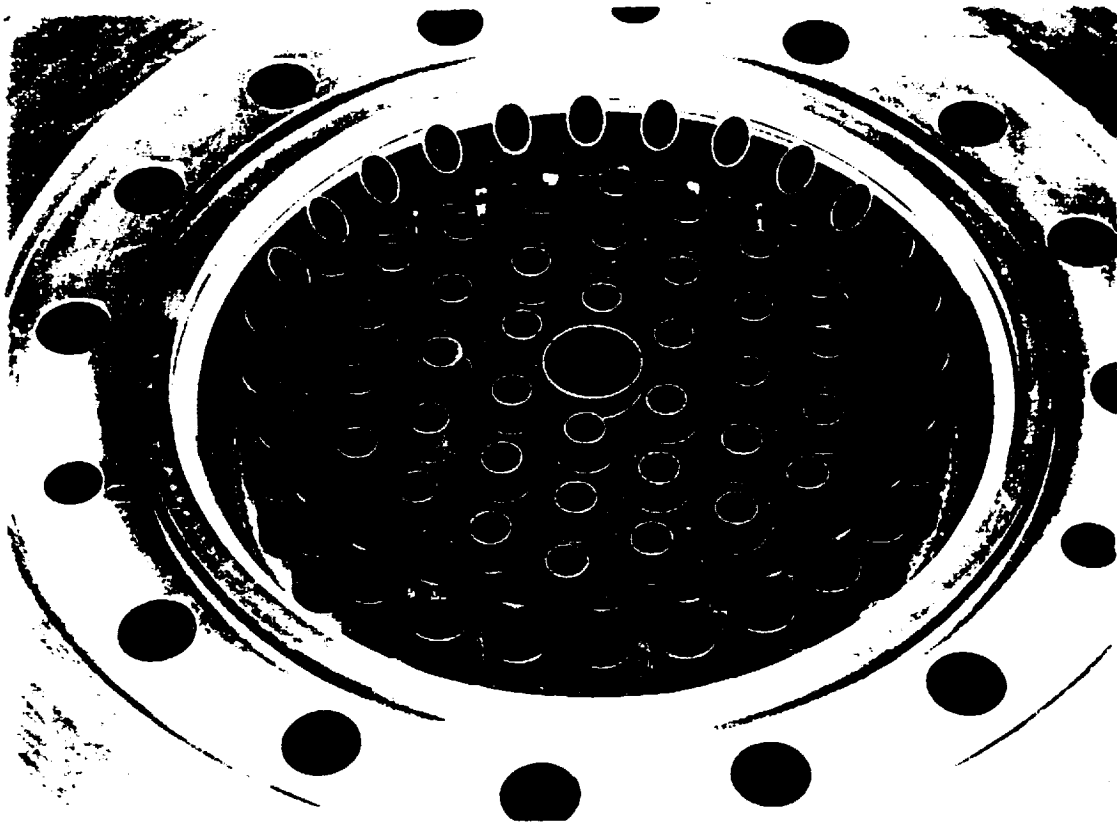
FE6068

Figure 2.1.3-18. Subscale Injector Assembly — LOX Side Closeup



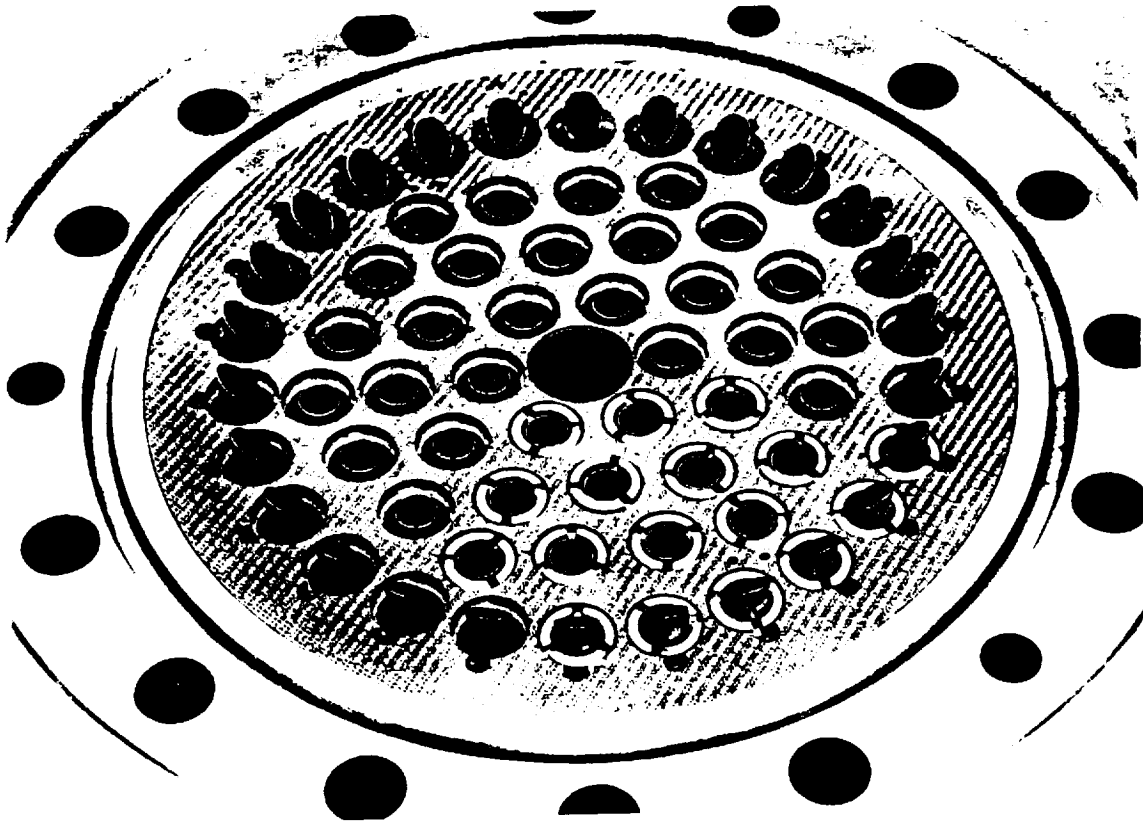
FE808823

Figure 2.1.3-19. Subscale Injector Assembly — Fuel Side Exploded View



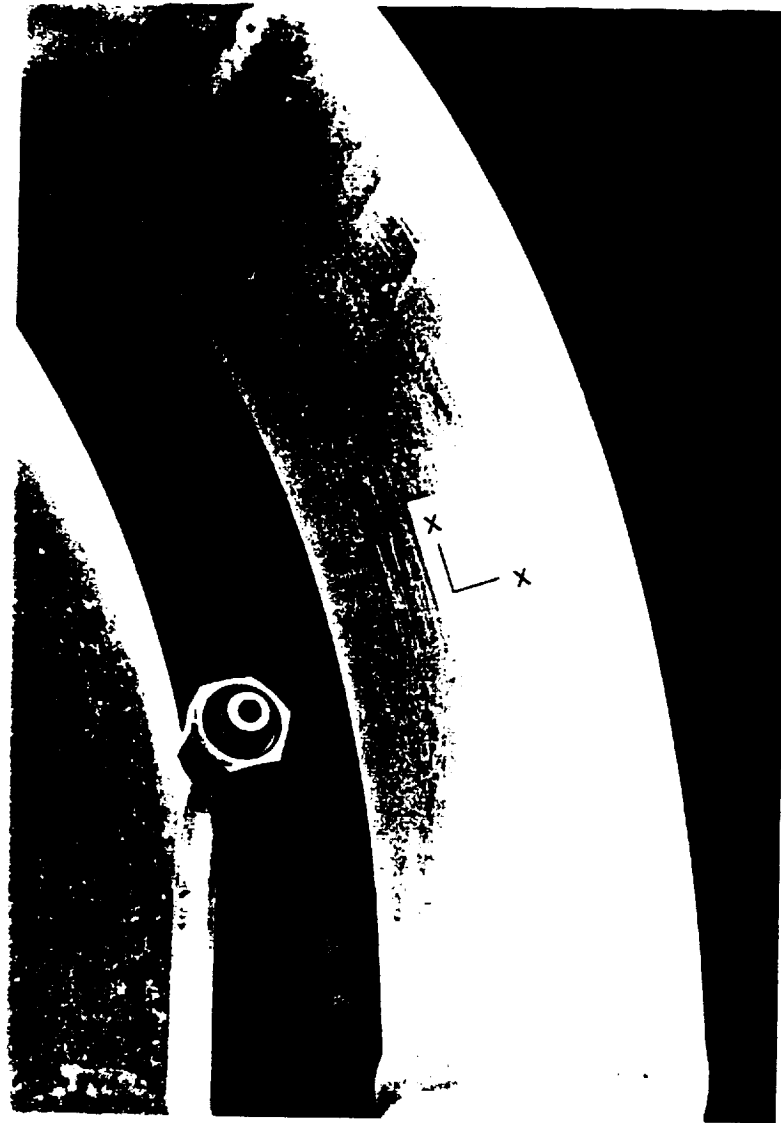
FE0088.

Figure 2.1.3-20. Subscale Injector Assembly — Fuel Side Closeup



FE608826

Figure 2.1.3-21. Subscale Injector Assembly — Fuel Side Closeup With Faceplate



FE008175

Figure 2.1.3-22. Typical Stresscoat Crack Pattern (Inside Radius of Elbow)

2.1.3.6 Water Flow Testing

Both the fuel and LOX circuits of the injector were water flow tested to verify the proper effective flow areas (Ac_d). The LOX circuit was flowed both with and without flow metering plugs installed. Flow testing of the LOX side with the flow metering plugs installed yielded an average Ac_d of 0.8346 in², which is within 2 percent of the predicted nominal. This is well within the desired 5 percent of nominal. The flow test of the LOX circuit without the metering plugs installed yielded an average Ac_d of 1.0052 in². The Ac_d average was slightly below the desired 5 percent of nominal, but it was within 6 percent of nominal. It was decided that this flow would be acceptable since it indicated a slightly lower area which would result in a higher differential pressure which would be conservative for testing. Figure 2.1.3-23 shows the injector mounted on the water flow test stand while Figure 2.1.3-24 shows the water flow spray pattern of the LOX circuit. As seen in Figure 2.1.3-24, the LOX flow pattern was uniform and the scarfed outer row elements acted to direct the spray away from the wall as intended.

Water flow testing of the fuel circuit revealed an Acd average of 0.9868 in^2 , 16 percent above the predicted nominal. Visual observation of the flow revealed leakage around the faceplate edge. A new seal was designed to provide additional crush. The seal was fabricated and installed but water flow still showed leakage around the faceplate edge. The edge of the porous faceplate was sealed with plasma spray and machined to provide a better sealing surface. Water flow showed that the edge of the plate had no leakage, however, there appeared to be areas of high flow through the porous plate and the Acd average was still 12.6 percent above that predicted.

The film cooling orifices were removed and blanks were installed to provide a better view of the actual flow at the edge of the plate. The installation of the blanks allowed a better view of the interior of the faceplate where some areas of high flow were also observed. Flow showed that there was leakage at the film cooling orifices and flow was also seen around the edge of the facenuts.

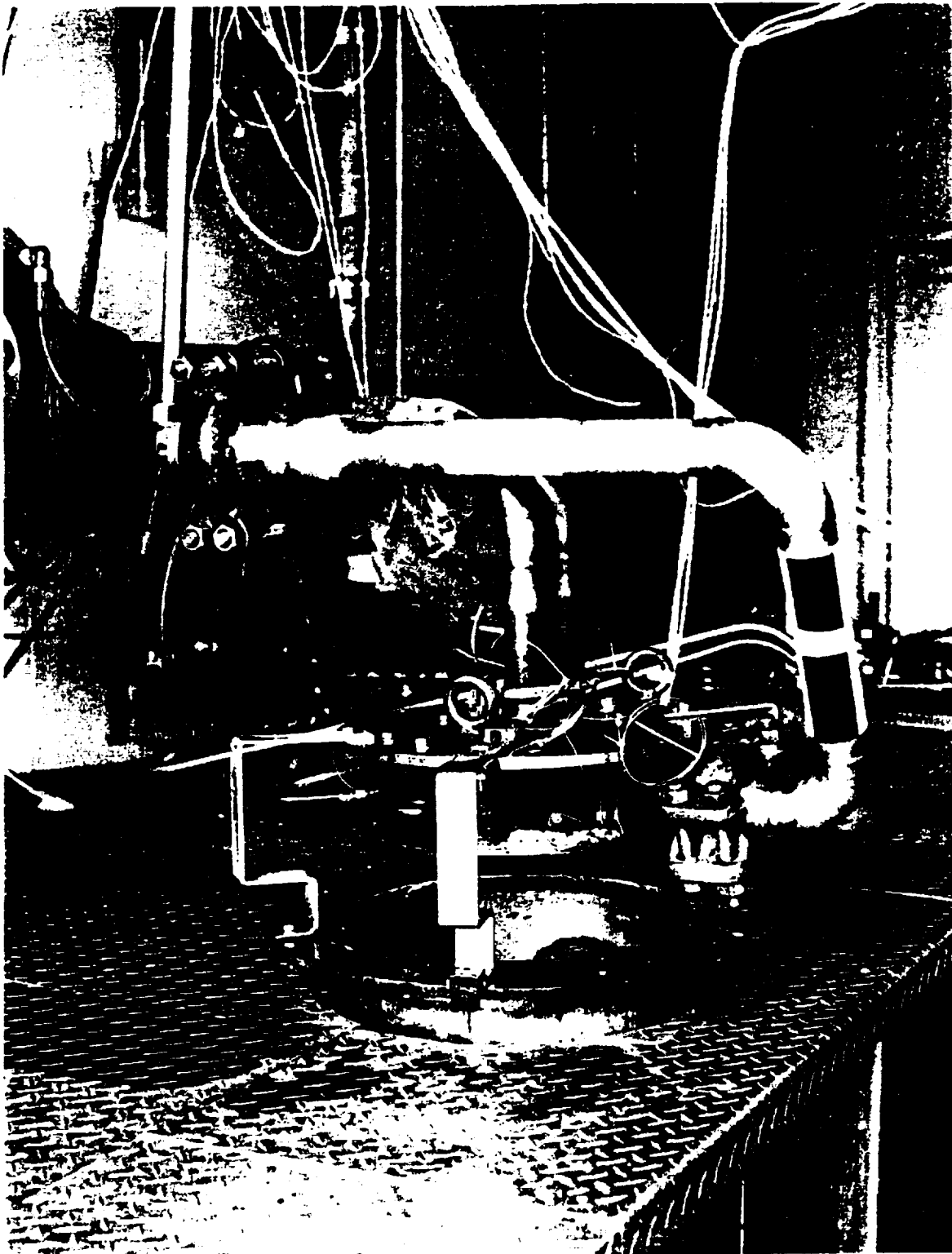
A portion of the porous plate used to make the faceplate was flow tested with air to confirm that it had the correct porosity. The test showed that the porosity was within the design requirements.

Although the effective area was in excess of that planned, it was decided that it was acceptable for testing, and the injector was delivered to NASA-MSFC.

Fixtures for flow testing faceplate samples were fabricated. These samples included sections of the faceplate, facenuts, fuel sleeves, and film cooling orifices, and were used to investigate possible causes of the excessive fuel circuit flow. Items investigated include leakage under the facenuts, leakage under the film cooling orifices, leakage around the igniter sleeve, and transverse leakage through the porous plate at the film cooling and facenut counterbores.

The samples confirmed that there was leakage around both the facenuts and film cooling orifices. Although there was transverse flow through the porous faceplate which exited at the counterbores for the facenuts and film cooling orifices, this flow was small and insignificant (Transverse flow exiting at the faceplate OD and seal groove was stopped by the plasma spray coating applied to those areas). The samples also showed that the most effective ways to restrict leakage around the facenuts was to increase the facenut torque. A Teflon seal placed on the back of the faceplate between the faceplate and the fuel sleeve was evaluated but not used due to a consideration of risk associated with having the faceplate "float" on the seals, and due to possible dislodging of seal pieces that could block the fuel flow. Also, the additional reduction in leakage over the higher facenut torque was small. Reducing the leakage around the film cooling orifices was considered more difficult, and no easily incorporated change was found. Thus, it was decided to replace the faceplate with the spare, which had simple film cooling holes rather than replaceable film cooling orifices. While eliminating the capability to vary the film cooling flow, this change did incorporate direct film cooling in which the fuel was directed to impinge on the chamber wall rather than being added outboard of the outer row element for reducing mixture ratio only.

The spare injector faceplate was installed onto the injector at MSFC. While the injector was dismantled, machining was done to provide clearance for installation of the combustion chamber dynamic pressure probes and to provide relief holes adjacent to the faceplate to facilitate faceplate removal if required again. Following this rework, the injector was cleaned for LOX service and reinstalled onto the combustion chamber. To secure the combustion chamber to the test stand while the injector was dismantled, a spacer was fabricated using the injector simulator plate that had been fabricated by P&W for use in welding the LOX inlet lines.



FE367728-2/3

Figure 2.1.3-23. Subscale Injector Mounted on Water Flow Stand

FE367729-3/4

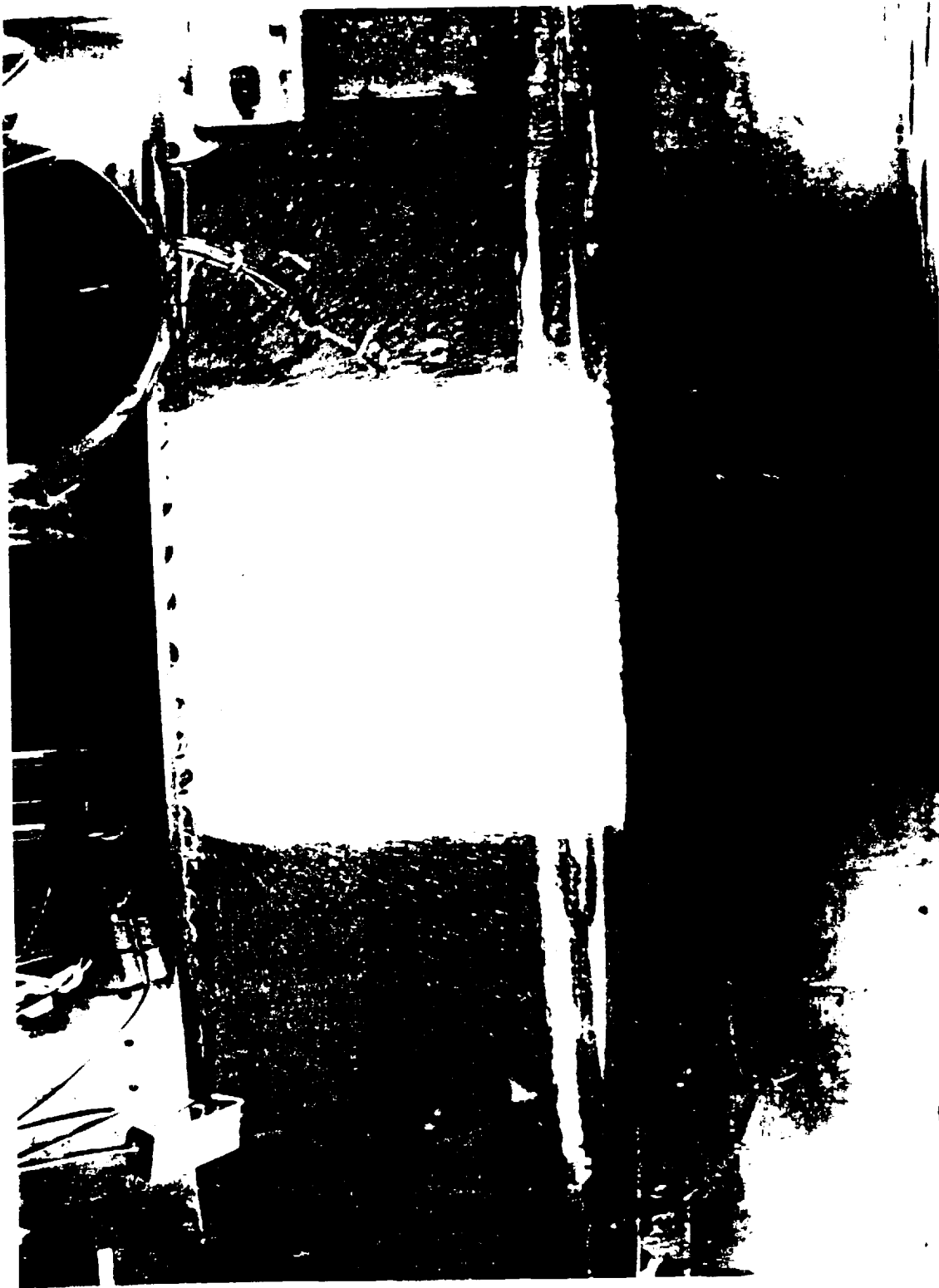


Figure 2.1.3-24. LOX Circuit Water Flow Spray Pattern

2.1.3.7 Outer Row Oxidizer Element Crack

Upon receipt of the injector at MSFC, a crack was noticed in the scarfed tip of one of the outer row oxidizer elements. As shown in Figure 2.1.3-25, a piece was missing from the tip, and a band of pitting and discoloration surrounded the crack. The crack was not seen before shipment of the injector from P&W. Close visual examination of the injector at MSFC showed that no other elements had any evidence of similar distress.

To allow testing to proceed, the damaged element tip was ground and milled flush with the injector face to avoid the risk of the crack propagating further down the element. This operation removed nearly all of the damaged area. Since the scarf was cut off, it was decided to plug the LOX element to prevent any oxidizer flow and avoid the possible risk of impinging LOX onto the combustor wall. The scarf feature is intended to prevent such impingement. A copper plug was installed to fill the entire internal diameter of the LOX element. This was threaded into the element in the same manner as the plugs used to control the tangential entry slot length and sealed with LOX compatible ceramic compound (Sauereisen cement) to completely prevent any LOX flow. Verification of the capability of this compound to withstand the thermal cycles was done on a sample element, which was prepared in the same manner as the injector element and dipped into liquid nitrogen several times. No evidence of cracking or dislodging of the compound was seen. The plugged element caused no problems during testing of the injector. The damaged tip was returned to P&W for analysis.

Analysis at P&W showed that the crack occurred in an area of material that had apparently melted and recast. A cross section of this area is shown in Figure 2.1.3-26. The remelt area extended from the element ID, at one point, all the way through the 0.020-inch wall. This area of recast was soft and porous and may have eroded and cracked during the water flow testing of the injector. The missing piece of the element may have broken loose during shipment of the injector, since this was not detected at P&W before shipment.

The origin of the remelt area remains unknown. Although a shallow recast layer is typical of the EDM process used to make the interpropellant plate with integral elements, the recast area in the damaged tip was in no way typical of an EDM recast layer. Typical EDM recast areas were 0.001 to 0.003 inch. This remelt area went completely through the 0.020-inch thick wall. In fact, this recast area does not appear to be caused by an electric arc, which tends to remove material, leaving craters with a thin recast layer rather than a thick area of melted material.

During manufacture of this part, the recast layer was removed from the outside of the element by hollow milling, and from the inside by reaming. The recast was removed from all other areas by chemical milling. Attempts to duplicate the remelt layer with EDM were performed at P&W on sample elements, but similar effects could not be duplicated. Thus, it was concluded that the damage was not a result of the intended manufacturing process, nor could it be duplicated by intentionally departing from good manufacturing procedures for making the integral element interpropellant plate.

There were no other steps in the manufacturing process that were suspect as being possible causes for the remelt area. The subcontractor who made this part was contacted regarding any departure from the planned processing that might have taken place and none was identified.

Although the cause of the damage remains unknown, it appeared to be isolated to this one element. Following the subscale testing, a thorough inspection of the interpropellant plate will be performed, including fluorescent penetrant inspection (FPI). FPI was accomplished at P&W on the interpropellant plate during the manufacturing process, and on an interpropellant plate sample as part of this investigation, and no cracks were found on either piece.

As a result of the above investigations, there is no concern that the problem found on this one element was due to the manufacturing process for an integral element interpropellant plate.

After the damaged element was plugged, the injector was remounted onto the combustion chamber on TS116 test stand for testing of the subscale rig.

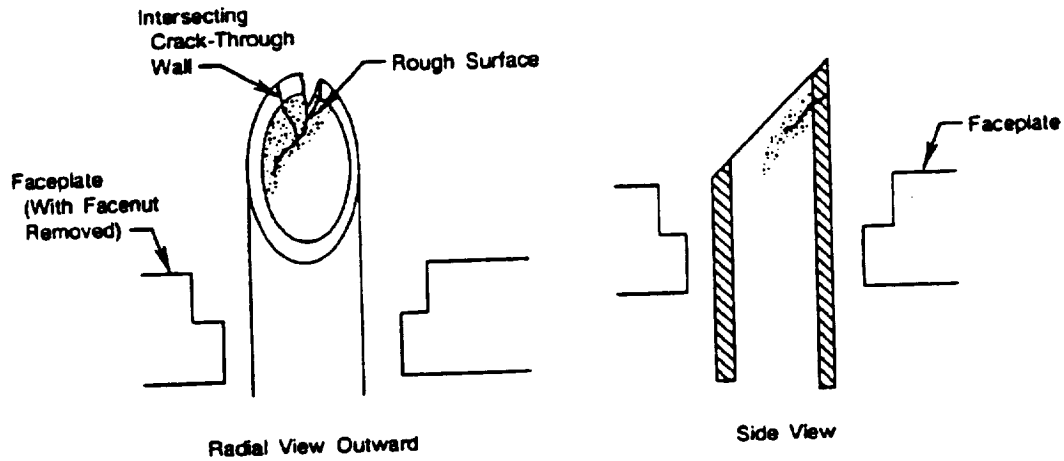
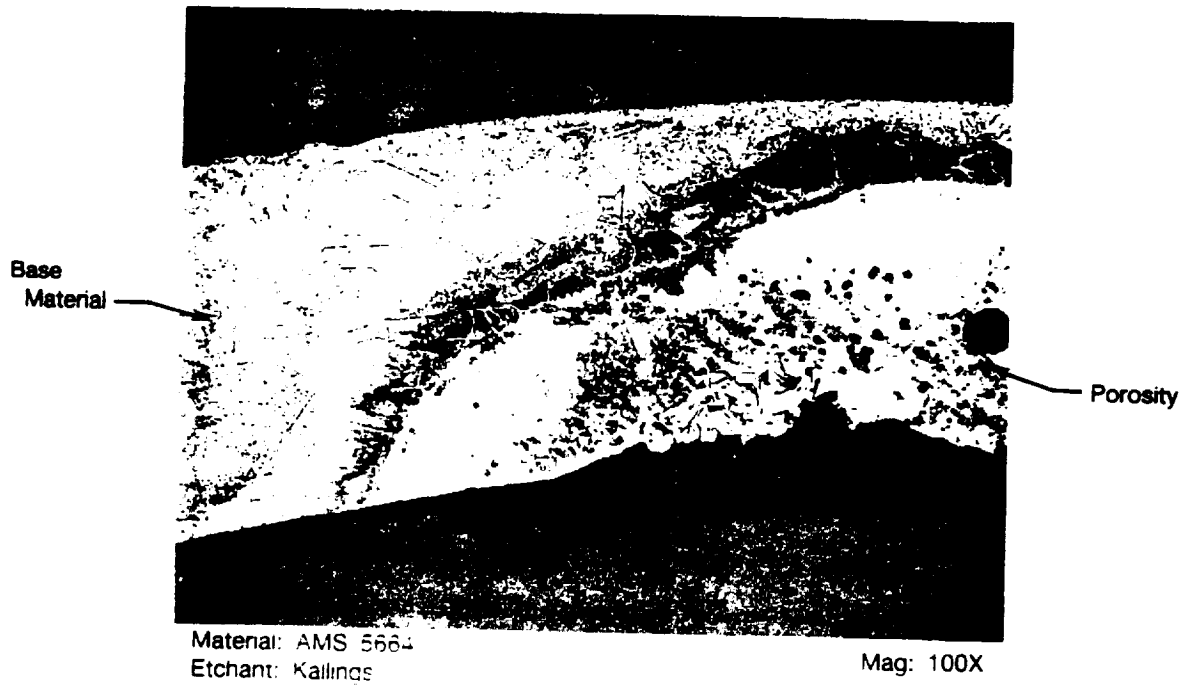
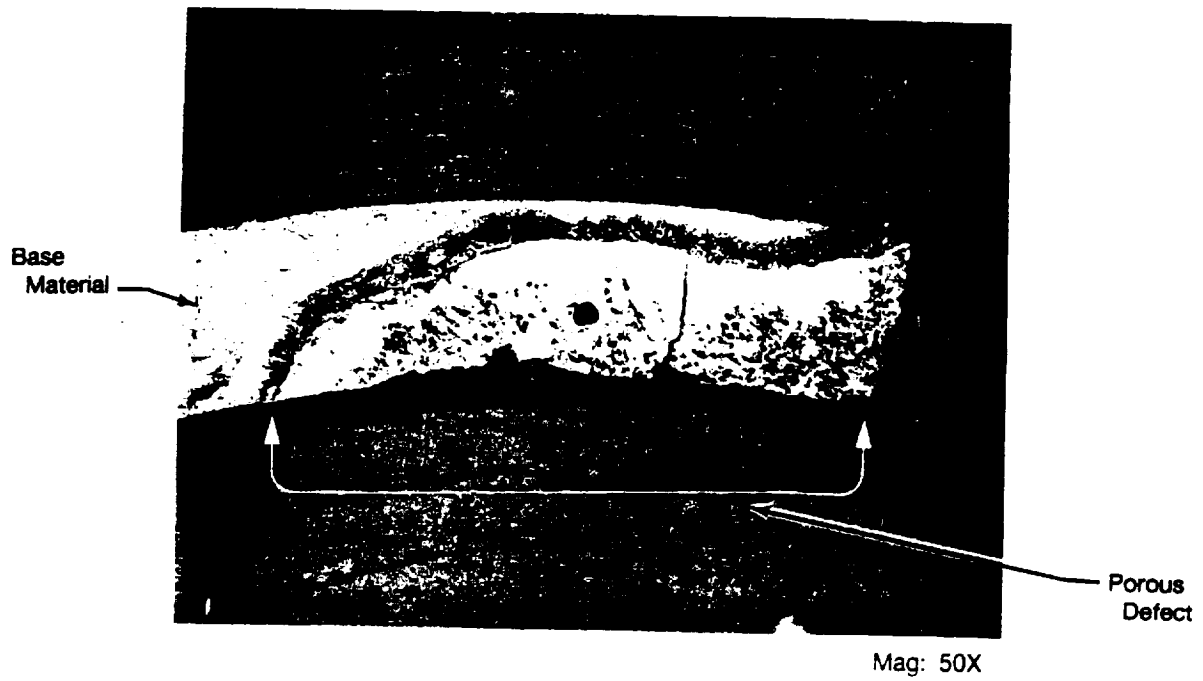


Figure 2.1.3-25. Cracked Outer Row Oxidizer Element



FE380190

Figure 2.1.3-26. Cross-Section of Element Wall Showing Area of Recast

2.2 IGNITER

2.2.1 Hypergolic Igniter Design

At the 23 May, 1989 program review, there was concern raised about the torch igniter operation and durability of the spark plug. This was based on NASA experience with other torch ignition systems and on the start sequence which was to be used for the subscale testing. As a result of these discussions, P&W produced a backup design for a hypergolic igniter using a triethylaluminum and triethylborane (TEA/TEB) mixture.

The design of the hypergolic igniter is shown in Figure 2.2.1-1. This design is little more than a piece of copper in the shape of the torch igniter with a straight hole through to the injector face to spray the TEA/TEB out into the combustion chamber. The flange and tube body is a single piece of AMS4602 OFHC copper. Thermal analysis of the face determined that no active cooling or thermal barrier coating would be required for chamber firing tests up to 10 seconds duration at the rated power level (RPL) test condition. The body outside diameter is tapered to permit unrestricted thermal growth. External dimensions are identical to the torch igniter facilitating direct replacement. A number 6 AN flared tube fitting was used to connect to the stand TEA/TEB supply. A TEA/TEB flowrate of 0.5 to 1.0 pps was specified since this igniter was similar to an igniter used for 40K testing at Marshall Space Flight Center (MSFC).

When the torch igniter experienced severe problems and was abandoned, the decision was made to incorporate the hypergolic igniter into the subscale injector design. The igniter was conventionally machined at a vendor from a single piece of OFHC copper.

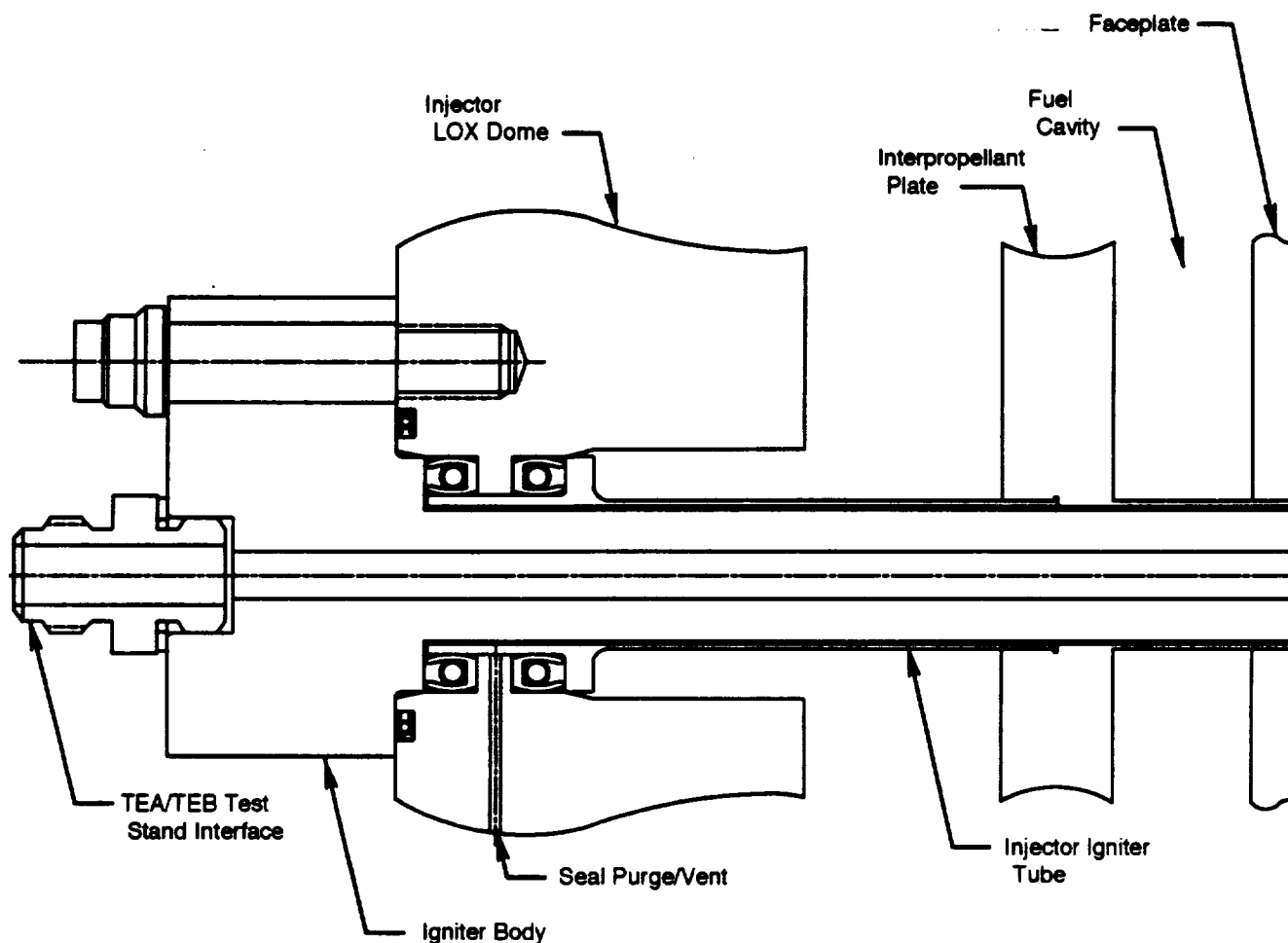


Figure 2.2.1-1. Subscale Hypergolic Igniter

2.2.2 Torch Igniter Design History

The torch igniter was designed to provide the start flame to the main combustion chamber (MCC) during engine start-up. The GOX flow was to be metered by an orifice at the inlet and injected into the igniter combustion chamber (ICC) through an inlet tube. Fuel flow was to be split at the inlet into two flowpaths, each metered by an orifice. One path has the fuel cooling the ICC wall, and the other path was for injecting fuel annularly around the GOX into the ICC.

An additional feature of the igniter was that as the hot gas leaves the ICC barrel and discharges into the MCC, the coolant bypass fuel impinges annularly around it. This initially causes a conically shaped flame front to form in the MCC. As the gas streams mix, the conical shape degenerates into a randomly shaped flame front. This fuel rich flame front combined with an oxidizer rich environment during rig startup would ensure a positive ignition source in the MCC.

The torch igniter was initially designed to operate with gaseous oxygen and gaseous methane. NASA/MSFC had indicated a preference for liquid oxygen, and P&W evaluated the impact of substituting liquid for gaseous oxygen on the design and operating characteristics of the torch igniter. Simply substituting a smaller upstream orifice in the LOX line resulted in an orifice size requirement of 0.003 in. diameter, which would have been unacceptably small (susceptible to blockage). During the design review, NASA agreed to provide gaseous oxygen to the igniter as originally designed.

The cross section of the initial igniter design is shown in Figure 2.2.2-1. Oxygen enters through a centrally located removable orifice and is injected into the torch combustion chamber. The igniter contains two fuel plenums which are fed from one supply. Removable orifices control the flow to each of these plenums. One feeds the gaseous methane to the ignition chamber through an annulus located around the LOX inlet tube. The other plenum feeds the coolant annulus through twelve crossover slots. This flow is discharged into the main combustion chamber. The propellants within the ignition chamber are ignited by an electric spark plug.

The flame front will be 0.500 inch from the oxidizer inlet. This allows the flange Haynes 230 material to extend that far from the inlet where it is brazed to the OHFC ignition chamber wall. This joint region also serves as a plenum to effect uniform flow of coolant through the annulus around the ignition chamber. The remainder of the pieces will also be Haynes 230 because of its excellent brazability and for thermal expansion compatibility.

When the igniter purge, starting, and steady flows had been defined, it became necessary, as a result of the flows required, to move the starting flow orifices off the igniter itself to allow introduction of the steady-state coolant flows downstream of the start orifices. The configuration for igniter orifices is shown schematically in Figure 2.2.2-2. This system will allow setting each flow independently without relying on internal metering and will permit using the same ignition system for both CH_4 and H_2 testing by changing these external orifices.

The energy requirements for the spark igniter were determined to be 25 millijoules at a rate of 50 sparks/sec. The requirements were determined from minimum spark ignition energies for methane and oxygen reported in "Combustion Flames and Explosions of Gases," Lewis and von Elbe, Academic Press, Inc., 1961.

Because of limited space on the igniter, the spark plugs had to be smaller than any other spark plugs in this energy range had ever been made before. The spark plug supplier had to develop a design and demonstrate in their laboratory that such a small diameter (0.125 inch) can be made to withstand the spark energy.

Instrumentation to detect ignition included two thermocouples routed along the chamber cooling annulus and installed at the tip of the igniter chamber to detect the copper liner temperature at the igniter discharge to the main chamber. In addition, a high response gas thermocouple was to be installed in the igniter combustion chamber dome. Ignition would be detected by the gas thermocouple with verification of hot gas discharge into the main chamber with the skin thermocouples.

The high-response thermocouple to be used to detect ignition of the torch igniter was an eroding tip thermocouple was manufactured by NANMAC corporation and is shown in Figure 2.2.2-3. The probe was to be installed in the dome of the torch igniter with an insertion depth into the torch combustion chamber of 0.100 inch. The probe used a platinum and rhodium ribbon encased in a zirconium oxide shell and is shown schematically in Figure 2.2.2-4. With this probe the junction is continuously formed as the tip erodes. The response was expected to be less than 0.100 second. At the 27 October 1989 program review, concerns were raised by NASA about the reliability of the eroding tip thermocouple to be used in the torch igniter. In previous testing at MSFC, this type of probe demonstrated rapid tip erosion during unstable subcritical combustion of hydrogen-oxygen. To mitigate risk a platinum-rhodium probe similar to that used successfully during recent testing at P&W under the Alternate Turbopump Development program was designed and fabricated.

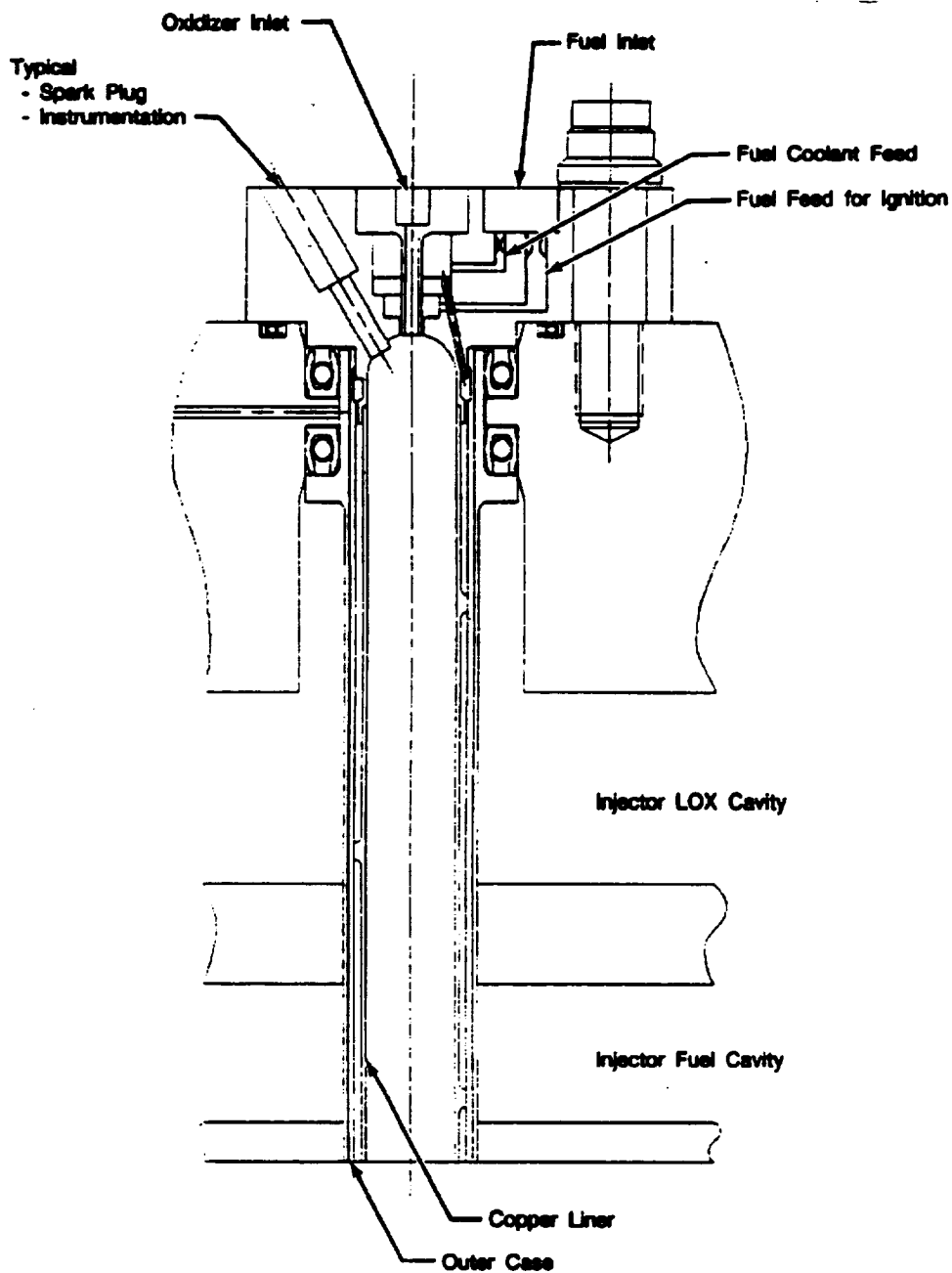
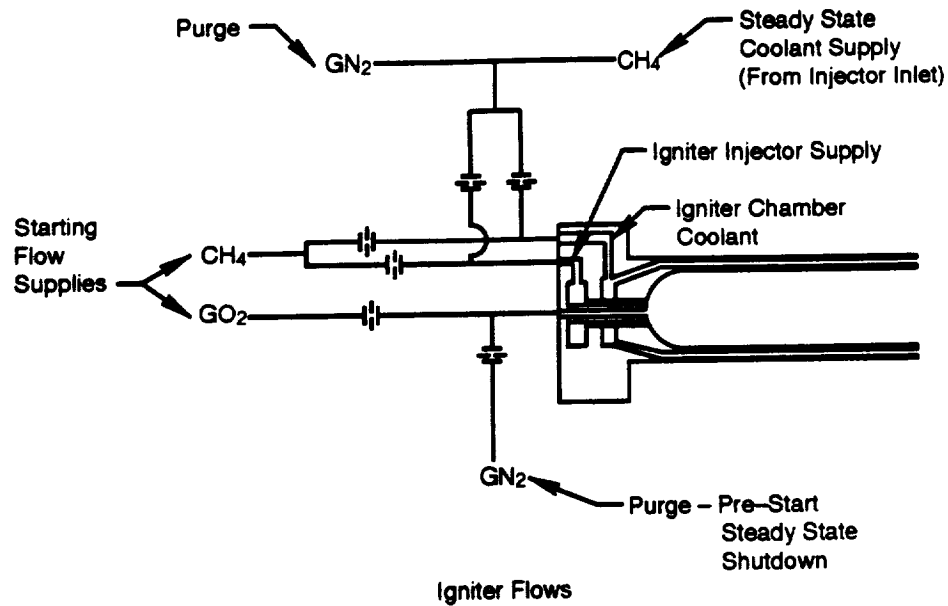


Figure 2.2.2-1. Torch Igniter Cross-Section



Igniter Flows

	Start	Steady State
Oxidizer Supply	GO ₂ - 0.00366 lbm/sec	GN ₂ - 0.180 lbm/sec
Fuel Injector	CH ₄ - 0.00229 lbm/sec	CH ₄ - 0.184 lbm/sec
Fuel Coolant	CH ₄ - 0.00597 lbm/sec	CH ₄ - 0.821 lbm/sec

Figure 2.2.2-2. Torch Igniter Orifice Setup

FE600378

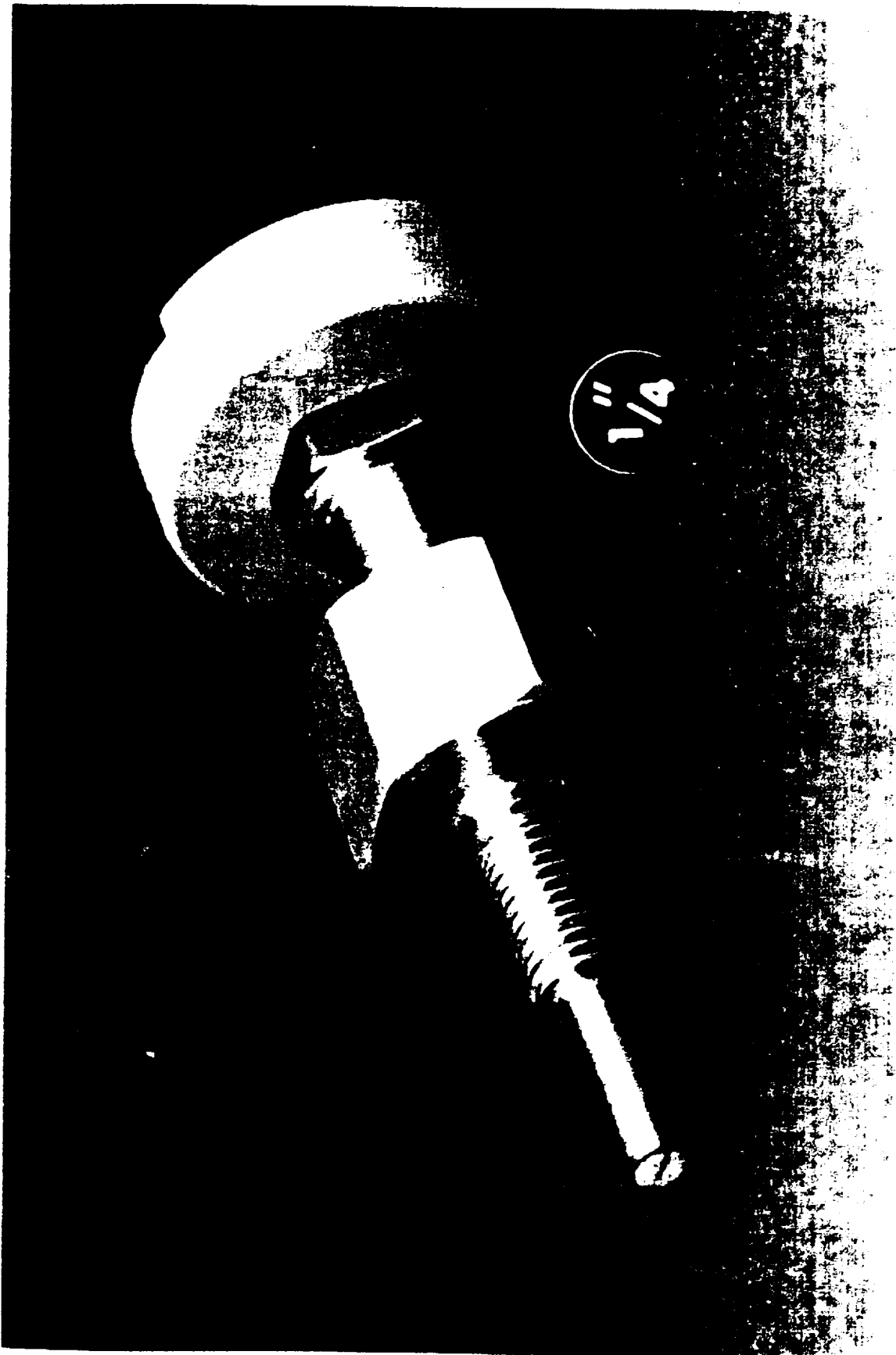


Figure 2.2.2-3. NANMAC High-Response Igniter Thermocouple

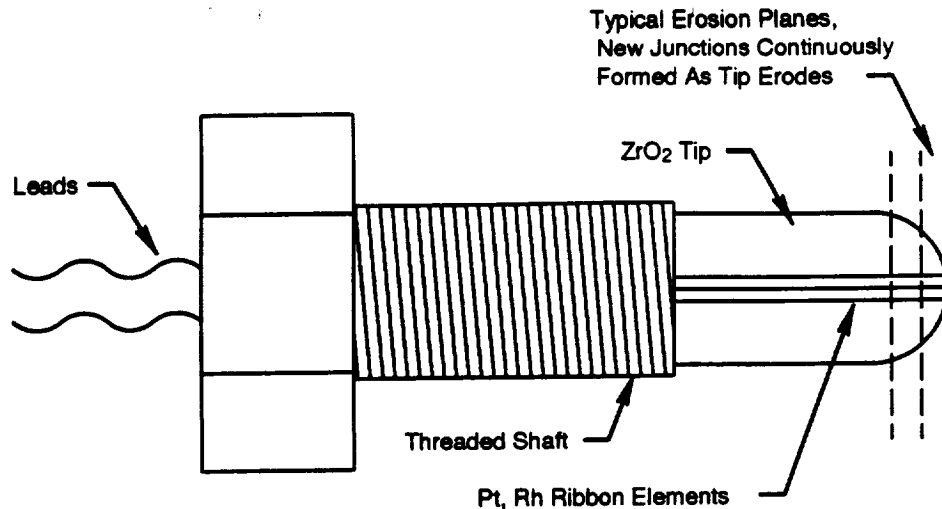


Figure 2.2.2-4. Torch Igniter Thermocouple

2.2.3 Torch Igniter Fabrication History

The spark plug, excitor, and high tension lead were purchased from vendors. The spark plug is shown firing in Figure 2.2.3-1 during a test of the system.

During fabrication of the torch igniter, several drill bits were broken during installation of the fuel coolant supply passages. Subsequent EDM removal of the bits enlarged the exits of three of the passages beyond a usable condition. A weld repair was made, and the passages were redrilled, returning the igniter to drawing specifications. Radiographic inspection revealed incomplete coverage in the joints between the igniter outer barrel and flange and igniter inner barrel and flange, however, it was determined that sufficient braze material existed to satisfy design requirements. The igniter was accepted, final machining was accomplished and the igniter was delivered to P&W. The completed igniter is shown in Figure 2.2.3-2.

During preparation for testing the igniter, it was discovered that one of the two barrel thermocouples (T/C) was broken at the housing junction. Due to the assembly configuration, this T/C could not be replaced. Trial fit-up with the injector assembly revealed an interference between the injector igniter sleeve and the remaining barrel T/C on the igniter, preventing assembly. Therefore, it was decided that following the testing, which would calibrate the barrel T/C to the dome T/C, the remaining barrel T/C would be removed from the igniter.

Delay in testing of the torch igniter at P&W due to SSME ATD test activity resulted in a mutual agreement with NASA to move the hot firing to MSFC TS116 stand. Before shipment of the igniter assembly to MSFC, the igniter was disassembled (supply fittings and orifices removed) for installation of replacement T/Cs on the outer surface of the copper hot wall. Only one of the two was operational and if it failed during checkout tests, the only indication of proper operation would be the spark dome gas T/C. Thus it was decided to remove the existing T/Cs and install larger diameter T/Cs more capable of withstanding the handling during installation and checkout testing. Having two reliable T/Cs would allow correlation with the spark dome T/C before their removal for the igniter installation into the injector.

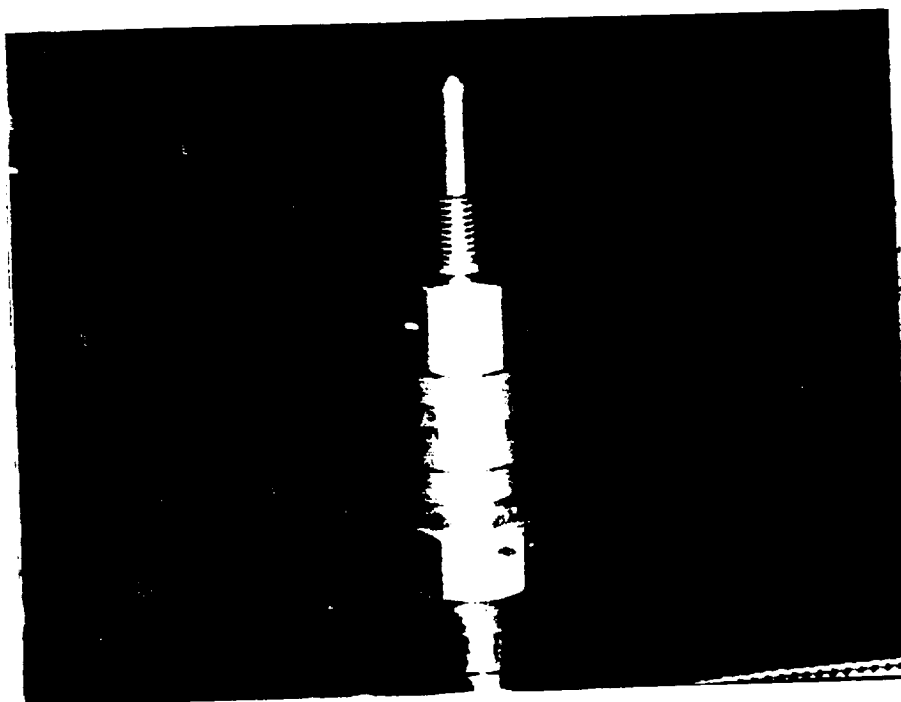
A port to provide a hydrogen purge to the injector sleeve into which the igniter is installed was also added to prevent freezing of combustion gases which would have filled this area during operation. This purge did not require additional actuation valves or sequencing, but was supplied directly from the hydrogen manifold in the injector body through an external line.

The rework was completed and the igniter and all ancillary parts were cleaned for LOX service, then assembled. All components required for hot firing were shipped with the igniter assembly to MSFC on 22 May 1990 and were received the following day.

The torch igniter was installed on TS 116 at MSFC for cold flow and hot fire testing. A cold flow test was accomplished on 9 July 1990. Review of the data showed that there was significant pressure buildup in both fuel supply tee fittings indicating a restriction in the flow downstream of the metering orifices. The fuel inlet lines were removed from the igniter and diagnostic flows were performed. These tests showed that there was very little flow through the igniter fuel injector circuit and no flow through the fuel coolant circuit. The igniter was removed from the test stand and returned to P&W for investigation.

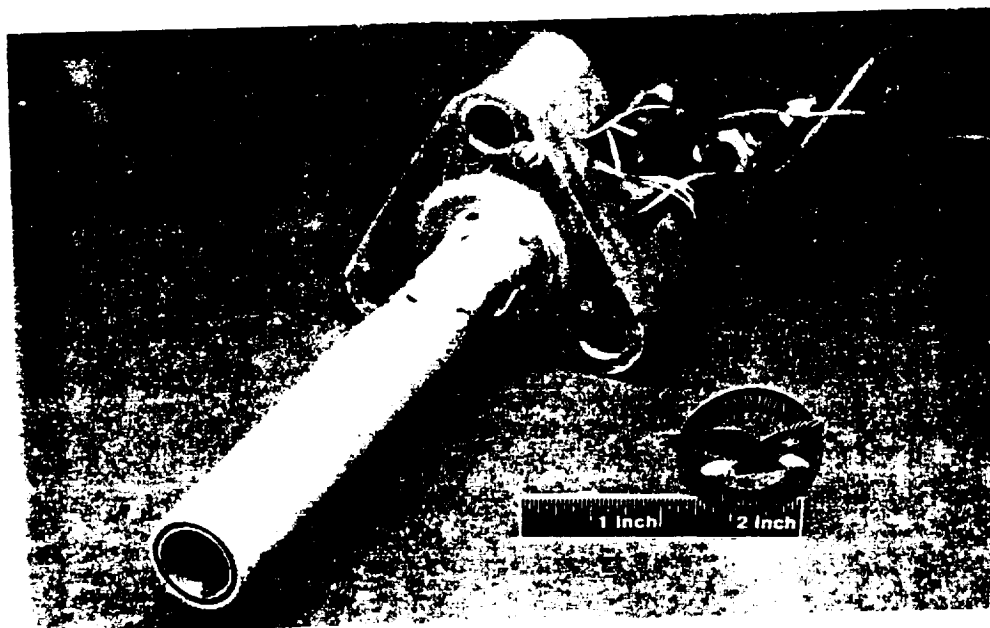
The igniter was machined to expose the internal passages which supplied fuel for cooling and injection. Inspection with a borescope showed incomplete machining of the fuel coolant passage and blockage of the injector passage. These restrictions were removed and flow was restored for both circuits. A cold flow was performed to verify proper performance and it was discovered that there was cross circuit flow between the injection and coolant circuits. Inspection showed an intersection between one of the passages that feeds the cooling annulus and the fuel injector supply passage. A sleeve was installed into the injector supply passage to correct this problem. This repair was partially successful and the cross circuit leakage was significantly reduced. Further investigation showed that a drawing error had allowed this intersection and another intersection of a cooling supply passage with the dome T/C hole. In addition, X-rays showed that blockage of the coolant annulus had occurred during installation of the T/Cs that had been intended for measuring the hot wall temperature. Since repair would require disassembly of the igniter to correct these problems, and this could not be accomplished in time to permit hot firing before the thrust chamber arrival at MSFC, it was decided to use the backup hypergolic igniter for thrust chamber testing.

The torch igniter was placed in stores with the possibility of being reworked for use on the large-scale injector with removal and replacement of the fuel coolant jacket and the copper liner to accommodate the longer installation length. After obtaining quotes for the repair of the torch igniter, and reviewing the reliability of the hypergolic igniter during the subscale testing, it was decided to use a hypergolic igniter for the full-scale testing. Therefore, the torch igniter was left in stores without repair and remains nonfunctional.



FE300910-4

Figure 2.2.3-1. Torch Igniter Spark Plug — Shown Firing



FE505773

Figure 2.2.3-2. Completed Torch Igniter

2.3 CALORIMETER COMBUSTION CHAMBER

2.3.1 Calorimeter Combustion Chamber Design

2.3.1.1 Mechanical Design

The mechanical design of the chamber provided two basic functions during this program. It served as the chamber for testing the subscale injector to determine performance and combustion stabilization, and is a calorimeter to provide data for analysis of the combustion chamber heat absorption. Figure 2.3.1-1 shows the subscale calorimeter combustion chamber. As shown, the chamber incorporates 144 circumferential passages for the water coolant. The coolant is introduced to eight manifolds from where it splits to nine individual flow circuits (72 circuits total for the combustor). This split provides metered flow to two passages each in all but four locations. The flow to each pair of passages is controlled by an orifice in the discharge of each of the 72 coolant circuits. The discharge line is located 180 degrees from the water inlet. The coolant circuit inlets are clocked at 22.5 degrees as they progress axially down the chamber length to permit ease of interface plumbing installation as well as to minimize circumferential temperature gradients in the chamber.

The coolant passages are machined circumferentially around the chamber to allow axial sectioning of the chamber so that the heat transfer along the length of the combustor can be determined. The chamber liner is made from NASA Z copper alloy which was forged and contour rolled to a near net shape to establish the needed material properties and minimize the usage of raw material. The water coolant passages are machined and closed out by an electroformed nickel structural shell. The coolant lines are made of 321 SST and welded to the nickel shell.

The calculated factors of safety for the combustor are presented in Table 2.3.1-1.

Table 2.3.1-1. Subscale Combustor Factors of Safety

Condition	Component	SF
Prestart — Full Coolant Pressure	Copper Liner	1.7 Yield
	Nickel Structure	1.25 Yield 1.5 Ultimate
Steady State	Coolant Lines	2.0 Yield 4.0 Ultimate

Chamber Life Prediction:

The copper liner wall of the subscale calorimeter chamber is predicted to have sufficient fatigue life for completion of all combustor tests without liner wall cracking. Based on the analytically predicted temperature distributions in the liner and electroformed nickel closeout, a minimum low-cycle fatigue life of 200 cycles was calculated.

Previous results of NASA LeRC subscale chamber tests (Reference 1) were used to determine the life of the P&W STBE subscale chamber design. Hot-fire testing of instrumented subscale combustion chambers at the NASA Lewis Research Center (NASA-LeRC) has shown significant mid-channel wall thinning and bulging following repeated cyclic testing. The large temperature difference between the liner hot wall and the thicker closeout material is a major cause of high cyclic strain in the liner wall, and therefore, is a prime cause for liner wall fatigue. The observed cyclic life of each hydrogen cooled chamber was plotted versus the maximum hot

wall to backside wall temperature difference (T). Figure 2.3.1-2 shows the NASA LeRC data and also the T of 1050°R for P&W's water cooled subscale chamber. The T value is based on an accel condition, where the liner hot wall surface quickly reaches steady-state temperatures, and the backside wall remains approximately at cooldown (ambient) temperature. Using this method, a typical liner wall fatigue failure would occur near 500 cycles of testing (assuming equal thermal gradients for each cycle). A conventional method for presenting the low-cycle fatigue (LCF) life characteristics of a given material is to plot strain range ($\Delta\epsilon$) as a function of cycles to failure (N_f). Numerous LCF specimen tests are conducted to represent the material fatigue characteristics at various strain ranges. The LCF curve for NASA Z is shown in Figure 2.3.1-3(Reference 2). A strain range of 2.2 percent in the liner wall was analytically predicted using the method described in(Reference 3). Figure 2.3.1-3 shows a typical curve fit through the NASA Z data, and an estimated minimum curve to account for the data scatter. The predicted strain range of 2.2 percent yields a minimum LCF life of 200 cycles.

Both methods described above demonstrated that the liner wall was designed to provide sufficient fatigue life for completion of all scheduled combustor tests with a low risk of liner wall fatigue failure.

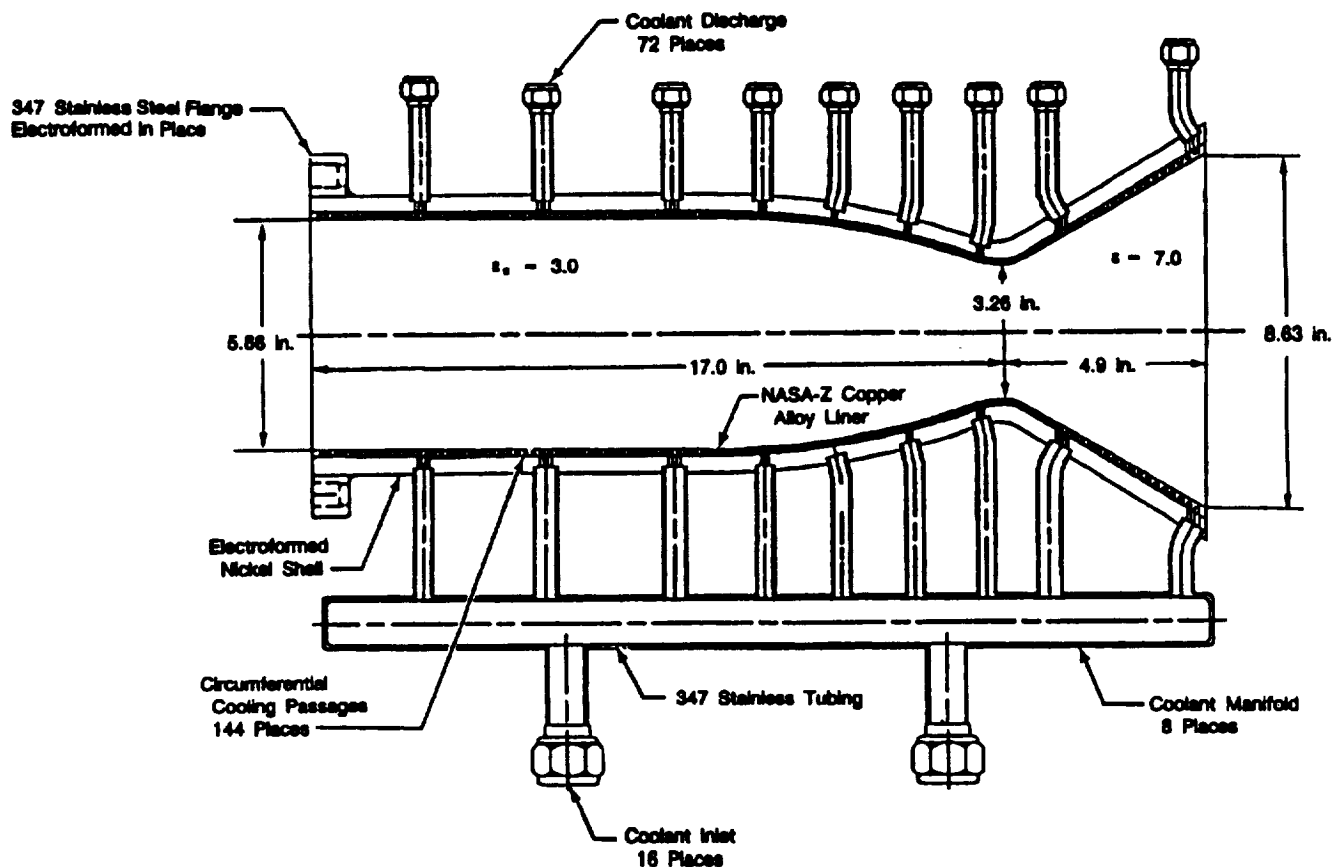


Figure 2.3.1-1. Subscale Calorimeter Combustion Chamber Design

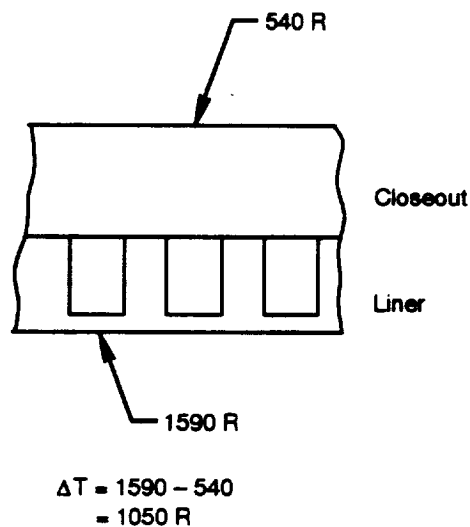
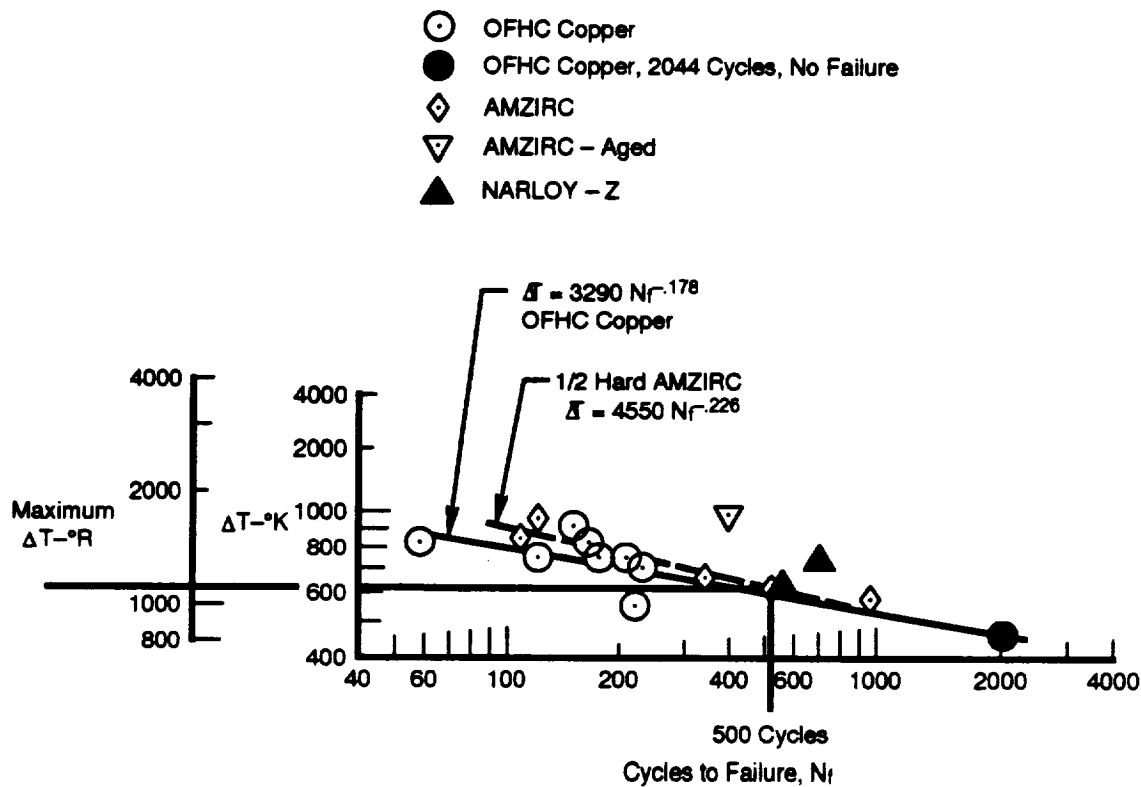


Figure 2.3.1-2. Maximum Hot Wall to Backside Wall Temperature Difference Versus Cycles to Failure

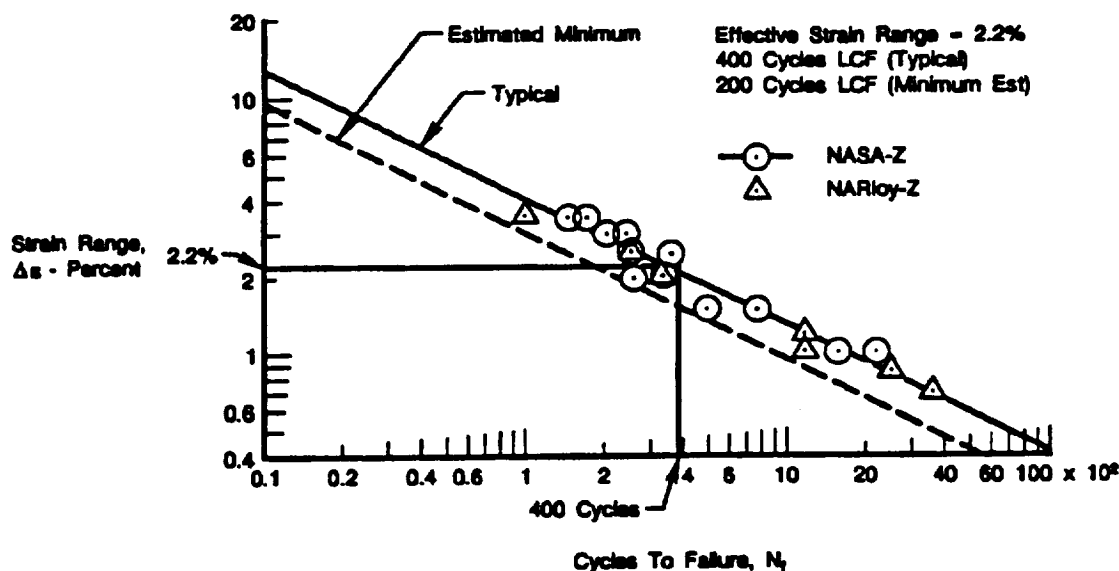


Figure 2.3.1-3. Low-Cycle Fatigue NASA Z

2.3.1.2 Analytical Design

Combustion Performance Analysis:

The combustion performance (η_{c*}), and stability characteristics were evaluated for the design of the P&W injector configuration. The subscale injection element dimensions used in this evaluation are given in Table 2.3.1-2. The characteristic velocity efficiency (η_{c*}) is provided as a function of characteristic length (L^*) and injected LOX drop size in Figure 2.3.1-4. The calculations for characteristic velocity efficiency are based on a P&W developed Supercritical combustion model, which is illustrated schematically in Figure 2.3.1-5. The model is based on analytical characterization of the following combustion related parameters:

- Droplet formation plane
- Droplet size and distribution
- Droplet heating
- Flame front location, including ignition delay effects
- Fraction of reactant burned.

Table 2.3.1-2. Subscale Injection Element Dimensions

LOX Spud ID (in.)	0.272
LOX Spud OD (in.)	0.312
Tangential Slot Width (in.)	0.030
Tangential Slot Length (in.)	0.426
Fuel Gap (in.)	0.020
Number of Elements	62

The drop formation plane for the P&W injector is approximately 0.6 inch from the LOX injector element tip. This distance was calculated from a P&W developed correlation of atomization plane vs LOX injector pressure drop which was developed from extensive tangential entry injection element spray testing.

The droplet size for the injected LOX was calculated from a P&W correlation which gives mass median diameter (MMD) as a function of geometry and operating conditions, for a tangential entry swirl coaxial injection element. This correlation was developed from extensive spray analysis of this type of injection element over a range of element sizes, injection pressure drops, mass flow rates, and test fluids. Figure 2.3.1-6 gives the LOX drop diameter distribution in cumulative volume (or mass) for the P&W injector.

Droplet heating is virtually instantaneous per the method of analysis proposed by Wieber(Reference 4). As shown in Figure 2.3.1-7, for chamber pressures in excess of 2000 psia, the LOX droplet reaches the critical temperature with virtually no vaporization from the drop before heating to the critical temperature at which the phase boundary between the drop and surrounding gas disappears.

The ignition delay time for the P&W injector is 0.5 milliseconds. This value was calculated from an ignition delay time correlation using References 5, 6, and 7. This delay locates the flame front approximately 0.6 inch from the injector face.

The calculation of combustion efficiency relies upon the model given in Reference 8. In this model, the combustion rate is controlled by diffusion once the liquid droplet reaches critical conditions (i.e., when the droplet reaches its critical temperature and the combustion process pressure is above the critical pressure of the fluid). Under these conditions, increasing the pressure increases the density of the diffusing reactants which reduces the rate of diffusion and therefore reduces the rate of combustion. A graphical representation of this process is shown in Figure 2.3.1-8, and the experimental verification is given in Figure 2.3.1-9(Reference 9).

An example of the application of the P&W supercritical combustion model can be found in Reference 10.

Combustion Stability Analysis:

The stability characteristics of the P&W injector were evaluated using the Sensitive Time Lag Theory(Reference 11). The evaluation was made using a computer code that P&W obtained from Dr. C. E. Mitchell of Colorado State University. This code is described in Reference 12. The results of the analysis are given in Figure 2.3.1-10, and show that the combustion system would be stable at the design operating conditions.

Heat Transfer Analysis:

Subscale Chamber Contour Selection — Ideally, the subscale chamber geometrical and operational characteristics should provide an environment that is identical to that of the full-scale chamber in the areas of combustion efficiency, combustion stability, local heat flux level and distribution to provide data that is directly applicable to the full-scale engine design. However, this is not possible due to restraints associated with the smaller thrust and flowrate size of the chamber. For example, certain more significant to evaluate/model parameters such as L^* and the throat entrance contour were retained while others, such as chamber cylindrical length allowed, were determined from the values selected. The proposed contour for the subscale chamber was selected to provide the same combustion chamber characteristic length, contraction ratio, throat heat flux level and a geometrically scaled divergent section comparable to that of the full-scale chamber.

Figure 2.3.1-11 depicts the chamber contour and identifies nomenclature. Table 2.3.1-3 summarizes contour characteristics. The R_c and R_{in} are approximately equal to those being used in the present analysis under Contract NAS8-36857. In choosing these, the assumption made is that the hot-side curvature enhancement is unaffected by throat radius; that is, it follows a flat plate analogy. The limited data available has not shown a dependence on throat radius. As noted above, retaining L^* equivalence the convergent section of the subscale chamber begins 10 inches downstream of the injector and for full-scale chamber it begins 5.5 inches downstream. An AIAA report(Reference 13) raises the concern of wall impingement versus axial length; however, this is considered

acceptable since the injector features outer ring injector element scarfing and an outer ring of porous Rigimesh between the elements and the chamber wall.

Table 2.3.1-3. Calorimeter Subscale Combustion Chamber Contour

Injector Radius (R _{inj}) - in.	2.83
Throat Radius (R _s) - in.	0.63
Chamber Inlet Radius of Curvature (R _{in}) - in.	8.6
Throat Radius of Curvature (R _c) - in.	2.50
Contraction Ratio	3.00
Chamber Length to Throat - in.	17.0
Chamber Volume - in. ³	380
Divergent Section Expansion Ratio	7.0
Divergent Section Length - in.	4.9
Divergent Section Angle (°) - degrees	30

Subscale Chamber Cooling Requirements — The subscale chamber coolant specified is pure de-ionized water. The inlet steady state pressure was defined as 4500 psia. Due to the inlet effects of flowing the coolant in the channel at high velocities needed for cooling, the static pressure in most of the passages will be less than the critical pressure of water (3206) psia. Therefore, the possibility of boiling in the coolant was analyzed.

The main criteria in designing with boiling is the prevention of burnout. This is a term that covers all physical occurrences that result in a sharp reduction in the heat transfer coefficient and wall temperature elevation. Reference 14 recommends the following, which is noted to be a very conservative equation for burnout:

$$Q_{BO} = 0.101 * (Vel) * (\Delta T_{sub})$$

Where:

Q_{BO} is Burnout heat flux in Btu/(in.²-sec)

Vel is coolant velocity in ft/sec

ΔT_{sub} is the difference between saturation temperature and bulk temperature in degrees R.

Experimental data in the reference shows this equation to be conservative by approximately 30 percent .

Using the design point, chamber contour and a hot wall temperature of 1560°R, a predicted heat flux curve was generated. This curve is presented in Figure 2.3.1-12. By using this generated wall heat flux curve and local geometry definition (passage width and fillet radius, land width, and hot wall radius), curves of burnout heat flux for different flowrates and passage heights were generated. Figure 2.3.1-13 presents a conservatively predicted burnout curve at the critical axial position 0.8 inch upstream of the throat.

The combustion chamber consists of circumferential passages through which high pressure water flows to cool the thin wall forming the chamber wall confirming the high-pressure combustion gas products. Each two to three passages are parallel flow controlled by a orifice in the manifold which is the coolant water discharge of these two to three passages. The 4500 psia inlet water is routed unrestricted to each group of several passages, thus inlet pressure and temperature are constant at each passage inlet.

In an attempt to minimize axial conduction effects which can lead to experimental data analysis uncertainties the thrust chamber was analytically divided into as few sections as possible, compatible with minimization of axial conduction. This resulted in two sections containing groups of separately manifolded two to three passage groups. The coolant flowrates were selected, compatible with the 250 lb/sec availability, to result in only two sections being required.

Using the coolant temperature rise, a mass flow rate was determined for each axial location. The optimum passage height was then determined from graphs similar to those of Figure 2.3.1-13. A thermal design deck (D5160) has been modified to model circumferential passages using water as the coolant. The effects due to passage inlet and curvature are included in the calculations.

The final design criteria imposed is associated with establishing as uniform a hot-wall temperature as practical. If the optimum passage height from the analysis resulted in a wall colder than 1560°R, the passage height increased until a wall temperature of 1560°R was reached. These adjustments were made from manufacturing considerations and held constant throughout each respective section of the chamber.

Using the finalized geometry, coolant pressure drops and in turn coolant static pressures were determined. Figure 2.3.1-14 presents chamber inlet and exit static pressures.

At the throat entrance the predicted ratio of burnout heat flux to coolant wall heat flux approaches unity and hot-wall temperature increases above 1560°R are predicted. However comparison with the experimental data in Reference 14 shows the actual burnout ratio to be closer to 1.3. This provides a margin approaching 30 percent.

Oxidizer/Fuel ratio (O/F) biasing of the outer row of elements significantly lowers wall heat flux which in turn improves both structural and burnout margin. Table 2.3.1-4 presents experimental data on O/F biasing for methane fuel as used in the initial rig design. Table 2.3.1-5 presents analytical results using a correlation where the wall conditions are adjusted for a lower O/F ratio, but the gaspath radiation is held constant. The analytical results are in good agreement with the available data. Figure 2.3.1-15 is a wall heat flux profile showing the effect of O/F biasing. When running methane, the effect at the throat of biasing from a core of 3.57 to a wall of 2.5 is a reduction in predicted hot-wall temperature from 1620°R to 1400°R. Burnout margin moves from a 1.11 to a 1.50 ratio using the burnout heat flux equation as reported by C. Dexter (Reference 14, Equation 6).

Table 2.3.1-4. O/F Biasing Experimental Data

Test No.	Pc	O/F Wall	O/F Core	Q/A Throat
28	1570	3.52	3.52	48.68
31	1789	2.52	3.36	40.95

Note: Test No. 28 Q/A Pc Correction: $Q/A_{corr} = 48.68 \left(\frac{1789}{1570} \right)^{0.8} = 54.04$

$$\% \text{ O/F shift} = \frac{3.52 - 2.52}{3.52} = 29\%$$

$$\% \text{ Q/A drop} = \frac{54.04 - 40.95}{54.04} = 24\%$$

Source: C. R. Bailey — High Pressure LOX/Natural Gas Staged Combustion Technology, 1984

Table 2.3.1-5. O/F Biasing Analytical Results

Pc	O/F Wall	O/F Core	Q/A Throat
3000	3.57	3.57	77.1
3000	2.50	3.57	59.1

Note: % O/F shift = $\frac{3.57 - 2.5}{3.57} = 30\%$
 % Q/A drop = $\frac{77.1 - 59.1}{77.1} = 24\%$

Since the subscale combustion chamber was designed to operate at a chamber pressure of 3000 psia with O₂/CH₄ propellants, heat transfer analyses were performed to determine the chamber pressure limit when testing with H₂/O₂. A simplified heat transfer analysis was performed where the wall temperature was held at 1460°R and a heat flux profile was generated. Chamber pressure was increased until there was a match in the highest heat flux to the design point. This comparison is shown in Figure 2.3.1-16. As shown, the heat flux in the combustion chamber is higher for the O₂/H₂ case, thus some of the coolant may have to be diverted to this section to keep the wall temperature below the design limit. This additional coolant is available in the nozzle section since the wall is running cooler in that area.

For brevity, and since the thermal models used in these analyses are for the most part mature, industry accepted standards, detailed description were not interwoven in the text. However, a brief description is provided as Appendix A to this report.

Design and analysis support for the calorimeter chamber continued during the fabrication of the chamber. During the machining of a sample chamber throat section, it was found that the coolant passage depths in the diverging section were deeper than those used in the heat transfer analysis. A heat transfer analysis showed that with these passages, there would be insufficient coolant available due to the requirement for more coolant in the deeper passages to maintain the required velocity. Another heat transfer analysis was completed and the passage heights were revised to reflect this latest analysis. With the more shallow passages, the analysis showed that it was possible to re balance the flow to require only 245 lbm/sec of the available 250 lbm/sec for a margin of 5 lbm/sec. Final flow balancing and orifice selection was accomplished when the coolant passages are flowed at P&W.

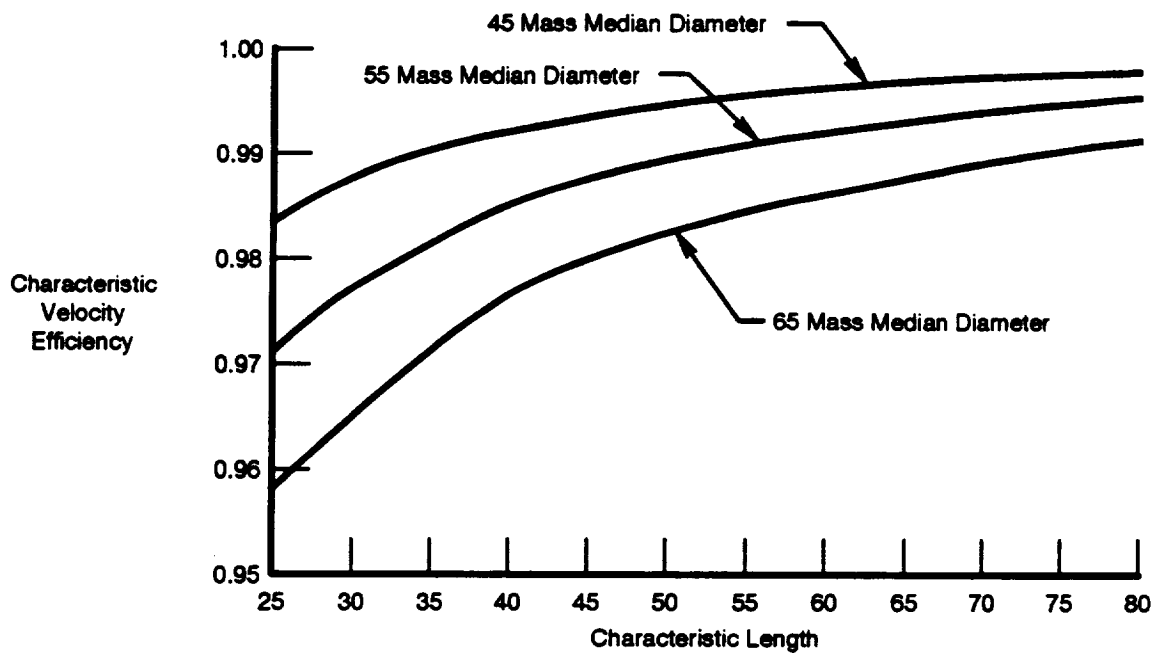


Figure 2.3.1-4. Effect of LOX Droplet Mass Mean Diameter on Subscale Chamber Characteristic Velocity Efficiency

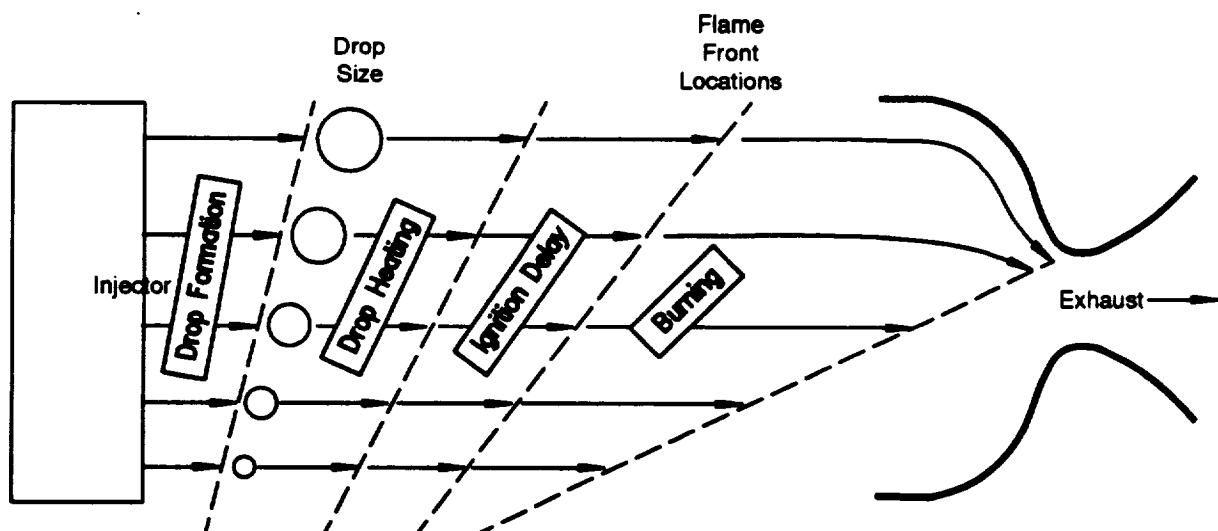


Figure 2.3.1-5. Supercritical Combustion Model

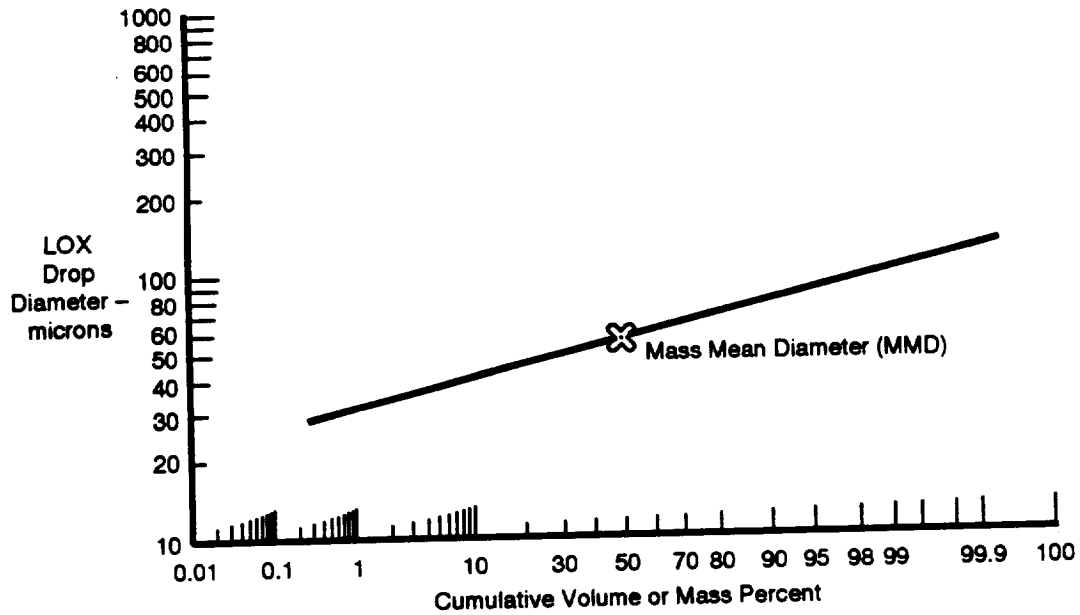


Figure 2.3.1-6. Predicted LOX Drop Diameter Distribution for the Subscale Combustion Chamber

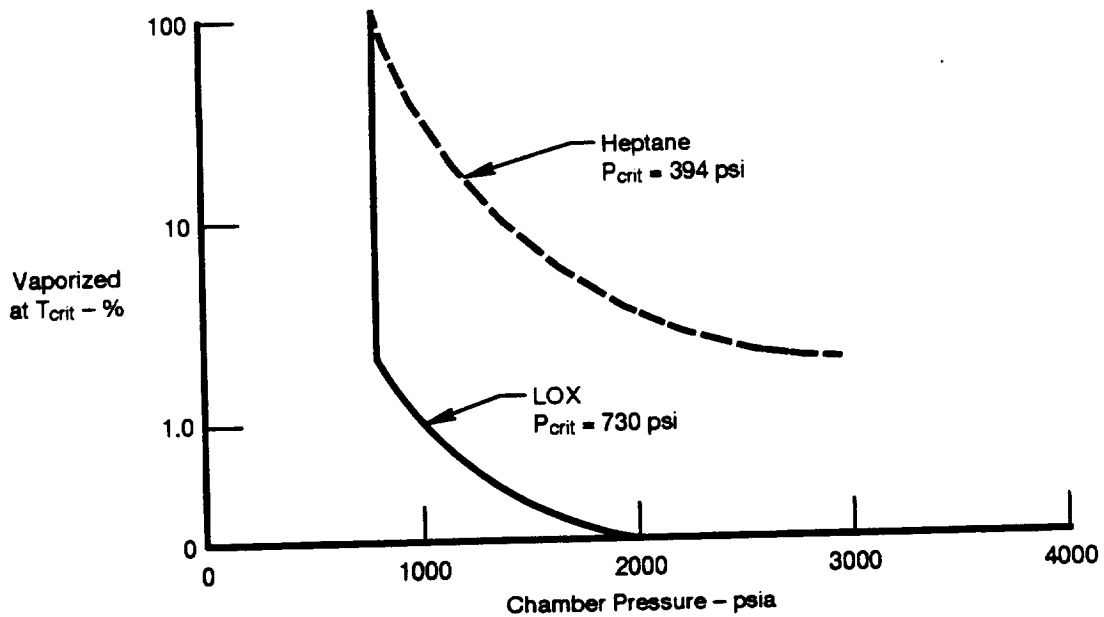
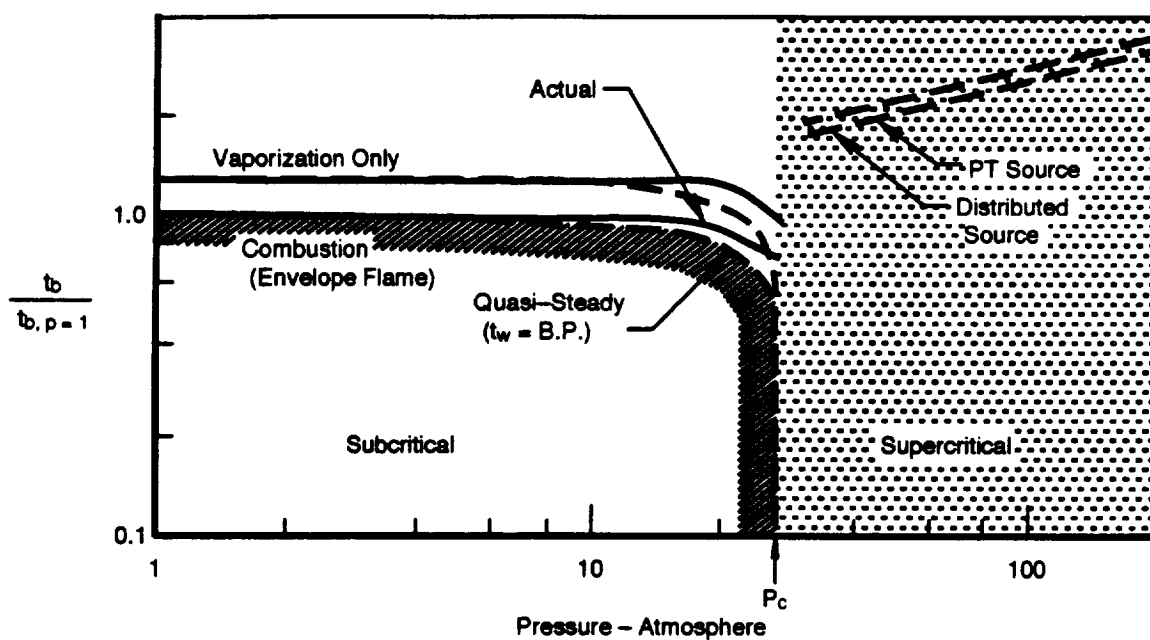


Figure 2.3.1-7. Subcritical Vaporization at High Pressure



Legend

t_b = Time to Burn Fuel Droplet
 t_w = Wet Bulb Temperature of Droplet
 B.P. = Boiling Point of Liquid Droplet

$\frac{t_b}{t_{b, p=1}}$ = Normalized Time to Burn or Vaporize – Time Required to Burn or Vaporize Same Size Droplet at 1 Atmosphere, Using Quasi-Steady Envelope Flame

P_c = Critical Pressure of Liquid
 PT = Pressure Temperature

Figure 2.3.1–8. Subcritical-Supercritical Burning Model Pressure Dependence of Normalized Combustion and/or Vaporization Time Typified by Kerosene Droplet in Air

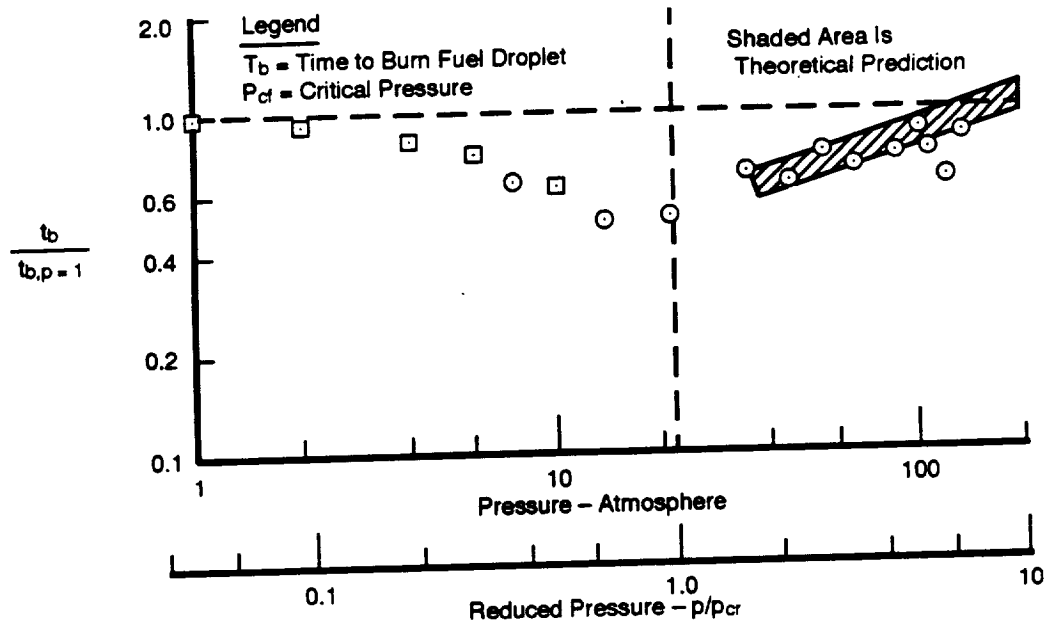


Figure 2.3.1-9. Experimental Effect of Pressure on Burning Rate Observed Time Required to Complete Combustion (Normalized by $P=1$ Atm) as a Function of Pressure for Normal Decane in Air

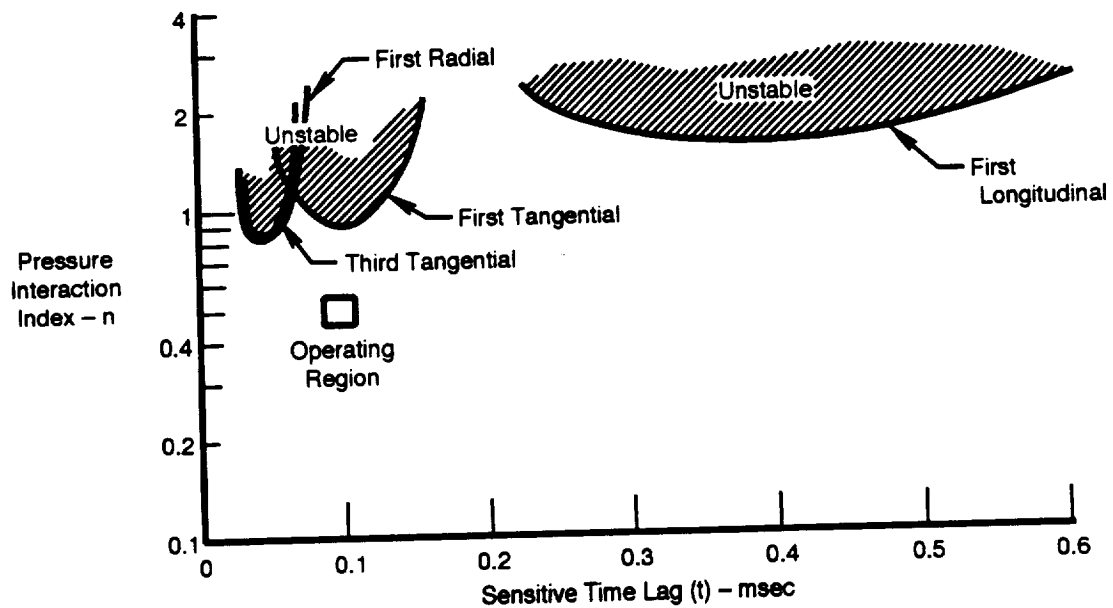


Figure 2.3.1-10. Stability Limits and Estimated n,t Zone for the Subscale Combustor

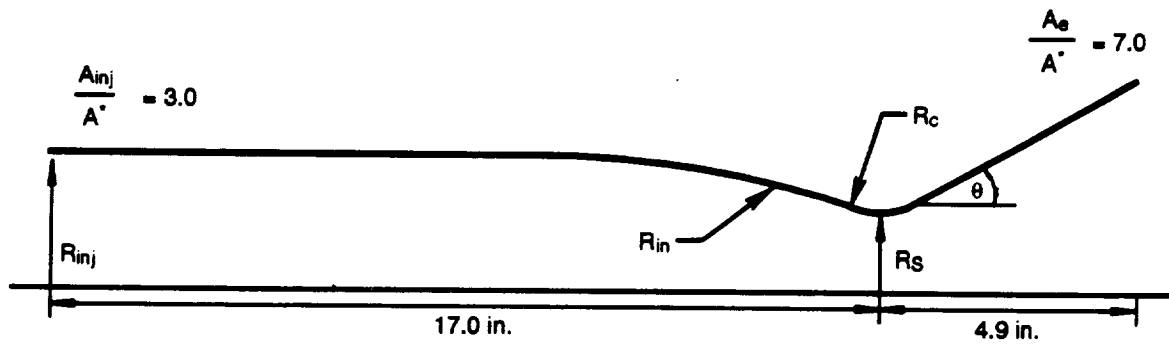


Figure 2.3.1-11. Schematic of Calorimeter Combustion Chamber Contour

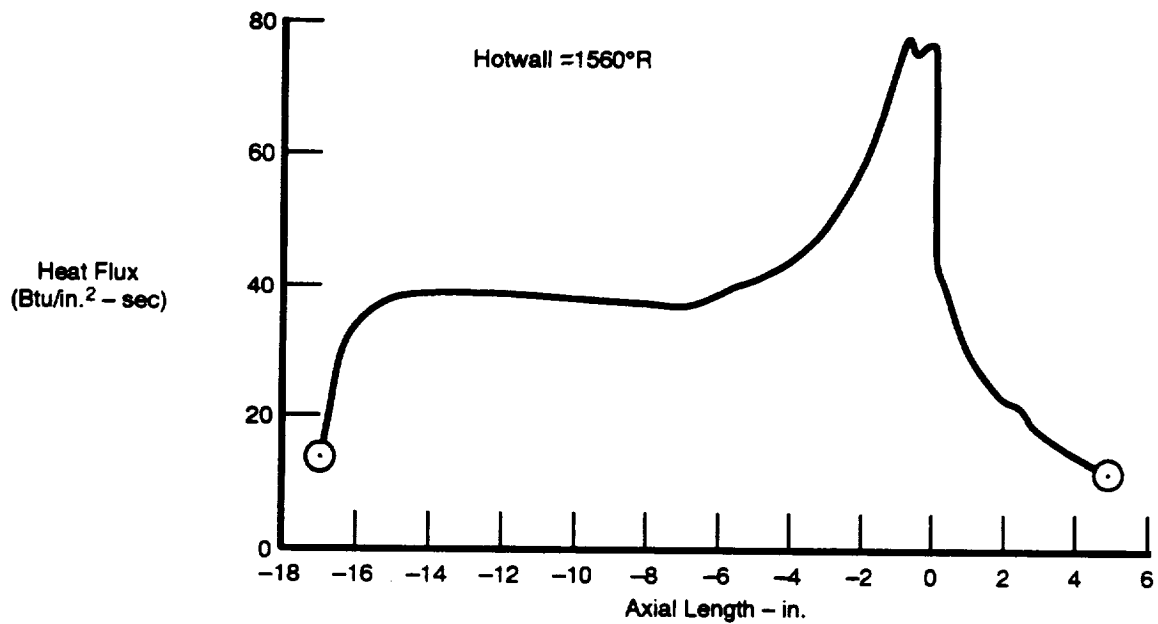


Figure 2.3.1-12. Calorimeter Thrust Chamber Predicted Combustion Wall Heat Flux Profile

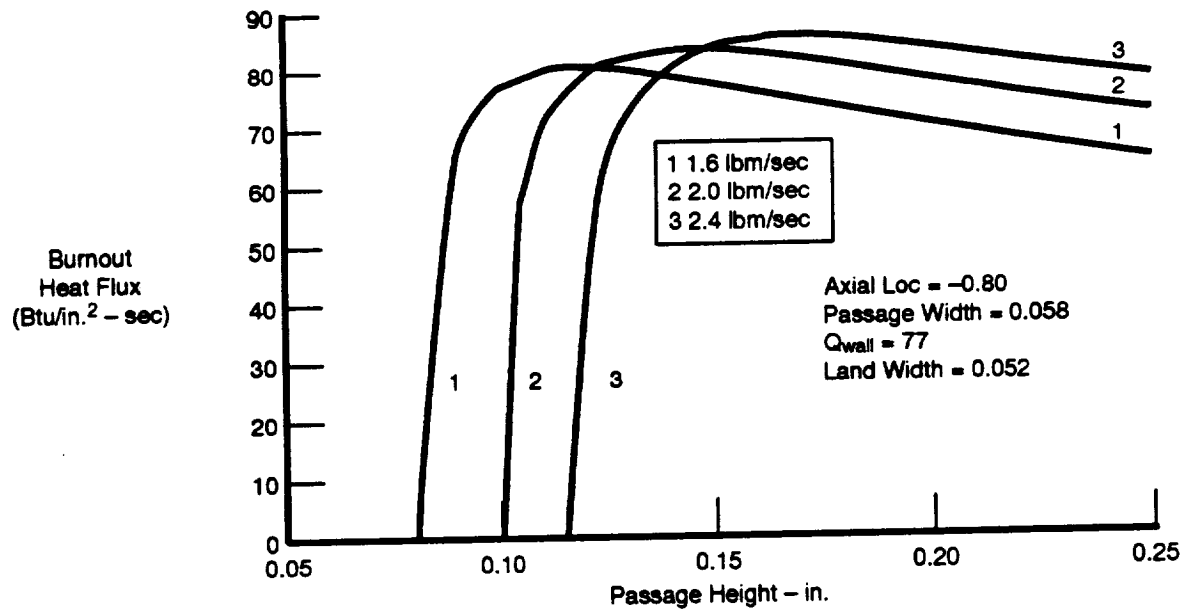


Figure 2.3.1-13. Calorimeter Thrust Chamber Burnout Heat Flux

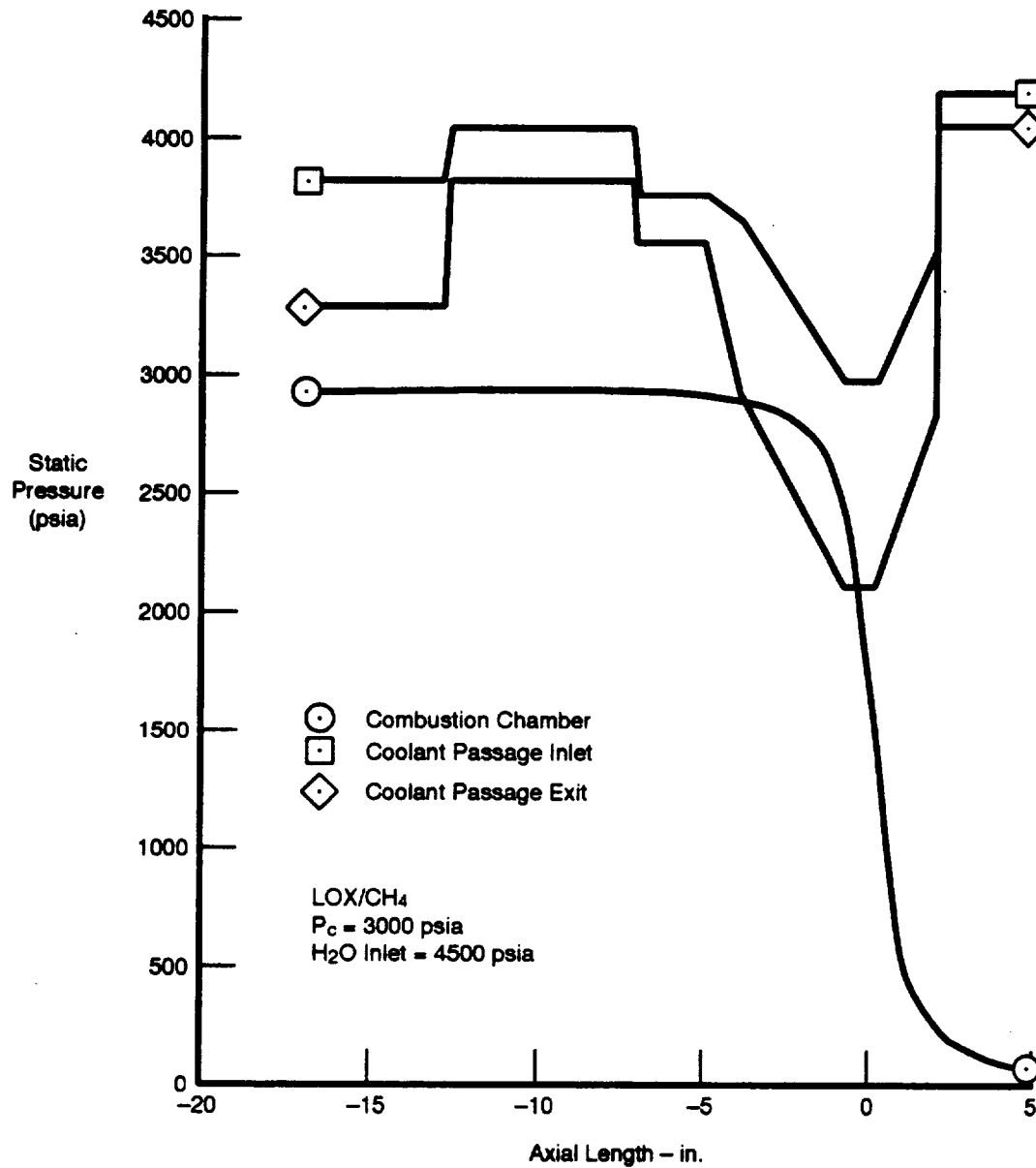


Figure 2.3.1-14. Subscale Combustor Static Pressures

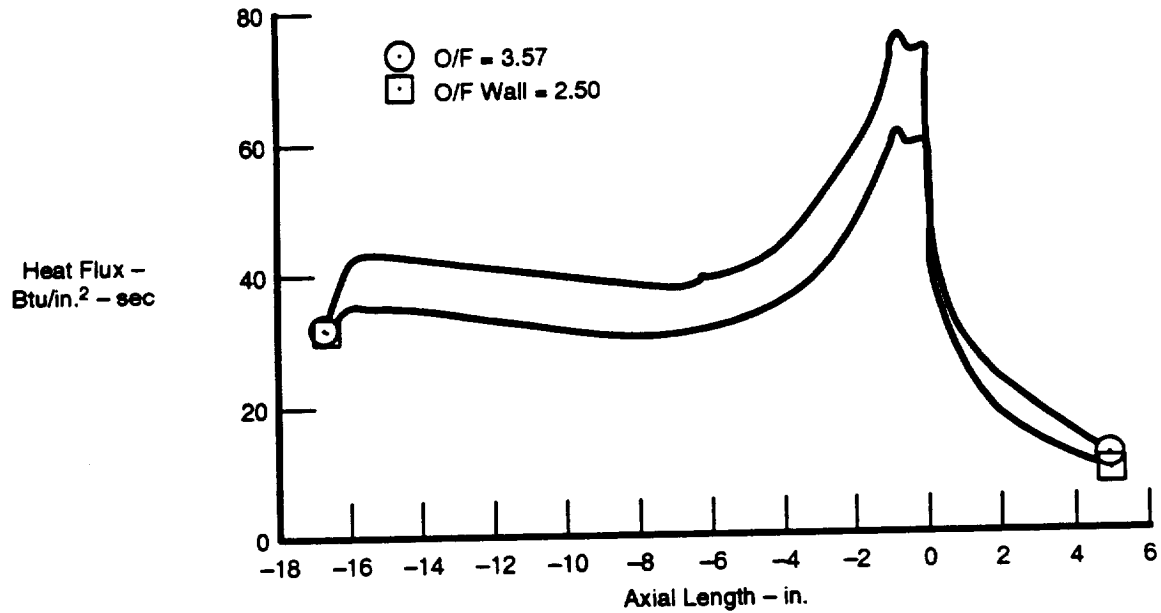


Figure 2.3.1-15. Combustor Wall Heat Flux

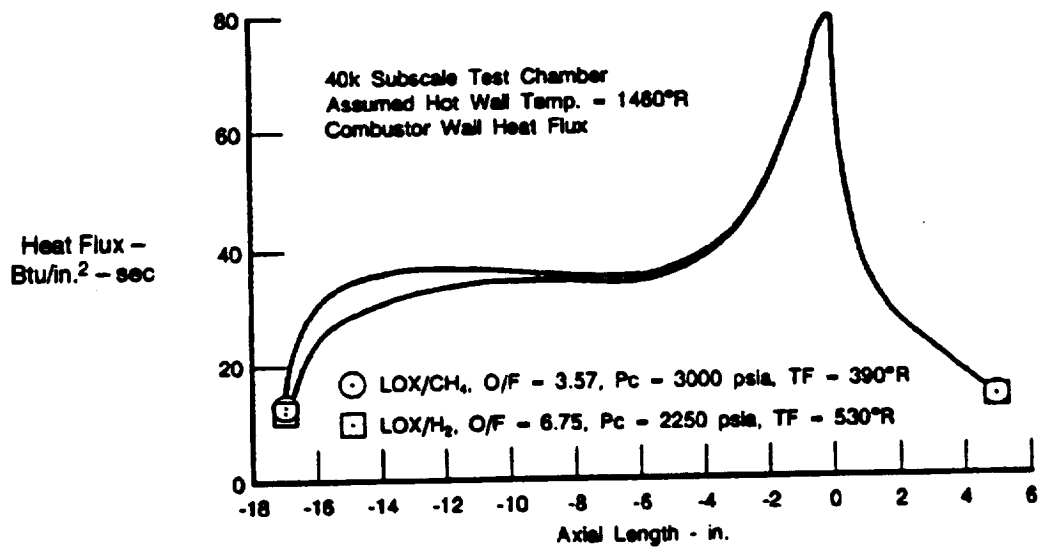


Figure 2.3.1-16. Combustor Wall Heat Flux for Two Propellants

2.3.2 Calorimeter Combustion Chamber Design History

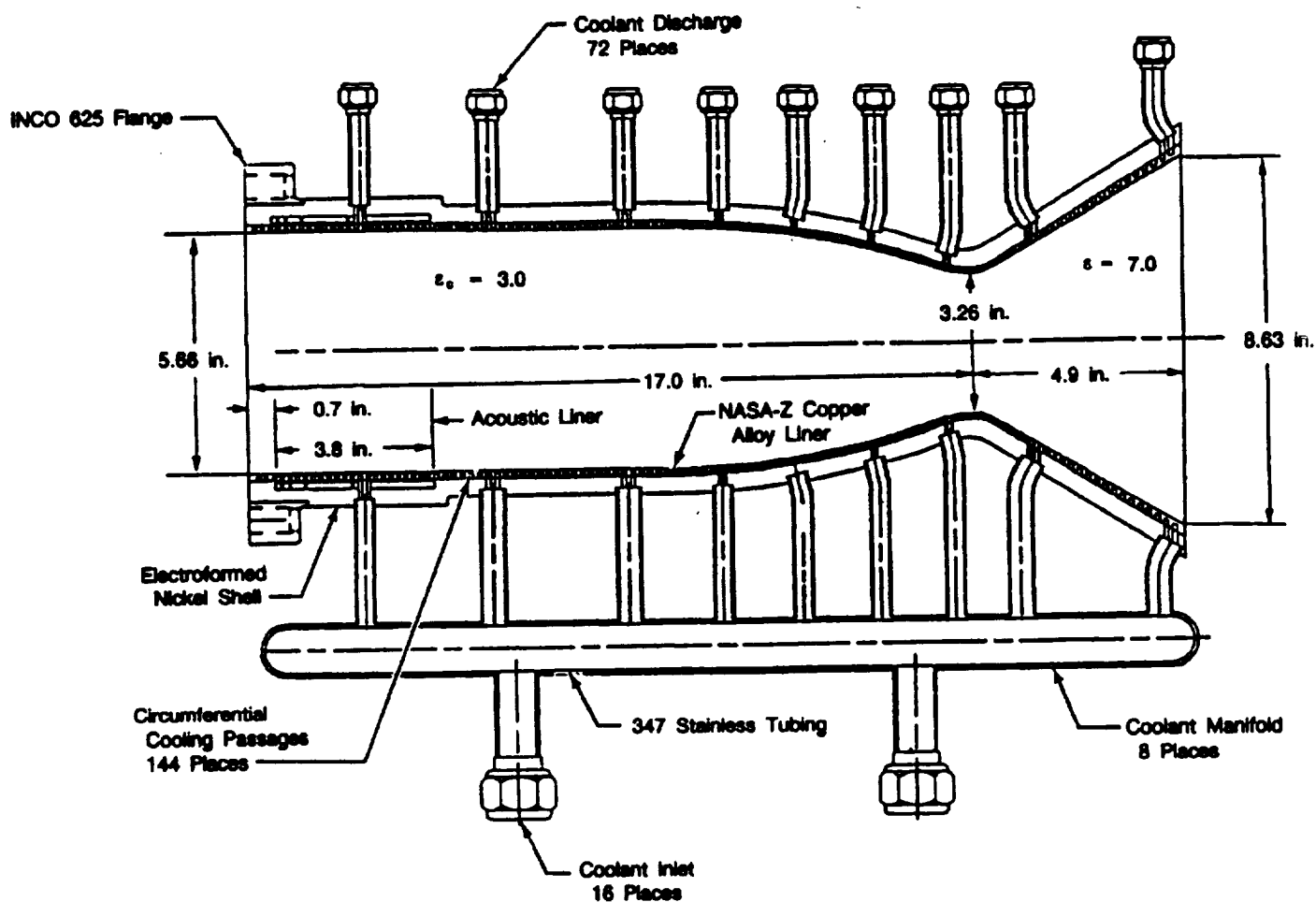
The initial design of the subscale calorimeter combustion chamber was essentially the same as that of the final design except for just a couple of significant differences. These differences include an acoustic liner in the original design as well as a different mounting scheme for the injector mounting flange. A cross-section of the initial design is shown in Figure 2.3.2-1.

In most locations, the coolant is fed directly from the coolant tubes into the pairs of channels as shown in Figure 2.3.2-1. Due to the proximity of the injector mounting flange to the upper two passages, this configuration could not be used. In the initial design, an alternate feed path to these channels was to be used as shown in figure 2.3.2-2. With this configuration, the water is routed through the flange and into a small internal manifold from where it then enters the coolant channels. The discharge is configured similarly.

The original design of the subscale chamber included an acoustic liner to absorb possible combustion instabilities. However, after methane was dropped from the program and hydrogen became the fuel, the risk of instability was low and the acoustic liner was considered to be unnecessary. So as a cost savings, the acoustic liner was eliminated from the subscale design.

In the initial subscale chamber design, The injector mounting flange was to be fashioned from INCO 625 and electron beam (EB) welded to the nickel closeout. However, the final weld sample trials revealed that a strong magnetization occurred when the electron beam was activated, bending the beam off course approximately 0.100 inch away from the intended path. Because of the schedule impact and cost of fabricating more weld samples to try to correct for the beam deflection, it was decided to revise the attachment configuration of the flange. The first alternate method for attaching the flange was to thread the two parts together using a buttress thread. The buttress thread was selected due to its high axial load-carrying capacity based on the success of similar designs in previous NASA-MSFC chambers.

Later, after working with the second electroforming vendor, a new flange attachment method was incorporated in which the flange design was revised from the buttress thread attachment method to an interference fit and subsequent encapsulation within the structural nickel closeout. A seal between the flange and the chamber would be created by electrodepositing a layer of copper (0.003 to 0.005 inch thick) onto the flange before installing it onto the chamber. The interference fit of 0.005 to 0.007 inch diametrical would cause deformation of the copper to assure a seal for the coolant from circuit to circuit. The external layer of nickel which would encapsulate the flange would provide the structure for the thrust load and acts as a seal to prevent external coolant leakage. This new design eliminated a possible leak path past the threads of the previous design that would have required a sealing braze, allowed machining of several port features into the detail flange ring, and saved time during the final fabrication by deleting the turning operation to machine the thread into the forward section of the chamber.



FD359893

Figure 2.3.2-1. Initial Subscale Combustor Assembly

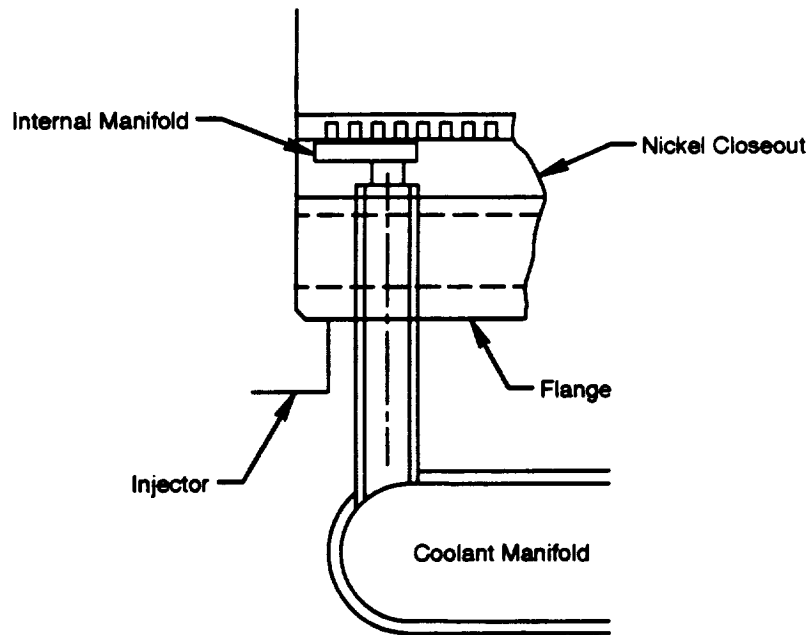


Figure 2.3.2-2. Forward Passages Coolant Feed

2.3.3 Calorimeter Combustion Chamber Fabrication History

Fabrication of the combustion chamber began with forging of the copper liner material. The copper liner was fabricated from a cast ingot of NASA Z copper alloy. This NASA Z material was spun forged to provide the needed material properties and to provide an hourglass shape from which to machine the liner. Two forgings were made. One was to be used to fabricate the chamber liner; the other would be a spare. NASA Z forgings were also obtained for fabrication samples of the acoustic liner and throat sections. These forgings were made from the same lot of material as the liner. Numerical control tapes were generated for the contour and coolant channel machining.

2.3.3.1 Machining Samples

Several trial machining samples were produced to provide confidence that the critical coolant passage and acoustic aperture liner machining could be done properly. These samples were used to set such machining parameters as speed and feed and to verify design of the cutters.

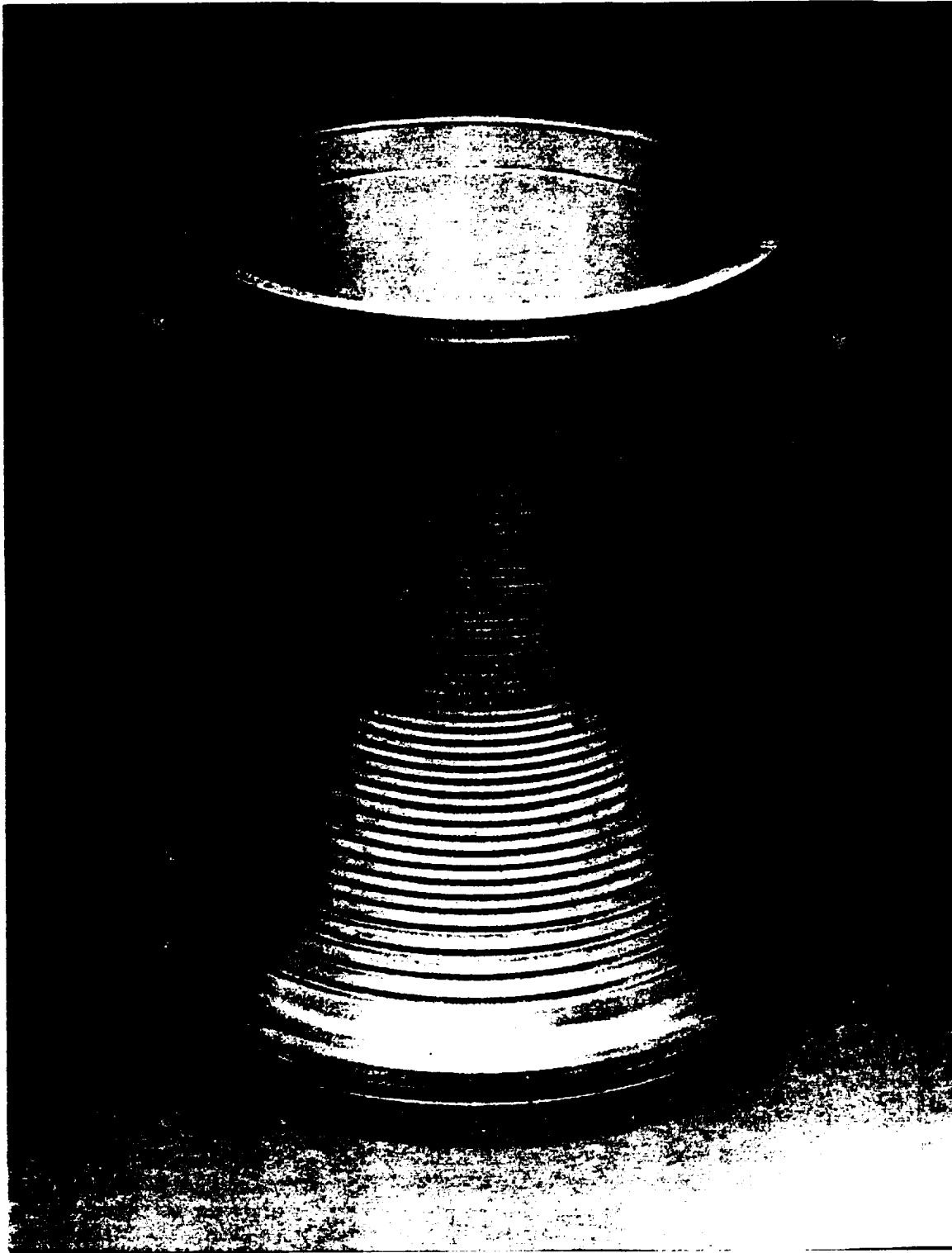
The first sample, an aluminum sample of the liner throat was machined to do the initial checkout of the numerical control (NC) tape. This sample is shown in Figure 2.3.3-1. During inspection of this piece an error was found in the angle of the external surface of the diverging section. The inspection record also showed that the channels in this section were cut deeper than originally assumed in the heat transfer analysis as discussed in the heat transfer section. During machining of this sample it was found that the cutters needed to be modified to provide additional clearance. During machining, in-process inspection of the contour dimensions and channel depths were accomplished. An acceptable agreement was found between these dimensions and those found with a coordinate measurement machine in the inspection area. Therefore, the in-process inspections could then be used on the other samples and the final part to determine the final depth of cut for the contour and the channels and to determine the internal contour final cut parameters to avoid a thin wall condition.

Next, an aluminum sample of the full liner was machined and is shown in process in Figure 2.3.3-2. The purpose of this sample was to check out the complete NC tape, check all cutters, and further investigate the

in-process measurement capability. In addition to these, since the tooling for the copper liner was available, this sample was used to provide tooling trials. During machining it was found that the tooling needed some minor modifications to provide additional support when turning the outside contour.

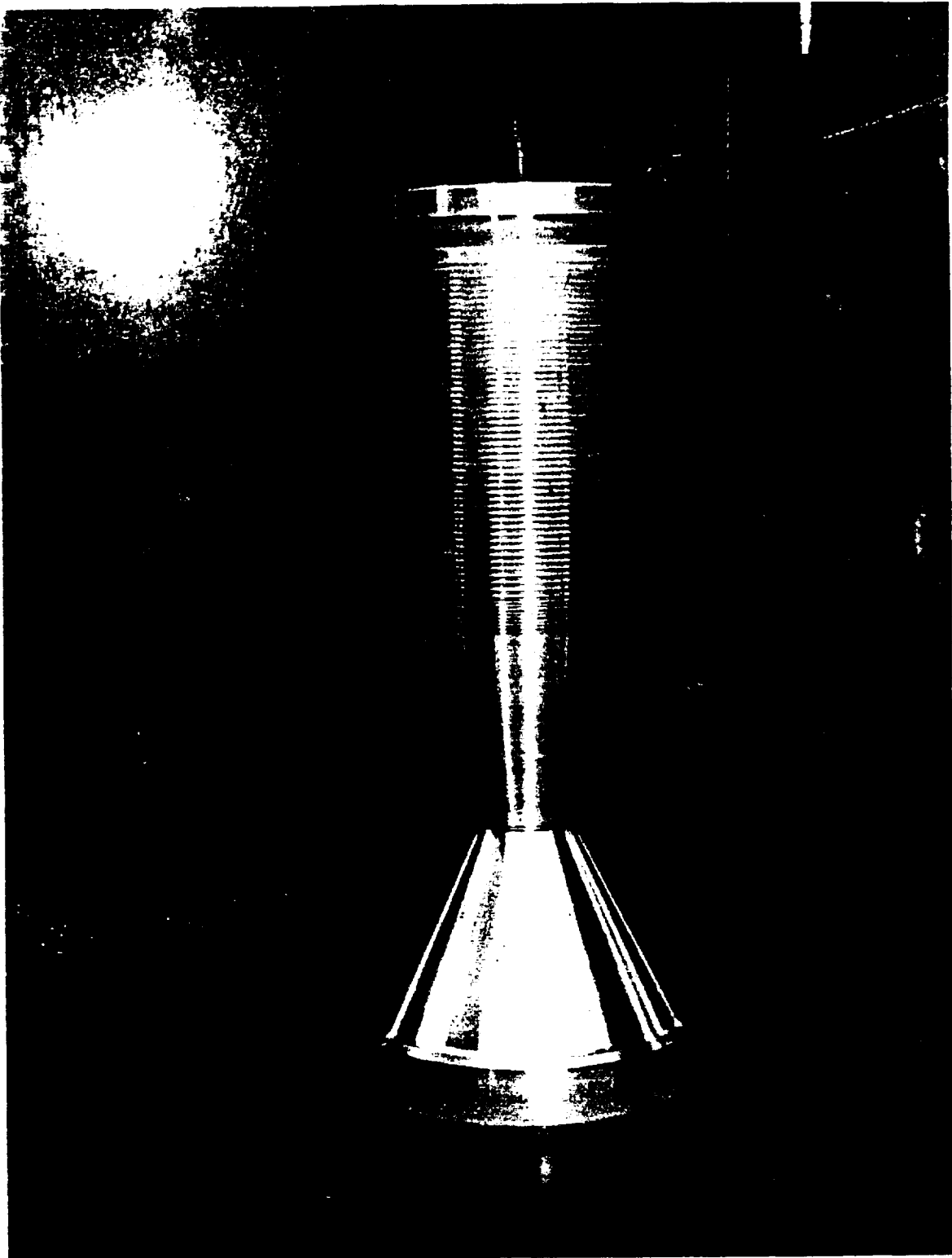
A NASA Z sample representing a section of the acoustic liner was machined and sent to a supplier for installation of the acoustic apertures. The purpose of the sample was to gain experience in machining of the NASA Z material and develop techniques for installation and electroforming of the acoustic apertures. Installation of apertures in a sample of a section of the acoustic liner was completed by a supplier. There were 168 apertures installed and no problems were encountered in meeting the blueprint dimensional requirements. This sample is shown in Figure 2.3.3-3.

A NASA Z sample of the liner throat was being machined as the final fabrication sample before committing the liner. During this machining it was found that the cutters for the contour needed additional modifications to cut the copper alloy that changes to the speed and feed rate were needed to achieve a satisfactory surface finish. This sample is shown during machining in Figure 2.3.3-4.



FE297667

Figure 2.3.3-1. Aluminum Liner Throat Machining Sample



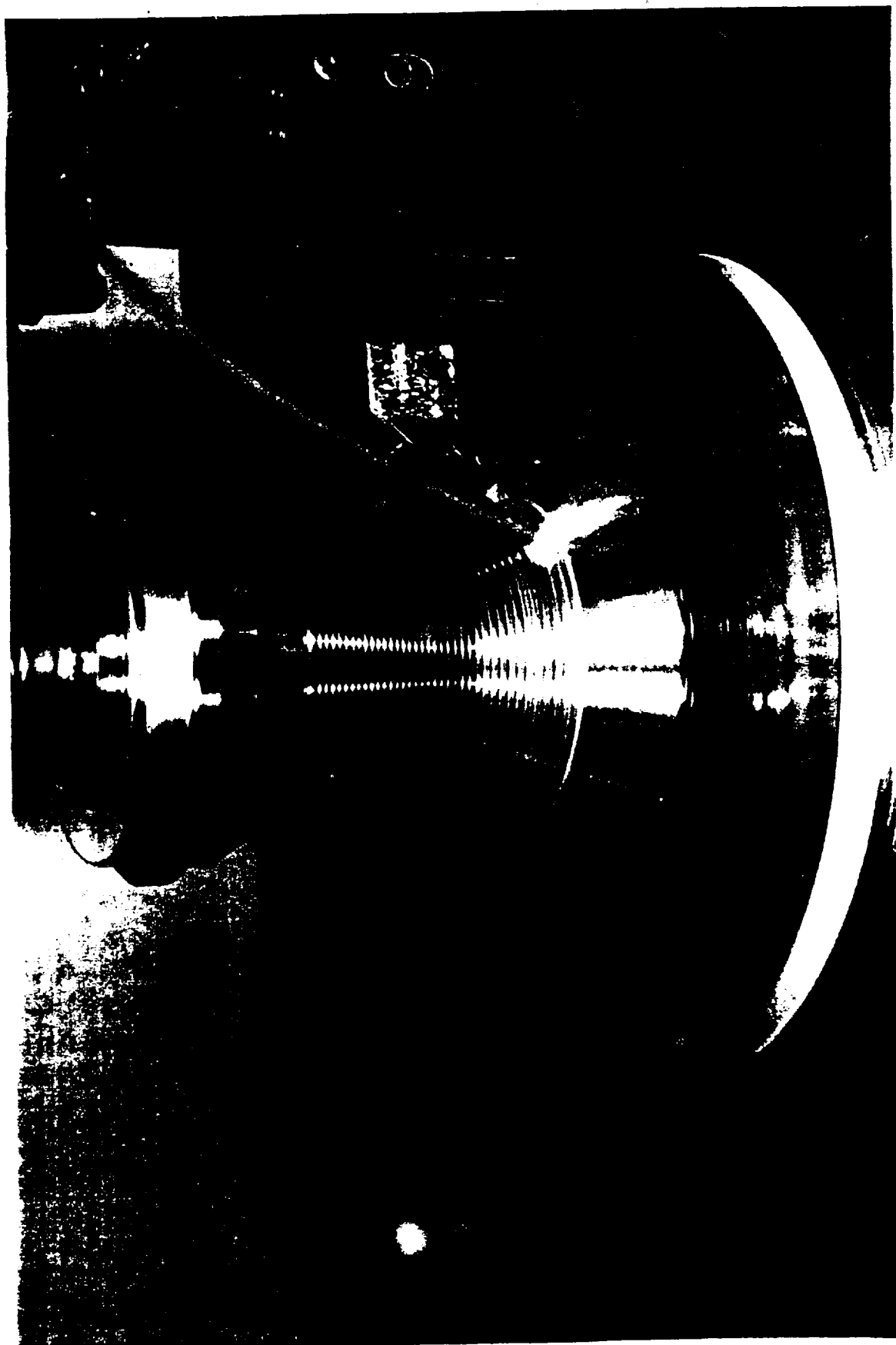
FE297661

Figure 2.3.3-2. Aluminum Liner Machining Sample During Machining



FE298102

Figure 2.3.3-3. NASA Z Acoustic Liner Machining Sample



FE 298420

Figure 2.3.3-4. NASA Z Liner Throat Sample During Machining

2.3.3.2 Copper Liner Machining

When the two NASA Z forgings for the combustion chamber were received and one was immediately released to the P&W shop to start fabrication. The other underwent sonic inspection to accurately determine the location of an inclusion found during the initial inspection at the vendor. This forging was obtained as a spare piece for manufacturing risk mitigation.

Machining of the chamber liner proceeded without incident until a chip hung during the installation of channel number 77. Machining of this liner is shown in Figure 2.3.3-5. This caused some damage to the adjacent lands. Machining was continued, since it was felt that this damage was not severe and could be cleaned up to provide acceptable performance. Channel 78 was installed without problem. However, during machining of channel 79 the cutter broke and caused severe land damage. This area was reviewed and it was determined that it could be repaired by removing the damaged lands, electrodepositing copper and remachining. Machining of the liner continued following this determination, however, three other areas of land damage occurred due to inadequate chip removal. An alternate method of machining was developed in which two passes were used to install a channel rather than a single plunge cut. This method was used to complete the liner machining without further problems. The damaged lands were removed as shown in Figure 2.3.3-6. P&W began machining the second liner forging after the second area of damage occurred.

Machining of the second liner forging was completed without incident using the approach demonstrated in completion of the first liner. In setting up this part, it was necessary to shift the machining center to assure that an indication found during ultrasonic inspection would be removed. Although it appeared that the indication would be removed during machining without a shift, a centerline shift of 0.015 inch was included to provide margin. The apertures for the acoustic liner were not installed because methane was dropped from the program and thus the acoustic liner was eliminated from the calorimeter chamber design. Once the machining of the second liner was complete, the damaged liner was cut in several pieces to be used in samples, and one piece was used to fabricate the transition spoolpiece.



FE298849

Figure 2.3.3-5. Machining of the First NASA Z Calorimeter Chamber Liner



Figure 2.3.3-6. First NASA Z Liner Showing Land Damage

FE 600511

2.3.3.3 Electroforming

Electroforming trials were conducted to determine the best method to closeout the combustion chamber coolant passages. The first attempts were made using a wax that contained silver powder. It was thought that this conductive wax would provide a more reliable and lower cost method to perform the closeout than the method traditionally used, in which nonconductive wax is used with a silver powder burnished into the wax to provide a conductive surface. The conductive wax would have eliminated the labor intensive burnishing step and avoided contamination of the copper surface with the silver powder. Samples were electroformed using this technique and an acceptable passage was formed; however, the resultant surface finish did not meet the design requirements. Since the conductive wax has silver suspended, it was not 100 percent conductive at the surface. When the plating was performed, it appeared that the plating initiated at the particles suspended in the wax and then bridged from particle to particle. This created a surface roughness which would have been unacceptable due to the large coolant pressure drop which would result. An additional sample was run using a nonconductive wax with silver burnished into the surface. This method produced a good passage shape and a surface finish ranging from 36 to 63 microinches. This was within the design requirement of 64 microinches. This was the method used to closeout the combustion chamber coolant passages. The combustion chamber is shown with the coolant passages filled with wax before burnishing with silver in Figure 2.3.3-7.

Bond samples were prepared from blocks of NASA Z to verify adequate strength and quality of the copper-nickel bond. The earliest samples demonstrated no delamination of the copper-nickel interface when subjected to chisel testing. A verification sample before liner processing revealed an unacceptable bond due to inadequate activation techniques. The sample result was later found to be due to contaminated activation solution, however, the result raised concerns about the bonding ability of the process. Investigation of various activation procedures resulted in the selection of a phosphoric/sulfuric process similar to the Space Shuttle Main Engine (SSME) procedure. Figure 2.3.3-8 shows a cross-section of a pressure test sample consisting of a serpentine channel in NASA Z and electroformed with 0.125 inch of nickel after being subjected to an internal hydrostatic pressure of 10,000 psi, with no failure of the bond joint. This pressure test subjected the bond and copper rib to 40,000 psi, while the actual liner will see less than 5,600 psi at the worst test condition.

A throat sample to measure cooling channel effective area (ACd) in the critical heat transfer area of the chamber throat was fabricated and then waterflowed. This sample was made by closing out some of the cooling passages on the NASA Z liner throat sample with ED-nickel. Ten coolant passages grouped into five flow circuits were flowed and measured for pressure loss and flow rate, and a system K ($K' = \Delta P / \dot{m}$) was calculated. The system losses were acceptable and within the predicted range.

A process was developed with the electroformer, in which the coolant passages through the nickel jacket were formed during the electrodeposit process. Nonconductive plugs were installed into the channels to form passages through the nickel jacket when the electrodeposition was accomplished. These plugs remained in place until the nickel deposition was complete (0.400 inch thick). The next step was to drill spot faces onto the chamber into which the coolant tubes would be welded. These spot faces were located using the nonconductive plugs as a guide. After the spot faces were drilled, the nonconductive plugs were removed exposing the copper liner and providing access to the channels. This method eliminated the electrodischarge machining (EDM) of the coolant passages that was originally planned; it was intended not only to save time, but also to eliminate the risk of EDM damaging the copper liner. This method is illustrated in Figure 2.3.3-9. Figure 2.3.3-10 shows the chamber with nonconductive plugs installed just before nickel deposition.

The combustion chamber electro-deposit process took about 6 weeks longer than scheduled due to a material transfer rate of 0.0006 in. per hour, rather than the predicted 0.001 in. per hour. Nodule growth around the nonconductive pins also slowed the process by requiring frequent removal of the liner from the plating tank to grind them off. Minor porosity was apparent in the throat region early in the process. This was determined to

be caused by insufficient surface speed to liberate the hydrogen gas bubbles formed during the process at this section due to the reduced diameter. Concentrated flushing of the electrolyte in the affected area resolved the problem. The final thickness at the forward flange end was achieved by shielding of the remainder of the liner, with the exception of the throat area (buildup lagged behind here due to increased distance from the anode and a shielding effect from the adjacent liner surface).

Weld samples were fabricated to prepare for the weld of the chamber flange to the closed out liner. Initial samples consisted of straight bars of INCO 625 (flange material) and NI-200 (simulating the electroformed nickel) to set the machine parameters, based on depth of weld and material properties. Afterwards, two samples of electroformed nickel were prepared. The first was an aluminum ring with nickel deposited. This was used to set up initial weld schedules and verify the depth of the weld heat affected zone. From this weld it was determined that a chill plug would be required to remove heat from the assembly in order for the weld to solidify rapidly. A fitted plug was machined for use with the next weld sample, which consisted of a section of a NASA Z liner built up with ED-nickel, dimensionally representative of the actual chamber. The intent of this sample was to closely duplicate the configuration of the chamber for establishing the final weld schedule and to ensure minimum distortion of the chamber due to the length (1.5 inch) of the weld as well as minimize heat input into the weld to protect the NASA Z to electroformed nickel bond.

In January 1990 the chamber completed nickel closeout and was delivered to the supplier for electron beam (EB) welding of the forward mounting flange. This weld would have consisted of a 1.5-inch deep full penetration weld to ensure complete sealing of the mating surfaces through which coolant ports will pass.

Final weld sample trials revealed that, although all parts were fully degaussed before welding, a strong magnetization occurred when the electron beam was activated, bending the beam off course and causing incomplete fusion of the two surfaces. The beam was deflected approximately 0.100 inch away from the intended path. Since further weld samples were required to correct for the beam deflection, and the lead time to produce geometrically accurate samples of ED nickel created an unfavorable impact on schedule, it was decided to revise the attachment configuration of the flange by threading the two parts together. A buttress thread was selected due to its high axial load-carrying capacity based on the success of similar designs in prior NASA-MSFC chambers. The chamber was delivered to P&W for modification, and fabrication of a new flange ring incorporating the thread was also started.

Upon receipt at P&W, the OD contour was machined to remove the nickel nodules which occur during electroforming and to provide a datum for installing the coolant tube spotfaces, followed by machining of the threaded portion for the flange. During the contour machining, delamination of nickel from the nickel substrate occurred in the throat region of the chamber. The thickness of the nickel in the throat was reduced to 0.152 inch (B/P requirement is 0.400 inch) before all evidence of delamination was removed. A structural evaluation was made to determine the strength capability of the resultant nickel shell. The chamber static pressure profile and the channel coolant pressure were used to calculate the maximum stresses in the nickel jacket over the length of the liner, along with the thickness required to maintain a factor of safety-to-yield of 1.2 or higher (Figures 2.3.3-11 and 2.3.3-12).

The thinnest nickel closeout remaining after final machining maintained a factor of safety greater than 4.0. Consideration was given to the heat-affected zone of the tube welds which locally reduces the nickel yield strength. Weld samples were metallurgically evaluated for depth of penetration to support the safety calculations.

Before continuing the scheduled machining operations, a hydrostatic proof test was conducted on selected channels to verify that all delaminated nickel had been removed and that the nickel-to-copper bond was sound. Four channels were tested, three in the throat region and one in the cylindrical section near the injector face. These were selected based upon remaining nickel thickness and maximum stresses. The channel in the cylindrical

section held 5400 psig (1.2 factor of safety over 4500 psig test condition) with no leakage. One of the throat channels also held the required pressure, but leaked slightly over into adjacent channels. The remaining two throat channels could not achieve full pressurization due to the volume of the leakage at adjacent channels above the pressure test system flow capability. Before-and-after helium leak tests revealed increased leakage following the proof test for the three throat channels. Visual observation indicated water leaking between nickel layers at the adjacent channel ports. Subsequent sonic inspection revealed areas of dis-bond within the nickel layer.

Three options were reviewed at this point: (1) continue processing, (2) remove the nickel in the throat area and replate at the original supplier (at no cost), or (3) remove all of the nickel and replate at a supplier with direct rocket thrust chamber closeout experience. Option 1 was dismissed as high technical risk due to the possibility of separating nickel layers under test conditions, exposing large surface areas to 4500 psig coolant water, with the resultant nickel layer thicknesses unknown. Option 2 was determined to be a moderate technical and schedule risk due to the still unknown condition of the remaining nickel-copper bond, and the development nature of the replating process at the original supplier. Partial nickel removal did not shorten the recovery period due to remaining processing requirements to ensure acceptability. Option 3 was selected as the lowest technical risk approach since it has the least remaining unknowns, and uses an experienced supplier with a proven closeout process.

Removal of the nickel was achieved by machining to within 0.010 inch of the original copper contour, followed by removal of the final layer using a commercially available stripping solution. The delaminated nickel layers revealed by the sonic inspection were confirmed as the machining progressed. Occasional unbonded regions were also revealed in the cylindrical section and at the conical exit area, reinforcing the decision to remove all of the nickel. The nickel-to-copper bond remained intact as the original contour was approached, mandating the use of the stripping solution to remove the final layer. A NASA Z/ED-nickel sample was run before the part to establish material removal rates and verify that no detrimental attack of the NASA Z occurred.

The nickel delaminations appear to have been caused by a multitude of conditions, depending on where they occurred on the liner. The throat area was a known low current density area (indicated by the slow rate of deposition during the plating cycle compared to the other areas) which could have resulted in insufficient electrochemical activation of each successive layer of nickel before re-immersion in the nickel solution. This low current density was due to the shielding effect of the surrounding larger diameters of the conical and cylindrical sections. Further aggravating the problem were the nonconductive plugs used to form the coolant ports, which in the throat section were very close to each other, again shielding the liner surface from full activation current. The areas on the cylindrical and conical sections were likely caused by contamination of the surface by activation solutions which were retained in the maskant foam used at either end of the part. The alternate supplier selected for redeposition of nickel used a refined process that concentrates current activation at the throat area, while shielding high density regions to prevent excessive buildup of nickel. Current density was also increased when using plugs, and the nickel was periodically machined back until a uniform surface is achieved from which to continue the plating. Not only does this remove any uneven nodular nickel growth which affects current density, but it also interrupts the enlarging grain growth and reduces residual stresses.

EF Nickel, Corona CA. was chosen as the replacement supplier due to their experience base in closeout of rocket chambers. Their chief metallurgist, Glenn Malone, had previous experience with copper chambers for NASA Lewis Research Center, and is currently engaged in contracts with NASA and Aerojet. They also had established procedures for the process techniques required; i.e., waxing the channels, silver burnishing, use of nonconductive plugs to form ports, etc. They were selected as the most capable of the vendors available to deliver a quality product without the development problems that occurred previously, and were able to meet the accelerated schedule requirements.

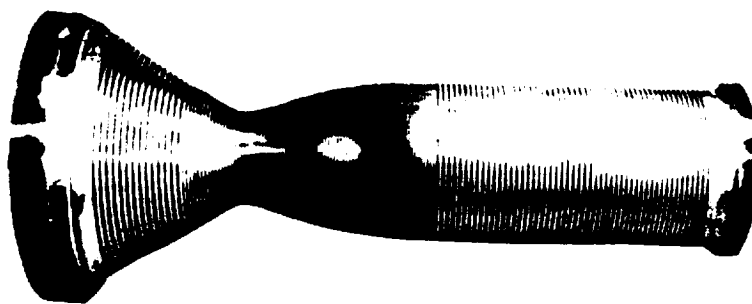
Working with the new electroforming vendor, the subscale thrust chamber forward flange design was revised from the buttress thread attachment method to an interference fit and subsequent encapsulation within the

structural nickel closeout. A seal between the flange and the chamber would be created by electrodepositing a layer of copper (0.003 to 0.005 inch thick) onto the flange before installing it onto the chamber. The interference fit of 0.005 to 0.007 inch diametrical would cause deformation of the copper to ensure a seal for the coolant from circuit to circuit. The external layer of nickel which would encapsulate the flange would provide the structure for the thrust load and acts as a seal to prevent external coolant leakage. This new design eliminated a possible leak path past the threads of the previous design that would have required a sealing braze. The change also allowed machining of several port features into the detail flange ring, deleted the turning operation to machine the thread into the forward section of the chamber after arrival at P&W, and saved time during the final fabrication.

Following removal of the initial electroformed nickel closeout the chamber was prepared (i.e., channels were filled with wax and burnished with silver, then immersed in the plating solution at EF Nickel in Corona, CA). Process techniques that differed from the prior electroforming company included nickel flash (0.002 to 0.005 inch) of the copper lands before wax filling and silver burnishing of the channels to prevent copper bleed-out contamination during activation, use of an activation solution tailored to nickel exclusively, and orientation of the liner horizontally to allow in-the-tank inspection during the electroforming process (Figure 2.3.3-13). In addition, individual plastic tabs were injection molded to provide the form needed to create the coolant passages through the nickel (Figure 2.3.3-14). These were inserted into the coolant passages following installation of the wax filler and burnishing with silver. The use of individual tabs was recommended rather than using an integral pair, as was done the first time, to allow for flushing of the plating solution between each channel. It is suspected that during the first electrodeposit attempt the solution stagnated at the tab pair, locally starving part of the required nickel and creating depressions at each coolant port.

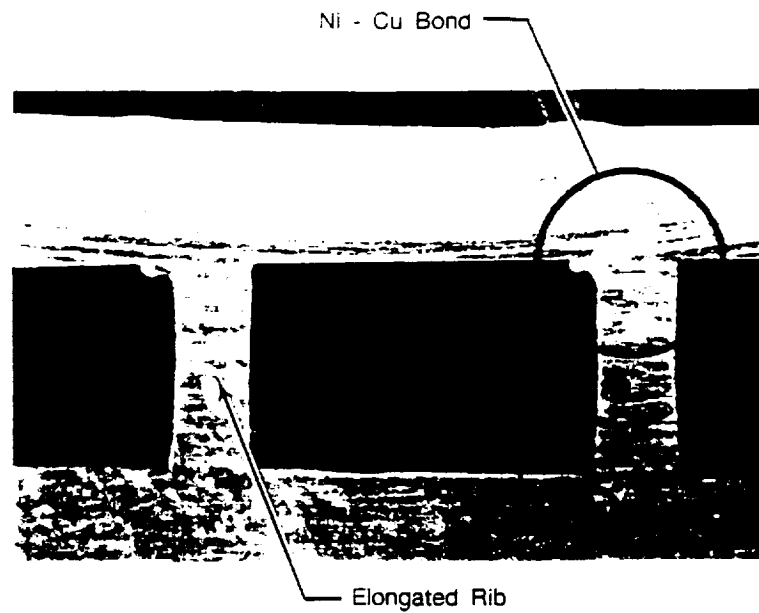
The primary technique that provides for a strong, reliable bond between subsequent nickel layers is the machining of the liner contour before reactivation. This interrupts the nickel grain growth and prevents large grain formation improving material properties while restoring the original contour to the chamber. In discussions with the current electroformer, it was indicated that one possible reason that we had previously experienced nickel delamination was the interim grinding of the nickel rather than machining, and because many of the abrasive grinding disks use silicon binders and the silicon was not removed with normal activation procedures, the surface was contaminated preventing a good bond.

Installation of the forward flange as discussed above was accomplished without difficulty, followed by the final nickel closeout of the liner and concurrent encapsulation of the flange (Figure 2.3.3-15). After completion of the electroforming, the chamber was shipped back to P&W.



FD368814

Figure 2.3.3-7. Chamber Liner — Waxed and Prepared for Silver and Plugs



FD368808

Figure 2.3.3-8. Electroformed Nickel to NASA Z Bond Sample

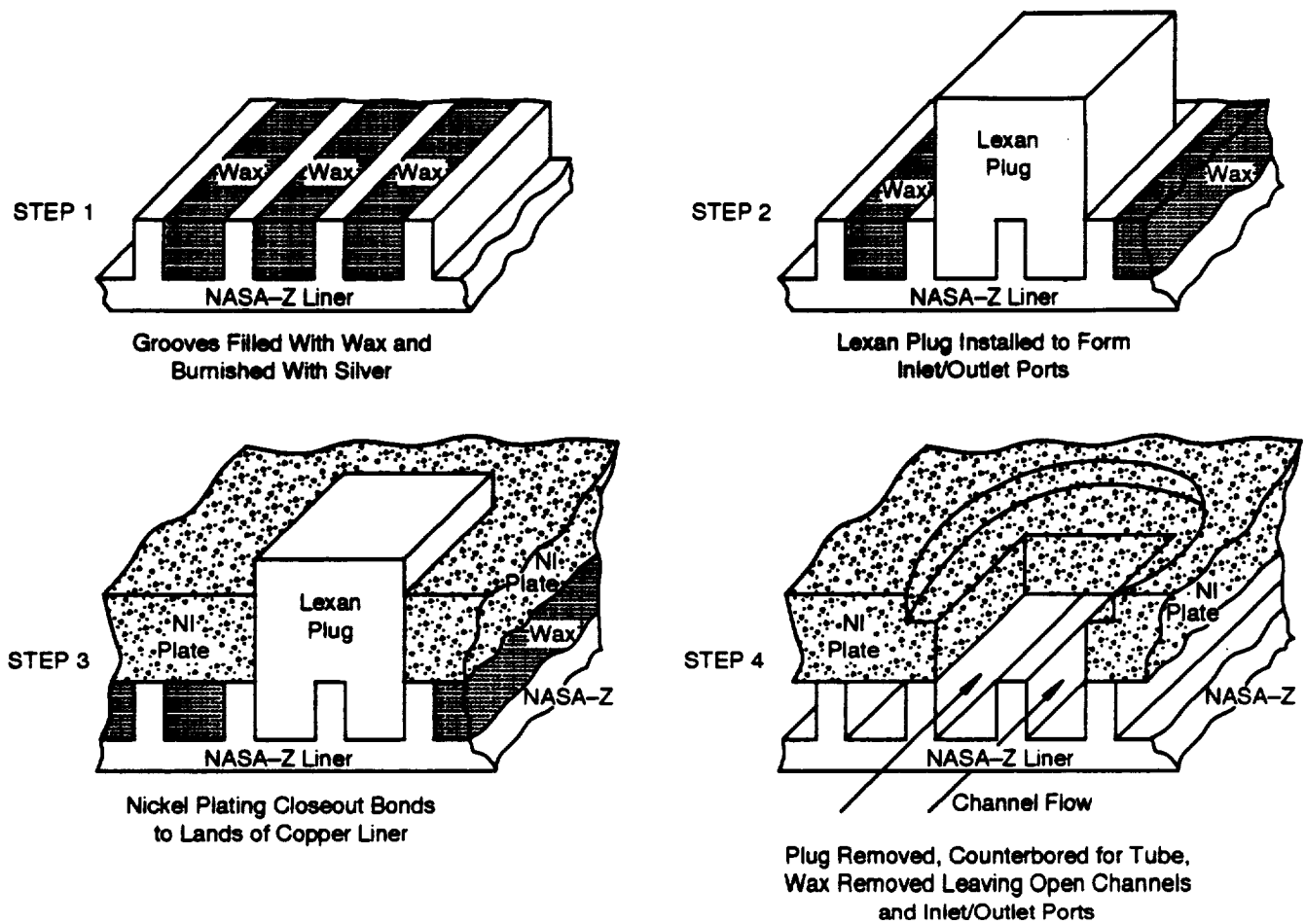


Figure 2.3.3-9. Nickel Deposition Process



FD368815

Figure 2.3.3-10. Chamber Liner Prepared for Nickel Deposition

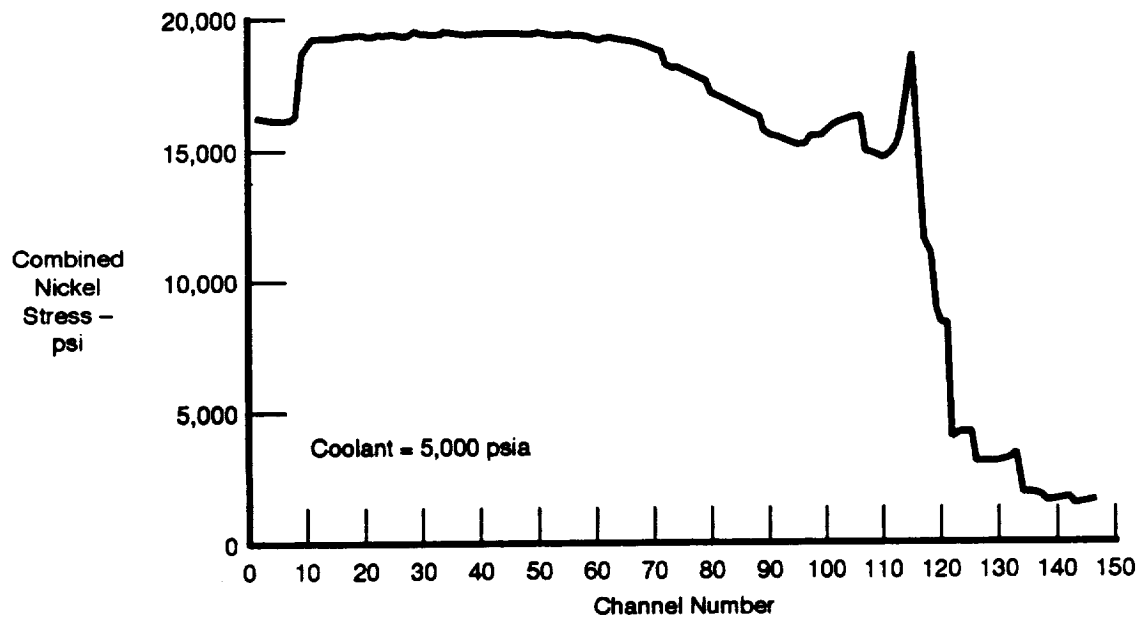


Figure 2.3.3-11. Nickel Stresses Due to Chamber Pressure and Coolant Pressure

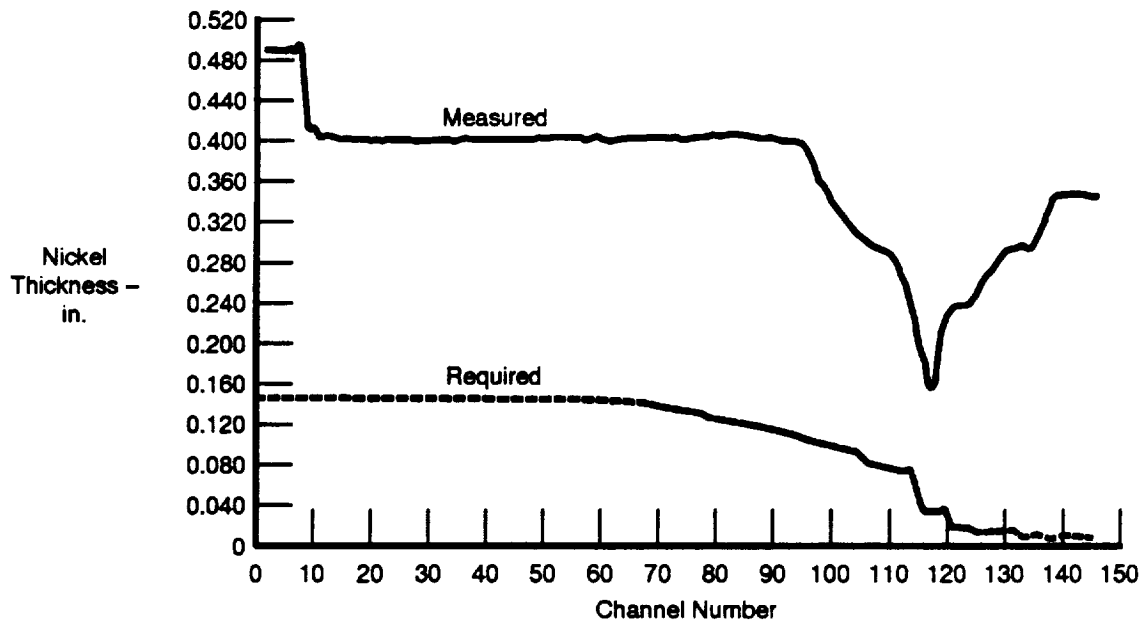
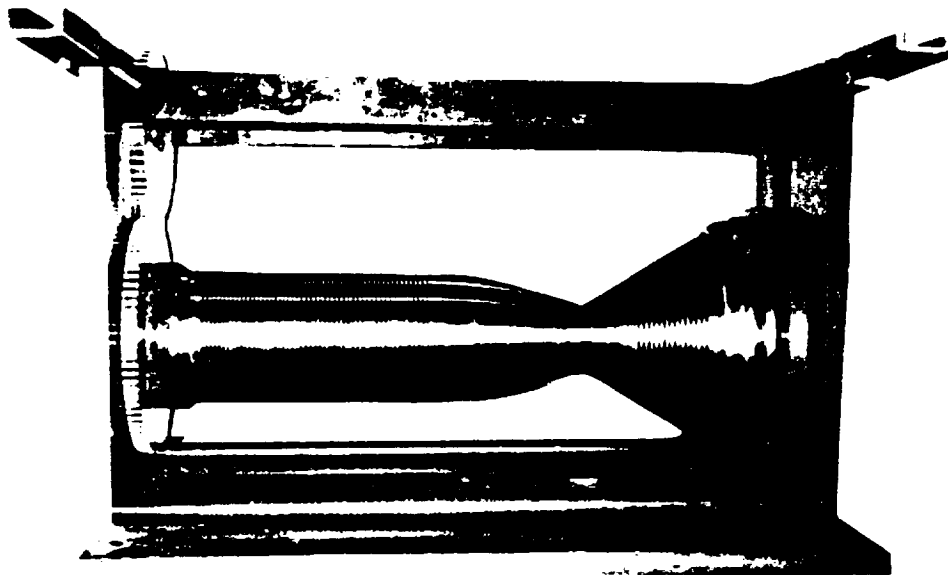
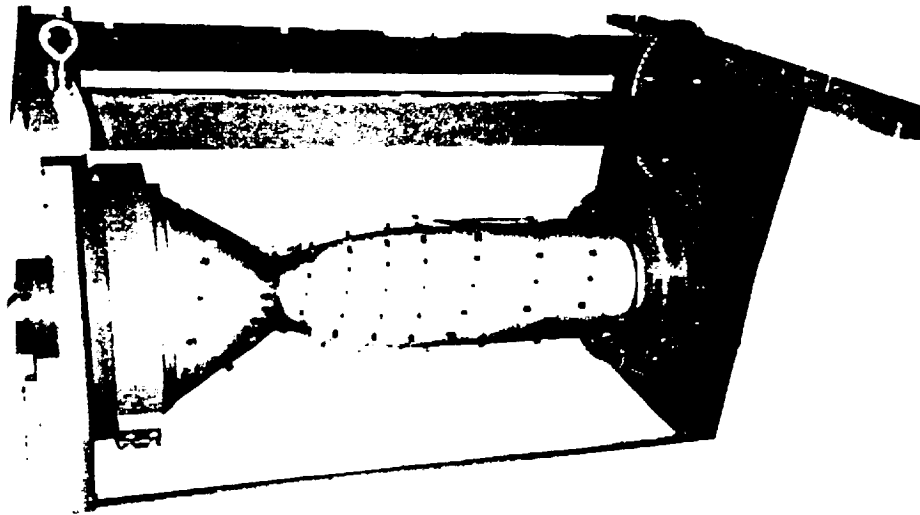


Figure 2.3.3-12. Nickel (59,300 Y.S.) Thickness Required for Calorimeter



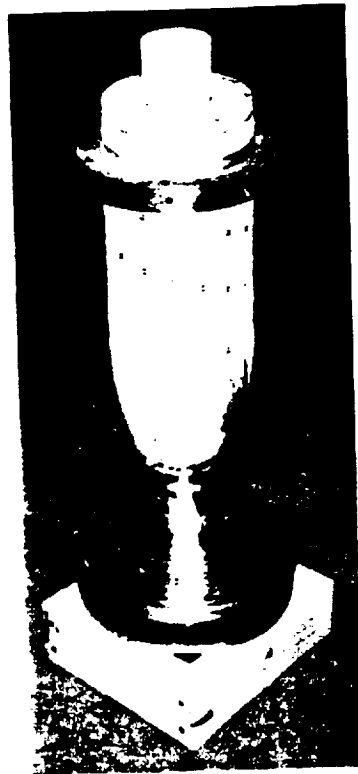
FC114669

Figure 2.3.3-13. Subscale Chamber With Wax-Filled Grooves Mounted in EF Fixture



FC114668

Figure 2.3.3-14. Subscale Chamber With Nickel Jacket and Port Tabs Installed



FC114670

Figure 2.3.3-15. Subscale Chamber With Mounting Flange Installed

2.3.3.4 Final Machining and Assembly

Machining of the chamber at P&W commenced with turning of the OD contour (Figure 2.3.3-16) followed by spot-facing of all inlet and outlet ports to accept the tubes. An interim proof test was then conducted with 5000 psig water to check the forward flange ports 1 through 5.

Proof testing of the forward flange cooling ports following initial machining revealed an internal leak path between ports 3 through 6. The volume of the leak was such that at 5000 psig the water escaped as a mist from port 6, and as a slow drip (approximately one drop per second) out of ports 3, 4 and 5. Since port 6 did not intersect the flange-to-chamber interface, it was concluded that a minute leak path connected it with adjacent channels. Based upon the low flowrate, the most probable cause was an axial scratch across the copper lands which was wax-filled during the plating process. Since the pressure differential across adjacent channels was minimal at operating conditions (i.e., all channels had 4500 psig supply), there would be no significant crossflow between these channels.

To seal any possible leakage between ports 1 through 5 at the flange-to-chamber interface due to operating stresses and pressures, both inlets and outlets of these ports were counterbored and tapped to receive threaded tubes with O-rings at the ends. The counterbores extend past the interface into the structural nickel jacket underneath, where the teflon O-ring seals the leak path around the end of the threaded tube. Before incorporation, a sample plate with a simulated interface was counterbored and assembled as described, then subjected to a 5000 psia hydrostatic proof test. Combinations of teflon O-rings with and without teflon tape on the threads were tested, with both performing flawlessly. The combination of O-ring and teflon tape was selected and incorporated into the chamber assembly (Figure 2.3.3-17).

Upon receipt of a small right-angle borescope, the coolant passages were inspected for blockage. At this time, all outlet tubes had been installed. Borecope inspection revealed blockage of all passages to varying degrees at the port entrances. The blockage was nickel flash from the electroforming process that formed in the small voids between the plugs used to form the ports and the adjacent wax (Figure 2.3.3-18). Several methods of removing the flash were investigated. Due to the narrow width of the channels and the chips resulting from a cutter, machining the slots larger was dropped from consideration. Abrasive media flow, or Extrude Hone™, was attempted on port 72, the last port at the nozzle opening. Sufficient media flow and pressure could not be achieved to remove the nickel flash without simultaneously removing an unacceptable thickness of surrounding copper in the channel. Therefore, EDM was selected as the lowest risk approach to remove the blockage by enlarging the port opening. For this process, all previously installed outlet tubes had to be removed. These were cut off and trimmed for reuse.

Following EDM removal of the nickel flash, a waterflow calibration was performed on all ports. Each slot within a port was separately calibrated to ensure equal flow split. Results were as predicted in the critical heat flux area of the converging section (Figure 2.3.3-19). Although the other areas did not flow as predicted, analysis shows that orifice sizing will provide flow to achieve the required heat flux into the coolant water. Initial orifice sizes were selected to achieve the required flow rates in each port. Slot-to-slot variation within each port was less than three percent in the worst case.

The fabrication of the chamber coolant supply and discharge tubes was done in parallel with the chamber fabrication. The tubes and manifolds were manufactured as subassemblies, which included the brazing of ferrules and nuts to tubes. The tube subassemblies were then welded to the combustion chamber.

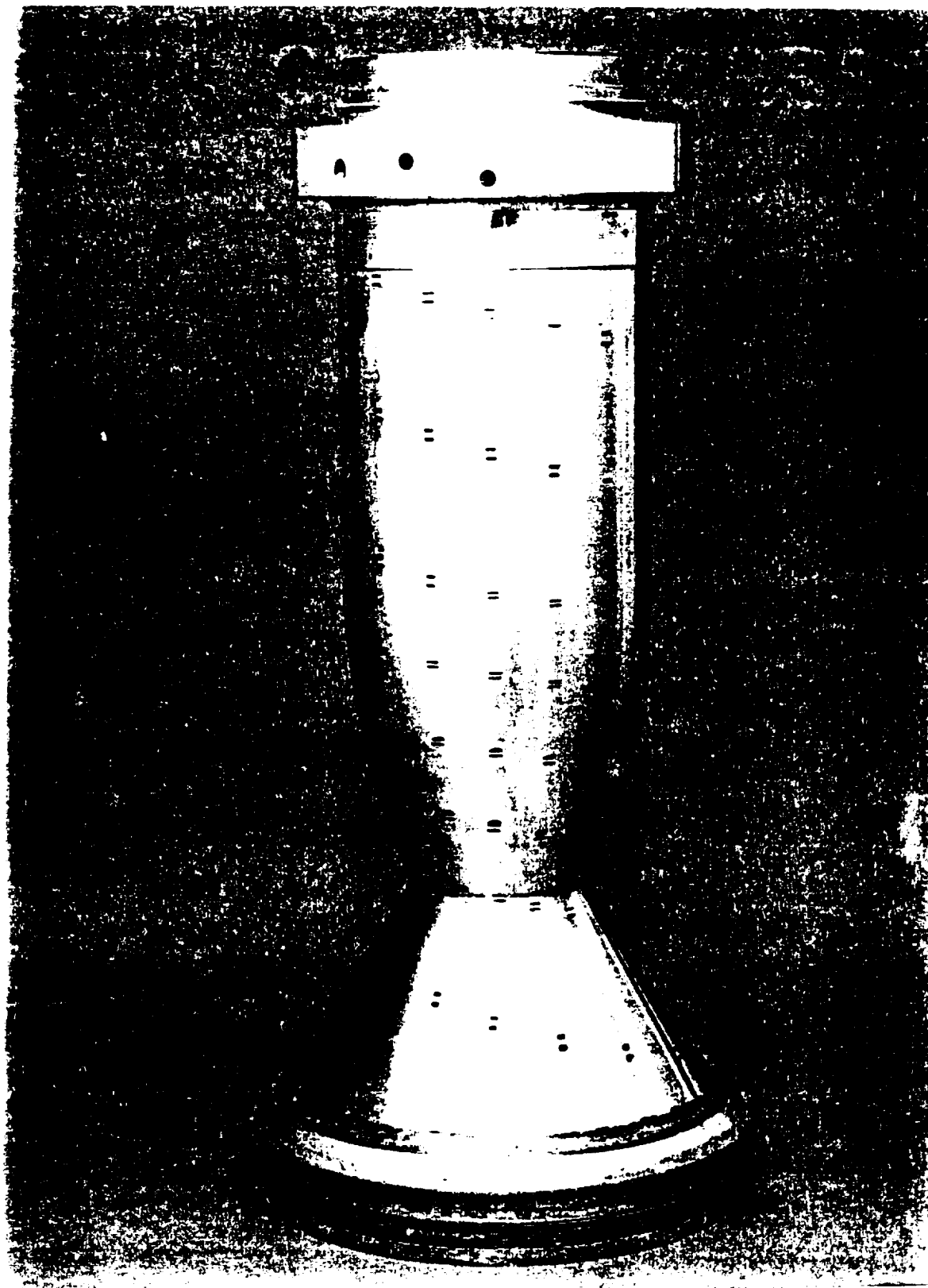
During producibility discussions with fabrication research, planning, and shop personnel concerning the welding of the tubes and manifolds, it was suggested that the manifolds be split axially to enhance welding to the inlet tubes. Following analysis of stresses across the resultant welds needed to rejoin the manifolds, the design

was revised to incorporate this suggestion. Welding in this manner allowed optimization of the weld sequencing and reduced the fabrication time required for these operations.

After the welding operations to install the inlet tubes, the outlet tubes, and the manifolds (over 240 separate welds) (Figure 2.3.3-20), the final proof test at 5400 psig of all channels and plumbing simultaneously was accomplished with no leakage. The chamber was cycled ten times from 0 psig to 5400 psig without incident.

Final machining of the chamber forward mounting flange and overall length followed completion of the proof test.

The chamber was cleaned, including the copper channels, by flushing with a copper brite dip for 20 seconds, followed by water rinsing; then final inspection was completed. Figures 2.3.3-21 and 2.3.3-22 show the completed combustion chamber. The chamber was then assembled to the injector for a fit check, successfully leak checked with 50 psi helium, and disassembled. Shipment to NASA was made on July 26, 1990.



FE008971

Figure 2.3.3-16. Subscale Chamber Following External Contour Machining

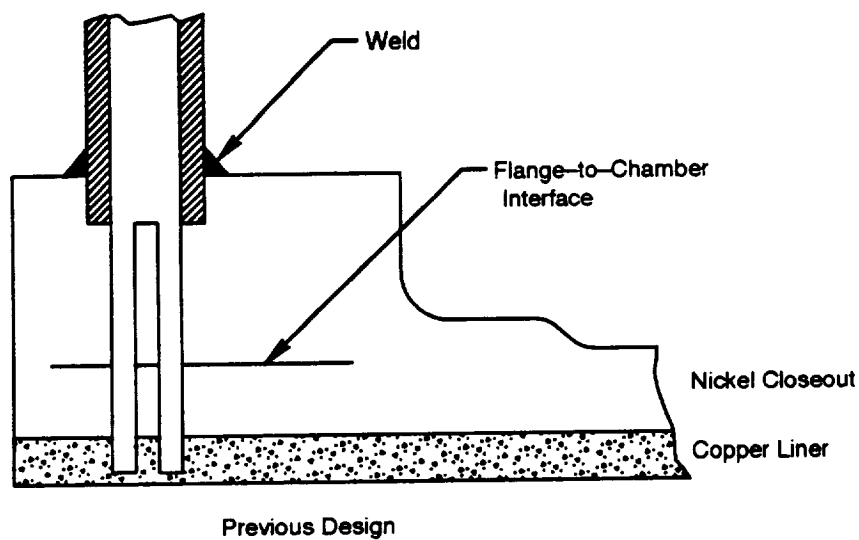
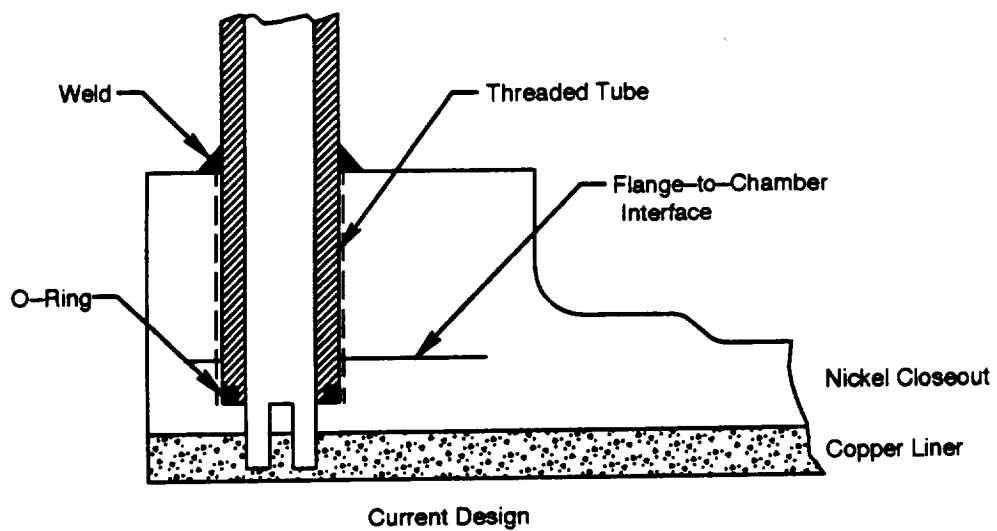


Figure 2.3.3-17. Flange-Chamber Interface — Current and Previous Designs

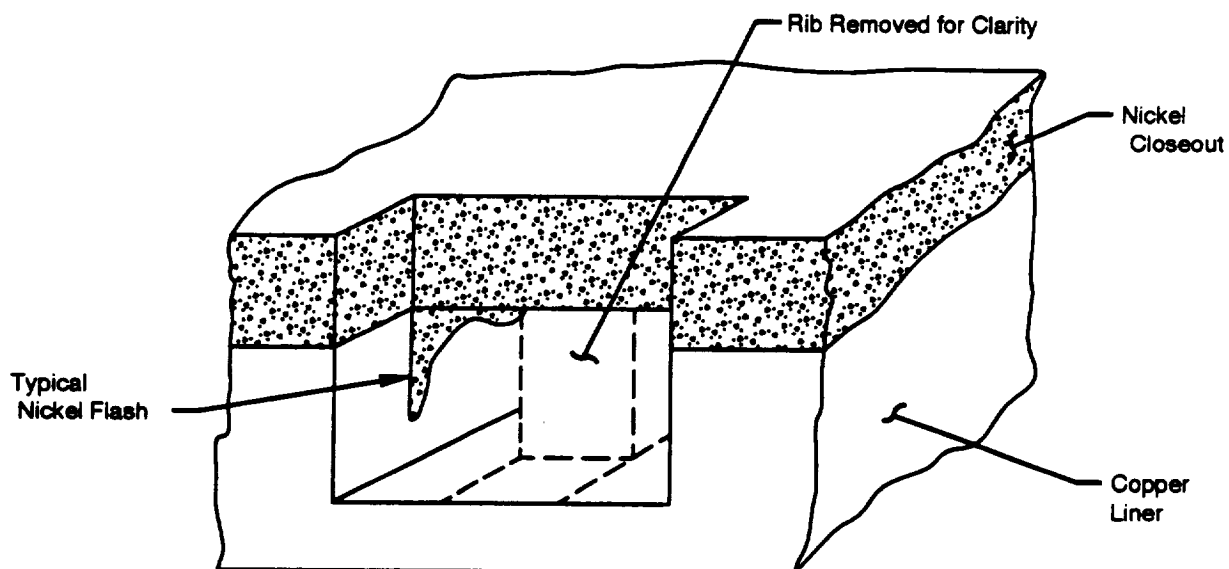


Figure 2.3.3-18. Nickel Flash at Port Entrances

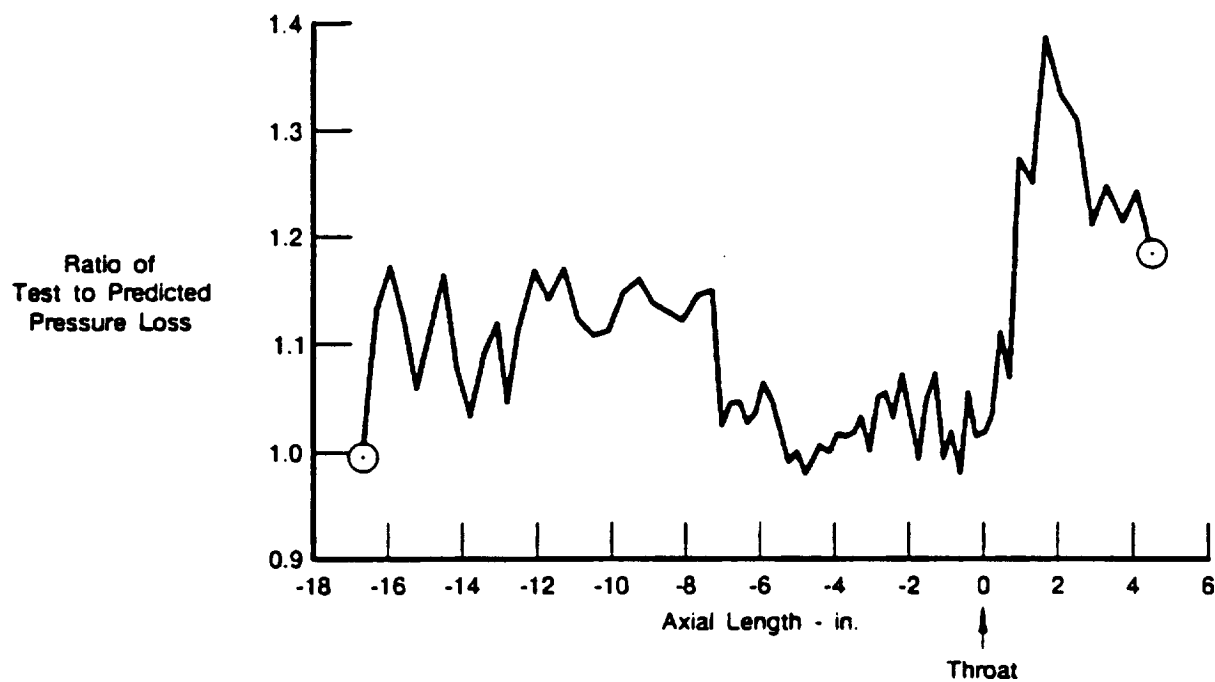
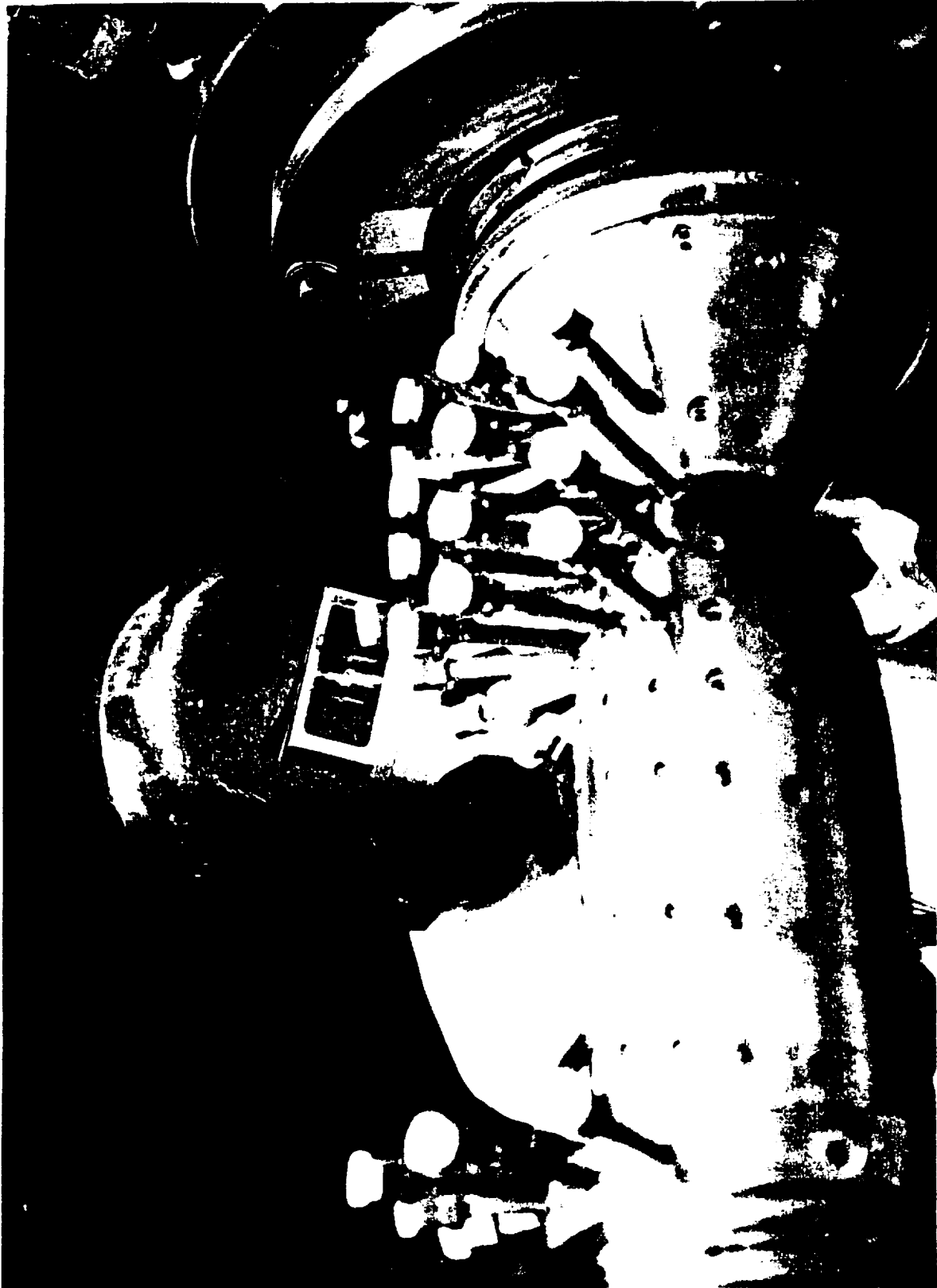
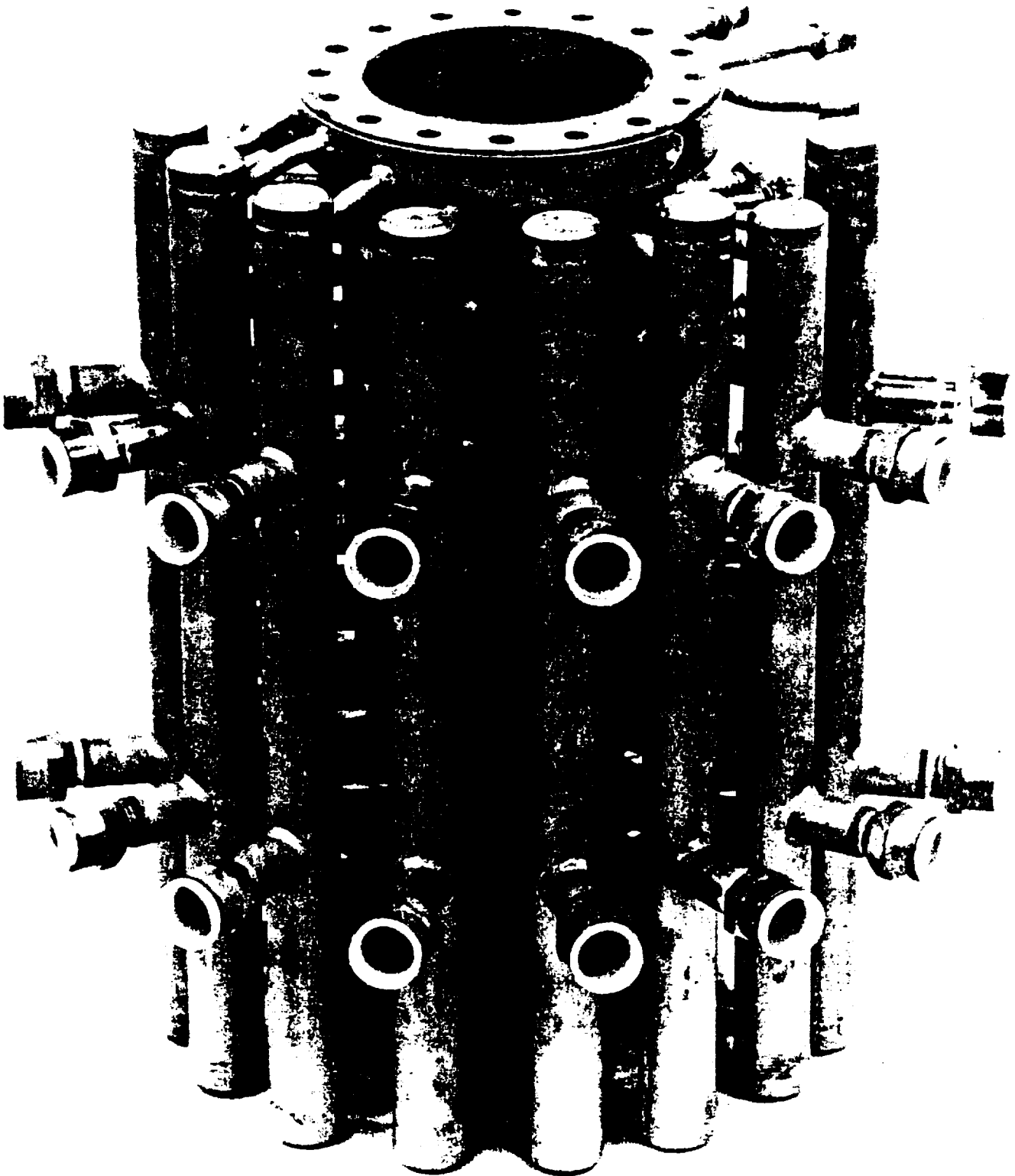


Figure 2.3.3-19. Subscale Chamber Water Flow Results



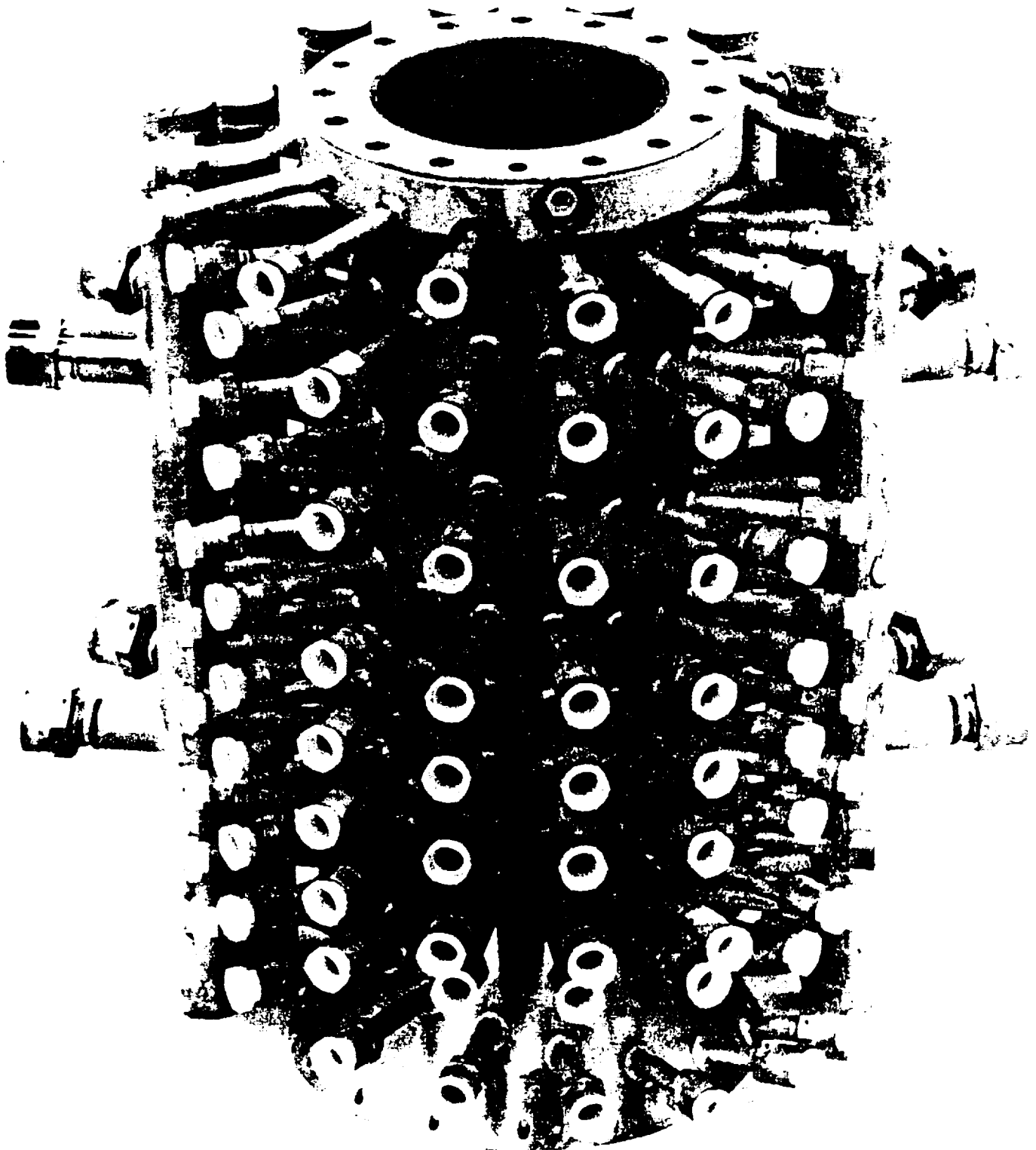
FE809653

Figure 2.3.3-20. Welding of Discharge Tubes on Subscale Chamber



FE010401

Figure 2.3.3-21. Completed Subscale Chamber Showing Inlet Tubes



FE610400

Figure 2.3.3-22. Completed Subscale Chamber Showing Outlet Tubes

2.4 TRANSITION SPOOLPIECE

2.4.1 Transition Spoolpiece Design

In August, 1989 a design was started for a spool piece that would allow the P&W injector to interface with a NASA combustion chamber. This calorimeter spool piece was to be available to permit use of the NASA chamber (reference contract NAS8-37575) as an option to the P&W full calorimeter chamber if required and could be used to investigate the effects of combustion chamber length since the NASA combustion chamber could be run with either a four or eight inch spool piece. This would permit testing of overall lengths of approximately 13 and 17 inches from the injector face to the throat. The concept for this spool piece is shown in Figure 2.4.1-1. Figure 2.4.1-2 presents the intended test article assembly.

A forward section of the damaged subscale combustor copper liner was salvaged and used for the spoolpiece liner. This liner was brazed to the ID of a stainless steel housing, while the coolant inlet and outlet tubes were brazed to the outside of the housing. The design contains 8 cooling circuits and 17 cooling channels in total: 1 circuit feeds 3 cooling channels, and 7 circuits feed 2 cooling channels each.

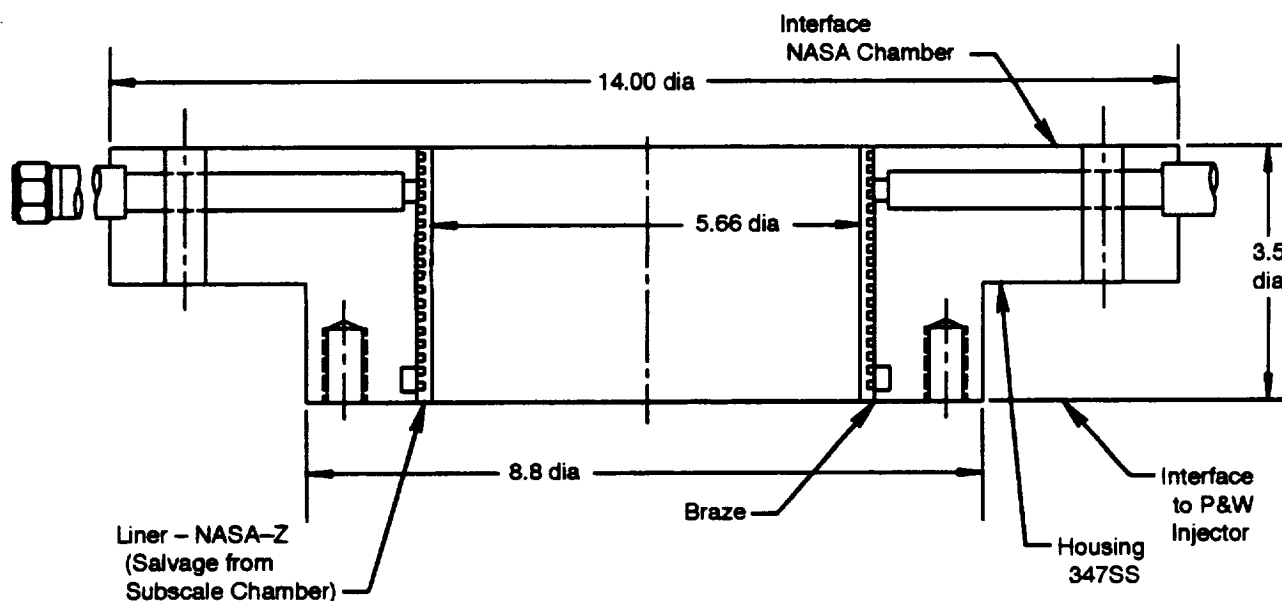


Figure 2.4.1-1. Transition Spoolpiece — P&W Injector to NASA Chamber

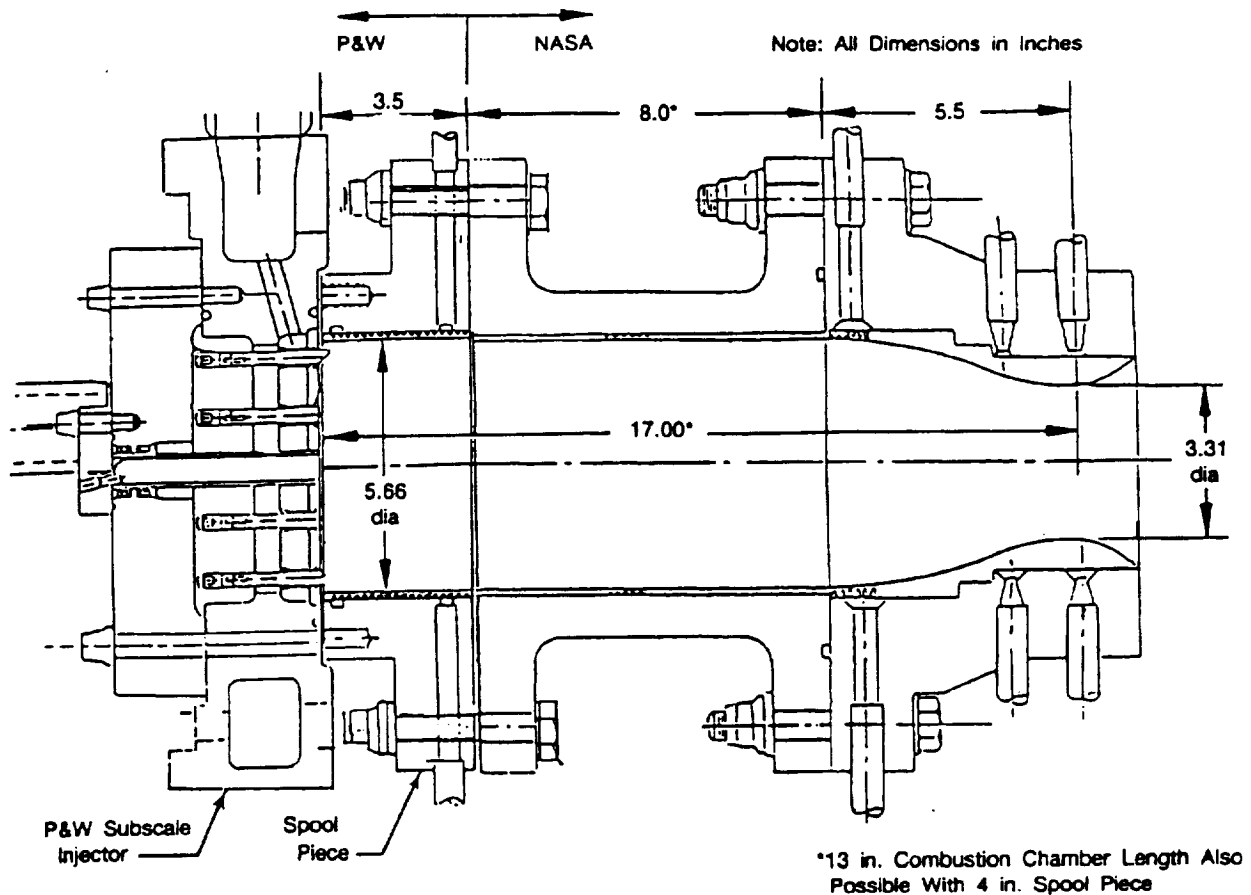


Figure 2.4.1-2. Transition Spoolpiece Installed in Rig

2.4.2 Transition Spoolpiece Fabrication History

Braze cycle evaluation was performed to determine the best braze cycle for the NASA Z liner to stainless steel housing braze. Braze samples were run to investigate Kirkendall voiding effects, diffusion of the braze material into the parent metals, erosion of the parent metals, effects of the thermal cycle on the chemistry, microstructure, and tensile properties of the parent metals, and the strength of the NASA Z to stainless steel braze joint. After reviewing available information on the brazing of NASA Z to stainless steel (304 or 347) an experimental methodology was employed to investigate braze variables. Three flat coupons of stainless steel were brazed to channel sections of NASA Z to investigate plating thickness, erosion, and wetting effects. The samples were evaluated and indicated the required set of conditions needed to ensure a proper braze. Those conditions were applied to two test rings. The rings were constructed to simulate the spool piece as close as possible. Test ring number one was brazed, hydrostatically pressure tested to 10,000 psi, and cut up for analysis. No leaks were observed at any joint on test ring number one during the pressure test, and nearly 100 percent coverage was achieved with no noticeable erosion or diffusion of any kind. Using results from test ring number one, test ring two was run through the braze cycle and hydrostatically pressure tested to 10,000 psi. Figure 2.4.2-1 shows test ring two. The eight supply tubes, visible in the figure, allow four individual cooling circuits to be tested. The pressure test of test ring two showed no channel-to-channel or external leakage.

The braze material for the NASA Z to stainless steel joint is 80 percent gold and 20 percent copper plating. During the first plating trials the copper was plated to the inner diameter of the stainless steel housing and a

gold-sulfite plating solution was used to plate the gold over the copper. This technique proved unacceptable since the sulfur in the gold plating solution attacked the copper before the gold was deposited. Replacement of the gold sulfite solution with a gold cyanide solution solved the problem. The resulting plating did not blister, crack, or peel away from the surface, after the bake cycle to remove hydrogen, thus indicating a good bond. Silcoro 75 braze foil will be used to attach the coolant supply and discharge tubes to the housing, samples of that joint have passed a hydrostatic pressure test of 10,000 psi with no leaks observed.

Tensile testing of NASA Z samples run with the test rings, indicated a yield strength of up to 40 percent below that specified for NASA Z. Material stresses during operation were reviewed and it was determined that the resulting NASA Z properties are sufficient to maintain acceptable design margins.

Based on information received from NASA, it was apparent that a fast cooldown from the braze temperature (1725°F) to the precipitation hardening temperature (900°F) is essential to limit grain growth and the corresponding reduction in NASA Z yield strength. The cooldown in the latest braze cycle was set as fast as the furnace would allow, and another braze sample was run to the latest cycle with an equivalent thermal mass to the actual spoolpiece to determine the actual cooling rate that could be expected for the spoolpiece. The braze proved acceptable, and a NASA Z tensile specimen run with the braze sample provided a yield strength of 12,400 psi, with a cooldown rate of 36°F/minute. This yield strength was lower than expected, based on the NASA supplied data, but was higher than that achieved with the previous braze cycle. Structural analysis showed that even the lower yield strength (11,800 psi) resulting from the previous braze cycle provides acceptable design margin for the NASA Z liner.

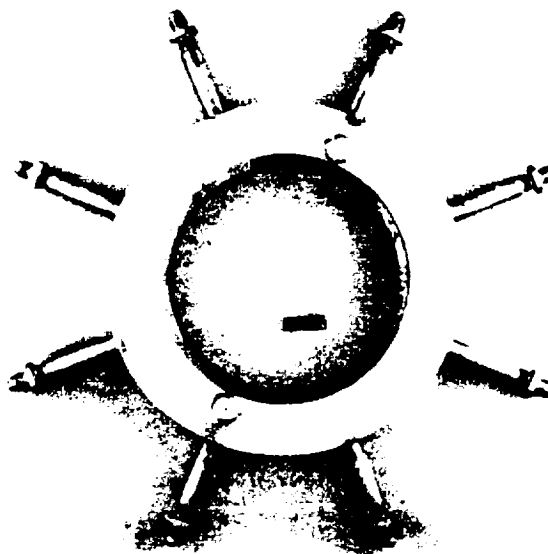
The stainless steel housing, NASA Z copper liner, and inlet and exit tubes for the transition spoolpiece were machined at P&W. The ID of the housing was plated with the 80 percent gold and 20 percent copper braze material for braze to the NASA Z liner. At the same time that the liner was brazed to the housing, the inlet and exit tubes were brazed to the housing, and ferrules were brazed to the tubes using Silcoro 75 braze alloy.

All ferrule-to-tube and tube-to-housing brazes proved to be acceptable, but an initial helium leak check found four small leaks in the copper liner to housing braze at either of the outermost channels to the outside. There was no channel-to-channel leakage. Several methods of repair were evaluated including a furnace braze repair, a local TIG braze repair, and a local repair with an electron beam welder. Repair options were evaluated using the braze samples which were run to initially develop the process for the transition piece. The method chosen was a local repair with a Yttrium Aluminum Garnet (YAG) laser welder using braze material as a filler. The laser introduced very little heat into the part, so the risk of degrading the properties in the NASA Z liner was low.

A leak check after the first laser repair attempt revealed that two tiny leaks still existed. Another laser repair corrected all leaks. The spoolpiece was then proof pressure tested to 5000 psi with water and helium leak tested again. There were no leaks during either test.

Due to a blueprint error, three bolt-holes on the injector interface were drilled through to the combustion chamber interface. Since these holes are inside of the sealing surface on the chamber interface and outside of the sealing surface on the injector interface, this condition creates a leak path for hot gases to escape from the combustion chamber to the outside. This will be corrected by inserting a threaded plug into the hole on the chamber interface and welding it shut to seal the leak path. As a result of the welding, the interface surfaces had to be ground flat. A post-grinding proof pressure test, again with 5000 psi water was conducted, as well as another helium leak check. Two small leaks were noted during the proof test at previously repaired areas. This occurred because the depth of penetration of the repair was kept low to avoid significant heat input to the part, and subsequent machining removed part of the repaired area. After the subscale testing was completed, there was no further scheduled use for this hardware, to save the cost required to complete the repair the spoolpiece was stored nonfunctional.

In reviewing the final processing of the transition spool piece, it was decided not to install the two dynamic pressure ports. This operation consisted of drilling a 0.070-inch nominal diameter hole through a 0.110-inch wide land at each location, then opening up this diameter through the structural shell to accommodate the transducer installation. This would require precise placement of the hole to avoid breaking through the land into the coolant passages. Although this could have been done with accurate measurements and the use of X-ray to confirm land locations, this feature might not have been needed for the transition spool piece. The intent of this piece was to provide a backup for the calorimeter chamber, if required. If the spoolpiece were needed for this purpose, the dynamic probe features could be installed. A second use for this piece was for possible testing to investigate chamber wall blanching. For this application, the dynamic probes would not be required, since testing would be conducted at points that were previously proven to be stable.



FE608822

Figure 2.4.2-1. Braze Sample Assembly for Transition Spoolpiece

2.5 40K SUBSCALE TESTING

2.5.1 Test Setup

This section intentionally left blank.

2.5.2 Instrumentation

The subscale test rig featured a wide array of instrumentation to provide data from which the stability and performance of the rig could be evaluated. Table M provides a complete list of the instrumentation for the subscale injector while Figure 2.5.2-1 shows the approximate locations of the subscale injector instrumentation. The LOX cavity featured 2 static pressure taps, 180 degrees apart, a high response Kulite probe for dynamic pressure, and a Rosemount RTD (resistance temperature device) for LOX cavity temperature. The fuel cavity featured two static pressure taps and a type E T/C for measuring the fuel cavity temperature. Another high

response Kulite probe measured the dynamic pressure in the fuel manifold. Two type C/A T/Cs were brazed to the faceplate (180 apart) to measure the faceplate temperature. Also brazed to the faceplate 180 degrees apart were two static pressure taps to measure combustion chamber pressure (P_c). One of these taps was aspirated with hydrogen fuel to prevent it from freezing. The combustion chamber has two ports 120 degrees apart near the injector face which were normally used for high frequency PCB transducers to measure the combustion chamber dynamic pressure but were also occasionally used for static pressure taps. Each of the chamber's 72 coolant outlet ports was fitted with a T/C to measure the temperature of the water leaving the chamber coolant passages.

The high-frequency pressure transducer selected for the subscale rig testing was the Kulite model CT-375-5000 for the injector LOX dome and fuel manifold. The Kulites were flush or near flush mounted and had a response of at least 75,000 Hertz before a 5 percent amplitude error occurs. The Kulite probes had the advantage of being able to indicate both the static and dynamic pressures. This model Kulite was designed for use in cryogenic temperatures for pressures up to 5000 psi and is compatible with both LOX and hydrogen. When methane was to be the fuel, the Kulite model HTM-375-5000 would have been used in the fuel manifold. The Kulite probes were calibrated at P&W before installation in the rig.

The PCB probe model 122A was selected for the combustion chamber since would be exposed to hot combustion gases and will require cooling. Due to the construction of the calorimeter combustion chamber, it was not possible to mount the probe flush to the combustion chamber wall. The mounting configuration is shown in Figure 2.5.2-2. With this configuration, it was predicted that the response error would be less than six percent at the first tangential acoustic frequency.

Concerns about the possibility of freezing of the chamber static pressure taps in the faceplate caused the evaluation of anti-icing concepts for these taps. This issue was raised by the fact that the hypotubing was routed to the faceplate through the fuel cavity, which contained cold (175 R) hydrogen gas. Experience from the RL-10 and SSME ATD programs has shown that, unless there is a positive outflow of gas from the hypotubing, the combustion product (steam) will tend to migrate into the hypotubing where the extremely cold temperature causes it to freeze. The resulting ice blocks the hypotubing and prevents accurate reading of chamber pressure. The SSME ATD program addressed this problem two ways. One tap was purged with high pressure gas through the start transient until steady state was reached. Once at steady state, the purge was turned off. The tap would operate normally, providing accurate pressure readings until it froze up after about 15 to 20 seconds. The second tap had a small pinhole in the hypotubing near the faceplate so that a small amount of hydrogen from the fuel cavity would bleed into the hypotubing and provide a positive outflow into the combustion chamber preventing steam from migrating into the hypotubing and freezing. This small hydrogen flow would cause an error in the pressure readings of about five psi.

Since the injector built under this program also had provisions for two chamber pressure taps, two types of pressure taps were used. One aspirated probe in which the probe is purged with hydrogen fuel during the run, and a non-aspirated probe, will not be purged with hydrogen fuel during the run. Since run times would be shorter than the 15 to 20 seconds it took for the taps to freeze in the ATD program, it was thought that the non-aspirated probe may not freeze at all. Data from this port will be used to correlate the error from the aspirated tap. The aspirated probe used the anti-icing scheme shown in Figure 2.5.2-3. This is a variation of the pinhole used in the ATD program. This scheme provides enough positive hydrogen outflow to assure the tap will not freeze while suffering a small error in the pressure readings, 1 to 3 psi. This tap will be able to continue reading chamber pressure should the first tap freeze.

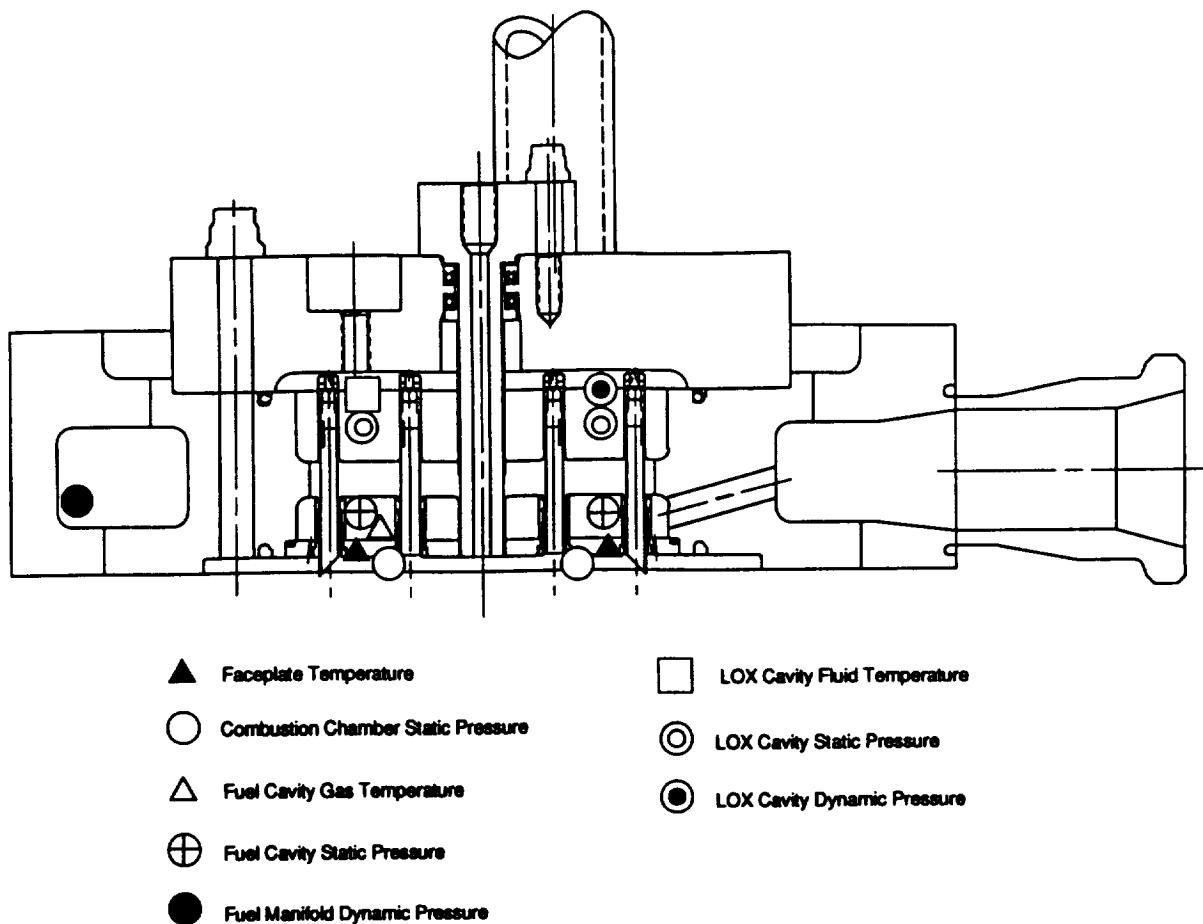


Figure 2.5.2-1. Subscale Injector Instrumentation

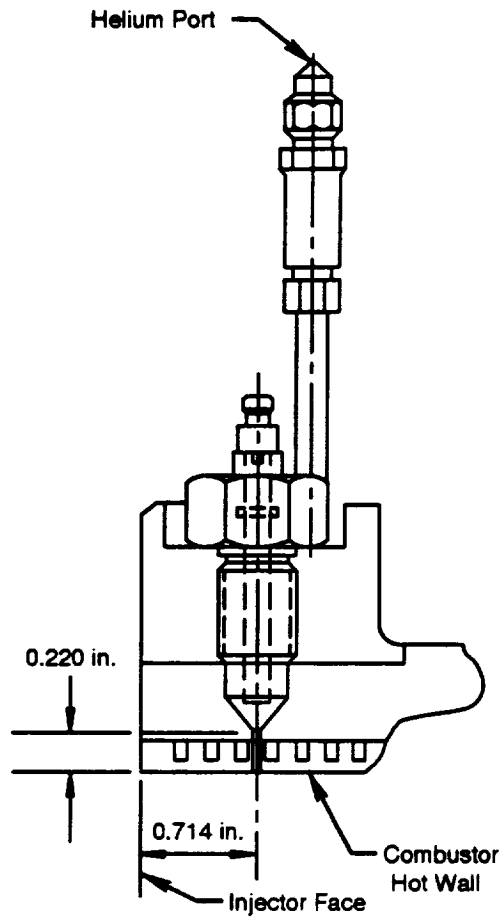
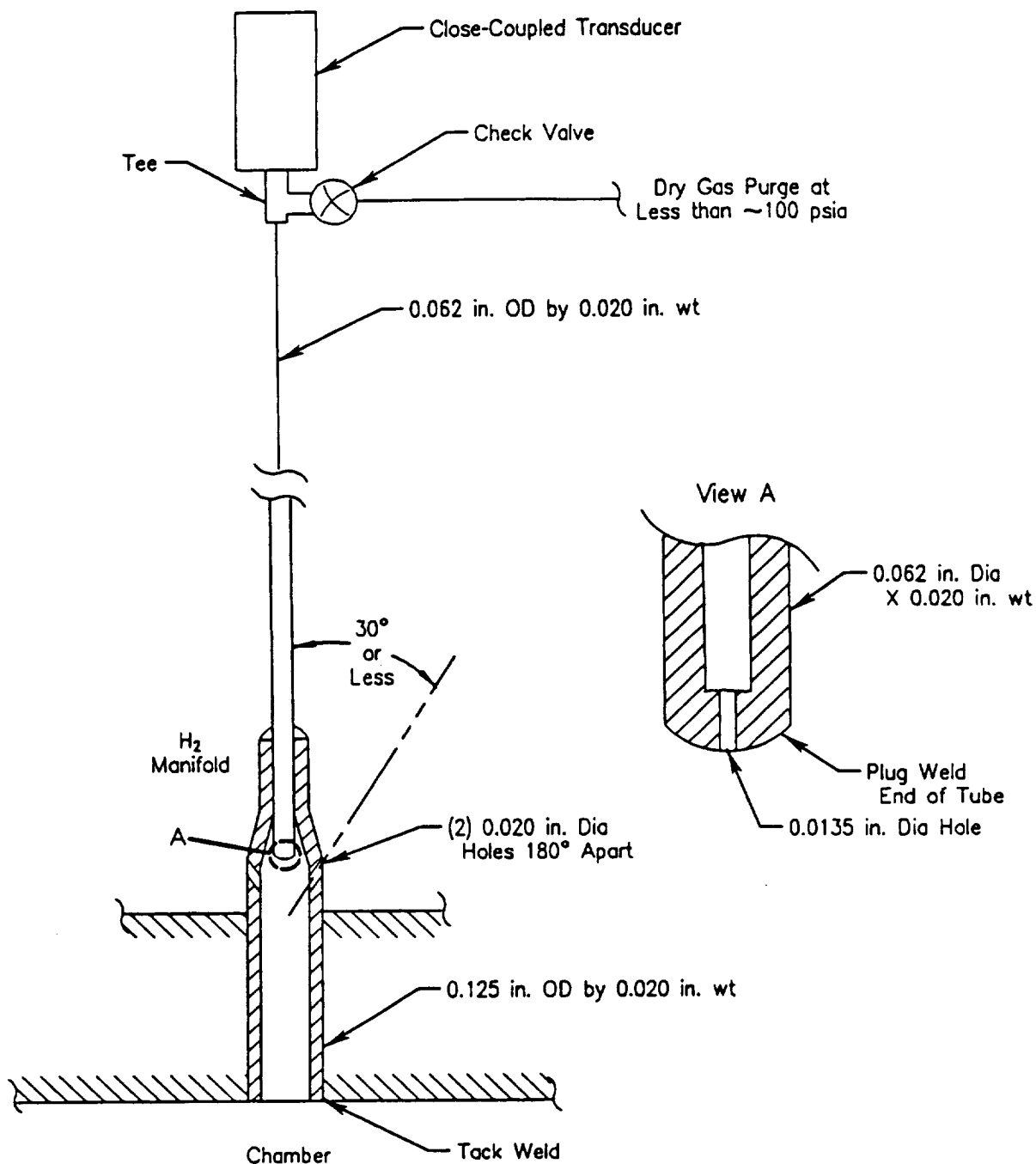


Figure 2.5.2-2. Combustor High-Frequency Pressure Transducer



FD375838

Figure 2.5.2-3. Subscale Chamber Pressure Tap Anti-Icing Scheme

2.5.3 Test Program Discussion

2.5.3.1 Analytical Model

An analytical model of NASA MSFC TS116 was created to assist in setting the run sequence. This simulation was a state variable model that relies on a routine which solves simultaneous equations. The model

incorporated volume dynamics in the LOX injector, fuel injector, and combustion chamber. It considered inertial and frictional line losses and ran steady-state or transient. It could be run with a choice of fuels (H_2 or CH_4) and includes injector purges. It has restart capability and graphics capability. It also had injector purge capability and LOX injector heat transfer. The test data from previous testing conducted at TS116 was used to calibrate the model. Following this calibration, the model was used to develop a safe start and shutdown sequence for the P&W subscale testing.

2.5.3.2 Original Test Matrix

The original subscale test plan was developed using a statistical design of experiment approach. Attempts were made to use a pure Taguchi approach to the experiments, however, this would have resulted in an L81 (81 test) matrix. Work continued on the matrix, with the P&W statisticians using alternate statistical techniques and with engineering assessing the variable and response requirements to develop the central composite matrix that resulted in a total of 21 tests. The testing was established in five phases to provide safe checkout of the test article, confirmation of design point performance, injector characterization, establishment of experimental repeatability, and exploration of the effects of film cooling. These phases are described as follows.

The first test series is presented in Table 2.5.3-1. The first test was planned to run to a chamber pressure of 450 psia and the second test to 1000 psia. As a result of discussions held with NASA, the decision was made to proceed directly to 1000 psia for the first test to allow for operation of the main oxidizer supply valve to verify valve scheduling. The second test would have been to run to the minimum power level of 1690 psia to establish valve scheduling to a steady-state level. The third test would be run to provide full test duration at a low chamber pressure.

Table 2.5.3-1. Early Phase 1 Test Matrix

Test Number	Oxidizer Flow (pps)	Fuel Flow (pps)	Oxidizer ACd/Element (Sq In.)	Fuel ACd/Element (Sq In.)	Fuel Temperature ($^{\circ}R$)	Fuel Elements (No.)	Chamber Pressure (psia)	Mixture Ratio (O/F)
Start	TBD	TBD	0.0137	0.0115	245	62	1000	5.5
Low Power	TBD	TBD	0.0137	0.0115	245	62	1690	5.5
Low O/F	TBD	TBD	0.0137	0.0115	245	62	1690	5.5

The second test series is presented in Table 2.5.3-2. This series was intended to demonstrate testing of the Space Transportation Engine (STE) minimum power level (MPL) and RPL design points. This series would have established the baseline performance of the test article for comparison to later testing to determine the test repeatability. In addition, these tests would have investigated the effect of outer row mixture ratio biasing on combustion chamber wall compatibility by running the two design points at two different levels of outer row mixture ratio. Although it was understood that the MPL design point had been deleted from the STE requirements, the testing at this power level was to be included in the test plan to provide a low chamber pressure point to bracket the STE, in the event that the baseline STE chamber pressure was reduced.

Table 2.5.3-2. Early Phase 2 Test Matrix

Test Number	O ₂ Flow	H ₂ Flow	O ₂ ACd/Element	H ₂ ACd/Element		No. of Elements	H ₂ Temperature	Film Coolant
				Inner	Outer			
1	MP	MP	L	L	L1	H	MP	H*
2	MP	MP	L	L	L2	H	MP	H
3	RP	RP	L	L	L1	H	RP	H*
4	RP	RP	L	L	L2	H	RP	H

Notes:

*STE Design Point (Current Phase B)

L - Variable set at Low Level

H - Variable set at High Level

MP - Equivalent to STE Minimum Power Level

RP - Equivalent to STE Rated Power Level

L1 - Outer Row set to Provide Design Point Outer Row Mixture Ratio (5.2)

L2 - Outer Row set to Provide Level 2 Outer Row Mixture Ratio (TBD)

The third test series is presented in Table 2.5.3-3. The purpose of this series was to provide complete characterization of the injector performance. Six test variables were established for this test series: ACd per oxidizer element, effective area per fuel element, oxidizer mass flow, fuel mass flow, fuel temperature, and number of elements. These variables represent the basic design and operation parameters and variations in these will affect such items as chamber pressure, mixture ratio, momentum ratio and propellant flow per element. This table shows how the characterization would have been set to provide an exploration of injector performance. During the actual testing, these tests would have been run in random order to reduce the effect of any time related changes (i.e. chamber wall erosion, instrumentation shift).

Table 2.5.3-3. Early Phase 3 Test Matrix

Test Number	O ₂ Flow	H ₂ Flow	O ₂ ACd/Element	H ₂ ACd/Element		No. of Elements	H ₂ Temperature	Film Coolant
				Inner	Outer			
1	L	LL	L	L	L	L	L	H
2	L	LH	L	H	H	H	L	H
3	L	LL	H	H	H	H	H	H
4	L	LH	H	L	L	L	H	H
5	H	HL	H	L	L	H	L	H
6	H	HH	H	H	H	L	L	H
7	H	HL	L	H	H	L	H	H
8	H	HH	L	L	L	H	H	H

Notes:

*Inner and Outer Fuel ACd in pairs for outer row and core elements to ensure proper O/F match

L - Variable set at Low Level

H - Variable set at High Level

LL - H₂ Flow set Low for Low P_c = 1690 psia LOX FlowLH - H₂ Flow set High for Low P_c = 1690 psia LOX FlowHL - H₂ Flow set Low for High P_c = 2250 psia LOX FlowHH - H₂ Flow set High for High P_c = 2250 psia LOX FlowH₂ Flows Nested in O₂ To Limit P_c and O/F

The fourth test series is presented in Table 2.5.3-4. The purpose of this series is to provide information on test repeatability. The two tests will be repeat points of the two STE design points run in the first test series. This repeat testing will provide information on the natural variation of test-to-test to permit evaluation of the actual effects due to varying test parameters or hardware configuration.

Table 2.5.3-4. Early Phase 4 Test Matrix

Test Number	O ₂ Flow	H ₂ Flow	O ₂ ACd/Element	H ₂ ACd/Element		No. of Elements	H ₂ Temperature	Film Coolant
				Inner	Outer			
1	MP	MP	L	L	L1	H	MP	H
2	RP	RP	L	L	L1	H	RP	H

Notes:

- L - Variable set at Low Level
- H - Variable set at High Level
- MP - Equivalent to STE Minimum Power Level
- RP - Equivalent to STE Rated Power Level
- L1 - Outer Row set to Provide Design Point Outer Row Mixture Ratio

The fifth test series is presented in Table 2.5.3-5. The purpose of this series was to determine what level of oxidizer/fuel ratio biasing and film-cooling would be required to prevent chamber wall blanching. The original intent of this series was to reduce the film-cooling to allow the combustor wall temperature to run at greater than 1000°F to determine if chamber wall blanching would occur. During the test plan review, the issue of time as related to blanching was discussed. The concern was that even though the wall temperature could be raised above 1000°F, blanching might not be seen since there was some evidence that it is related to exposure time. This series would, however, provide information on the effects of varying the amount of film cooling on combustion chamber wall heat flux through the length of the chamber.

Table 2.5.3-5. Early Phase 5 Test Matrix

Test Number	O ₂ Flow	H ₂ Flow	O ₂ ACd/Element	H ₂ ACd/Element		No. of Elements	H ₂ Temperature	Film Coolant
				Inner	Outer			
1	MP	MP	L	L	L1	H	MP	L
2	MP	MP	L	L	L2	H	MP	L
3	RP	RP	L	L	L1	H	RP	L
4	RP	RP	L	L	L2	H	RP	L

Notes:

- L - Variable set at Low Level
- H - Variable set at High Level
- MP - Equivalent to STE Minimum Power Level
- RP - Equivalent to STE Rated Power Level
- L1 - Outer Row set to Provide Design Point Outer Row Mixture Ratio (5.2)
- L2 - Outer Row set to Provide Level 2 Outer Row Mixture Ratio (TBD)

Because of tight schedules at TS 116 test stand at MSFC, there was not enough time allowed for the P&W subscale testing to run all of the tests in P&W's original test plan. Therefore, a new test plan was developed to fulfill testing requirements within the allotted time frame.

2.5.3.3 Final Test Matrix

The subscale test plan was revised at the request of NASA to reduce the number of tests. This reduction was prompted by NASA budgetary restrictions and by test schedule restraints resulting from the recent delivery slippage of the P&W calorimeter combustion chamber and the NASA combustion chamber throat section. The revised plan had only 15 tests over three test series. The basic approach using statistical Design Of Experiment (DOX) was retained, but repeat tests and demonstrations of the predicted optimum configurations were eliminated. A mid-power point test during the Series 1 checkout was also eliminated.

In addition to these changes, the testing which involved elimination of injection elements was also deleted. This was a result of concerns raised by NASA relative to early SSME development experience regarding the blockage of the oxidizer elements and potential for LOX leakage causing local burning and element damage. It was felt that minor leakage could be tolerated in the core elements, but that the scarfed outer row elements might be damaged. As a result, the plan had been to block only some of the core elements; however, if only the core elements are blocked the LOX flow to the outer row is increased and the outer row mixture ratio is increased. This could be compensated for by changing the outer row facenuts to increase the flow and lower the mixture ratio. This however, would introduce another dependency in the test matrix requiring additional tests.

The final test matrix for the subscale test article is presented in Table 2.5.3-6 and consists of three test series as follows:

- **Series 1 Initial Checkout:** The purpose of this test series is to safely demonstrate test article ignition and transition to steady-state flows.
- **Series 2 Statistical Injector Characterization and Performance:** The purpose of this test series is to fully characterize the injector performance. This is a statistically designed experiment during which 5 variables at 2 levels each will be evaluated: LOX element ACd, fuel element ACd, fuel temperature, fuel flow and LOX flow. These parameters were specifically chosen because they are the variables which characterize the combustor and hence its design. From these parameters, the traditional injector characterization variables such as injection velocities, chamber pressure, and mixture ratio can be obtained. In a traditional test matrix, 32 tests would be required to investigate every combination of two values for each variable, but only 8 tests were required using the Taguchi DOX. Chamber pressures of approximately 1710 psia and 2400 psia and core O/F mixture ratios between 5.5 and 7.5 were run to bracket the expected STE operating conditions.
- **Series 3 Wall Compatibility:** The purpose of this test series is to evaluate the effects of scarfing, film cooling and outer row mixture ratio biasing on the chamber hot wall temperature and heat flux as well as injector performance. Outer-row mixture ratio biasing increases the fuel flow area of the injection elements nearest the chamber wall, while film cooling allows extra hydrogen gas to flow directly through the injector faceplate so that the gas impinged directly on the chamber wall. Also, the exits of the outer-row LOX injector elements were scarfed to direct most outer-row LOX away from the chamber wall. All three schemes sought to reduce wall heat flux by reducing the near-wall O/F ratio, which lowered combustion temperatures there. Mixture ratio biasing and film cooling use fuel redistribution upstream of the injector, while scarfing depends on LOX redistribution downstream of the injector. All three wall-durability enhancements were present in the Series 2 tests; they were sequentially removed in the Series 3 tests.

Table 2.5.3-6. Final Subscale Test Matrix

Series 1 - Initial Checkout												
Test Number	O ₂ Flow (pps)	O ₂ Inlet Press (psia)	Oxidizer ACdElem Sq. in.	O ₂ ApPc (%)	Fuel Flow (pps)	H ₂ Inlet Press (psia)	Fuel Temp Deg R	H ₂ Core ACdElem Sq. in.	H ₂ Outer ACdElem Sq. in.	H ₂ ApPc (%)	No. of Elem.	O ₂ Flow/Element (pps)
1	Level 1	TBD	0.0137	TBD	TBD	N/A	N/A	0.0115	0.0148	N/A	61	TBD
2	Low	TBD	0.0137	TBD	TBD	N/A	N/A	0.0115	0.0148	N/A	61	TBD
Power	44.9	1800.5	0.0137	7.5	8.2	1871	245	0.0115	0.0148	10.6	61	0.73606

Test 1 will be level 1 LOX and TEA/TEB only to determine the P_c rise at ignition to set the ignition select redline.

* 0.46% film on engine = 1.64% on rig

** Upper number is element O/F. Lower number is effective O/F including porous plate flow.

Series 2 - Injector Characterization

Test Number	O ₂ Flow (pps)	O ₂ Inlet Press (psia)	Oxidizer ACdElem Sq. in.	O ₂ ApPc (%)	Fuel Flow (pps)	H ₂ Inlet Press (psia)	Fuel Temp Deg R	H ₂ Core ACdElem Sq. in.	H ₂ Outer ACdElem Sq. in.	H ₂ ApPc (%)	No. of Elem.	O ₂ Flow/Element (pps)
3	53.36	1874	0.0172	4.5	9.7	1961	220	0.0115	0.0146	9.4	61	0.87475
4	53.36	1805	0.0137	7.5	8.07	1776	170	0.0115	0.0146	5.8	61	0.87475
5	53.36	1917	0.0137	7	9.7	1879	170	0.0148	0.01854	4.9	61	0.87475
6	53.36	1761	0.0172	4.8	8.07	1765	220	0.0146	0.01854	5	61	0.87475
7	68.63	2442	0.0137	5.7	12.48	2430	170	0.0115	0.0146	5.2	61	1.12508
8	68.63	2593	0.0172	9	12.48	2541	220	0.0115	0.0146	9.8	61	1.12508
9	68.63	2281	0.0137	6.1	10.37	2286	170	0.0148	0.01854	6.1	61	1.12508
10	68.63	2371	0.0137	9.7	10.37	2275	220	0.0146	0.01854	5.2	61	1.12508
Baseline	53.36	1805	0.0137	7.5	8.07	1776	170	0.0115	0.0146	5.8	61	0.87475

* 0.46% film on engine = 1.64% on rig

** Upper number is element O/F. Lower number is effective O/F including porous plate flow.

Series 3 - O/F Blasting and Film Cooling Evaluation

Test Number	O ₂ Flow (pps)	O ₂ Inlet Press (psia)	Oxidizer ACdElem Sq. in.	O ₂ ApPc (%)	Fuel Flow (pps)	H ₂ Inlet Press (psia)	Fuel Temp Deg R	H ₂ Core ACdElem Sq. in.	H ₂ Outer ACdElem Sq. in.	H ₂ ApPc (%)	No. of Elem.	O ₂ Flow/Element (pps)
12	53.36	1805	0.0137	7.5	8.07	1776	170	0.0115	0.0146	5.8	61	0.87475
13	53.36	1805	0.0137	7.5	8.07	1776	170	0.0115	0.0146	5.8	61	0.87475
14	53.36	1805	0.0137	7.5	8.07	1776	170	0.0115	0.0146	5.8	61	0.87475
15	53.36	1805	0.0137	7.5	8.07	1776	170	0.0115	0.0146	5.8	61	0.87475

* 0.46% film on engine = 1.64% on rig

** Upper number is element O/F. Lower number is effective O/F including porous plate flow.

Prior to Test 13 remove the outer row LOX element scarfing features.

Prior to Test 14 plug weld closed the film cooling holes

2.5.3.4 Subscale Testing

The subscale test article was installed onto NASAMSFC TS 116 with no significant problems. Figure 2.5.3-1 shows a schematic of the subscale test rig, the injector mounted on the calorimeter combustion chamber.

Six series of water blow-downs were accomplished to calibrate the calorimeter combustion chamber coolant passages and to set the size of the discharge orifices. During each of these blow-downs, three different levels of coolant inlet pressure were run. The purpose of this testing was to determine and set the size of the discharge orifice which sets the flow through each of the seventy-two coolant circuits. The intent was to provide sufficient flow for cooling while maintaining control of the flow with the orifice rather than with the pressure drop in the channels. Initial sizing of the orifices was based upon preliminary flow testing performed at P&W during the fabrication process. Although these flows were accomplished at only 50 psia inlet pressure, there were only a few orifice sizes required to be changed when the calibrations were performed at pressures up to 4500 psia.

The following is a summary of the subscale tests:

- Test No. P242-001 (Matrix Test No. 1) occurred on 8/25/90. This was an ignition only test to determine the level of chamber pressure that would result from level 1 (partial) LOX flow and TEA/TEB. The purpose of the test was to establish this level to allow setting the no-ignition abort chamber pressure level.
- Test No. P242-002 (Matrix Test No. 2) occurred on 8/27/90. The purpose of this test was to provide a low chamber pressure and low O/F checkout of the test article. The test was terminated due to a low fuel temperature. A chamber pressure of approximately 1300 psig was achieved before the cutoff. The fuel temperature was set by flowing through a bypass valve, and when the main fuel valve was opened to allow flow to the injector, the temperature dropped below limit. The temperature was on manual control and could not be brought into limit within the time allotted. Following this test the gas valve which controls the temperature was been ramped to a preset position when the main fuel valve was opened, thus requiring less manual adjustment of the gas valve to assure that the temperature was met. During this firing, there was significant combustion outside of the test article due to hydrogen leakage at the fuel inlet line joints.
- Test No. P242-003 (Matrix Test No. 2) occurred on 8/28/90. This was another attempt to perform the checkout testing. A cutoff occurred due to low fuel venturi pressure. This parameter is checked after the main fuel valve reaches open and must be within limits within two seconds. The absolute cause of the cutoff was not determined, but believed to be related to several items. The LOX valve did not achieve the desired position, causing a lower than expected chamber pressure, and subsequently, a lower venturi pressure. It was also suspected that an error occurred in the venturi pressure transducer reading due to leakage through a partially open bleed valve. For the next test, the LOX valve position was increased to ensure that the LOX valve was sufficiently open and the bleed valve was removed from the transducer line.
- Test No. P242-004 (Matrix Test No. 2) occurred on 8/29/90. This was a successful firing lasting for 9.9 seconds. A chamber pressure of approximately 1550 psig was attained for 3.6 seconds. An observer cutoff occurred at 0.100 second less than planned due to combustion outside of the test article. Post test inspection of the test article showed it to be in good condition.
- Test No. P242-005 (Matrix Test No. 3) occurred on 8/31/90. This test was cut off due to no-ignition detect. This was due to insufficient LOX flow, and even though ignition did occur, the chamber pressure level attained was below that determined from the cold flow and ignition tests. For the next test, the

LOX valve position was increased from 4.4 percent to 5.0 percent to assure that the valve would open to a position required to make the no-ignition cutoff level. In addition, the no-ignition abort sample time was increased to 1.0 second from 0.5 second. The cutoff level was also reduced by 5 psi to 35 psig.

- Test No. P242-006 (Matrix Test No. 3) was completed on 9/5/90, but test objectives were not met due to test stand LOX valve malfunction. The main oxidizer valve did not achieve a five-second open indication until eight seconds after the sequencer start due to a valve indicator error. After the indication was received, the TEA/TEB valve was opened, ignition occurred, then the main fuel valve started to open. Cutoff occurred at the planned 10 seconds duration, thus full fuel flow was not achieved. The start sequence was changed to permit proceeding to the TEA/TEB flow one second after the LOX valve leaves the closed position or after the valve reaches the desired position.
- Test No. P242-007 (Matrix Test No. 3) was completed on 9/6/90. A run of 8.6 seconds was accomplished with 2.4 seconds at steady-state conditions of 1790 psia chamber pressure at an overall mixture ratio of 5.66. The planned 10-second run was terminated by the test conductor due to fire on the test stand as a result of hydrogen leakage. Visual observation of the test article showed no distress. This test firing is shown in Figure 2.5.3-2.
- Test No. P242-008 (Matrix Test No. 4) was completed on 9/7/90. The test sequence duration was approximately 13 seconds during which three different levels of hydrogen temperature were attained. A chamber pressure of approximately 1750 psia was attained. Before the testing, the fuel inlet line was removed and the seals were replaced; there was no evidence of fire during the test.
- Test No. P242-009 (Matrix Test No 5) was completed on 9/10/90. The test sequence duration was approximately 13 seconds, during which two different levels of hydrogen temperature were attained. A chamber pressure of approximately 1760 psia was attained. After this test, a small area of nickel delamination was noticed at the chamber discharge end. The delamination occurred between three adjacent bolt holes at approximately 0.200 inch from the nickel/copper interface. Since there was sufficient nickel at this location to withstand the loads, there was no action taken. This delamination was monitored throughout the remainder of the test program, and no growth was noted.
- Test No. P242-010 (Matrix Test No. 6) was attempted on 9/12/90 but was cut off after six seconds due to chamber pressure dropping below the low limit. A faulty LOX valve feedback indicated that the valve had opened too far, so the valve was closed, causing chamber pressure to drop.
- Test No. P242-011 (Matrix Test No. 6) was completed on 9/12/90 and was a successful full-duration run of fifteen seconds. Two levels of hydrogen temperature were run, and a chamber pressure of approximately 1740 psia was attained.
- Test No. P242-012 (Matrix Test No. 7) was attempted on 9/13/90 but the test was terminated when the LOX valve did not open.
- Test No. P242-012 (Matrix Test No 7) was accomplished on 9/14/90, but due to a drop in LOX run tank pressure, the desired conditions were not achieved. The pressure continued to decrease throughout the run and was believed to be due to a malfunction of the valve that controls nitrogen pressurization of the LOX tank.
- Test No. P242-013 (Matrix Test No. 7) was accomplished on 9/15/90. The full-duration 15-second test achieved a chamber pressure of 2336 psia. There was no distress to the test article at this high chamber pressure level.

Several attempts to complete the next test in the matrix were made between 9/17/90 and 9/20/90. These were cut off for a variety of reasons including low fuel pressure, low fuel temperature, problems with the LOX valve position potentiometer, and a faulty T/C on the calorimeter chamber.

- Tests P242-020 (Matrix Test No. 8) and P242-021 (Matrix Test No 9) were accomplished on 9/21/90. All test objectives were met during both full-duration 15-second firings.
- Tests P242-022 (Matrix Test No. 10) and P242-023 Matrix Test No. 11) were accomplished on 9/22/90. All test objectives were met during the full-duration firings. These were the final tests of the Taguchi injector characterization test matrix.
- Test P242-024 (Matrix Test No. 12) was accomplished on 9/24/90. The 15-second duration run reached a chamber pressure of about 1750 psi. This was the first of a series of wall compatibility tests, which was reinstated into the test program to determine the effect of outer row mixture ratio biasing, film cooling, and outer row element tip scarfing on combustion chamber wall temperature and heat flux as well as on injector performance. This injector was configured without mixture ratio biasing by changing the outer row facenuts to be the same as in the core. On 9/25/90 the injector was dismantled from the thrust chamber so that the scarfed tips of the outer row LOX elements could be removed. The scarfed tips were ground and milled to be flush with the injector face, and following cleaning, the injector was remounted on the test stand the next day.
- Test P242-025 (Matrix Test No. 13) was run on 9/26/90 but was cut off by an observer due to a fire caused by a hydrogen leak at the injector fuel inlet. The seals were replaced before the next run attempt.
- Test P242-026 (Matrix Test No. 13) was accomplished on 9/26/90 for the full duration of 15 seconds and reached a chamber pressure of 1821 psi. Post test examination of the test article showed no distress as a result of removing the outer row scarfing. The injector was again removed from the thrust chamber on 9/27/90 so the film cooling feature could be removed. The 52 holes were welded shut and the injector was remounted onto the chamber.
- Test No. P242-027 (Matrix Test No. 14) was accomplished on 9/28/90 for the planned 15-second duration. This test was run without any wall compatibility features. There was no distress noted on the test article following this test.
- Test No. P242-028 (Matrix Test No. 15) was accomplished on 9/28/90 for the planned 15-second duration to complete the subscale testing. Before this test, the mixture ratio biasing was reinstated by changing the outer row facenuts. The test article was removed from the test stand on 9/29/90. Teardown and post-test inspections were accomplished in early October 1990.

Throughout the test series, the fuel temperature was varied approximately 10R during each run. The resulting decrease in H_2 flowrate led to small variations in chamber O/F ratios. Therefore, up to three data points at approximately 3 second intervals were obtained for a given test. The data were sequentially tagged A, B and C; A summary table of the test results is shown in Table 2.5.3-7. Figure 2.5.3-3 presents typical chamber pressure traces for two of the runs. The total test duration of all runs was 286.3 seconds

Table 2.5.3-7. Preliminary Subscale Test Results

Test No.	Time of Data	Pc (psia)	Fuel Flow pps	LOX Flow pps	Mixture Ratio				Fuel Temp Deg. R	Fuel Acid (in2)	Fuel ΔP/Pc %	LOX Acid (in2)	LOX ΔP/Pc %	Eta C*	Peak Q/A		Comburstor Ave. Q/A,++
					All	Wall	Outer	Core							Value	Ch.No.	
001 (1)												0.836					
004 (2)	9.707	1572	8.95	45.12	5.04	3.77	4.19	5.04	230	1.069	7.9	0.850	5.9	0.976	42.6	57.0	18.0
007 (3)	8.586	1808	9.67	54.02	5.59	4.15	4.64	6.51	229	0.959	8.7	1.001	5.4	0.968	46.5	55.0	20.0
008A(4)	8.985	1750	8.95	53.56	5.98	4.45	4.97	6.97	193	0.977	6.5	0.856	7.7	0.966	44.9	55.0	18.5
008B(4)	13.23	1712	8.43	53.45	6.34	4.72	5.27	7.39	206	0.969	6.5	0.854	7.8	0.966	46.5	57.0	19.3
009A(5)	9.007	1784	9.31	53.38	5.73	4.38	4.8	6.63	183	1.179	4.5	0.865	7.4	0.973	47.4	57.0	19.1
009B(5)	12.61	1732	8.58	53.35	6.22	4.75	5.21	7.19	202	1.174	4.5	0.867	7.5	0.970	48.7	57.0	19.7
011A(6)	7.988	1752	8.77	54.20	6.18	4.68	5.15	7.18	204	0.989	6.4	0.992	5.8	0.966	46.2	55.0	18.6
011B(6)	15.03	1719	8.48	54.07	6.38	4.83	5.31	7.41	213	0.991	6.5	1.009	5.6	0.960	47.5	57.0	19.6
013A(7)	10.3	2360	12.19	70.15	5.75	4.36	4.8	6.68	175	1.118	5.0	1.031	6.4	0.981	56.2	56.0	22.9
013B(7)	14.71	2327	11.73	70.17	5.98	4.55	4.99	6.94	183	1.111	5.0	1.034	6.4	0.978	57.5	56.0	23.5
020A(8)	8.123	2355	12.64	69.55	5.5	4.14	4.57	6.41	220	0.859	10.9	0.858	9.3	0.973	52.5	57.0	22.1
020B(8)	11.12	2326	12.26	69.69	5.68	4.28	4.72	6.62	228	0.855	10.9	0.862	9.2	0.968	53.6	57.0	22.8
020C(8)	15.04	2311	12.09	69.59	5.75	4.32	4.79	6.7	234	0.856	11.0	0.863	9.3	0.966	54.1	57.0	23.2
021A(9)	8.037	2277	11.39	70.16	6.16	4.55	5.1	7.2	176	0.840	8.0	1.040	6.4	0.968	51.8	57.0	21.8
021B(9)	15.04	2243	11.04	69.99	6.34	4.69	5.24	7.41	180	0.835	8.0	1.014	6.9	0.965	53.5	56.0	22.6
022A(10)	8.036	2248	10.95	69.78	6.37	4.77	5.31	7.41	219	1.052	6.1	0.843	10.0	0.970	50.8	57.0	21.2
022B(10)	10.99	2241	10.92	69.76	6.39	4.77	5.31	7.43	220	1.045	6.2	0.851	9.9	0.969	53.7	56.0	22.5
022C(10)	15.04	2239	10.98	69.74	6.35	4.73	5.28	7.39	219	1.052	6.2	0.854	9.7	0.966	55.7	56.0	22.5
023A(11)	8.018	1802	9.45	54.40	5.76	4.26	4.76	6.73	183	0.861	8.3	0.846	7.6	0.967	44.3	54.0	18.0
023B(11)	11.02	1758	8.94	54.38	6.08	4.49	5.03	7.11	197	0.864	8.3	0.867	7.4	0.961	45.6	54.0	18.7
023C(11)	15.02	1739	8.71	54.43	6.24	4.61	5.16	7.28	204	0.866	8.3	0.872	7.4	0.958	46.3	54.0	19.0
024A(12)	8.02	1800	9.49	53.80	5.67	4.59	5.22	6.03	183	0.766	10.4	0.860	7.4	0.973	45.7	54.0	18.8
024B(12)	11.02	1761	8.97	53.76	5.99	4.85	5.52	6.37	196	0.759	10.6	0.857	7.6	0.969	47.2	54.0	19.6
024C(12)	15.02	1742	8.74	53.72	6.15	4.97	5.67	6.53	202	0.759	10.6	0.862	7.5	0.968	47.8	54.0	20.0
026A(13)	8.03	1834	9.47	54.28	5.73	4.65	5.3	6.06	188	0.818	9.1	0.846	7.5	0.967	55.8	54.0	24.8
026B(13)	12.51	1798	8.92	54.24	6.08	4.92	5.61	6.45	201	0.808	9.3	0.869	7.3	0.982	57.5	54.0	25.6
026C(13)	15.03	1774	8.74	54.23	6.2	5.03	5.73	6.58	206	0.804	9.4	0.864	7.4	0.981	57.9	54.0	25.9
027A(14)	8.04	1806	9.28	53.23	5.74	4.99	5.43	5.97	192	0.788	9.9	0.830	7.8	0.991	56.3	54.0	25.0
027B(14)	11.28	1797	9.08	53.31	5.87	5.1	5.57	6.1	197	0.785	9.8	0.844	7.6	0.993	57.2	54.0	25.5
027C(14)	15.04	1780	8.86	53.28	6.02	5.23	5.7	6.25	203	0.786	9.8	0.840	7.8	0.991	58.2	54.0	26.1
028A(15)	8.03	1835	9.93	54.64	5.82	4.55	4.82	6.8	187	0.842	8.4	0.844	7.6	0.986	56.8	54.0	25.1
028B(15)	11.03	1816	9.03	54.62	6.05	4.72	5.12	6.42	193	0.838	8.3	0.837	7.6	0.989	57.6	54.0	25.6
028C(15)	15.03	1793	8.75	54.59	6.24	4.88	5.28	7.14	203	0.840	8.4	0.852	7.5	0.987	58.4	54.0	26.1

Following the testing, the subscale test article was removed from the test stand at MSFC and disassembled for visual inspection. The injector was in excellent condition following the testing. The faceplate and LOX dome were removed to facilitate inspection of the fuel and LOX cavities, respectively. A powdery residue covering both sides of the porous faceplate and the fuel cavity was analyzed and identified as products of combustion of the TEA/TEB hypergolic and oxidizer. It was determined that due to the low flow capability of the helium purge system used during the ignition period of the start transient, backflow of the ignition products into the fuel cavity occurred. However, there was a sufficient volume of purge gas in the fuel lines when the fuel was turned on to expel the ignition products from the fuel cavity before the fuel arrived at the injector. There was no residue present in the LOX cavity, but one outer row element had one tangential entry slot blocked by a piece of copper foil or plating. The foreign object was determined to have been introduced from the upstream oxygen supply line. There was no visible effect on the chamber wall downstream of the element due to the blockage of the element slot.

Concentricity of the facenuts to the elements, which had no specific design feature for maintaining position relative to the elements, was unchanged from build and the fuel annulus gap was symmetrical within drawing limits. One outer row scarfed element exhibited a small area of erosion (approximately 0.150-inch long along tip of element) following test No. 23.

The interpropellant plate electron beam (EB) welds to the injector housing showed no visible evidence of cracking or distress. The injector was fluorescent penetrant inspected (FPI) after it was returned to P&W, and, again, no evidence of cracking or distress was found. The injector was fully serviceable without repair, except that it required replacement of the faceplate chamber pressure and temperature instrumentation.

The combustion chamber was in excellent condition following the testing. There was no blanching or erosion of the hot wall. All coolant tubes and welds were in excellent condition, which FPI at P&W confirmed. A local delamination of the structural nickel jacket occurred following the ninth hot firing at the aft face of the nozzle portion of the chamber between two seal plate bolt holes. No further growth of the delamination occurred during the remainder of the testing. The combustion chamber was fully serviceable without repair.

The hypergolic igniter was also in excellent condition, although heavy deposit of TEA/TEB residue was present on the outer wall of the igniter. The igniter was fully serviceable without repair.

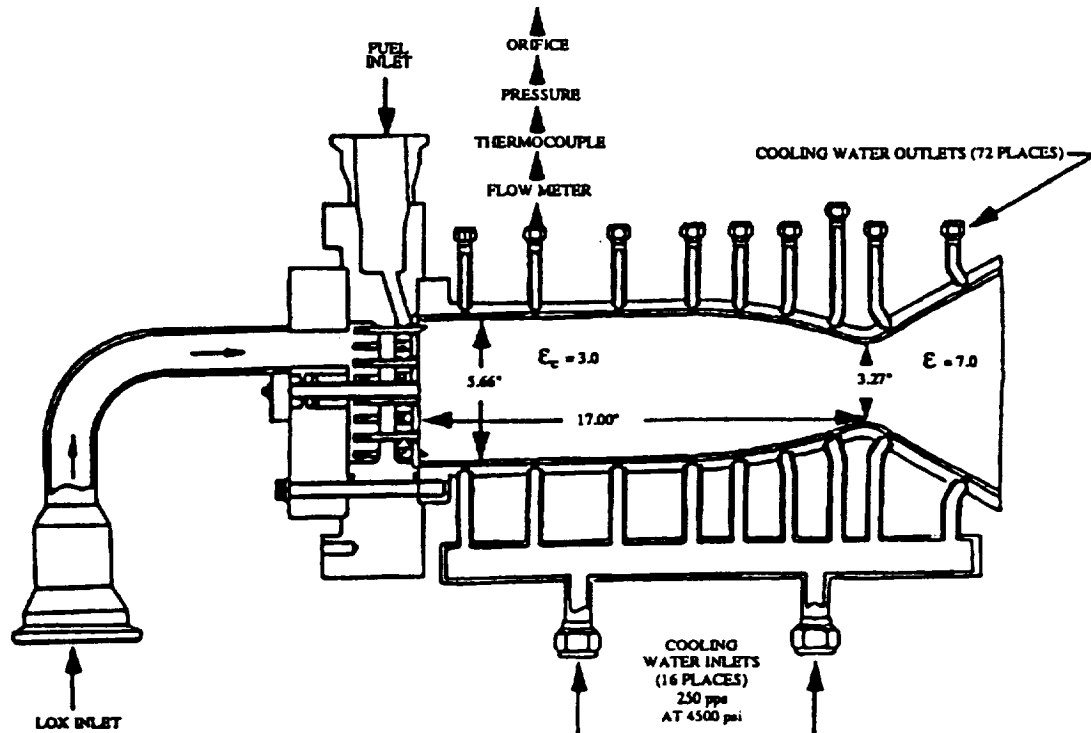


Figure 2.5.3-1. Subscale Test Rig



Figure 2.5.3-2. Subscale Rig Test Firing — Test No. P242-007

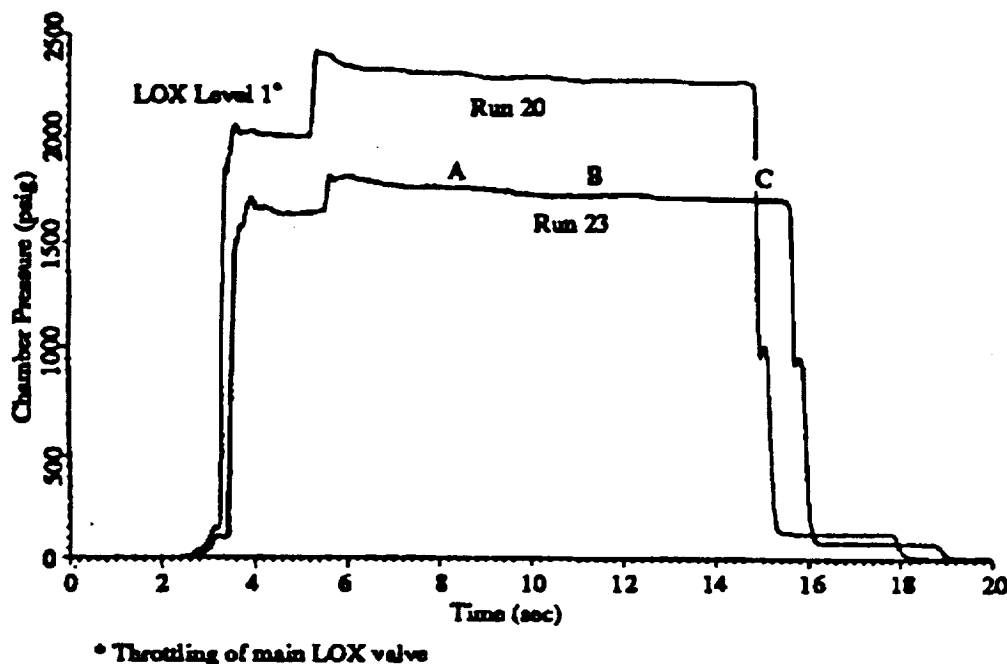


Figure 2.5.3-3. Typical Chamber Pressure Traces

2.5.3.5 Aspirated Chamber Pressure Probe

The readings from the aspirated chamber pressure (P_c) probe in the injector faceplate were found to read consistently lower than the non-aspirated and chamber wall static readings. The reason for the lower measurements were due to the jet pump effect inherent in the aspirated design. Ejection of the high-velocity fuel through the probe orifices creates a suction at the instrumentation tube inlet. This results in a pressure reading that is lower than the actual chamber pressure. An analytical correction was derived using momentum and continuity considerations and subsequently applied to the chamber pressure measurements. The correction, when compared to available wall static pressure readings, is accurate to within 5 psi for the majority of cases. The magnitude of the correction ranged from 0.5 to 1.3 percent of the chamber pressure, depending on the velocity of hydrogen jet through the probe orifices.

2.5.4 Analysis of Test Results

2.5.4.1 Injector Performance Analysis

Nomenclature

- A^* — chamber throat area
- A_{cd} — injection area times discharge coefficient
- A_w — faceplate area in wall zone
- c^* — characteristic velocity
- F — fuel
- MR — mixture ratio (mass basis)
- \dot{m} — mass flow rate
- P_c — chamber pressure (injector plane)
- P_f — fuel pressure upstream of injection

P_o — oxidizer pressure upstream of injection
 $P_{o,throat}$ — total pressure at chamber throat
 O — oxidizer
 Q/A — wall heat flux
 r^2 — coefficient of multiple determination
 S — striation factor (Equation 4)
 T — temperature
 η_{c*} — characteristic velocity efficiency
 $\eta_{c*,diff}$ — supercritical, diffusion limited characteristic velocity efficiency
 $\eta_{c*,mix}$ — mixing limited characteristic velocity efficiency

Subscripts:

f — fuel
 o — oxidizer
 t — total

Overall, much useful information was extracted via analysis of the combustion performance data. The success of the testing and the wealth of information are due in part to the Taguchi test matrix and in part by the sequential removal of the outer row mixture ratio biasing, scarfing, and film cooling. As a result of the variation in conditions and geometry, a broad range of c^* efficiencies were obtained. Tests involving radially-uniform mixture ratio profiles produced c^* efficiencies above 99 percent; non-uniform profiles associated with wall durability-enhancement schemes resulted in lower efficiencies. The reliable combustion data is complemented by the fact that the chamber was stable at steady-state conditions throughout the test series. Peak-to-peak steady-state chamber pressure fluctuations were always less than four percent of the average pressure. It should also be noted that the pressure drop across the injection elements was varied from 4.5 to 11.5 percent of the chamber pressure by varying the propellant flow areas. Though all three wall protection methods proved successful at reducing wall heat flux, scarfing of the outer-row, swirl-coaxial injection elements was the technique which resulted in the least debit in c^* efficiency per unit reduction in heat flux.

Data Analysis.

Injector performance for the test series is based on the characteristic velocity efficiency, defined as:

$$\eta_{c*} = c^*_{Real}/c^*_{Ideal} = (P_{o,throat} A^* / \dot{m}_t c^*_{Ideal}) \quad (1)$$

For all the data, $P_{o,throat}$ was calculated by standard Rayleigh loss methods. It was assumed in the $P_{o,throat}$ calculation that the static pressure at the faceplate is essentially the total pressure at the injection plane, and the average gas composition at the throat corresponds to the overall injected mixture ratio. The standard NASA computer model presented in Reference 15 was employed to obtain c^*_{Ideal} . Heat loss to the calorimeter chamber was accounted for by modifying the propellant enthalpy input required to generate c^*_{Ideal} . The resulting c^* efficiencies for the injector characterization series of tests (run numbers 7 through 23) were analyzed statistically relative to the five variables used to generate the test matrix. A statistical regression model was thus derived:

$$\eta_{c*} = 0.931 + 0.00555\dot{m}_f - 0.000572\dot{m}_o + 0.0081A_{Cd,o} + 0.0308A_{Cd,f} - 8.06 \times 10^{-5} T_f \quad (2)$$

where mass flows are in lbm/sec, areas are in in², and T_f in °R. Of the five variables, \dot{m}_f , \dot{m}_o , and $A_{Cd,f}$ had the dominant impact on η_{c*} . The r^2 for equation (2) is 0.91. Also of importance in equation (2) are the positive and/or negative influences of the variables as seen in their respective multipliers. In terms of engine parameters, the end result is that the lower levels of overall O/F mixture ratio (≈ 5.7) and lower levels of the relative $H_2 - O_2$ injection velocities ($DV/V_o \approx 4$) tended to increase c^* efficiency.

Mixture ratio nonuniformities caused by the biasing of the mixture ratio near the chamber wall were a dominant factor on the experimental η_{c+} due to the high percentage of injection elements in the outer row (42 percent). To analyze the mixture ratio striation, a streamtube model, defined in Figure 2.5.4-1, was employed. Streamtube models have been widely used and are based on the assumption that relatively little mixing occurs in the thin shear layer existing between zones (References 16,, 17,, 18,, and 19).

Table 2.5.4-1 presents the predicted O/F mixture ratios corresponding to the test numbers given in Table 2.5.3-7. The calculations are based on measured and calculated flow splits and the assumption that 67 percent by mass of the outer row LOX is directed into the mid-zone while only 33 percent of that LOX is shifted into the wall streamtube when scarfing is present. Note also that by the convention of Figure 2.5.4-1, the H_2 film coolant resides in the wall zone, based on the assumption that the H_2 film is perfectly mixed with the flow from the outer-row elements.

Table 2.5.4-1. Predicted Streamtube Flow Splits

Test No.	Mixture Ratio					LOX Flow pps			Comments
	Overall	Core	Outer	Mid	Wall	Core	Mid	Wall	
004 (2)	5.04	5.86	4.19	6.29	2.51	26.63	12.33	6.16	Chamber Checkout
007 (3)	5.59	6.51	4.64	7.03	2.76	31.88	14.76	7.38	
008B(4)	6.34	7.39	5.27	7.94	3.15	31.54	14.61	7.30	Baseline Configuration
009B(5)	6.22	7.19	5.21	7.67	3.17	31.48	14.58	7.29	
011B(6)	6.38	7.41	5.31	7.79	3.23	31.91	14.77	7.39	
013B(7)	5.98	6.94	4.99	7.37	3.03	41.41	19.17	9.59	
020C(8)	5.75	6.70	4.79	7.15	2.88	41.07	19.01	9.51	
021B(9)	6.34	7.41	5.24	7.94	3.12	41.31	19.13	9.55	
022C(10)	6.35	7.39	5.28	7.97	3.15	41.16	19.06	9.52	
023C(11)	6.24	7.28	5.16	7.83	3.07	32.13	14.87	7.43	Baseline w/ Biasing, Scarfing, Film Cooling
024C(12)	6.15	6.53	5.67	8.76	3.32	31.70	14.68	7.34	Baseline w/ Scarfing, Film Cooling
026C(13)	6.20	6.58	5.73	6.65	5.03	32.00	11.11	11.11	Baseline w/ Film Cooling
027C(14)	6.02	6.25	5.70	6.28	5.23	31.45	10.92	10.92	Baseline w/ No wall Compatibility Features
028C(15)	6.24	7.14	5.28	5.74	4.88	32.22	11.19	11.19	Baseline w/ Biasing

When the results of the wall compatibility runs are compared with the initial series of tests, the effect of mixture ratio striation is evident. Figure 2.5.4-2 contains η_{c^*} as a function of the regression equation and wall O/F ratio. As each wall compatibility enhancement feature was removed, the mixture ratio across the injector face became more uniform and η_{c^*} increased proportionally. In fact, c^* efficiencies above 99 percent were obtained for run number 27 because of a near-uniform O/F distribution across the injector face. To better represent this conclusion, a different linear regression model can be formulated which includes a striation factor (s):

$$\eta_{c^*} = s (1.0156 + 0.001644r_{hf} + 0.0000689r_{h0} - 0.02383A_{Cd,o} + 0.01397A_{Cd,f} - 0.00018T_f) \quad (3)$$

where:

$$s = (1/r_{hi}) \sum_i [r_{hi} (c^*_{calc})_i / c^*_{ideal}] \quad (4)$$

In equation (4) above, $(c^*_{calc})_i$ is the characteristic velocity associated with the O/F mixture ratio of the i th streamtube (as in Table 2.5.4-1). The r^2 associated with the above equations is 0.92 and is represented in Figure 2.5.4-3.

Theoretical Predictions:

Correlation between the P&W analytical combustion model and the subscale data has been achieved with good results. The combustion model20 can be described by the following physical processes:

1. Supercritical, diffusion-controlled combustion
2. Mixture ratio variations
3. Propellant mixing.

The first process listed is the original combustion model used by P&W for the subscale injector predictions. The model uses droplet size and distribution, the heating of the droplets to their critical temperature, the location of the flamefront, and the diffusion-controlled combustion of the resulting mixture to predict the injector performance. The mixture ratio variations and propellant mixing processes were used to modify the model to enhance the correlation with the subscale test data. Analysis of the results led to the addition of a mixing model which takes into account the relative difference between the fuel and LOX velocities upon injection. It has been found that for the range of velocities encountered, the mixing process is dominated by swirl and that lower fuel velocities improve the mixing. This is as opposed to a mechanism dominated by shear in which higher fuel velocities are more conducive to higher efficiency.

The overall η_{c^*} is based on the product of a diffusion (combustion) c^* efficiency and a mixing c^* efficiency, mass-weighted for each streamtube:

$$\eta_{c^*} = (1/r_{hi}) \sum_i (\eta_{c^*, diff} \times \eta_{c^*, mix}) r_{hi} \quad (5)$$

where i represents a single streamtube. The resulting combination of c^* efficiencies (combustion, mixing, and streamtube) leads to the agreement between the analytical calculations and the test data as seen in Figure 2.5.4-4. Most of the predicted η_{c^*} values are within 0.5 percent of their measured counterparts, and all are within 1.0 percent.

The loss in performance due to the wall durability enhancements has been quantified by the results of the test series. The losses are caused by mixture ratio variation across the injector face (to provide a lower mixture

ratio near the wall) which results in the mass-weighted streamtube effect. An injector which has a uniform mixture ratio across the face would inherently have higher performance than an injector which has the core elements operating at a high mixture ratio to achieve low wall mixture ratio. During the test series, it was seen that scarfing had the dominant effect on wall mixture ratio and hence on efficiency. However, the percentage of outer row elements on the subscale chamber is 42 percent as compared with the full-scale chamber which is closer to 10 percent. Therefore, the effect of a low mixture ratio at the wall is not as dominant in the full-scale chamber. The subscale test article, because of the higher percentage of outer row elements provided appropriate sensitivity to injector stream tube effects and the opportunity for enhanced combustion streamtube modeling.

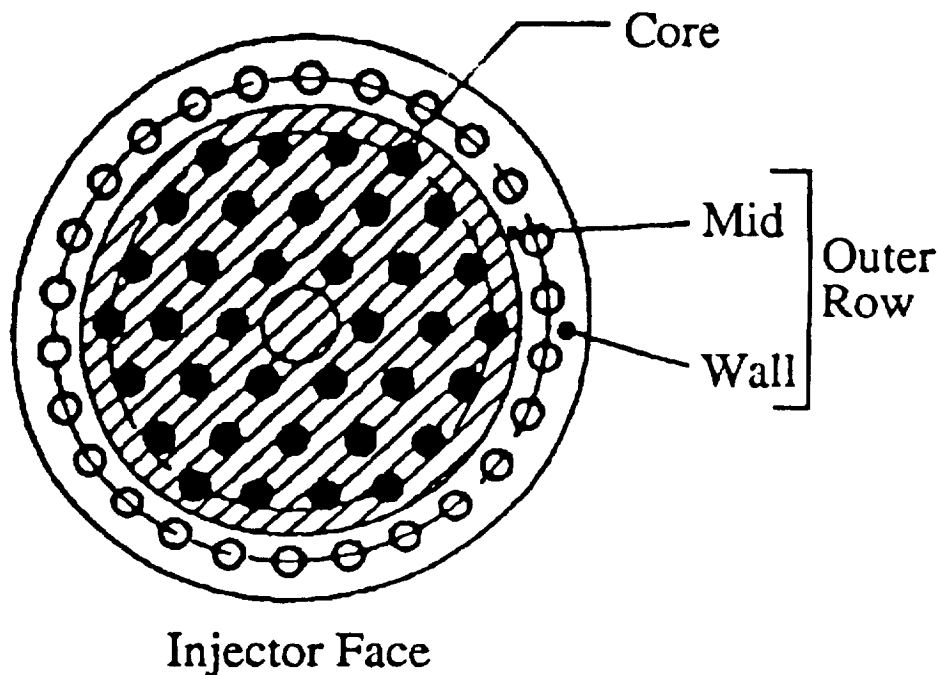


Figure 2.5.4-1. Streamtube Model of Propellant Distribution

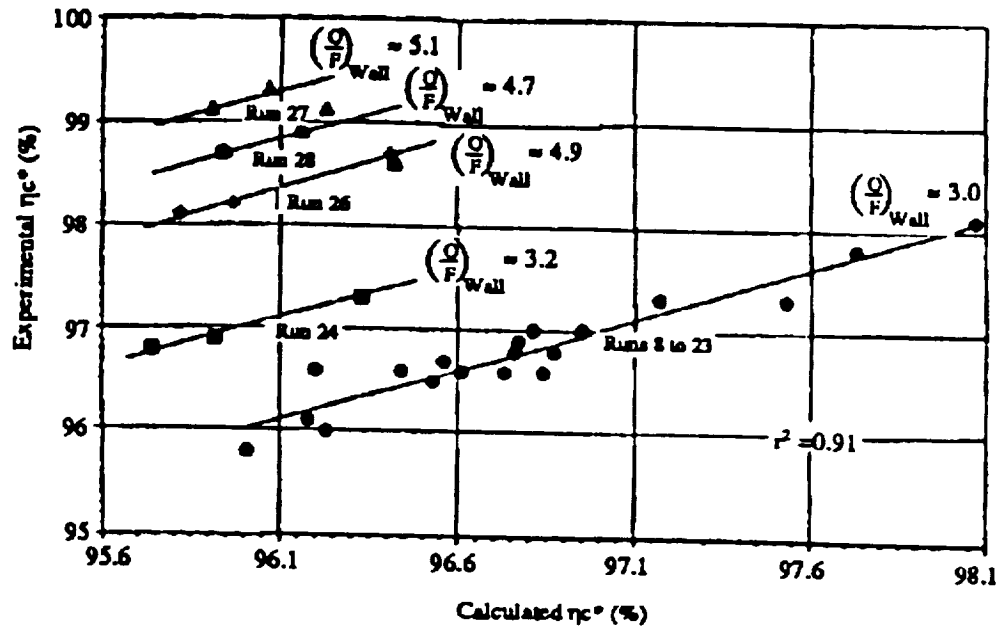


Figure 2.5.4-2. Correlation of Performance Data Using Statistical Regression Model

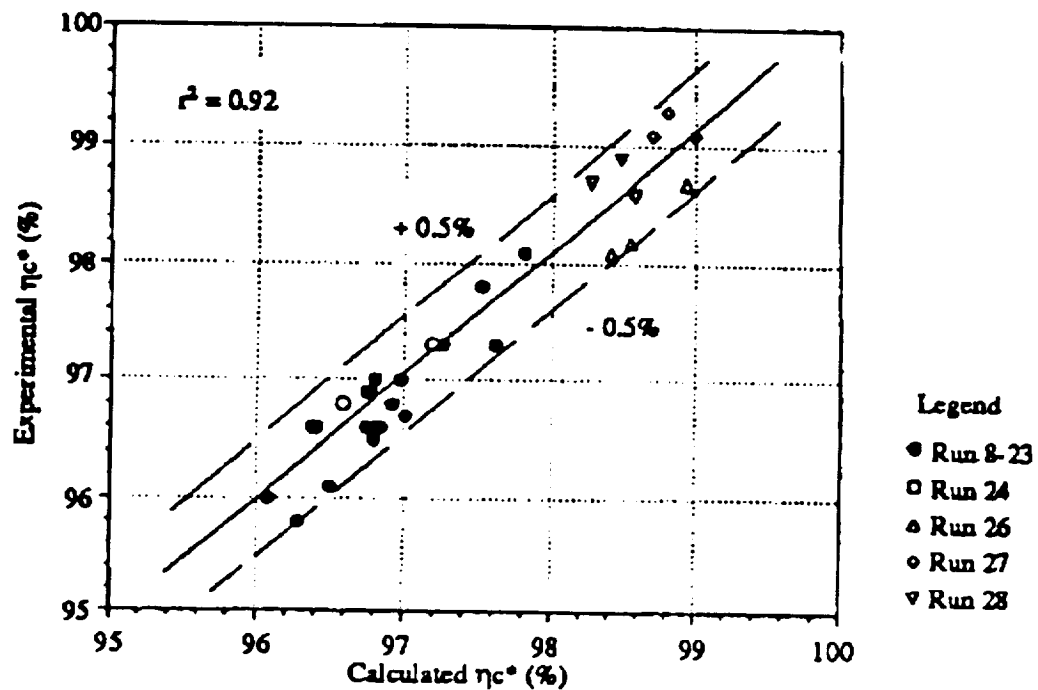


Figure 2.5.4-3. Performance Data Correlation With Striation Effects

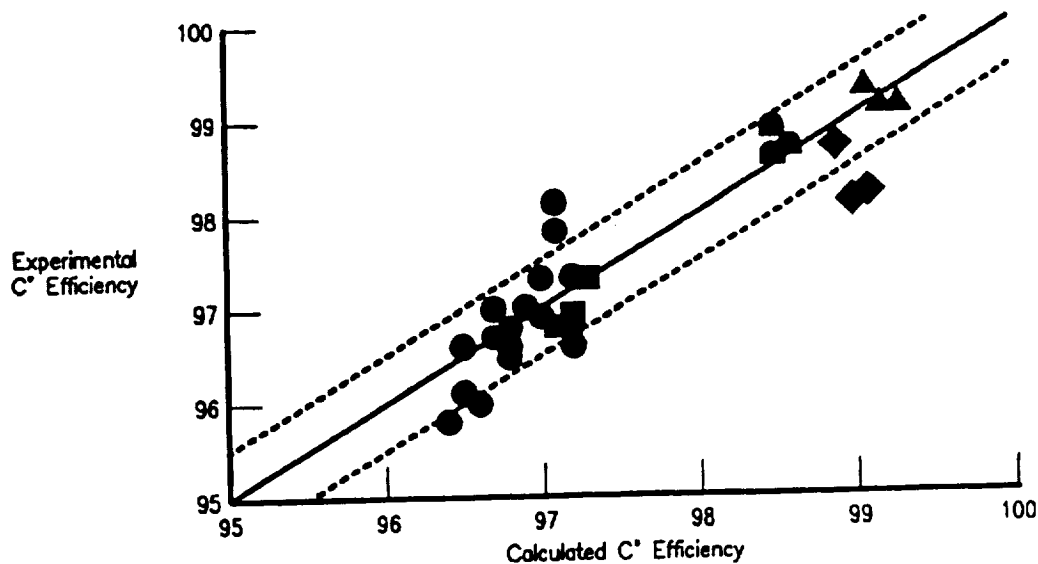


Figure 2.5.4-4. Experimented Versus Calculated c^* Efficiency

2.5.4.2 Combustor Heat Transfer Analysis

Data Analysis:

Throughout the injector characterization portion of the test program, there was negligible effect on the peak heat flux or the heat flux through the cylindrical portion of the chamber due to the injector variables. The final four tests provided the majority of the data concerning the chamber heat flux when the three wall compatibility features, scarfing, film cooling, and mixture ratio biasing were sequentially removed. Of these, the scarfing of the outer row elements provided the dominant effect on the heat flux.

Experimental data confirm a reduction in wall heat flux resulting from the use of scarfed-tipped, LOX, tangential-swirl elements. A summary of the predicted O/F mixture ratios are presented in Table K, which shows an approximate 40 percent reduction in predicted wall O/F attributable to a 45 degree scarfed tip. The scarfed cases show approximate reductions in heat flux of 16 percent and 30 percent at the throat and seven inches downstream of the injector, respectively. This effect can be seen in Figure 2.5.4-5. These reductions correlate with the predicted wall O/F mixture ratio behavior and support the theory that the wall mixture ratio is the driver for wall heat flux and that scarfing provides a significant shift in the wall.

The benefit-to-cost ratio of the three methods is compared in Figure 2.5.4-6. Though scarfing had the largest negative impact on efficiency, its c^* reduction per unit change in wall O/F ratio (i.e., its slope) is lower than the other two wall heat flux reduction methods, which means that scarfing is the method of choice for enhancing chamber wall durability while minimizing the associated performance debit.

Applied to the full-scale, 812 element STME injector, scarfing would have much less impact on η_{c^*} because of the significantly smaller percentage of outer-row injection elements (the only ones scarfed). Also, though the subscale tests only involved a 45 scarf angle, a different scarf angle could be used to trade wall durability for performance. Thus scarfing offers the same adjustability as film cooling or mixture ratio biasing with less of a performance debit for the same near-wall O/F ratio.

As a comparison of two wall treatments, mixture ratio biasing and scarfing, consider an injector with 25 percent of its elements on the radius nearest the wall and a common near-wall mixture ratio and a common overall mixture ratio. Of the two methods, scarfing provides the more uniform mixture ratio profile relative to the overall O/F mixture ratio, which is the key to minimizing the c^* efficiency debit. The greater nonuniformity of the mixture-ratio biasing approach is a result of shifting fuel from the core to the wall. In contrast, scarfing does not rob the core of fuel, it robs the wall region of oxygen, which keeps more of the chamber nearer the overall O/F ratio.

Figure 2.5.4-7 presents calculated c^* efficiencies for a range of percentages of injectors in the chamber core. This figure shows that c^* efficiency should be at least one percentage point higher than film cooling and at least two percentage points higher than mixture ratio biasing when each is the sole means of achieving a wall O/F mixture ratio of 3.0, with an overall mixture ratio of 6.94.

Analysis of the data also revealed that LOX tangential-swirl elements provide an additional reduction in barrel heat flux levels when compared to SSME subscale data. Figure 2.5.4-8 is a comparison of the wall heat flux profile of a representative SSME subscale data point (test 36,(Reference 21)) and a representative, unscarfed injector configuration (test 27C). Results for a scarfed injector case are also shown. The two important points of this figure are: (1) the throat wall heat fluxes are similar between the SSME subscale and test 27C; and, (2) the wall heat flux in the barrel region is significantly reduced for the unscarfed injector configuration. Figure 2.5.4-9 confirms that LOX tangential-swirl injectors reduce barrel wall heat flux when compared to the SSME subscale data. In this figure the wall heat flux was scaled by both the chamber pressure and the barrel contraction ratio to the 0.8 power. The additional test point is from a LOX, recessed, tangential-swirl injector configuration tested at NASA/MSFC immediately following the P&W test program(Reference 22); this tangential-swirl injector resulted in a heat flux profile similar to the P&W unscarfed, tangential-swirl injector.

Theoretical Predictions:

Comparison of the test data with the pre-test analytical model revealed that the model was underpredicting the heat flux to the chamber. This was traced to the model assumption that enthalpy and temperature were correlated, primarily affecting transport properties. This was corrected and then modifications were developed to improve the correlation with the test data in the subsonic portion of the chamber.

An adjustment to the model was made using a constant front end heat transfer coefficient number (cm) to account for a suppressed mixture ratio at the wall. This suppression is a function of the additional fuel flow area outboard of the outer row of elements which forms a low mixture ratio stream tube at the chamber wall. With this modification the model accurately correlates the test data for all of the subscale runs, including those with the wall compatibility features (scarfing, mixture ratio bias, and film cooling) removed. It also accurately correlates with previous 40K test data collected by R. Bailey for NASA-MSFC (Refer to "Test Evaluation of Oxygen-Methane Main Injectors").

In the supersonic section, a flat mixture ratio profile and a reduced cm factor was used successfully to correlate with all test data, including prior SSME 40K data.

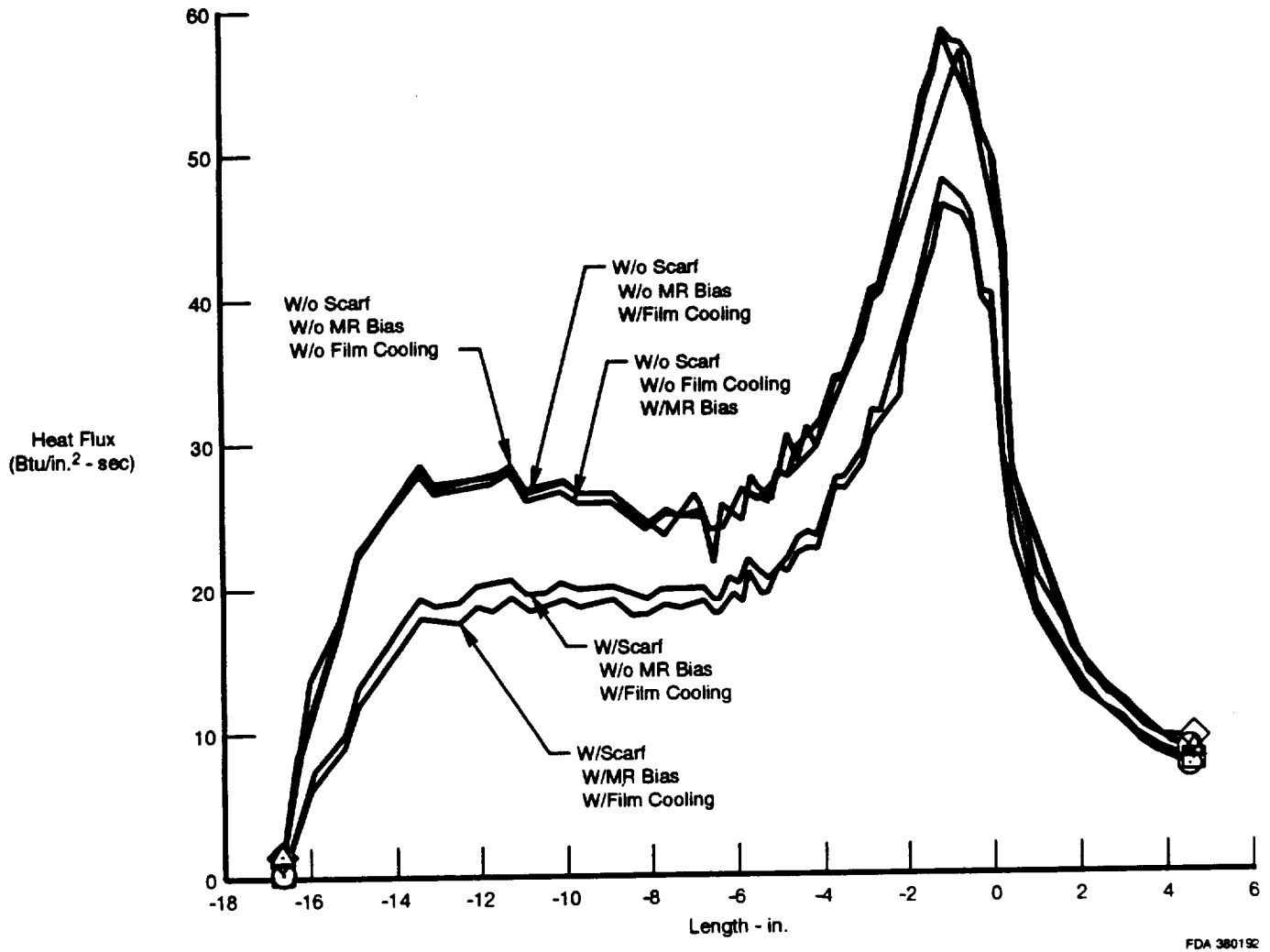


Figure 2.5.4-5. Experimental Wall Heat Flux in Subscale Thrust Chamber

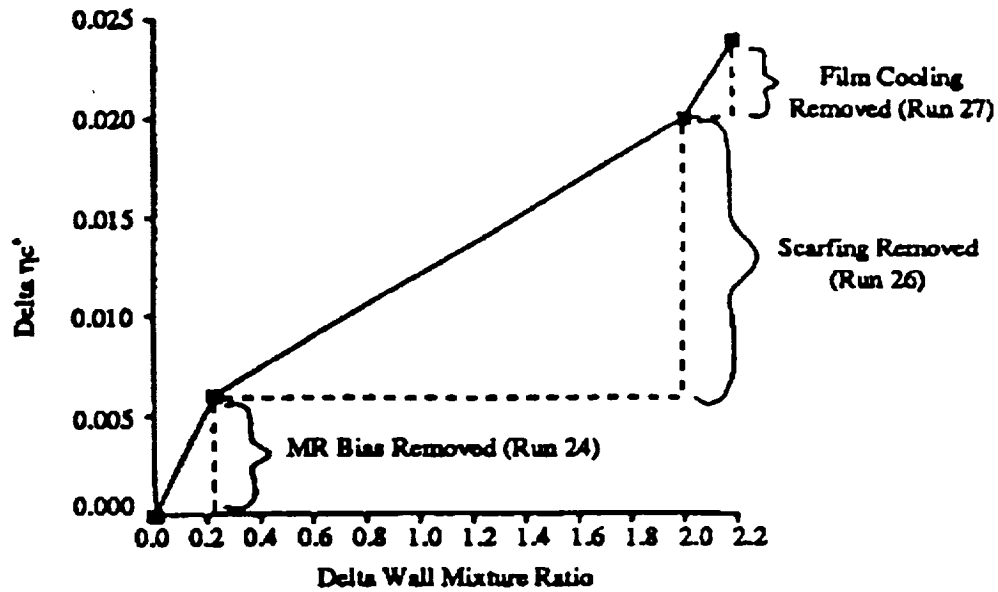


Figure 2.5.4-6. Performance Debit Relative to Amount of Wall Cooling

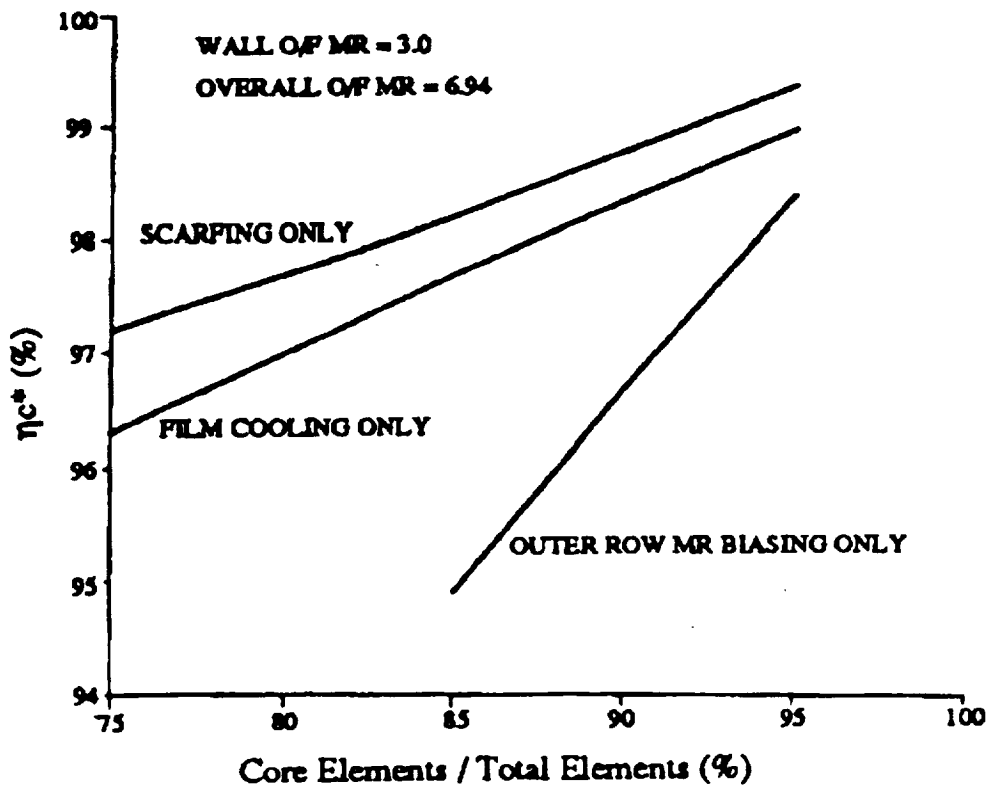


Figure 2.5.4-7. Performance Benefits of Scarfing

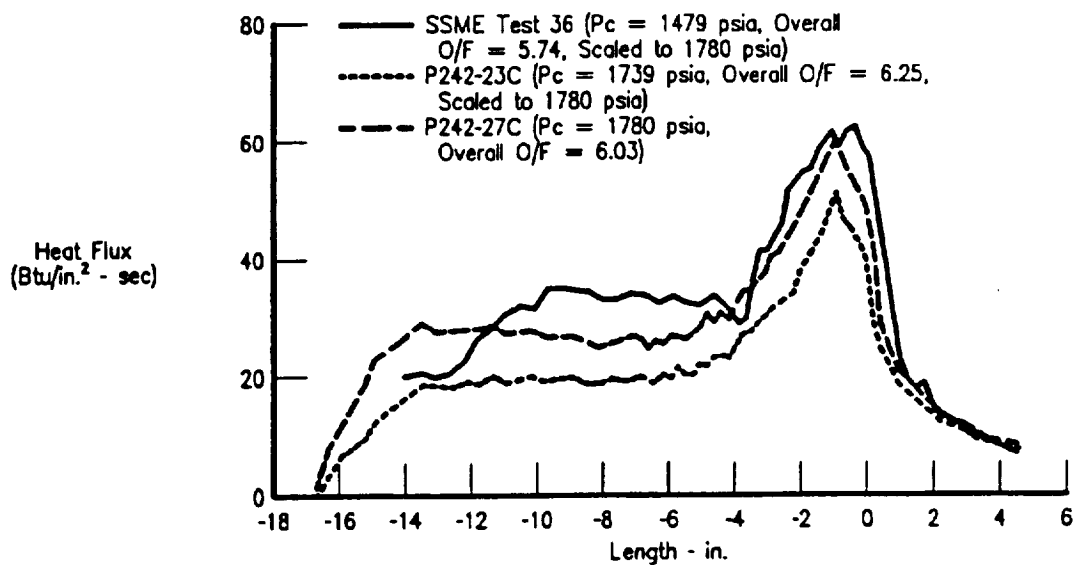


Figure 2.5.4-8. Comparison With SSME Subscale Data

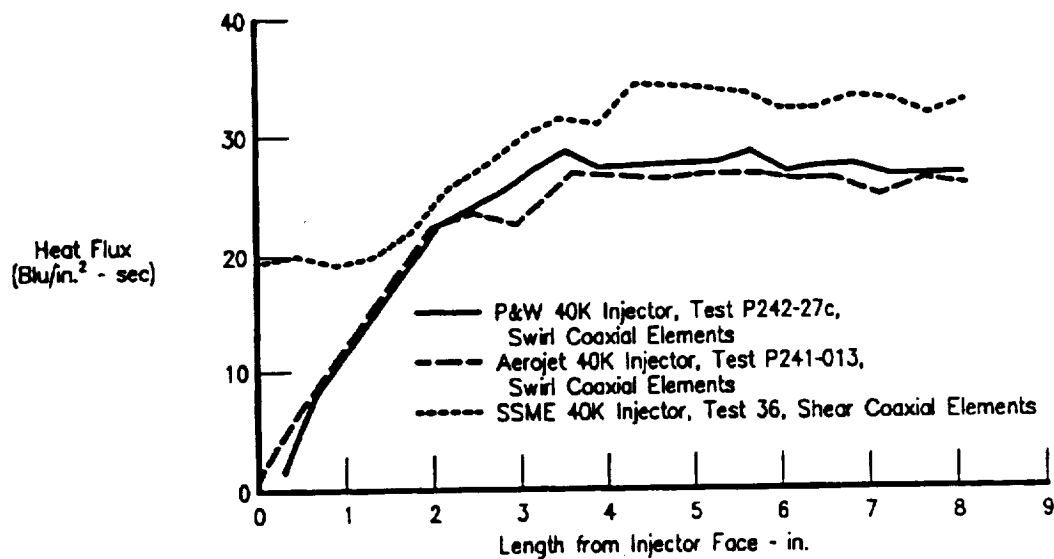


Figure 2.5.4-9. Swirl Element Versus Shear Element Heat Flux

SECTION 3.0 LARGE-SCALE TASK

3.1 LARGE-SCALE INJECTOR

3.1.1 Large-Scale Injector Design

Figure 3.1.1-1 shows a cross section of the current large-scale injector design. Hydrogen fuel enters through a INCO 625 Greyloc flange and passes into the INCO 718 manifold. This manifold is electron-beam (EB) welded at two locations to the INCO 718 injector housing. The fuel passes through sixty crossover holes into the fuel cavity, from which it is fed into the combustion chamber through either INCO 718 fuel sleeves or annuli between the INCO 718 LOX elements and the 347 stainless steel porous faceplate. Some fuel also passes through the faceplate to transpiration cool the injector face. LOX enters through two six-inch schedule XX, INCO 625 pipe elbows. From there it travels into the LOX elements through tangential entry slots and into the combustion chamber. Each of the 808 LOX injectors are tangential-entry, swirl-coaxial elements which produce a hollow-cone spray with an average drop size of 15 to 20 microns at normal operating conditions. The tangential entry swirl concept is shown in Figure 3.1.1-2. The injector is also designed with 4 inactive elements, two of which are used as aspirated combustion chamber pressure taps. The other two are bomb ports, where the bombs for stability testing are mounted and connected to lead wires.

Figure 3.1.1-1 shows the injector element pattern. 108 of the 812 elements form a circular outer row, and 12 elements form a circular inner row while the remaining elements fall into a hex pattern in the infield. The igniter comes through the very center of the injector. Like the subscale, the large-scale injector features a one-piece electrodischarge machined (EDMed) interpropellant plate with integral LOX elements. The advantages of the one-piece interpropellant plate design are described in the subscale injector design section. The large-scale injector does not incorporate the fuel and LOX flow area flexibility features which were incorporated into the design of the subscale injector elements. Performance was optimized using subscale test data. While the large-scale injector does not incorporate film cooling or outer row mixture ratio biasing, it does have scarfed outer row elements for combustion chamber wall compatibility. Scarfing is described in detail in the subscale injector design section.

The faceplate is mechanically attached to the injector with facenuts which are screwed into fuel sleeves, which are in turn brazed onto the LOX elements. This configuration is similar to the subscale injector and is seen in Figure 3.1.1-2. A major difference from the subscale, however, is that, in the large-scale injector the faceplate is attached at only a limited number of elements, 234 out of 812. This is the number of attachment points required for structural integrity. Cost is reduced because fewer facenuts and fuel sleeves must be made. Fuel flow through the attachment elements is controlled by the gap between the LOX post and the facenut. For non-attachment elements, the fuel flow is controlled by the gap between the LOX post and the hole in the faceplate. The LOX flow for all elements is controlled by the tangential LOX entry slots on the upstream side of the LOX posts. The facenuts are secured with purple Loctite, a low-strength thread-locking compound. The OD of the faceplate is welded to the housing to provide a seal between the faceplate and the housing. Each of the fuel sleeve to LOX element brazes was axially load tested in the same manner as the subscale. Because the gold-nickel braze is ductile the load testing does not damage the braze. Because this braze is structural only and is not required to seal between oxidizer and fuel, this braze does not need to undergo the scrutinizing inspection of a prime reliable braze joint.

The hypergolic igniter for the large-scale injector is integral with the injector housing, and is nothing more than a small hole which runs through the center of the injector. A threaded copper (NASA Z) insert was incorporated into the design to direct the triethyl aluminum/triethyl boron (TEA/TEB) hypergolic ignition fluid outward in multiple (4) streams to aid in mixing with the oxidizer. If necessary, the insert can be removed through the chamber exit. This Insert is shown in Figure 3.1.1-3.

Review of the bomb attachment lug design with Rocketdyne personnel prompted the addition of a spacer between the bomb and the bomb port element. The spacer is required to compensate for the excess lug penetration into the fuel cavity. The long lug would not allow enough clearance for provision of a large-radius bend in the wire conduit to ease the bomb wire installation. The spacers were fabricated from stainless steel would be and film cooled by the cold gaseous hydrogen as it exited the porous faceplate. Figure 3.1.1-4 shows the bomb installation configuration.

The bomb lead wires are routed to the bomb port elements through the fuel manifold, crossover holes, and fuel cavity in 347 stainless steel conduit. This 0.165-inch OD tube serves two purposes. First, it guides the lead wire to the bomb ports allowing the installation of the lead wires without removal of the faceplate or even removing the injector from the test stand. Secondly, the conduit protects the lead wires from forces caused by possible turbulent hydrogen flow. Instrumentation which is routed to the faceplate or fuel cavities, is also routed through the 347 stainless steel conduit.

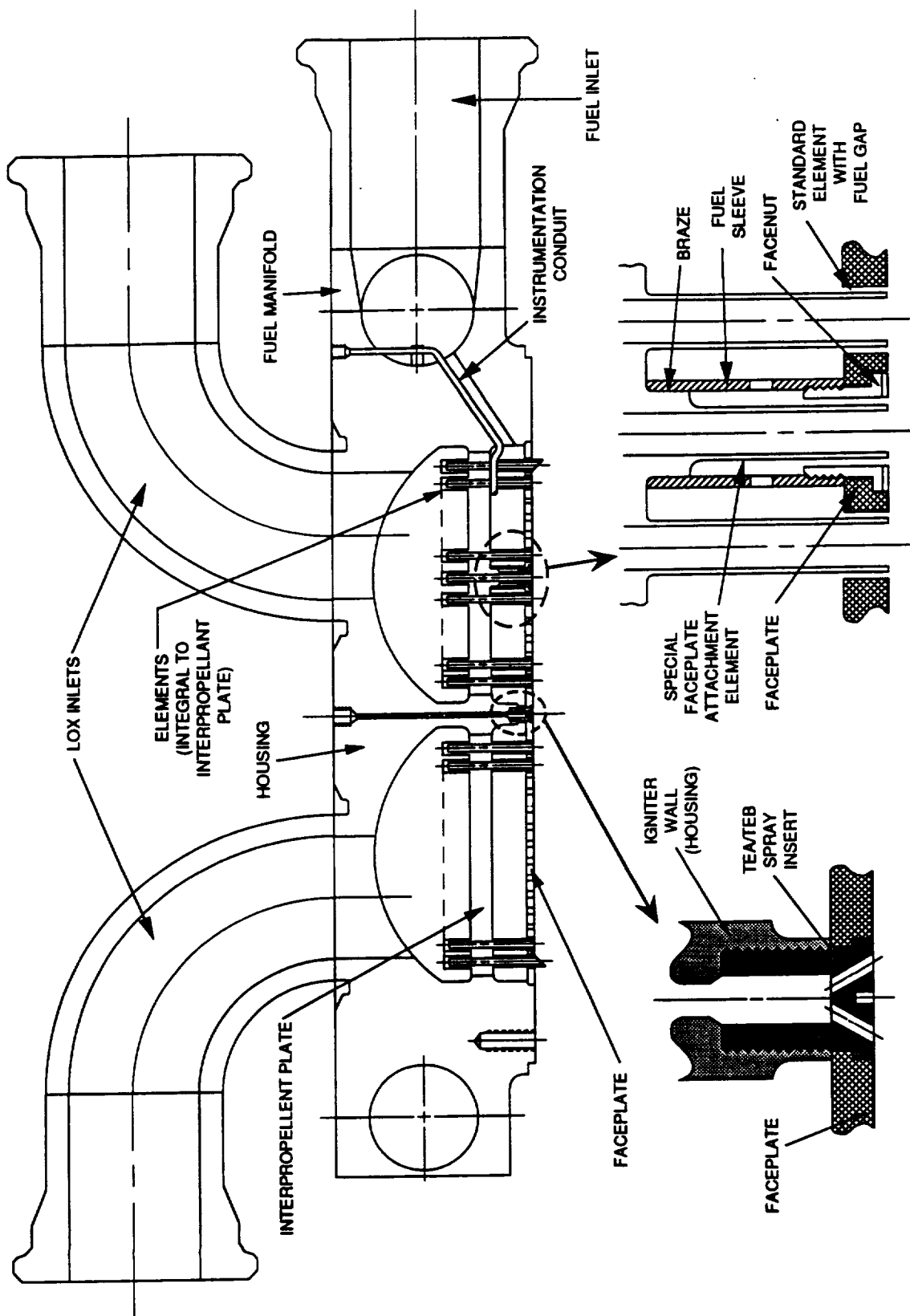


Figure 3.1.1-1. Large-Scale Injector Cross-Section

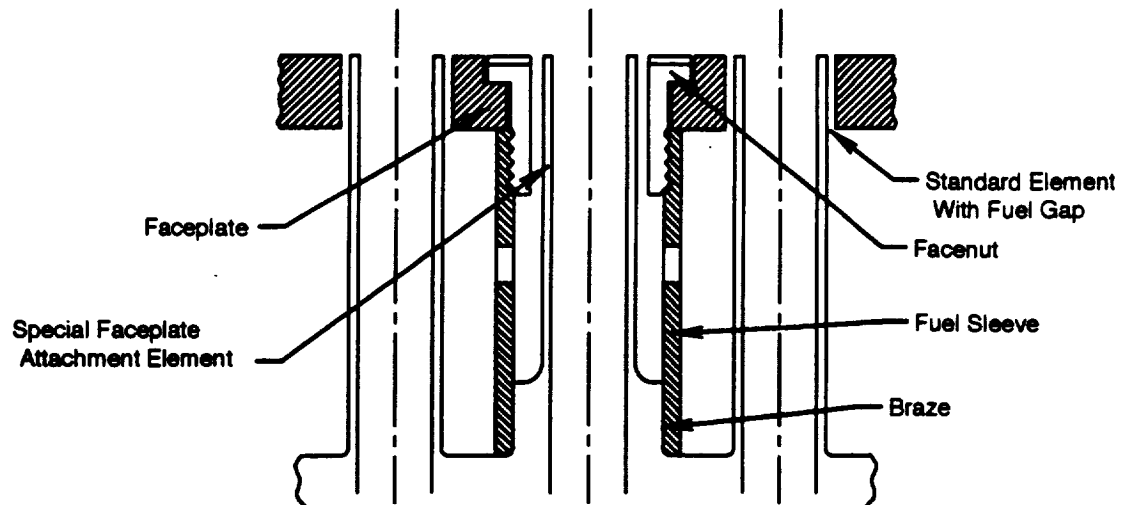


Figure 3.1.1-2. Low-Cost Faceplate Attachment Scheme

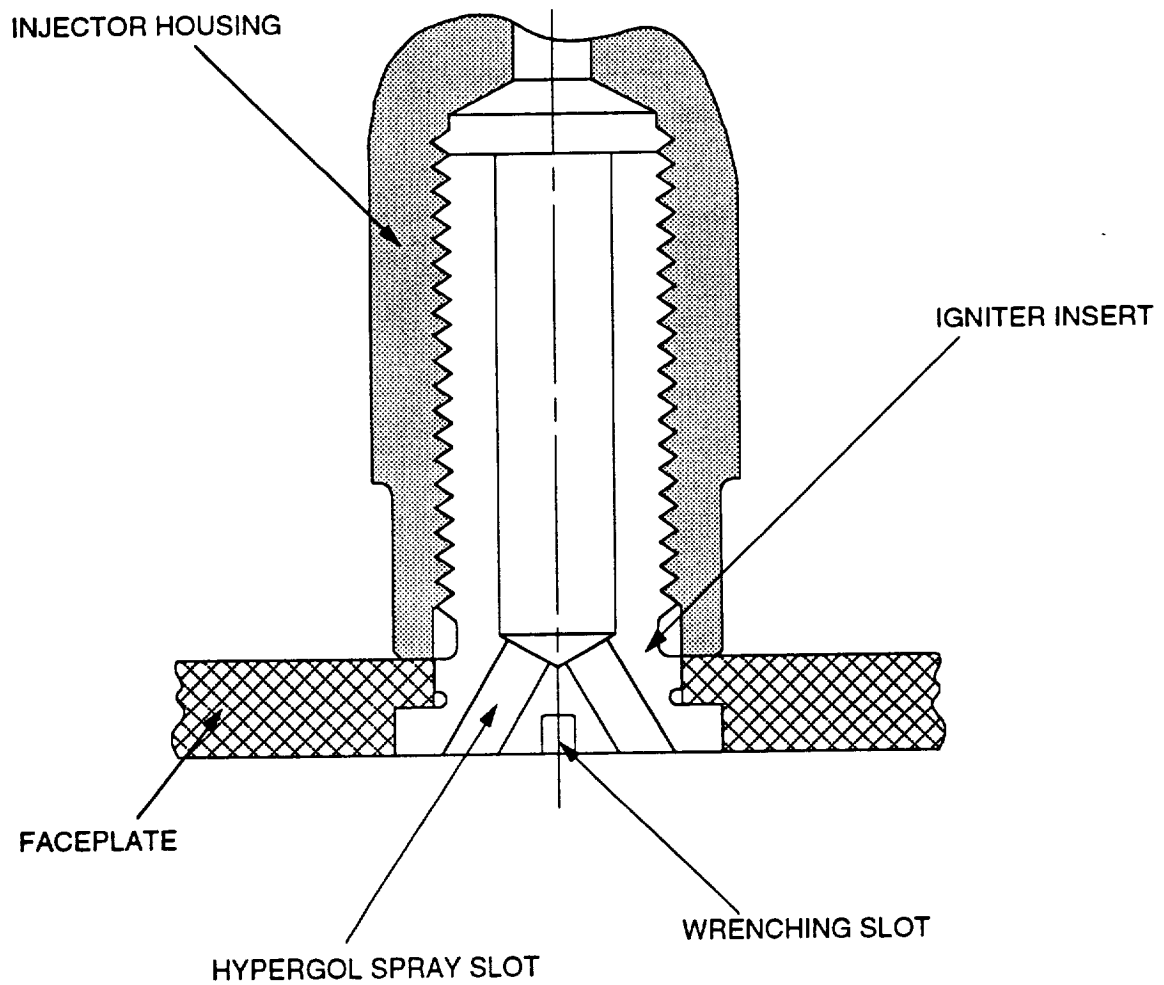
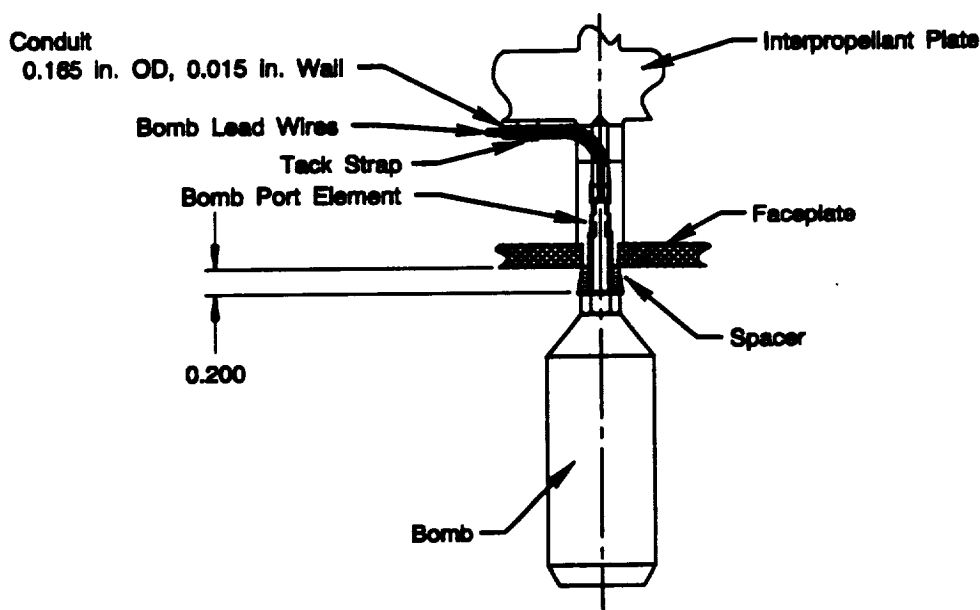


Figure 3.1.1-3. Large-Scale Injector Igniter Insert



FDA 384230

Figure 3.1.1-4. Bomb Installation for Combustion Stability Testing

3.1.2 Large-Scale Injector Design History

Like the subscale injector, the large-scale injector was originally designed to operate on oxygen methane. Initially, it was designed to include flexible geometry to allow running three design points (STBE Unique at 3158 Pc, STBE Derivative at 2250 Pc, and STME Unique at 2250 Pc). This would have required removable fuel face nuts and LOX element plugs similar to the configurations used for the subscale injector. It would have an integral element interpropellant plate manufactured using a potential low-cost method. A removable fuel manifold was also considered to permit changing the mounting configuration. With this removable manifold it would have been possible to test this injector in the baseline configuration, a direct feed configuration, with a partial flow combustion chamber (part of the fuel flow through the liner, the remainder entering through an injector manifold and mixed in the injector), or mounted directly to the government furnished combustion chamber. Some of these other configurations would have required additional manifolds.

Early in the design of the large-scale injector and acoustic liner spoolpiece, P&W considered the use of a direct fuel feed concept for the large-scale testing. With this concept all of the fuel needed for the injector would be routed through the acoustic liner spoolpiece and fed directly from the discharge of the liner into the injector fuel cavity. P&W had coordinated the requirements for this concept with NASA since the fuel inlet pressure required for this concept is higher than that needed to supply fuel directly to the injector. With the maximum available pressure of 4200 psia as indicated from NASA, it was determined that it would be possible to run at chamber pressure of approximately 3000 psia when burning methane. Although this was slightly lower than the STBE Unique design point (3158 psia), it was felt that this would still provide a credible demonstration of the injector performance and the low-cost configuration concept. Although it would be desirable to demonstrate this low-cost configuration during this program to provide credibility for the direct feed concept, this approach was determined to be higher risk than the baseline plan to use hydrogen coolant from the combustion chamber to cool the spoolpiece and feed the injector independently. This is due to two primary reasons. First, there was concern for the effects on life of the injector and the acoustic liner spoolpiece. Secondly, there was concern about using this direct feed concept due to the accurate pressure drop prediction that was needed. This was due to the fact that the pressure drop in the spoolpiece would affect the injector fuel supply. Because this was to be primarily an injector technology program, it was desirable to be able to explore various areas of injector

operation to determine operating margins. With a direct feed concept such variations in operation may not have been possible either due to the pressure drop in the spoolpiece or to coolant flow requirements which restrict the amount of fuel flow variation. P&W decided to proceed with the baseline configuration of cooling the spoolpiece independently of the injector flow.

Later, it was decided to incorporate as many flight-type features as possible into the large-scale injector design. The use of a removable fuel manifold was abandoned to allow the use of a one-piece injector body and the removable LOX dome was eliminated. These changes will make the injector more representative of a flight configuration which would use near-net forgings or castings.

At the request of NASA, P&W reviewed the possibility of using two oxidizer inlets instead of one as originally planned. This request came as a result of consideration being given in the large-scale facility design to use two oxidizer supply lines. The impact of going to two inlets was reviewed based on the velocity of the oxidizer entering the injector and the subsequent distribution in the injector. P&W reviewed the use of one inlet on the injector performance and found that the pressure distribution in the LOX cavity was acceptable as far as its effect on injector performance and combustion chamber wall heat variations. In reviewing the request to evaluate running two inlets, P&W also considered the impact on demonstration of the injector performance. Since pressure distribution will be more difficult with one inlet than with two, it is desirable to demonstrate this in the testing. However, in order to provide compatibility with the test stand which will use two inlet lines and two LOX control valves, P&W incorporated two oxidizer inlets into the injector design.

These decisions led to the injector design shown in cross section in Figure 3.1.2-1. This design incorporated low cost features, where considered feasible, and rig features elsewhere. The low cost features included an integral element interpropellant plate, similar to the plate the one used in the subscale test rig, and fuel sleeves integral to the LOX posts, unlike the subscale rig where fuel sleeves incorporating threads for face nut changeout were brazed to the oxidizer elements. The integral fuel sleeve concept is shown in Figure 3.1.2-2. Also shown in that figure is an option for brazing of the fuel sleeves. The other features of the injector were designed as rig components incorporating large factors of safety with simplified geometry for ease of machining.

As requested by NASA, The LSI design was revised to incorporate the interface to the injector to an instrumentation spoolpiece. This spoolpiece would be used to allow testing of the large-scale injector without a stability aid. The instrumentation ring would be used in place of the acoustic liner spoolpiece. Only a minor change to the injector interface was needed to accommodate mounting to the instrumentation spoolpiece.

For a given geometry and chamber pressure, wall mixture ratio was shown to be the primary driver in heat flux. To provide a uniform circumferential heat flux profile, the full-scale injector element pattern was revised from a full hexagonal pattern to a circular outer row with a hex pattern for the infield elements (based on the subscale injector design). By positioning all of the outer row elements an equal distance from the chamber wall, the occurrence of coolant flow maldistribution would be minimized due to the even heat flux profile.

The integral fuel sleeve concept was evaluated in machining samples. It was determined that with the present technology, this concept could not reliably and inexpensively produce fuel sleeves which met tolerance requirements. Since the time and money were not available to develop the potential of the integral fuel sleeve concept, The injector was redesigned to incorporate a new faceplate attachment scheme. This scheme, shown in Figure 3.1.1-2, uses a simple, reliable braze to attach the fuel sleeves to the elements. Also, since this braze is structural only and is not required to seal between oxidizer and fuel, this braze does not need to undergo the scrutinizing inspection of a prime reliable braze joint. A simple load test is sufficient.

Cost is further reduced by eliminating the complex braze of the faceplate to the injector elements in favor of mechanically attaching the faceplate with facenuts as was done on the subscale injector. Additional cost reduction

was realized by attaching the faceplate at only a limited number of element locations; only the number of locations required for structural integrity. The number of facenuts and fuel sleeves required is thus greatly reduced. Since variable propellant flow areas were not required on the large-scale injector, the fuel flow area of non-attachment elements could be controlled by the LOX post and the hole in the faceplate rather than by facenuts.

Analysis of the test data for the 40K subscale injector showed that differential pressures across the interpropellant plate and the faceplate were much higher than expected. The maximum ΔP across the interpropellant plate was 1200 psi from the fuel cavity to the LOX cavity (at shutdown) and 200 psi from the LOX cavity to the fuel cavity (at start-up). The maximum ΔP across the faceplate was 1200 psi (at shutdown). Since the full-scale injector was originally not designed to take pressures of greater than 300 ΔP across the interpropellant plate, it was decided to redesign the full-scale injector to handle the larger ΔP s. Although the full-scale injector was to be tested on a new test stand which was expected to have better control over the ΔP s than the subscale stand, the level of uncertainty required the full-scale injector to be able to withstand greater ΔP s. To increase the P capability across the interpropellant plate, the plate thickness was increased from 0.750 to 1.250 in., and the LOX cavity radii was increased, as shown in Figure 3.1.2-3, to reduce the pressure-limiting stresses. Also since the torch igniter was eliminated from the injector design in favor of a hypergolic igniter it was possible to make the igniter integral to the injector housing. This not only significantly reduces cost (the only separate igniter component required is a simple threaded insert at the injector face to create the hypergol spray pattern) but also allows the center hole size to be reduced and thus the wall thickness increased. This change can also be seen in Figure 3.1.2-3. To increase the P capability across the faceplate, the number of element locations at which the faceplate is attached was increased.

As a result of the redesign the new maximum allowable ΔP across the interpropellant plate at start-up (from the LOX side to the fuel side) was 700 psi, while the new maximum allowable ΔP across the interpropellant plate at shutdown (from the fuel side to the LOX side) was 1400 psi. The new maximum allowable ΔP across the faceplate was 1500 psi. These maximum allowable ΔP s are higher than the ΔP s seen in the subscale testing. At this point the design was essentially the current large-scale injector design.

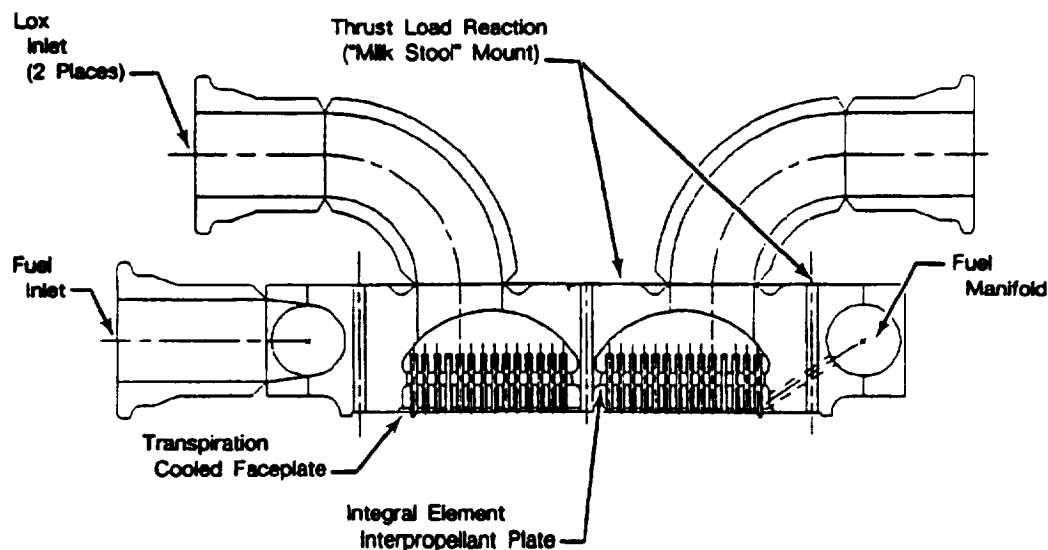


Figure 3.1.2-1. Early Full-Scale Injector Cross-Section

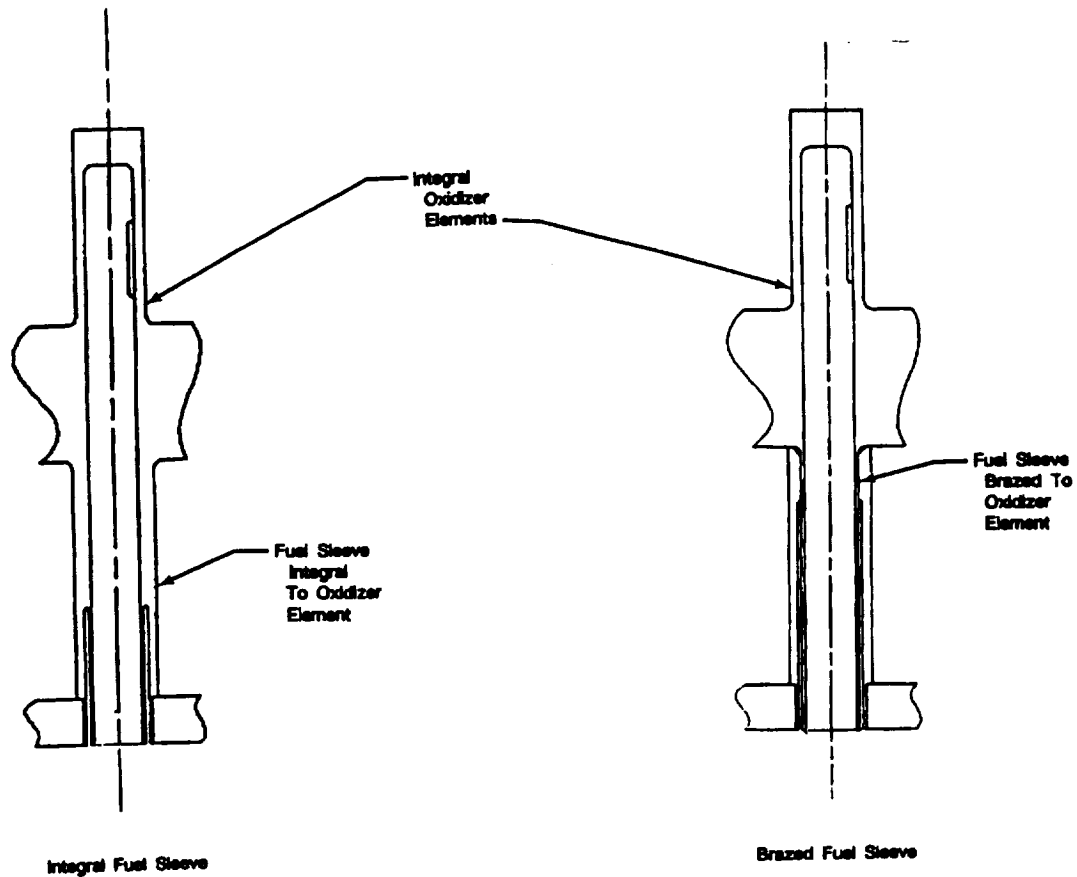


Figure 3.1.2-2. Early Full-Scale Injector Fuel Sleeve Options

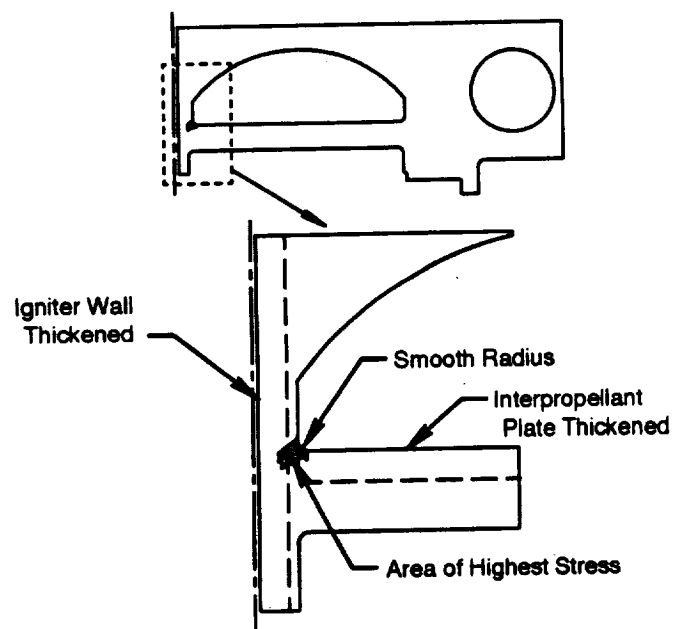


Figure 3.1.2-3. Redesign of Injector Housing and Interpropellant Plate

3.1.3 Large-Scale Injector Fabrication History

3.1.3.1 Interpropellant Plate

By far the most challenging detail of the large-scale injector to manufacture was the interpropellant plate with its 812 integral elements.

After receiving the pancake forging, the interpropellant plate vendor turned the forging to rough size and then rough EDM the element posts on both the LOX and fuel sides of the interpropellant plate to about 0.50 inch greater than their finished diameters. All of the elements on either side of the plate were "gang" EDMed. That is they were all EDMed together at one time. After rough EDM, the interpropellant plate was stress relief heat treated to eliminate stresses and movement caused by the removal of a large amount of material from the pancake forging. A photo of the inter propellant plate after rough EDMing is shown in Figure 3.1.3-1. Figure 3.1.3-2 shows a typical carbon electrode that was used during the rough EDMing of the LOX elements.

However, during the EDM and subsequent stress relief cycles the interpropellant plate experienced radial shrinkage, effectively moving the outer row elements inward by as much as 0.032 in. and increasing the thickness across the center of the plate by about 0.015 in. The plate also experienced bowing, making it concave on the oxidizer side. This alone could have been compensated for within the remaining machining stock envelope, but the additional movement of the elements due to the radial shrinkage required adjustment of the element pattern to maintain the dimensional requirements of the element features.

The radial shrinkage was thought to be due mainly to residual stresses resulting from the rapid quench performed following the forging heat treat cycle. Another factor which may have contributed to the shrinkage is that the interior of the plate may have spent some time at the precipitation hardening temperature during heat treat cycles at the vendor, which had cool down rates slower than required. INCO 718 shrinks during precipitation hardening.

The interpropellant plate was subjected to an additional solution heat treat cycle to remove any remaining residual stresses. A thermocouple imbedded in an INCO 718 plug was inserted into the center hole of the plate to monitor the core temperature response and ensure that the solutioning temperature was reached throughout the material thickness. Additional mass used during the previous stress relief heat-treat cycles in an attempt to flatten the plate was discarded to aid in attaining the maximum cooldown rate possible. Dimensional inspection afterwards revealed a recovery of 0.010 in. of the radial shrinkage. The element pattern was adjusted to compensate for the remaining offset of the elements. As a result the rigimesh faceplate hole pattern also had to be adjusted to compensate for the relocation of the elements.

Following solution heat treatment of the interpropellant plate, a material sample was taken from an element near the center of the plate. The microstructure of this sample was examined and found to meet all microstructure requirements.

The vendor that would be performing the gundrilling of the core holes in each element completed drilling of small INCO 718 samples to establish the process parameters based on tool wear and hole finish, along with a full-scale steel sample to verify true position of each hole. When this sample was drilled, a subsequent inspection revealed an error in the element locations as much as 0.007 inch in the outer row. The gundrilling machine was laser calibrated and the inaccuracy identified as inherent in the machine positioning system. Historically, gundrilling has not been performed on a part that has required close tolerance control over a large (21-inch diameter) area, therefore, the deficiency had gone previously undetected. To correct the inaccuracy, a software compensation package was installed that corrects for the repeatable positional deviation.

With the compensation package installed, recalibration verified that the required tolerance could be attained. A second sample plate was drilled to verify the modified hole pattern developed to compensate for the interpropellant plate shrinkage. After this sample was received and inspected, The holes in the LOX elements of the actual interpropellant plate were drilled. Figure 3.1.3-3 shows an overall view of the fuel side of the interpropellant plate after the gundrilling of the holes in the LOX elements. Dimensional inspection indicated that several of the holes were drilled outside of the parallelism tolerance allowed relative to the element centerline, with the worst being 0.015 inch out of parallel from the element tip to the central location of the LOX entry slots. Additionally, many of the holes were nonconcentric with the element OD. It is thought that these gundrilling inaccuracies were due to a lack of stiffness in the positioning table of the gundrilling machine. The machine flexed slightly when drilling the deep holes in INCO 718, which is a very tough material. The problem did not show up on the small INCO 718 samples because it was a large moment created when the outer holes far from the center were drilled that caused the deflections in the machine. The small samples did not have holes far enough away from the center to have a large enough moment arm to cause a measurable deflection in the machine.

The positions and diameters of the holes and the element ODs were thoroughly inspected and recorded for each element, and the finishing electrode pattern was adjusted to compensate for the concentricity and parallelism of the holes. There was adequate stock remaining on the element ODs to correct the concentricity, resulting in wall thickness variations within blueprint limits on all but a small number of elements on the fuel side (only one of these elements later proved unacceptable for structural and functional requirements). Similarly, there was sufficient material remaining on the LOX side of the elements such that the final position of the OD of the post could be adjusted to match the centerline of the element ID at the LOX entry slot location within defined limits on all of the elements.

The elements were then finish EDMed in two steps to about 0.005 in. greater than the final diameter. The extra stock was to allow for removal of the recast layer left by the EDM process. These EDM operations were also "gang" EDM operations where all of the elements on one side of the plate were EDMed at one time. The interpropellant plate was then chemical milled to remove the recast layer. After chem-milling, the tight-tolerance diameters, such as the ends of the fuel sides of the elements and the bases of the attachment elements where the braze joint would be, were hollow milled to the proper dimensions. The gundrilled holes required no recast layer removal and were masked off during chem-milling. The thin walled elements on the fuel side were also masked off during chem-milling since there was not enough extra stock left on these elements for both chemical and hollow milling.

During the hollow milling of the fuel side elements, damage occurred to four of the fuel side elements. One element was damaged when the coordinate for the depth of cut was improperly input into the machine and approximately 0.75 inch of the element tip was cut off. Three additional elements were damaged when an incorrect coordinate for the positioning of the tool was entered, resulting in damage to the elements, one of which is an attachment element for the faceplate. After the hollow milling was completed, a crack was discovered in one of the thin walled elements. The wall at one point on this element was so thin that the hollow miller broke through the wall. All of the elements were leak checked, and no other wall break-throughs were found. The locations of all five of the damaged elements are shown in Figure 3.1.3-4.

Since the tangential LOX entry slots had yet to be installed at that time, it was possible to remove the damaged portion of the elements and leave these elements inactive, without affecting the integrity of the one-piece design. Optionally, brazed replacement elements could have been incorporated at these locations to preserve the number of active elements, but this would have had a negative impact on the reliability of the plate by including five prime-reliable joints between the LOX and fuel systems. The effect on injector performance was determined to be negligible if the five elements were made inactive since the injector would still feature 803 active elements. The faceplate will not have regular holes installed at the locations of the three inactive non-attachment elements but instead had a pattern of eight small holes at each of these locations. This pattern of holes had the same

effective flow area as a standard fuel annulus on an undamaged element in order keep the fuel distribution the same as it was before. The one attachment element would receive a fuel sleeve as originally designed, but would employ a solid facenut with coolant holes fed from the fuel cavity, and would secure the faceplate through a standard hole in the faceplate.

Samples were fabricated to study the EDMing of the tangential LOX entry slots. Samples which simulated a long row of elements were used to determine the maximum number of element slots that can be "gang" EDMed simultaneously to reduce processing time and cost, while successfully maintaining the required positional tolerances. Machine parameters were also determined, along with tooling and electrode requirements. Figure 3.1.3-5 shows a segment of an electrode used to EDM several slots along a row of elements simultaneously.

To allow in-process evaluation and process control of the EDMing of the tangential entry slots, a waterflow facility was established at the supplier to evaluate each element for the correct A_{Cd} and spray cone angle. Waterflow samples were fabricated and tested before EDMing the LOX entry slots of the interpropellant plate to ensure that the correct machine parameters are set to provide the correct propellant flow rates and mixing characteristics. These samples were also water flow tested at a P&W flow facility as a check of the vendor's water flow facility.

After the samples were tested with satisfactory results, LOX entry slots were installed in the twelve elements in the innermost row (closest to the center), and these elements were water flow tested. The center elements were done first because these would pose less risk the chamber wall if they were machined improperly. After the water flow results on these elements proved acceptable, The LOX entry slots were installed in the remaining infield elements. Because of the hexagonal pattern of the infield elements, a whole straight row of slots in one direction could be "gang" EDMed at once. This could not be done on the outer row or the inner row since these rows were circular and had no straight lines. The LOX entry slots in the outer row elements were the last to be installed.

Occasionally during the EDMing of the infield LOX slots, the plate would be taken off the EDM machine for water flow testing of completed elements to ensure that the slot EDM process was under control. Figure 3.1.3-6 shows a schematic flow testing of the interpropellant plate elements on the vendor flow facility. Some elements could not be water flowed. Because of their proximity to other elements, The flow fixture would not fit over them. In these cases the LOX entry slots were dimensionally inspected to verify that they had the same dimensions as slots that could be tested and had good water flows. If the slot dimensions of two elements are the same the flows should also be the same. Thus if an element had slots with the same dimensions as one that flowed correctly then that element should also flow correctly. The water flows of all the LOX elements proved to be within acceptable limits. Two elements did have higher than expected flows but this was easily compensated for by drilling the holes in the faceplate at those locations slightly larger than normal. The resulting higher fuel flow will combine with the high LOX flow to give the proper mixture ratio.

Because it was thought that the scarfed tips would be too vulnerable to damage, the operation to EDM the 45-degree angles on the outer row elements was deleted. The interpropellant plate was delivered to P&W without scarfs but with extra length on the outer row elements so that they could be scarfed as late as possible after the interpropellant plate was installed into the injector.

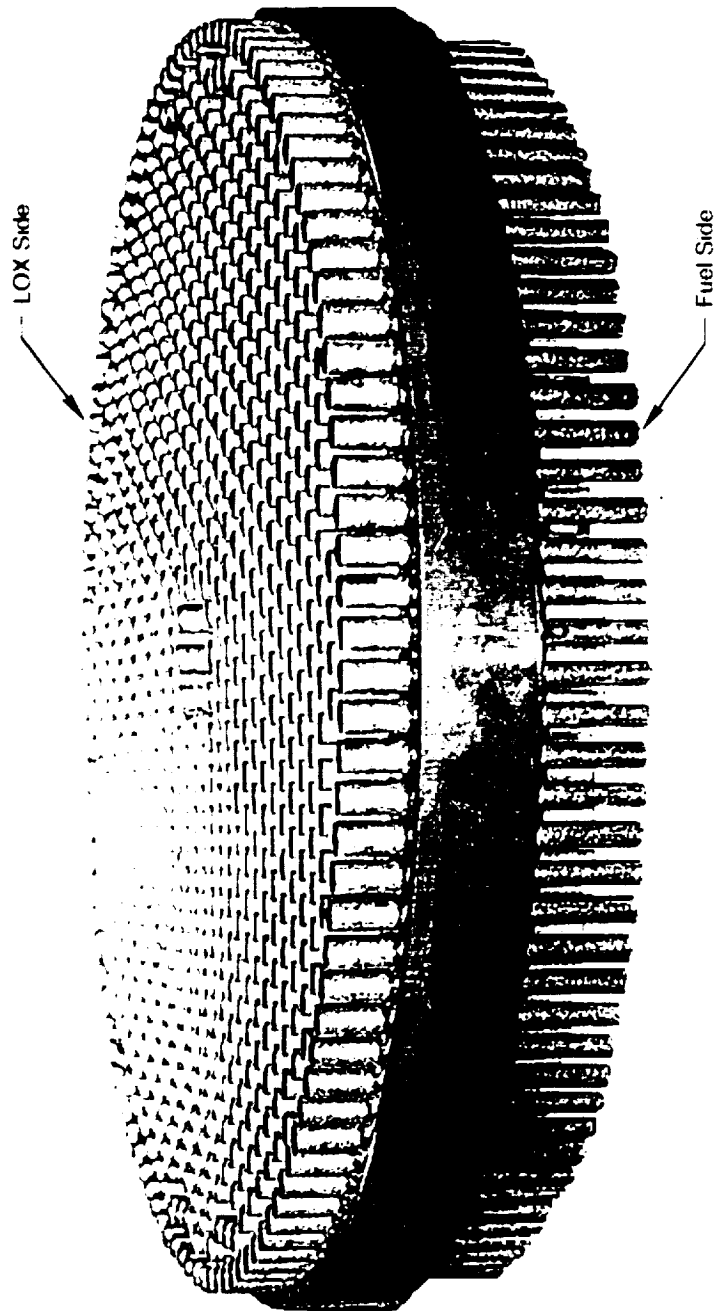


Figure 3.1.3-1. Large-Scale Interpellant Plate After Rough EDM

FE622362

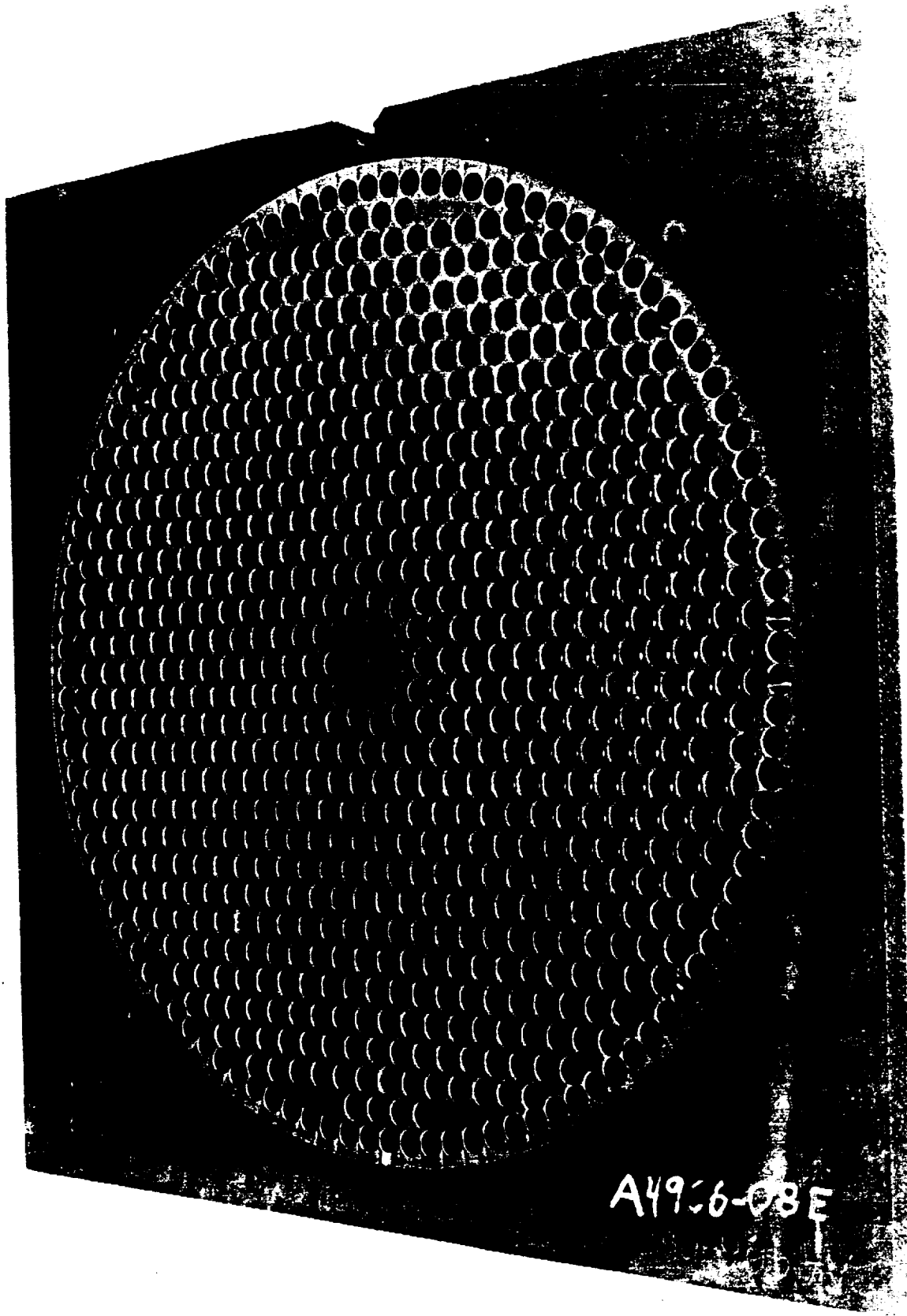


Figure 3.1.3-2. (h EDMing Electrode



FEB2373

Figure 3.1.3-3. Large-Scale Interpellant Plate After Gundrilling

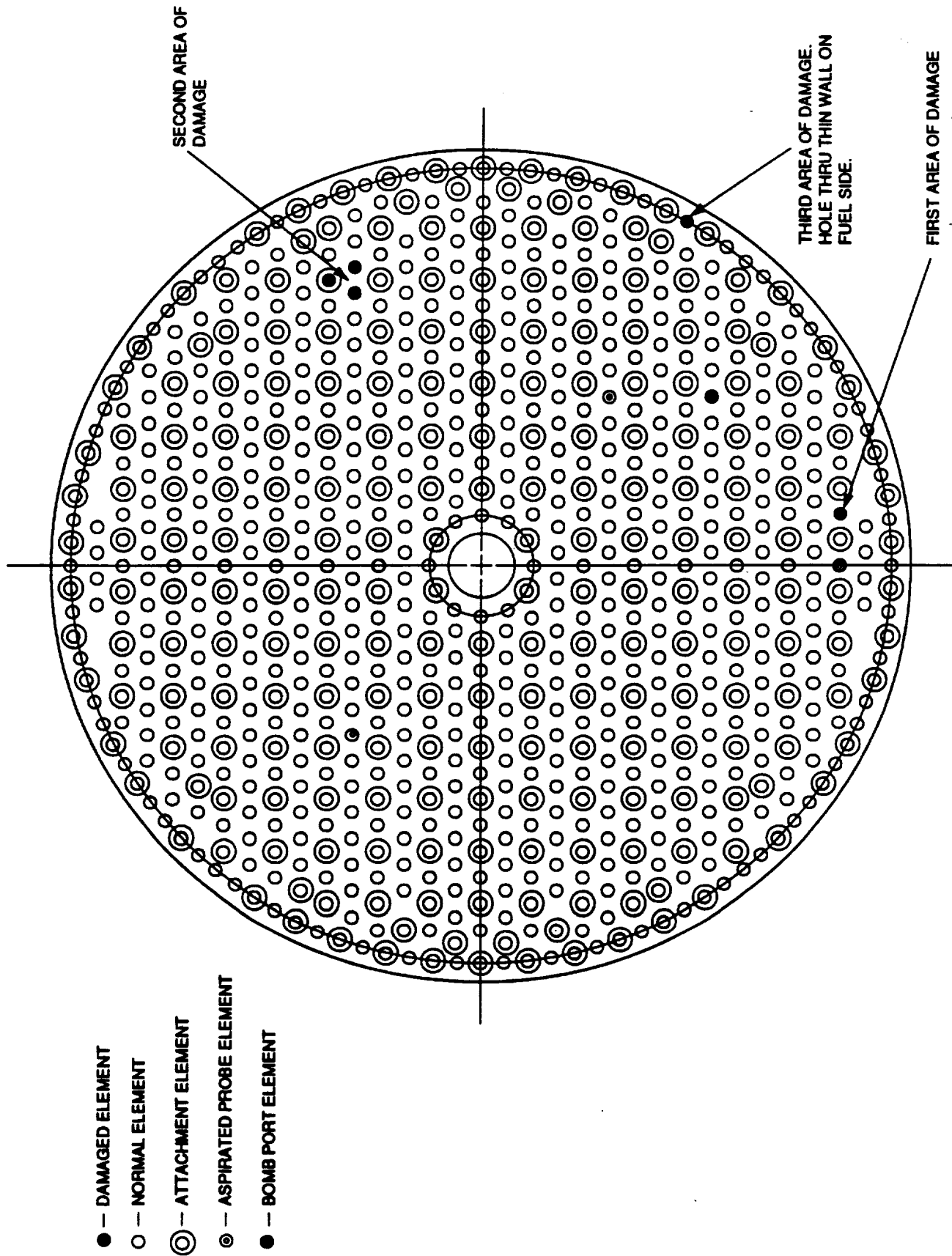


Figure 3.1.3-4. Locations of Damaged Fuel Elements (Looking Up at Fuel Side)

FE82281

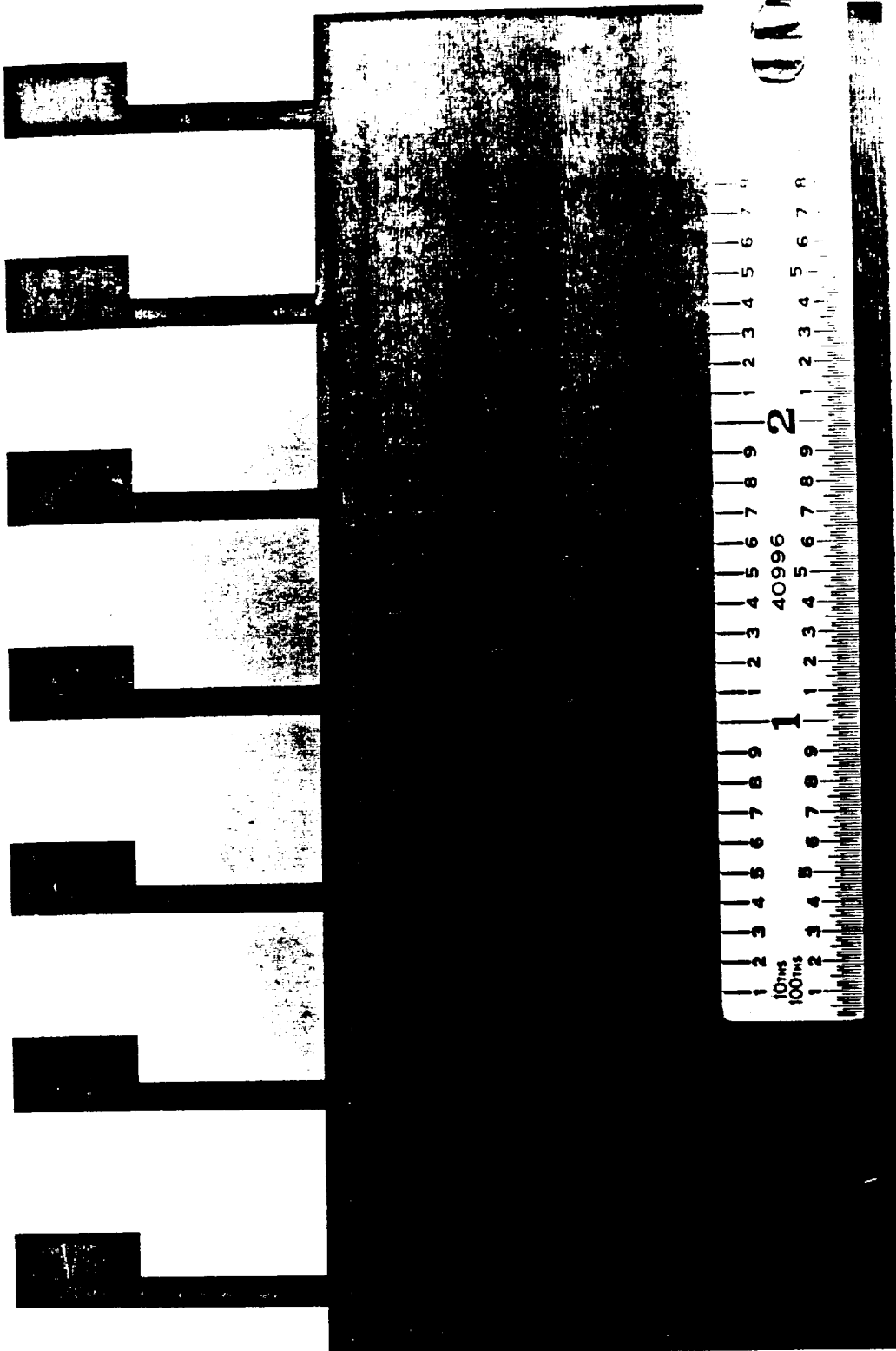


Figure 3.1.3-5. Segment of Electrode for "Gang" EDMing LOX Entry Slots

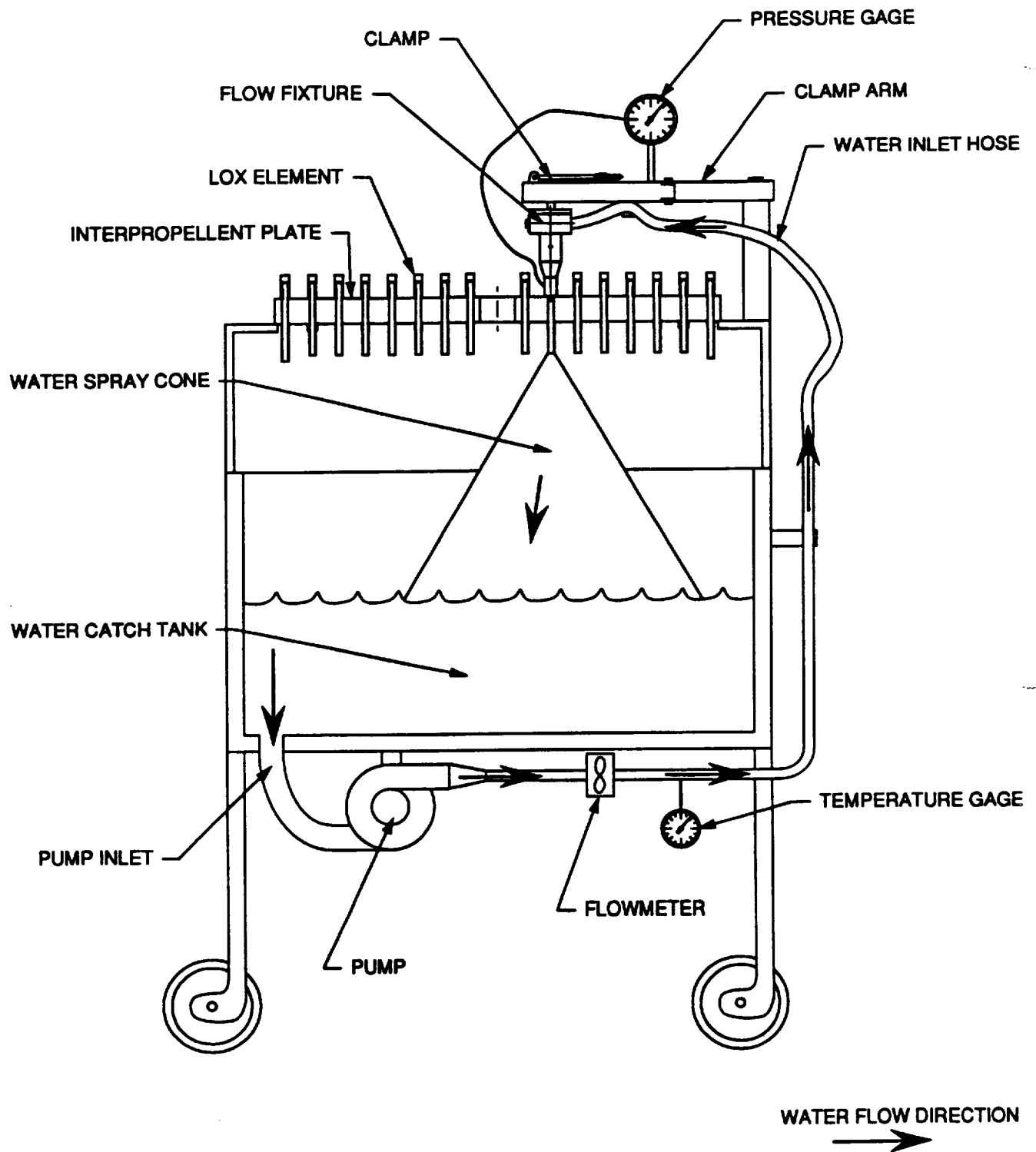


Figure 3.1.3-6. Waterflow Setup for the Large-Scale Interpropellant Plate

3.1.3.2 Injector Fabrication

The injector fuel manifold was conventionally machined from a forged INCO 718 ring in the P&W shop. The fuel sleeves and facenuts, both made from INCO 718, were purchased from vendors. The first thread on most of the facenuts was found to be defective preventing the facenuts from being started in the fuel sleeve threads. These facenuts were returned to the vendor and replaced with good facenuts. The igniter inserts were machined from NASA Z copper alloy in the P&W shop.

The injector housing was conventionally machined from a large INCO 718 pancake forging in the P&W shop. After rough machining, the housing was subjected to a dimensional stabilization heat treat cycle to relieve any internal stresses present in the large forging and prevent any gross movement of final features during subsequent operations. Following the stabilization cycle, a material sample was taken from the center of the housing in the area that would have received the least amount of work during the forging process, and analyzed. Microstructural analysis showed that the forging met the material metallurgical requirements of grain size and nondissolved precipitates in the grain boundaries. Tensile specimens were taken from this same sample and were tested to verify that the mechanical property requirements were met.

The faceplate was made from 1/4-in. thick 347 stainless steel porous plate identical to that used on the subscale faceplate. This porous plate was made by sintering together sheets of wire mesh. The plate had a flow rate of 190 SCFM/ft² per minute at 2 psig. Because the shrinkage and gundrilling problems with the interpropellant plate moved the injector elements from their proper positions, the faceplate holes had to be drilled to fit the elements on the interpropellant plate. A concentricity of 0.004 in. was desired between the element OD and the faceplate hole ID for even fuel distribution around the fuel annulus for the non-attachment elements. Because of the potential for further movement during heat treat cycles used in the injector fabrication, it was decided to wait until after all heat treat cycles were complete before measuring the element locations. This data was given to the faceplate vendor to match the faceplate holes to the element locations.

Electron beam (EB) weld samples were run for the fuel manifold to injector housing welds and the interpropellant plate to injector housing weld. EB weld samples for the faceplate to housing weld were also run. These samples were used to establish machine weld schedules and verify proper weld results. The weld joint samples were X-ray inspected and no voids or cracks were found. Cut-ups of the welded samples revealed small (0.020-in. long) microfissures, just like those found in one of the subscale EB welds. This microcracking is not uncommon in INCO 718, especially with the AMS 5664 heat treat, and is not considered significant. Fracture analysis of the welds yielded sufficient life with ample margin.

Before EB welding began, the interpropellant plate was nickel plated in preparation for brazing on the fuel sleeves. In order to prevent nickel plating on the critical surfaces of the elements, all of the elements were masked before plating except for the bases of the attachment elements where the braze joint was to be. Also in preparation for the braze operation, the fuel sleeves were also nickel plated, and the braze concentricity tools were fabricated.

A pair of INCO 718 lifting eyes were first welded to the fuel manifold. Next, the interpropellant plate was nickel plated in preparation of the fuel sleeve braze and then was EB welded to the injector housing. Figure 3.1.3-7 shows the interpropellant plate being installed into the injector housing in preparation for the EB weld. X-ray and fluorescent penetrant (FPI) inspection of this weld revealed no flaws. At this point the instrumentation conduit was bent to shape, installed and tack strapped in place. In order to seal the conduit from the fuel in the fuel manifold, welds were performed where the conduit tube meets the injector housing. The fuel manifold was then EB welded to the injector housing, and these joints were X-rayed and FPIed. Figure 3.1.3-8 shows the injector after the EB weld of the fuel manifold. Despite masking efforts, a considerable amount of weld splatter resulted in the LOX cavity and fuel manifold from the EB welds. With much effort from P&W deburr personnel, the weld splatter was successfully removed, even from hard to get to locations.

The LOX inlet elbows and flanges as well as the fuel inlet flange, all made from INCO 625, were purchased from vendors with no major problems. The LOX inlet flanges were first manual tungsten inert gas (TIG) welded to the elbows and then the elbows were TIG welded onto the injector housing. The fuel inlet flange was then TIG welded to the fuel manifold. Fluorescent penetrant and X-ray inspections were performed on all of these weld joints.

The LSI flange locations were dimensionally inspected after final heat treat. Deviations from the Interface Control Document interface dimensions were caused by excessive weld shrinkage during manual TIG welding. The deviations were coordinated with NASA-George C. Marshall Space Flight Center (MSFC) and are reported to be within the TS 116 experience band.

Braze samples of the fuel sleeve to injector element braze were fabricated and brazed. These samples were just like those done for the subscale except that they were made to full-scale dimensions. The large-scale braze samples, however, did not have any problems with the concentricity tool bonding to the element like the subscale samples did because the methods which resolved the problem for the subscale were employed when making the large-scale concentricity tools.

Because the large-scale braze joints were to be load tested at a much higher load than the subscale (2500 lb versus 150 lb), three of the large-scale braze samples were load tested to failure. All three samples failed at over 8000 lb. However, none of the three samples failed at the braze joint. Instead they all failed at the fuel sleeve thread undercut. There was no evidence of damage to any of the brazes. These tests demonstrated that there was sufficient margin in the braze joint (and fuel sleeve) to perform the load tests safely.

The fuel sleeve braze operation was concurrent with a solution heat treat to stress relieve the weld joints and was successfully completed with no problems. No concentricity tools bonded to the elements. Subsequent load test of all 234 sleeves was successfully completed to verify adequate braze strength.

The injector assembly final precipitation heat treat cycle was completed following the fuel sleeve load tests. Final injector element locations were inspected and documented following the heat treat cycle. Computer files of the element locations were transferred to the faceplate vendor to aid in machining the faceplate fuel annuli holes. An aluminum plate was fabricated by the vendor and successfully fit checked before machining the faceplate began. To improve the ability to obtain maximum hole to injector element concentricity the rigimesh outer diameter-to-housing clearance was increased. Consequently a manual weld of the faceplate to the injector housing was required in place of the planned EB weld. In addition an injector element adjustment tool was fabricated to tweak the injector elements if necessary to obtain the required element-to-faceplate hole fuel annulus concentricity for each element.

Critical bolt holes and seal surfaces were machined after all heat treats were completed so that no movement of these features could occur during heat treat.

The LSI facenut design was modified slightly during this period to eliminate the interrupted fuel annulus outer diameter created by the torque tool slots. Elimination of these wall discontinuities was done to improve the fuel exit velocity profile. A comparison of the cross sections of the previous and final facenut designs are shown in Figure 3.1.3-9.

The proof pressure test of the LOX cavity and interpropellant plate was accomplished by sealing off the injector elements using the method shown in Figure 3.1.3-10. A silicone rubber RTV compound was placed in the elements and allowed to cure. Next a sheetmetal ring was placed into the proof pressure test plate and filled with melted Rigidex tooling wax. Then the injector was lowered onto the proof test plate so that the element sank into the Rigidex. The proof test plate and injector were bolted together, and the Rigidex was allowed

cool off and solidify. Then all instrumentation ports were sealed off and the injector was pressure tested. The RTV provided the seal, while the Rigidex held the RTV in place and prevented it from blowing out.

At this point, the outer row elements were scarfed to a 45-degree angle with a tool designed to hold a cutting wheel at the proper angle and at the proper position. This tool was also designed to scarf the outer row elements at 30- and 15-degree angles as well as cut off the scarf altogether. This tool was designed to be used at NASA-MSFC during rig testing to change the scarf angle so that the effects of scarf angle on performance and wall compatibility could be studied.

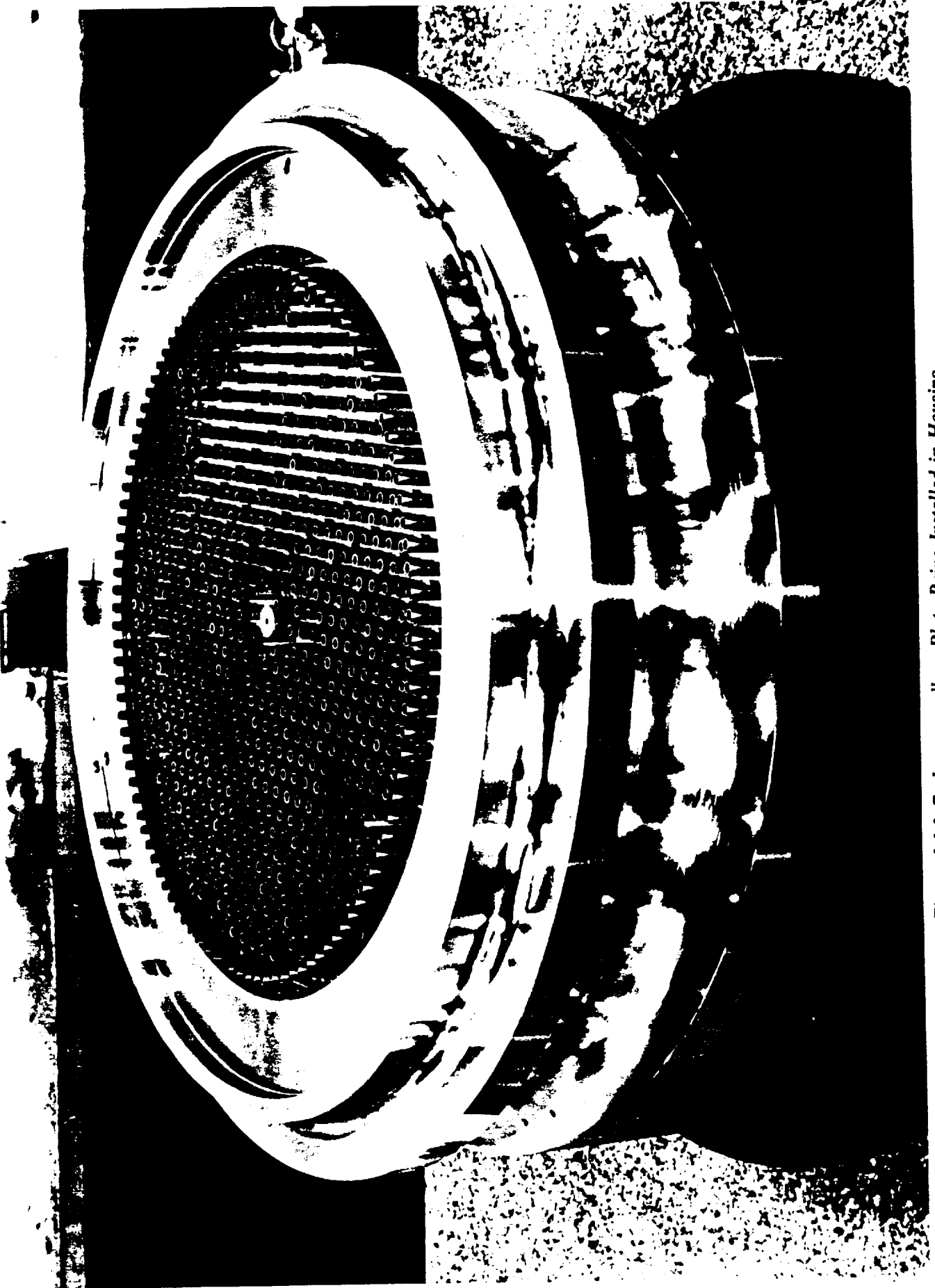


Figure 3.1.3-7. Interpropeller Plate Being Installed in Housing

FEB28547

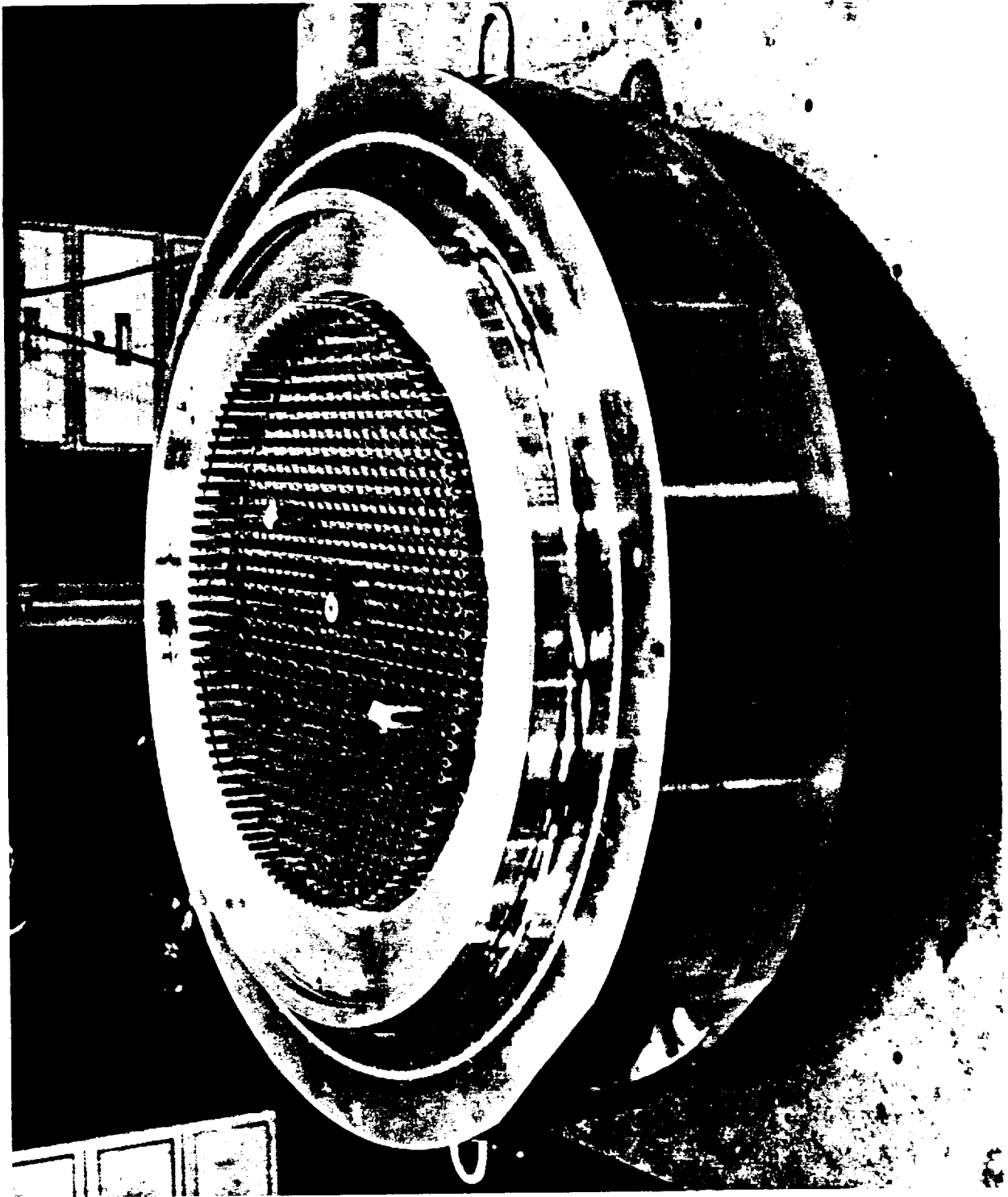


Figure 3.1.3-8. Large-Scale Injector After EB Weld of Fuel Manifold

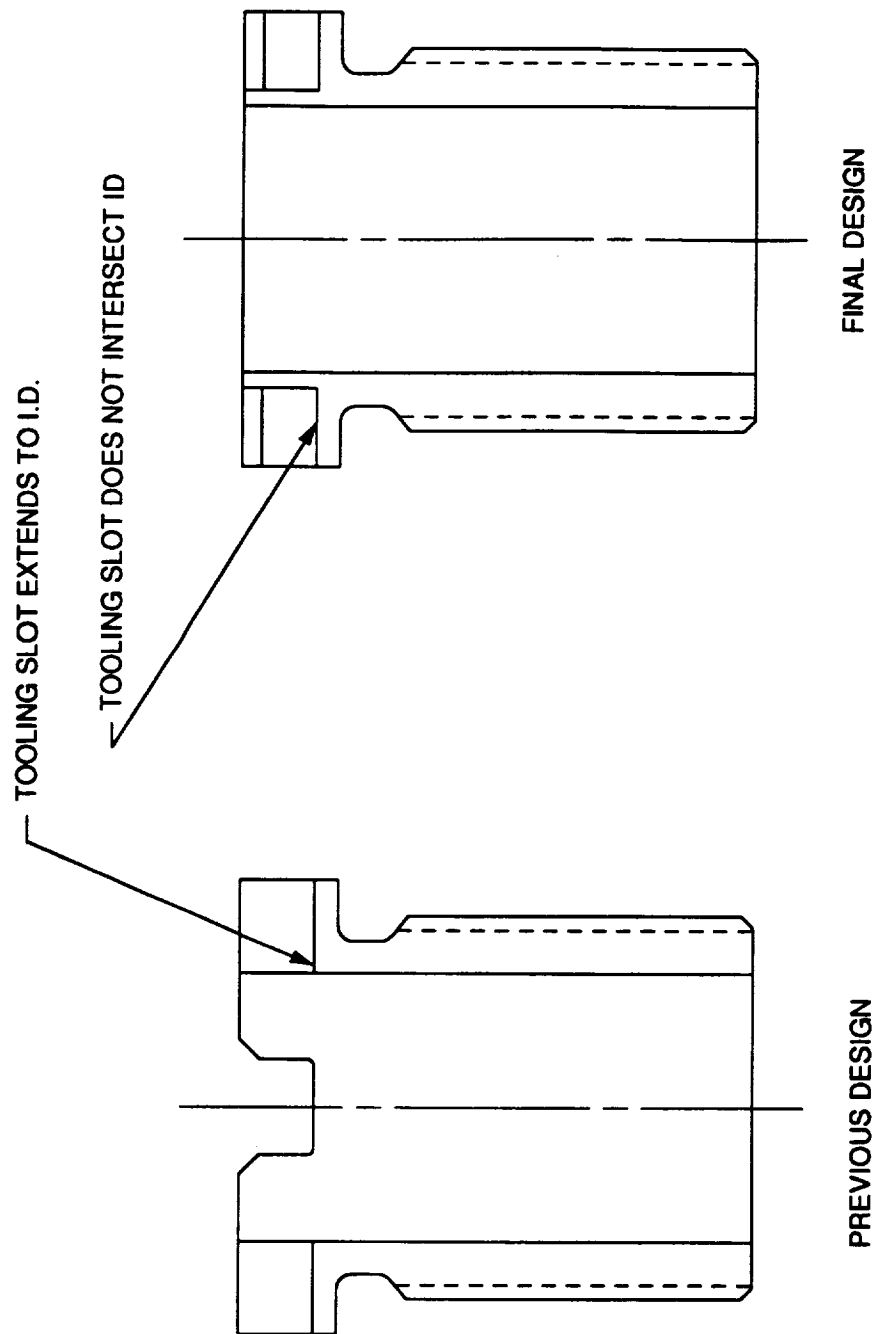


Figure 3.1.3-9. Cross-Sections of Previous and Final Facenut Designs

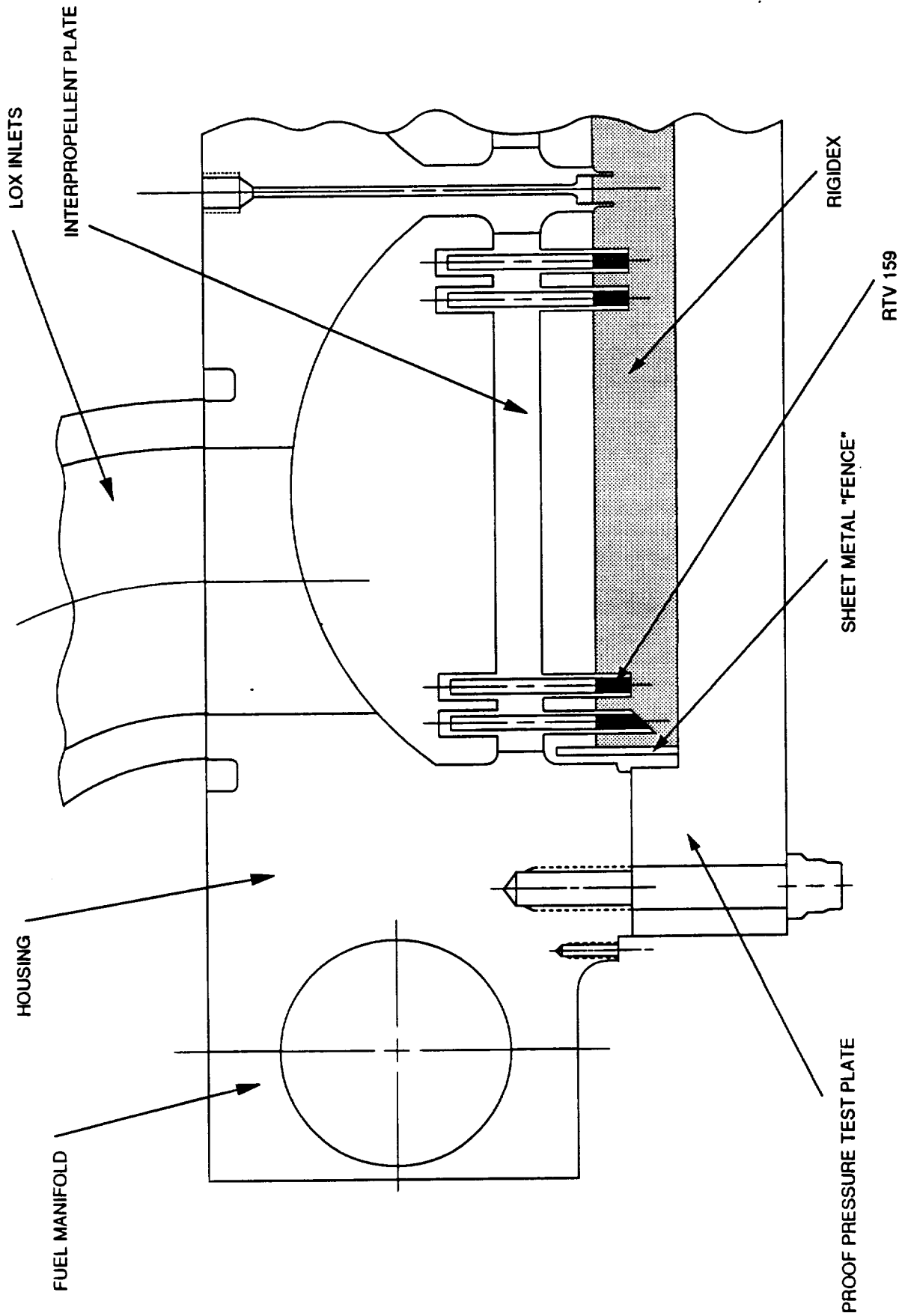


Figure 3.1.3-10. LOX Cavity Proof Pressure Test Method

3.1.4 Large-Scale Injector Instrumentation

The large-scale injector featured a wide array of instrumentation similar to the subscale to provide data from which the stability and performance of the injector could be evaluated. Table 3.1.4-1 provides a complete list of the instrumentation for the large-scale injector while Figure 3.1.4-1 shows the approximate locations of the large-scale injector instrumentation. Like the subscale, the large-scale injector the LOX cavity of the large-scale injector featured 2 static pressure taps, 180 degrees apart, a high response Kulite probe for dynamic pressure, and a Rosemount RTD (resistance temperature device) for LOX cavity temperature. The fuel cavity featured two static pressure taps, 180 degrees apart, and two type E thermocouples (T/C), 180 degrees apart, for measuring the fuel cavity gas temperature. The fuel manifold featured two static pressure taps, 180 degrees apart, and another high-response Kulite probe to measure the dynamic pressure in the fuel manifold. Two type C/A T/Cs attached to the faceplate (180 degrees apart) measured the faceplate temperature. The large-scale injector also featured two static pressure taps, 180 degrees apart, to measure combustion chamber pressure (P_c). These taps were aspirated with hydrogen fuel to prevent them from freezing. All T/C,s and pressure taps routed to the fuel cavity or faceplate were routed through the stainless steel conduit described in the injector design section.

The high-frequency pressure transducer selected for the large-scale rig testing was, like the subscale the Kulite model CT-375-5000 for the injector LOX dome and fuel manifold. The Kulites were made by the manufacturer to P&W's length specifications so they could be flush or near flush mounted and had a response of at least 75,000 Hertz before a five percent amplitude error occurs. The Kulite probes had the advantage of being able to indicate both the static and dynamic pressures. This model Kulite was designed for use in cryogenic temperatures for pressures up to 5000 psi and is compatible with both LOX and hydrogen.

The readings from the aspirated chamber pressure (P_c) probe in the subscale injector faceplate were found to read consistently lower than the non-aspirated and chamber wall static readings. The reason for the low measurements were due to the jet pump effect inherent in the aspirated design. Ejection of the high velocity fuel through the probe orifices creates a suction at the instrumentation tube inlet. This results in a pressure reading that is lower than the actual chamber pressure. Although an analytical correction was used for the subscale testing analysis, it was decided to redesign the aspirated probe to eliminate the jet pump effect to give accurate readings. This was done by drilling the aspiration holes at a 90-degree angle to the probe centerline so that the hydrogen has no forward velocity when it enters the probe. Figure 3.1.4-2 shows this new probe design. Because the probe is integrated into an element, it does not have to be attached to the faceplate before the faceplate is installed. This will save much of the trouble and time lost due to problems installing the faceplate with instrumentation attached. The faceplate T/C attachment was also redesigned so that the faceplate T/C does not have to be attached to the faceplate before installing the faceplate.

Table 3.1.4-1. Large-Scale Injector Instrumentation List

Header	Description	Loc	Supplier	Range	Acc	Remarks
TMLSIFP1	Faceplate Temperature #1	AW, AG	P&W	160-1100°R	±5%	Type C/A T/C
TMLSIFP2	Faceplate Temperature #2	AW, AG	P&W	160-1100°R	±5%	Type C/A T/C 180° from #1
PSLSICC1	Combustion Chamber Static Pressure #1	AX, AK	MSFC	0-4000 psia	±5%	Aspirated with H2 Fuel.
PSLSICC2	Combustion Chamber Static Pressure #2	AX, AK	MSFC	0-4000 psia	±5%	Aspirated with H2 Fuel. 180° from #1
TFLSIFC1	Fuel Cavity Gas Temperature #1	AU, AH	P&W	160-600°R	±5%	Type E T/C
TFLSIFC2	Fuel Cavity Gas Temperature #2	AU, AH	P&W	160-600°R	±5%	Type E T/C 180° from #1
PSLSIFC1	Fuel Cavity Static Pressure #1	AV, AJ	MSFC	0-4000 psia	±5%	
PSLSIFC2	Fuel Cavity Static Pressure #2	AV, AJ	MSFC	0-4000 psia	±5%	180° from #1
PSLSIFM1	Fuel Manifold Static Pressure #1	AR	MSFC	0-4000 psia	±5%	
PSLSIFM2	Fuel Manifold Static Pressure #2	AR	MSFC	0-4000 psia	±5%	180° from #1
PHLSIFM1	Fuel Manifold Dynamic Pressure #1	AP	P&W	1K-10K Hz	±10%	Kulite Probe. Length = 1.22"
TFLSILC1	LOX Cavity Fluid Temperature #1	AN	P&W	160-600°R	±5%	Rosemount RTD
PSLSILC1	LOX Cavity Static Pressure #1	AS, AL	MSFC	0-4000 psia	±5%	
PSLSILC2	LOX Cavity Static Pressure #2	AS, AL	MSFC	0-4000 psia	±5%	180° from #1
PHLSILC1	LOX Cavity Dynamic Pressure #1	AM	P&W	1K-10K Hz	±10%	Kulite Probe. Length = 1.88"

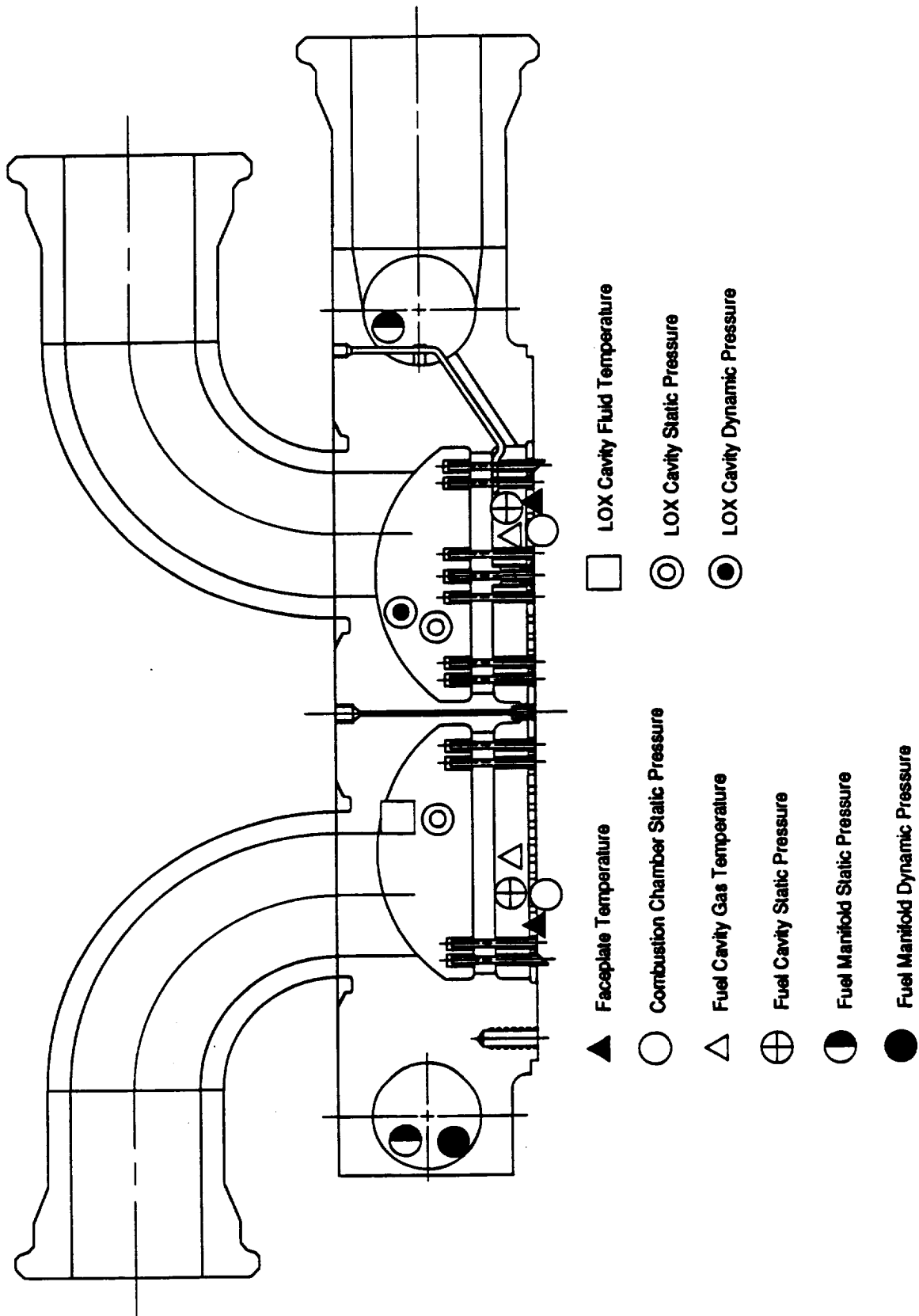


Figure 3.1.4-1. Large-Scale Injector Instrumentation

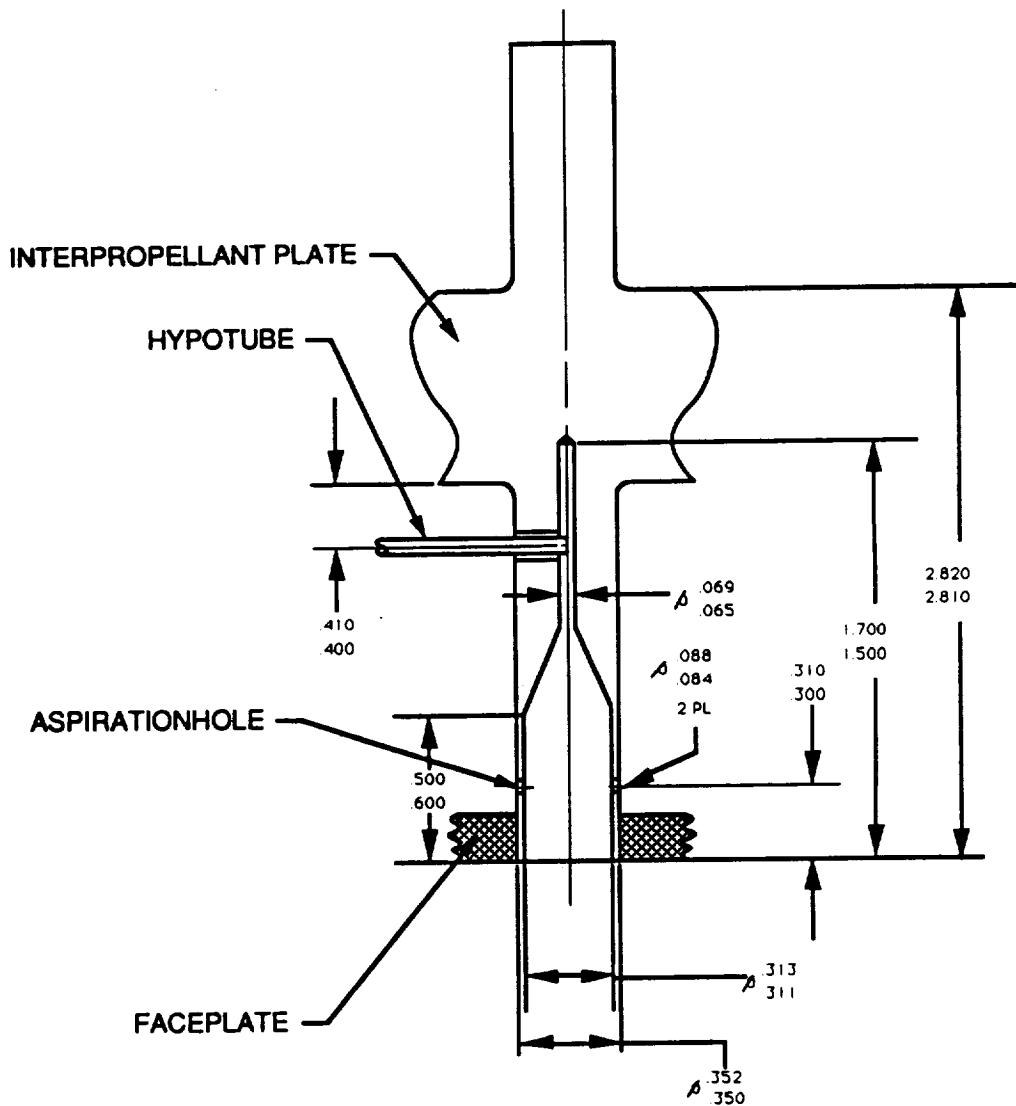


Figure 3.1.4-2. Large-Scale Injector Aspirated Probe

3.2 THRUST MOUNT DESIGN AND FABRICATION HISTORY

The original thrust mount design is shown in Figure 3.2-1. This design incorporated two formed cones with either one or two longitudinal welds. These cones were to be welded to plates to mount the injector and to interface with the test stand. Following welding the two end faces would be machined parallel to avoid creating side loads. The rig assembly using this type of thrust mount is shown in Figure 3.2-2. In an effort to reduce cost, the thrust mount was redesigned in early 1990 to achieve, essentially, the current thrust mount design. This design, which is shown in Figure 3.2-3, makes use of more readily available components. This configuration uses standard plate thicknesses and a rolled cylinder for the main thrust load carrying member. Eccentric loading is carried by gussets around the main cylinder. It was estimated that the cost of this configuration would be 25 percent that of the original design. The rig assembly using the current thrust mount is shown in Figure 3.2-4.

The deletion of the acoustic liner from the test plan resulted in the addition of 5.5 in. to the length (to compensate for the removal of the acoustic liner). The thrust mount assembly with the additional length was

reviewed for structural capability and was found to be within the margin of safety limits set by NASA-MSFC Handbook 505A. The combustion chamber support rods proposed in the NASA interface control document (ICL) will increase that margin by absorbing any vibratory side loads and removing the moment resulting from the overhung weight of the chamber.

The thrust mount was fabricated at a vendor and consists entirely of stainless steel components, which were conventionally machined and then welded together. After welding, the welds were X-ray inspected, and then the assembly was stress-relieved before final machining of test stand and injector interfaces. After the thrust mount was received at P&W it was dimensionally inspected to verify critical interface dimensions. All dimensions were found to be within blueprint requirements. Figure 3.2-5 is a photograph of the thrust mount during the inspection.

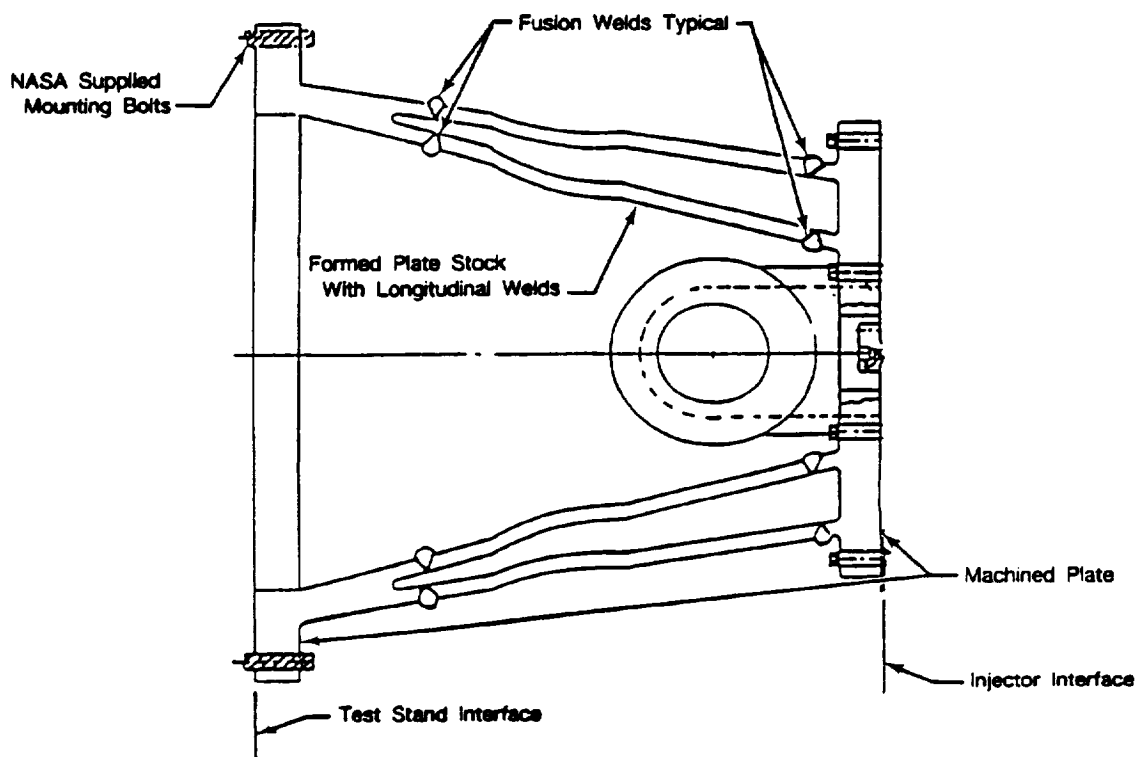


Figure 3.2-1. Original Large-Scale Thrust Mount Design

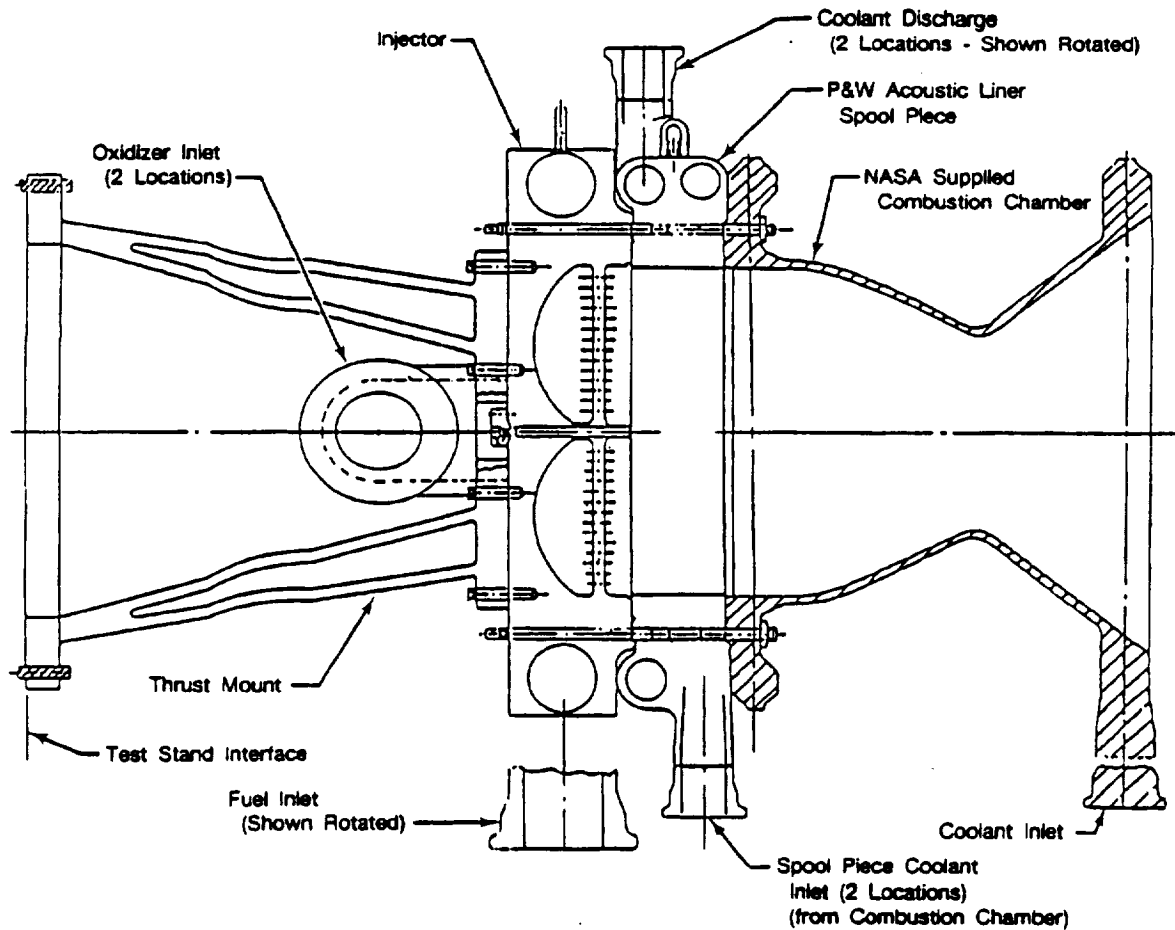


Figure 3.2-2. Original Large-Scale Thrust Mount on Rig

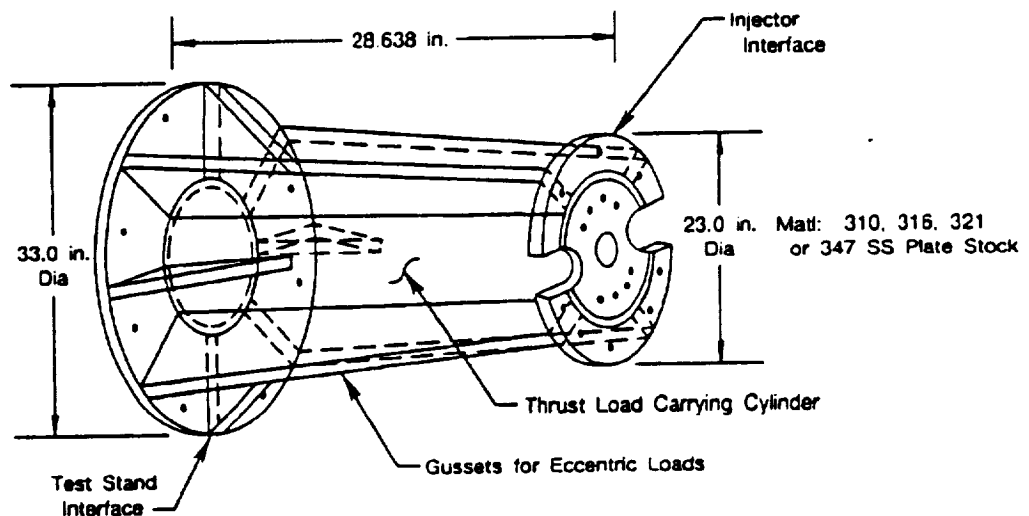


Figure 3.2-3. Large-Scale Thrust Mount Configuration

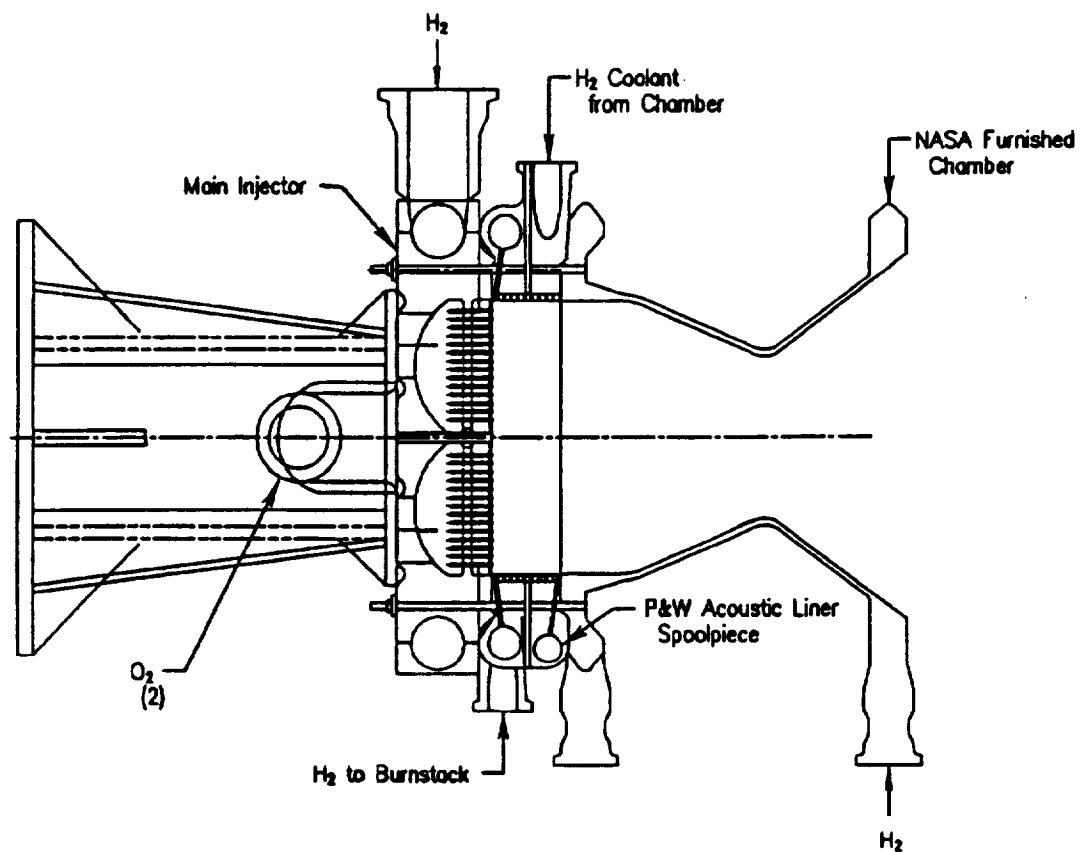
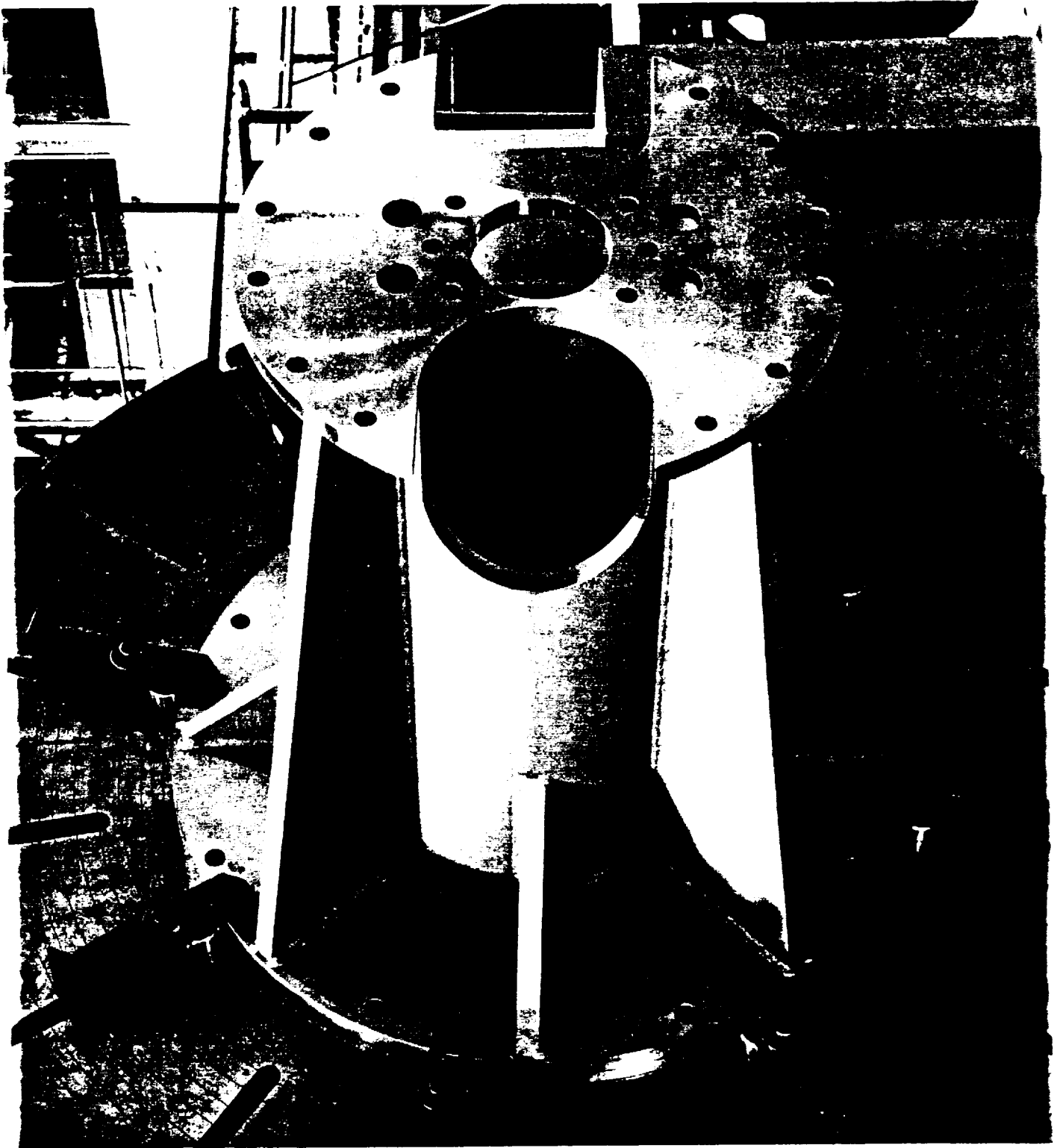


Figure 3.2-4. Large-Scale Thrust Mount on Rig



FE628041

Figure 3.2-5. Large-Scale Injector Thrust Mount

3.3 ACOUSTIC LINER

3.3.1 Acoustic Liner Design History

3.3.1.1 Methane Design

During the early phases of the program, methane (CH_4) was the fuel to be used in the P&W main injector technology rig. Although the stability analysis with methane indicated that the combustion system would be stable with satisfactory margin, P&W had incorporated an acoustic liner into both the subscale and large-scale thrust chambers in view of the uncertain nature of combustion stability with hydrocarbon fuels. The liners were designed using a computer code developed by P&W, and updated with test results obtained under AFAL Contract F04611-86-C-0115.

The design specifications for both the subscale and large-scale acoustic liners are listed in Table 3.3.1-1. These parameters were set to achieve maximum acoustic absorption at the first tangential mode frequency and have adequate chamber wall coverage for stable combustion. Sketches of the subscale and preliminary large-scale acoustic liners are shown in Figure 3.3.1-6. The predicted acoustic absorption for the subscale and large-scale acoustic liners is shown in Figures 3.3.1-7 and 3.3.1-8, respectively. These absorption curves were calculated with the aid of the P&W acoustic design deck (5612). The results of this deck were recently verified by acoustic test work done on AFAL Contract F04611-86-C-0115, "LOX/Hydrocarbon Acoustic Liner Technology Program." A brief description of how the acoustic liner design parameters were set is given below:

1. **Area Ratio** — The 0.06 area ratio (acoustic area/total liner area) was set based on past parametric studies which have shown this value to be close to optimum. Larger area ratios would increase the required number of acoustic apertures (holes) and the heat transfer to the backing cavity without any significant improvement to the acoustic absorption.
2. **Hole Diameter** — The hole diameter was set to be as large as possible within the available cooling channel land width of the combustion chamber. This minimizes the total number of acoustic apertures in the liner. Increasing the hole diameter also causes an increase in the acoustic absorption although this effect is relatively small compared to other factors such as acoustic liner cavity gas temperature.
3. **Hole Length** — The acoustic liner hole lengths are set by the cooling channel land thickness. Like hole diameter, increasing the hole length causes a relatively small increase in the acoustic absorption.
4. **Backing Cavity Depth** — The backing cavity depth was set to maximize the acoustic absorption at the first tangential mode frequency 5121 Hz for the subscale and 1395 Hz for the large-scale chamber. The backing cavity depth has a very strong influence on the frequency at which a liner has peak acoustic absorption.
5. **Liner Length** — The liner length was set by a P&W design criteria governing the minimum acceptable liner absorptivity and chamber coverage for stable combustion. The criteria requires a minimum liner length of 1/4 the chamber equivalent length (chamber volume - injector area) with an acoustic liner absorptivity of at least 20 percent at the frequency of interest (first tangential in STBE).
6. **Backing Cavity Partition** — Circumferential partitions are needed in the acoustic liner backing cavity to prevent hot chamber gases from flowing through the backing cavity due to the combustion

chamber pressure gradient. The partitions were placed to keep the pressure gradient from the first and last rows of apertures in each acoustic cavity less than 25 psi. Axial partitions which run the full length of the acoustic liner are also included in the liner at four locations, 90 degrees apart. These partitions suppress tangential oscillations in the backing cavity which could reduce liner performance.

7. Acoustic Liner Placement — The acoustic liner was placed so that the first row of acoustic apertures is parallel to the predicted flame front in the combustion chamber. This puts the first hole at 0.070 in. from the injector face for this design. This placement will maximize the acoustic liner effectiveness.

Table 3.3.1-1. Acoustic Liner Design Parameters

	<i>Subscale</i>	<i>Large-Scale</i>
Area Ratio	0.05	0.06
Hole Diameter - in.	0.07	0.08
Hole Length - in.	0.23	0.35
Backing Cavity Depth - in.	0.15	0.60
Liner Length - in.*	3.8	4.3
Total Number of Holes	882	2848
* Length from leading to trailing edge of backing cavity		

The acoustic cavity temperature is very important to the acoustic liner operation. Temperatures too high can cause structural distress of liner materials. Temperatures too low can reduce the acoustic liner performance as seen in Figures 3.3.1-7 and 3.3.1-8. Past tests with acoustic liners have shown the backing cavity temperature to be primarily a function of the acoustic behavior of the chamber. Temperatures as high as 2000°R have been recorded in unstable tests while 600°R temperatures have been recorded in the same chamber during stable tests. These data suggest that the liner backing cavity temperature will naturally increase until the liner has sufficient absorptivity to stabilize the combustion process and that the temperature during stable operation should be on the order of 600 to 1000°R.

To protect the liner from the potentially high temperatures of unstable operation, each liner cavity would have been purged with fuel (methane). The maximum temperature limit for the wall was set at 1500°R and would have been controlled by the rate of purge. A total flow of 2.0 lb/sec would have been provided to the subscale liner and 7.4 lb/sec to the large-scale liner. These flows should have provided sufficient purge through the acoustic apertures to control the cavity gas temperature. Care would be taken during the chamber testing not to flow too much methane to the backing cavity, which could effectively neutralize the acoustic liner absorptivity and cause unstable operation. To determine if a methane purge is necessary, instrumentation would be added to the liner to monitor its temperature. Thermocouples placed in the acoustic cavities would measure the cavity gas temperature and back wall temperature. In addition, a pressure measurement would be taken near the first and last rows of acoustic apertures to measure the axial pressure gradient across the liner.

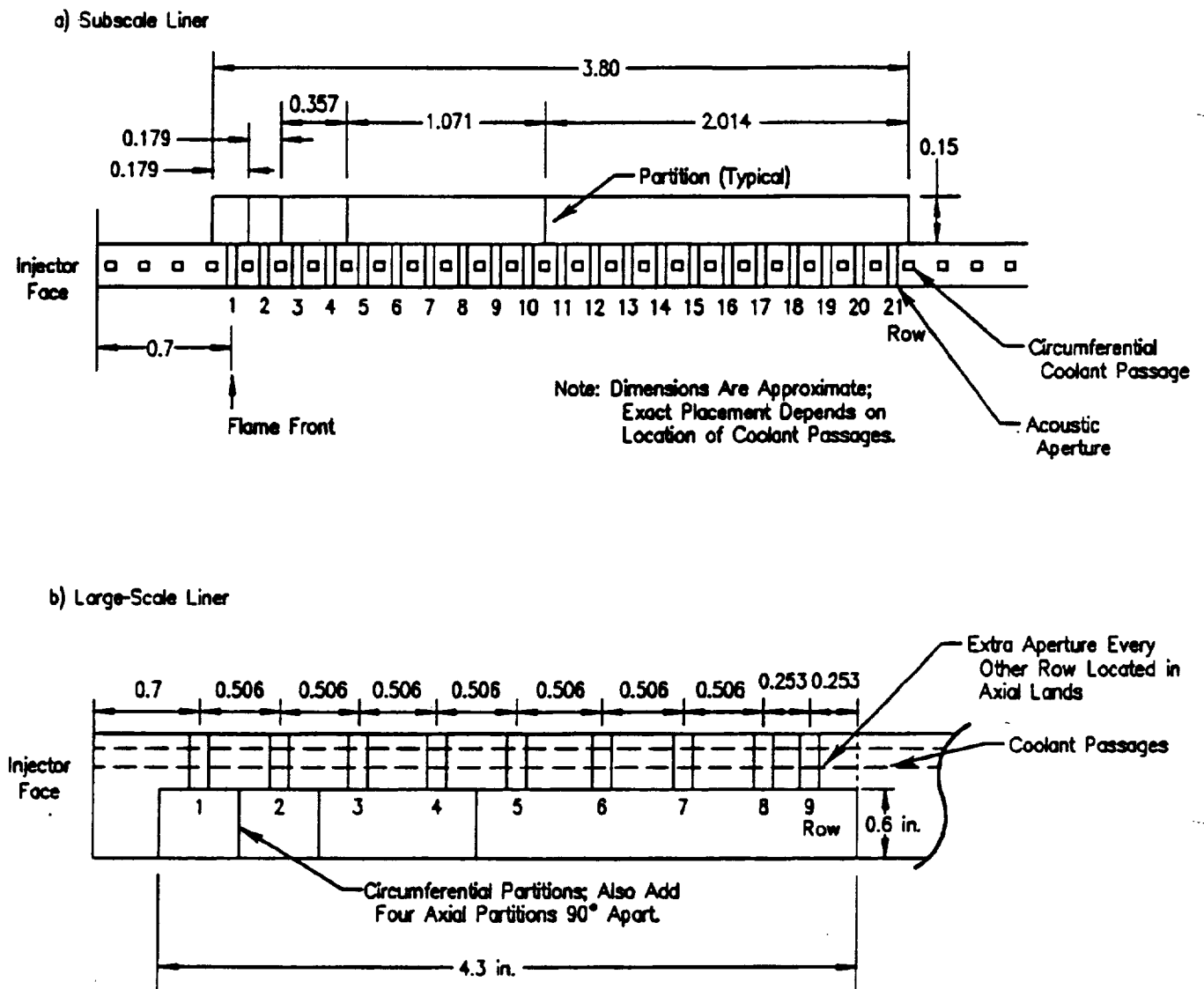


Figure 3.3.1-6. Subscale and Full-Scale Acoustic Liners

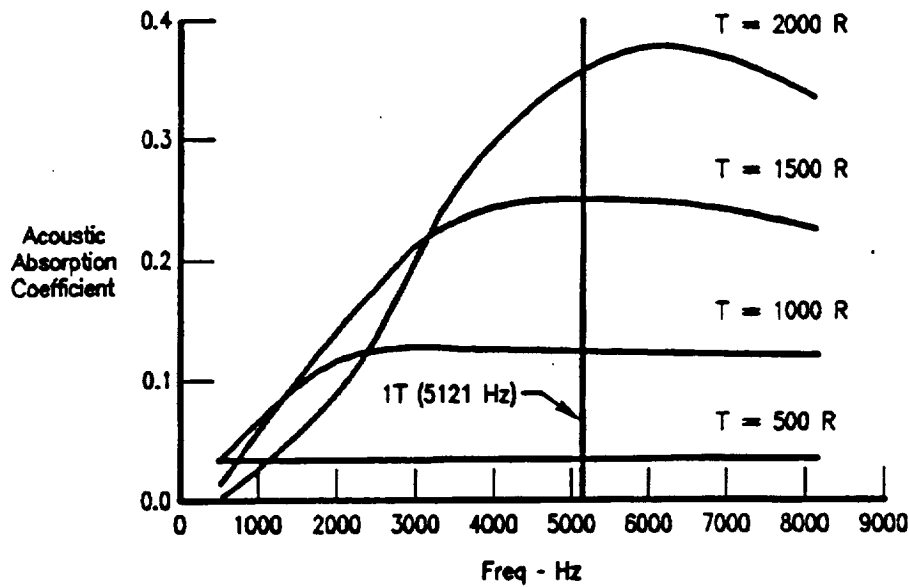


Figure 3.3.1-7. Subscale and Full-Scale Acoustic Liner Predicted Performance

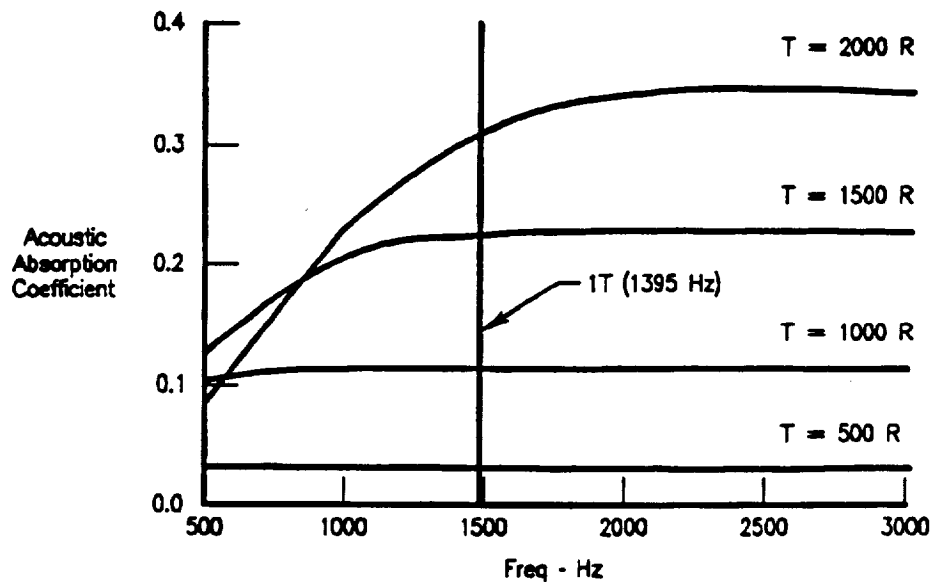


Figure 3.3.1-8. Full-Scale Acoustic Liner Predicted Acoustic Performance

3.3.1.2 Hydrogen Design

When the liner was originally designed for operation with methane, the backing cavity was approximately 0.600 inch deep to provide the minimum of 20 percent absorption at the first tangential acoustic mode with combustion gases in the backing cavity. When the change was made to run with hydrogen the liner response was reevaluated. Since the P&W baseline STE did not include a stability device, it would have been desirable to operate the large-scale test article with the acoustic liner ineffective. With the backing cavity set at 0.600 inch it was not possible to detune the liner to drop its absorption to a very low (<5 percent) level. To be able to detune the liner the backing cavity depth was reduced to 0.300 inch. The target absorption of 20 percent can be attained by purging the cavity with nitrogen or allowing combustion gases to fill the cavities. To detune the liner, the cavity

can be purged with hydrogen. This will provide the capability to run with and virtually without a stability aid. The response of the acoustic liner with these three media in the backing cavities is presented in Figure 3.3.1-^c

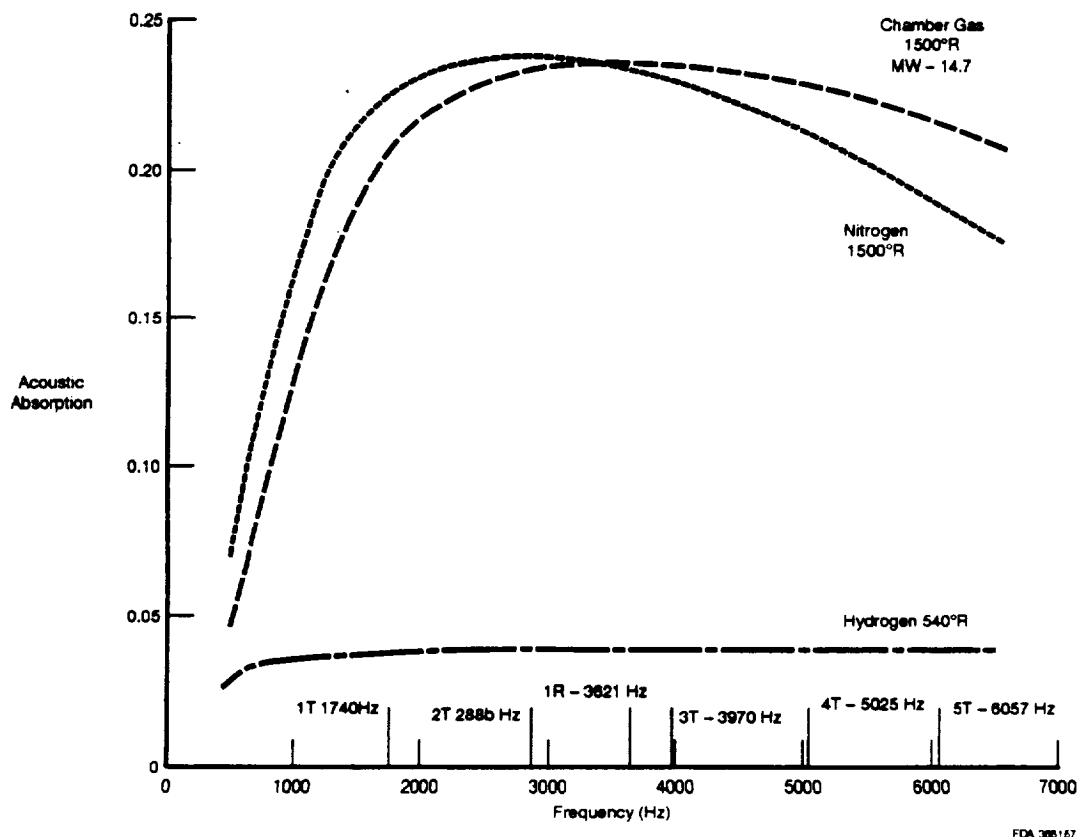
The temperature of the acoustic cavities during steady-state operation were evaluated to determine the capability to detune the liner to reduce its absorptivity by lowering the cavity gas temperature. In addition, the cavity gas temperature with no steady-state purge was reviewed. The acoustic liner was designed to operate effectively when running with O_2/CH_4 and with a CH_4 purge to control the backing cavity gas temperature and acoustic absorptivity. Among the objectives of the subscale testing was an evaluation of the chamber heating rates and demonstration of performance. With the backing cavity purge active, additional gas would be introduced into the chamber, affecting the chamber heat transfer by establishing a film coolant along the upper part of the chamber; performance would also be affected by adding fuel (or if N_2 is used, an inert gas) that would not fully combine in the combustion process. For the CH_4 testing, this would be a true demonstration of what would be expected in the large-scale design; however, for the H_2 testing it was expected that an acoustic liner would not be needed, thus it was necessary to determine chamber heat rates and combustion performance without the purge. Analyses were performed to determine what the acoustic cavity gas temperature would be without an active purge. Analyses were also performed to determine the effectiveness of the liner for the H_2/O_2 testing should a stability device be needed.

The acoustic cavity would have experienced recirculation of combustion gases when the liner was operated without a purge due to the axial static pressure gradient created by heat addition from combustion. To minimize the hot gas recirculation the liner is compartmented axially with circumferential partitions. The forward section of the liner, which would experience the highest axial static pressure gradient, had only one circumferential row of apertures per partition, which prevents hot gas recirculation, since inflow and outflow would have to occur in the same aperture. The liner was partitioned so that no section with two or more rows of apertures would experience more than 25 psi axial static pressure gradient, thus limiting the recirculated hot gas mass flow. With these restrictions the acoustic cavity gas temperatures was calculated to be $1580^\circ R$ with H_2/O_2 combustion when there was no active purge. This temperature level would not create a thermal problem in the cavity back wall because of the low film coefficient associated with the low flow rate of the recirculated hot gas. The resulting back wall temperature for the expected eight second firing was $313^\circ F$ which was below the design temperature of $500^\circ F$. This acoustic cavity temperature level improves the acoustic absorption effectiveness of the liner, (i.e., the higher the acoustic cavity gas temperature, the higher the acoustic absorption). With H_2/O_2 combustion products, the acoustic absorption coefficient of the liner should have exceeded 0.2 for all frequencies above 1500 Hz with no active purge. With an active H_2 purge the acoustic absorption coefficient would be 0.12, which is not adequate for effective acoustic damping. With an active GN_2 purge the acoustic absorption coefficient exceeded 0.2 for all frequencies above 2300 Hz, because the higher molecular weight of the GN_2 (compared to H_2) greatly improves acoustic absorption. The calculated first tangential instability frequency for the subscale H_2/O_2 testing was 5100 Hz, thus the acoustic liner could have been functional during this testing.

During the cool down period, the spoolpiece was expected to be exposed to full coolant pressure without any chamber pressure. For the purpose of the design, it was assumed that the liner would be subjected to a coolant pressure of 6300 (dead headed supply pressure) and a temperature of $-75^\circ F$ before test article ignition. This provides the worst case differential pressure across the coolant passages and crossover areas. The resulting area of maximum stress occurs at the interface to the NASA-supplied chamber. On this side of the spoolpiece Rocketdyne had incorporated a gap which was used to supply film cooling to the combustion chamber. With this gap, the spoolpiece had to be fully self supported to limit deflection into this gap. The need to support the crossover area made necessary the use of extended ribs in the NASA Z liner to limit the deflection. During steady-state operation, the differential pressure between the coolant path and the combustion chamber would have been low and stresses reduced to very low levels. At the injector end, the spoolpiece would be supported by the injector body and no deflection would occur.

Maximum thermal stresses would also occur during test article cool down. At this time coolant is flowed through the liner to condition it before test article startup. This cooldown period causes the liner to achieve a temperature of -75F minimum while the structural shell is assumed to be near ambient temperature. This temperature differential would produce strains at each end of the liner where it would be welded to the structural shell. With the rigidity needed to achieve acceptable pressure induced stresses, there would have been some local yielding of the liner at the attachment points. This was not considered a problem since the strain was limited and the resulting low-cycle fatigue (LCF) life was high.

When the possibility of running hydrogen, as well as methane, arose, it was considered desirable to deactivate the acoustic liner during the hydrogen tests. Therefore, a method to physically block the acoustic cavities during the hydrogen testing was investigated. Since it was desirable to be able to return the liner to its original functioning configuration, a configuration was considered which would incorporate a removable liner that could be inserted into the combustion chamber. Materials that were considered are carbon/carbon, silicon phenolic and quartz phenolic. It was believed that the ablation rate of these materials would be sufficiently low to permit obtaining steady-state data with the apertures physically blocked. Since this method would have entailed some risk due to uncertainties in the thermal mismatch and ablation rates, it would only have been considered if it was shown that the liner could not be made ineffective by cooling the backing cavity gas temperature to reduce the acoustic absorptivity.



FDA 388167

Figure 3.3.1-9. Effect of Purges on Acoustic Liner at Rated Power

3.3.2 Acoustic Liner Fabrication Plans

3.3.2.1 Subscale

Figure 3.3.2-1 presents the detail of the subscale acoustic liner configuration. As shown, the acoustic liner cavities are formed into the electroform construction of the acoustic liner section of the combustor would have required the installation of 882 acoustic apertures, the acoustic cavities, and coolant crossover passages while maintaining the integrity of the water coolant passages in the copper liner. A flat pattern of a section of the acoustic liner showing these features is presented in Figure 3.3.2-2. The planned method of construction is presented in Figure 3.3.2-3. First the cooling passages in the copper liner would be machined and the acoustic apertures would be installed. The passages would be filled with a compound (i.e., wax) to permit conventional electroform closet of the coolant passages, and non conductive pins would be installed into the acoustic apertures. Then, the entire liner would have nickel deposited to a thickness just beyond that required to form the acoustic cavities (approximately 0.200 inch). Next, the acoustic cavity features would be machined into the nickel leaving the cavities, water crossover pads and partitions. The pins would be removed from the acoustic apertures at this time and, following completion of machining, the acoustic cavities would be filled with a compound to permit final closeout of the acoustic cavities and forming of the structural shell. Coolant passages to the liner channels and the interface for the coolant tubes would then be machined. An option for machining the coolant passages after the initial electroforming is also being considered.

3.3.2.2 Full Scale

Several meetings were held to coordinate the fabrication of the acoustic liner spoolpiece. These meetings were attended by representatives from Analytical Design, Mechanical Design, Drafting, Manufacturing, and Project Engineering. This team performed complete reviews of the detail drawings to assure that parts could be made within existing manufacturing capabilities and meet the design intent. As a result, much more manufacturing information was incorporated into the drawings to facilitate the actual fabrication, and more consideration to dimensional control was given to avoid unnecessarily tight tolerances and subsequent quality review activity. This early coordination was to minimize problems during the fabrication process.

Construction of the full-scale acoustic liner spoolpiece would follow the same procedure as the process described for the subscale acoustic liner section. The configuration of the full-scale acoustic liner spoolpiece is shown in Figure 3.3.2-4.

Machining of the liner was to be accomplished at P&W using information gained in an IR&D effort to optimize machining of NASA Z for combustion chambers. A Taguchi statistically designed experimental approach was taken to vary speed, feeds, depth of cut, cutter type, and other key machining parameters to optimize dimensional control, surface finish, and machining time.

The results of this experiment are being analyzed and will be applied to the machining of this liner.

3.3.2.3 Elimination

After the fuel selection was switched to hydrogen (H_2), the risk of combustion instability became so minor that the subscale acoustic liner was deemed unnecessary and dropped from the program.

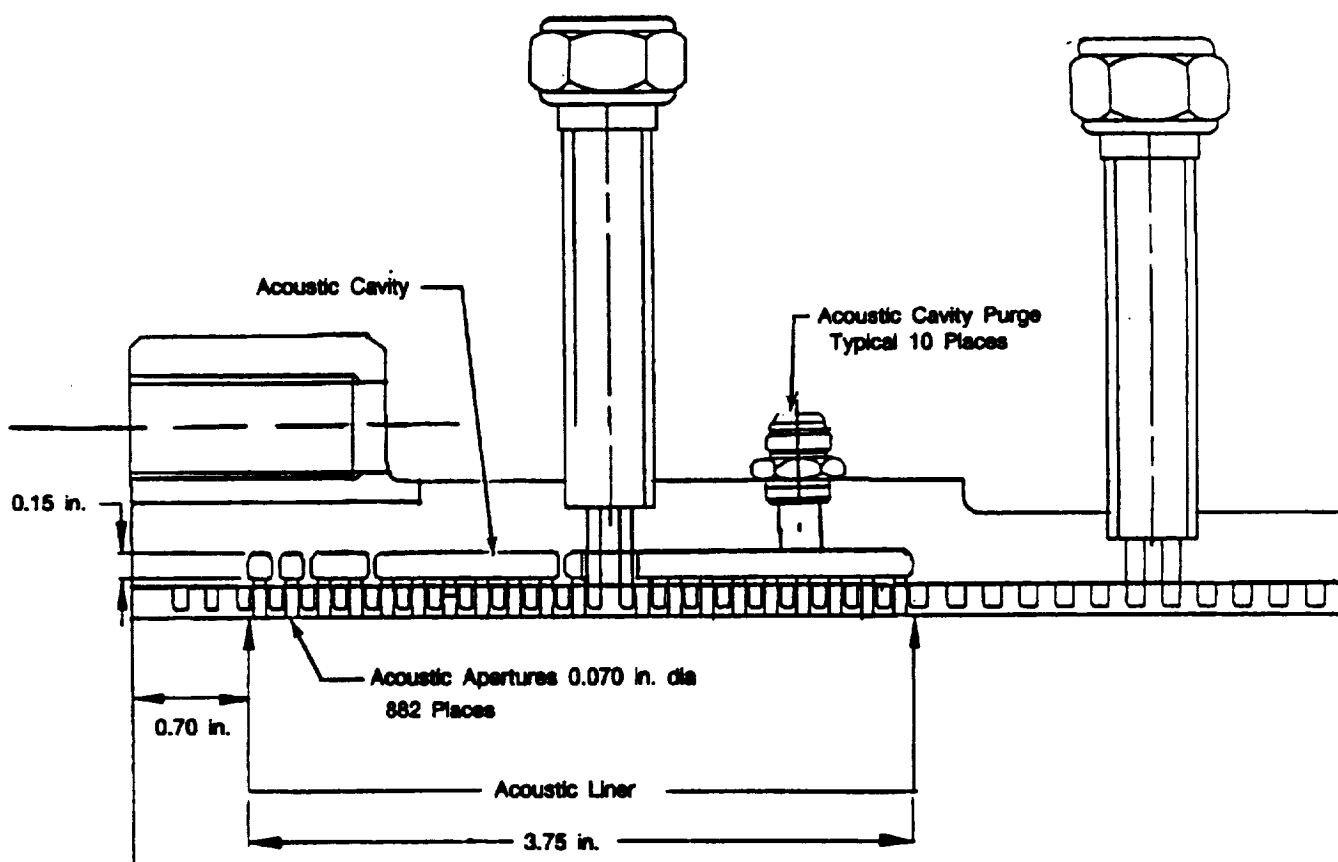


Figure 3.3.2-1. Subscale Combustion Chamber Acoustic Liner

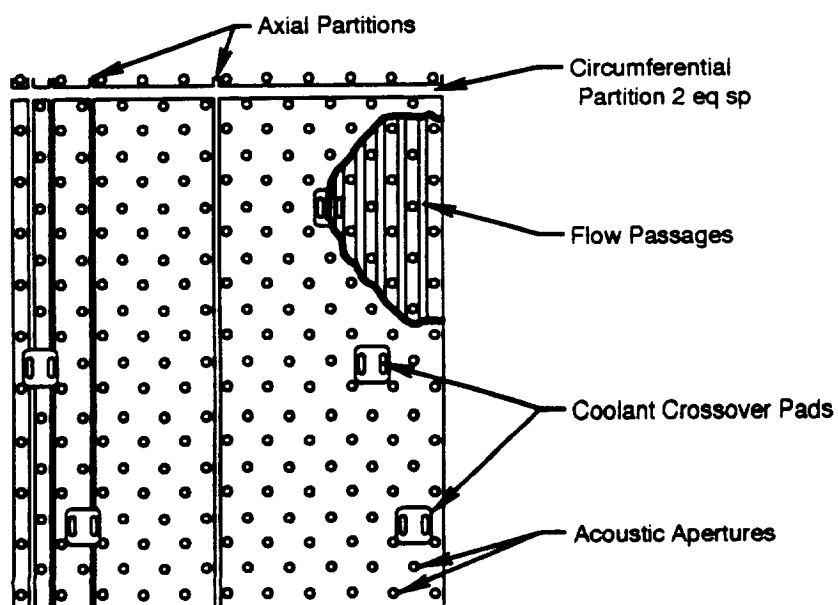


Figure 3.3.2-2. Subscale Acoustic Cavity

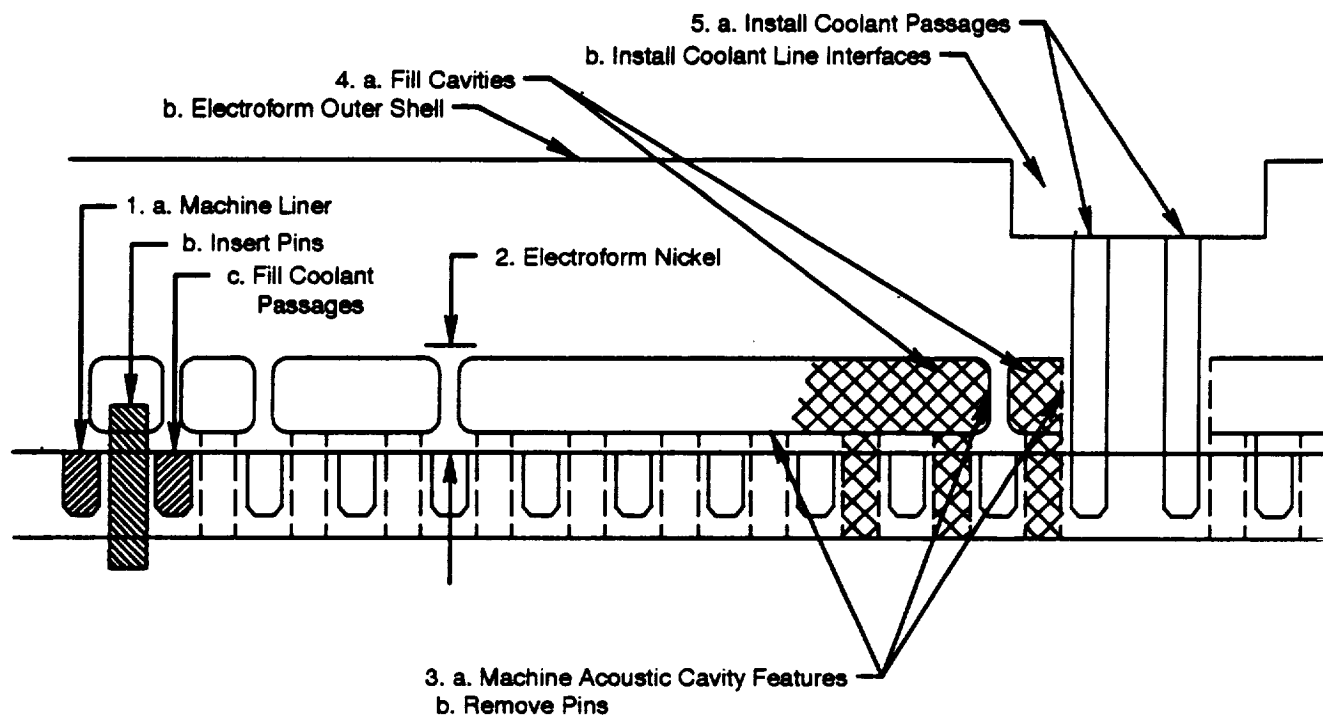


Figure 3.3.2-3. Subscale Acoustic Liner Construction

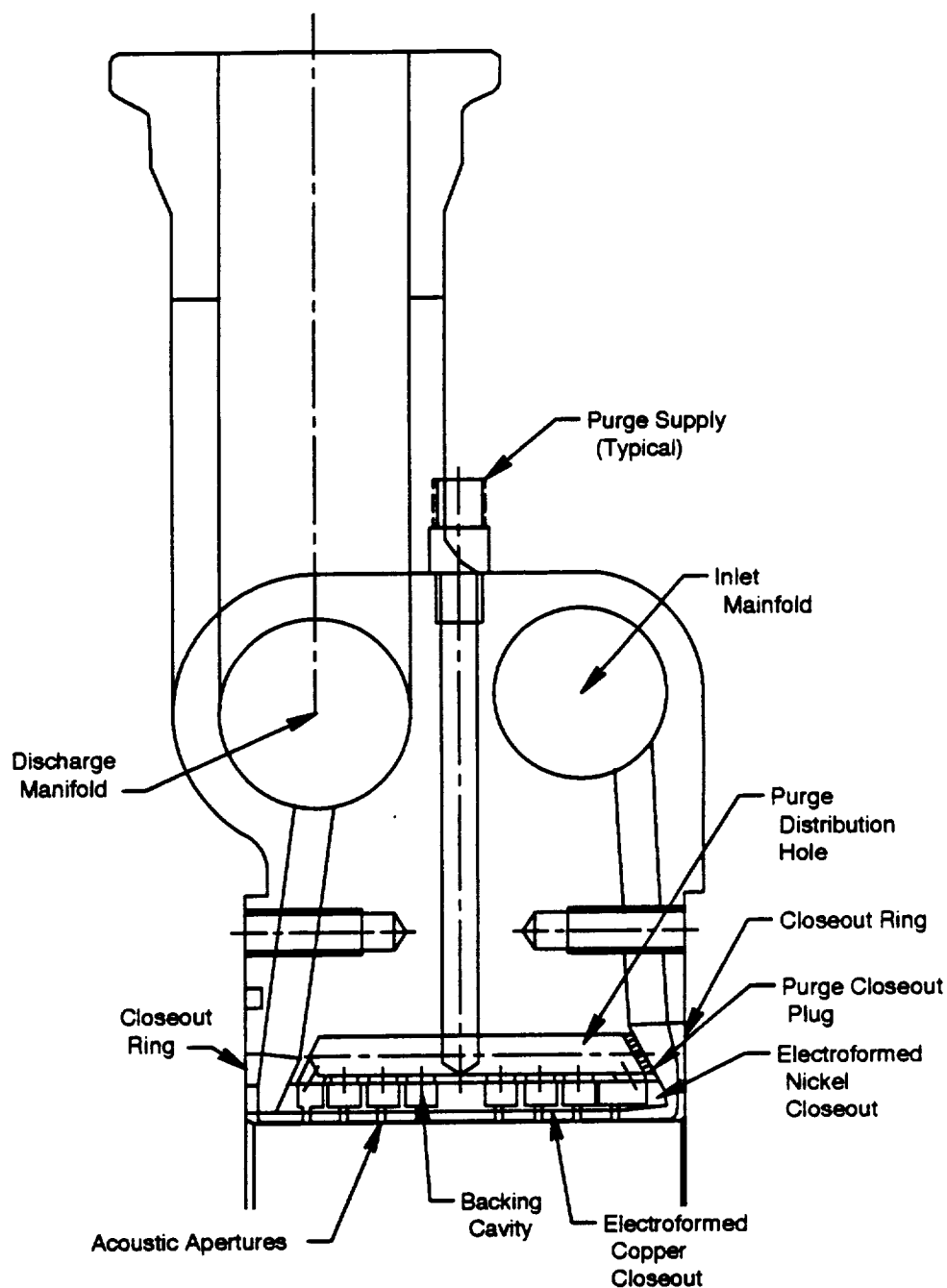


Figure 3.3.2-4. Large-Scale Acoustic Liner Spoolpiece

3.4 TEST SUMMARY

The large-scale injector task was terminated before testing of the hardware described in the preceding sections and therefore this section is blank.

SECTION 4.0

NOZZLE SKIRT FABRICATION TRIALS

The nozzle skirt fabrication demonstrations support the STME Phase B Preliminary Design (Contract NAS8-38170).

The objective of this program is to provide demonstration of key fabrication technologies that offer the greatest potential for developing a robust, highly reliable, low-cost nozzle skirt. The skirt fabrication trials provide the initial demonstration required to assess the feasibility in achieving these objectives.

The fabrication demonstrations are structured around a two-phase approach consisting of a process development phase (Phase I) and a large-scale verification phase (Phase II). Nondestructive testing and mechanical properties testing are used in conjunction with the manufacturing producibility results to aid in the selection of the optimum fabrication method.

Phase I uses flat samples representing the various fabrication techniques, two of three materials (INCO 625, Haynes 188, Haynes 230), and two tube geometries (round and square) for evaluation in assessing their relative abilities to provide a process that can support the program objectives of high reliability and low cost. Each of the fabrication method trials uses statistical design of experiments (DOX) matrices based on Taguchi methods where applicable to reduce the overall number of experiments required to evaluate the large number of independent variables involved. The objectives of Phase I are as follows:

- Address all major technical concerns of each manufacturing method
- Identify process related sensitivities
- Select the alloy most suited to each manufacturing method
- Assess the impact of the tube geometry on each process
- Identify viable inspection techniques
- Assess repairability
- Establish accurate cost estimates for each method.

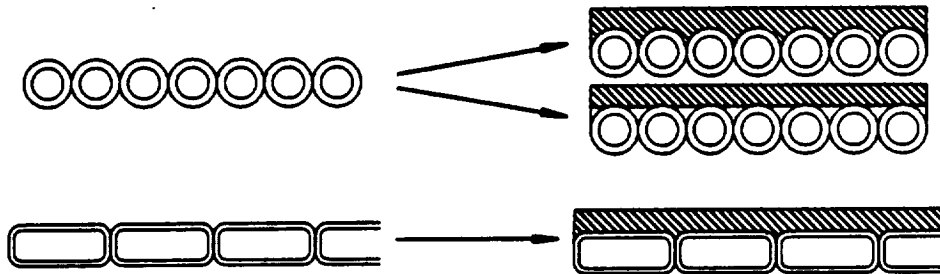
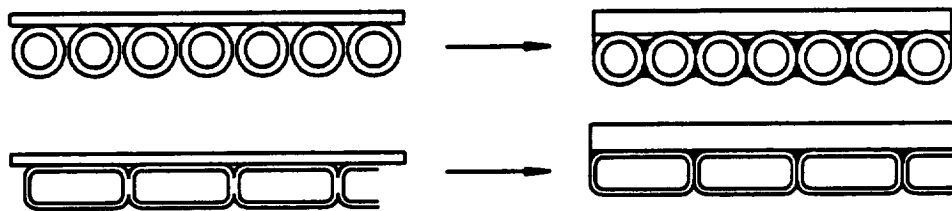
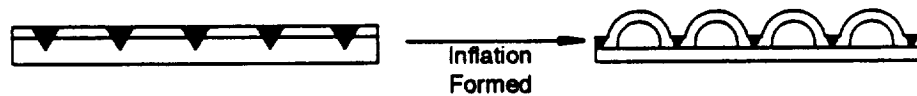
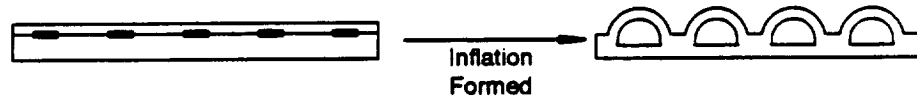
Nondestructive (NDT) test methods were employed where applicable to assess fabrication flaws, both naturally occurring and induced, and identify viable inspection techniques, such as X-ray, fluorescent penetrant inspection (FPI), and ultrasonic inspection. Mechanical properties of the materials and the bond joints will be evaluated using tensile and fatigue testing methods, while metallographic cross-sections will be prepared and evaluated using conventional light microscopy, scanning electron microscopy (SEM), transmission electron microscopy (TEM), and microprobe mass spectrometry where applicable.

Figure 4-1 illustrates the various fabrication methods investigated. These are divided into two basic categories:

- Tubular concepts
 - Inflation formed/diffusion bonded (IF/DB) tubes
 - Hypervelocity oxygen/fuel spray (HVOF) jacketed tubes
 - Brazed tubular assembly
- Sheetmetal concepts
 - Explosive formed/welded convolute (EF/W) sheet
 - Welded/inflation formed (W/IF) sheet
 - Diffusion bonded/inflation formed (DB/IF) sheet.

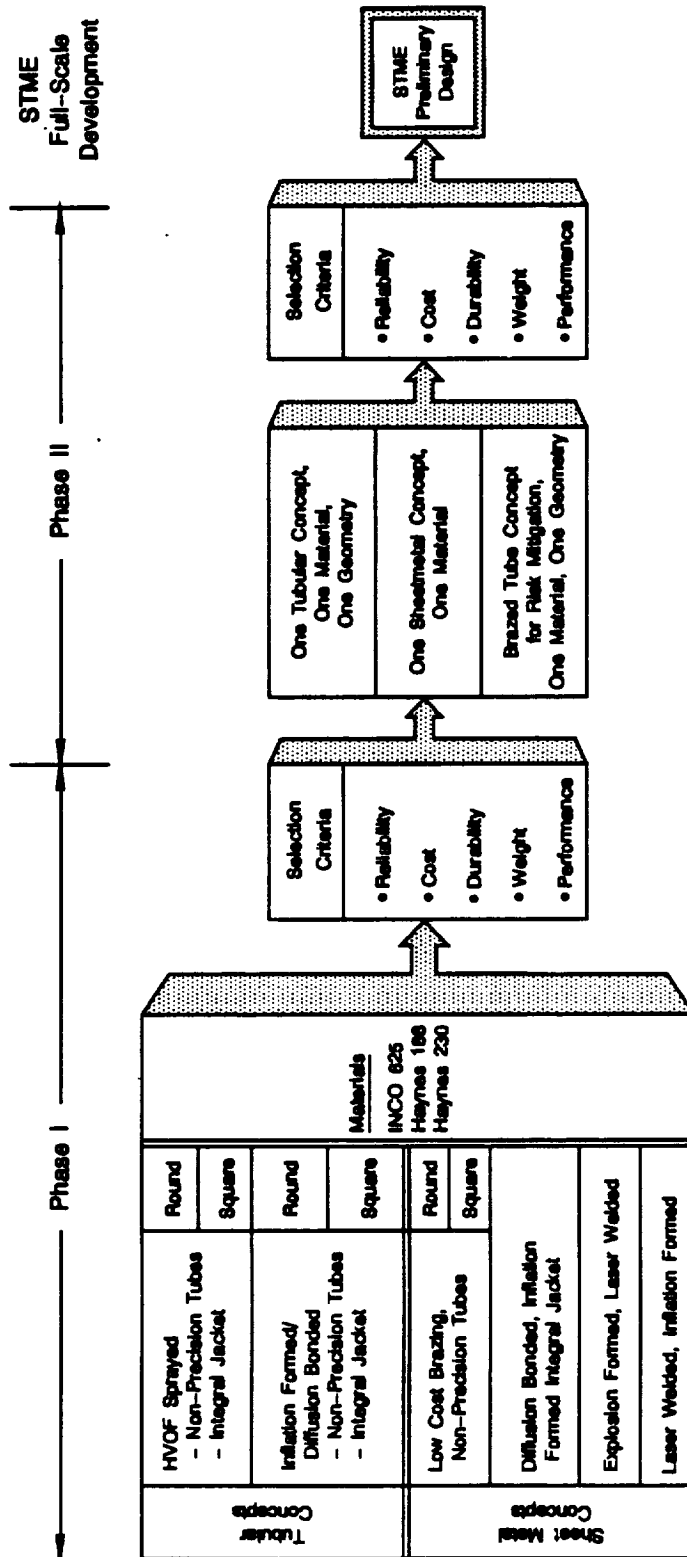
Following the completion of Phase I, two to three of these methods were to be selected for further evaluation in the Phase II portion of the program. Based on the downselect criteria presented in Figure 4-2, one sheetmetal fabrication method and at least one tubular fabrication method was to be selected. The brazed tubular method will also be included, if it is not downselected, for risk mitigation since this is currently the standard method of nozzle fabrication, of which P&W has over thirty years of RL10 experience. Only the optimum material for each method was to be selected for continued evaluation based on bond strength, mechanical properties, and metallurgical condition. One tube geometry (round or square) was to be selected for each method based on the ability to obtain the desired form within the design and cost requirements.

The Phase II portion of the program then proceeds to assess the large-scale related process capabilities and sensitivities of each of the downselected fabrication methods. Full-length panels at least 10 to 20 tubes wide and a large-diameter short cylinder will be fabricated and bonded according to the process developed in Phase I. Inspection and repair methods established in Phase I will be validated on flaws induced in the test panels, and cross-sections will be taken through some sections of the panels for metallographic inspection. Conceptual designs of the tooling required for a full-size nozzle will be supplied to assist in the selection decision for the STME nozzle design. Following the completion of Phase II, the optimum fabrication method was selected for the STME nozzle design. Depending on the technical and programmatic risks, the brazed tubular nozzle may be dropped or carried forward for risk mitigation.

TUBULAR CONCEPTSInflation Formed/Diffusion Bonded Tubes (IF/DB)Hypervelocity Oxygen Fuel Spray Jacketed Tubes (HVOF)Brazed Tube AssemblySHEETMETAL CONCEPTSExplosive Formed/Welded Convolute (EF/W)Welded/Inflation Formed (W/IF)Diffusion Bonded/Inflation Formed

5121

Figure 4-1. Fabrication Technologies Selected for Nozzle Skirt



FDA 394229

Figure 4-2. Nozzle Skirt Fabrication Trials

4.1 NOZZLE SKIRT FABRICATION TRIALS — PHASE I

4.1.1 Tubular Concepts

4.1.1.1 Inflation Formed/Diffusion Bonded (IF/DB) Tubes

Figures 4.1.1-1 and 4.1.1-2 illustrate the tooling concept used to perform the experiments. Tooling and raw materials were sent to P&W Development Operations-North, where the experiments were performed. The vacuum press to be used in the process was capable of providing pressures in excess of 2000 psi. Initial trials were performed at the maximum pressure, temperature, and time variables to determine the feasibility of the process for each material, followed by parameter optimization using a statistical design of experiments (DOX) matrix.

The first IF/DB trial was completed, using the Inconel 625 round tubes. The sample is shown in Figures 4.1.1-3. The trial was successful, with substantial inflation forming and tube bonding occurring during pressurization to 1500 psi and 2150°F. However, due to a leak in the tooling sample, the scheduled pressurization cycle was not completed to the maximum pressure of 2000 psi.

The tooling plates, shown as the thicker sections on the top and sides of the tubes, were not originally intended to bond to the tubes but rather to form a shell to create square tubes. A release agent was applied to the tooling inner walls before assembly to prevent tube bonding to the tooling plates. The effectiveness of the release agent was poor, resulting in substantial bonding of the tooling to the tubes. Based upon these results, other release agents are being tested to prevent future unintentional bonding.

Upon microscopic examination of the IF/DB sample bond joints, it was noted that carbides had formed on the bond lines. The presence of these carbides may result in a structurally inadequate bond joint and are not desirable. Various heat treatments are being investigated to limit or prevent the formation of carbides in future tests.

Examination of the tube cross sections also showed that slight cracks occurred on the tube corner inner radius. The corner area experiences the highest total strain during the forming process and is therefore the most susceptible to failure during the high pressure and temperature forming environments. After microscopic evaluation, it was found that the minute cracks were due to Inter-Granular Attack (IGA) on the inner walls due to the presence of air (an oxidizing atmosphere) inside the tubes during the forming process. The cycle procedures are being adjusted to prevent atmospheric contamination during the forming process by purging the tubes with an inert gas and evacuating the volume before subjecting the sample to the high pressures and temperatures.

Based upon this single IF/DB process, several design improvements were incorporated into the remaining test samples to prevent similar problems.

A parallel effort was undertaken that will offer significant benefits in terms of reducing tooling, raw material and complexity. This similar process makes use of a Hot Isostatic Pressure (HIP) facility, wherein the tubes and sheetmetal jacket are placed in a tool with reduced wall thicknesses. The sample is evacuated to remove any air between the tubes/sheetmetal and the tool walls, and welded to create a vacuum between the tubes and the tooling. The sample was placed in a HIP furnace, where it was brought up to pressure and temperature in the same manner as the IF/DB process. Because the entire furnace is held at the high pressure, the tubes are formed square against the structural jacket and the tool walls at temperature.

Both the IF/DB process and the HIP forming process described above were also tested using preformed square tubes. Since the preformed square tubes will undergo significantly less strain in the forming process than using round tubes, better material properties can be achieved at reduced forming pressures for producing the same final design.

The first IF/DB samples using the HIP furnace were successfully completed with round Inconel 625 tubes. The first two samples are shown in Figure 4.1.1-4. The right sample was formed in a HIP furnace held 2100°F and 17,000 psi. The extreme pressure, which is the maximum pressure available in that furnace, was used to ensure bonding was achieved in the first trial. Due to the pressure acting on all sides of the sample, the sheetmetal simulating the jacket and the thin tooling deformed inward on the tubes before the tubes fully expanded. The left sample was inflated at 2100°F and 5000 psi. Similar inflation forming and bonding also occurred at the significantly lower pressure. Both of these samples were screening trials intended to gather sufficient knowledge to design a more thorough test matrix.

A screening trial using preformed square Haynes 230 tubes was completed at 2100°F and 17,000 psi in a HIP furnace. In this trial, green "Stop-Off" was painted on the sides of the tubes to prevent tube-to-tube bonding. The sample was successful, in that only tube-to-jacket bonding occurred, as shown in Figure 4.1.1-5. The sample was intentionally bent to clearly show that the sides of the tubes were not bonded together. The concept for using non-bonded tubes is currently being structurally analyzed for the full-scale nozzle design. It offers the potential for reduced tensile stresses in the tube inner wall during nozzle cooldown by allowing the hot wall of the tube to freely contract. In the tube-to-jacket areas of this sample, full bonding was achieved.

The next screening trial, shown in Figure 4.1.1-6, used round Inconel 625 tubes at 2100°F and 3000 psi in a HIP furnace. This trial also used tooling "bags" rather than the thicker tooling plates that are used in the IF/DB trials performed in a standard furnace with an externally supplied pressurization source. The bags are actually thin sheetmetal enclosures designed only to hold a vacuum between the tubes and between the tubes and the sheetmetal jacket. In this sample, full diffusion bonding was achieved although somewhat less inflation formed than in the higher pressure samples due to the bag configuration. This type of arrangement actually allows the tube inner wall to retain a somewhat rounded shape, which would be desirable in a regeneratively cooled nozzle configuration. Part of the tooling bag has been included in the figure for clarity.

A fifth screening trial using round Inconel 625 tubes was conducted at 2100°F and 1000 psi in a HIP furnace. This sample is shown in Figure 4.1.1-7 and is directly comparable to the samples in Figure 4.1.1-4. At the HIP furnace pressure of 1000 psi, significant bonding and inflation forming was achieved. The lower pressure did not create fully square tubes, and a small gap is left between the tube walls at the sheetmetal interface.

The results of these initial screening trials were used to design a more thorough test matrix for the remainder of the IF/DB HIP fabrication samples. Each of the three materials, using preformed square tubes, will be tested at a range of pressures. To demonstrate more closely the full-scale nozzle configuration, there are two geometry configurations that were used. The first, shown as Configuration A in Table 4.1.1-1, was intended to simulate the tube geometry at the forward section of the nozzle by placing the wide sections of the tubes together. Configuration B is intended to simulate the tube geometry at the aft section of the nozzle by placing the narrow sections of the tubes together. For all materials and geometries, both masked and unmasked samples were to be run to verify the ability to prevent bonding between the tubes. Tables 4.1.1-1, 4.1.1-2, and 4.1.1-3 show the sample configurations selected for each of the candidate materials.

Table 4.1.1-1. Inconel 625 — 25 Samples

Pressure (psi)	Configuration A		Configuration B	
	8 Masked	5 Unmasked	8 Masked	9 Unmasked
7000	2	2	2	1
3000	2	1	2	1
1000	2	1	2	1
500	2	1	2	1

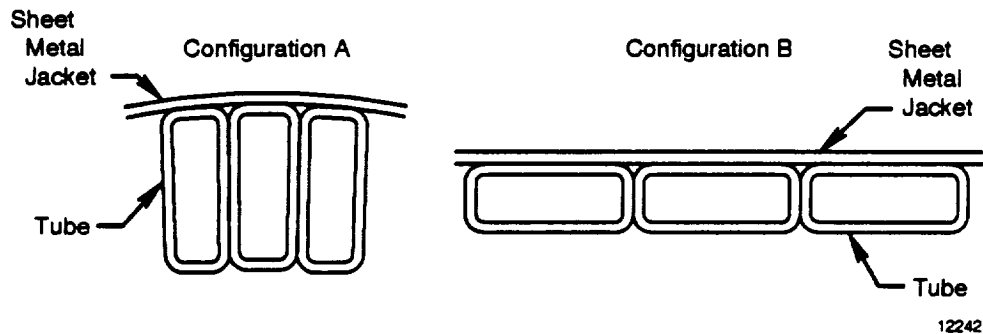


Table 4.1.1-2. Haynes 230 — 13 Samples

Pressure (psi)	Configuration A		Configuration B	
	4 Masked	3 Unmasked	4 Masked	2 Unmasked
7000	1	1	1	1
3000	1	1	1	1
1000	1	1	1	-
500	1	-	1	-

Table 4.1.1-3. Haynes 188 — 12 Samples

Pressure (psi)	Configuration A		Configuration B	
	4 Masked	2 Unmasked	4 Masked	2 Unmasked
7000	1	1	1	1
3000	1	1	1	1
1000	1	-	1	-
500	1	-	1	-

All of the test matrix samples underwent weld repairs to fix cracks found in the perimeter welds. These cracks were due to the use of tooling materials with a larger coefficient of expansion than the tubes. The samples were reworked and welded to repair the existing cracks, and a sheetmetal "bag" that is made of the same material as the tubes was welded to the existing tooling to encase it and hold a vacuum. Neither the samples nor the process demonstration was adversely impacted by this revised configuration.

Manufacturing planning for the full-scale nozzle has showed that tooling costs can be greatly reduced by providing thinner section tooling. This thinner section tooling can be achieved by the use of a pressurized furnace rather than the inner tube walls pressurized in the furnace from an external source. Using a HIP furnace, the space between the tubes and the sheetmetal jacket or tooling can be evacuated before placing the part in the furnace. Because the pressure is acting on all sides of the part, the tooling is not required to act as a pressure vessel but only to hold the vacuum and retain the finished shape of the part. In the standard IF/DB configuration, the pressure inside the tube walls used to inflate and bond the tubes is provided from a source external to the furnace. The tooling is thus required to hold the pressure and is significantly larger. The cost advantage of the tooling appears to outweigh the cost differential between the HIP furnace and the standard furnace.

Based upon these full-scale nozzle manufacturing studies, the remaining IF/DB trials were conducted using the HIP furnace. Since the bonding and inflating processes are essentially the same, the HIP samples demonstrate both methods of IF/DB.

Additional IF/DB samples using the HIP furnace (HIP-IF/DB) were successfully completed with round and square Inconel 625, Haynes 188, and Haynes 230 tubes. These samples were run at a range of pressures as discussed in the test matrix (Table 4.1.1-1). Figure 4.1.1-8 shows a successful Inconel 625 HIP sample. This sample was processed at 7000 psi, and the tubes were unmasked to form a tube-to-tube bond as well as the tube-to-jacket bond. Figure 4.1.1-9 shows a HIP sample that was processed at 3000 psi with the tubes unmasked. Both of these samples show both forming and bonding, and used preformed square tubes. Figure 4.1.1-10 shows a HIP sample of Inconel 625 tubes that was processed at the relatively low pressure of 500 psi, with the tubes intentionally unbonded. This sample had experienced contamination due to inadequate cleaning procedures and masking techniques.

Figures 4.1.1-11 and 4.1.1-12 show Haynes 230 samples that used preformed square tubes and were bonded at 3000 psi. The microcracks in the tube radii are evident at the outside corners and are due to high total strain rate during forming. In the first sample, the tubes were unmasked to form tube-to-tube bonds. In the second sample, the tubes were intentionally left unbonded.

The test matrix samples were fabricated during the previous reporting period, and some of the samples underwent weld repairs to fix cracks found in the perimeter weld. However, several of the samples were run in the HIP furnace before the tooling thermal coefficient of expansion mismatch was found to be a problem. These samples were irreparably damaged and thus no significant forming or bonding occurred before the samples leaked. Of the samples that had not yet been run before the crack problem was discovered, all of the Inconel 625 samples were repaired by reworking and rewelding the material, and a sheetmetal bag made of the same material as the tubes was welded to the existing tooling to encase it and hold a vacuum. Neither the samples nor the process demonstration were adversely impacted by this revised configuration. The remaining Haynes 230 and Haynes 188 samples were not repaired because the material downselect decision to Inconel 625 had been made and there was no need for further Haynes 188 test samples.

The results of the metallographic testing have been completed for several of the previously completed IF/DB samples. Figure 4.1.1-13 shows the sample cross section at the bond locations and tube corner radii of an Inconel 625 sample that used preformed rectangular tubes and was HIP-IF/DB processed at 7000 psi and 2100°F. The photo shows several microcracks at the tube inside corner radii, which were caused by oxides that had formed

at the metal surface due to an impure furnace gas environment. Since the presence of oxygen was confirmed during the chemical analysis, and also because no cracks are found in the tube outer walls, the cracking is not an indication of Inconel 625 strain rate or total strain sensitivity to the process.

Figure 4.1.1-14 shows the same Inconel 625 sample, at the bond locations. The tube-to-tube bond appears to be somewhat better than the tube to jacket bond, although both bonds contain oxides and voids along the bond lines. The oxides also show some indication of penetration into the base metal, which was caused by either particle contamination (dirt or oil) or air trapped between the surfaces. The uniformity of the oxides suggests that they most likely arose from a nonvacuum condition. Note that once base metal oxides are formed on either mating surface, the diffusion bond cannot occur. In addition, oxides cannot be diffused out of a nickel-based alloy (unlike titanium alloys), and therefore must be completely removed by chemical cleaning before the bond cycle and prevented from forming during the bond cycle by removing all air. Once a part is satisfactorily cleaned, however, it can remain free of oxides throughout the handling and processing, because clean nickel alloys will not form oxides at room temperature conditions. Figure 4.1.1-15 shows an etched photograph of the same sample, which shows the carbides present in the base metal and at the bond locations. Many of these carbides are naturally occurring in the nickel-based alloy, and can migrate to the surface of the metal during the high-temperature processing. Some of these secondary carbides may precipitate back out of the base metal with sufficient time at the high processing temperature. Other types of carbides, some of which are not normally found in the base metal, may be formed when contamination such as dirt or oil comes into contact with the base metal. These primary carbides will stabilize in the presence of oxygen, and therefore will not precipitate out of the metal. Based upon these results, further analysis was performed on additional samples to determine the type of carbides present at the bond locations to see if they came from the base metal (which is not preventable).

At the highest diffusion bonding pressure of 17,000 psi, the tube-to-tube and tube-to-jacket bonds show similar characteristics, as shown in Figures 4.1.1-16 and 4.1.1-17. Figure 4.1.1-16 indicates that the bond location and base metal was more severely affected by the environment, most likely due to the higher pressure causing greater diffusion of oxides into the part, as well as oxygen stabilized carbides. Figure 4.1.1-17 shows a network of concentrated, continuous carbides that most definitely indicates contamination was present. The extent of carbides is not affected by the degree of processing pressure.

Figure 4.1.1-18 is a photograph of Inconel 625 tubes that were bonded at 7000 psi and 2100°F. The lack of cross-grain growth at the tube to tube boundary indicates that a longer bond cycle may help recrystallize grains and improve bond characteristics. There is also some evidence that the amount of metal deformation at the bond location may have excellent grain size characteristics (ASTM 6-8) that are actually better than the tube metal grain size before the HIP-IF/DB processing. The longer diffusion bonding times proposed in this report will likely cause the base metal grain size to become larger, which adversely impacts material properties.

Figure 4.1.1-19 shows the results of a HIP-IF/DB sample that was heat treated at 2150°F for 2 hours with a fast cool, following the IF/DB process cycle. The purpose of the subsequent heat treat was to see if the carbides at the bond line were reduced by precipitating out of the metal. There was, however, no change from the original metallographic analysis, which indicates that the presence of oxygen had stabilized these carbides.

One of the early Haynes 230 samples, which was HIP bonded at 3000 psi and 2100°F, is shown in Figure 4.1.1-20. The tube outer walls were severely damaged by the forming process, which is similar to the results found in the Haynes 230 sheetmetal forming processes. The sample was analyzed for the presence of oxygen (which can accelerate cracking) but was found to be free of oxygen. The Haynes 230 material is obviously very sensitive to total strain or strain rate during the forming process, and therefore less robust for this type of fabrication process. Figure 4.1.1-21 shows the same sample, etched to reveal grain size, structure, and the presence of carbides at the bond lines. These carbides are most likely due to the contamination problems experienced during fabrication and processing.

Based upon the above results and previous samples, several significant processing lessons learned have been incorporated into Fabrication Trials Phase II planning and full-scale nozzle manufacturing master planning. These lessons learned are listed below:

Processing Parameters — A processing temperature of 2100 to 2150°F was used for the test matrix samples. This temperature has been shown to allow substantial forming, and some bonding of the tubes. Since 2100°F is a relatively high temperature for any thermal processing (equal to the heat treat temperature of Inconel 625), further studies should include whether lower temperatures can produce the same good forming and bonding results, and what effects it may have on grain growth and carbide formation.

A processing time of 6 hours was used for all samples in order to allow for a direct comparison between samples at different pressures. The 6-hour time allowed for some bonding to occur at the pressures of 3000 psi and higher, but the lower pressure samples had poorer bond quality. Additional time at the processing temperature and pressure will provide better bonds, but will adversely affect tooling creep life and base metal grain structure. Longer processing times may be further investigated to understand the extent of improved bonding versus decreased tooling life and grain structure.

Pressures of 500, 1000, 1500, 3000, 5000, 7000, and 17000 psi have been used in the IF/DB and HIP-IF/DB fabrication trials. The highest pressures provided the greatest tube forming and bonding, with pressures greater than 5000 psi giving roughly similar results. The squareness of the tubes at the higher pressures is not desired from a structural standpoint, because the sharper corner radii in the tube will have a higher stress concentration than a smooth corner. However, the sharper outside corner provides greater bonding surface for the tube-to-jacket bonds. Because the lower pressures (less than 5000 psi) provide the more desirable rounded corner tube geometry and offer reduced thickness tooling for the IF/DB and reduced furnace pressure requirements for both the IF/DB and the HIP, further fabrication samples should focus on investigating processing pressures in the 1000 psi to 5000 psi range.

Surface Condition — General cleanliness requirements for fabricating the samples proved to be of significant importance. Several contaminants were found in the processed samples, which included residue from the tape used to mask the jacket side of the tubes when stop-off was applied to prevent tube-to-tube bonds. The HIP furnace undoubtedly has an impure environment (presence of oxygen in the furnace inert gas), which causes oxides to form at the bond surfaces and prevents bonding of the parts. The relatively simple cleaning procedures initially used will need to be modified to more stringent cleaning procedures to chemically remove all oxides, dirt, oil, and other common manufacturing facility contaminants.

Release Agents — The green stop-off that was used to prevent bonding of the tubes to the tooling and to each other worked well. The possibility of contamination to the bond surfaces from the outgassing of this release agent should be determined. In addition, the ability to mask the tubes with the release agent without contaminating the bond surfaces (due to the residue left from the masking tape) should be examined. As illustrated in Figure 4.1.1-10, the tube was masked with tape and then covered with the release agent. The tape was removed when the release agent dried, and wiped clean with alcohol. The tape residue appears to have contaminated the surface, as indicated by the yellowish hue, and alcohol does not seem to adequately remove this residue.

Additional Samples for IF/DB and HIP — To answer some of the remaining processing, cleaning, and environment concerns, additional small scale tubular HIP and IF/DB samples will be fabricated. These samples will be used to finalize the Phase II subscale nozzle processing parameters, minimize contamination problems, and optimize the bonding and strength of the bond joint. In addition, simple tensile tests will be conducted on existing samples as well as the additional samples to characterize the strength of the bond joint. Concurrent full-scale nozzle design and analysis will establish limits for bond strength and bond coverage to determine minimum acceptable conditions.

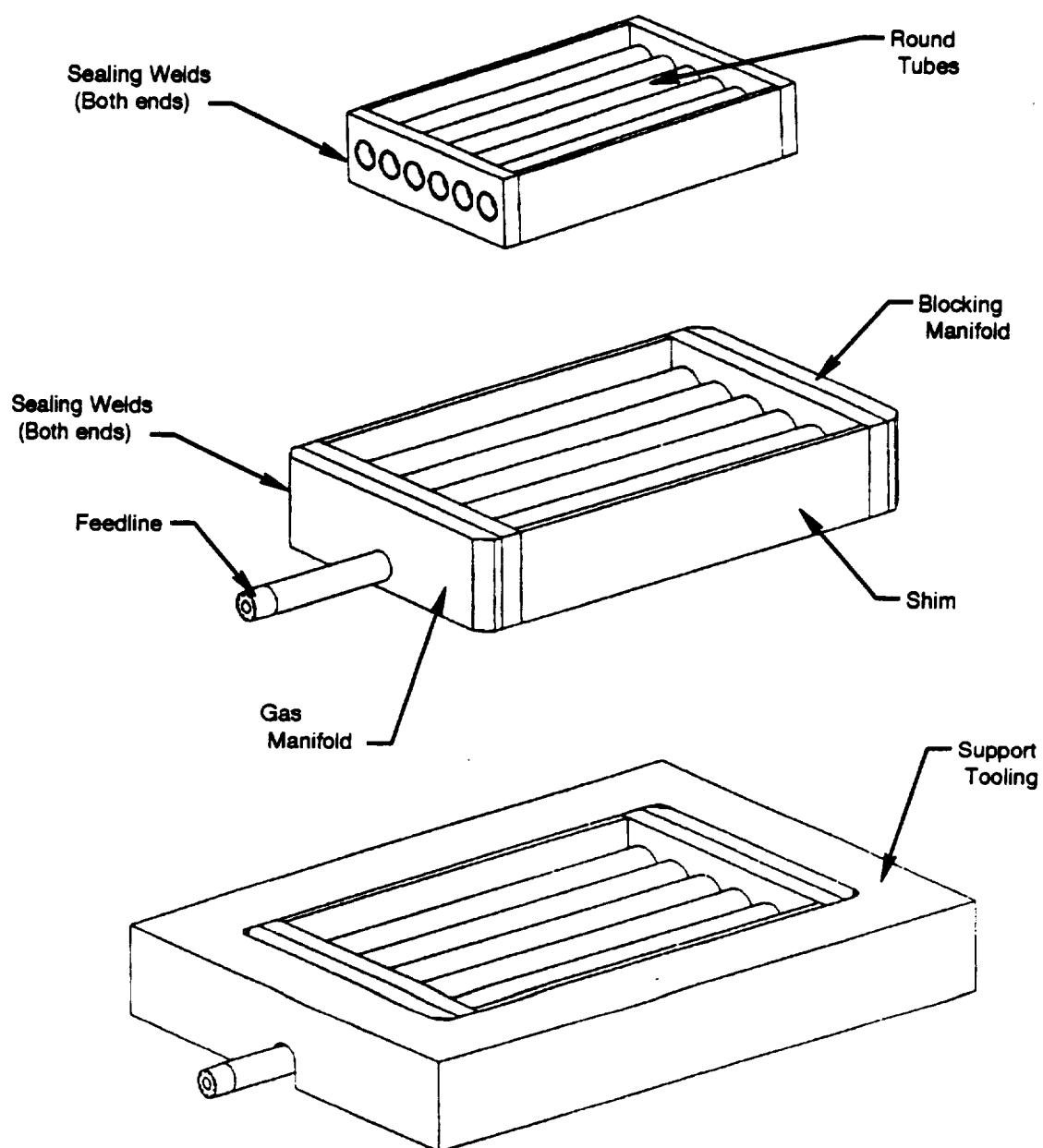
Laboratory diffusion bonding experiments were conducted to determine the capability for Inconel 625 to diffusion bond both with and without special preparation procedures. As discussed in the previous bimonthly report, many of the small tubular diffusion bonded samples contained oxides and carbides at the bond locations. This laboratory study was undertaken to determine the best possible bond joint, using nickel plating, descaling, or chemical milling preparation procedures.

The samples used mating AMS 5599 (Inconel 625) sheetmetal 0.02 in. thick samples, approximately 2 x 2 in. size. Three specimens were run in a 100 ton vacuum press at 10⁻⁴ Torr vacuum level using a 1900°F bond temperature with a 5000 psi pressure applied for 6 hours. The 1900°F bond temperature was selected to avoid grain size coarsening during the diffusion bond cycle, which indicates reduced parent material properties.

The three sets of samples were prepared using standard production methods for diffusion bonding. The first set of samples received approximately 0.0002 in. thick nickel plating on both mating surfaces. A second set was descaled using a standard descaling procedure, which includes a hydrochloric acid solution and a caustic potassium permanganate descaling solution. The third set of samples was cleaned using a standard chemical milling procedure, which involves using several different acids in solution.

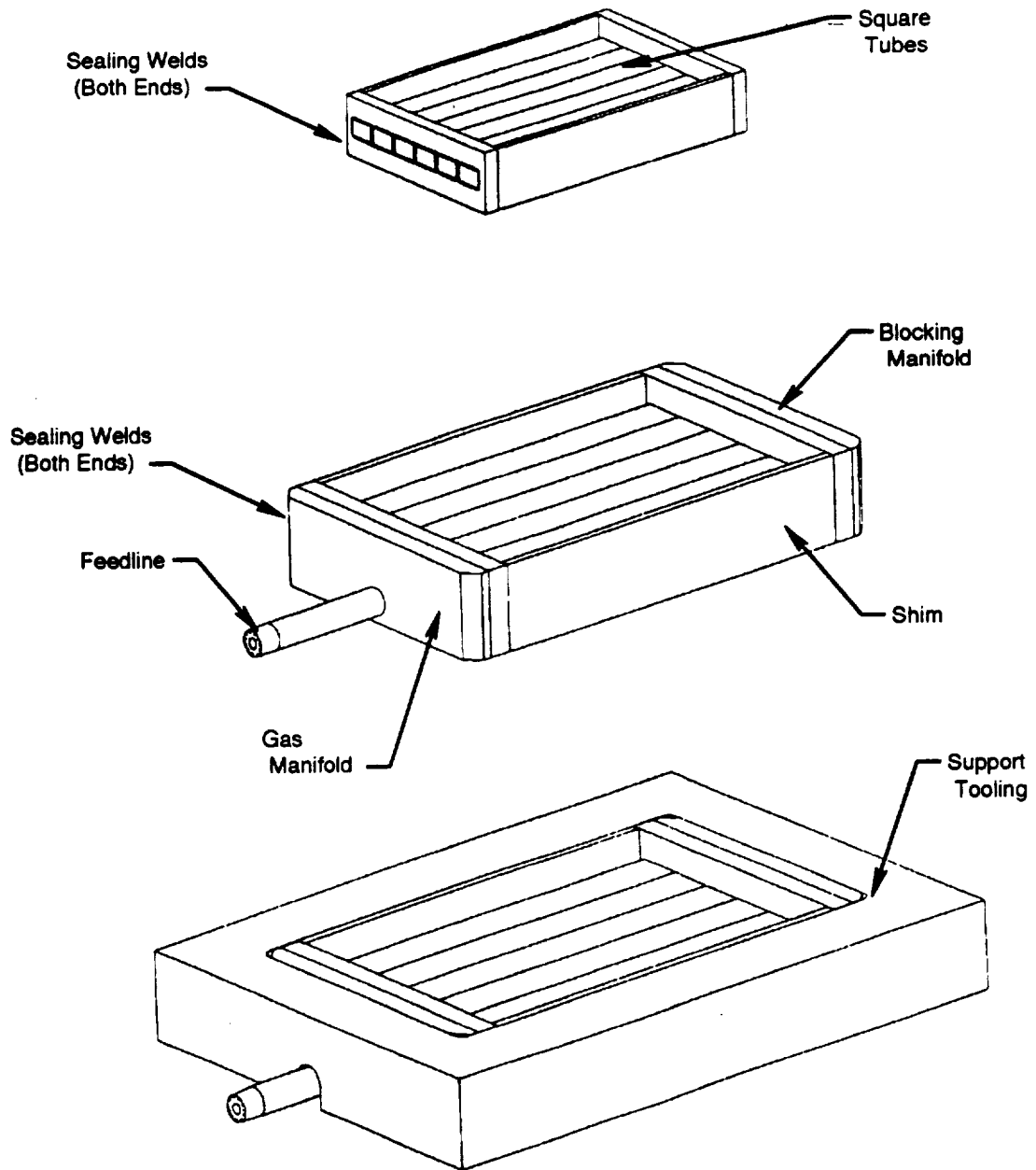
The resultant bond quality was evaluated by both the extent of the grain growth across the bond interface and the elimination of a visible interface. The more extensive grain growth across the bond indicates a stronger bond, and the less apparent the bond interface, the closer the bond strength will be to parent material strength. Metallurgical examination of the sample cross-sections through the bonded samples indicated that the nickel plated surfaces produced the highest bond quality of the three samples (see Figure 4.1.1-22), as both of the desired features were attained to a high degree. Examination of the remaining two unplated samples, which used the descaling and chemical milling surface preparations only, revealed interfacial contamination with no apparent grain growth across the bonds, as shown in Figures 4.1.1-23 and 4.1.1-24.

One of the samples also underwent subsequent thermal cycling at 2150°F in order to simulate a secondary braze cycle for the nozzle which would join the stiffening bands and the nozzle inlet manifold attachment to the tubular skirt subassembly. The post-bonding treatment further enhanced bond integrity in the nickel plated sample by causing additional grain growth across the interface as shown in Figure 4.1.1-25.



7243

Figure 4.1.1-1. Round-Tube Specimen Tooling



7245

Figure 4.1.1-2. Square-Tube Specimen Tooling

FE02156

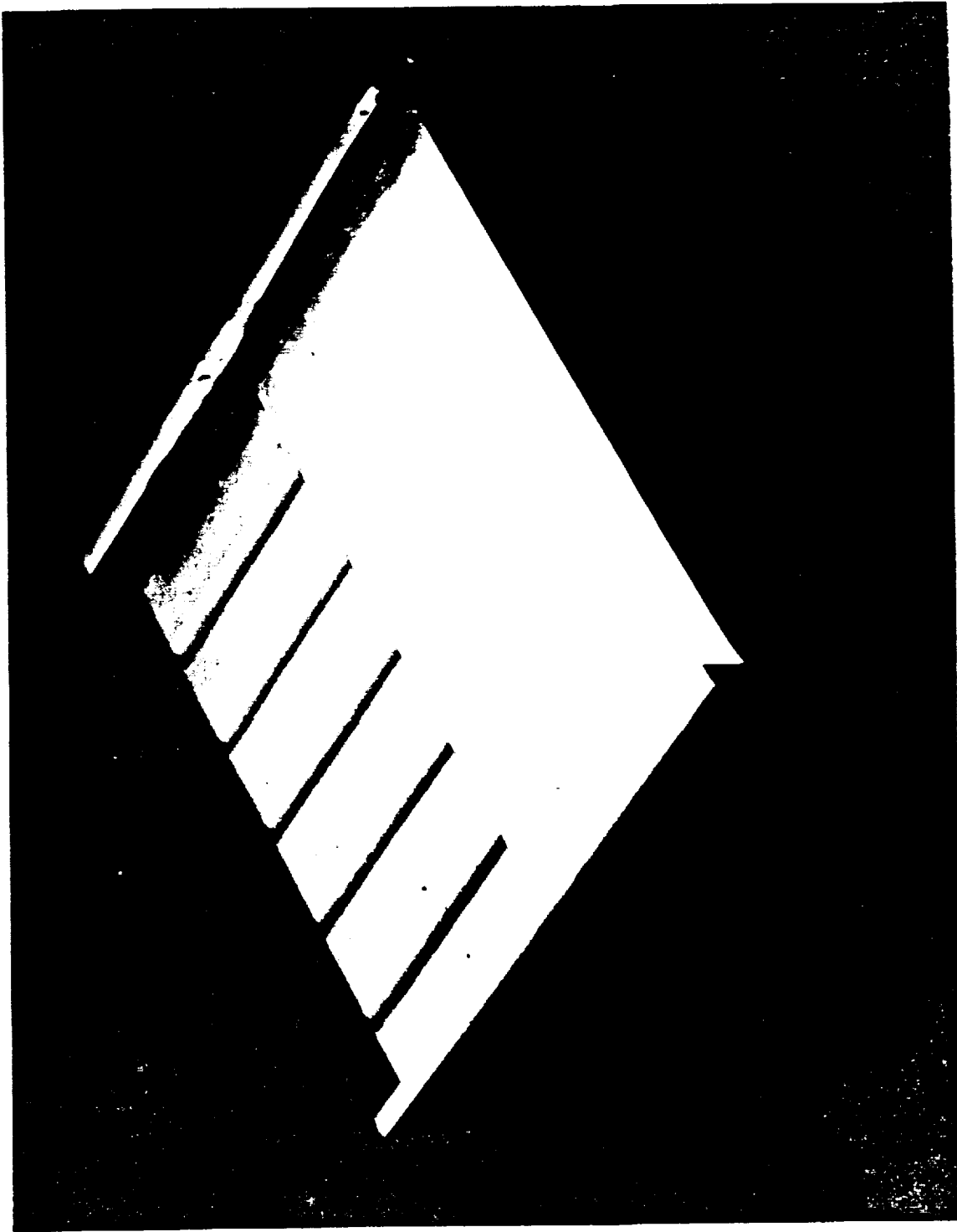


Figure 4.1.1-3. Diffusion Bonded/Inflation Bonded Inconel 625 Sample Using Round Tubes

FE824004

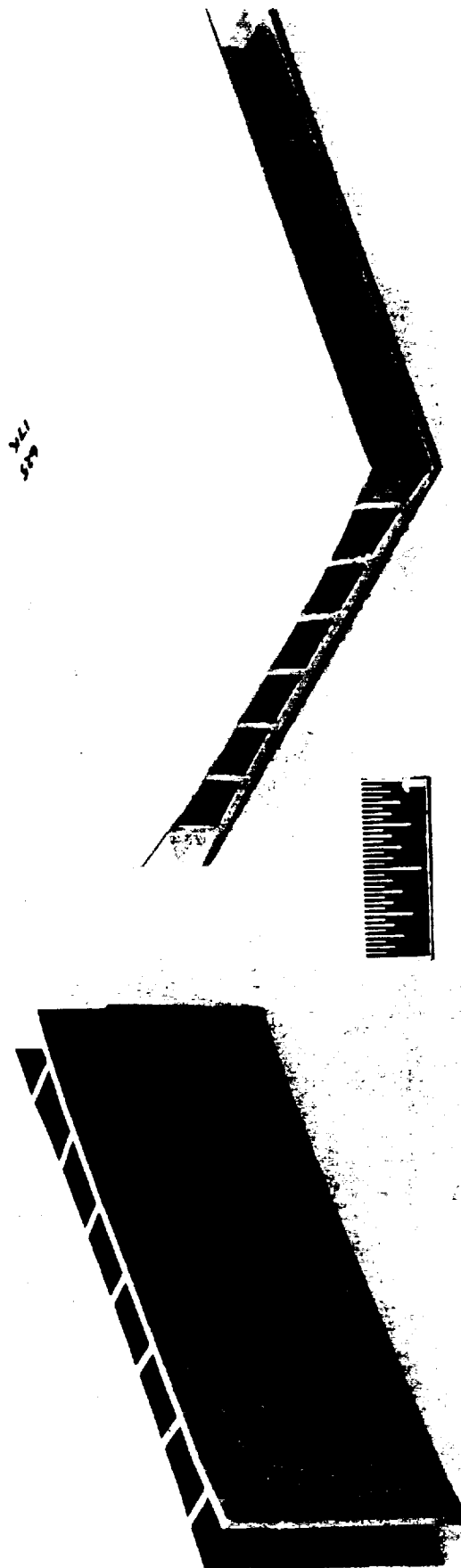


Figure 4.1.1-4. Diffusion Bonded/Inflation Formed Inconel 625 Round Tubes in an HIP Furnace (Left, 2100 F and 5000 psi; Right, 2100 F and 17,000 psi).

FE824007

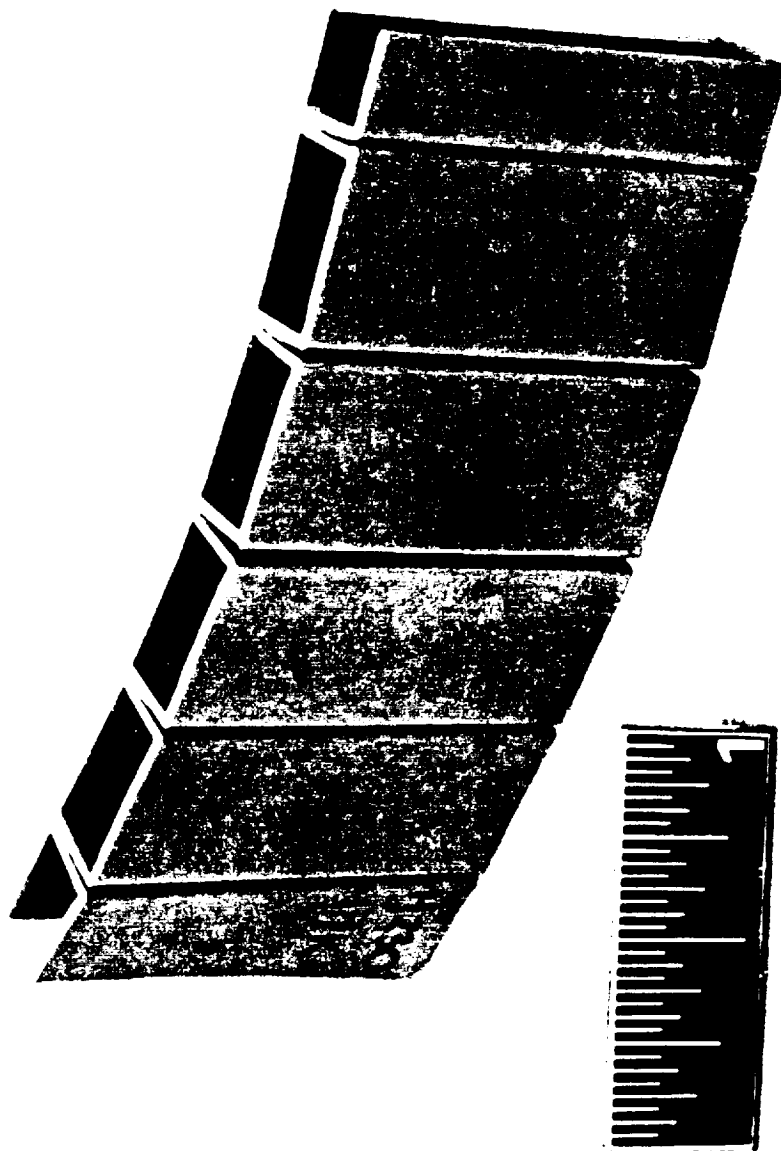


Figure 4.1.1-5. Diffusion Bonded/Infiltration Formed Haynes 230 Preformed Square Tubes in a HIP Furnace at 2100°F (17,000 psi) With No Tube-to-Tube Bonds

FE824007

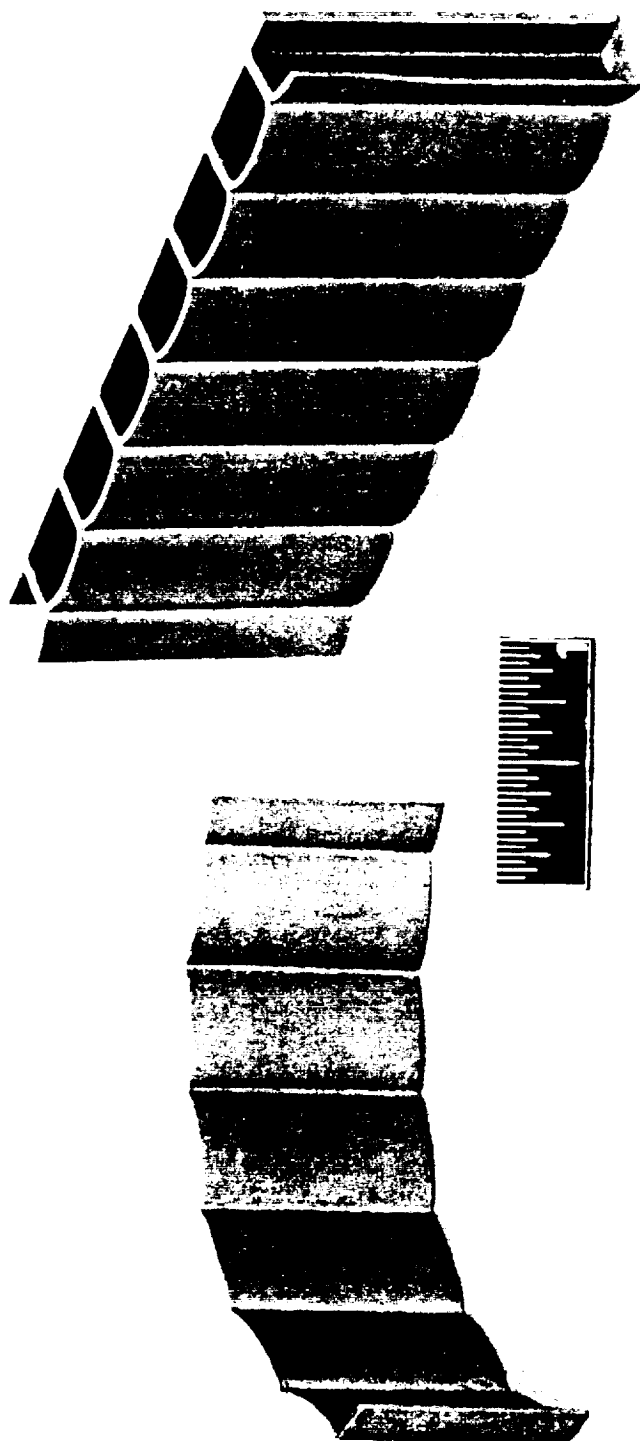


Figure 4.1.1-6. Diffusion Bonded/Inflation Formed Inconel 625 Round Tubes in an HIP Furnace at 2100°F and 3000 psi With Tooling Bags

FE824006

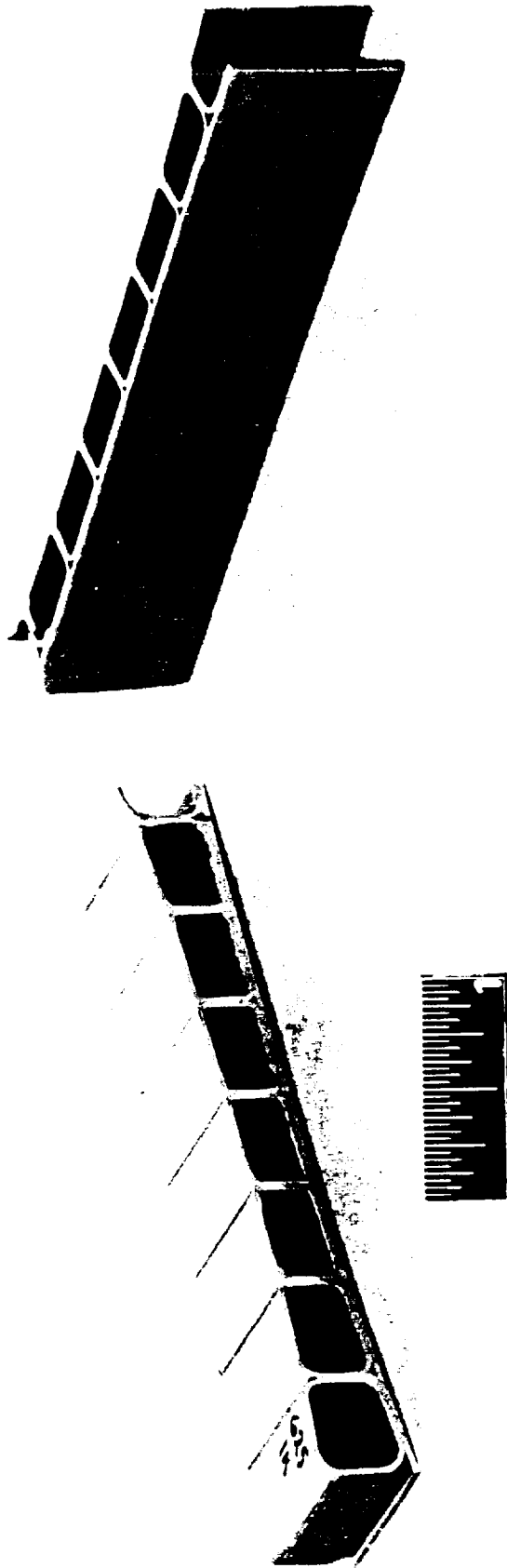
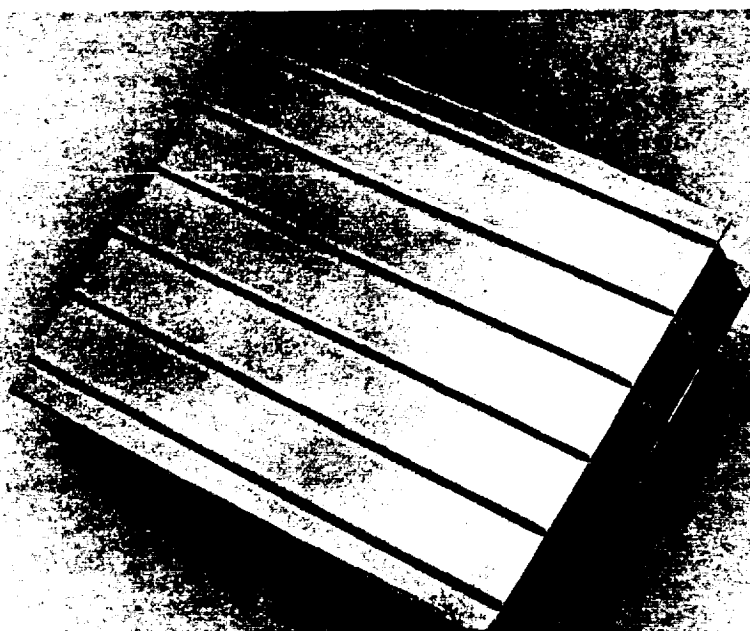
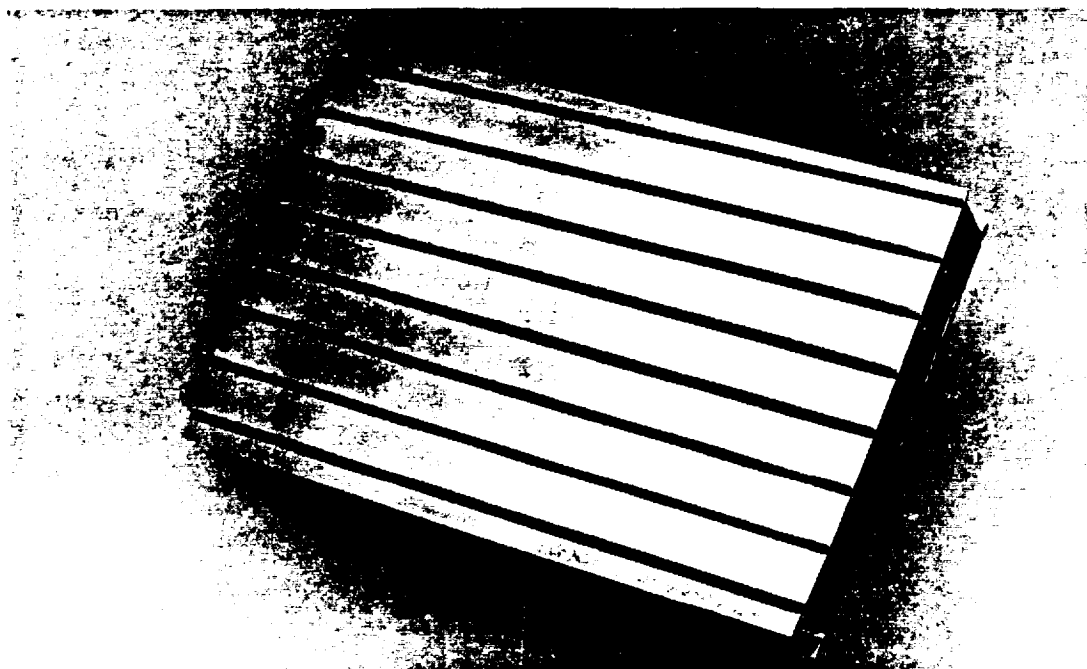


Figure 4.1.1-7. Diffusion Bonded/Inflation Formed Inconel® 25 Round Tubes in an HIP Furnace at 2100°F and 1000 psi



FE025836

Figure 4.1.1-8. Preformed Square Inconel 625 Tubes Inflation Formed/Diffusion Bonded in a Hot Isostatic Press Furnace at 7000 psi and 2100°F With Tubes Unmasked To Form Tube-to-Tube Bonds



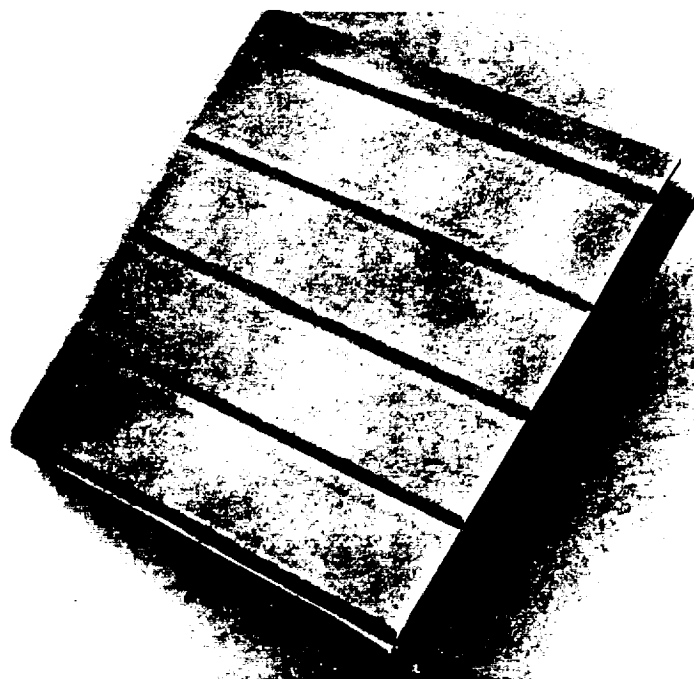
FE025839

Figure 4.1.1-9. Preformed Square Inconel 625 Tubes Inflation Formed/Diffusion Bonded in a Hot Isostatic Press Furnace at 3000 psi and 2100°F With Tubes Unmasked To Form Tube-to-Tube Bonds



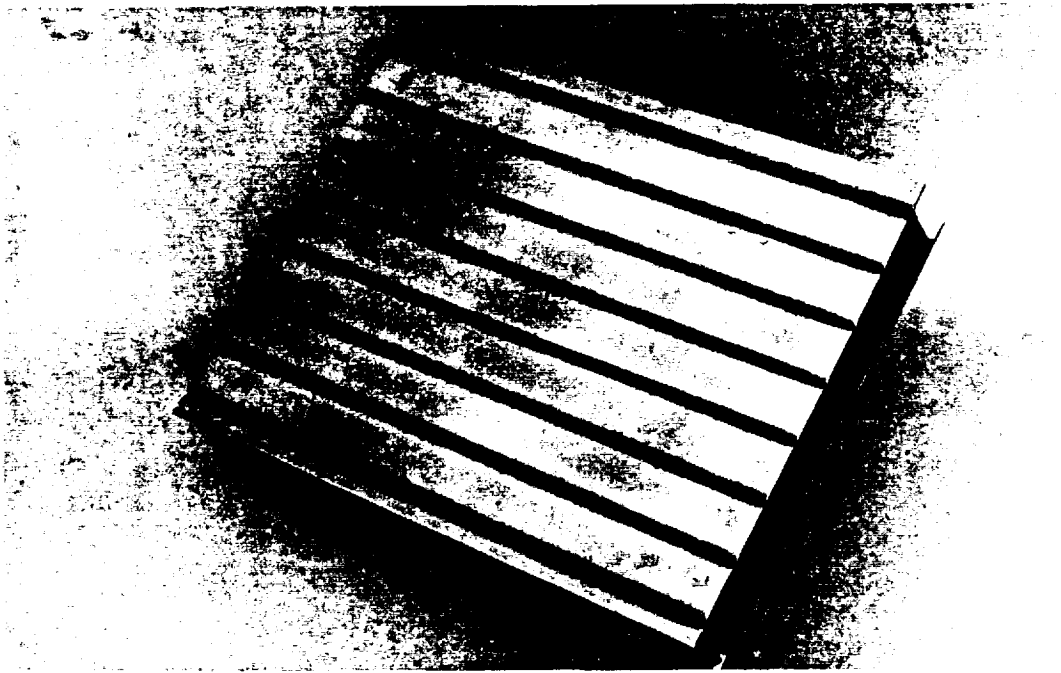
FE625840

Figure 4.1.1-10. Preformed Square Inconel 625 Tubes Inflation Formed/Diffusion Bonded in a Hot Isostatic Press Furnace at 500 psi and 2100° F With Tubes Masked To Prevent Tube-to-Tube Bonds, and With Contamination Present Due to Masking



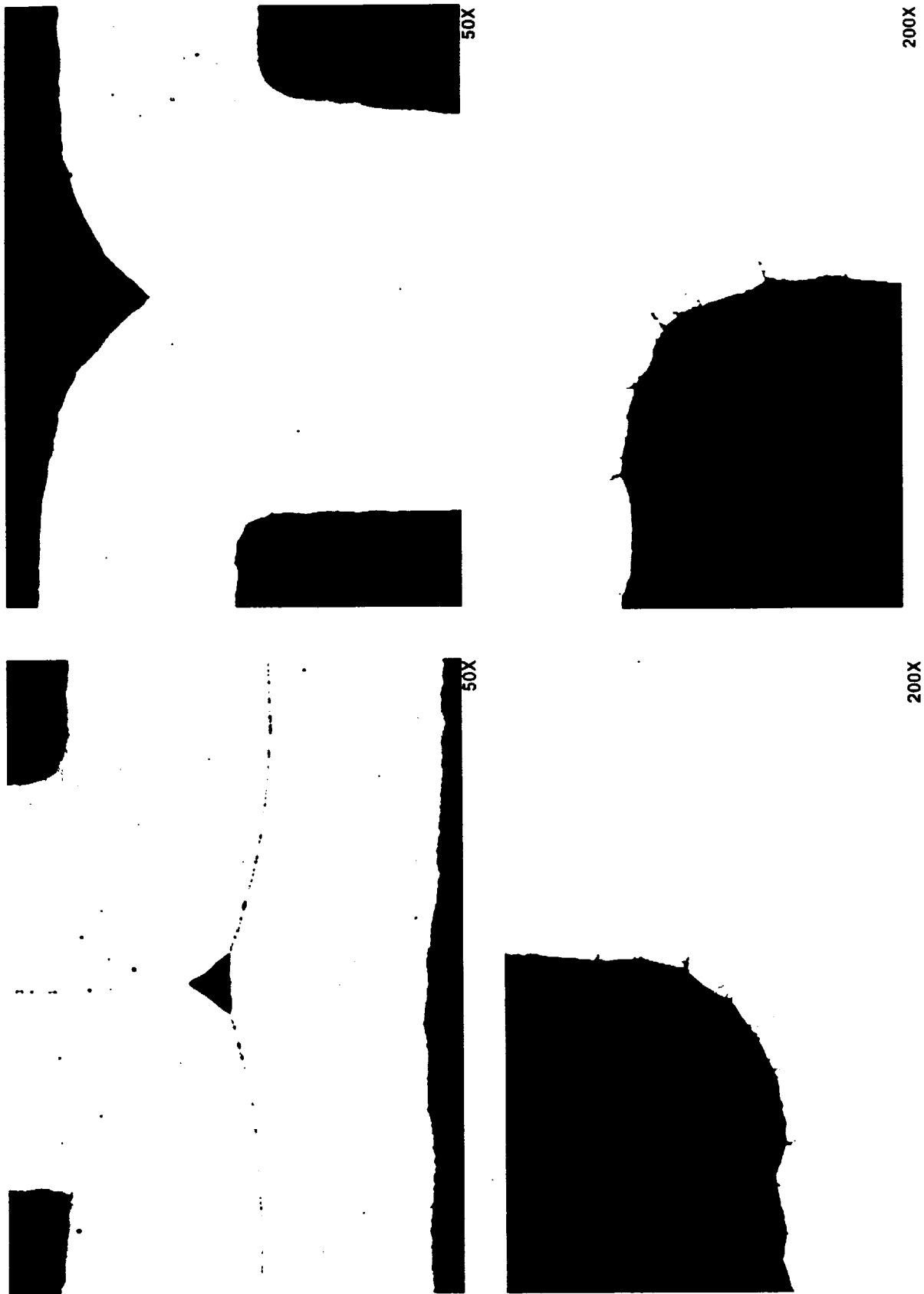
FE625837

Figure 4.1.1-11. Preformed Square Haynes 230 Tubes Inflation Formed/Diffusion Bonded in a Hot Isostatic Press Furnace at 3000 psi and 2100° F; Microcracking Occurred in Outside Corner Radii Due to High Material Strain and Strain Rate



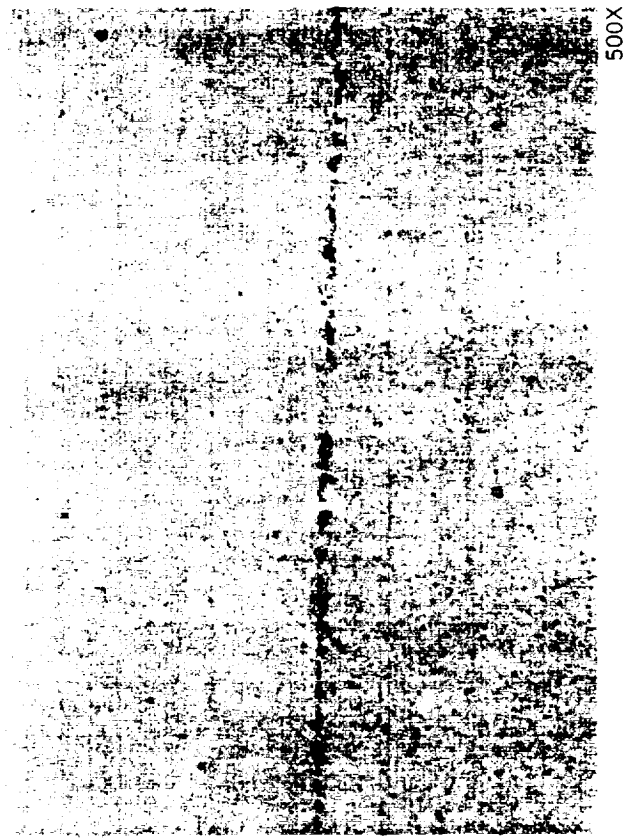
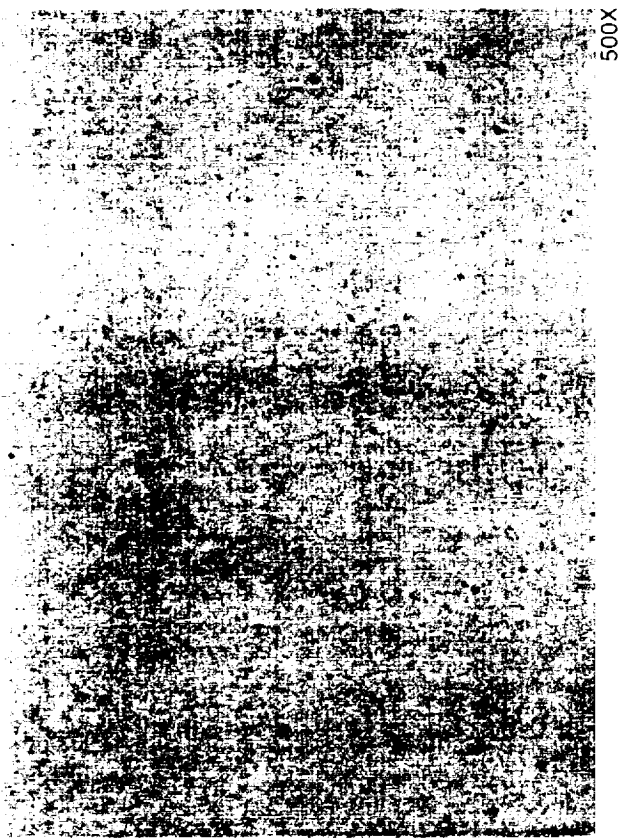
FE625838

Figure 4.1.1-12. Preformed Square Haynes 230 Tubes Inflation Formed/Diffusion Bonded in a Hot Isostatic Press Furnace at 3000 psi and 2100° F; Microcracking Occurred in Outside Corner Radii Due to High Material Strain and Strain Rate

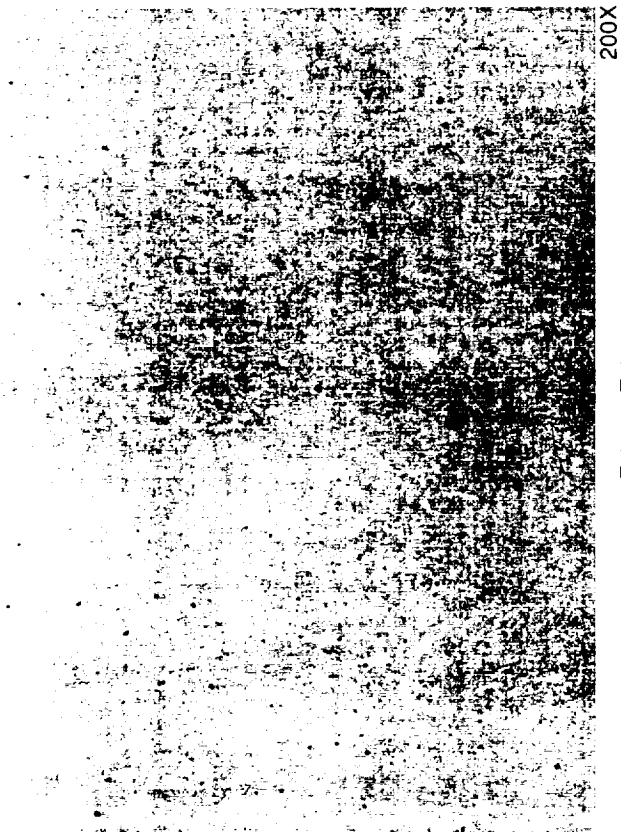


14594

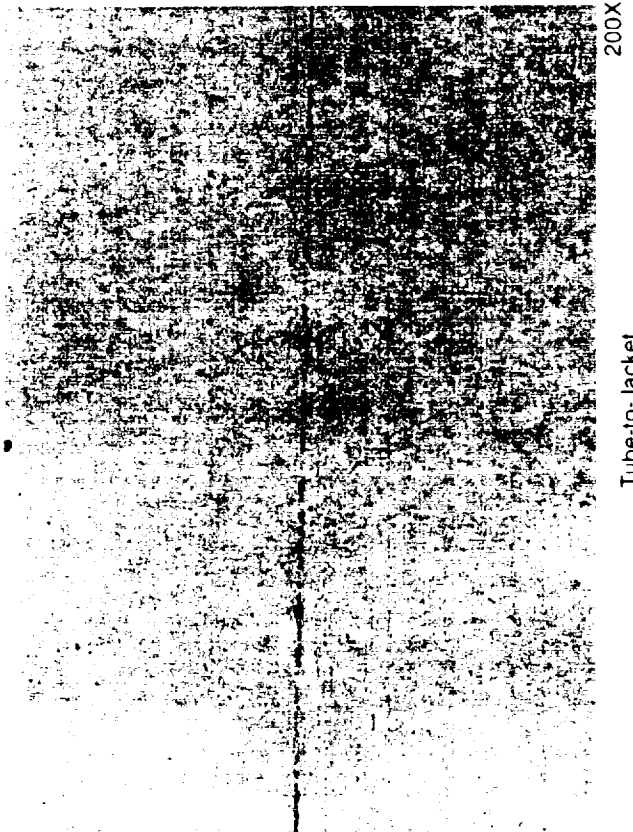
Figure 4.1.1-13. Preformed Square Inconel 625 Tubes Inflated Formed/Diffusion Bonded in a Hot Isostatic Press Furnace at 7000 psi and 2100°F Showing Microcracks on Inside Corner ii Due to Oxide Formation from a Nonvacuum Environment



14597



Tube-to-Tube



Tube-to-Jacket

Figure 4.1.1-14. Preformed Square Inconel 625 Tubes Inflation Formed/Diffusion Bonded in a Hot
Isostatic Press Formed at 7000 psi at 121000 F Showing Tube-to-Tube and Tube-to-Jacket Bond



500X



500X

14598



200X

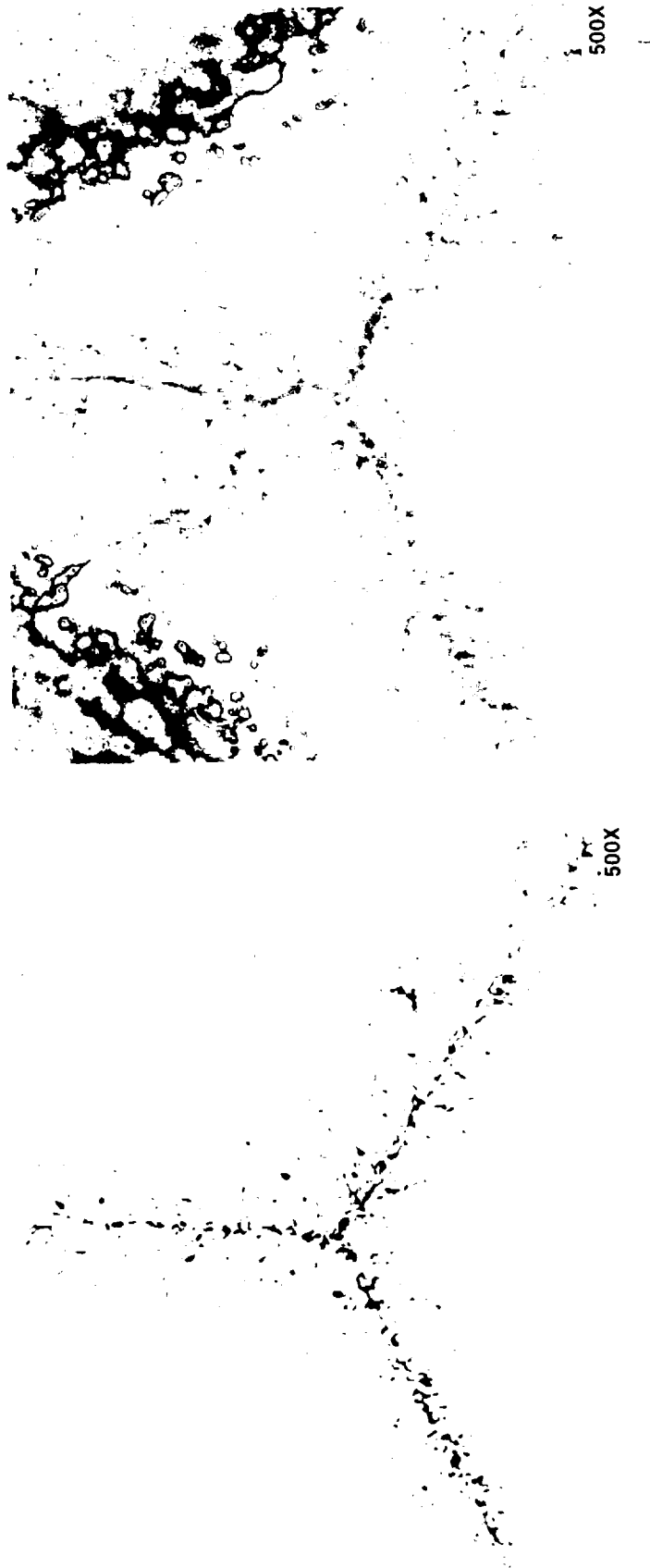
Tube-to-Tube



200X

Tube-to-Jacket

Figure 4.1.1-15. Preformed Square Inconel 625 Tube-to-Tube Inflation Formed Diffusion Bonded in a Hot Isostatic Press Furnace at 7000 psi and 2100°F Showing Gaps Present in Base Metal and at Bond Locations



14600

Figure 4.1.1-16. Inconel 625 Tubes Inflation Formed Diffusion Bonded in a Hot Isostatic Press Furnace at 17,000 PSI and 2100°F Showing Oxides and Oxygen-Stabilized Carbides

500X

500X

500X

500X

Figure 4.1.1-17. Inconel 625 Tubes Inflation Formed/Diffusion Bonded in a Hot Isostatic Press Furnace at 17,000 psi and 2100° F Showing a Network of Concentrated, Continuous Carbides

14801

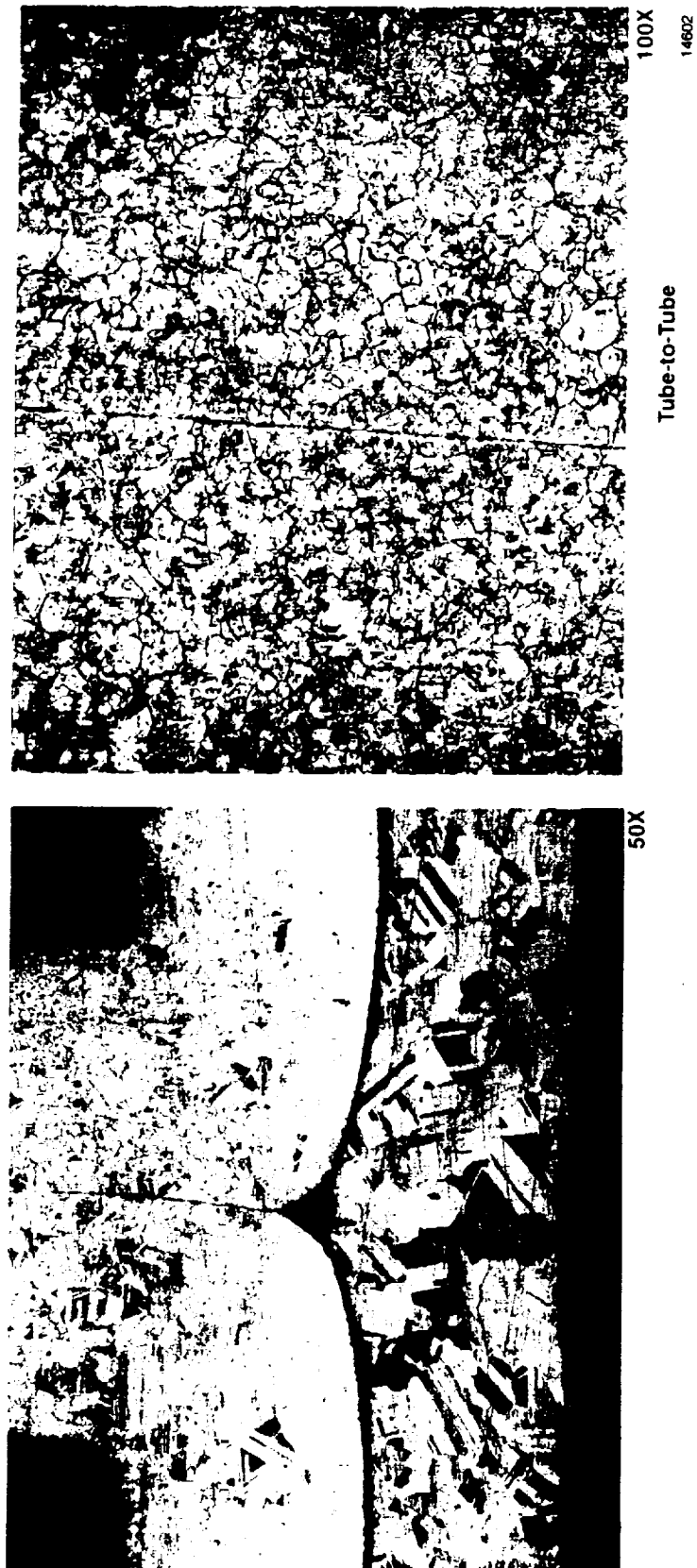


Figure 4.1.1-18. Preformed Square Inconel 625 Tubes Inflation Formed/Diffusion Bonded in a Hot Isostatic Press. Exposed at 7000 psi and 2100°F. Showing Fine Grains at Bond Location and In Tube Parent Material.

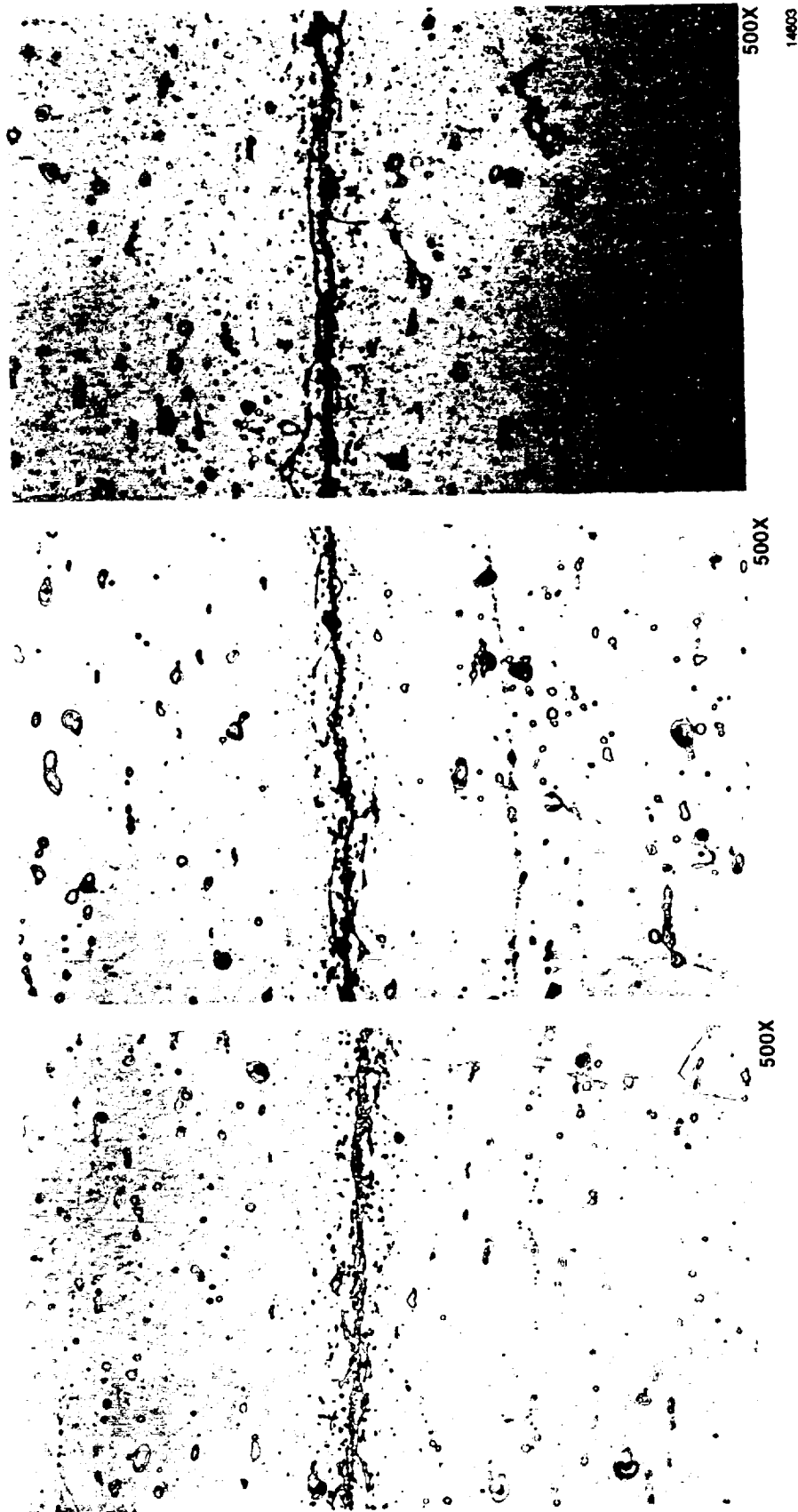


Figure 4.1.1-19. Preformed Square Inconel 625 Tubes γ -irradiation Formed/Diffusion Bonded With a Subsequent Heat Treat at 2150°F for 2 Hours With a Fast Cooldown γ -irradiation Formed/Diffusion Bonded With a Subsequent Heat Treat at 2150°F for 2 Hours With a Fast Cooldown

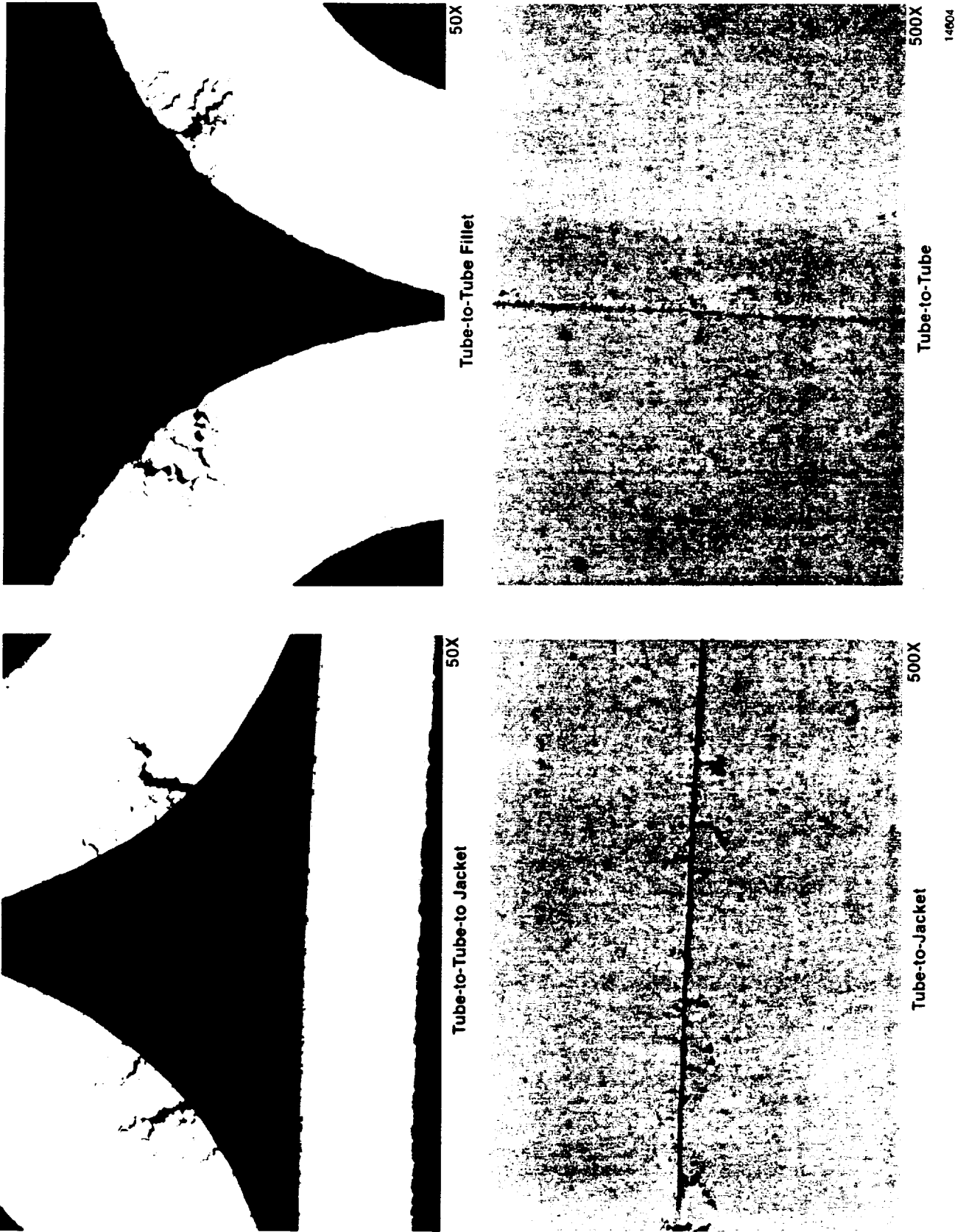


Figure 4.1.1-20. Preformed Square Haynes 230 Tubes Inflation Formed/Diffusion Bonded in a Hot Isostatic Press Furnace at 3000 psi and 2100°F Showing Tube Outer Walls Cracked Due to High Strain in Forming Process



500X



500X

14605



200X

Tube-to-Tube



200X

Tube-to-Jacket

Figure 4.1.1-21. Preformed Square Haynes 30 Tubes Inflation Formed/Diffusion Bonded in a Hot Isostatic Press Furnace at 3000 μ and 2100 $^{\circ}$ F Showing Carbides at Bond Lines

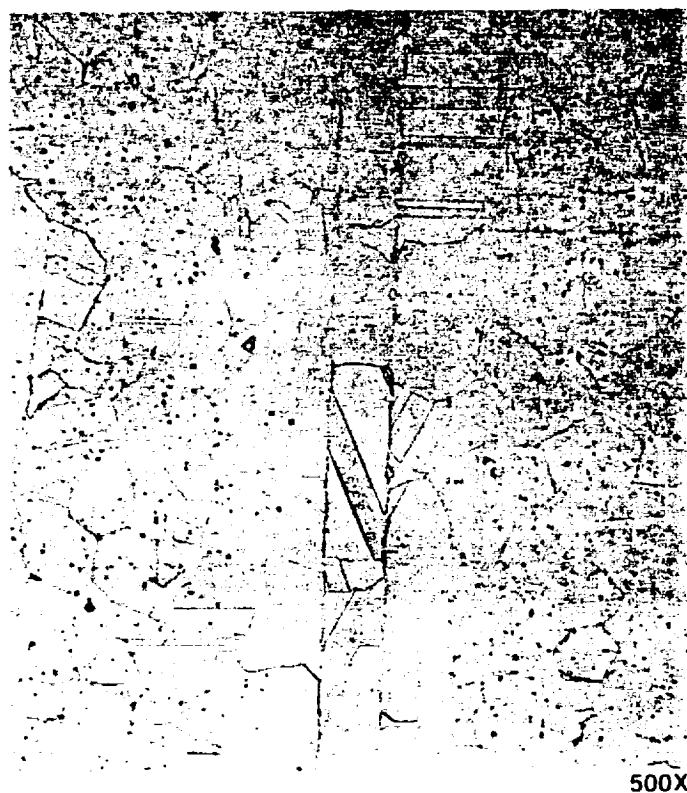
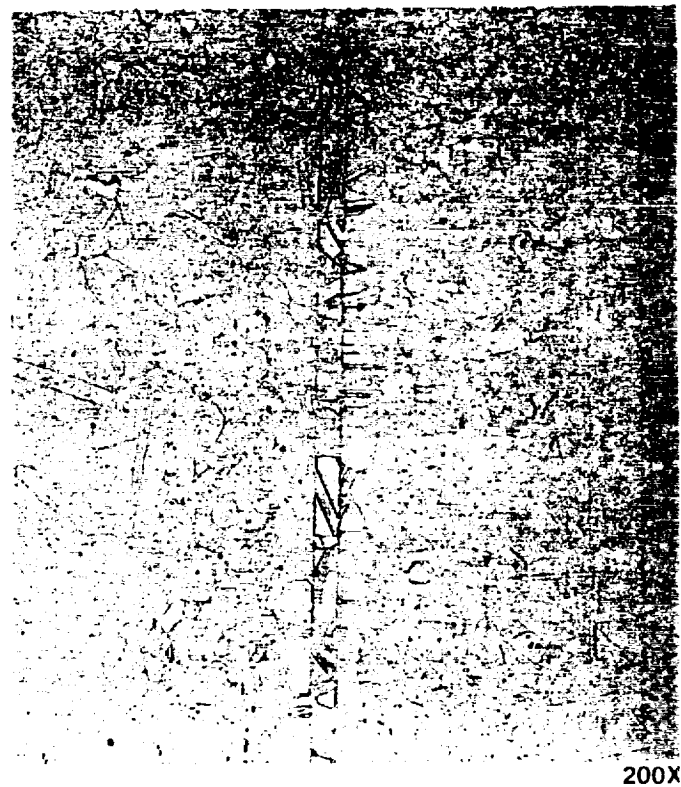
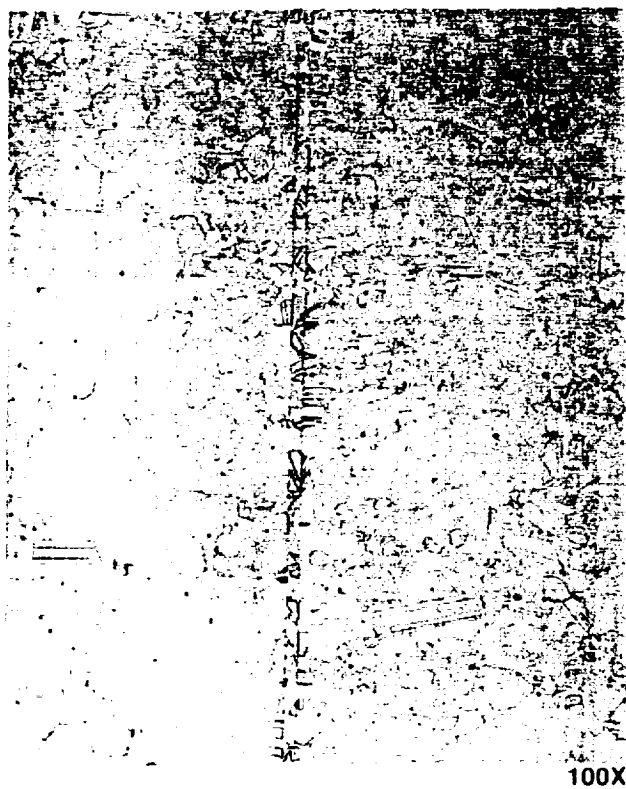
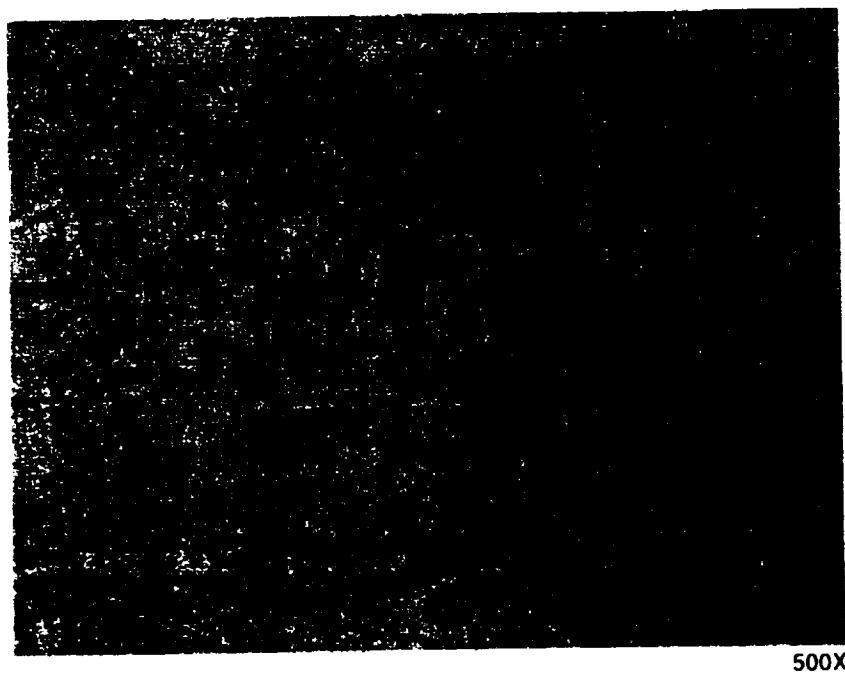


Figure 4.1.1-22. Inconel 625 Tubesheet Metal Nickel Plated and Diffusion Bonded at 5000 psi and 1900°F for 6 Hours



16533

Figure 4.1.1-23. Inconel 625 Tubes Sheetmetal Cleaned With Descaling Solution and Diffusion Bonded at 5000 psi and 1900° F for 6 Hours

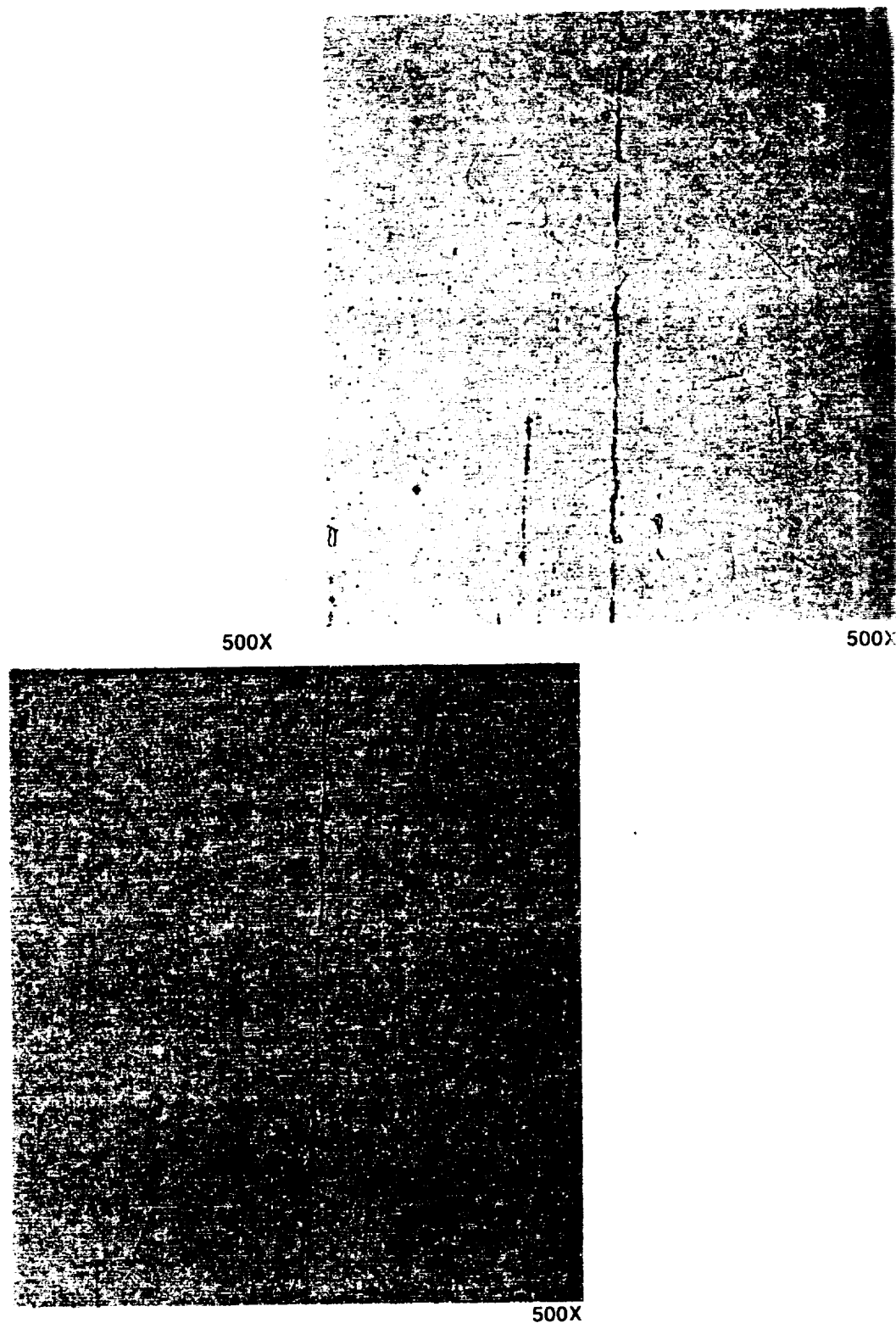


Figure 4.1.1-24. Inconel 625 Tubesheetmetal Cleaned With Chemical Milling Solution and Diffusion Bonded at 5000 psi and 1900°F for 6 Hours

16534

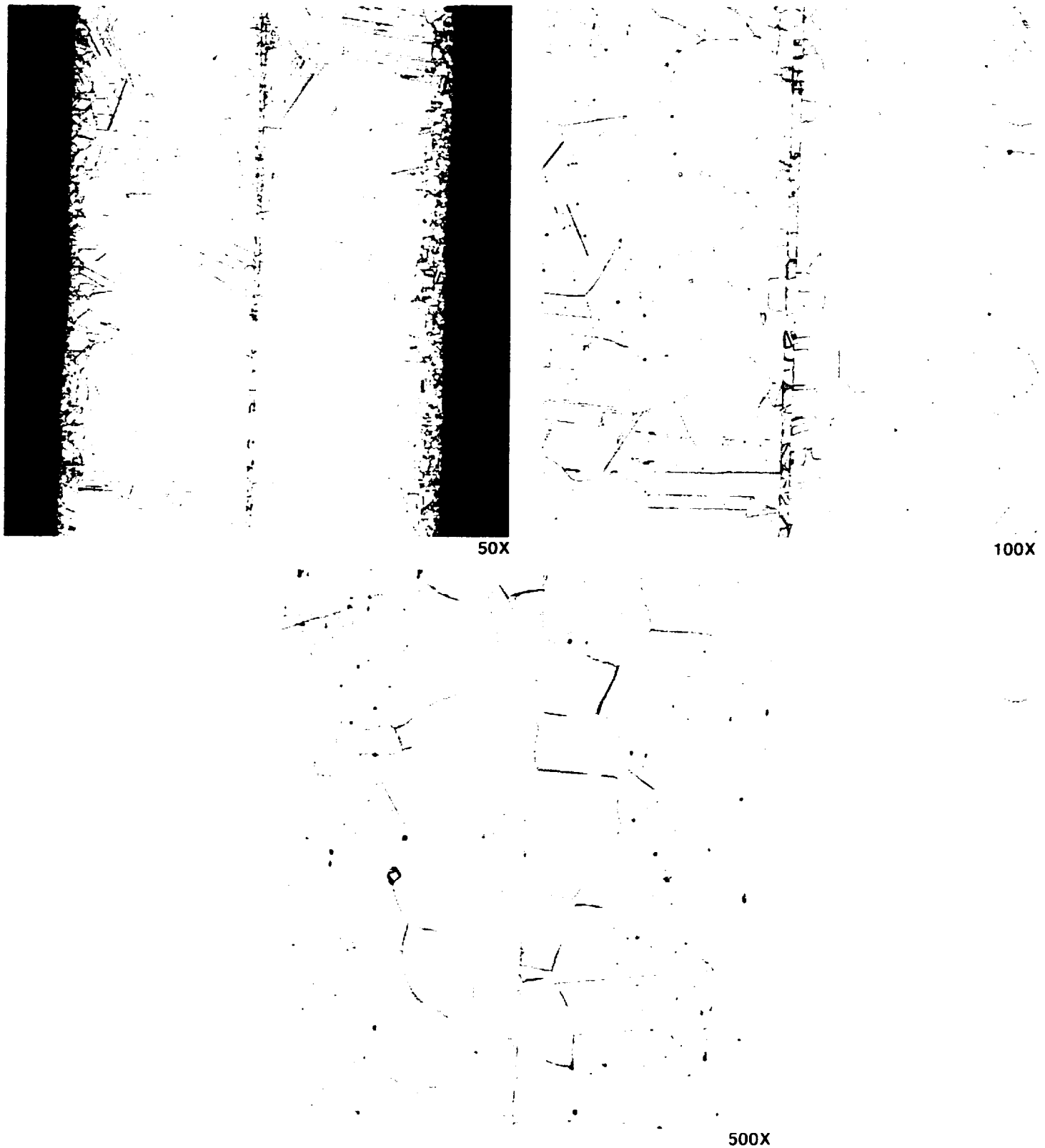


Figure 4.1.1-25. Inconel 625 Tubesheetmetal Diffusion Bonded at 5000 psi and 1900°F for 6 Hours, Then Heated at 2150°F To Simulate the Secondary Braze Cycle

16535

4.1.1.2 Thermal Sprayed Tubes

This effort focused on reduction of the oxide content in the sprayed coatings, and has been limited to testing with INCO 625 tube material. Samples that were sprayed with hydrogen-rich parameters and using argon both as the cooling and carrier gas showed no appreciable decrease in the oxide content of the coatings. Reduced oxygen content powders were procured for further testing. In an attempt to determine the origin of the oxygen in the coating (incoming powder or oxygen in the air), a sample was sprayed in an inert chamber constructed of aluminum and filled with argon. This allowed an oxygen content of 200 ppm to be maintained within the chamber atmosphere and resulted in reduced oxygen content of the sprayed coating; however, the porosity of the coating increased significantly due to the higher density of the argon atmosphere. From these samples, it is evident that the majority of the oxygen is being entrained in the spray from the ambient atmosphere during the process. Figures 4.1.1-26 and 4.1.1-27 are photomicrographs of air sprayed HVOF versus inert chamber sprayed HVOF, respectively. Additional samples were sprayed in the inert chamber in an attempt to improve the density of the coatings. Other oxide reducing experiments were conducted as the lower oxide content powders arrive, but due to the apparent oxygen entrainment, these are not expected to significantly reduce the oxide content of the coatings.

Inert arc-wire spray was also evaluated as an alternative spray process. Several samples have been sprayed with an arc-wire gun in the inert chamber. Results thus far have again shown a significant amount of oxide reduction compared to those sprayed with the same gun in air. Figures 4.1.1-28 and 4.1.1-29 provide a comparison of air sprayed arc-wire versus inert chamber arc-wire. Porosity increased with this set of samples also, and additional arc-wire experiments will be conducted in an attempt to reduce the porosity.

Initial evaluation of the inert HVOF spray compared to the inert plasma spray revealed that when using identical powders, a much lower oxide level is achievable with the inert plasma process than with the inert HVOF process. This is attributed to one of two phenomena. One theory is that the oxygen in the HVOF combustion process is not entirely being consumed by the hydrogen and is migrating into the coating. The second theory is that the inert plasma process is reducing the oxide on the powder (due to spraying with argon and hydrogen), resulting in a low oxide coating. The inert HVOF sample is shown in Figure 4.1.1-30, and the inert plasma spray sample is shown in Figure 4.1.1-31. Further testing was done in this area using samples with thick spray, so that the bulk oxygen measurements can be taken and compared with the level of oxygen in the initial powder. Further metallurgical studies will also be conducted to measure the extent of grain growth and ductility that can be achieved with different heat treatments.

Test pieces have been fabricated for follow-on work using vacuum plasma spray over Inconel 625 tubes. The initial work was completed under an IR&D program in 1990, and the results are shown in Table 4.1.1-4. The mechanical properties shown indicate that the higher heat treatments significantly improve elongation and reduction of area properties when compared to the lower temperature heat treatments. However, the effects of both the 2150°F heat treatment and the high pressure need to be investigated further.

Table 4.1.1-4. Average Room Temperature Tensile Properties for Vacuum Plasma Sprayed Inconel 625 Tubes

<i>Condition</i>	<i>PL (ksi)⁽¹⁾</i>	<i>YS (ksi)</i>	<i>UTS (ksi)</i>	<i>Elongation (%)</i>	<i>Ra (%)</i>
As Sprayed	131	163	169	1.9	4.2
Heat Treat 900°F/4 hrs	132	166	170	1.7	4.7
Heat Treat 1200°F/24 hrs	136	175	175	0.8	1.1
Heat Treat 1800°F/1 hr	120	147	166	7.0	11.0
HIP'ed 2150°F/15 ksi/1 hr	67	77	142	20.2	19.8

(1) Proportional Limit

Based on these results, remaining testing will focus on three areas: (1) ductility enhancement without hot isostatic pressing (HIP'ing), (2) filling the interstices between the tubes, and (3) bond strength improvements without grit blasting the tubes.

Results of the inert wire sprayed specimens during this reporting period indicate the effects of varying heat treatments to improve ductility and modifying spray parameters to improve density of the sprayed material. Table 4.1.1-5 shows that with the standard spray parameters and standard heat treatments, the elongation properties are unacceptably low. Based on these results, additional samples were sprayed with modified spray parameters and underwent the standard heat treatment of 2000°F for one hour in a vacuum. The metallographic evaluations in Figures 4.1.1-32 and 4.1.1-33 show a slight improvement in density with the modified spray parameters. Metallographic results to determine effects on ductility are pending.

*Table 4.1.1-5. Tensile Properties of Inert Wire Sprayed
Inconel 625 Heat Treated at 2000°F for One Hour in Vacuum*

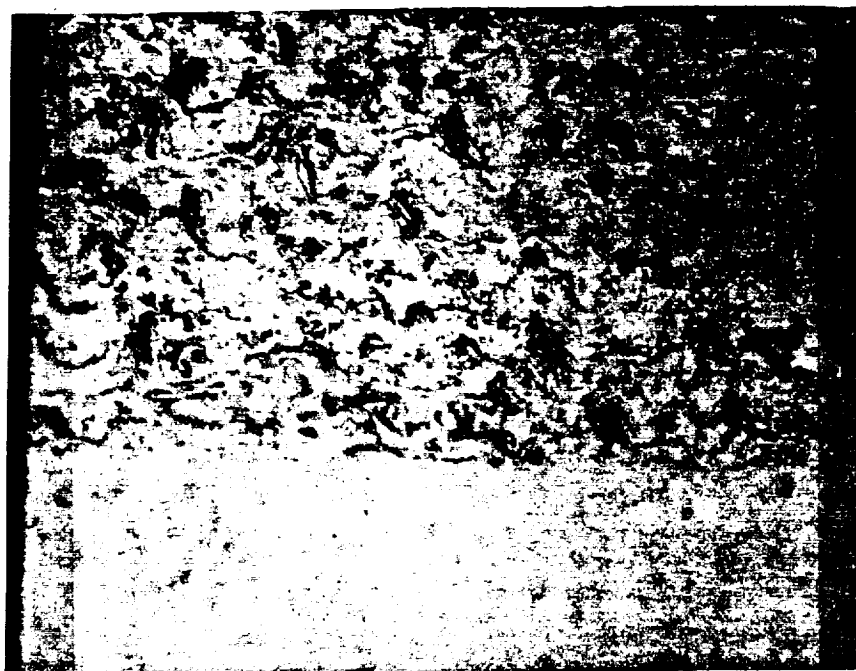
<i>Specimen No.</i>	<i>Temperature (°F)</i>	<i>0.2% Offset YS (psi)</i>	<i>Tensile Strength h (psi)</i>	<i>Elongation (%)</i>	<i>Ra (%)</i>
1	Ambient	31,100	31,100	0.6	—
2	Ambient	41,800	41,800	0.7	—
3	Ambient	39,500	39,500	0.4	—

Note: Percent elongation taken from the graph.

As reported previously, the vacuum plasma spray material has exhibited unacceptably low ductility when sprayed without high-temperature heat treatments. The only heat treatments found to be effective are at temperatures greater than 1800°F and with the use of a HIP furnace. However, the elevated temperatures required to improve ductility in the plasma sprayed material reduce yield strength of both the plasma sprayed material and the tubes.

Results of the inert wire sprayed specimens during the previous reporting period indicated the effects of varying heat treatments to improve ductility, and of modifying spray parameters to improve density of the sprayed material. Using the standard spray parameters and standard heat treatments, the elongation properties were unacceptably low. Based upon the previous results, additional samples were sprayed with modified spray parameters and underwent the standard heat treatment of 2000°F for one hour in a vacuum. The metallographic evaluation showed a slight improvement in density, however, ductility testing showed no improvement.

Preliminary sizing of the sheetmetal jacket for the full-scale nozzle indicates that sections are as thin as 0.060 inch to approximately 0.150 inch. The thermal sprayed concepts are not as attractive to the thin sections because of the difficulty in bonding, and in reduced material properties when compared to sheetmetal. In addition, the high porosity and low ductility of the thermally sprayed materials require significant heat treatments and processing to improve properties to an acceptable level. Based upon these results and the full-scale nozzle manufacturing planning studies, further investigations of thermal sprayed tube concepts will primarily support the final investigations for the low oxide powders and the thermal spraying of braze material in support of the braze tube fabrication trials.

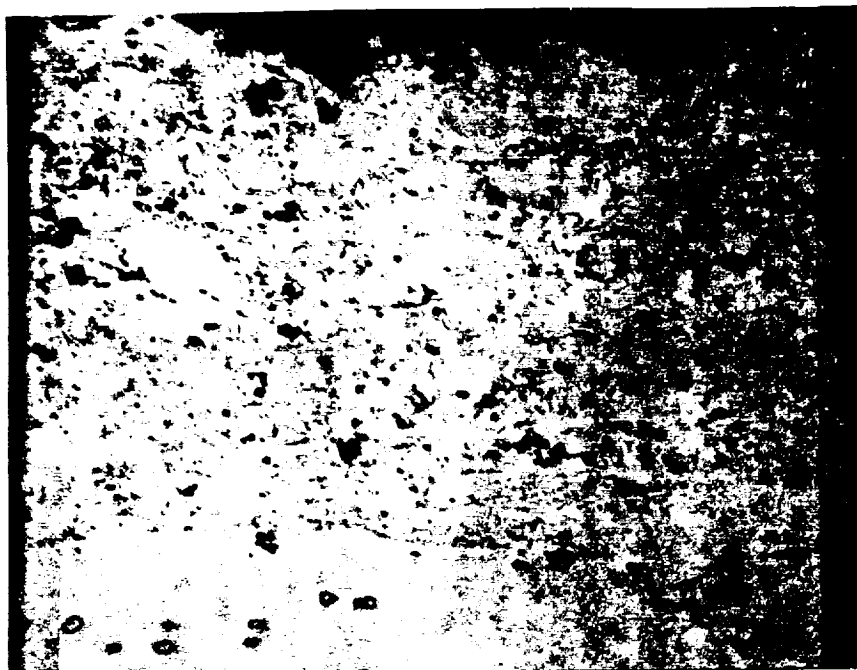


HVOF-5

Mag: 400X

7247

Figure 4.1.1-26. Air-Sprayed HVOF

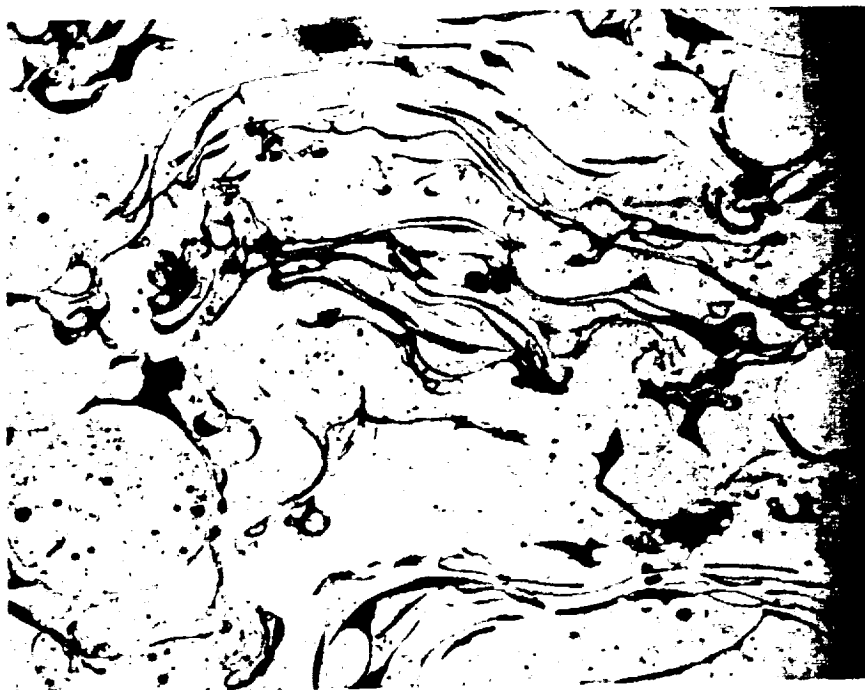


HVOF-9

Mag: 400X

7252

Figure 4.1.1-27. Inert Chamber HVOF Spray



Mag: 400X

7255

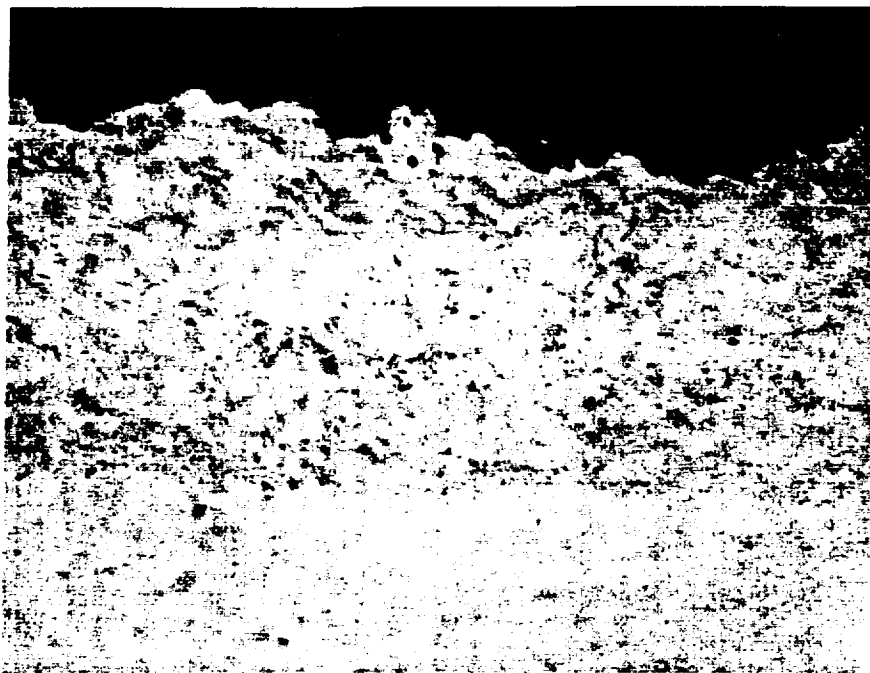
Figure 4.1.1-28. Air-Sprayed Arc-Wire



Mag: 100X

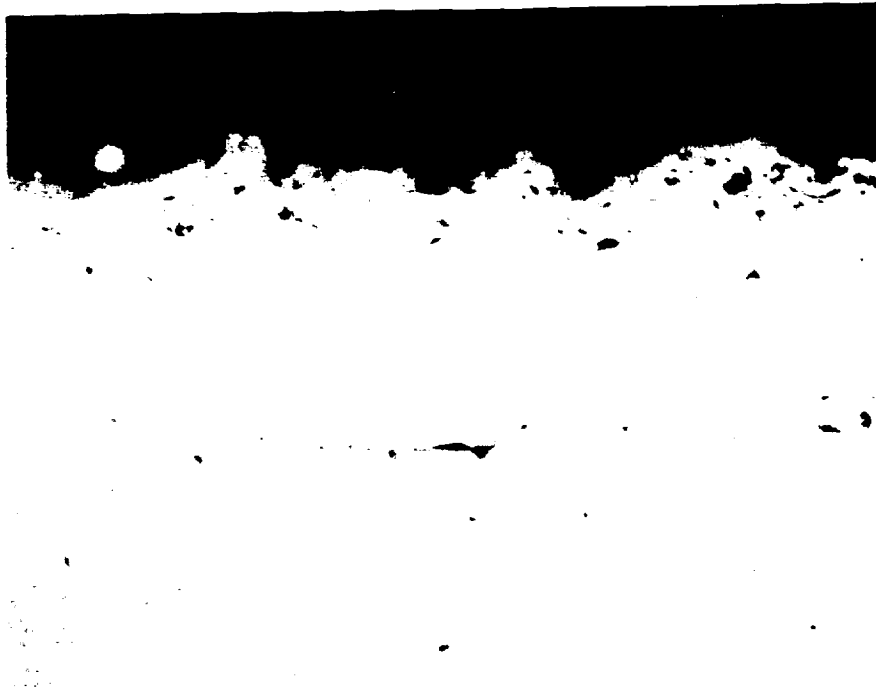
7256

Figure 4.1.1-29. Inert Chamber Arc-Wire



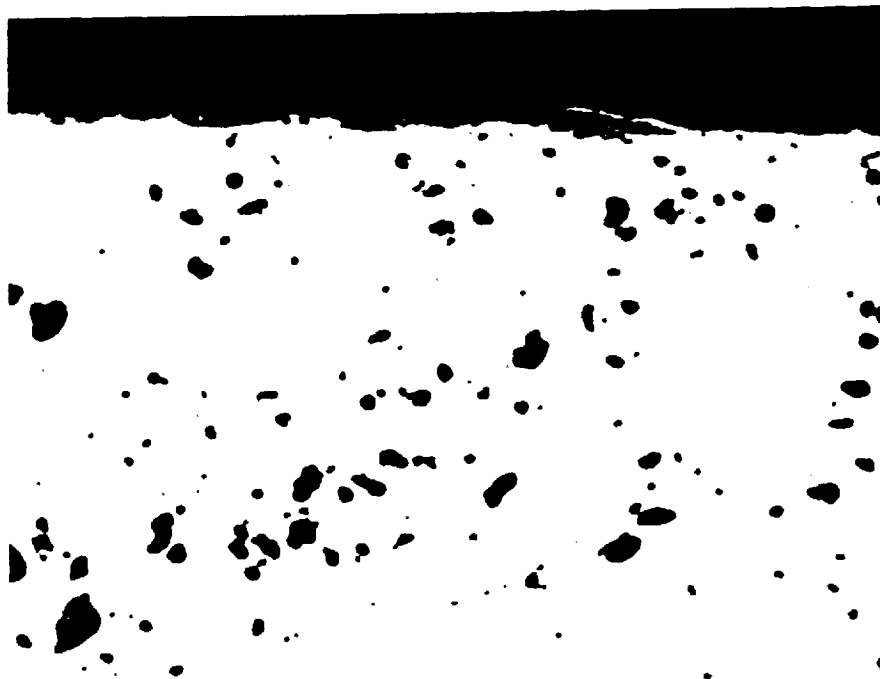
FC119235

Figure 4.1.1-30. Inert HVOF Spray Heat Treated at 2000° F for 1 Hour (400×)



FC119238

Figure 4.1.1-31. Inert Plasma Sprayed Inconel 625 (400×)



FC119236

Figure 4.1.1-32. Inert Wire Heat Treated at 2000° F for 1 Hour in Vacuum (50×)



FC119237

Figure 4.1.1-33. Inert Wire Heat Treated at 2000°F for 1 Hour in Vacuum (50×)

4.1.1.3 Brazed Tubular Assembly

The Segment 1 braze alloy screening trials were completed. Nine braze alloys were evaluated in this segment (Table 4.1.1-6). All of the samples have been brazed and evaluations are complete. Evaluations performed on the braze samples include: visual inspection, microstructural evaluation, micro-hardness testing, and microprobe mass spectrometry. Figures 4.1.1-34, 4.1.1-35, and 4.1.1-36 are examples of the variety of microstructures observed in these screening trials. The results are currently being reviewed by an expert panel consisting of representatives from Materials Engineering, Design Metallurgy, and Manufacturing Engineering, with expertise in the field of brazing. A downselect decision to three candidate braze alloys will be made by the team after the results are evaluated. The three candidate braze alloys will then be further evaluated in the Segment 2 parametric study.

Table 4.1.1-6. List of Braze Alloys Being Evaluated in Segment 1

<i>Trade Name</i>	<i>Specification</i>	<i>Composition</i>	<i>Solidus (°F)</i>	<i>Liquidus (°F)</i>
Nicrobraz 10	AWS BNi-6	Ni, P-11%	1610	1610
Nicrobraz 30	AMS 4782	Ni, Cr-19%, Si-11%	1975	2075
Nicrobraz 50	AWS BNi-7	Ni, Cr-14%, P-10%	1630	1630
Nicrobraz 3002	N/A	Ni, Cr-15%, Si-8%	N/A	N/A
Nicrobraz 5025	N/A	Cu, Ni-38%, Cr-7%, P-5%	N/A	N/A
Nicrobraz 150	N/A	Ni, Cr-15%, B-3.5%	1930	1930
Nicrobraz 210	AMS 4783	Co, Cr-19%, Ni-17%, Si-8%, W-4%, B-0.8%	2025	2100
Amdry 930	AWS BNi-8	Ni, Mn-2%, Si-7%, Cu-5%	1820	1870
Amdry 300	N/A	Ni, Cr-19%, Mn-9.5%, Si-9.5%	1950	2000

A design of experiments for the Segment 2 study was outlined. The DOX was structured to optimize the ductility of the base material/braze alloy combinations based on the controllable parameters listed in Table 4.1.1-7. Testing methods are currently being defined. As a baseline comparison, Gold-Nickel (AMS 4787, braze specimens will also be produced since this best simulates the SSME brazed tubular nozzle for comparative purposes to the current state of the art. Fabrication of test specimens for this segment have begun.

Table 4.1.1-7. Parameters to be Investigated in Segment 2

<i>Parameter</i>	<i>Values</i>
Braze Alloy	Three Candidates
Base Material	Haynes 230, 188 and Inconel 625
Braze Temperature	High, Medium and Low
Time at Braze Temperature	1.5, 1.0 and 0.5 Hours
Diffusion Time	0, 1.5 and 3.0 Hours
Diffusion Temperature	High, Medium and Low

The Segment 1 trials evaluated nine braze alloys to downselect three for Phase 2 testing. Each of the braze specimens was subjected to a series of tests to evaluate the quality of the braze joint formed. Examinations were performed to determine the flow and melting characteristics of the braze alloy, to look for defects, and to determine alloying depth and diffusion into the tube material. Micro-hardness readings were taken to characterize the relative strength and ductility of the brazements, as well as the effect of the braze alloy and corresponding thermal cycling of the tube material. Finally, where additional information on diffusion bonding phenomena was desired, microprobe mass spectrometry was used to determine the composition of various phases and regions found in several of the brazements.

Based upon Segment 1 braze alloy trials, several of the alloys were eliminated due to unsatisfactory material properties. Nicrobraz 10 and 50 were eliminated due to their relatively low melting points. Nicrobraz 210, 5025, and AM 930 were eliminated due to their poor melting and flow properties. Based upon the characteristics judged most important for the braze alloys (relative ductility or micro-hardness, and diffusion effects), and past experience, the following three braze candidates were selected for further study. AM 300 demonstrated the lowest hardness with readings ranging from HRC 35-49 in the braze joint. Nicrobraz 30 was selected based on successful history of applications in gas turbine engines. Nicrobraz 150, containing boron, showed promising hardness results. However, a review of research performed by Pratt & Whitney's Materials Laboratory suggests that the alloy AMS 4779 should produce significantly better results than the Nicrobraz 150.

The Segment 2 braze alloy screening trials are summarized in Tables 4.1.1-8, 4.1.1-9, and 4.1.1-10. The parameters to be investigated in Segment 2 include the three candidate braze alloys, the three base material candidates (Inconel 625, Haynes 188, and Haynes 230), the braze temperature, and the braze time. The braze cycle retort procedure shown in the tables is similar for all three candidate braze alloys, with only slight differences in hold time and braze temperature.

Table 4.1.1-8. AMS 4782 Braze Trials

Run Number	Sample No. *	(A)-Braze Temperature (° F $\pm 10^\circ$ F)	(B)-Hold Time (hrs + :15/- :00)
1	1	2200	1:00
4	2	2200	2:00
3	3	2200	4:00
6	4	2150	1:00
2	5	2150	2:00
5	6	2150	4:00

* Due to our experience with this alloy on gas turbine hardware, the amount of experimentation that is required is limited.

Table 4.1.1-9. Amdry 300 Braze Trials

Run Number	Sample No.	(A)-Braze Temperature (° F $\pm 10^\circ$ F)	(B)-Hold Time (hrs + :15/- :00)
2	1	2050	1:00
8	2	2050	2:00
6	3	2050	4:00
7	4	2100	1:00
3	5	2100	2:00
5	6	2100	4:00
9	7	2150	1:00
4	8	2150	2:00
1	9	2150	4:00

Table 4.1.1-10. AMS 4779 Braze Trials

Run Number	Sample No. *	(A)-Braze Temperature (° F $\pm 10^\circ$ F)	(B)-Hold Time (hrs + :15/- :00)
6	1	2000	1:00
3	2	2000	2:00
2	3	2000	4:00
1	4	2075	1:00
4	5	2075	2:00
5	6	2075	4:00

* Due to our experience with this alloy on gas turbine hardware, the amount of experimentation that is required is limited.

The Segment 2 braze alloy testing was completed for AMS 4782. This testing consisted of varying braze temperature and hold times to determine the most cost-effective solution. All of the samples have been completed and underwent a bend test to verify braze and bond strength properties. The bend test parameters were finalized to ensure repeatable test procedures for each sample.

The full-scale nozzle manufacturing planning and preliminary design studies selected a two-step braze process as the baseline configuration. The first step uses a high-temperature braze to join the tubes to the sheetmetal jacket. The second step joins the skirt to the stiffening bands and to the manifold attachment. This two-step braze process requires that the second braze process be at a significantly lower temperature than the first so as not to remelt or affect the bonding achieved by the first braze. The only candidates for the two-step braze process are AMS 4782, which has a braze temperature of about 2200°F, and AMS 4787 (gold-nickel) for the second braze, which has a braze temperature of about 1850°F. The other candidates, Armdry 300 and AMS 4779 have braze temperatures of 2050 and 2000°F respectively. Either of these materials would remelt or undergo recrystallization during the second braze cycle. Based upon these studies, the remaining braze fabrication trials will focus only on the AMS 4782 and AMS 4787 braze processes.

Other manufacturing planning studies conducted for the brazed nozzle configuration have shown that the existing P&W gas box furnace equipment is too small for the 580K or larger nozzle. Pratt & Whitney currently owns a large vacuum furnace that is suitable for a full-length 580K nozzle, or truncated nozzle up to 800K thrust. Therefore, since a vacuum furnace would most likely be used in the full-scale nozzle development program, all of the braze materials are being run in a vacuum furnace. The results to date show that there is no discernible effect between the hydrogen environment of a gas box furnace and the vacuum furnace.

Three samples using the plasma sprayed braze alloy process have been successfully brazed with AMS 4782 braze alloy. One of these samples is shown in Figures 4.1.1-37 and 4.1.1-38. Small segments of sheetmetal were inserted between the tubes to create a gap to verify bonding with a specified gap size. The sheetmetal thicknesses were 0.005, 0.010, and 0.020 inch. The resulting 0.005 and 0.010-inch gap sizes were easily filled by the braze alloy, but the 0.020-inch gap was too large. This sample was sprayed with 0.009-inch thick AMS 4782 powder, which required nine spray passes. The use of the plasma sprayed braze alloys offers the potential for a significant reduction in the labor time typically required for braze material application.

Other full-scale nozzle manufacturing issues addressed in future braze trials include: 1) inflating the tubes to a low internal pressure to ensure proper braze fit is maintained, 2) investigate masking techniques to prevent tube-to-tube bonding and allow only tube-to-jacket bonding, and 3) further testing and evaluation of plasma sprayed braze alloys to reduce labor time required for braze application.

The Segment 2 braze alloy testing was completed for AMS 4782. This testing consisted of varying braze temperature and hold times to determine the most cost-effective solution. All of the samples have been completed and will now undergo a bend test to verify braze and bond strength properties. The bend test parameters have been finalized to ensure repeatable test procedures for each sample, and are now underway.

The full-scale nozzle manufacturing planning and preliminary design studies selected a two-step braze process as the baseline configuration. The first step uses a high-temperature braze to join the tubes to the sheetmetal jacket. The second step joins the skirt to the stiffening bands and to the manifold attachment. This two-step braze process requires that the second braze process must be at a significantly lower temperature than the first so as not to remelt or affect the bonding achieved by the first braze. Figure 4.1.1-39 illustrates the brazing temperature versus melting temperature ranges for the three primary braze candidates and the two secondary braze candidates. As shown in the graph, AMS 4779 is no longer being considered as a primary braze alloy candidate because the solidus is only 1800°F, which is well below the secondary braze temperature for AMS 4787 of 1800 to 1850°F. This remelting of the primary braze alloy has been verified in the fabrication trials.

Additional studies have occurred to determine the effect of the interaction between the primary and secondary braze alloys. The presence of silicon in AMS 4782 (Ni-19Cr-10Si) causes the gold in the secondary braze (82Au-18Ni) to form a low melting point alloy. Figure 4.1.1-40 is a plot of the gold silicon melting temperature (liquidus phase shown above the curved line). The melting point of gold drops dramatically as silicon is added, until a minimum melting point of 685°F (363°C) at the eutectic composition of 97.2-percent Au—2.8-percent Si. The metallographic evaluations of this interaction are shown in Figure 4.1.1-41, with the low melting point alloy shown as the dark region between the tube-to-tube fillet braze. This sample was tested at 1500°F for 150 minutes to determine the degree to which the operating environment of the nozzle will affect the braze alloy. Additional samples of the step braze process are shown in Figures 4.1.1-42 and 4.1.1-43 for AMS 4779 and AMDRY 300 respectively, with an AMS 4787 subsequent braze process.

The sample designed for the step braze techniques is shown in Figure 4.1.1-44, and uses preformed square tubes placed side by side with 0.025-inch thick shims between every other tube. The shims will intentionally create gaps in the tube mating surfaces to determine the ability of the braze to adhere to both surfaces when a large gap is present. The excellent gap coverage shown so far has only been demonstrated on round tubes, where capillary action or gravity might have more of an impact on drawing braze into the gap than on square tubes.

Other manufacturing planning studies conducted for the brazed nozzle configuration have shown that the existing P&W gas box furnace equipment is too small for the 580,000-pound thrust size or large nozzle. Pratt & Whitney currently owns a large vacuum furnace that is suitable for a full-length 580,000-pound thrust nozzle, or truncated nozzle up to 800,000 pounds thrust. However, the hydrogen gas environment used in the gas box furnace assists the braze because of the reducing properties of hydrogen. In addition, a new gas box furnace large enough to hold the nozzle for the 650,000-pound thrust size STME would be significantly less expensive than a vacuum furnace of the same size. Since there appears to be advantages for brazing in both types of furnaces, several braze samples were run in both environments to see if any significant differences exist. Figure 4.1.1-45 is a specimen that used round Inconel 625 tubes with the AMS 4782 braze alloy in a hydrogen environment. Figure 4.1.1-46 shows another sample that used square Inconel 625 tubes and the same braze alloy, but was processed in a vacuum furnace. Both samples show no porosity, excellent braze coverage, good adhesion to both tube and sheetmetal base materials, and even indicate a small diffusion region (where the braze diffused into the base material), which improves bond properties. The gap size is approximately 0.025 inch at the cross-section at which the photo was taken. Microhardness readings were taken on the braze and the base metal for both samples, and no significant differences were found. There are no significant differences between the samples for the AMS 4782 braze material.

Figure 4.1.1-47 is a photograph of a round tube braze sample that used AMDRY 300 braze material in a vacuum environment. Shims were placed between the tubes to determine the capability of the braze to cover gaps in mating surfaces. Figures 4.1.1-48 and 4.1.1-49 show the metallographic analysis for the AMDRY 300 braze material on Inconel 625 tubes in a hydrogen and vacuum environment, respectively. As with the AMS 4782 braze samples, there is no discernible difference between the samples, and excellent braze coverage and bond results were achieved.

As discussed in the last bimonthly, the plasma spray method of applying braze material offers a significant reduction in labor costs typically found in brazed tube nozzle assemblies. The fabrication trials sample design, shown in Figure 4.1.1-50, illustrates how the tube assembly is placed on top of the sheetmetal plate that has been previously plasma sprayed with braze alloy. A low pressure is applied to the inside surface of the tubes to physically mate the tube assembly to the plate, and the sample is placed inside the furnace. Figure 4.1.1-51 shows a cross-section of one of the Haynes 230 tube samples that was brazed at 2175°F in a vacuum after being plasma sprayed with AMS 4782. The braze coverage is excellent, and the photographs show the braze partially diffusing into both the sheetmetal and the tubes, which provides good bond joints. Microhardness readings indicated a slight reduction in hardness compared to the AMS 4782 conventionally applied braze, which

implies better braze material ductility. Figure 4.1.1-52 shows a brazed tube sample in which the sheetmetal jacket was plasma sprayed with AMS 4782.

Bend testing was done to determine which of the three candidate braze alloys (AMS 4782, AMS4779, or AMDRY 300) is the most ductile. A total of 82 specimens were fabricated and tested in the device shown in Figure 4.1.1-53. The bend tester uses flat Inconel 625 plates .050 and .078 in. thick, which contains a 0.008-0.012 in. groove filled with the braze alloy. The plate is pushed into the u-groove in preset increments and inspected before and after each increment for cracks in the braze alloy. Figures 4.1.1-54 and 4.1.1-55 show samples undergoing testing.

Thirty-five of the specimens were tested in compression, another 35 in tension, and the remaining 12, which serve as control specimens, have been brazed with AMS 4787 (gold nickel secondary braze material) and tested in both compression and tension. The same sample design is used for both types of tests, with the braze-filled groove on top of the sample for the compression test and the braze-filled groove on the bottom of the sample for the tension test.

The tension tests were conducted in 0.100 in. increments, after which the samples are fluorescent penetrant inspected, failures are recorded, and the samples are cleaned for further testing. Compression tests are conducted in 1.000, 0.100, and 0.250 in. increments and processed in the same manner as the tension tests.

The specimens were fluorescent penetrant inspected after each increment of bending and were either accepted or rejected for porosity or cracking. Results indicate a ductility advantage of AMS 4779 over both AMS 4782 and AMDRY 300, based upon tension tests alone. However, compression tests showed similar results between all three primary braze alloys.

Bend testing results were evaluated to obtain a comparison of braze alloy ductility between the three primary braze alloy candidates: AMS 4782, AMS 4779, and AMDRY 300. The braze bend tests were modeled after "Standard Method for Guided Bend Test for Ductility of Welds," ASTM E190-80. The specimens were bent in both compression and tension and then fluorescent penetrant inspected for porosity or cracking. Additional tension testing was conducted to gather more data since it was believed that some specimens may have failed as a result of porosity rather than cracking. Since porosity is a function of the application method plus the inherent braze alloy properties, it is a complicating factor that may have skewed the results.

Each of the 72 specimens were reinspected under a high powered microscope and none of the specimens showed any signs of porosity. The braze alloys have been cracked in both tension and compression and the results have been summarized in Table 4.1.1-11.

Table 4.1.1-11. Braze Alloys Tension/Compression Cracking

<i>Braze Alloy</i>	<i>% Elongation (Tension)</i>	<i>Standard Deviation</i>
AMS 4779	5.58	3.12
AMS 4782	1.15	0.05
AMDRY 300	0.98	0.17

<i>Braze Alloy</i>	<i>%Elongation (Compression)</i>	<i>Standard Deviation</i>
AMS 4779	13.18	0.08
AMS 4782	14.45	0.04
AMDRY 300	13.91	0.79

The elongation measurements listed in Table 6-1 are valid for comparison between braze alloys. They are not representative of actual alloy elongation properties due to differences between the standard elongation tests and the above comparison tests.

These results showed that AMS4779 possesses a higher percent elongation in tension than does AMS 4782 or AMDRY 300. However, the difference in the standard deviations of AMS 4779 and AMS 4782 is significant and indicates that the two alloys must not be significantly different. In addition, the test results show that the AMS 4782 possesses a higher elongation in compression than the other two alloys. Based upon these results, either AMS 4779 or AMS 4782 would be an appropriate braze alloy selection for ductility requirements. These findings are also consistent with the bend testing and qualitative evaluations that were previously completed in Phase I. Pratt & Whitney will proceed with the plans to use AMS 4782 as the primary braze alloy candidate for all Phase II and full scale nozzle development work.

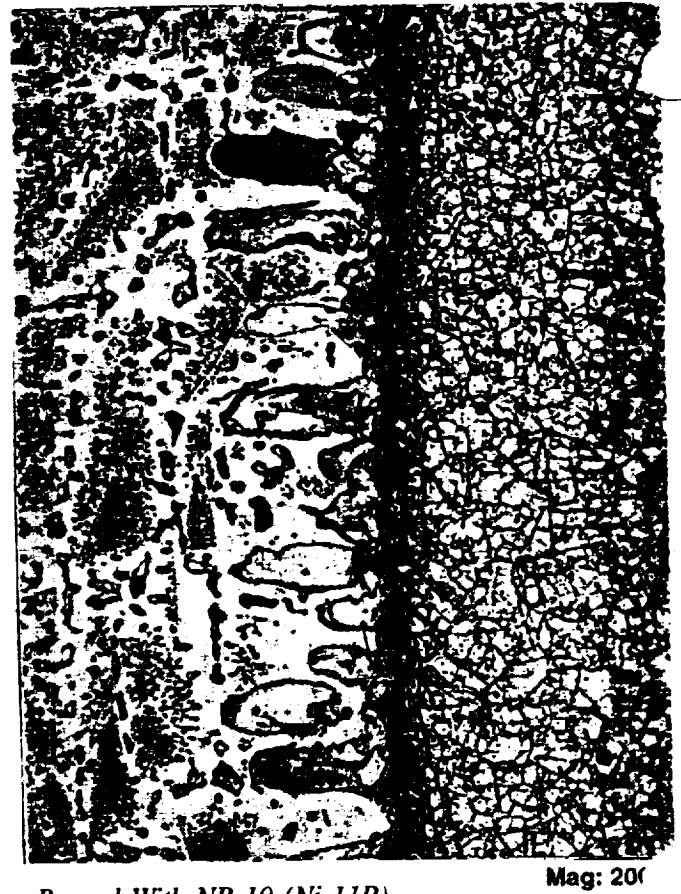
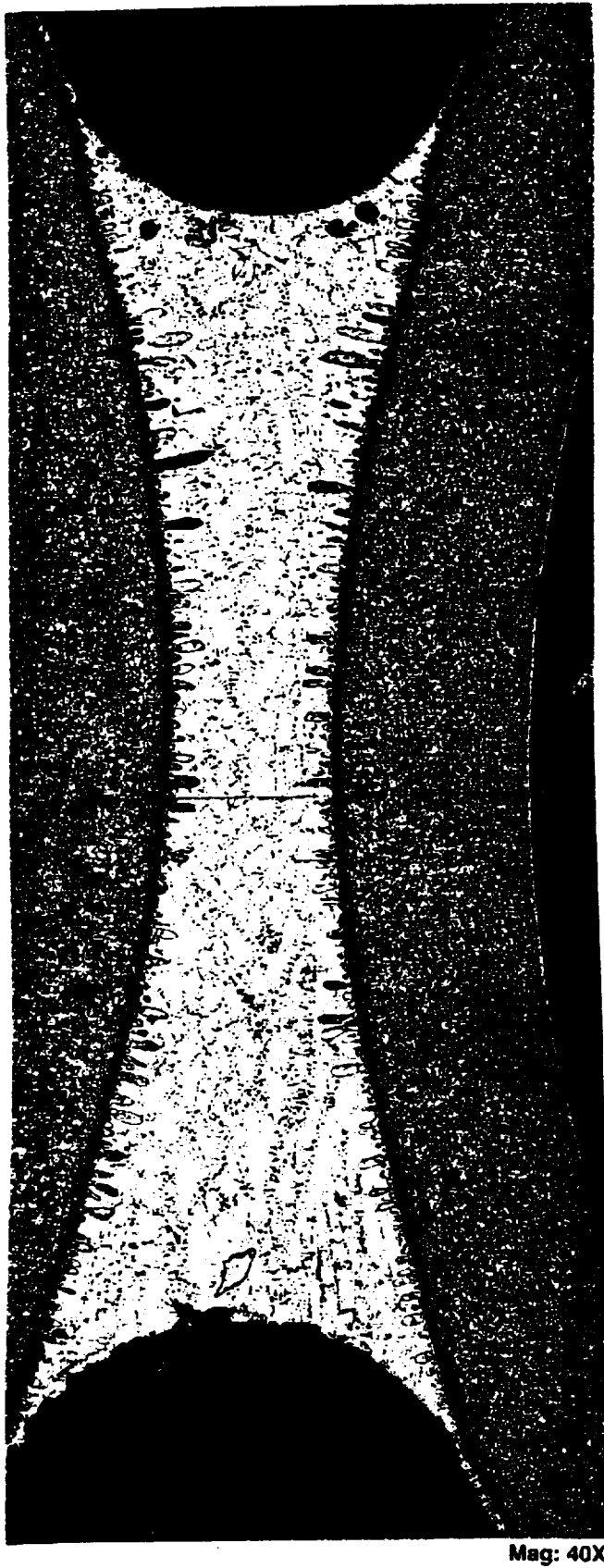
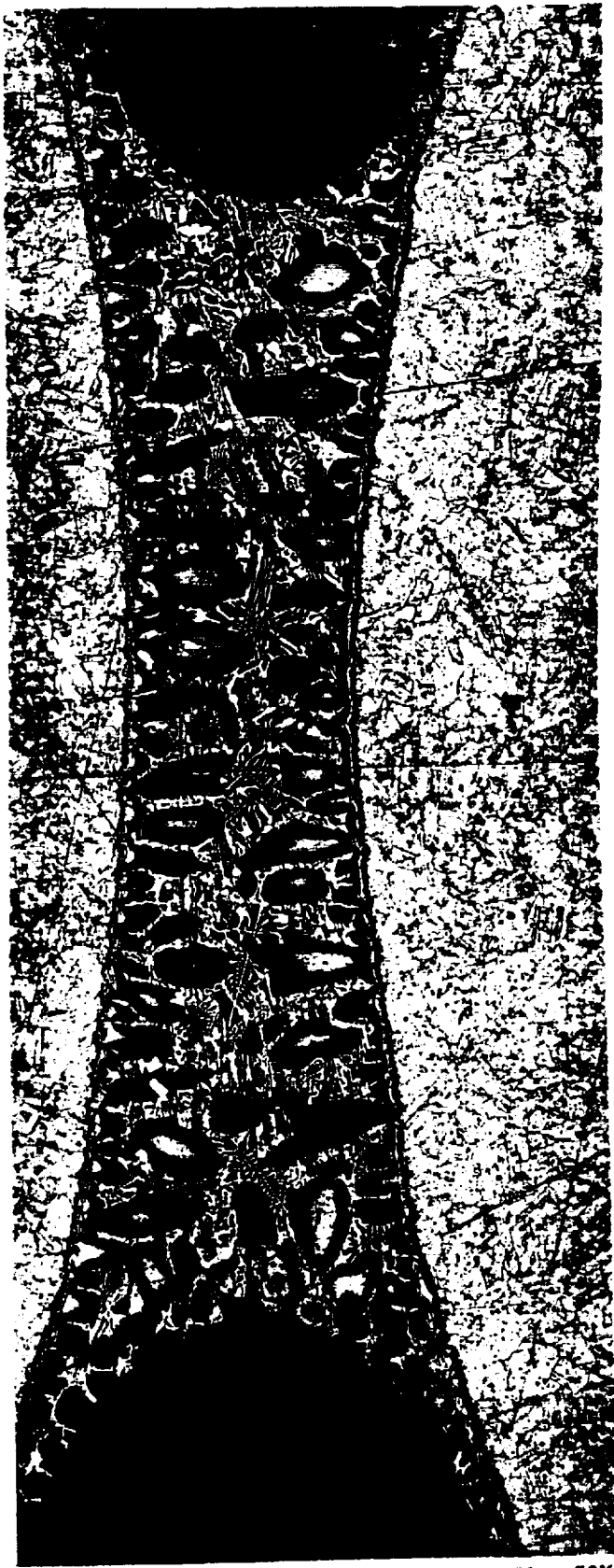
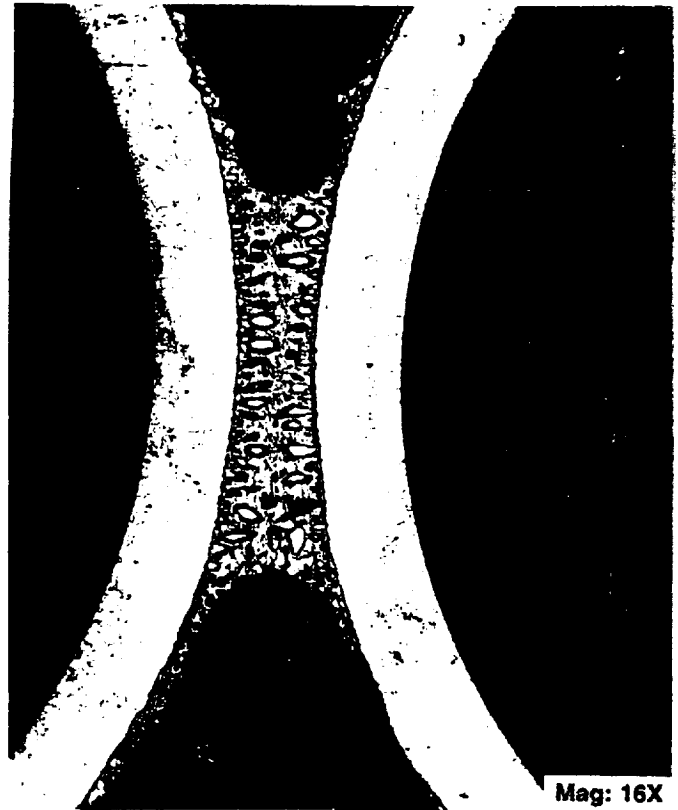


Figure 4.1.1-34. INCO 625 Tubes Brazed With NB-10 (Ni-11P)



Mag: 50X



Mag: 16X



Mag: 100X

Figure 4.1.1-35. INCO 625 Tubes Brazed With NB-30 (Ni-19Cr-10Si)

7265

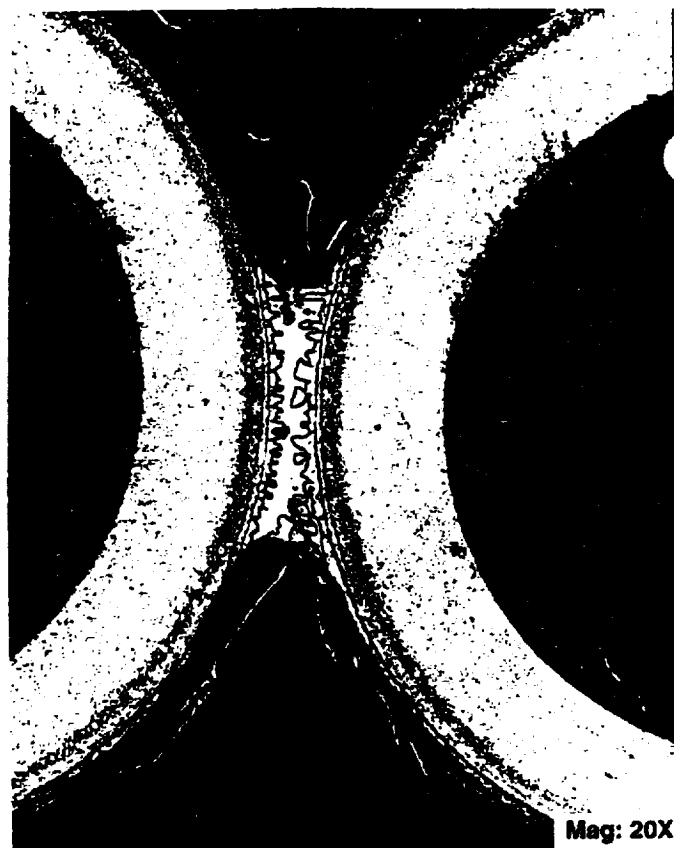


Figure 4.1.1-36. Haynes 230 Tubes Brazed With NB-150 (Ni-15Cr-3.5B)

FE62573

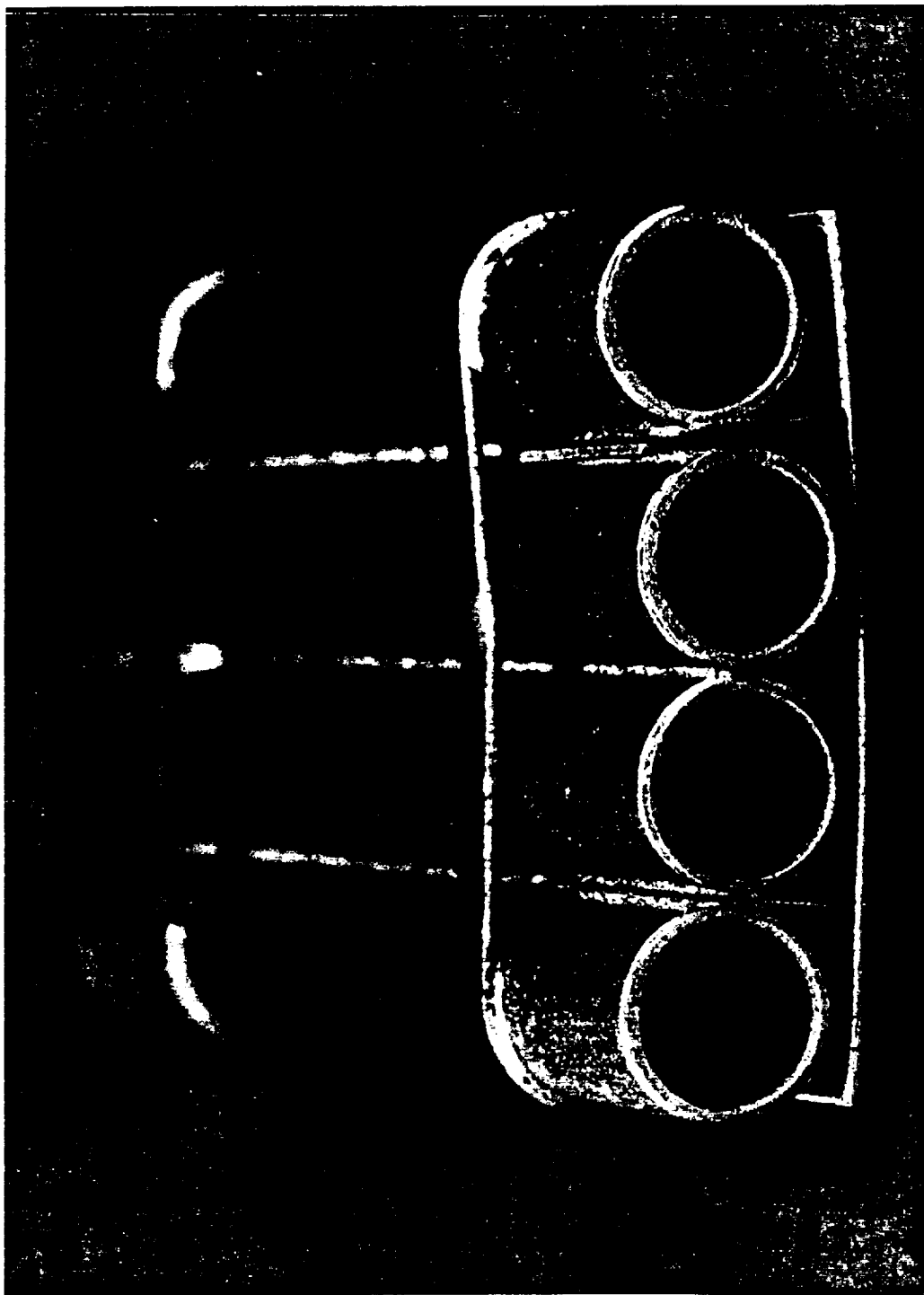


Figure 4.1.1-37. Inconel Tubes With AMS 4782 Braze Alloy Plasma Sprayed 0.009 Inch Thick

FER03672

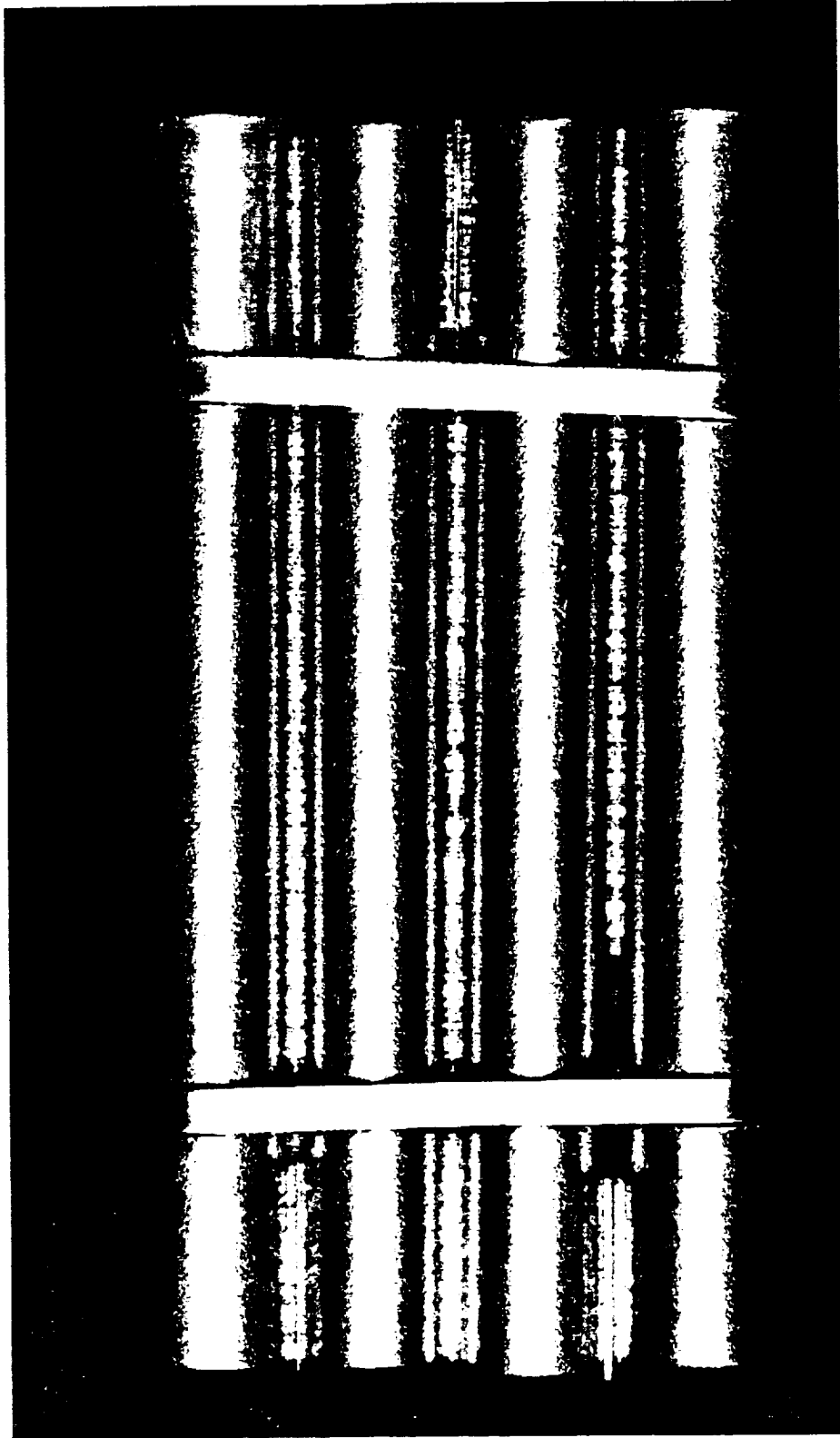
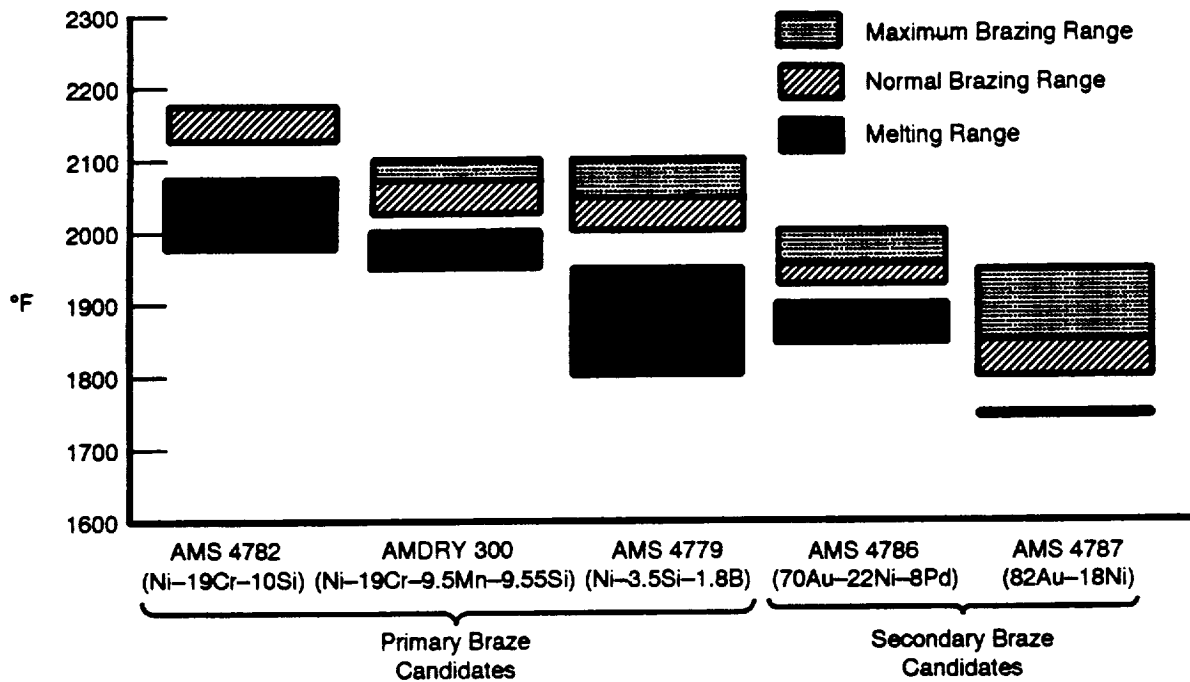
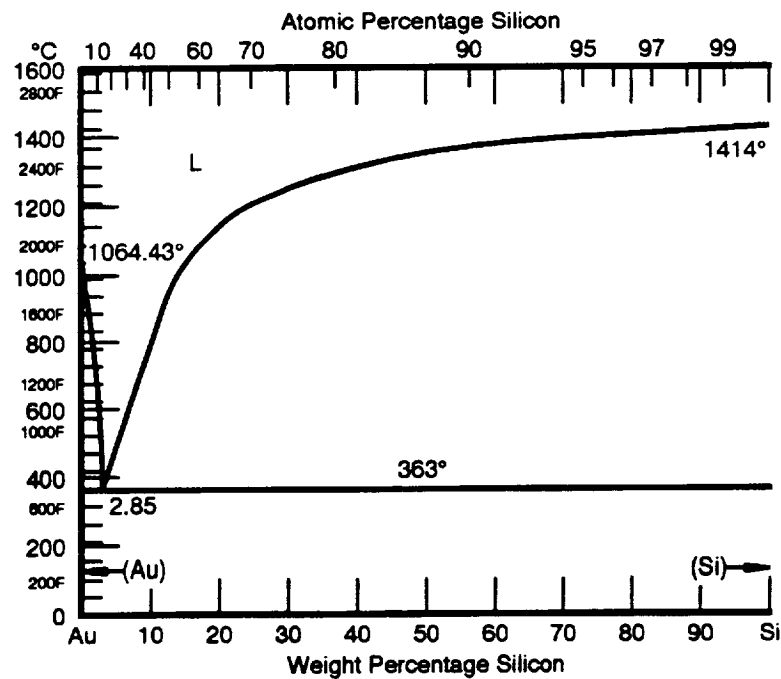


Figure 4.1.1-38. Inconel Tubes With AMS 9772 Braze Alloy Plasma Sprayed 0.009 Inch Thick



14582

Figure 4.1.1-39. Brazing Ranges for Nozzle Braze Alloy Candidates



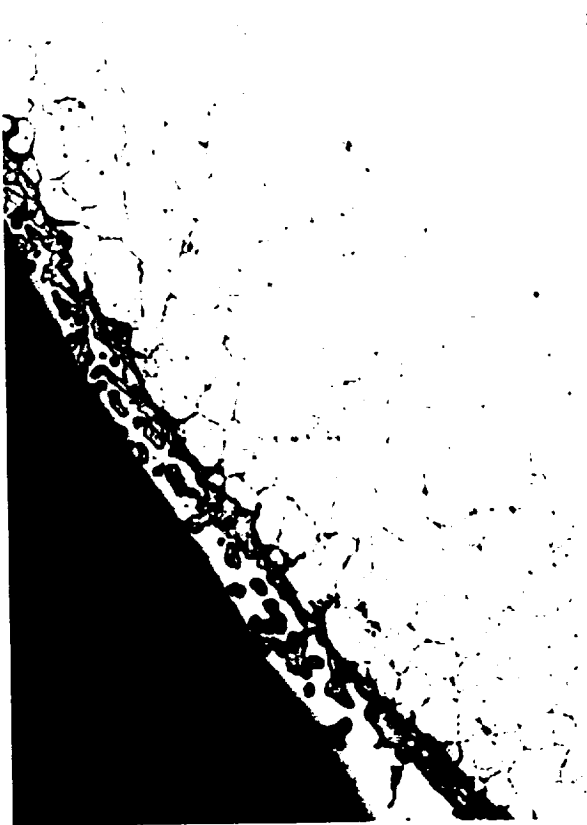
14583

Figure 4.1.1-40. Phase Diagram for Gold-Silicon Eutectic



100X

Tube-to-Tube Fillet



200X



50X

Tube-to-Jacket



200X

14606

Figure 4.1.1-41. Preformed Square Inconel Tubes Brazed With AMS 782 (Ni-19Cr-10Si) at 2150° F in Vacuum, Then Rebrazed With AMS 4787

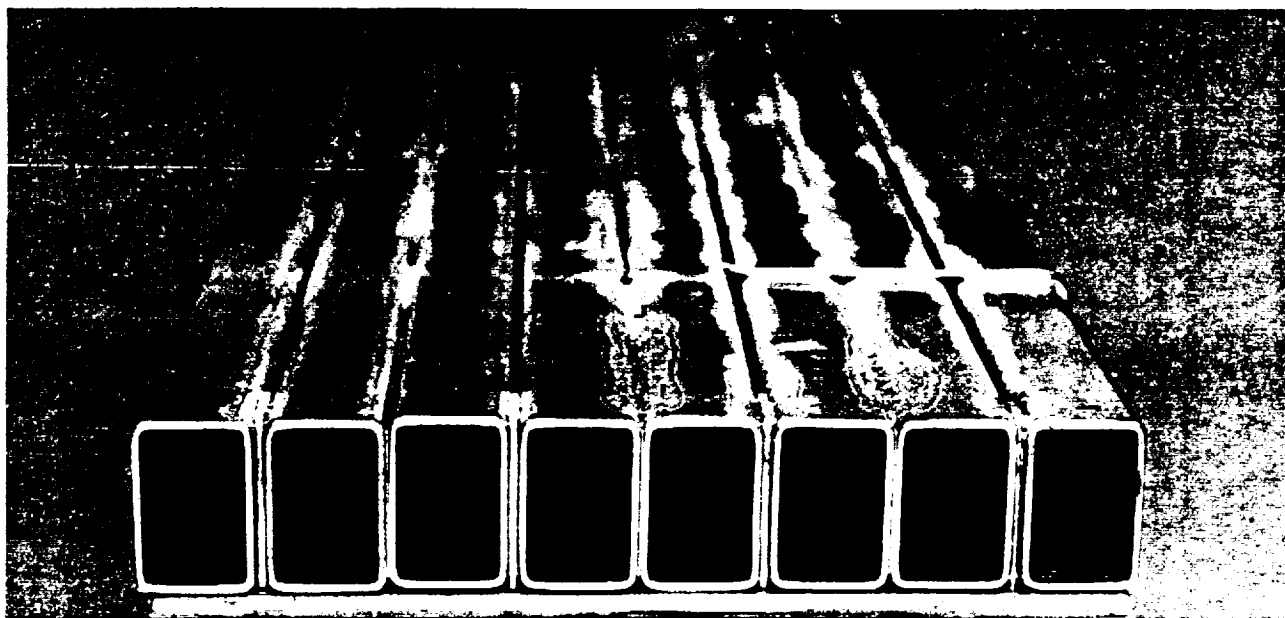


Figure 4.1.1-42. Step Braze Sample — Tubes and Jacket Were Plasma and Brazed With AMS 4779 (Ni-3.5Si-1.8B), Then a Second Braze of Alloy AMS 4787 (82Au-18Ni) Was Applied and the Sample Brazed in a Lower Temperature Cycle

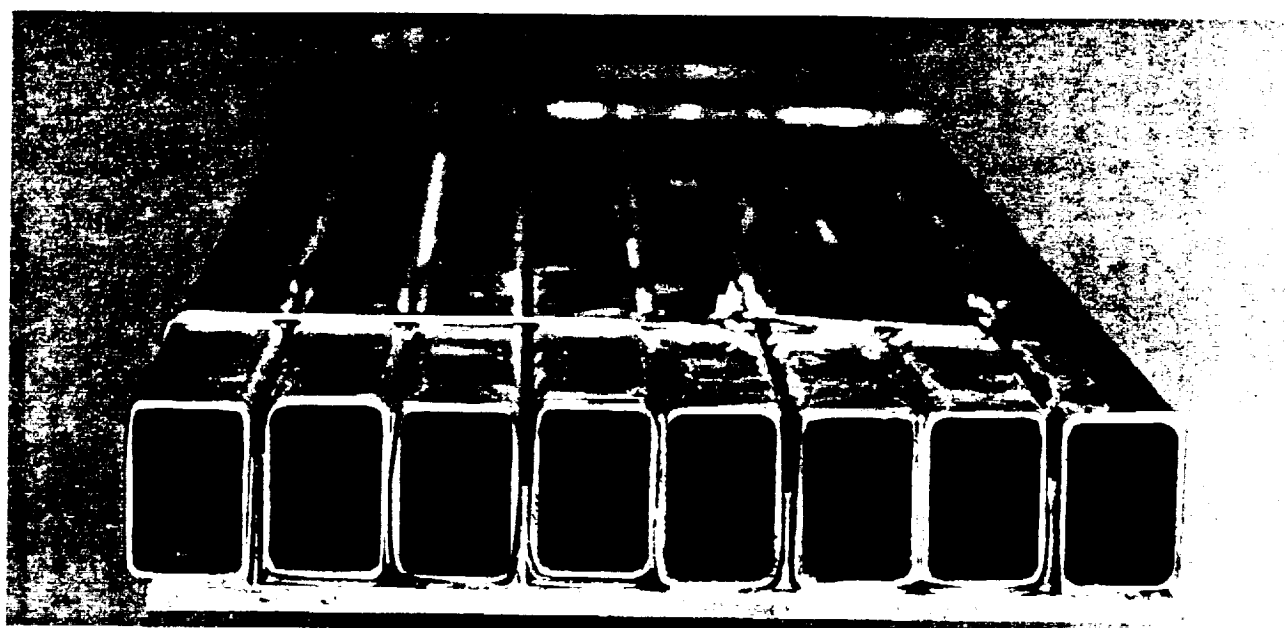
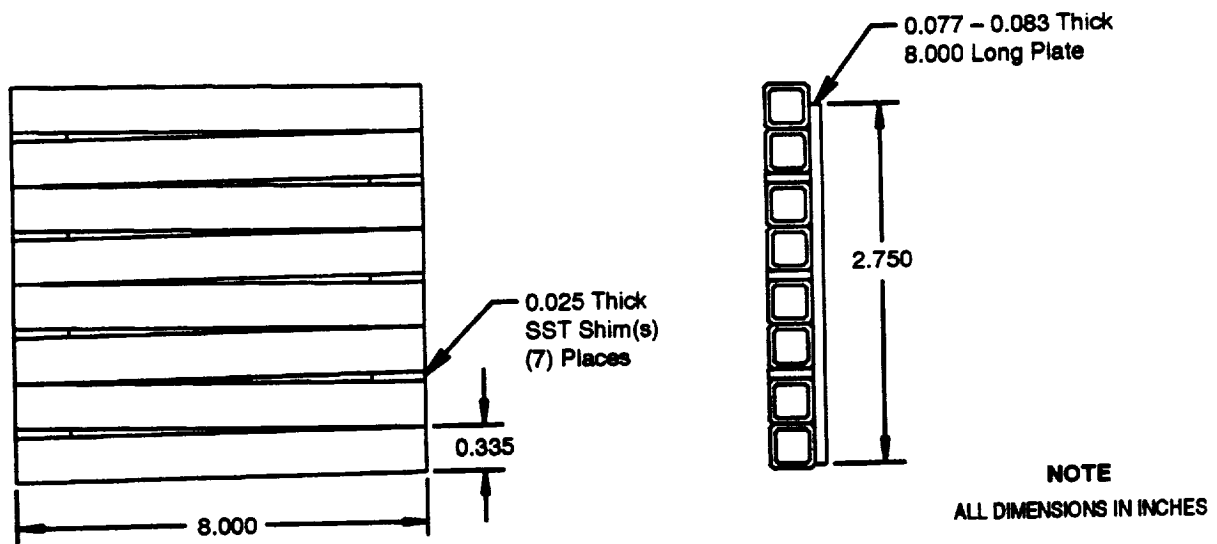
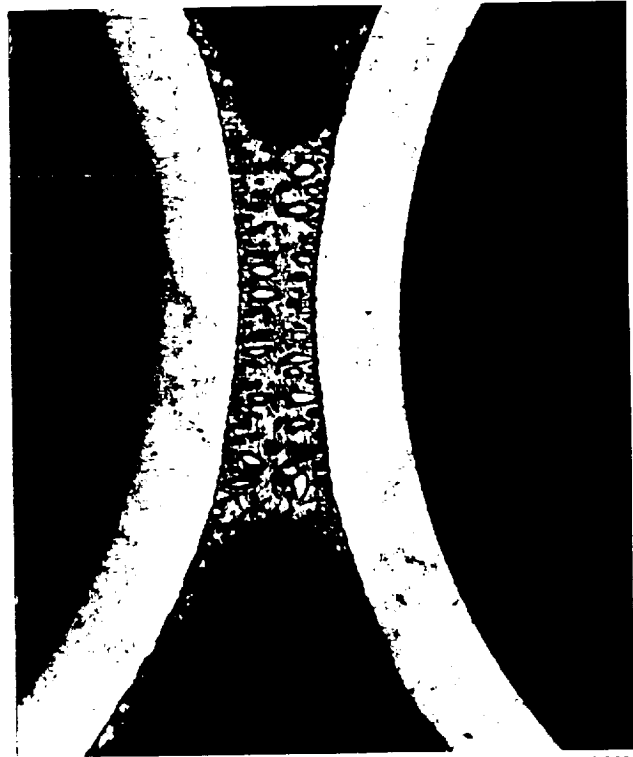


Figure 4.1.1-43. Step Braze Sample — Tubes and Jacket Were Plasma and Brazed With AMDRI 300 (Ni-19Cr-9.5Mn-9.5Si), Then a Second Braze of Alloy AMS 4787 (82Au-18Ni) Was Applied and the Sample Brazed in a Lower Temperature Cycle



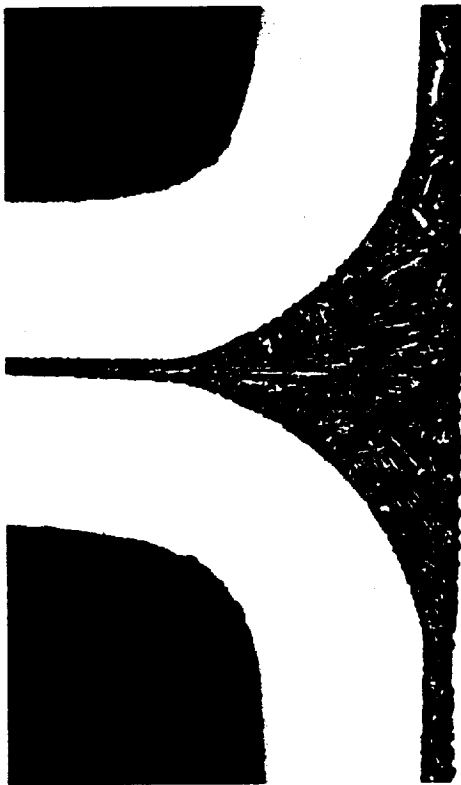
14584

Figure 4.1.1-44. Fabrication Sample Design for the Step Braze Trials



14607

Figure 4.1.1-45. Round Inconel 625 Tubes Brazed With AMS 4782 (Ni-19Cr-10Si) in Hydrogen Showing No Porosity and Excellent Braze Coverage

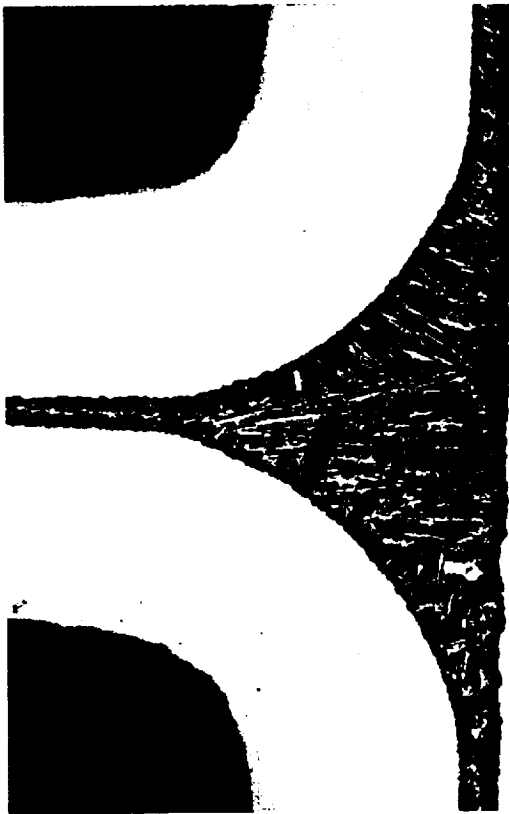


32X



100X

14609

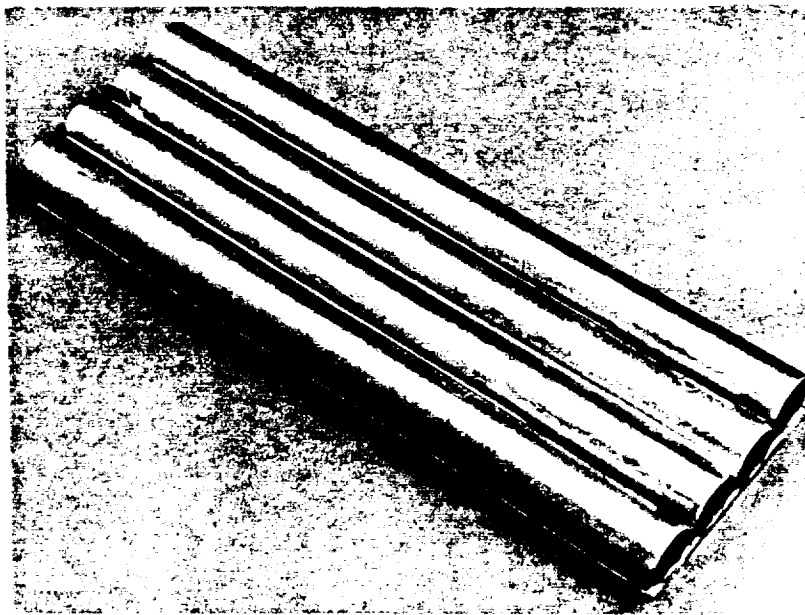


40X



100X

Figure 4.1.1-46. Preformed Square Inconel 718 Tubes Brazed With AMS 4782 (Ni-19Cr-10Si) in a Vacuum Environment Showing Porosity and Excellent Braze Coverage



FE024127

Figure 4.1.1-47. Inconel 625 Tubes Brazed With AMDRY 300 (Ni-19Cr-9.5MN-9.5Si) in a Vacuum Environment Showing Excellent Gap Coverage

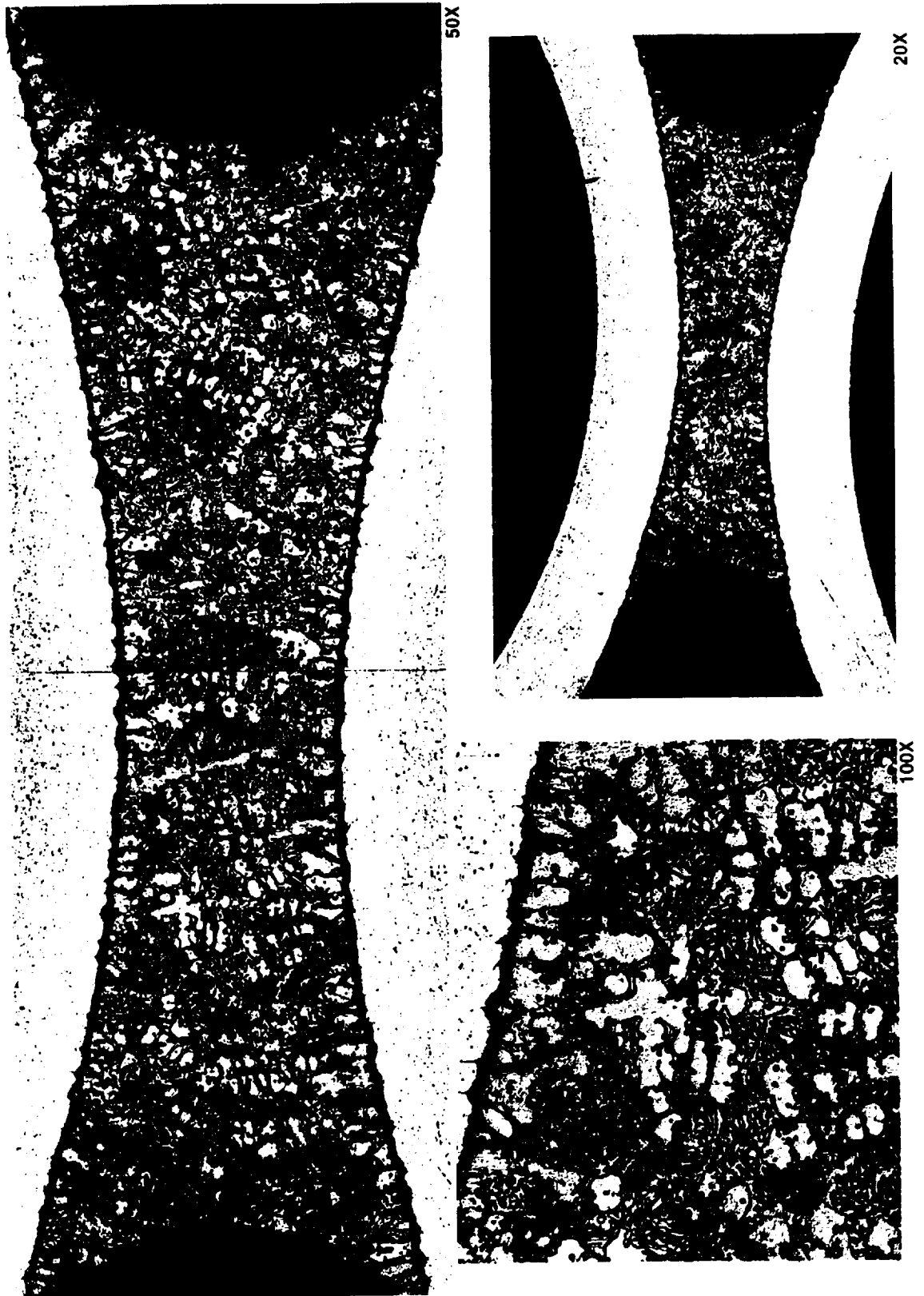


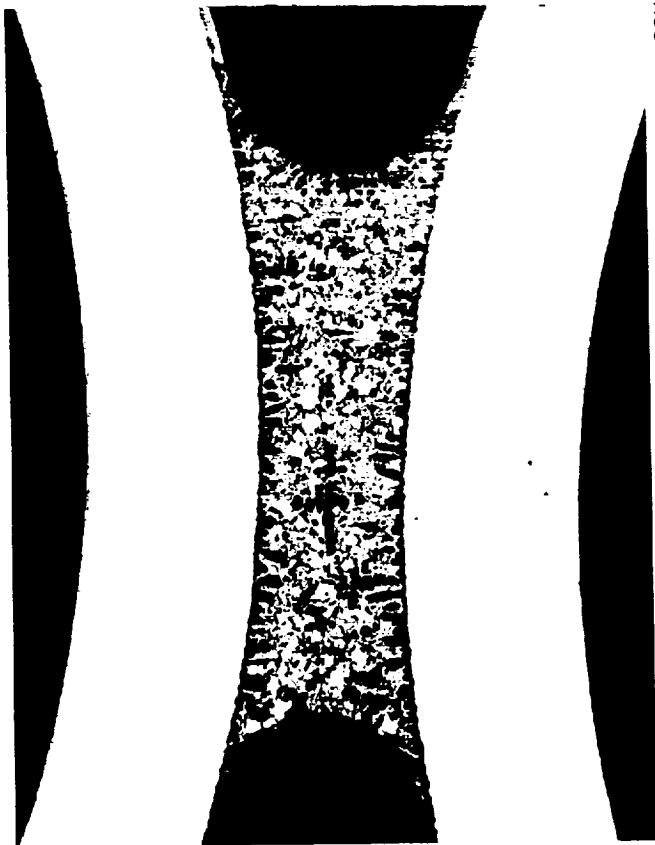
Figure 4.1.1-48. Inconel 625 Tubes Brazed With AMDRY 300 (Ni-19Cr-9.5MN-9.5Si) in a Hydrogen Environment Showing Excellent Braze Coverage



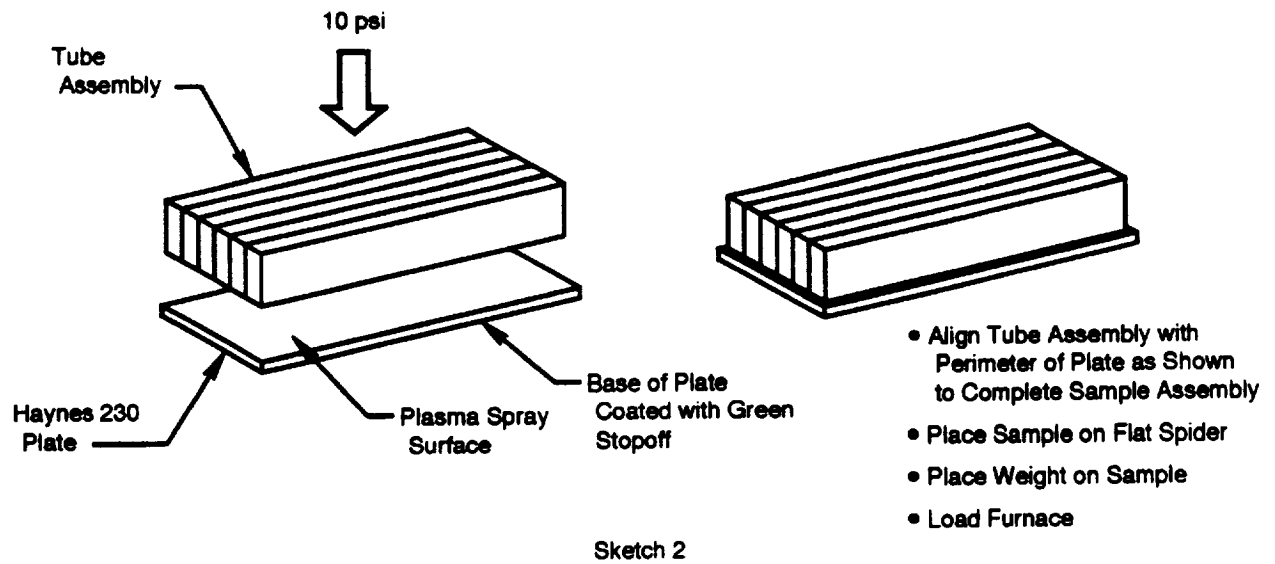
100X



500X

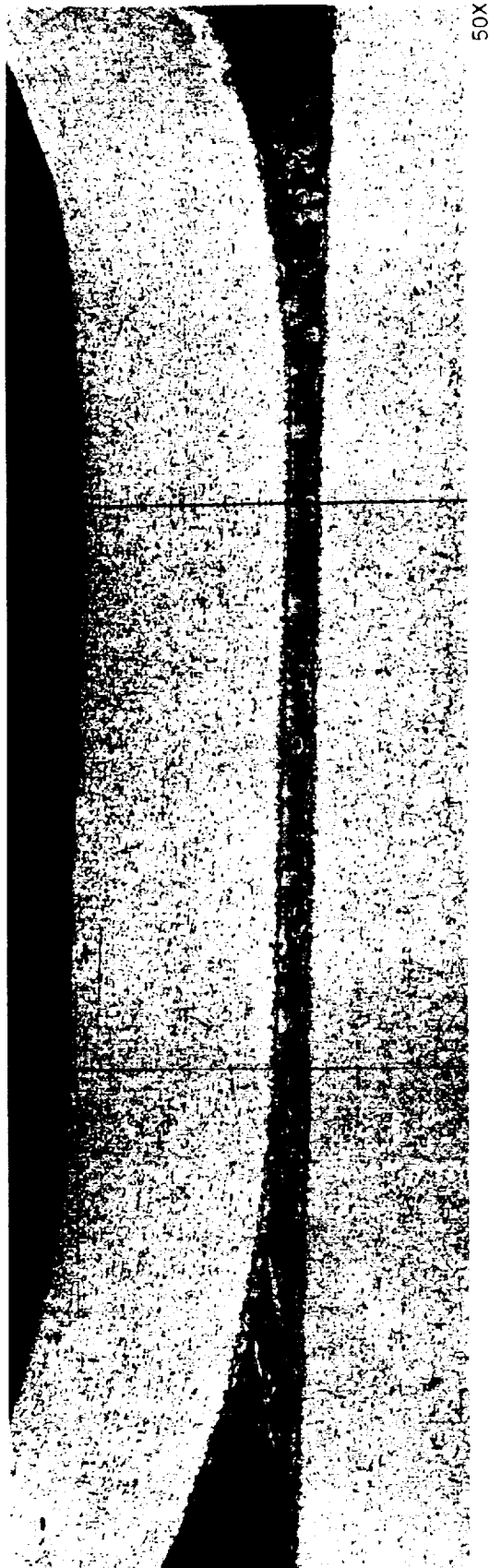


32X

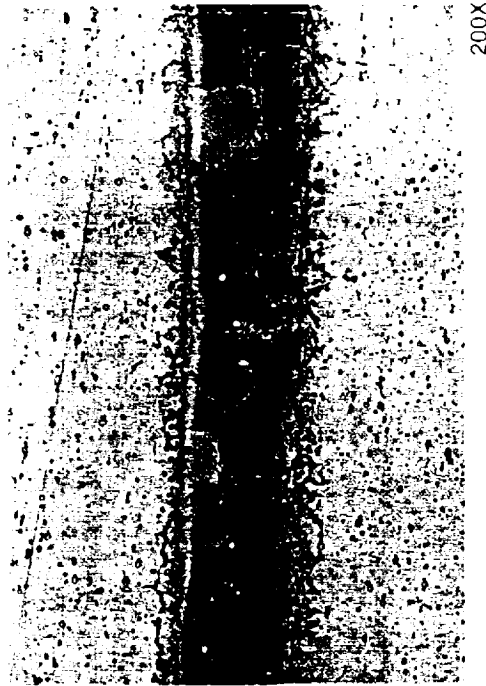


14585

Figure 4.1.1-50. Fabrication Sample Design for the Plasma Spray Braze Application Method

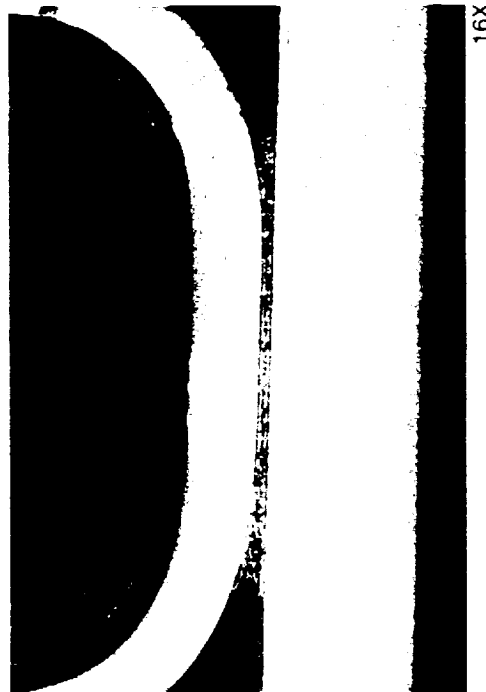


50X



200X

14612



16X

Figure 4.1.1-51. Preformed Square Haynes 230 Tubes Brazed at 2175°F With
AMS 4762 (Ni-19Cr-10Si) Applied to the Steelmetal Using Plasma Spray Method.

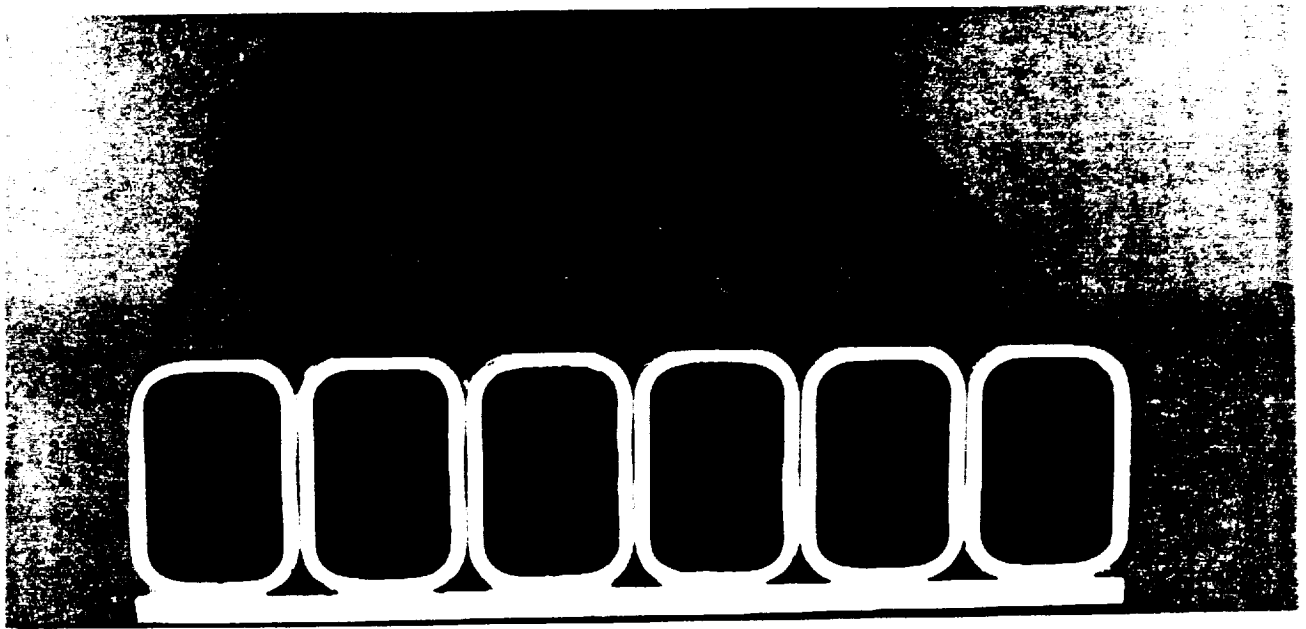
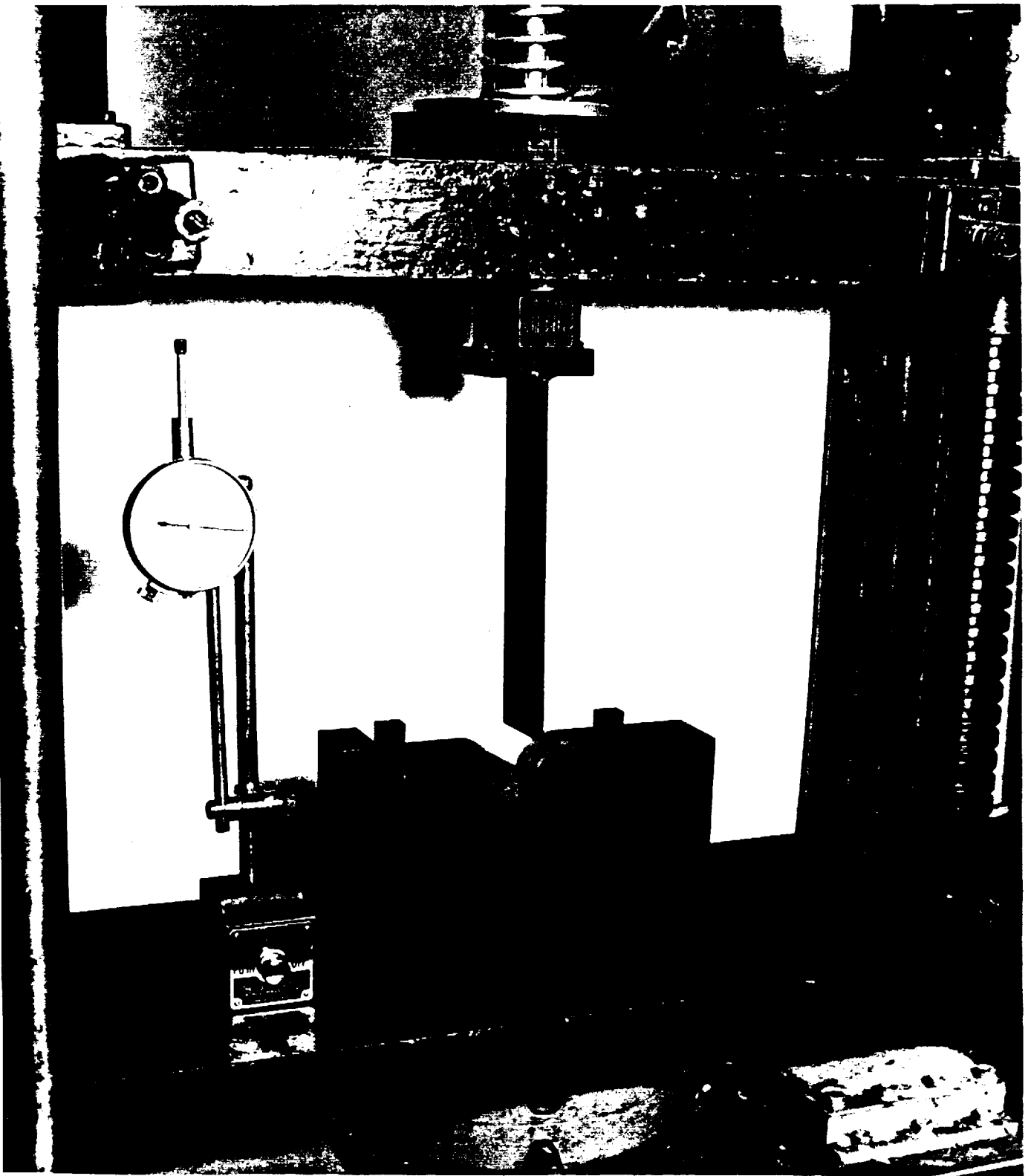
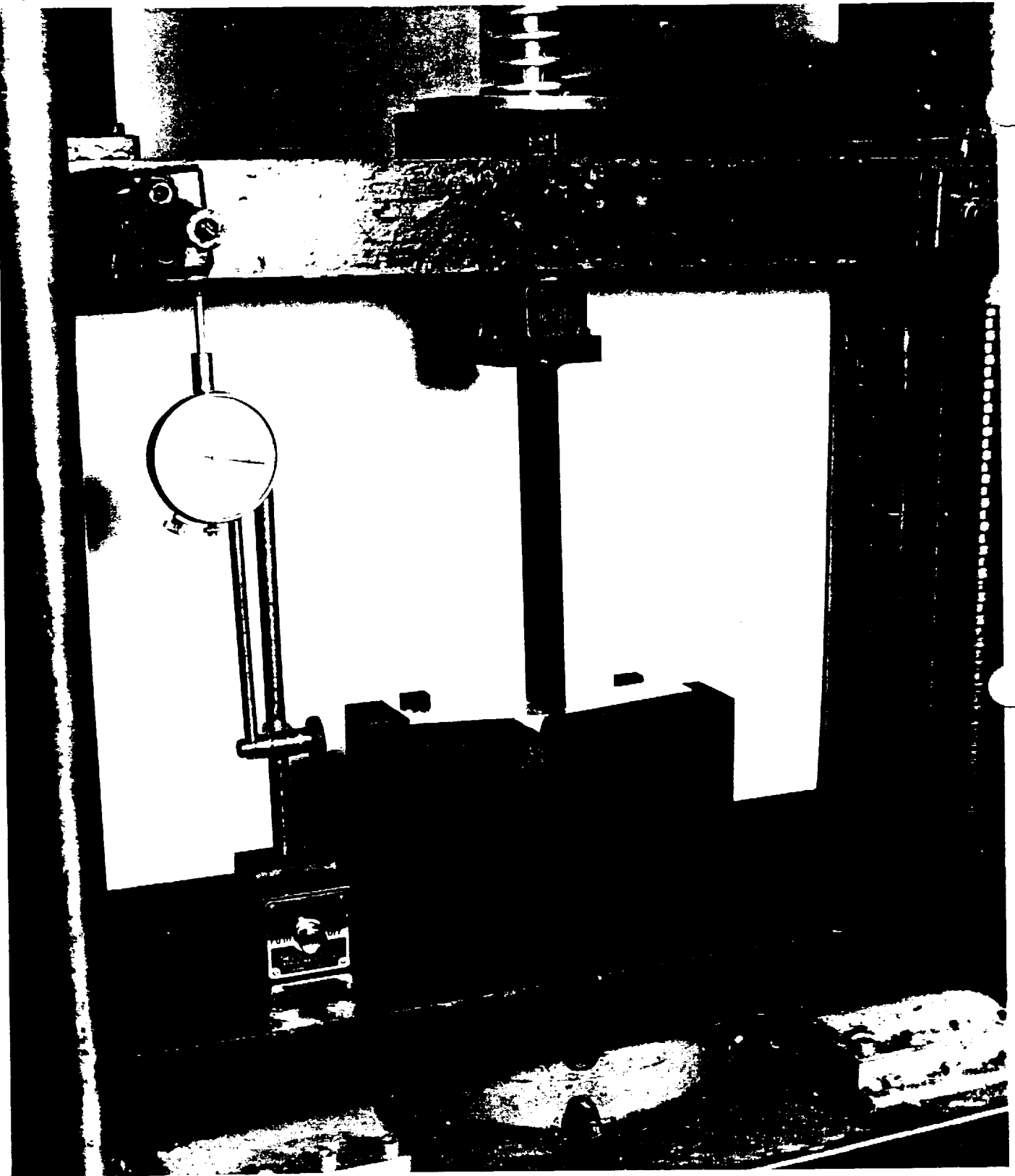


Figure 4.1.1-52. Brazed Tube Sample — Sheetmetal Jacket was Plasma Sprayed With AMS 4782 (Ni-19Cr-10Si)



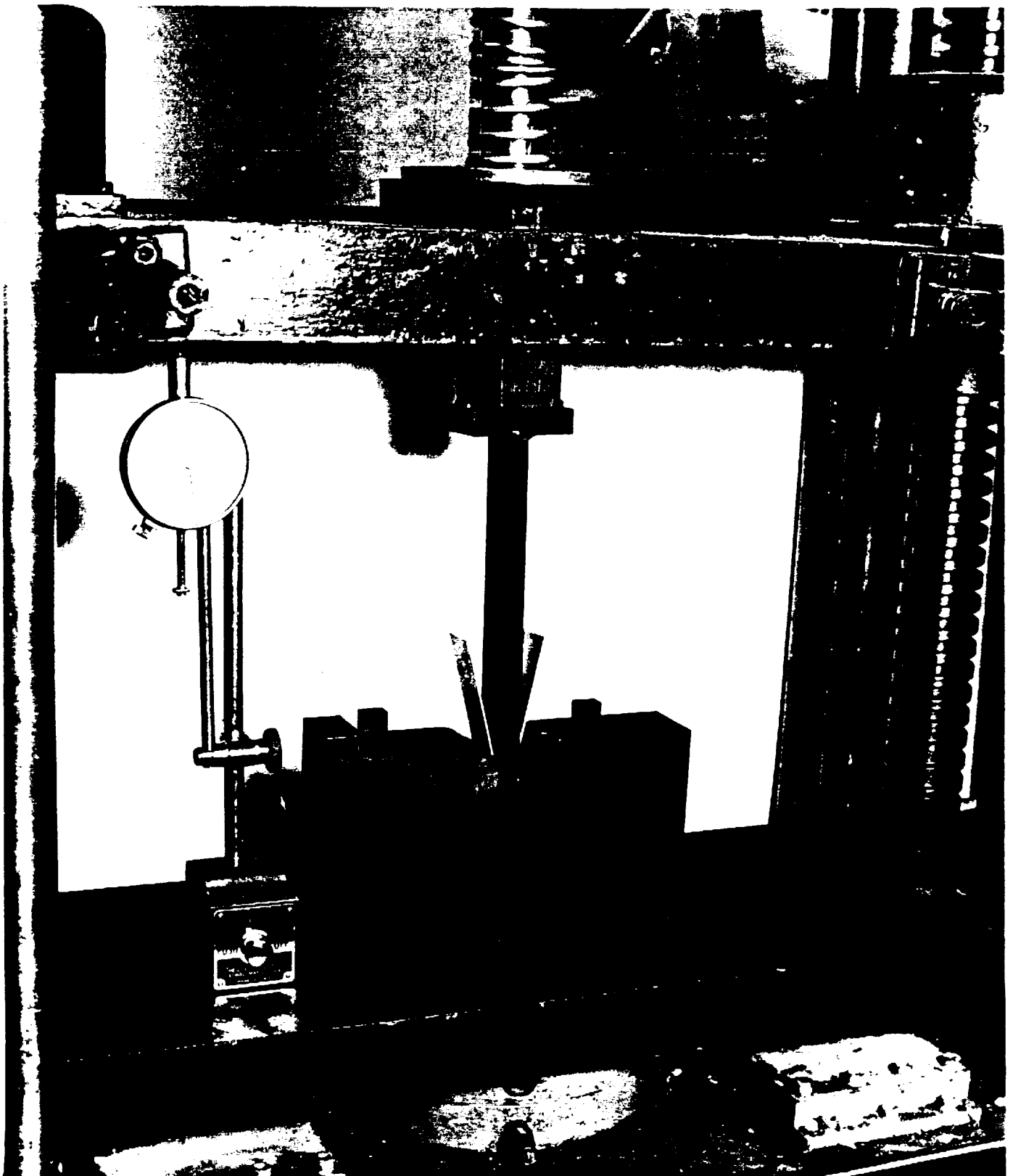
FE020994

Figure 4.1.1-53. Braze Sample Bend Tester



FE 626994-6

Figure 4.1.1-54. Braze Sample Undergoing Bend Testing



FE 628694-6

Figure 4.1.1-55. Braze Sample Undergoing Bend Testing

4.1.2 Sheetmetal Concepts

4.1.2.1 Explosion Forming/Laser Welded Convolute

Tool design of the flat specimen explosion form dies was completed and the fabrication of the three dies was completed. Figure 4.1.2-1 shows one of the explosion form dies during fabrication with the removable/replaceable convolute forms.

All explosion forming trials were conducted by Explosive Fabricators, Inc. located in Louisville, Colorado. The trials investigated if the sheetmetal will take the desired convolute form, what minimum convolute land width is obtainable by explosion forming, the extent of material thinning that occurs, and which of the two materials is best suited for explosion forming.

Preliminary results indicate that the current full-scale nozzle sheetmetal convolute passage design, with an aspect ratio of over 2:1, is too severe for consistent explosive forming. The same material strain present in the LW/IF and DB/IF trials is found in the explosion forming process, with similar material thinning near the attachment location. The first sample, shown in Figure 4.1.2-2, has been received and achieved passage heights of up to 0.600 inch, which is close to the full-scale nozzle passage height of 0.620 inch. All of the samples required multiple explosion forming and stress relief cycles to keep the sheetmetal ductile and able to form the high aspect ratio geometry. The supplier indicated that the Inconel 625 material required less forming and fewer stress relief cycles than the Haynes 230 material.

All explosion formed samples were finally received from the explosion formed supplier, Explosion Fabricators Inc. The supplier provided a detailed report and recommendations for both the fabrication trials sample configuration and full-scale nozzle manufacturing configuration. These recommendations were included into the full-scale nozzle Master Planning Summaries, and full-scale nozzle cost data has been updated for Phase I downselect. Excerpts from the Explosive Fabricators report are provided below:

The purpose of the program was to determine the feasibility of forming Inconel 625 or Haynes 230 panels, 23 inches square by 0.032 inches thick, to the desired contour. Three dies designed and built by were provided.

Forming Procedures:

- 1. The panels were formed using explosive force with water as the driving medium. In addition, a vacuum was pulled behind the panels to prevent burning of the material during the forming operation.*
- 2. The dies and panels were lubricated to decrease the friction between them and allow a more uniform elongation over the surface of the panels.*
- 3. Several explosive geometries were tested: line charges situated parallel and normal to the convolutes, and net-shaped charges. The distance and amount of charge for the various configurations were varied till the optimum results were obtained.*
- 4. An anneal was performed on the panels between the forming operations. A forming operation consisted of one to three explosive shots.*

Results:

1. *The maximum depth of valleys between the inserts of the die before the first interim anneal was 0.33 to 0.36 inch.*
2. *The maximum depth of valleys between the inserts of the die before the second interim anneal was 0.43 to 0.46 inch.*
3. *The maximum depth of valleys between the inserts of the die before the third interim anneal was 0.50 to 0.54 inch.*
4. *The maximum depth of valleys between the inserts of the die before the fourth interim anneal was 0.55 to 0.60 inch.*
5. *The panels reached the base of the die between the insert after the final anneal but failed. The failures occurred at various locations ranging from half way into the valley down to the bottom of the valleys. This type of failure seems to be the result of excessive thinning.*
6. *Previously formed panels created by a break press were also used to evaluate their ability to conform to the desired contour. This resulted in considerably deeper deflection after the initial shot. With subsequent shots, the panel started to touch between the inserts, with no interim anneals. The benefit of this approach was that the thinning problem decreased and the panels could be produced to full depth with fewer forming and annealing operations; however, wrinkling occurred at the ends of the convolutes.*

Conclusions:

1. *Overall, the project worked as expected. Although the dies that were provided did not lend themselves to explosive forming due to the limited amount of flange area to draw in and the size and location of the vacuum ports, the panels were formed to approximately 95 percent of full contour.*
2. *Of the two materials used, Inconel 625 and Haynes 230, the Inconel seemed to form more readily. The Haynes 230 failed when formed to an amount equal to the Inconel, resulting in additional forming and stress relieving operations.*
3. *The best results occurred with the preformed panels, though more evaluation will be required to produce a finished part. The primary obstacle to overcome is to eliminate the wrinkles at the convolutes lead in during the forming operation.*
4. *Of the dies provided, die No. 3 provided the best formed panels. This can be attributed to larger flat in the bottom of the valleys (0.08 inch).*

Recommendations:

1. *In our opinion, to produce this nozzle in the sizes required, modification to the final shape and/or preform will be essential.*
2. *The final contour would lend itself more readily if the depth of the hoops were less in respect to their width. One possible configuration would be using an arc depth that is less than half its width. Additionally, the length of the flat and the radius at the bottom of the valleys should increase in size.*

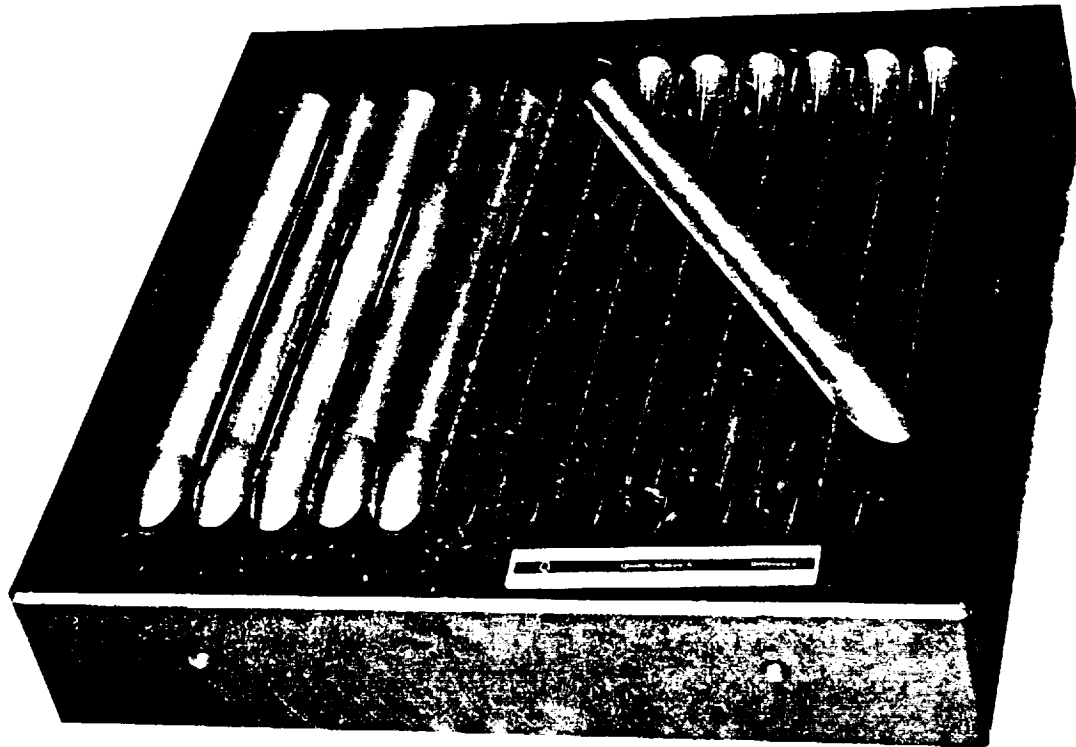
3. *A possible modification to the flat panel preforms would be to have them pre-bent (Figure 4.1.2-3). This approach will lessen the amount of the elongation required to conform to the final contour. The die required for this would need to have an area outside of the finished panel press area to draw the material into where convolutes taper off to eliminate the wrinkling problem (Figure 4.1.2-4).*
4. *After a number of panels are formed, they may be welded together. Any distortion then can be eliminated using a final sizing operation in a full female die. This will also planish the weld.*
5. *Another possibility is to use brake formed panels for the lower nozzle sections and a separate part for the convolute lead in. The two parts after forming can be welded together. This will alleviate the wrinkling problem but add a welding operation.*

A total of 24 Inconel 625 panels and 5 Haynes 230 panels were returned to P&W. Six of these Inconel 625 panels were selected for laser welding trials, based upon which had formed closest to the 0.620-inch required convolute height and which had the fewest cracks caused by the explosion formed process. Figure 4.1.2-5 shows a fully formed panel with no cracks. Additional panels were preformed using a brake press, which allows the material to be preformed without significantly reducing wall thickness. However, the preforming also causes the material gathers as shown in Figure 4.1.2-6. The remaining 27 samples had cracks near the base of the convolute, as shown in Figures 4.1.2-7 and 4.1.2-8. Figure 4.1.2-9 shows random cross-sections away from the weld, which were taken to determine the extent to which the material thinned nonuniformly during the explosion formed process. As shown in the figure, the cross-section is fairly uniform.

Photomicrographs of the welded sample at two random locations are shown in Figures 4.1.2-10 and 4.1.2-11. The weld parameters that were developed in the first sample will be used to weld the six selected panels to 0.085-inch thick sheetmetal section that simulates the structural jacket. To determine the maximum allowable gap that can be tolerated by the laser weld, shims will be placed between the convoluted sheet and the jacket. This test will provide data for use in full-scale nozzle planning to estimate the process sensitivity to sheetmetal dimensional and layup tolerances, which can significantly impact costs.

Recent full-scale nozzle design studies have indicated that a double convolute shape is feasible for the sheetmetal jacket. This double convolute is achieved by explosive forming or machining the outer jacket, and explosive forming the inner sheetmetal nozzle. This design allows reduced height-to-width ratios for the explosive formed inner wall, thereby reducing the total material strain and material thinning. To better understand the welding process, during the welding trials one of the Inconel 625 panels will be cut in half and welded to itself to simulate the double convolute design.

The weld parameters that were developed for the explosion formed Inconel 625 panels were used in the welding of the best explosion-formed samples. A successfully welded sample is shown in Figures 4.1.2-12 and 4.1.2-13. The final task for completion of Phase I was to simulate the double convolute shape of the sheetmetal nozzle design. Figures 4.1.2-14 and 4.1.2-15 show the double convolute sample, which was created by cutting one of the explosion formed panels in half and tack welding the two sections together in preparation for laser welding. The sample was not completed because the sheetmetal nozzle studies were discontinued following the February Component Development Team meeting. At this meeting, the results of the fabrication trials were discussed and the explosion formed/laser welded fabrication process was eliminated from further consideration due to high cost and low producibility. Additional information on the nozzle downselect rationale is provided in Section 5.



FAL106136

Figure 4.1.2-1. Explosion Form Die With Removable/Replaceable Convolute Forms

FE824001

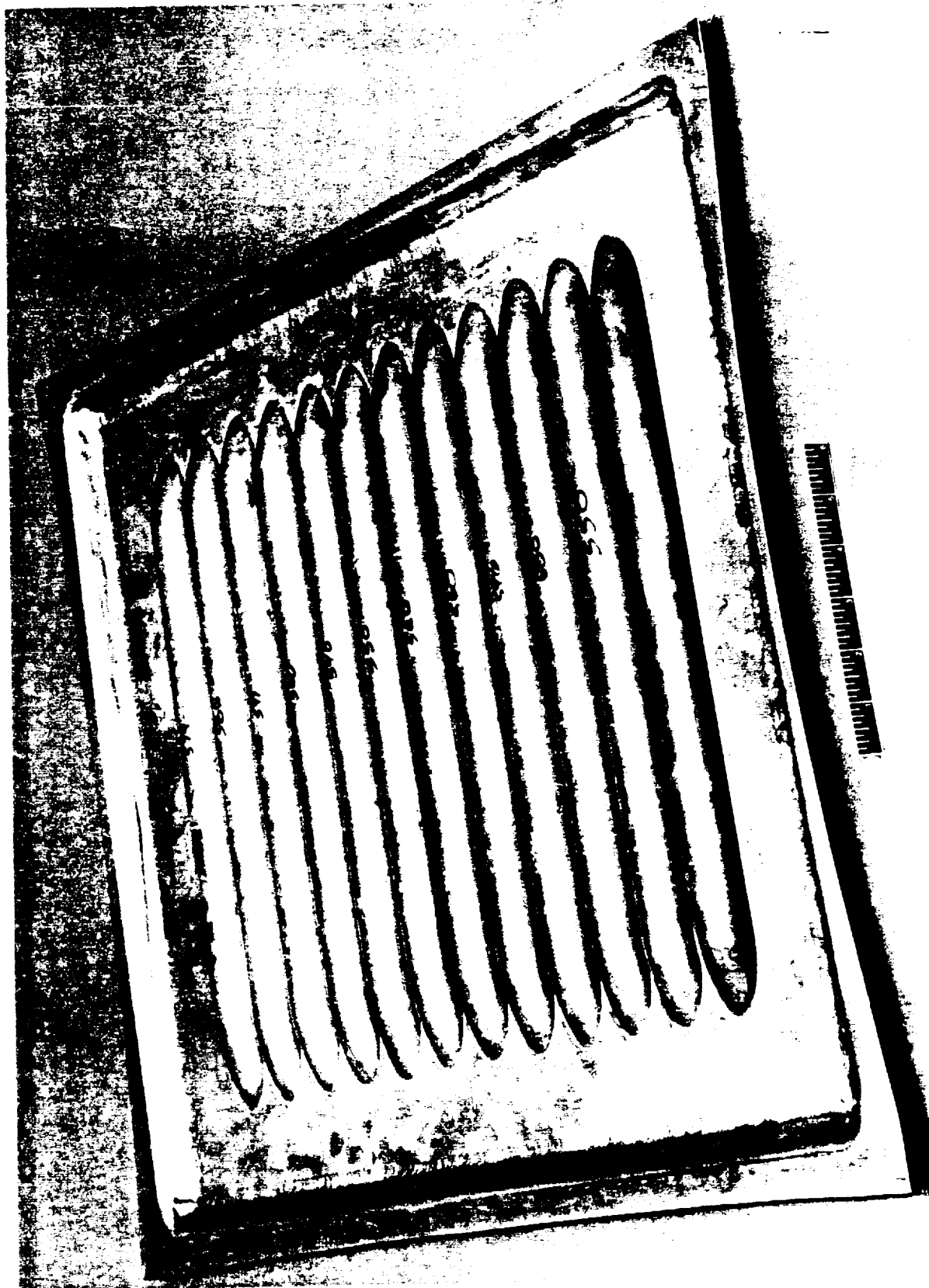
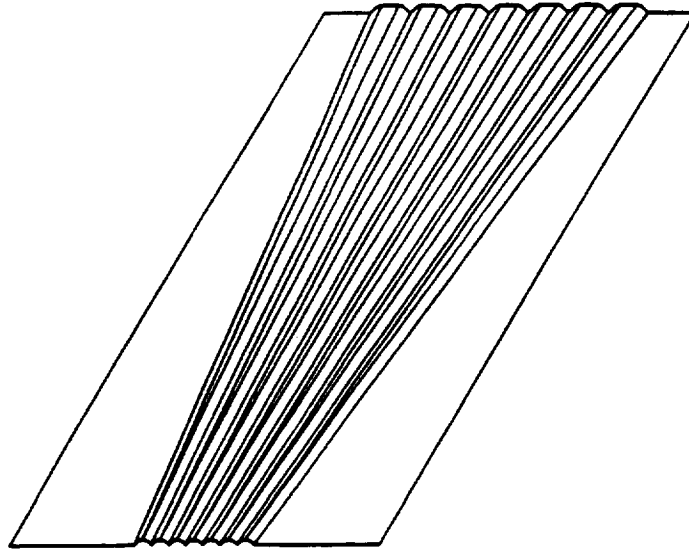
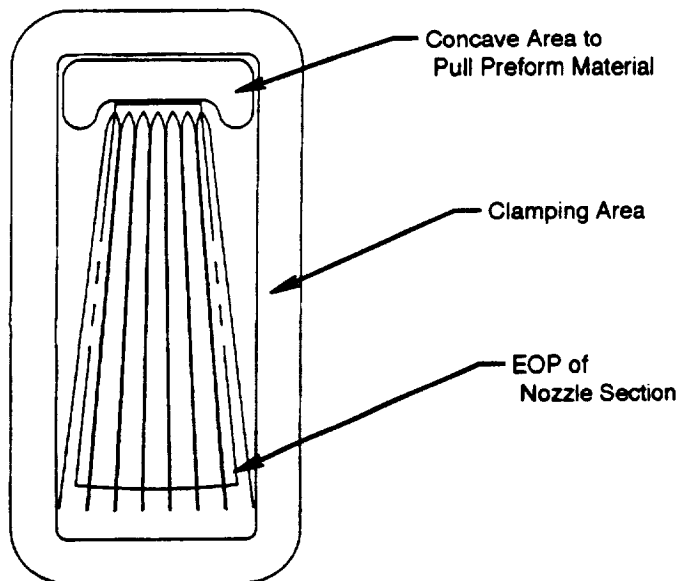


Figure 4.1.2-2. Explosior Formed Inconel 625 Sample



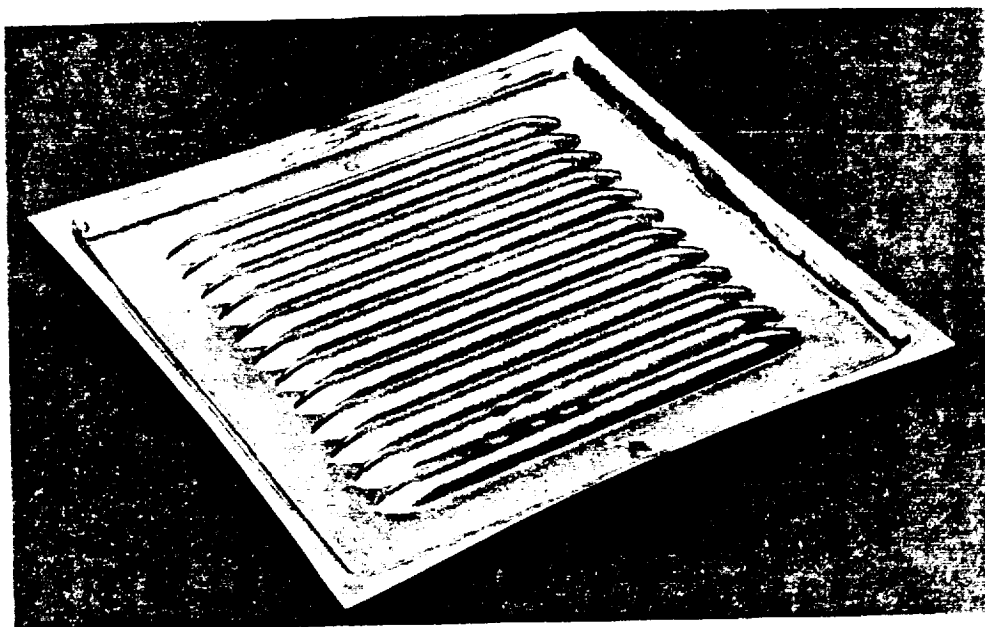
14636

Figure 4.1.2-3. Explosive Fabricators, Inc Nozzle Proposed Preform Blank



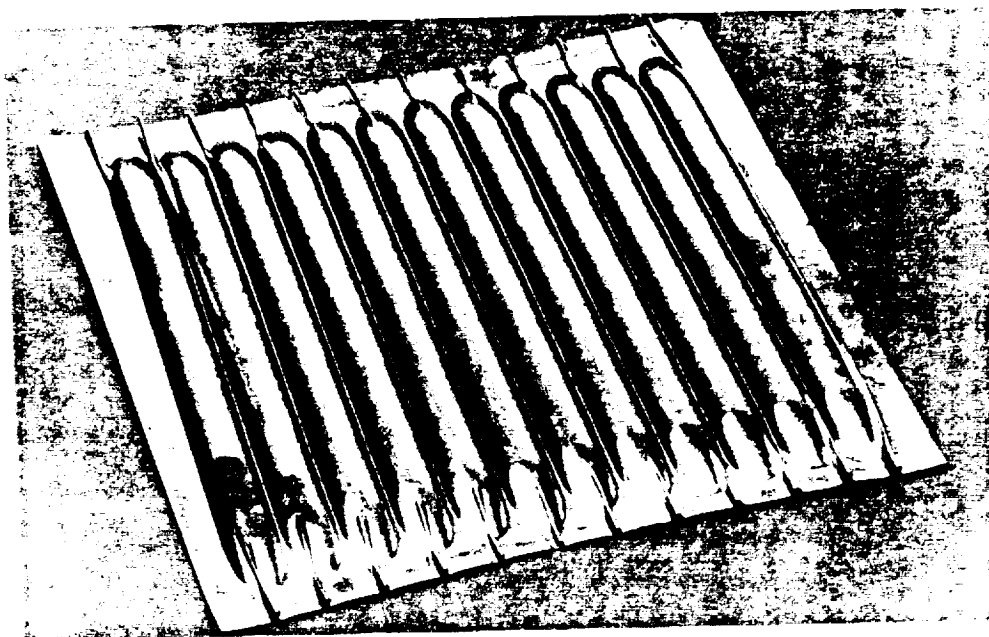
14638

Figure 4.1.2-4. Explosive Fabricators, Inc Nozzle Die Concept



FE625314

Figure 4.1.2-5. Inconel 625 Panel Explosion Formed With No Cracks



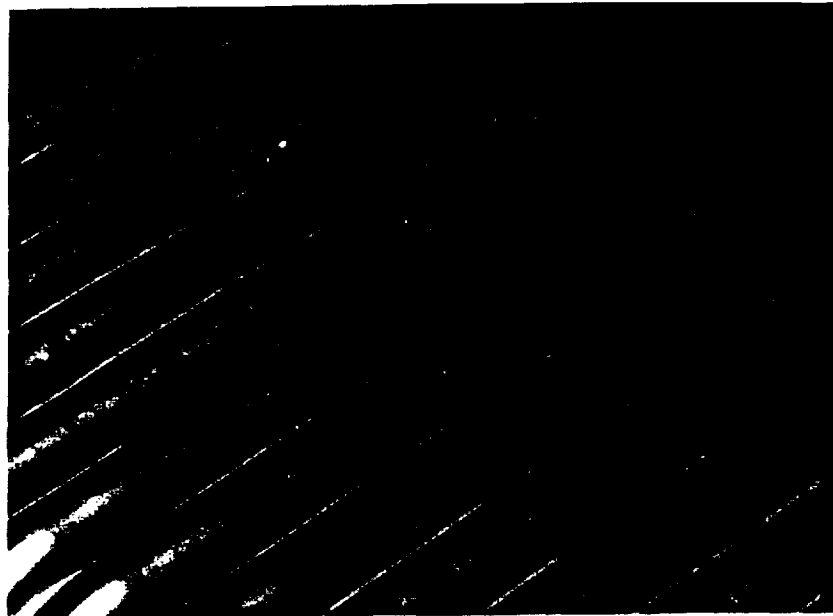
FE625309

Figure 4.1.2-6. Inconel 625 Panel Preformed Using a Brake Press and Explosion Formed to the Final Geometry



FE625317

Figure 4.1.2-7. Inconel 625 Panel Showing Typical Failure Due to the Explosion Forming Process



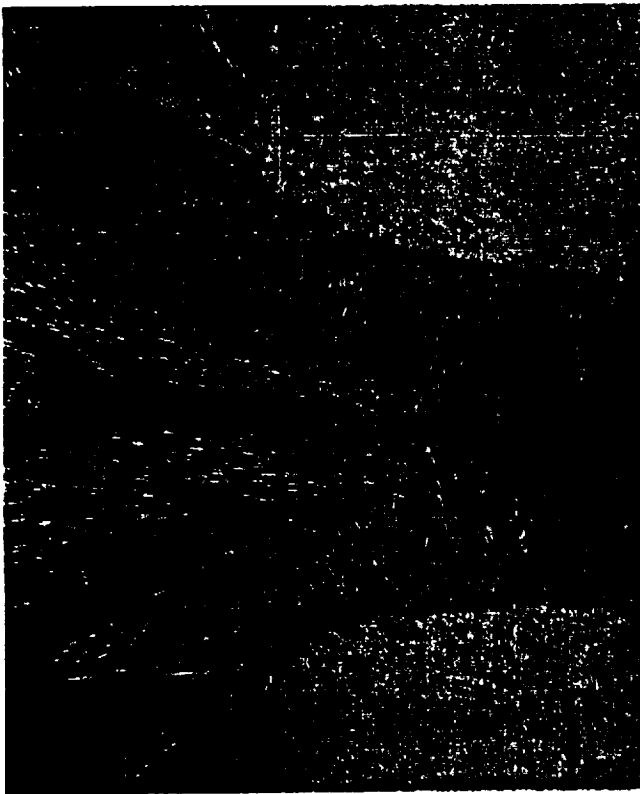
FE625315

Figure 4.1.2-8. Inconel 625 Panel Showing Typical Failure Due to the Explosion Forming Process

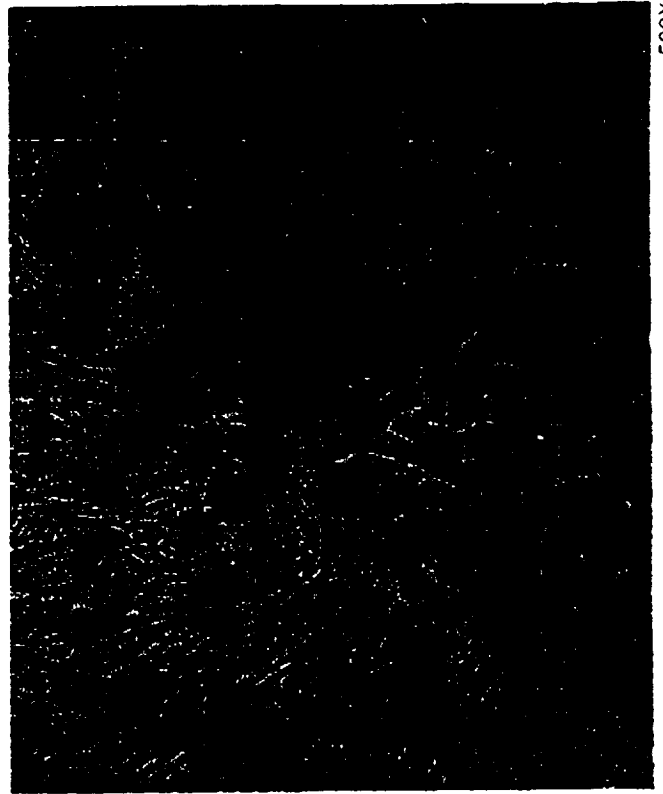


14613

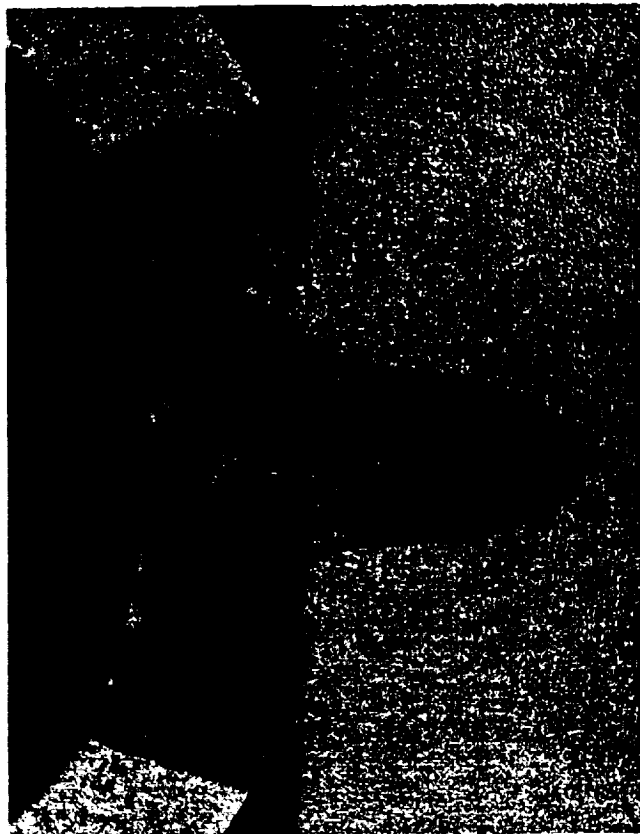
Figure 4.1.2-9. Random Cross-Sections Taken through an Explosion Formed Inconel 625 Panel



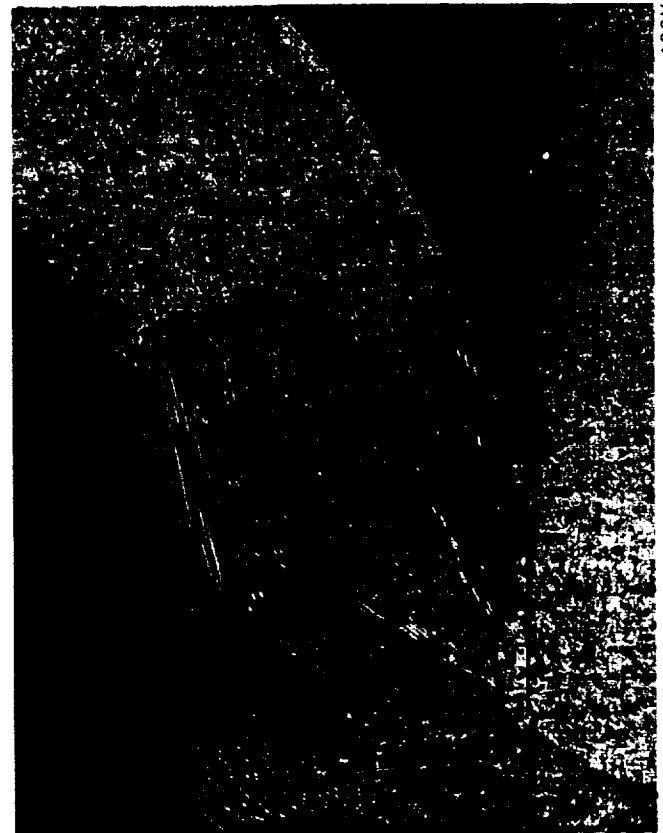
100X



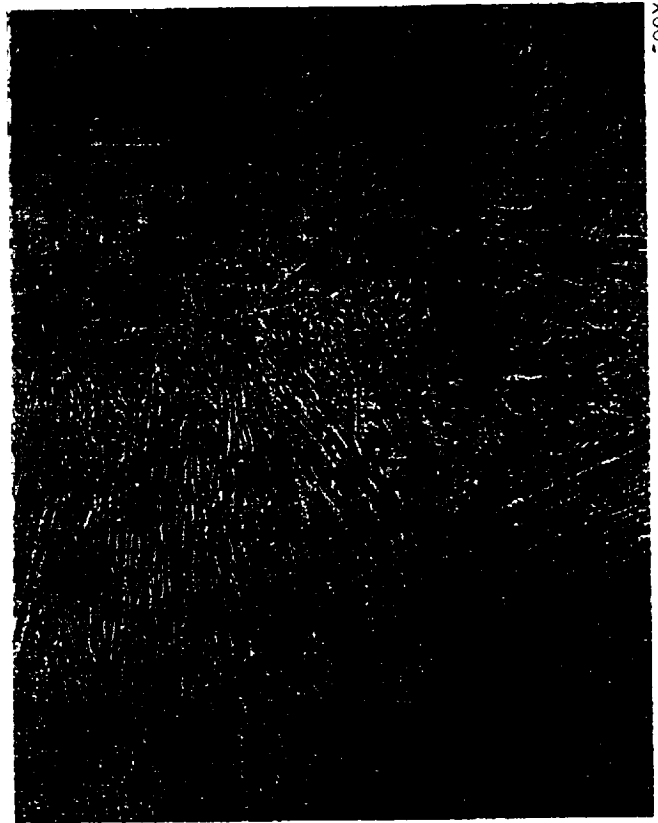
500X



50X



100X



4616

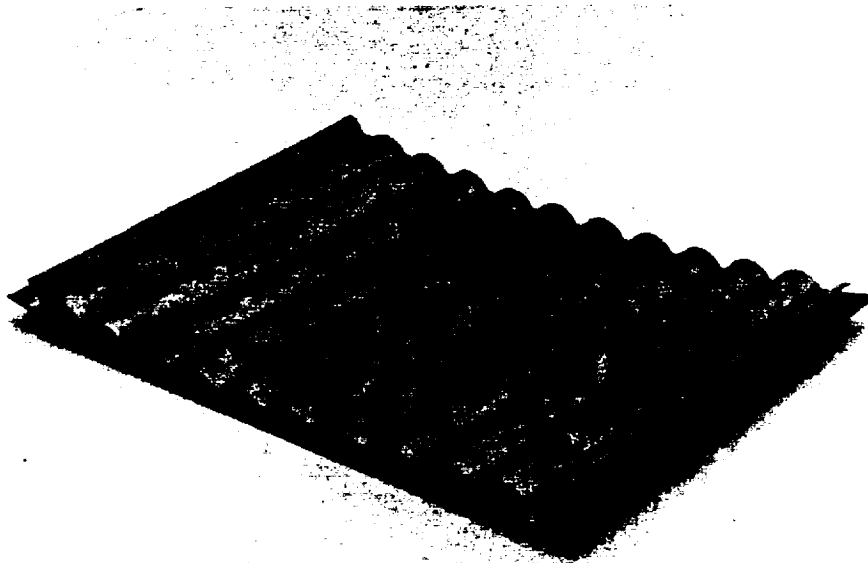
Figure 4.1.2-11. Inconel 625 (a) Explosion Formed and Laser Welded





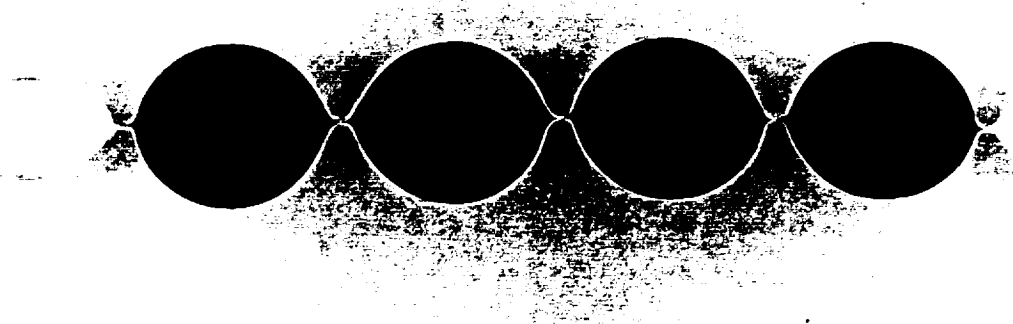
FE02681

Figure 4.1.2-12. Explosion Formed/Laser Welded Sample



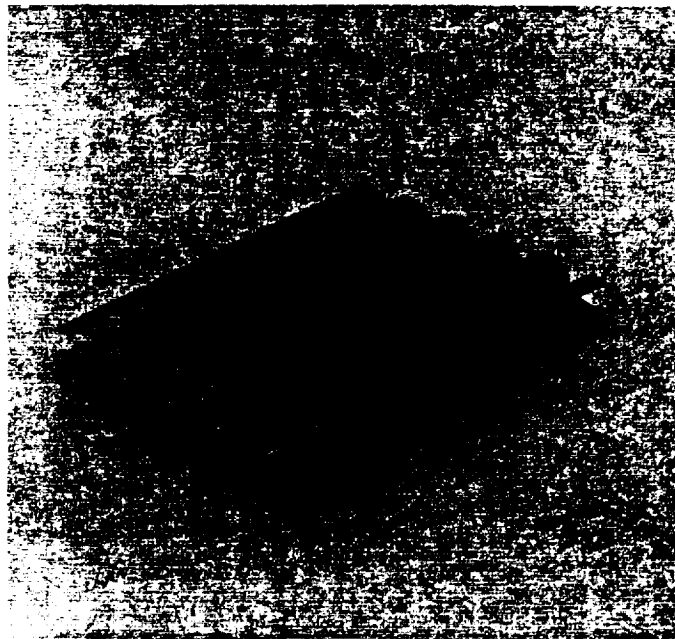
FE026878

Figure 4.1.2-13. Explosion Formed/Laser Welded Sample



FE026880

Figure 4.1.2-14. Explosion Formed/Laser Welded Double-Convolutd Sample



FE026879

Figure 4.1.2-15. Explosion Formed/Laser Welded Double-Convolutd Sample

4.1.2.2 Laser Welded/Inflation Formed Sheetmetal

The first sample (Figure 4.1.2-16) was used to test the inflation apparatus and the test specimen configuration. The laser weld land width of 0.060 inch was selected based on heat transfer requirements. Testing of the first sample proved that the sensitivity of the pressure gauges is critical to proper inflation forming, especially during the initial introduction of pressure. The first sample inflation formed to a height of 0.160 inch before rupture occurred in the welds due to the pressure increasing at a rate that was more rapid than intended. Metallographic evaluation of the welds before and after inflation form indicated that the welds were severely damaged by the forming process and that signs of excessive strain rate were present (Figure 4.1.2-17). Failure initiated at the high stress concentration point between the sheetmetal that simulates the nozzle hot wall and the plate that simulates the nozzle structural jacket, and propagated through interdendritic tears in the weld metal (Figure 4.1.2-18).

The second sample was intended as an upper limit screening test of the inflation forming process on Haynes 230. The intent of the test was to determine if the sheetmetal would form to a height of 0.620 inch using the highest temperature (2150°F) at the lowest practical strain rate for forming (10 psi increase in pressure every five minutes). Results of the second test indicated that a change in specimen design was required to accommodate the method of gas introduction into the convolutes. The specimen redesign was completed and incorporated into the remaining specimens. Rupture of the second specimen occurred at 70 psi in the areas where the laser welds are terminated (at the bifurcation point) on the sample (Figure 4.1.2-19). The convolutes reached a height of 0.150 inch before rupture occurred.

The first two Haynes 230 LW/IF test specimens were completed using a 0.060-inch weld land width. The first sample was inflation formed to a height of 0.160 inch before rupture occurred in the welds due to an abnormally high rate of pressure increase during the test. Metallographic evaluation of the first sample showed that the welds were severely damaged by the forming process and signs of excessive strain rate were present. The failure initiated at the high stress concentration point between the sheetmetal (which simulates the nozzle hot wall) and the plate (which simulates the nozzle structural jacket), and propagated through interdendritic tears in the weld metal.

The second sample was intended as an upper limit screening test of the inflation forming process on Haynes 230. The intent of the test was to determine if the sheetmetal would form to a height of 0.620 inch using the highest temperature (2150°F) at the lowest practical strain rate for forming (10 psi increase in pressure every five minutes). Results of the second test indicated that a change in specimen design was required to accommodate the method of gas introduction into the convolutes. The specimen redesign was completed and incorporated into all future specimens. Rupture of the second specimen occurred at 70 psi in the areas where laser welds are terminated (at the bifurcation point) on the sample shown in Figure 4.1.2-20. The convolutes reached a height of 0.150 inch before rupture occurred. Metallographic evaluation of the specimen has indicated that forming at the slower strain rate eliminates the weld related cracking. However, severe weld heat affected zone and base metal defects are created as shown in Figure 4.1.2-21.

Based upon the unsatisfactory results found from the first two samples as described above, the LW/IF candidate using Haynes 230 is not considered a viable candidate for the full-scale nozzle fabrication method. The first sample indicated that using high strain rates causes fracture in the weld metal and resultant failure between the base metal and the weld. The second sample showed that using slower strain rates shifted the failure location from the weld to the heat affected zone of the base metal, with unacceptable overstress and resultant failure in that region. The two samples failed at total strains much less (approximately 1/5) of the total strain that would be required to achieve 0.620-inch passage height configuration. Based upon the fabrication trial results described above, Haynes 230 was not continued as a candidate for the LW/IF process.

Three of the Inconel 625 LW/IF samples completed testing, at an inflation rate of 10 psi/5 minutes at 1800°F. The first sample ruptured at an area of incomplete weld penetration in one of the welds, shown in Figure

4.1.2-22, after reaching a height of 0.210 inch. The incomplete penetration in the weld was caused by improper focusing of the laser beam onto the workpiece. Metallographic evaluation of the welds revealed cracking in the heat affected zone of the welds, as shown in Figure 4.1.2-23.

The second sample was a repetition of the first sample using the proper laser beam focus. This sample inflated to a height of 0.225 inch before rupture. Metallographic evaluation of the welds also revealed cracking in the heat affected zone as shown in Figure 4.1.2-24, in much the same manner as the first.

The third sample was completed using the same forming parameters as the first, but with a special form of Inconel 625 known as Low Cycle Fatigue (LCF) Inconel 625. This material is reported to have improved LCF capabilities and was expected to be an improvement in ductility at elevated temperatures compared to the conventional Inconel 625. This third sample inflated to a height of 0.390 inch before rupture occurred, which is the best inflation performance of any material to date, shown in Figures 4.1.2-25 and 4.1.2-26. Results of the metallographic evaluation are pending.

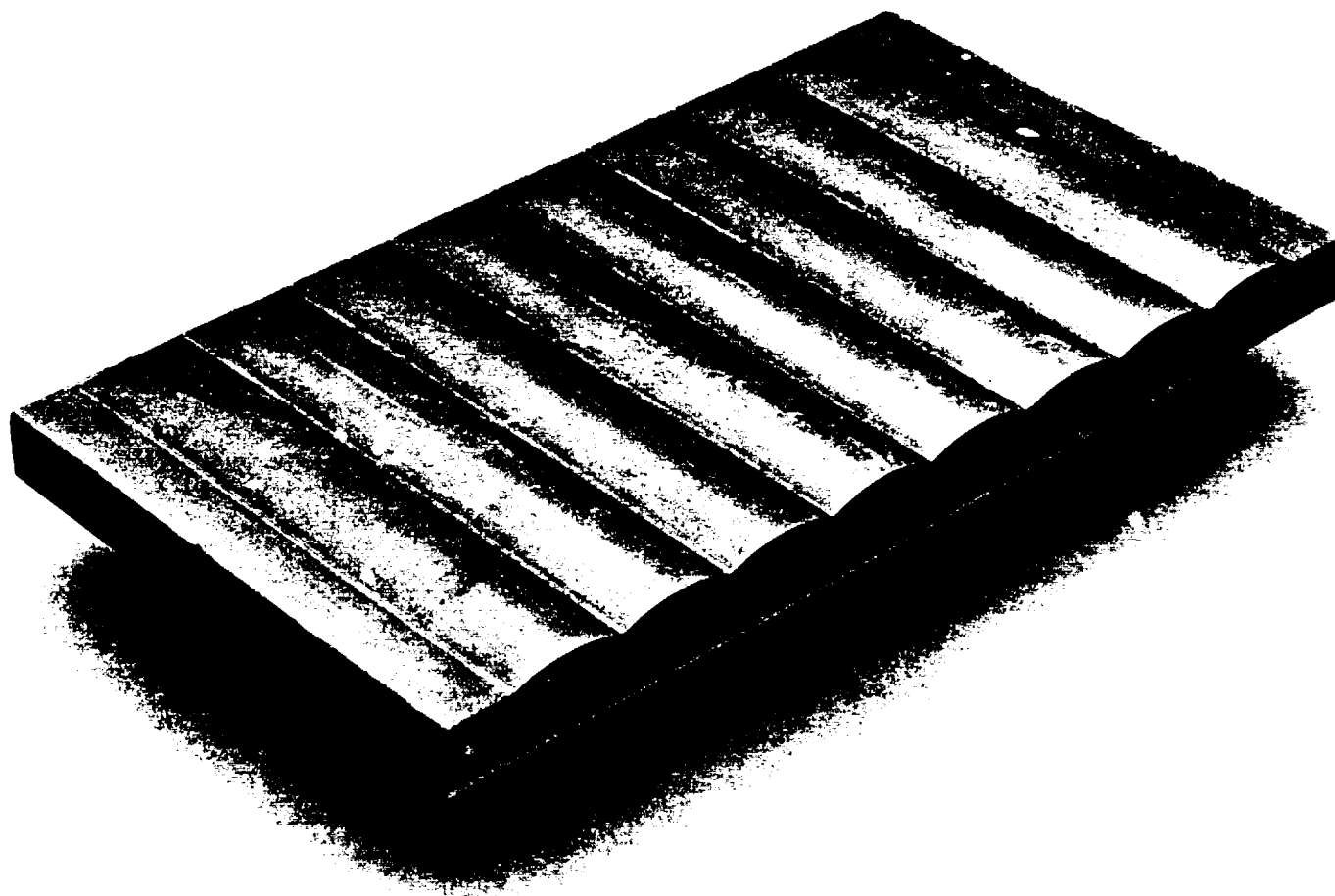
A sample using 300 series stainless steel was performed to investigate the Aerojet (Babcock & Wilcox) sheetmetal nozzle fabrication demonstration configuration. Because limited data is available on the Aerojet concept, a concept demonstration was performed with the 300 series stainless to verify the feasibility of the Aerojet process.

The sample was inflated at 1800°F at a rate of 10 psi/5 minutes. The sample inflated to a height of 0.340 inch before rupture, which is 0.040 to 0.090-inch higher than the Aerojet design. A preliminary strain calculation was performed to compare the two design concepts, and it was determined that the Pratt & Whitney concept using 1.2 x 0.620-inch passages undergoes roughly four times the total strain of the Aerojet 1.25 x 0.25-inch passages. The difference in passage geometry is significant in terms of the degree to which the sheetmetal must stretch to reach the desired height. This last sample, shown in Figures 4.1.2-27 and 4.1.2-28, also showed that the process reaches a configuration limit in the neighborhood of aspect ratios at about 4:1.

Metallographic evaluation of the 347 stainless steel sample, which was performed to investigate a welded/inflation formed concept similar to that studied by Aerojet in their Thrust Chamber Technology ADP contract, was completed. The investigation shows that fracture occurred in the high stress concentration interface at the weld location. Results of the metallographic evaluation are shown in Figures 4.1.2-29 and 4.1.2-30.

All of the screening trials performed using LW/IF concepts show unsatisfactory results at passage aspect ratios at about 2:1. The full-scale nozzle passage geometry for the sheetmetal configurations is not conducive to the LW/IF process due to the reduced parent material properties near the weld before forming, and the high strain experienced at these locations. Based upon the fabrication trial results and the full-scale nozzle preliminary design and manufacturing planning studies, the LW/IF concepts will no longer be considered a viable fabrication process candidate.

As discussed in the previous bimonthly report, all screening trials performed using laser welded/inflation formed (LW/IF) concepts show unsatisfactory results at passage aspect ratios at about 4:1. The full-scale nozzle passage geometry for the sheetmetal configurations is not conducive to the LW/IF process due to the reduced parent material properties near the weld before forming and the high strain experienced at these locations. Based upon the fabrication trial results and the full-scale nozzle preliminary design and manufacturing planning studies, the LW/IF concepts will no longer be considered as a viable fabrication process candidate.



FE621172

Figure 4.1.2-16. Haynes 230 Laser Welded/Inflation Formed Test Specimen (6-inch × 12-inch)

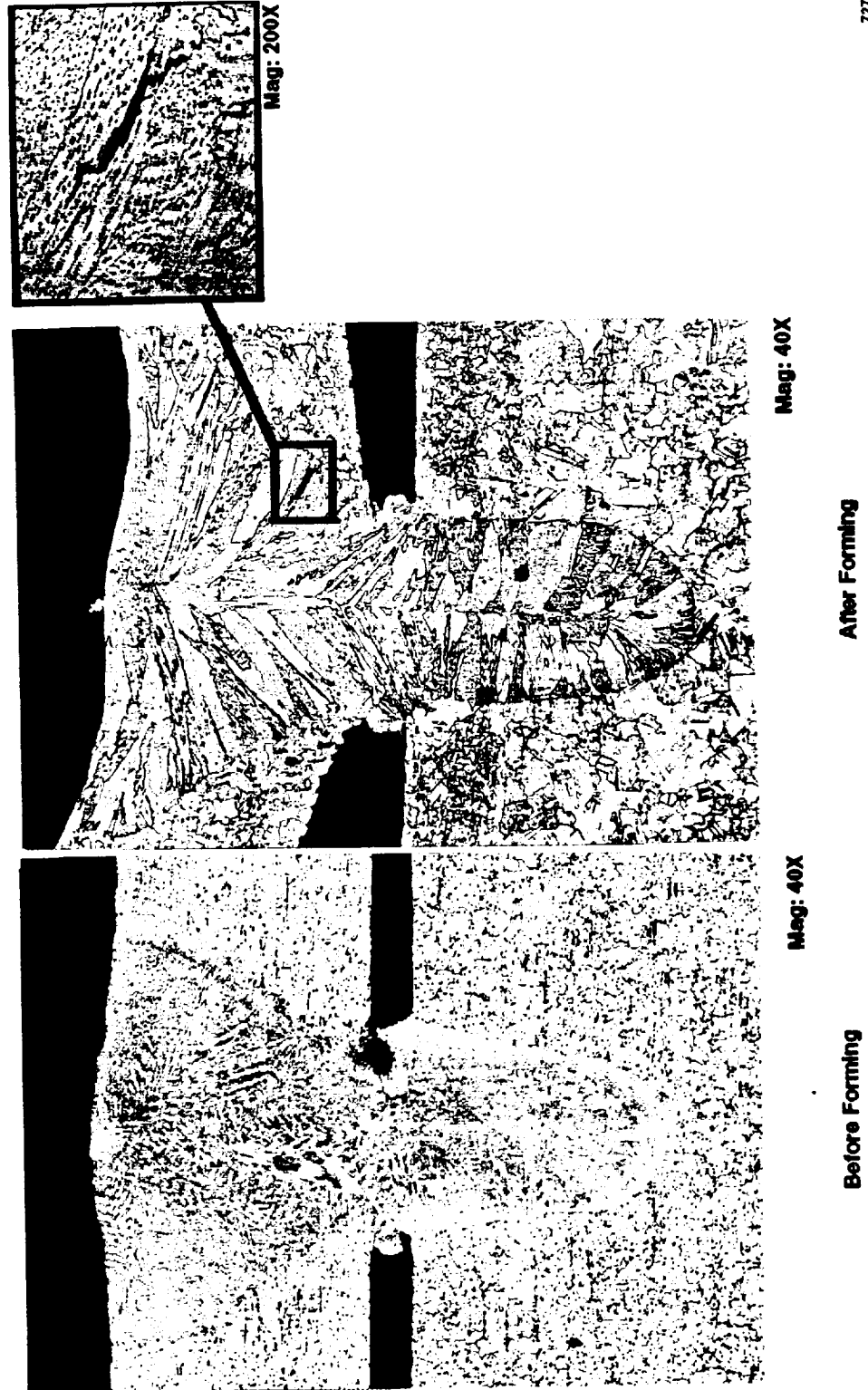
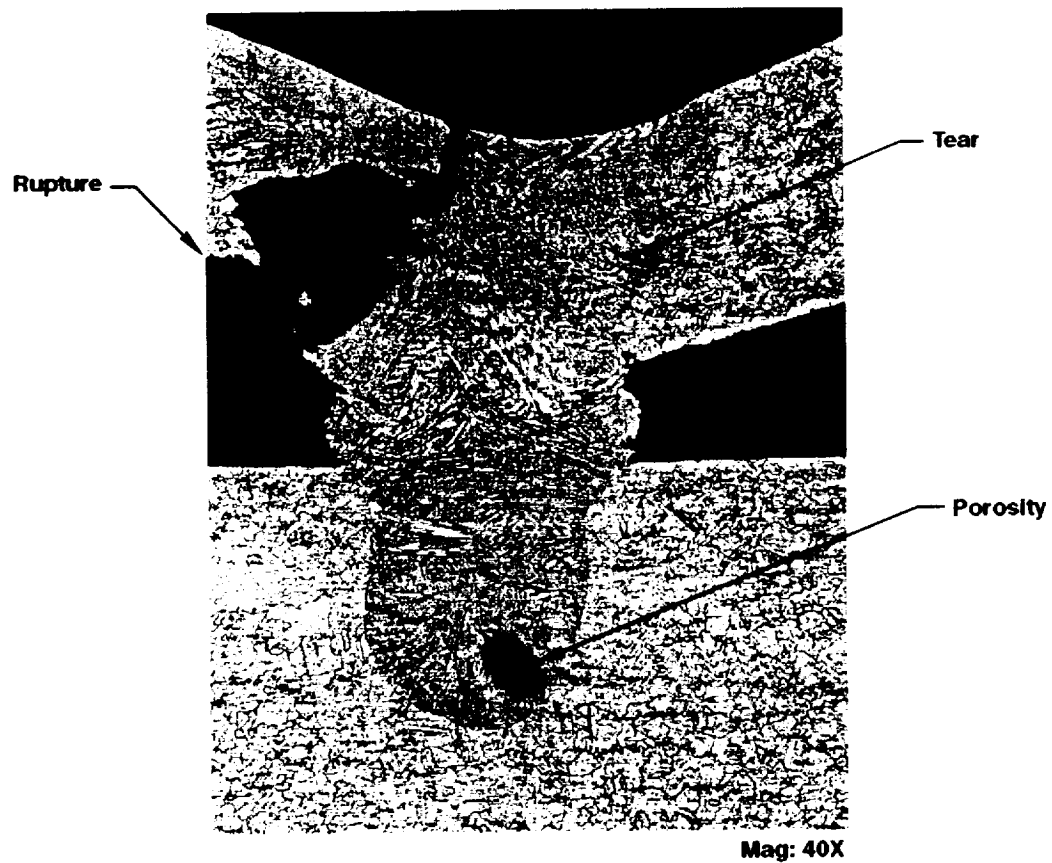


Figure 4.1.2-17. Photomicrograph of Haynes 230 Laser Welds Before and After Inflation Forming Showing Inflation Caused by the Forming Process



7278

*Figure 4.1.2-18. Photomicrograph of Laser Weld Rupture
Caused by Inflation Forming Process (Material = Haynes 230)*



Figure 4.1.2-19. Haynes 230 Laser Welded/Inflated Formed Sample Showing Rupture at Bifurcation Point



F021008

Figure 4.1.2-20. Laser Welded/Inflation Formed Haynes 230 Sample No. 2

FC119230

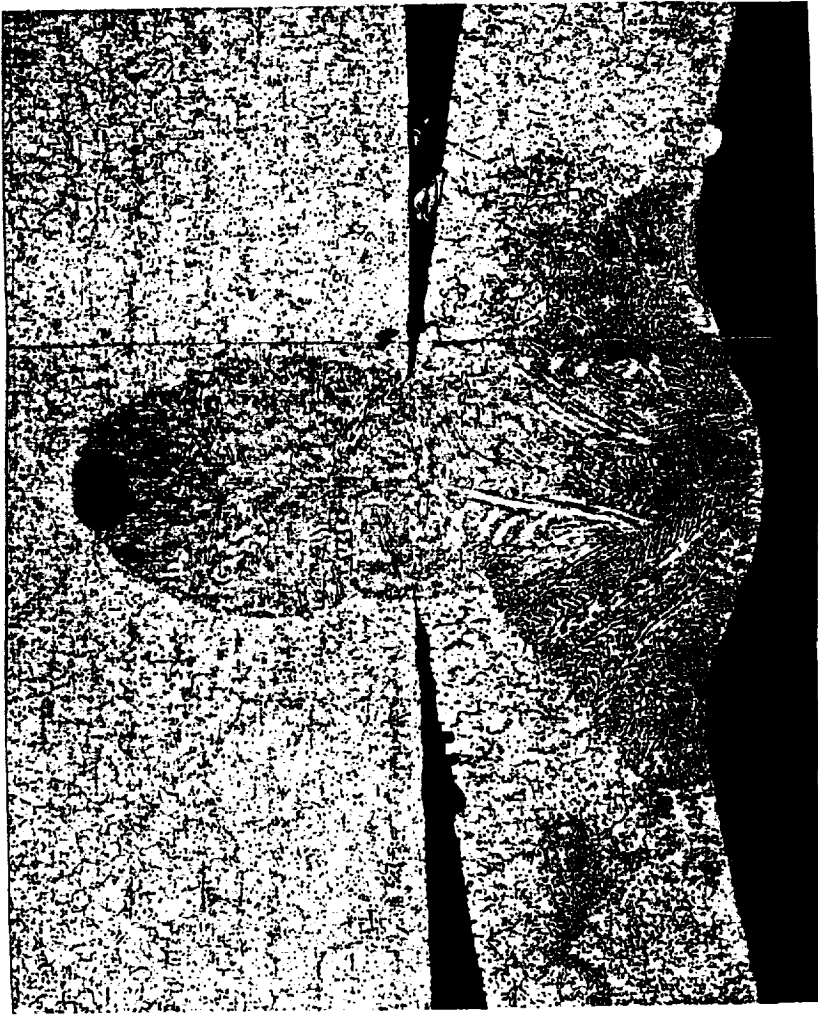


Figure 4.1.2-21. Laser Welded/Inflation [redacted] Haynes 230 Cross-Section Sample No. 2

FE62080

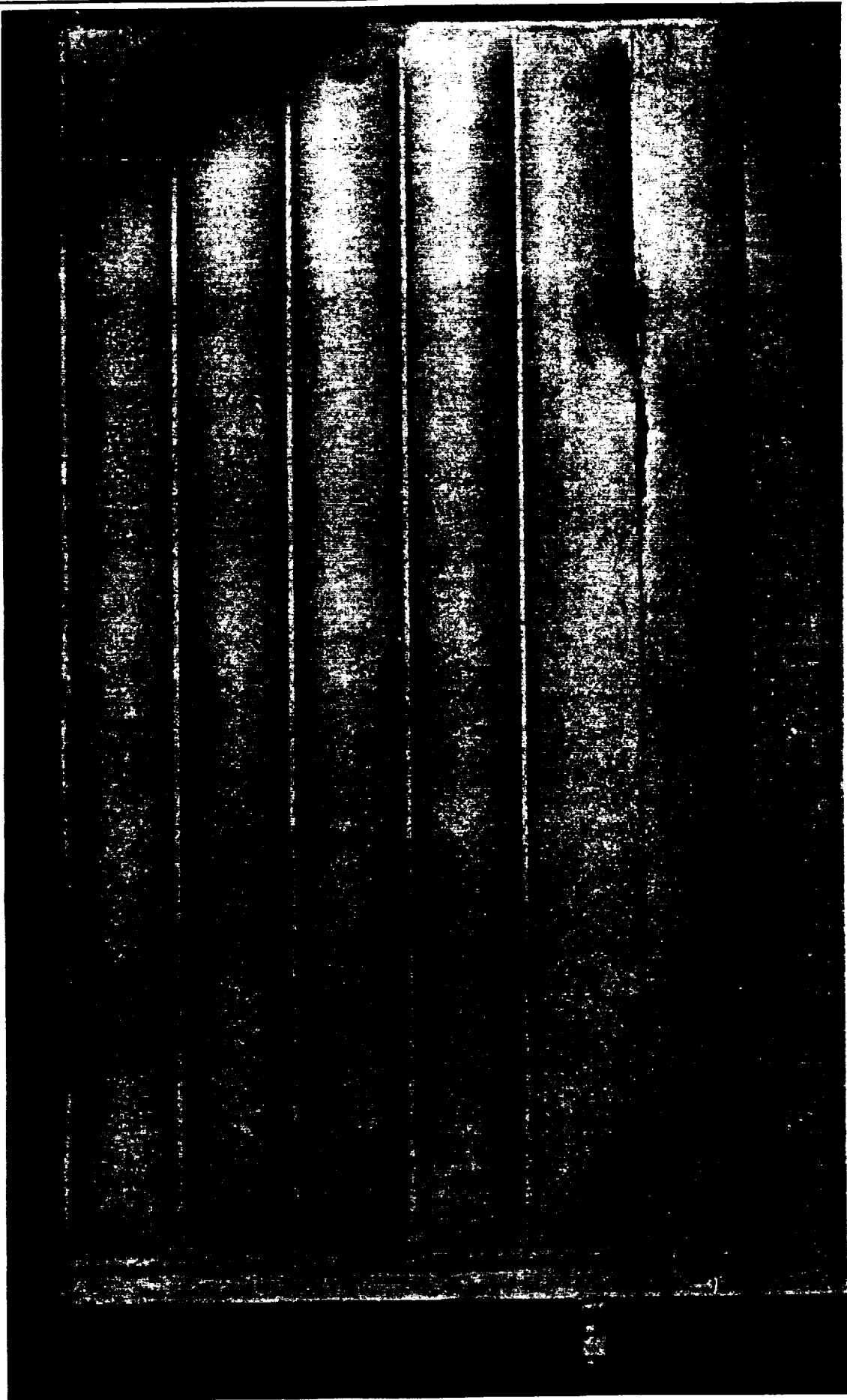
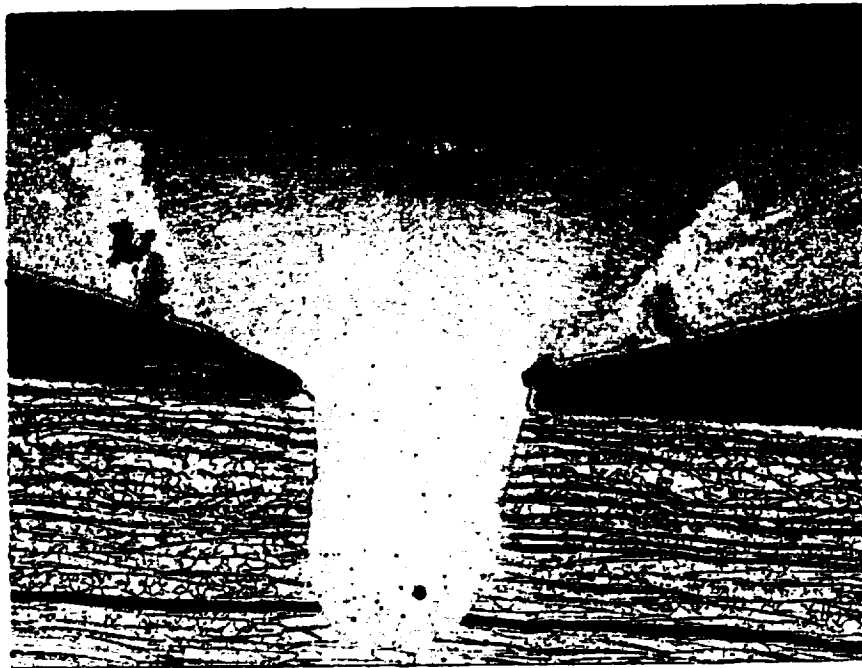


Figure 4.1.2-22. Laser Welded/Inflation Formed Inconel 625



FC119231

Figure 4.1.2-23. Laser Welded/Inflation Formed Inconel 625 Cross-Section Sample No. 1 (40×)



FC119232

Figure 4.1.2-24. Cross-Section Through Laser Welded/Inflation Formed Inconel 625 Sample No. 2 (32×)

FE82524



Figure 4.1.2-25. Laser Welded Inflation Formed "Low-Cycle Fatigue" Inconel 625

FE82314

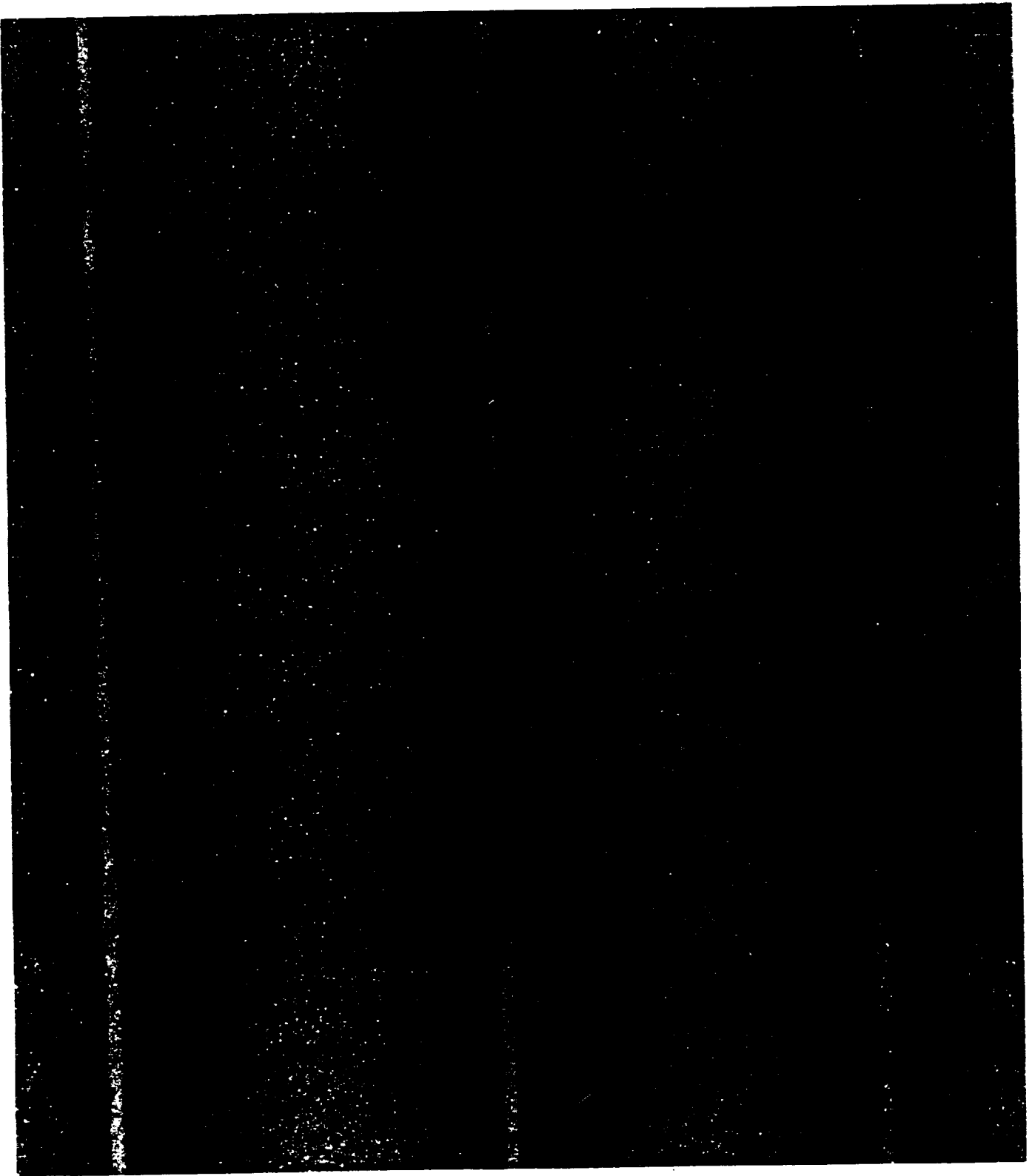
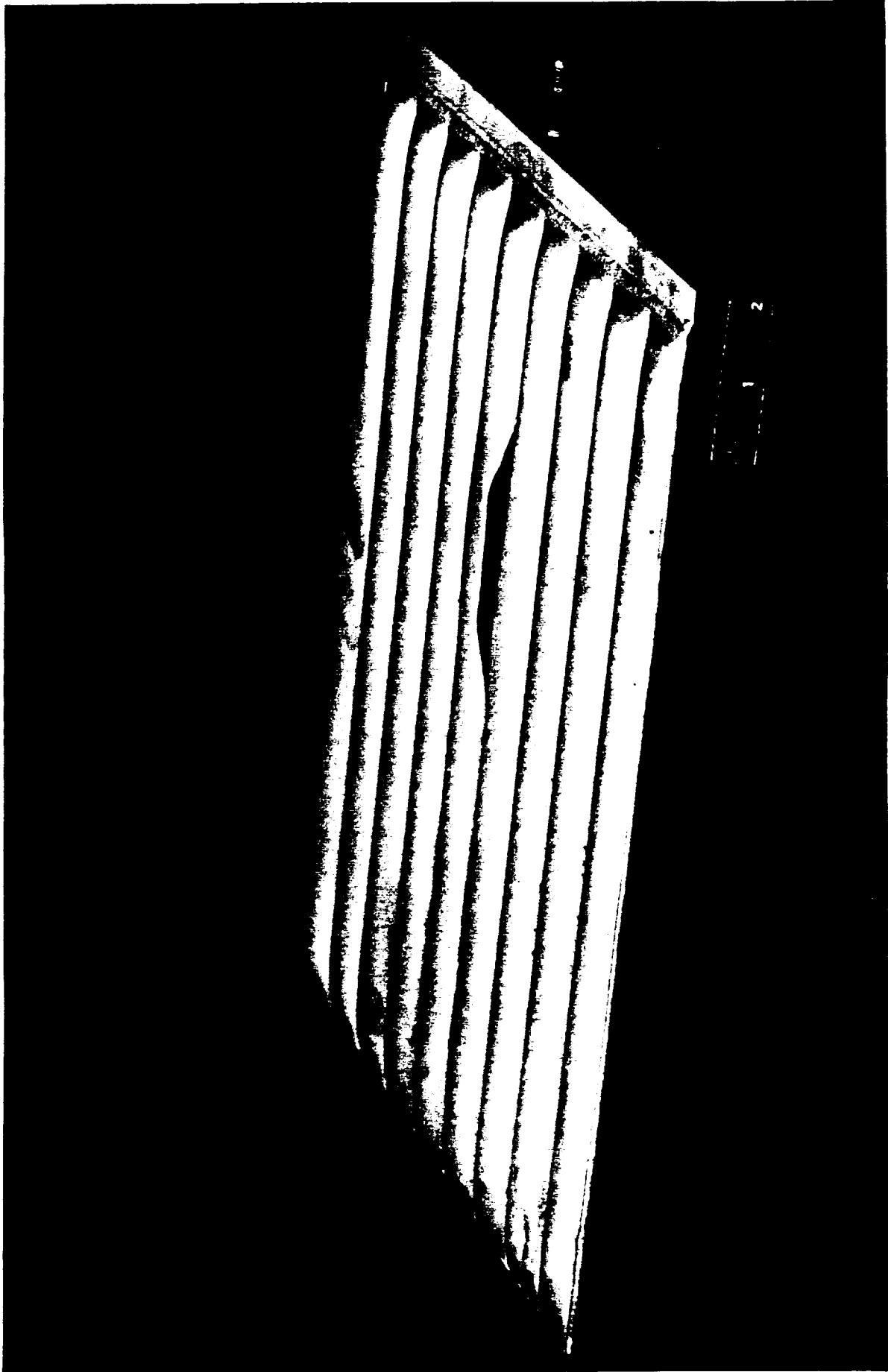


Figure 4.1.2-26. Laser Welded/Inflated Formed "Low-Cycle Fatigue" Inconel 625



FE82209-43

Figure 4.1.2-27. Laser Welded/Inflation Formed 347 Series Stainless Steel



FE82329-50

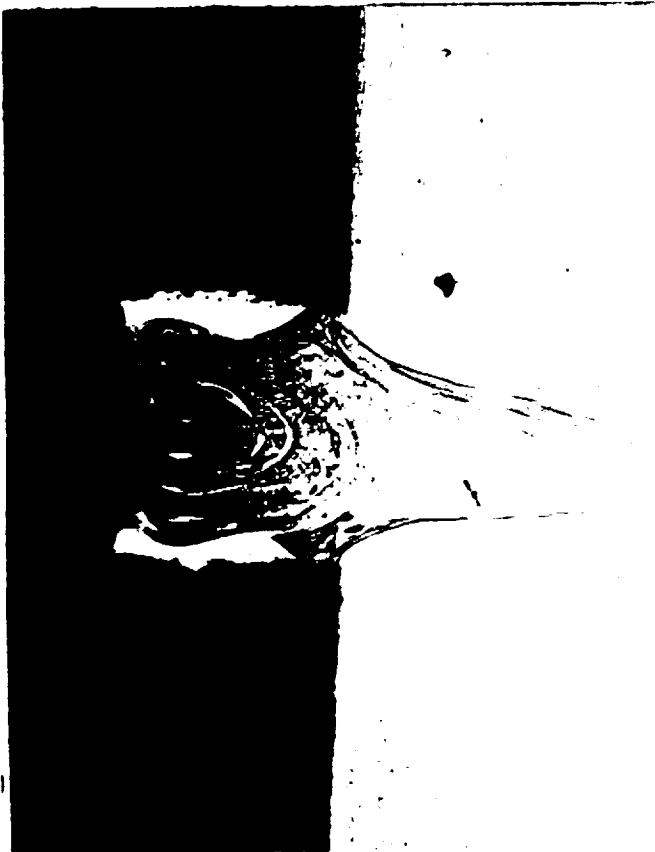
Figure 4.1.2-28. Laser Welded Infil Formed 347 Series Stainless Steel



50X



100X



20X



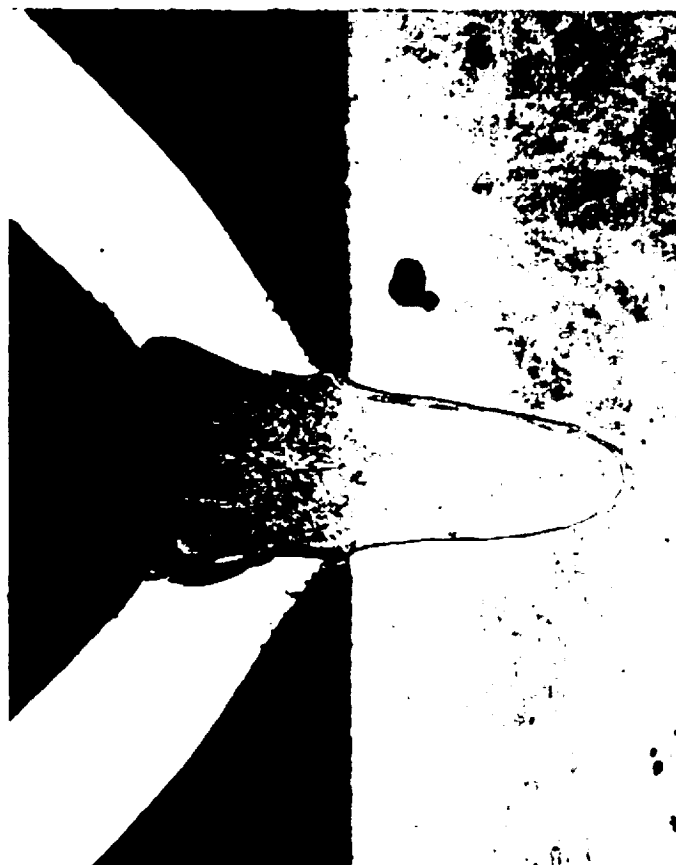
100X



500X



100X



20X



100X

Figure 4-12-20 Laser Welded Inflation Formed 347 SST Sheetmetal Sample

4.1.2.3 Diffusion Bonded/Inflation Formed Sheetmetal

Small samples of the DB/IF sheetmetal fabrication process were fabricated with available molybdenum tooling material. The molybdenum tooling is used in the small samples because it is a high strength, low alpha material that provides the high diffusion bonding pressure at a high temperature in lieu of a high temperature hydraulic press. The required forming temperature of Haynes 230 is 2150°F, which prohibited using the existing hydraulic press that has a temperature capability of 1850°F. The molybdenum tooling provided the bonding pressure between the sheetmetal parts by clamping the two tooling plates around the test specimen.

Four small samples were tested: two Haynes 230 and two LCF Inconel 625 samples. All will be diffusion bonded in a vacuum and then inflation formed in a hydrogen retort. One of each of the different materials will be inflated in a slow strain rate and one each at a high strain rate. Results of the first Haynes 230 prematurely failed in a specimen perimeter weld, after the convolutes reached a height of 0.270 inch. The perimeter weld has been repaired and the sample will undergo another inflation cycle to complete the trial. The sample, shown in Figure 4.1.2-31, is before the second inflation cycle.

The larger DB/IF samples had been delayed due to raw material unavailability. However, all raw material has now arrived and the samples are being fabricated. Inconel 625 thus was the only material used in the large DB/IF trials due to the temperature limit of the hydraulic press used to press the material to form the diffusion bonding.

The first larger Inconel 625 DB/IF sample was completed. The sample was diffusion bonded in a hydraulic press at 1800°F for six hours. The sample was mislocated in the press during bonding, which prevented inflation forming of the sample. Metallographic evaluation of the sample shows that good bonding was achieved between the sheetmetal jacket and the liner, as shown in Figure 4.1.2-32. During the bonding process, some plastic deformation of the die was noted. This deformation indicates that a convoluted die for a full-scale nozzle may have a limited life at the high temperature forming environment.

The first small Inconel 625 DB/IF sample was completed as shown in Figure 4.1.2-33. The sample underwent a vacuum diffusion bond cycle at 2000°F for two hours, with bonding pressure applied by Moly tooling. The bonding cycle was followed by an 1800°F inflation form cycle, with pressure increasing 10 psi/5 minutes. During the inflation cycle the specimen ruptured at 390 psi, where the edge of the convoluted tool applied pressure onto the specimen. Visual examination of the sample indicated that no diffusion bonding occurred. The failure to diffusion bond the sample is attributed to the inadequate surface finish and flatness of the sample. The remaining samples were ground flat and parallel within 0.001 inch, and will have a lapped surface finish. The metallographic evaluation of the sample, shown in Figures 4.1.2-34 and 4.1.2-35, confirmed that no diffusion bonding had occurred and that the sheetmetal was damaged by the forming process.

Both of the remaining small Inconel 625 samples were completed with unsuccessful results. Neither sample reached the required convolute height of 0.620 inch before sample rupture occurred, as shown in Figures 4.1.2-36 and 4.1.2-37. The samples also did not diffusion bond, as shown in Figure 4.1.2-38. The metallographic evaluation has shown base metal defects where the tooling force was applied to the sample. Material thinning and porosity is evident in the location of highest stress, which was similar to results found in previous samples.

One of the Haynes 230 samples was completed, but did not achieve the required 0.620-inch height before rupture. The final Haynes 230 DB/IF sample was completed and ready to undergo DB/IF processing. The DB/IF tooling that had been used for all of the samples was experiencing significant plastic deformation, or creep, due to the long duration at high temperature and pressure. Following the Haynes 230 processing, the tool was to be cut up and undergo metallographic evaluation to determine the extent of tooling deformation experienced.

Final evaluation of this process was completed. Based upon unsuccessful results to date, this process has several limitations that make it not a viable candidate for full-scale nozzle fabrication:

1. Zero-gap requirements for bonding to occur. The process is not tolerant of normal sheetmetal surface and dimensional variations. Mating surfaces must be ground flat and parallel within 0.001 inch, with a lapped surface finish. This would require expensive preparation and tooling in the full-scale nozzle.
2. Short tooling life due to plastic deformation, or creep. After a few cycles the tool geometry changes due to creep, rendering the tool unacceptable for further use.
3. High material strain and thinning causes rupture of the material near the tool mating edges. The high aspect ratios (height = 0.62 inch, width = 1.2 inch) of the specimens caused a failure in each trial, before the sheetmetal reached full height.

Further investigation of the laser welded/inflation formed sheetmetal concepts was discontinued as discussed in the preceding section.

FE02528

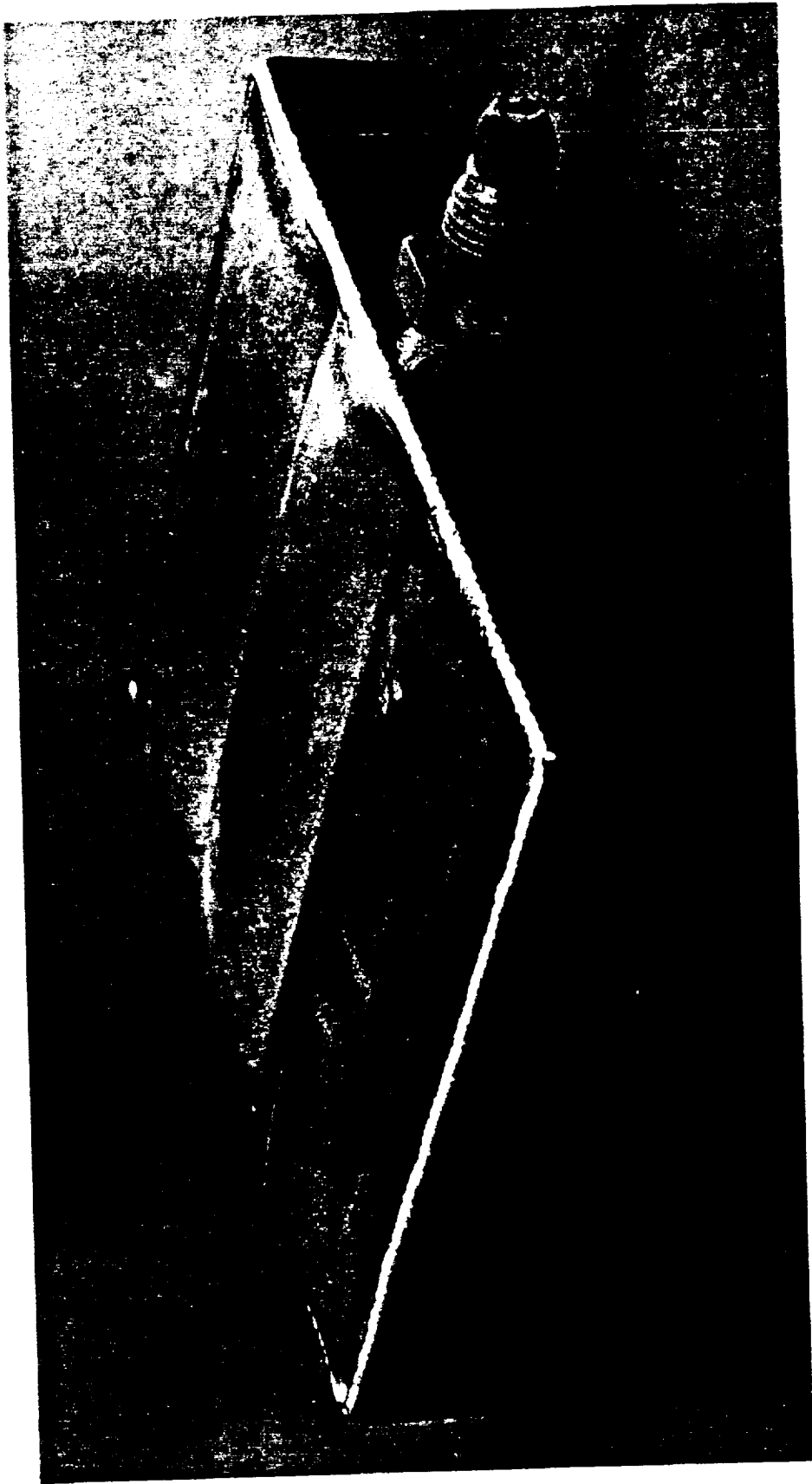


Figure 4.1.2-31. Diffusion Bonded/Inflation Formed Haynes 230 Sample

500X
FC119485

1000X

Figure 4.1.2-32. Diffusion Bonded/Inflation Formed Incorporated 625 Sample Showing Diffusion Bond at 1800°F for 6 Hours

500X

16X

FEB2551-46

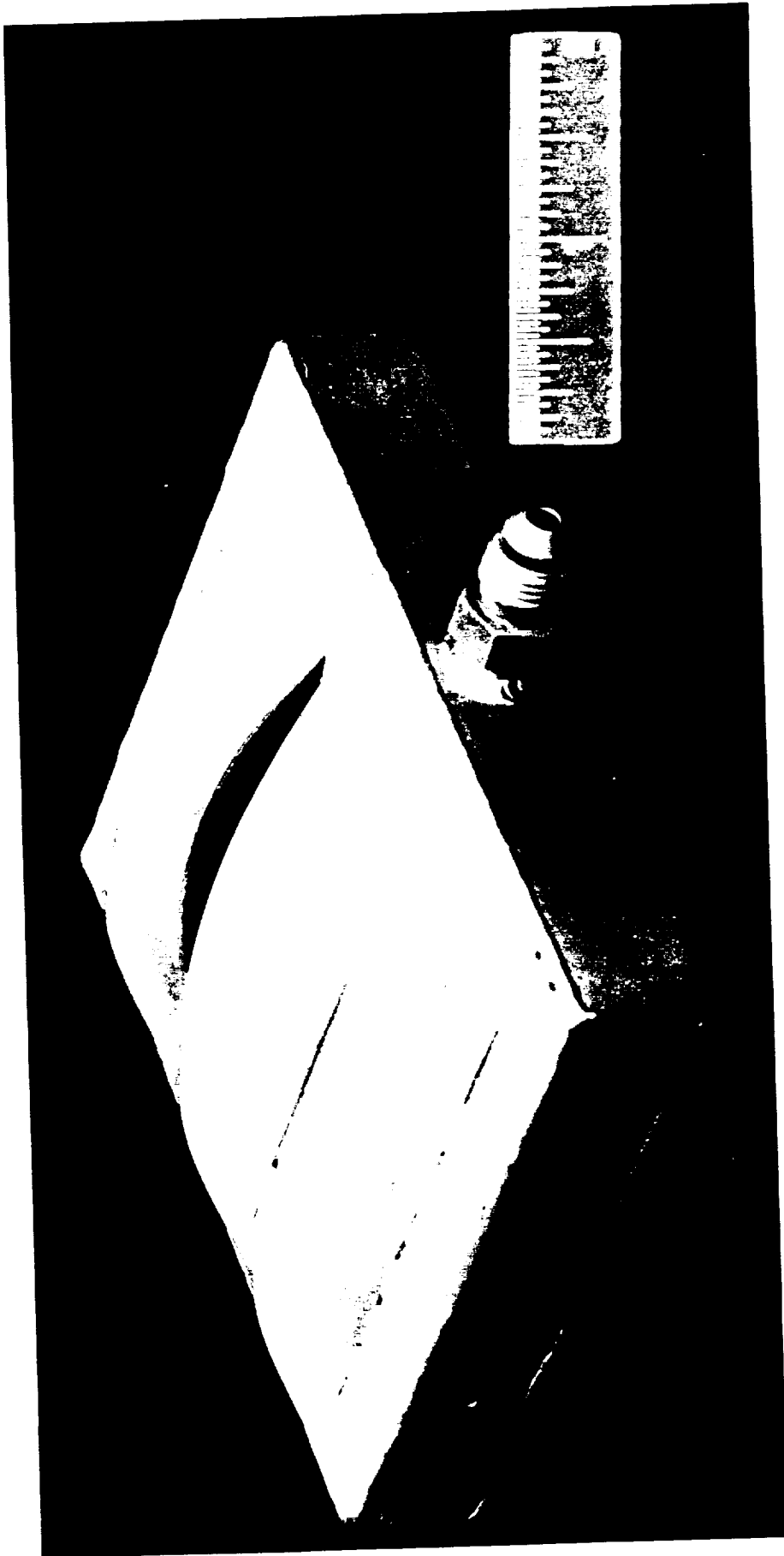


Figure 4.1.2-33. Diffusion Bonded/Inflation Formed Inconel 625 Sample Showing Failure at Diffusion Bond Location

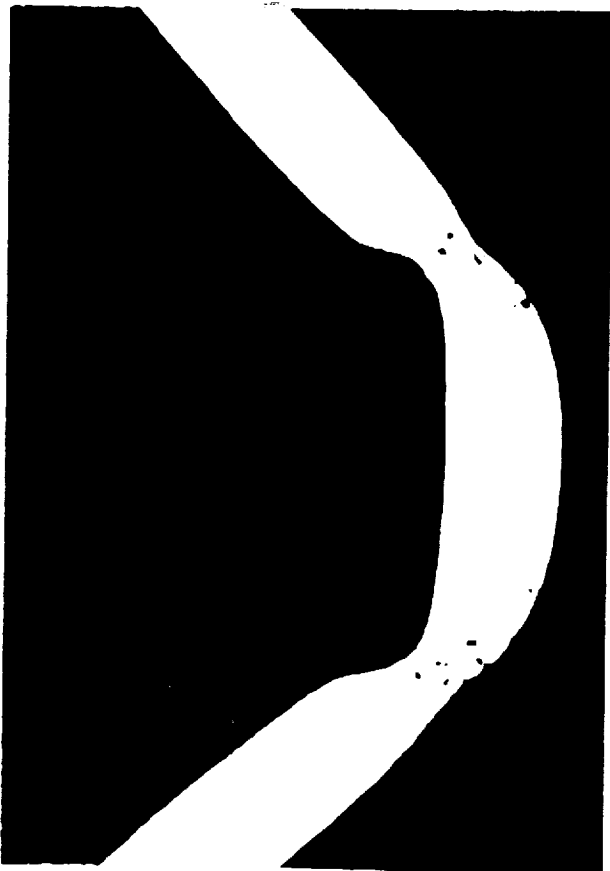


32X



100X

FE119486



20X



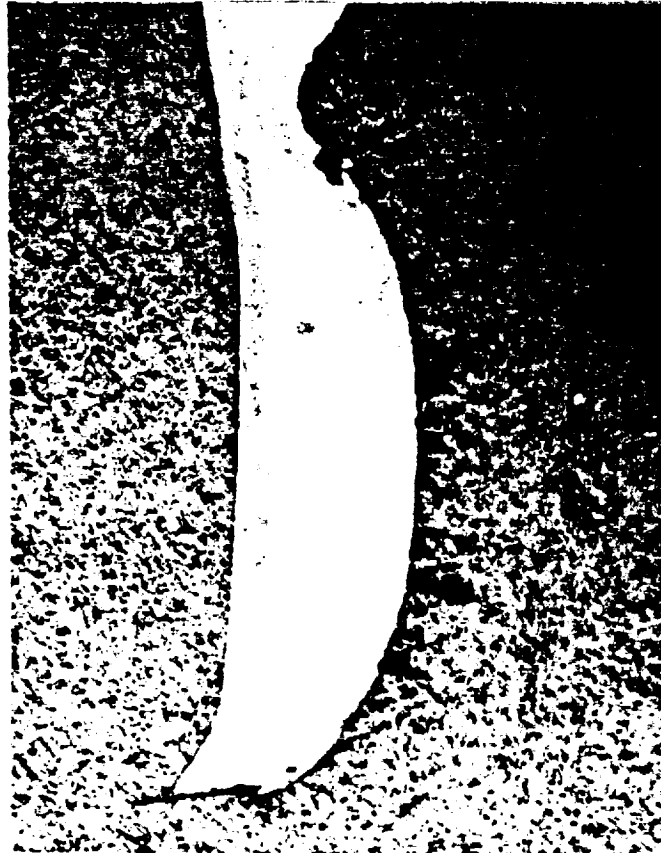
50X

Figure 4.1.2-34. Diffusion Bonded/Inflation Formed Inconel 625 Sample Showing Metal Thinning and No Diffusion Bonding



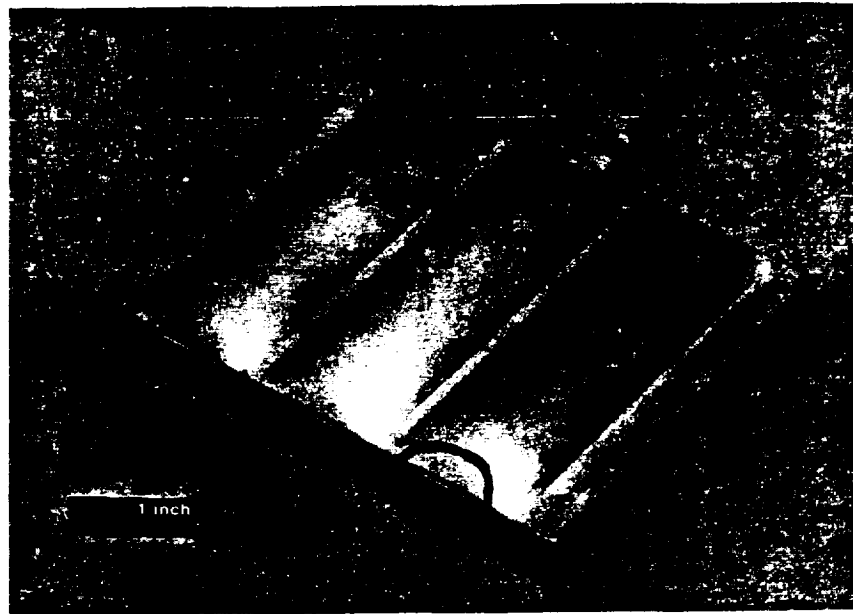
100X

FC119487



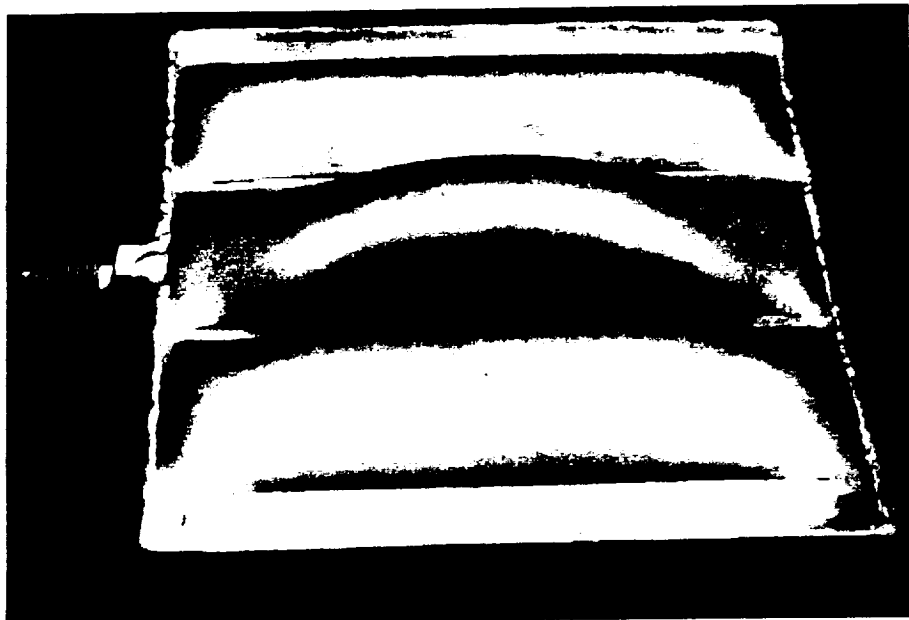
32X

Figure 4.1.2-35. Diffusion Bonded/Inflation Formed Inconel 625 Sample Showing Fracture Due to Thinning



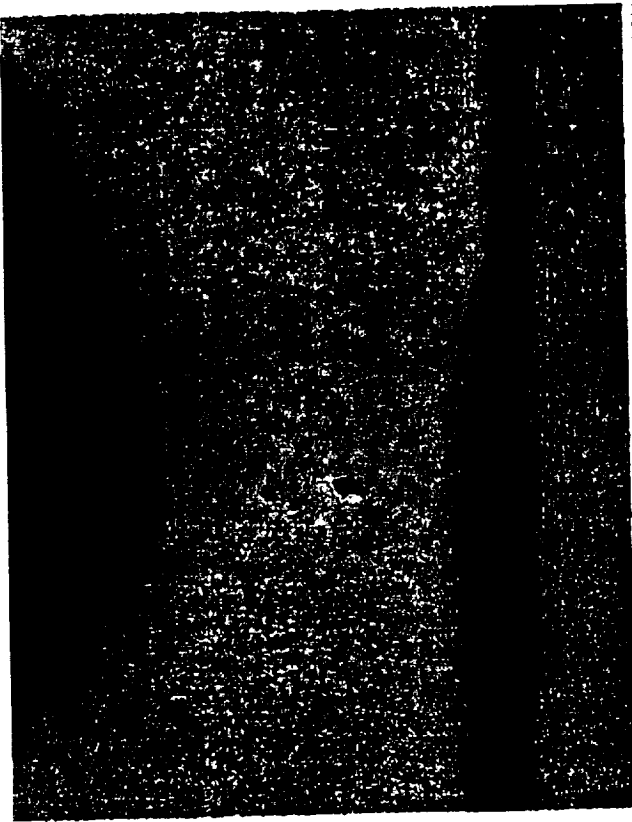
FE025164

Figure 4.1.2-36. Diffusion Bonded/Inflation Formed Sheetmetal Sample Showing Typical Failure in Weld Perimeter Location

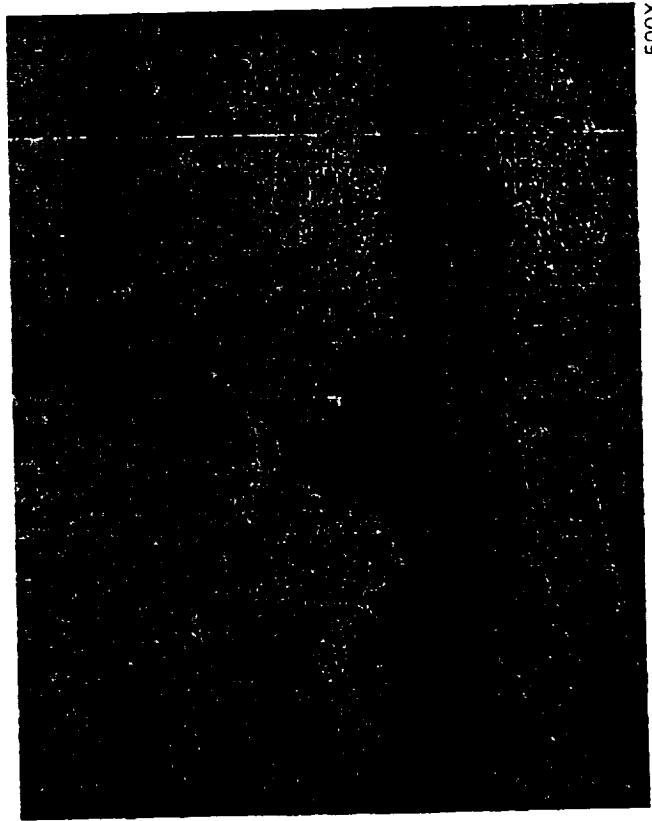


FE024064

Figure 4.1.2-37. Diffusion Bonded/Inflation Formed Sheetmetal Sample Showing Typical Failure Near Bond Location

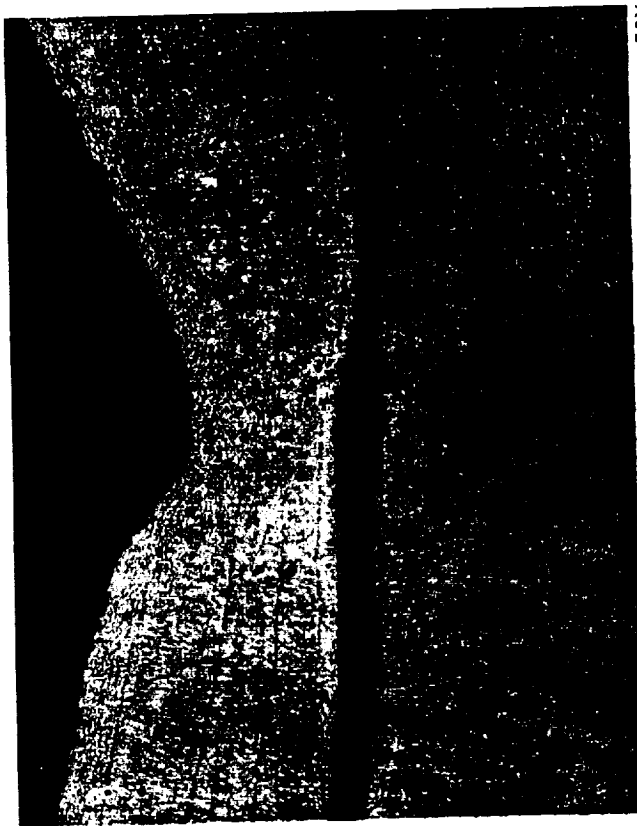


100X

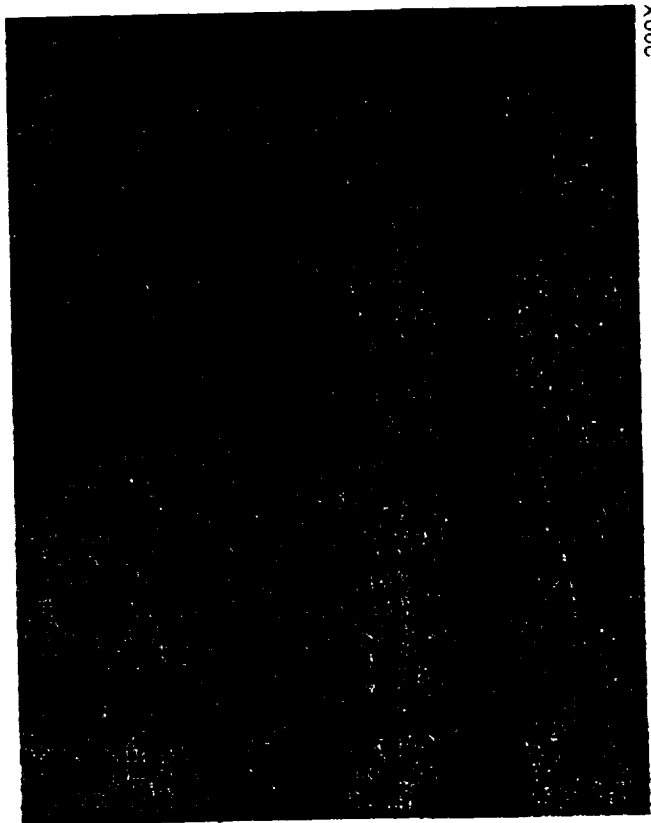


500X

14817



50X



200X

Figure 6 40 Diffusion Bonded Inflation Formed Sheetmetal Sample Showing

4.2 NOZZLE FABRICATION TRIALS — PHASE II

4.2.1 40K Subscale Nozzle Sample

The Phase II sample configuration, which will use a bell-shaped, quarter scale (~40K thrust), full-contour nozzle was established for the second phase of the fabrication trials program. This configuration was the best choice for larger scale samples to mimic large-scale process requirements, tooling designs, tube shape, and fabrication-induced material stresses.

The detailed tool designs were completed for the IF/DB tube, brazed tube, and HIP tube processes. Figure 4.2.1-1 shows the tooling and nozzle assembly design for the IF/DB and brazed nozzles. Both the IF/DB and brazed subscale nozzles will use the same IN100 mandrels. The HIP IF/DB tool design (Figure 4.2.1-2) uses a thinner inner mandrel that is also centrifugally cast IN100. The HIP design does not require an outer mandrel because the pressure acts on all sides of the part, and therefore the tooling is not required to also act as a pressure vessel. IN100 was chosen as the best tool material for the subscale nozzle fabrication processes because of its good creep properties and compatible thermal coefficient of expansion. The best tool material, MAR-M-247, is not readily available in the sizes required for the this tooling, but will be used for the full nozzle fabrication tooling. MAR-M-247 has a significant better creep life than IN100, although the IN100 tooling currently being procured will have a creep life that is more than adequate for the Phase II fabrication trials requirements.

The nozzle Component Development Team completed the Phase I Nozzle Fabrication Trials, the nozzle skirt downselect evaluation process, and the recommendations for Phase II Nozzle Fabrication Trials program. The pros and cons of each fabrication process that was studied in Phase I were discussed, and the conclusions are summarized below:

- All of the major manufacturing technical concerns for each process have been addressed
- Tubular concepts are the most viable, and are applicable to both round and square tubes
- Of the sheetmetal concepts evaluated, only the explosion formed/laser welded concept is producible for the full-scale nozzle
- Key critical process parameters have been identified including temperature, time, cleanliness, passage geometry limitations, and tube gaps for brazing
- Potential inspection techniques have been identified
- Inconel 625 has been selected as the best material choice for all methods
- A preliminary assessment of repairability and reliability has been completed for each process
- The inflation formed/diffusion bonded process using an HIP furnace is the lowest cost option of all processes
- The tubes and jacket hardware for the inflation formed/diffusion bonded process and the brazing process are identical, which allows both processes to be developed on a larger scale in parallel, reducing full-scale nozzle manufacturing risk.

The completed cost analysis and producibility rankings developed for each viable fabrication procedure is shown in Table 4.2.1-1. The inflation formed/brazed tube process using an HIP furnace ranks the highest in producibility and is the second lowest in production unit cost. The inflation formed/diffusion bonded process using an HIP furnace ranks third in producibility but is the lowest in production cost. Both of these processes will require a large HIP furnace in order to meet these projected production costs. A separate study was performed to accurately estimate the costs and resources needed to design, install, and operate this new facility for the nozzle development program. The inflation formed/brazed tubes in a conventional furnace ranks second in producibility but third in production unit cost, and the inflation formed/diffusion bonded process in a conventional furnace ranks fourth in both producibility and unit cost. Both of these processes are higher in cost than the HIP furnace processes because of the difference in recurring tooling costs. The explosion formed/laser welded sheetmetal process ranks fifth in producibility and is also the highest cost option of those studied in Phase I. The bar chart shown in Figure 4.2.1-3 compares all of the skirt fabrication options to a traditionally brazed tube regeneratively cooled nozzle that uses precision tubes and a traditionally high-cost gold braze alloy.

Table 4.2.1-1. Nozzle Skirt Fabrication Options — Producibility Rankings and Costs

<i>Fabrication Procedure</i>	<i>Producibility Ranking</i>	<i>FY91 Cost in \$k - 500th Unit</i>
HIP Inflation Formed/Brazed Tubes	1	576k
Inflation Formed/Brazed Tubes	2	634k
Inflation Formed/Diffusion Bonded Tubes in an HIP Furnace	3	564k
Inflation Formed/Diffusion Bonded Tubes in a Conventional Furnace	4	717k
Explosive Formed/Laser Welded Sheetmetal	5	1147k

Based upon the results of the Phase I fabrication trials and the nozzle skirt evaluation process conducted in the Phase B preliminary design study, the inflation formed/diffusion bonded and brazed processes were selected for further fabrication trials in Phase II. All of the sheetmetal concepts as well as the thermal sprayed tube concepts will not be pursued due to higher cost and feasibility problems.

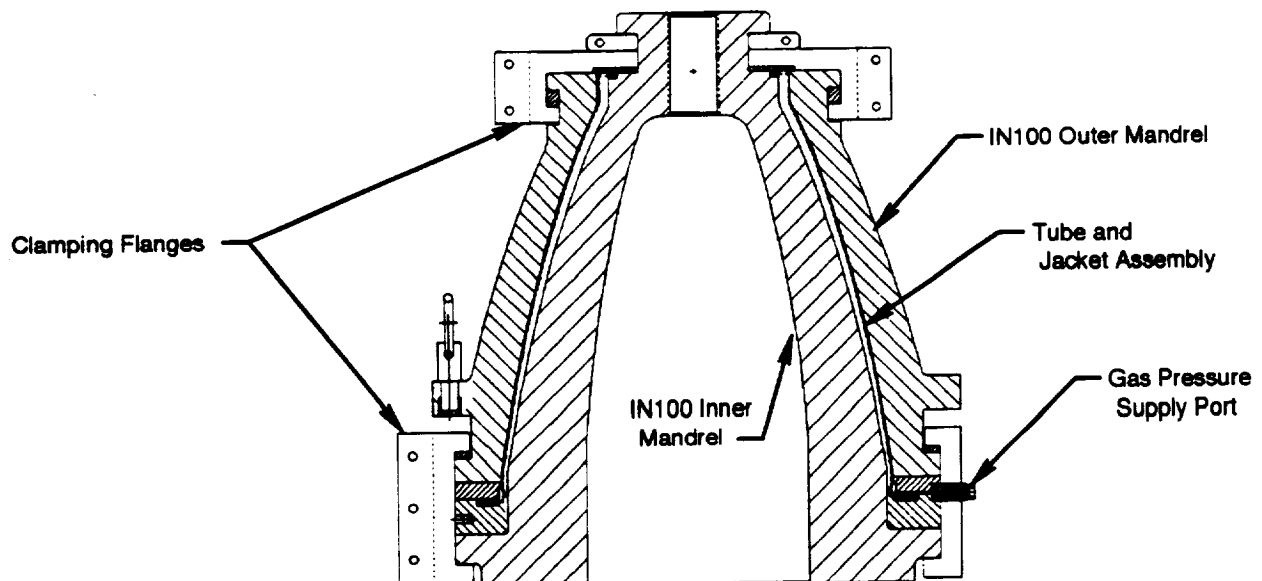
The subscale nozzles, 40K size manufacturing technology demonstrators (40K MTD) that are approximately one-quarter scale of the full-size STME nozzle are shown again in Figures 4.2.1-1 and 4.2.1-2. Both the inflation-formed diffusion-bonded sample using an HIP furnace and the inflation-formed brazed sample using a conventional HIP furnace were to be fabricated in Phase II. The tooling mandrels for the IF/Braze process are made of centrifugally-cast IN-100 material. The HIP mandrel is made of centrifugal cast Inconel 625. The structural jackets for the 40K MTD nozzles were fabricated in the P&W shop. The Inconel 625 round tubes were received and formed to the finished square cross-section geometry and nozzle contour. The tube dies were completed in the P&W tool shop. Due to the long lead time associated with the tooling mandrels for the 40K MTD nozzles and the uncertainty of the optimized inflation formed/braze process parameters, additional samples were designed and procured before assembly of the 40K MTD nozzles.

These new samples were to optimize inflation forming/braze process parameters before building the 40K MTD nozzles, so that all of the processing variables (pressure, temperature, time, and pressure ramp rate) are optimized and sensitivity to the various parameters are identified and controlled. The proposed sample design is shown in Figure 4.2.1-4. It is a cylindrical, constant tube cross-section, a short version of the nozzle assembly that simulates tooling, end caps, and pressurization and fabrication methods in either a full- or partial-hoop design. The cylindrical samples were to use IN-100 forgings with grain size modified to simulate cast properties, constant cross-section rectangular Inconel 625 tubes, and a cylindrical sheetmetal structural jacket. All other

details are similar to the 40K MTD nozzles, including the method of pressurization and the tube end caps. Phase II plans were for two complete cylindrical sample tooling assemblies. The number and type of samples to be fabricated was determined by using Design of Experiments (DOX) based on Taguchi techniques to achieve the minimum number of tests required to incorporate all process variables and their interactions.

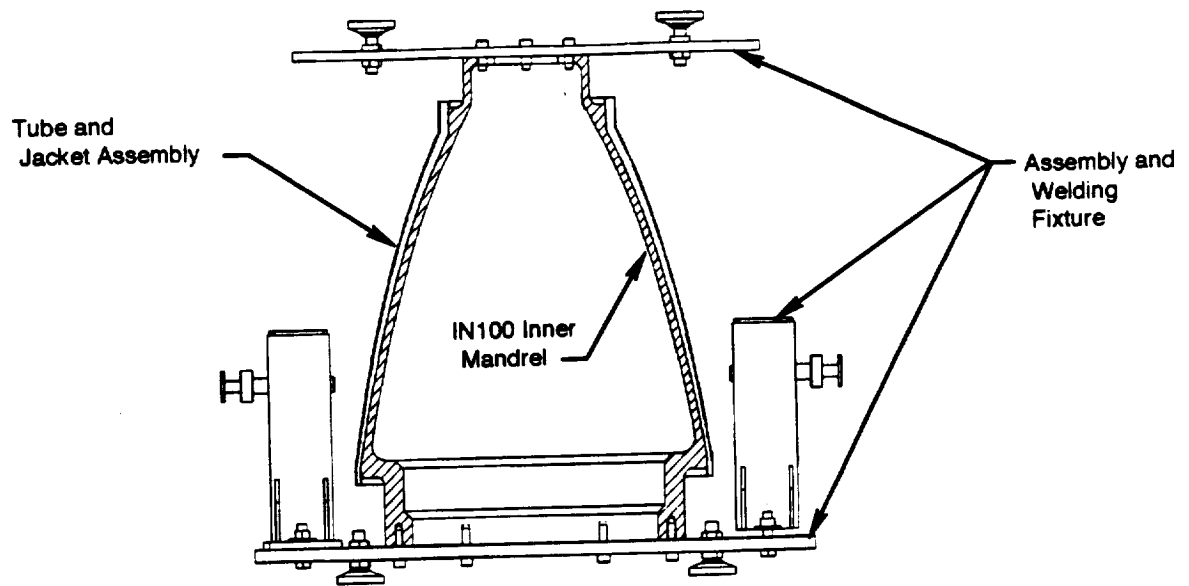
Additional process information was obtained for tube forming parameters using single-tube sample testing conducted in an HIP furnace. The proposed single-tube forming sample design is shown in Figure 4.2.1-5, and includes a single rectangular constant cross-section tube inserted in a tooling block that has a pre-cut hole that simulates the finished (after inflation-forming/brazing) dimensions of the full-scale nozzle near the front end. Small shims were tack welded to the tube sides near the ends before it is inserted into the tooling block, and the tube will then be welded to the ends of the tooling block. The shims provide a known offset of the tube to the tooling block, providing forming information for various gap sizes that could be expected in full-scale nozzle fabrication. The front end geometry was selected because it will be the most difficult to form in order to close down gaps in the diametral fit-ups (tooling inner mandrel outer diameter [OD] fit-up with tube inner surface, and tube outer surface fit-up with structural jacket inner diameter [ID] surface). These single-tube samples were fabricated and processed to gather information on requirements for successfully inflating tubes to achieve proper braze fit-up, and to narrow the temperature, time, and pressure ranges in the cylindrical sample experiments using low cost, rapid turnaround samples.

Based upon results of the Phase I fabrication trials and the nozzle skirt evaluation conducted in the Phase B preliminary design study, the IF/DB and the brazed processes were selected for further fabrication trials in Phase II. Sheetmetal and thermal-sprayed tube concepts were not pursued due to higher cost and feasibility problems.



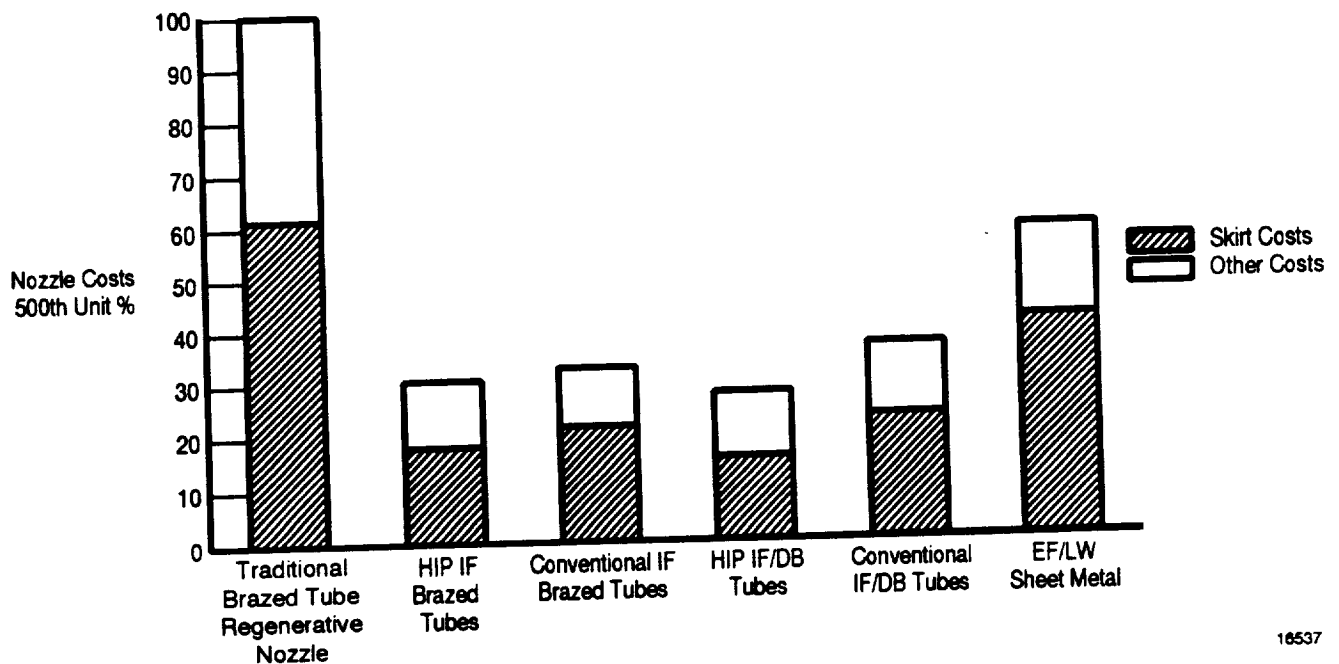
145RA

Figure 4.2.1-1. Phase II Tooling and Nozzle Assembly for the Brazed Tube Process and the Inflation Formed/Diffusion Bonded Tubes in a Conventional Furnace



14587

Figure 4.2.1-2. Phase II Tooling and Nozzle Assembly for the Inflation Formed/Diffusion Bonded Tubes in a Hot Isostatic Press Furnace



18537

Figure 4.2.1-3. Nozzle Cost Comparison for Various Fabrication Options

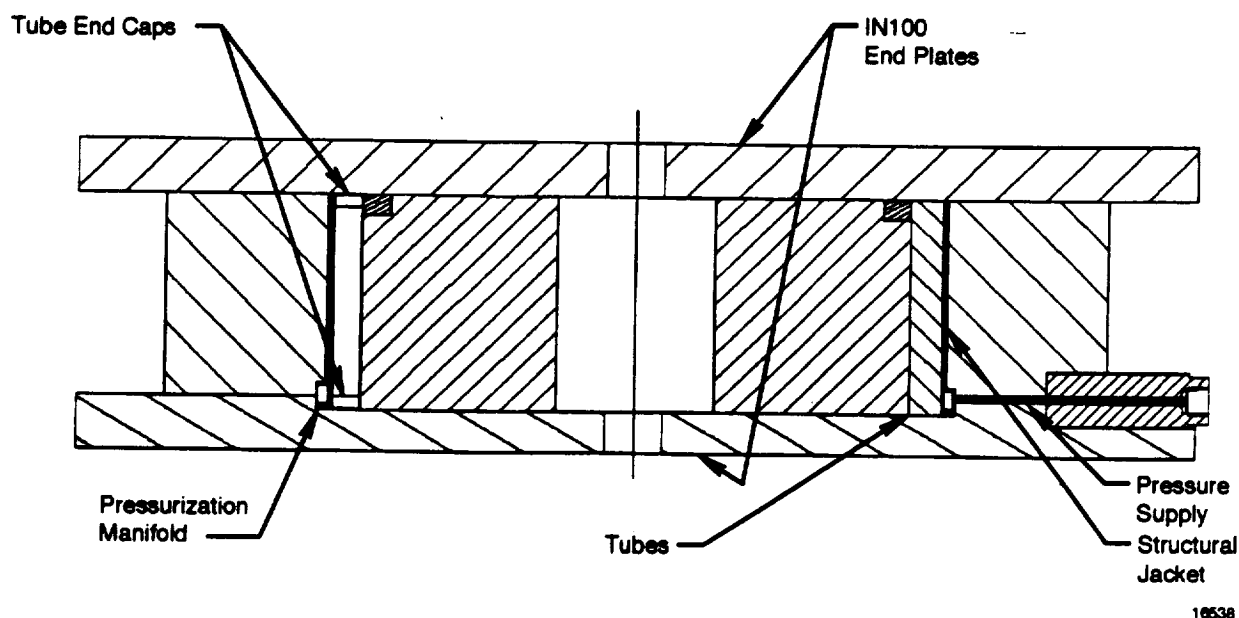


Figure 4.2.1-4. Cylindrical Sample Design for Inflation Formed/Brazing Process Parameter Optimization

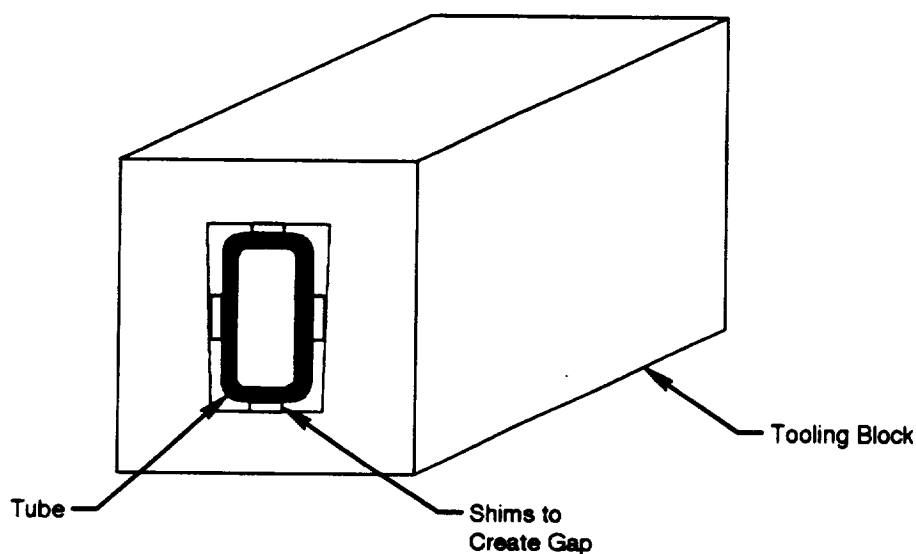


Figure 4.2.1-5. Single-Tube Inflation Forming Sample Design

4.2.2 Single-Tube Samples

The single-tube samples were designed to provide IF process parameters for tube forming. The tube blocks were machined and the trapezoidal hole, which simulates the space that a rectangular tube would fill for a 40K MTD size nozzle, was installed. Thirty tube blocks were fabricated, some of which are shown in Figure 4.2.2-1. Rectangular tubes were to be inserted into the blocks in different locations to simulate the gap sizes that could be found in the nozzle assembly. Figure 4.2.2-2 shows a block with a tube inserted in the hole. The space between the tube outer wall and the block was evacuated and seal welded shut. Each block was processed in a pressurization furnace under different conditions to provide the required lowest combination of pressure, temperature, and time needed for forming the tubes to fill the required space.

The first four samples were run in a hot isostatic press furnace (HIP) in the Pratt & Whitney Materials Lab using preformed rectangular tubes welded in place, with the tube interior exposed to furnace pressure. Table 4.2.2-1 summarizes the operating conditions that were used for the forming experiments.

Table 4.2.2-1. Operating Conditions Used In Forming Experiments

<i>Sample Number</i>	<i>Temperature (°F)</i>	<i>Pressure (psi)</i>	<i>Time (Hours)</i>
1	1925	500	1
2	1950	500	6
3	1950	700	6
4	1950	700	12

The samples were assembled, leak checked, then sealed off and placed in the HIP furnace. The furnace was brought to full temperature at near ambient pressure, then the furnace pressure was ramped up to the T_i 4.2.2-1 values and held for the time shown. After removal from the furnace, the samples were cut open using electrodischarge machining (EDM) and metallurgically examined.

Figure 4.2.2-3 is a transverse cross-section taken through the single tube AMS5581 sample No. 2 (HIP processed at 1950F at 500 psi for 6 hours), and shows extensive cracking in the hot formed tube wall, as indicated by the arrows. The predominately intergranular cracks were believed to have propagated from pre-existing base metal defects (See Figures 4.2.2-4 and 4.2.2-5) in the tubing of a specific heat lot from one supplier. The probable loss of internal pressure during the HIP cycle due to leakage through the cracks, may account for the tube wall inability to have expanded further and thus contacted the die backwall surface, as indicated by the bracket.

Figure 4.2.2-6 is a transverse cross-section taken through sample No. 3 (HIP processed at 1950 F at 700 psi for 6 hours) showing extensive cracks in the tubing that was from the same heat lot and supplier as the previous sample. The same pre-existing base metal defects were present causing similar cracking and probable loss of internal pressure during forming.

Figure 4.2.2-4 are sections taken through defective tubing, showing extensive cracks in the longitudinal orientation after cold forming the as-received round tube to the rectangular shape. The cracks are indicated by arrows on the upper photo, while the lower photo shows a closer view of the cracks taken from sample No. 3.

Figure 4.2.2-5 are sections through the round, unprocessed, as-received AMS 5581 tubing from the original raw material order (heat code HW1Q)), showing numerous intergranular voids (indicated by dark spots) in the transverse orientation of the left photo. The right photo indicates extensive cracks and voids associated with carbide stringers in the longitudinal direction.

FEB 20 1968

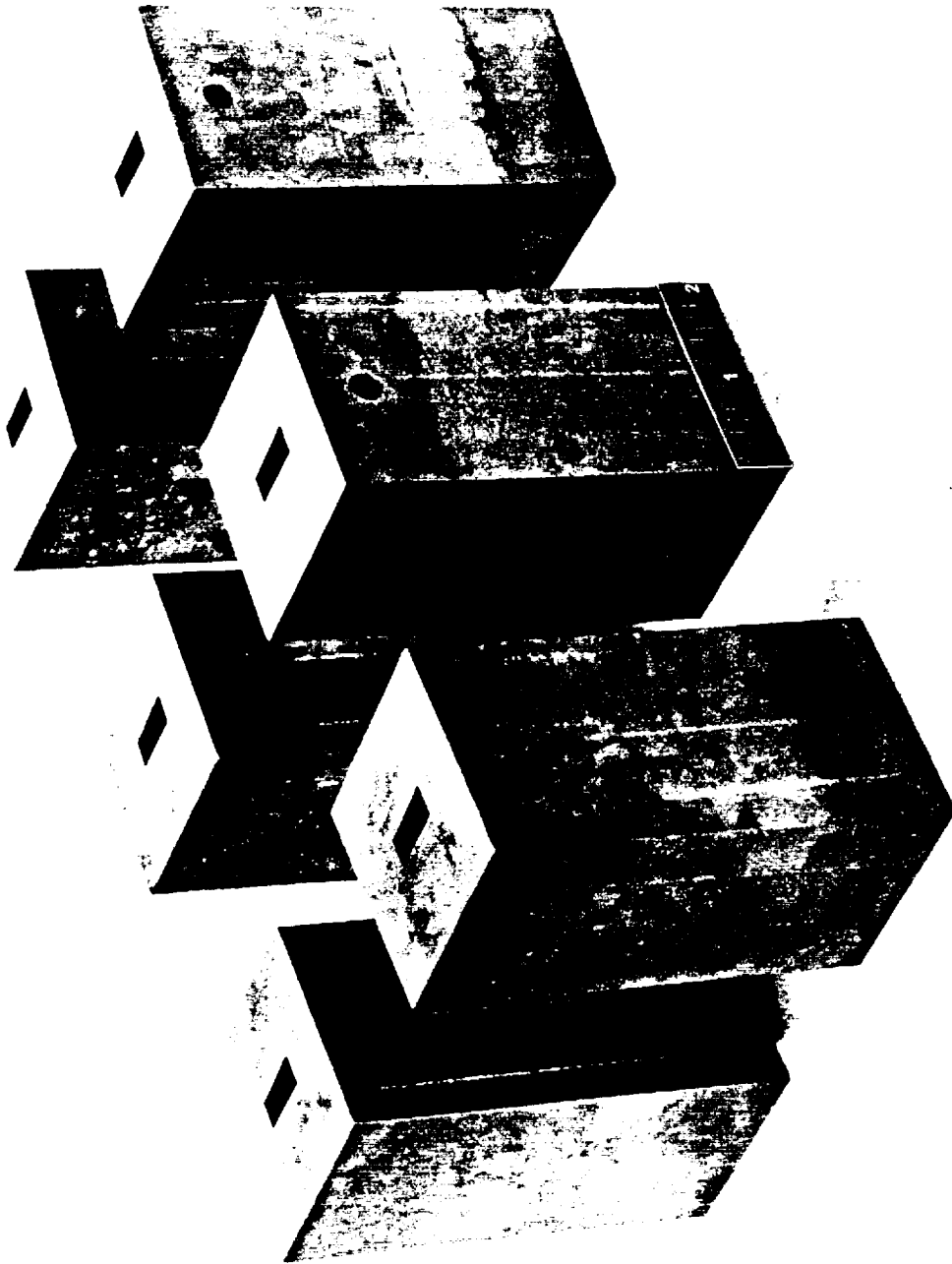
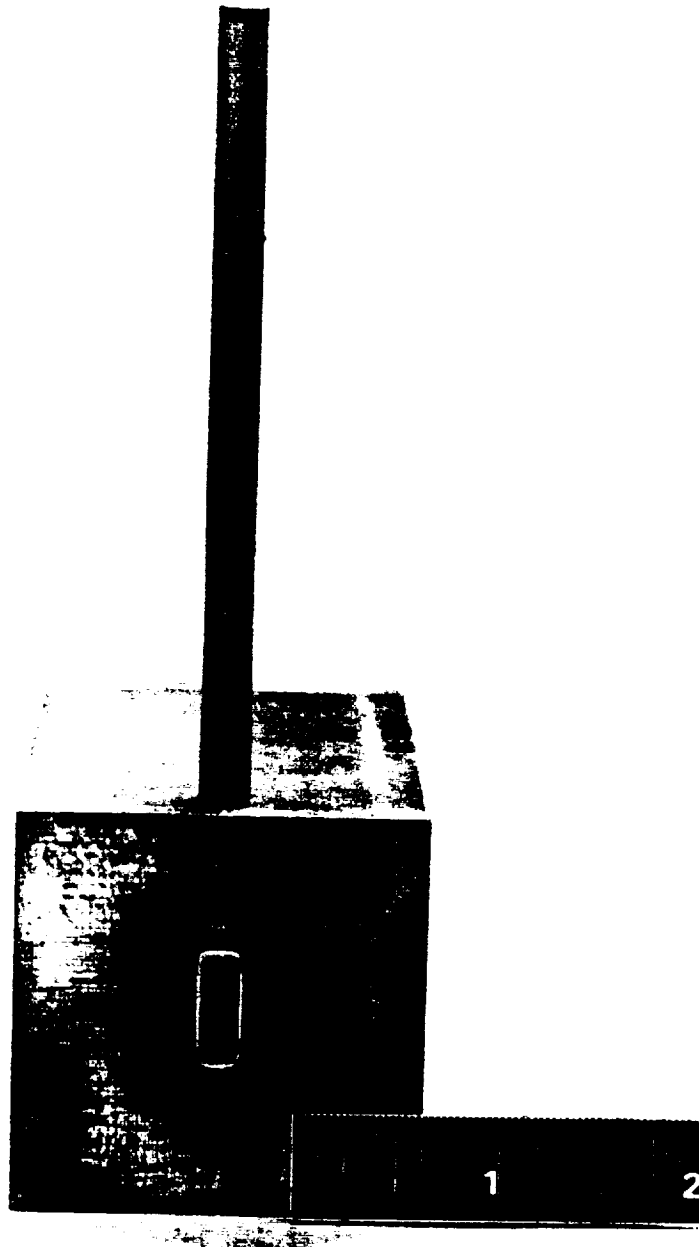
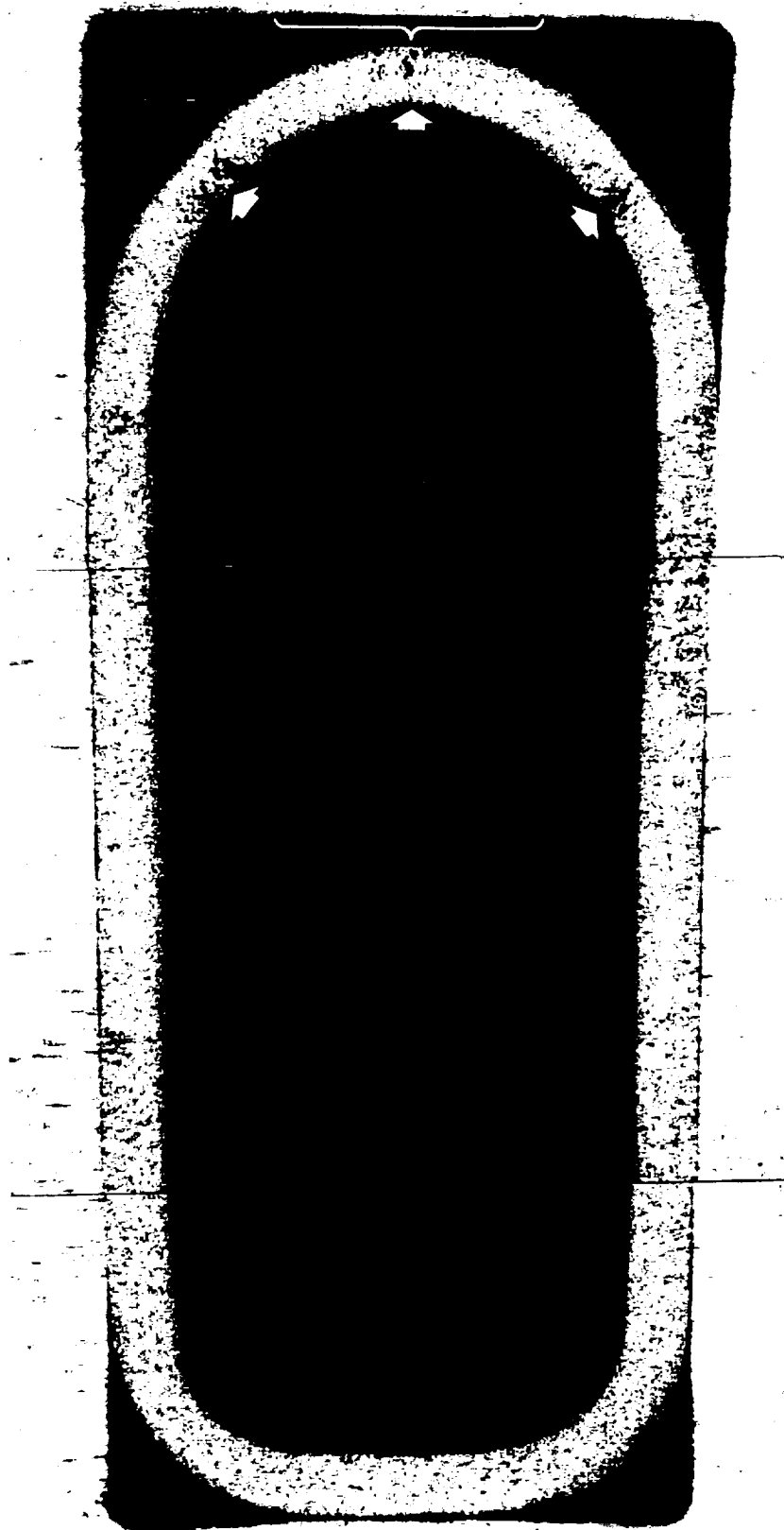


Figure 4.2.2-1. Single-Tube Sample — Blocks



FE629839

Figure 4.2.2-2. Single-Tube Sample Assembly

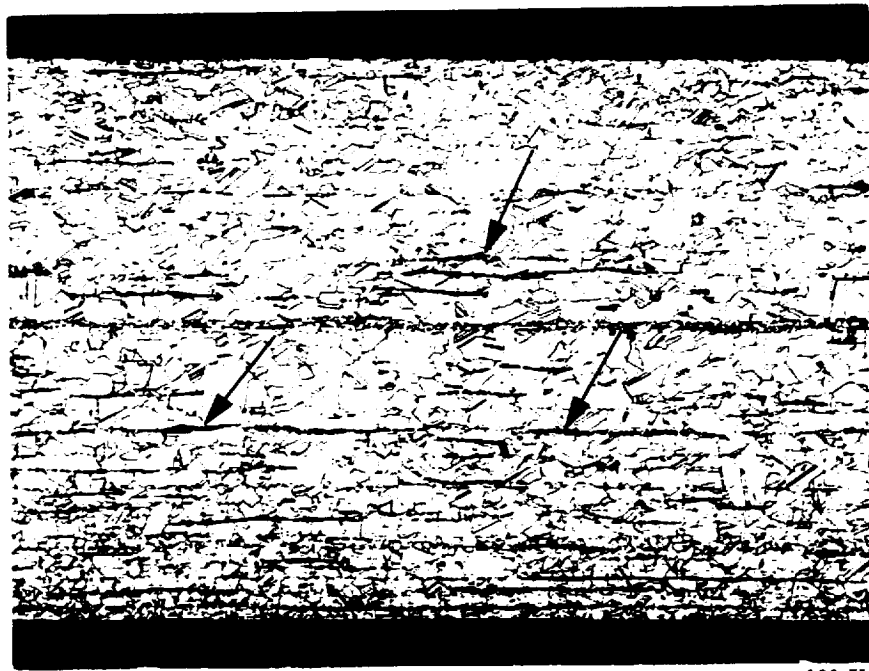


12.8 X

AMS 5581

Formed at 1925 °F, 500 psi, 6 hours

Figure 4.2.2-3. Transverse Cross-Section Taken Through Single Tube AMS5581 Sample No. 2



AMS 5581

Cold-Formed to Rectangular Shape

100 X

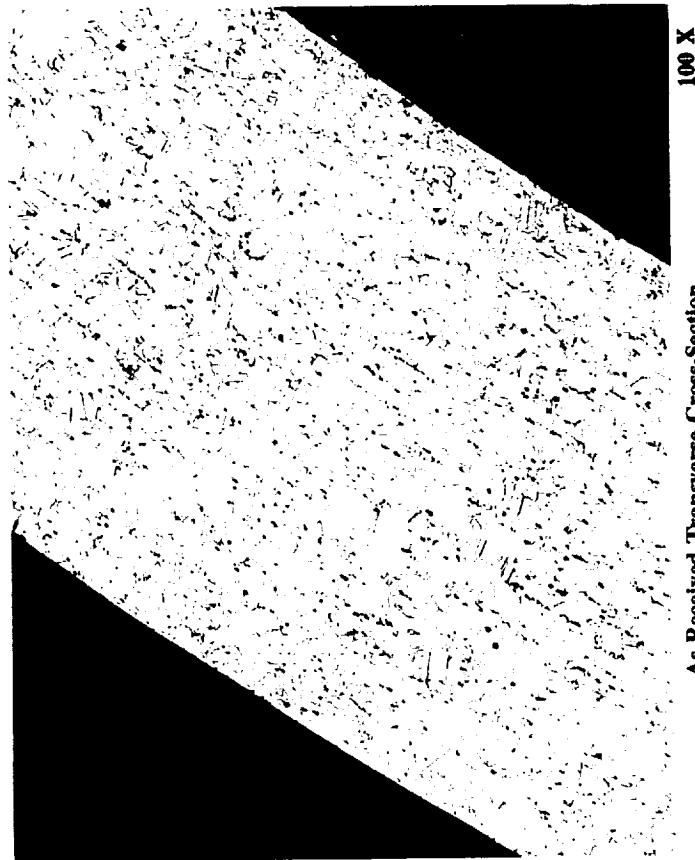
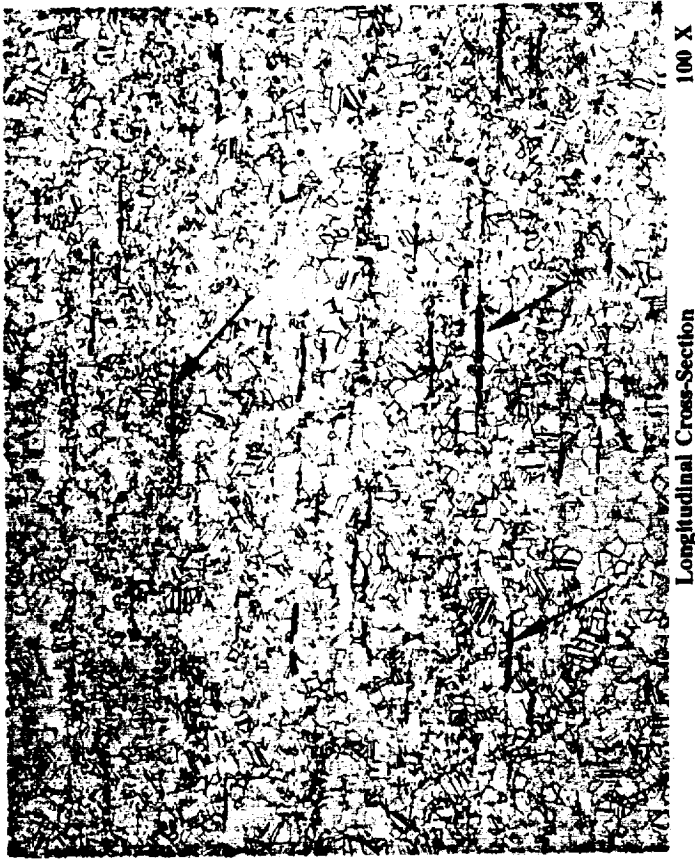


AMS 5581

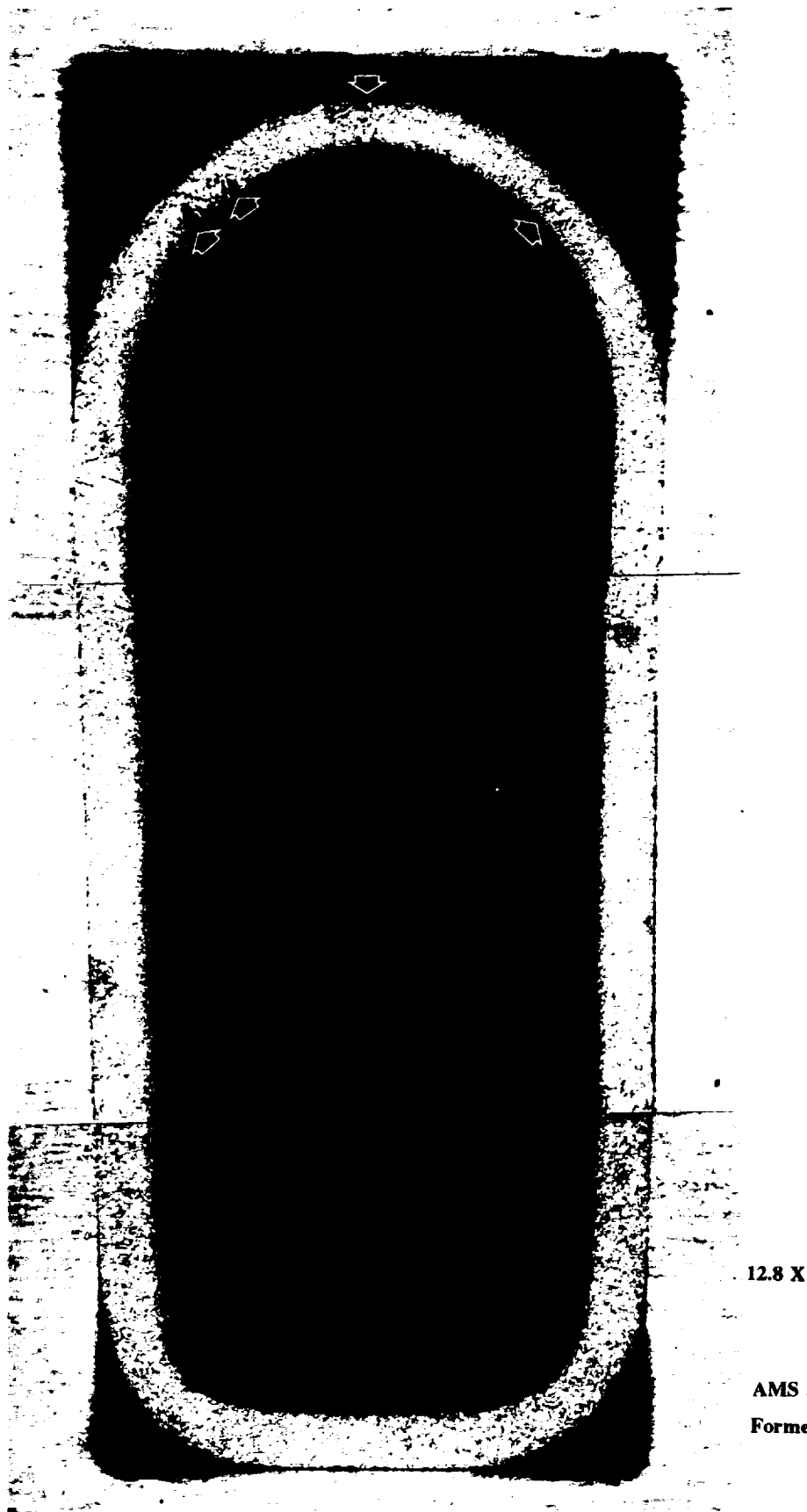
Formed at 1950 °F, 700 psi, 6 hours

40 X

Figure 4.2.2-4. Sections Taken Through Defective Tubing



Through the Round Unprocessed. As-Received AMS 5581 Tubing



AMS 5581

Formed at 1950 °F, 700 psi, 6 hours

Figure 4.2.2-6. Transverse Cross-Section Taken Through Sample No. 3

4.2.3 Cylindrical Samples

IF/Braze Samples

Since the IF/Braze process was downselected to only the pressurized furnace/lightweight tooling configurations, the IN100 mandrels ordered from P&W-Georgia were no longer needed. The associated tooling details on order from the tool supplier were cancelled.

A new lightweight mandrel was designed and built using an existing Inconel 625 forging. It was to be used to demonstrate the IF/Braze process in a pressurized furnace. The mandrel is shown in Figure 4.2.3-1. During the next reporting period, the 4-inch tube details will be completed and the first IF/Braze cylindrical sample can be assembled using this mandrel, as shown in Figure 4.2.3-2.

An additional mandrel will be formulated in the next reporting period using the remainder of the same Inconel 625 forging. This mandrel will be used to demonstrate the bag-braze process on a cylindrical sample with a hard OD mandrel.

Bag-Braze Samples

The bag/braze cylindrical samples were designed to simulate the bag/braze technique of forming tubes during nozzle brazing. Figure 4.2.3-3 shows the bag/braze sample design that is currently being fabricated in the P&W manufacturing shop. All of the structural jackets, tube details, weldment cover rings, and inner bag details were completed. The jackets will be plasma sprayed with the braze alloy and the first samples assembled during the next reporting period. The first two samples will be assembled in a nozzle top-end and aft-end configuration as shown in Figures 4.2.3-4 and 4.2.3-5. These samples will provide preliminary information on process feasibility and process parameters required for tube forming. Limited structural analysis indicates that a delta pressure of 14 psi may not be sufficient to push the tubes against the structural jacket; therefore, a pressurized furnace may be required for this process. These sample details can easily be adapted to run in a pressurized furnace by eliminating the weldment cover and seal welding directly to the tube ends.

The bag-braze cylindrical samples have been completed and are ready for processing in a HIP furnace. Four samples have been fabricated, two of which use the "top end" tube configuration, and two use the "bottom end" tube configuration so that process parameters can be verified on a cylindrical sample for both geometries. Although the tube material used in these samples is not acceptable for demonstrating inflation forming, the bag/braze technique uses tube bending to achieve braze fit-up rather than inflation forming, and will be acceptable for pressure demonstration. Figure 4.2.3-6 shows all four samples, while Figure 4.2.3-7 and 4.2.3-8 shows one of each type. All samples have been leak checked and are ready for shipping to a HIP supplier and processing during the next reporting period.

Sample Processing

The HIP suppliers were originally asked to quote on an in-process hydrogen purge system so that the cylindrical and quarter scale samples could be formed and bonded at the same conditions as designed for the full scale nozzle. However, neither furnace supplier would provide the low pressure hydrogen purge in their HIP furnaces due to schedule and safety concerns with existing furnaces. The intent of the hydrogen purge was twofold :

1. To remove oxides for greater braze and bond cleanliness
2. To provide a continuous monitoring and pump-down system inside of the sample in case of a leak

A leak that occurred during the forming or bonding operations would allow furnace argon (which provides the furnace pressure) to leak into the sample. This would reduce the delta pressure which allows the form and permits impurities into the sample that could hamper brazing. Both vendors did, however, agree to provide a vacuum pump-down and monitoring system that will be used for all cylindrical and quarter scale samples. This allows the real time monitoring and evacuation that is needed to continue processing even with a small amount of leakage into the part, thus saving costly rework, repair, and furnace abort cycles.

A team technical review was held to verify the manufacturing and assembly conditions and processes that were used to fabricate all four samples. These technical reviews were held before each sample was released to the shop, and before each sample was released to the HIP supplier. This will ensure hardware integrity, incorporate recent lessons learned, and establish process parameters for manufacturing, assembly and HIP processing. The first two samples will be formed at the same HIP furnace conditions (selected to be 250 psi at 1925 F for 6 hours) followed with the standard braze process of 15-50 psi, at 2150 F for 30 minutes.

FE-630760

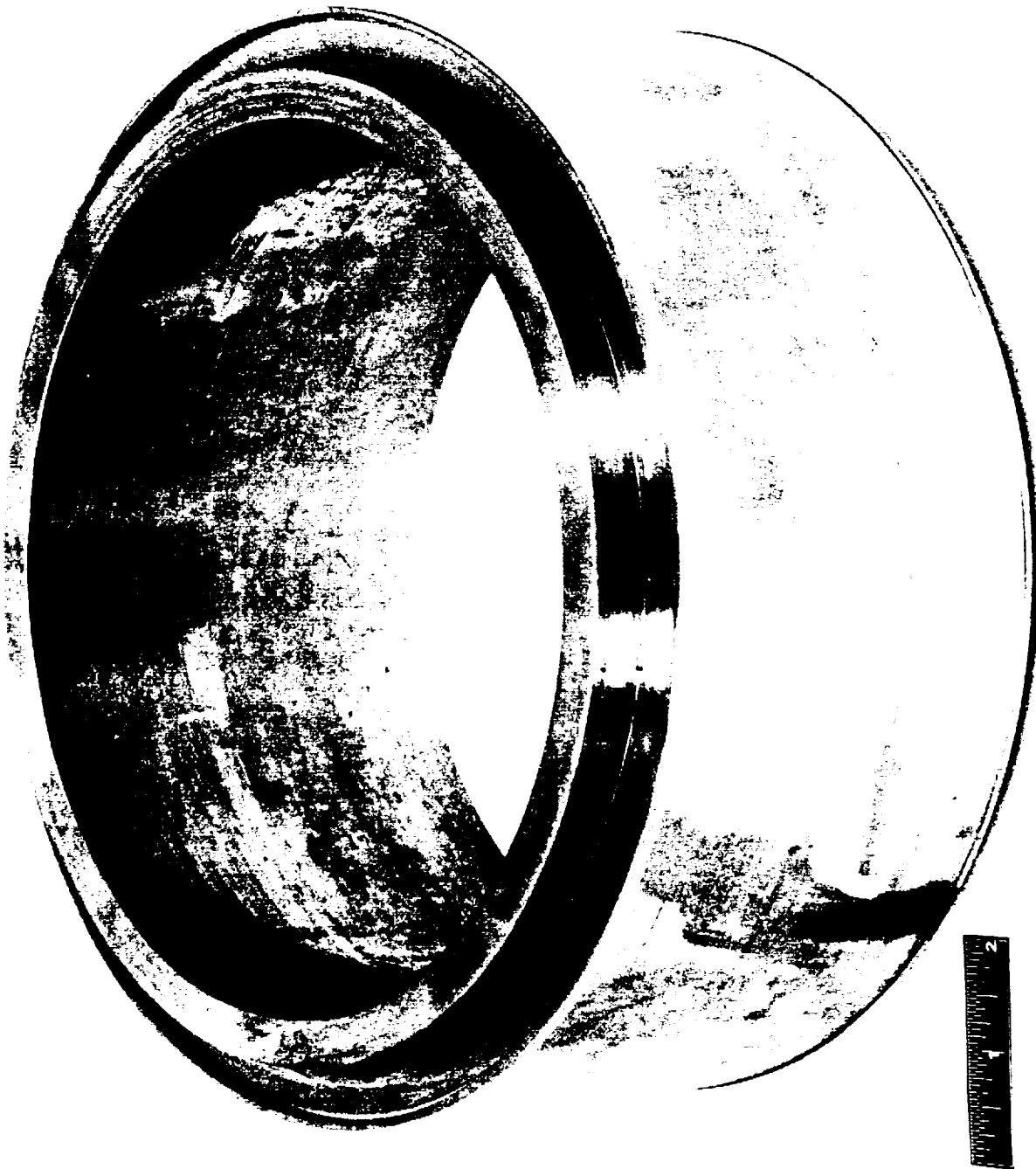
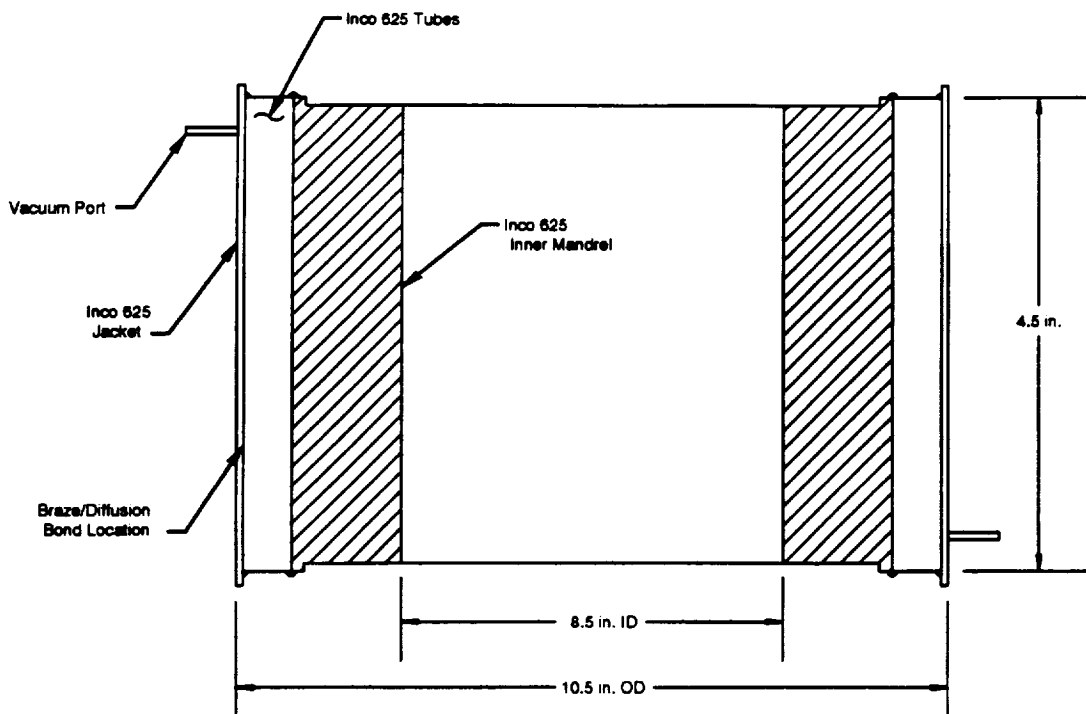
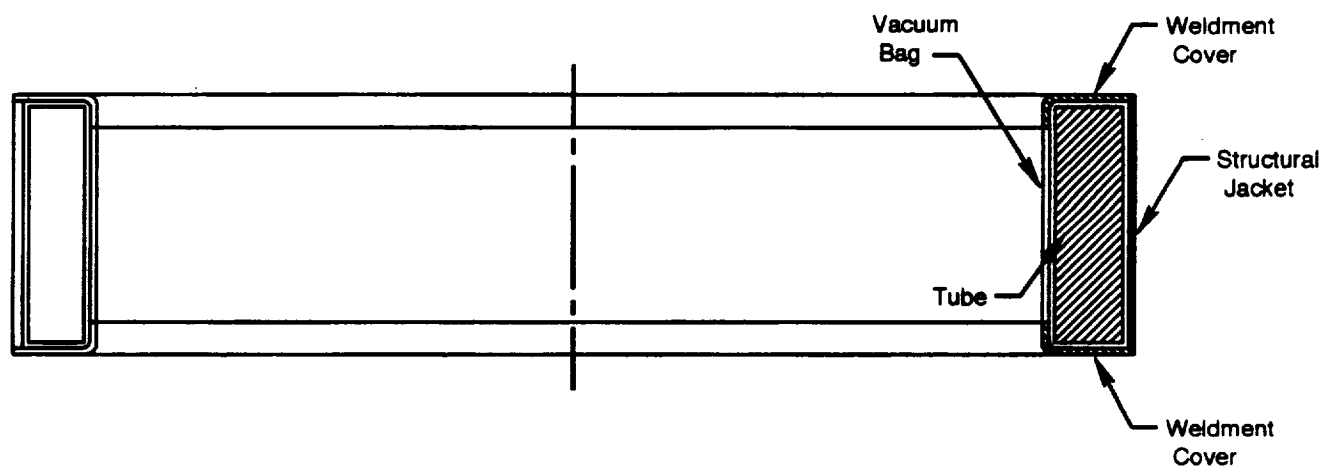


Figure 4.2.3-1. Cylindrical IF/Braze Mandrel



24837

Figure 4.2.3-2. Inflation Formed/Brazed and Diffusion Bonded Cylindrical Samples



21889

Figure 4.2.3-3. Cylindrical Sample Bag-Braze Design

FE-429840

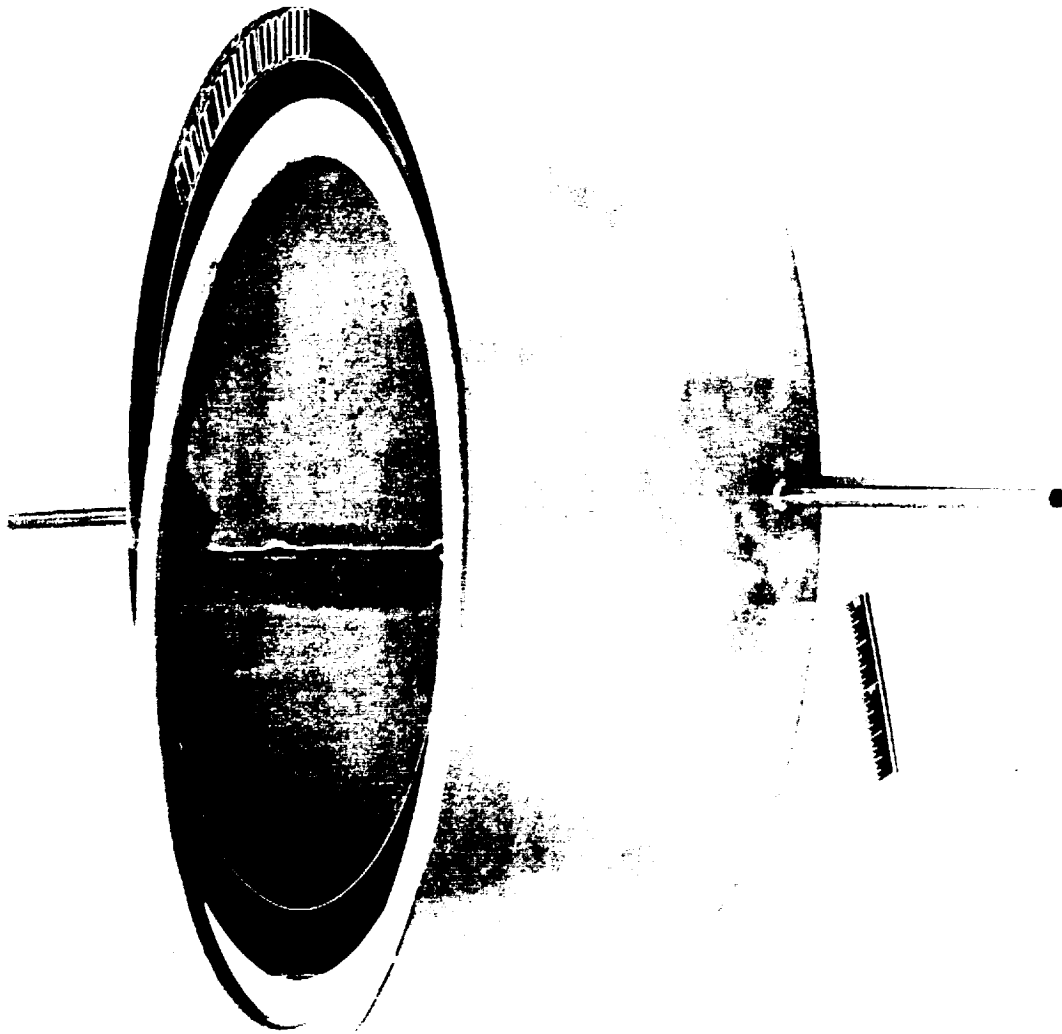


Figure 4.2.3-4. Cylindrical Sample Hardware — Outer Jacket, Tubes, Inner Vacuum Bag, and Weldment Cover

FE-629842

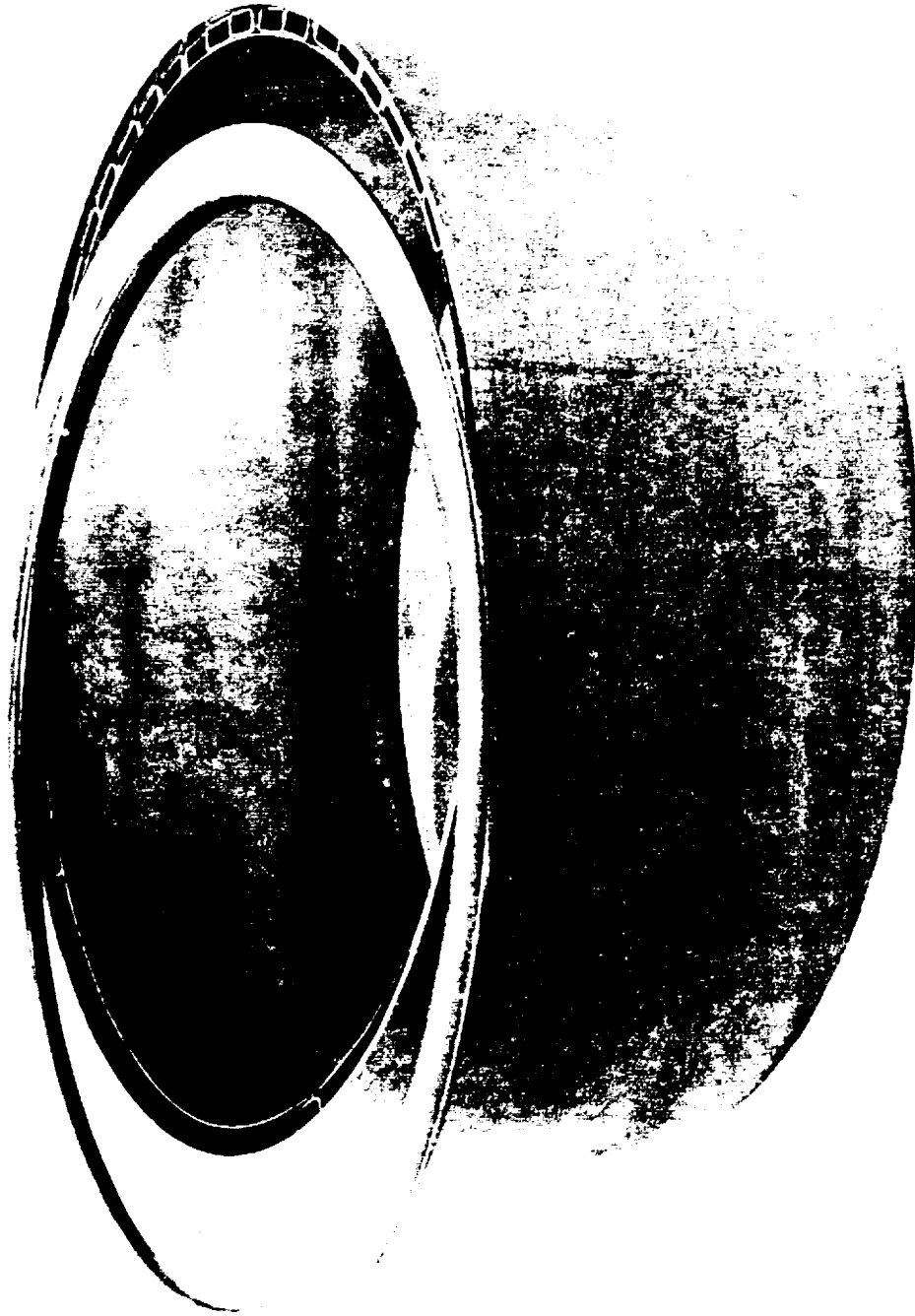


Figure 4.2.3-5. Cylindrical Sample Hardware — Outer Jacket, Tubes, Inner Vacuum Bag, and Weldment Cover

FE-000761

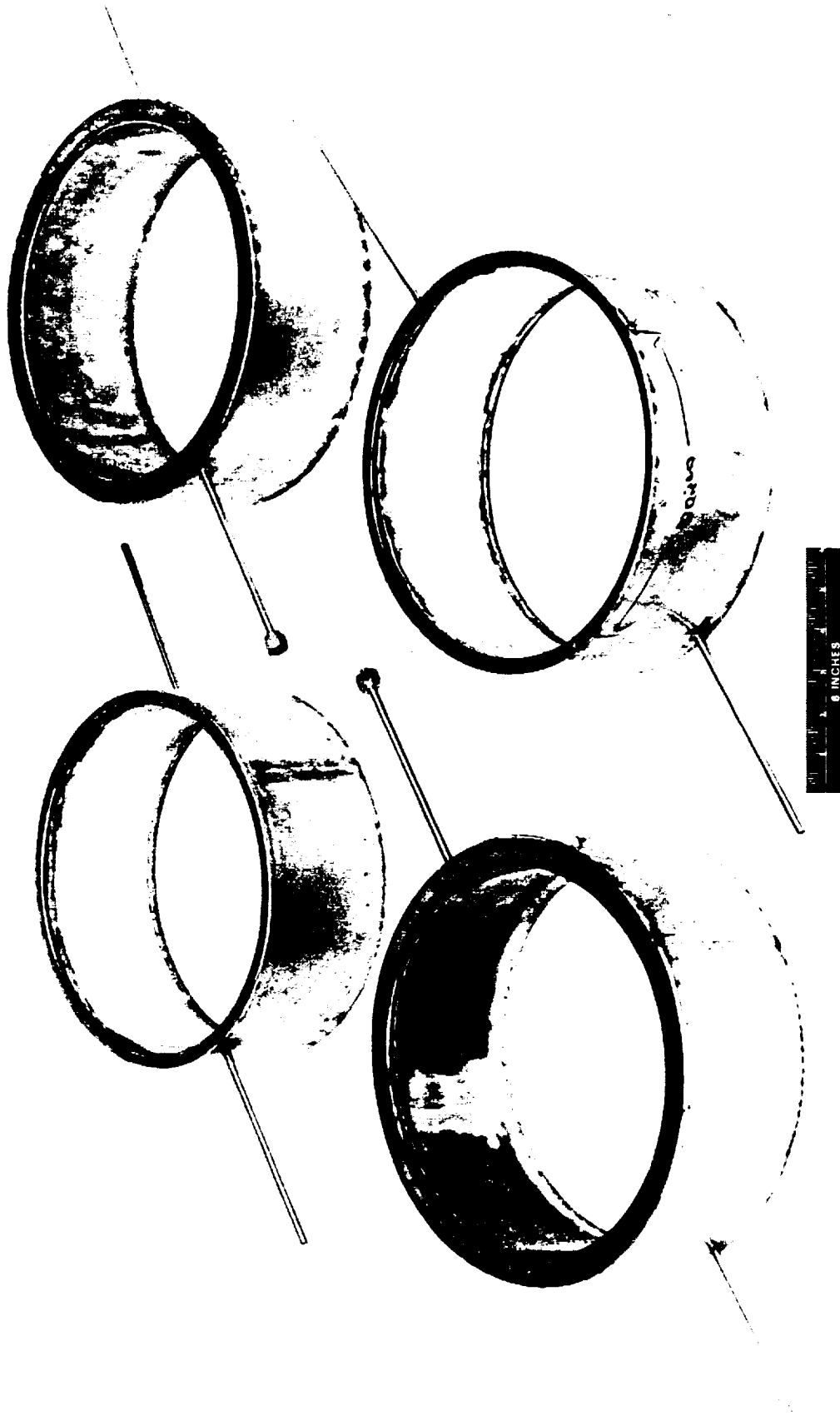


Figure 4.2.3-6. Cylindrical Bag-Braze Nozzle Sample Assembly

FE-630757

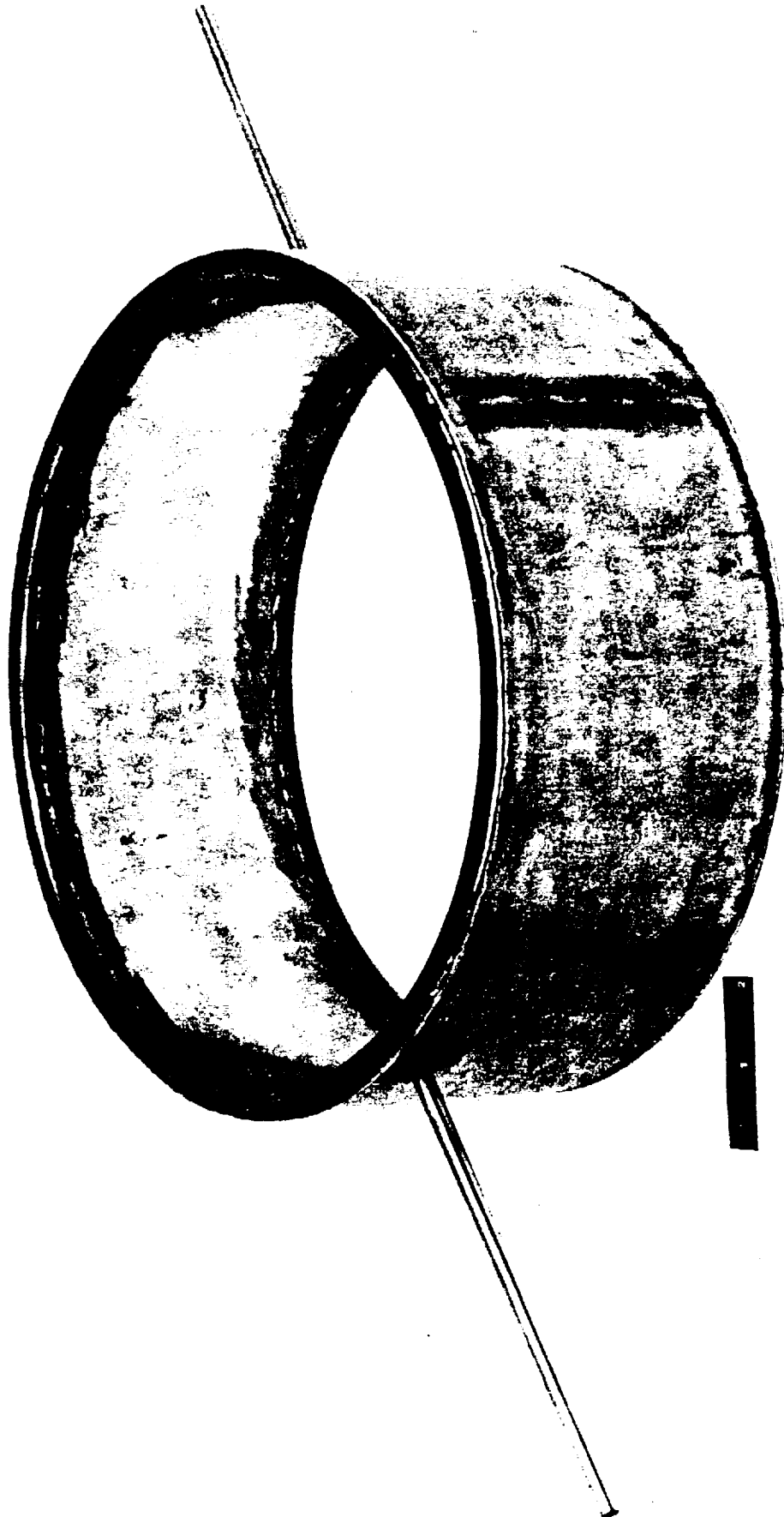


Figure 4.2.3-7. Cylindrical Lag-Braze Sample Assembly

FE-030759

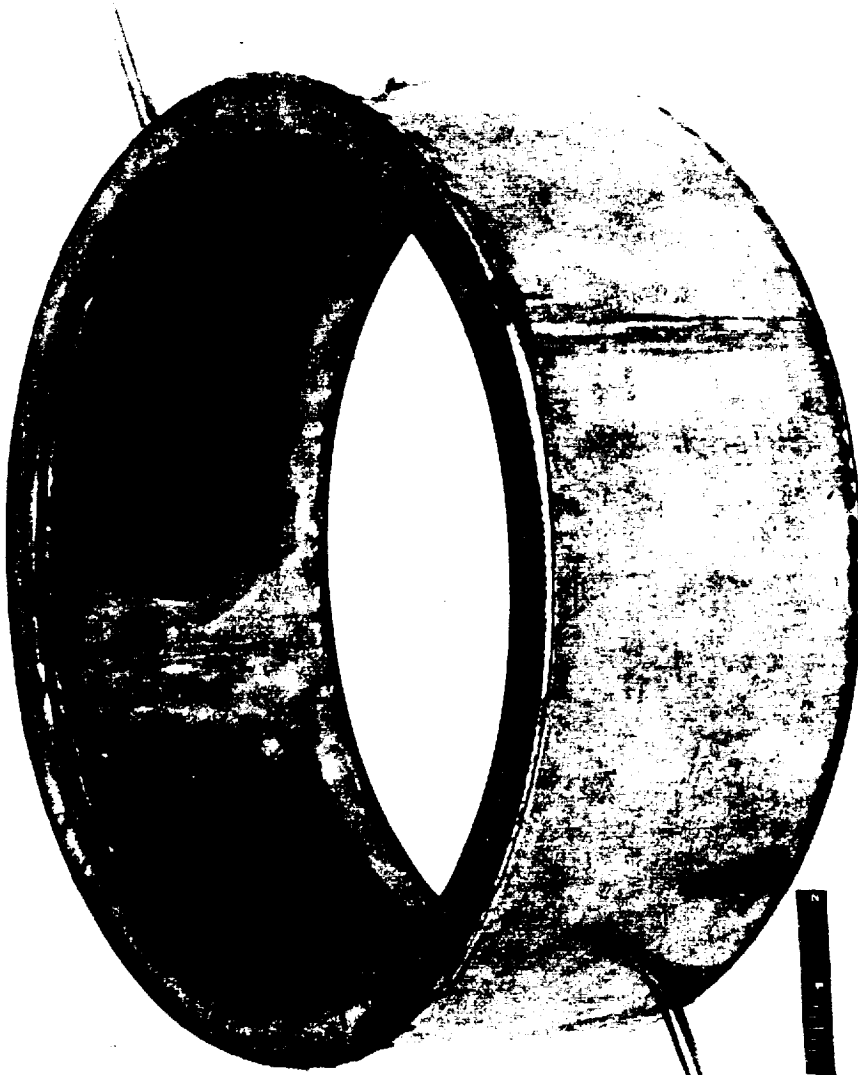


Figure 4.2.3-8. Cylindrical Bag-Braze Sample Assembly

4.2.4 40K MTD Nozzle Samples

IF/Braze Samples

Procurement of the heavy IF/braze tooling mandrels for use in a nonpressurized furnace was terminated, although the mandrels were already centrifugally cast at the time of the termination order. The OD mandrel will now be used to fabricate up to three bag-braze samples in a pressurized furnace, as discussed below.

The tube raw material and sheetmetal for forming the structural jackets were received. The first 24 tube test pieces were formed using the first of three tube-forming dies designed and built specifically for the 40K MTD nozzle. The first die was reworked to accommodate higher than expected tube springback. The 24 tubes are currently being formed to the finished front-end rectangular shape in the first die. The second and third dies were then used to create the aft-end rectangular shape and the nozzle contour, respectively. All tube dies and the contour/trim fixture were completed.

Three of the 40K MTD structural jackets were completed; one is shown in Figure 4.2.4-1. These structural jackets are the first of 12 that will be completed for all the 40K MTDs during the next reporting period. Each jacket will be plasma sprayed with braze alloy before use in one of the 40K MTD nozzle assemblies. The spin mandrel used to fabricate the structural jackets is shown in Figure 4.2.4-2, together with the spin mandrel used to fabricate the vacuum bags.

Bag-Braze 40K MTD Nozzle

The bag-braze 40K MTD nozzle design does not require an inner or outer mandrel for structural jacket support during the braze cycle; however, results from the cylindrical bag-braze trials determined the final configuration of the 40K MTD sample tooling. Should the structural jacket need support during the bag-braze process, several options can be pursued:

1. Use a thicker structural jacket to prevent jacket yielding/creep during the forming/brazing process.
2. Use the thin inner mandrel currently being procured for the IF/braze and IF/DB 40K MTD nozzles.
3. Reoperate an existing subscale calorimeter nozzle heat treatment fixture to accommodate the slightly smaller diameter of the 40K MTD nozzle.

These options were evaluated so P&W can proceed directly from the cylindrical bag/braze samples to the 40K MTD bag/braze samples using one of the above options, if required.

Bag/Braze Samples

The quarter scale bag-braze sample design is shown in Figure 4.2.4-3. The two variations on the bag-braze techniques are also shown. The use of weld rings will enclose the tubes and structural jacket within the bag (thin inner sheetmetal piece) and the tool. Their usage causes the furnace pressure to act only to bend the tubes for braze fit-up. The alternate configuration eliminates the weld rings, and the tubes are welded to each other, to the inner bag, and to the jacket and tool. This leaves the tube interior wall exposed to the furnace pressure, so both inflation forming and bending are used to achieve braze fit-ups. The cylindrical braze samples will provide the basic process feasibility information needed to downselect between these two concepts during the next reporting period. The OD mandrel, due in mid-October, will be machined here at P&W to accommodate either configuration.

Using test pieces, the tube forming trials were continued and two of the three dies were completed. The third die, which forms the tube contour, was reworked to accommodate higher than expected tube springback. A tube sample shown in Figure 4.2.4-4, is very close in final shape but with an undersize bend in the aft section.



FE629844

Figure 4.2.4-1. 40K MTD Structural Jacket



FB20836

Figure 4.2.4-2. Spin Chucks for 40K MTD Outer Jacket and Vacuum Bag

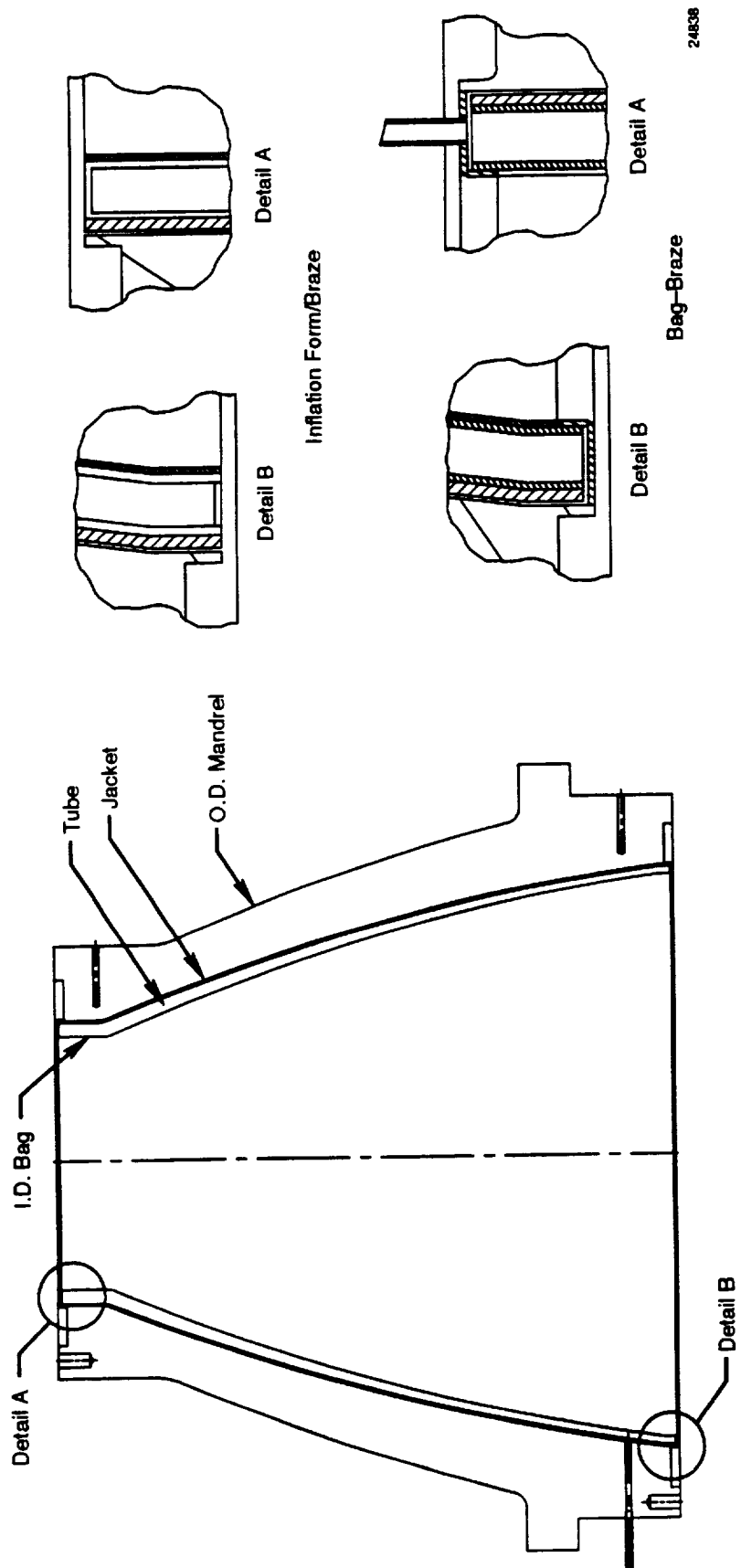


Figure 4.2.4-3. Quarter-Scale Bag-Braze Sample Tool Design

FE-630754

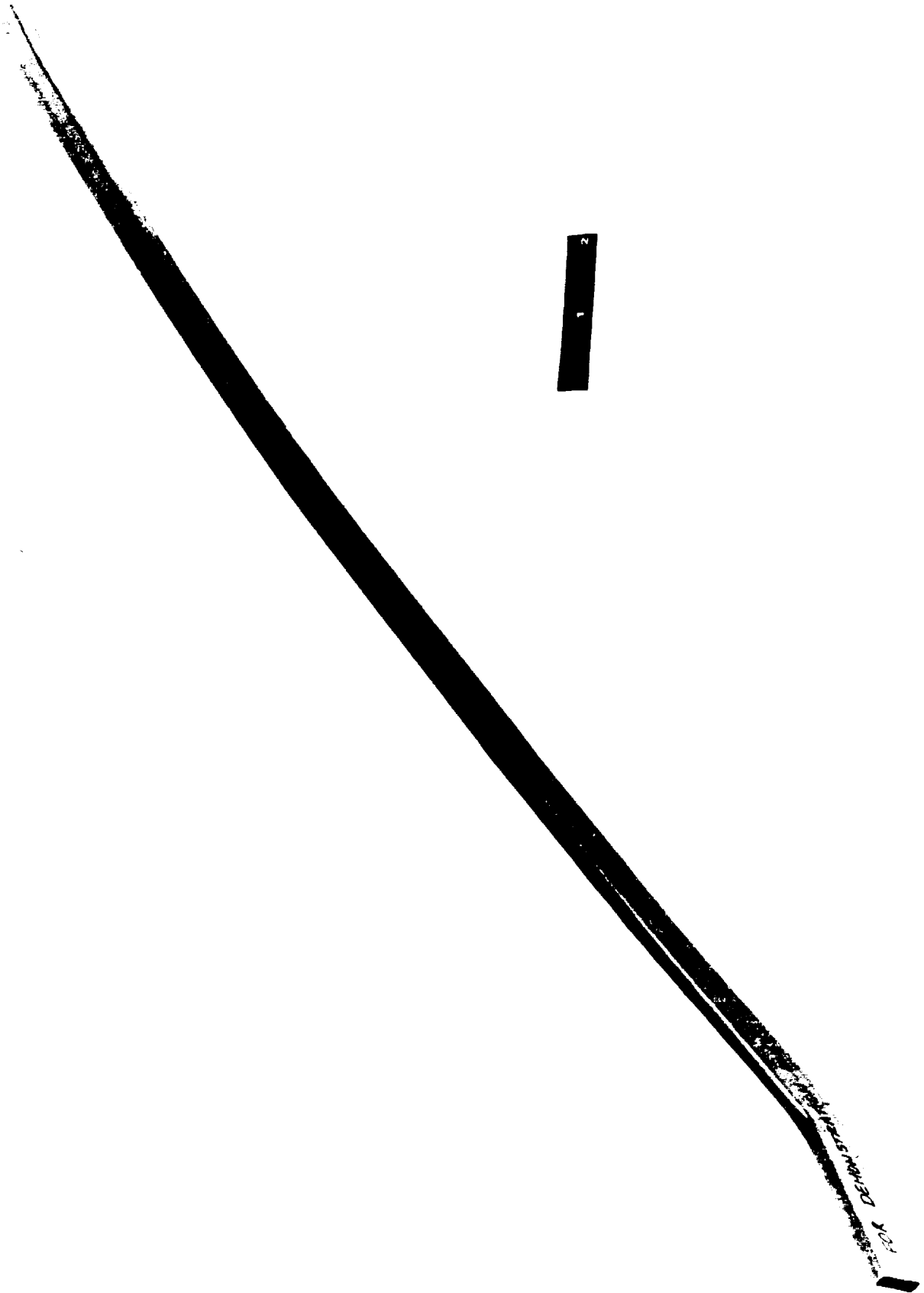


Figure 4.2.4-4. Quarter-Scale Nozzle Tube Sample

SECTION 5.0 SUBSCALE NOZZLE TASK

5.1 SUBSCALE NOZZLE FABRICATION AND TEST SUPPORT

The subscale nozzle fabrication and test program was planned to address several of the key full-scale nozzle prioritized risk issues, including the following:

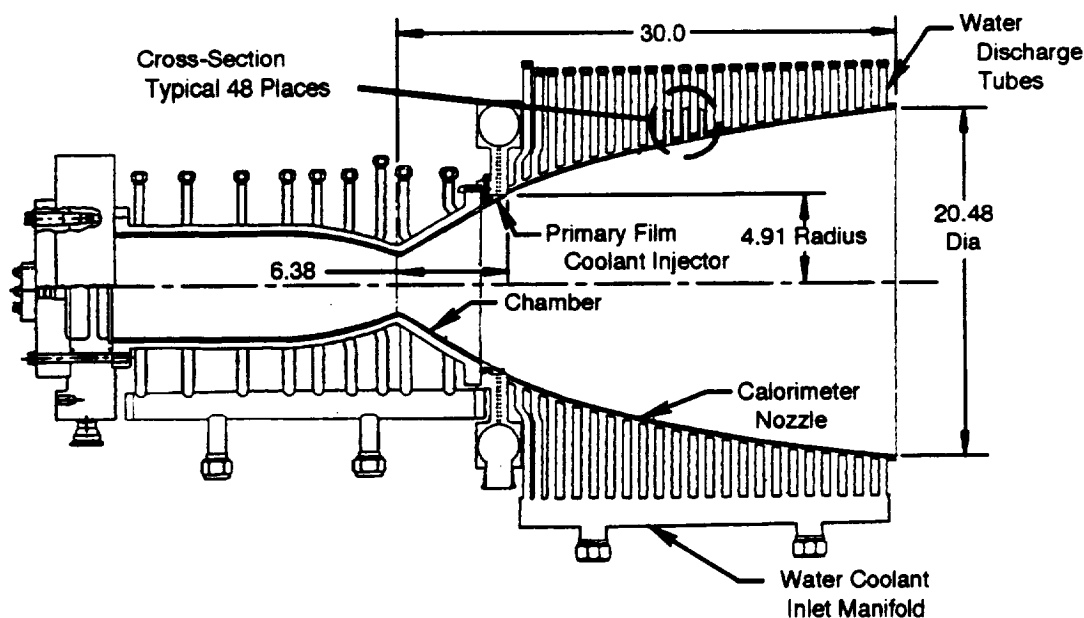
- Effect of film cooling on nozzle hardware
- Effect of thermal mismatch between the chamber and the nozzle resulting in a step in the wall contour and possible nonconcentric alignment
- Nozzle accelerating core flow effect on film layers
- Transient aerodynamic effects on nozzle hardware.

The preliminary design concept, as shown in Figure 5.1-1, mates with the existing P&W/NASA 40K subscale injector and calorimeter chamber that successfully completed 28 firings in August and September of 1990 at the MSFC TS116 test stand.

Originally three different subscale nozzle concepts were considered for use: a film/water cooled calorimeter nozzle, a tubular film/convective cooled nozzle, and a sheetmetal Columbium film cooled nozzle. The calorimeter nozzle was selected as the optimum test vehicle because of the distinct advantages in the areas of heat transfer data analysis, fabrication, durability, and instrumentation capability. The relative advantages and disadvantages of the three nozzle configuration options, from a technical standpoint only, are summarized in Table 5.1-1. In addition to the technical advantages, the calorimeter nozzle offers a slight advantage in cost and schedule.

Table 5.1-1. Subscale Nozzle Configuration Comparison

	Calorimeter Nozzle (Baseline)	Columbium Sheetmetal Nozzle (Option)	Tubular Nozzle (Option)
Heat Transfer Data Analysis:	• Film cooling effectiveness can be determined with minimum uncertainty	• Film cooling effectiveness can be determined with minimum uncertainty	• Greater uncertainty due to convective cooling
Performance Analysis:	• Use static pressures and temperatures to calculate thrust	• Use static pressures and temperatures to calculate thrust	• Use static pressures and temperatures to calculate thrust
Fabrication:	• Turned circumferential channel liner-minimum tooling costs • Electroformed nickel closeout • Welded Tubes	• Sheetmetal columbium - expensive tooling required for welding and forming operations • Silicide coating - easily damaged and difficult to repair	• Brazed or diffusion bonded tubes - expensive tooling required for one-time braze or bonding operations • Raw material (tube) costs are high for small quantity
Test Durability:	• 900°R average wall temperature	• 3050°R maximum wall temperature • Potential for severe oxidation if coating damaged	• 1200°R average wall temperature
Test Requirements:	• Water coolant supply 150 to 300 gpm at 250 psi • Hydrogen coolant supply 2 to 5 lb/sec at 285 psi maximum • Instrumentation easily installed (thermocouples, static pressure probes)	— • Hydrogen coolant supply 2 to 5 lb/sec at 285 psi maximum • Thermocouples cannot be used on nozzle aft end (>2100° F)	— • Hydrogen coolant supply 2 to 5 lb/sec at 285 psi maximum • Instrumentation installation moderately difficult
		• Infrared camera	



FDA 381692

Figure 5.1-1. Subscale Thrust Chamber Assembly

5.1.1 Design and Analysis

The focus of the design and analysis work performed was to establish preliminary nozzle and film injector geometry, based on the full-scale STME nozzle. Using the established full-scale STME nozzle length, area ratio, and contour, a preliminary subscale nozzle contour was designed to simulate the predicted full-scale nozzle aerodynamic and thermal conditions. From the preliminary subscale nozzle contour, which features an area ratio of 45 to 1 and a length of approximately 27 in. from the chamber throat, the film cooling injector geometry can be established. Consistent with the proposed test plan, P&W was to provide four unique primary film coolant injector pieces, each with a unique film injector orifice design. Two of the injectors will inject the primary film coolant parallel to the nozzle wall, both sonic and supersonically. The other two will be designed to direct flow parallel to the nozzle centerline, both sonic and supersonically. Figure 5.1.1-1 is a conceptual design illustrating the film coolant redistribution between subsonic and the primary supersonic injection locations, which closely simulates the full-scale design. The subsonic film coolant injected at the forward lip of the injector helps smooth the hot gas flow past the step in the wall contour which is intended to simulate the discontinuity in wall contour found in the full-scale design. The subsonic film coolant also helps cool the primary injector lip. The subsonic flow, metered by small orifices, and the sonic/supersonic flow, metered by the primary orifice passages, will be varied during the nozzle characterization tests. Metering of the coolant flows in this way offers precise control over the flow distribution to enhance the accuracy of the resultant data analysis. These passages will be electrodischarge machined (EDM) into a ring forging made of Inconel 625. A two-piece cover ring will then be brazed to close out the passages, eliminating the possibility of leakage flow around the injector orifices. The four preliminary passage geometries were evaluated for producibility, EDM tooling, brazing, and structural considerations. The primary issues in designing and producing these injector rings are holding close tolerances in the orifice flowpaths, limiting braze fillet encroachment into the orifice flowpath while achieving strong braze bonds, and limiting thermal loads on the injector ring for maximum durability.

The preliminary liner coolant passage geometry was established and structurally analyzed. Materials considered for the liner include centrifugally cast Inconel 625 and wrought Inconel 625 made by spinning sheetmetal. Although the centrifugally cast material offers slight advantages in lead time and improved flexibility in the raw material geometry, the wrought Inconel 625 offers better material properties. The liner geometry was being analyzed for creep strain ratcheting (CSR) life, creep life, and low-cycle fatigue life as an initial screening method for material selection. Further structural analysis of the liner passages included simple elastic/plastic finite element modeling to determine the influence of thermal gradients and other static loads on the liner passages.

The hydrogen inlet manifold, the water coolant tubes and water coolant inlet manifolds, and the nozzle liner closeout geometry were rough sized and reviewed for producibility, tooling, assembly, packaging, and structural considerations. The manifold is made from Inconel 625 forgings welded together and to the nozzle liner before the electroformed nickel plating and final machining.

The conceptual subscale nozzle design was analyzed with the General Aerodynamic Simulation Code, GASP. This computer code was developed for NASA-Langley by Dr. R. Walters of Virginia Polytechnic Institute. The subscale nozzle flow field was assumed to be inviscid and frozen. Both the normal subsonic injector and the tangential sonic injector were modeled. The static pressure field shown in Figure 5.1.1-2 reveals distinct pressure waves that emanate through the flow domain. The impact of the injectors on the main stream hot gas is shown in Figure 5.1.1-3. The temperature contours in Figure 5.1.1-4 clearly illustrate that the cold region of nozzle is adjacent to the walls.

The existing subscale calorimeter chamber reoperation procedures were established and the final mechanical design and analysis completed. The procedures have not significantly changed since the proposal, as shown in Figures 5.1.1-5 and 5.1.1-6. Three of the aft water coolant tubes and three of the corresponding water coolant discharge tubes will be removed, as well as the aft end of all eight of the larger water coolant inlet manifolds.

The chamber will be inspected, cleaned, and shipped to EF Nickel for plating of the aft chamber/nozzle flange. Following the flange buildup procedure, the chamber will undergo final machining, cleaning, and reattachment of the water inlet tubes and manifolds at P&W. As shown in Figures 5.1.1-5 and 5.1.1-6 the process is simple and well within the current capabilities of the supplier's processes. The flange has been sized to standard structural criteria based on MSFC Handbook 505A as modified for ground test rig hardware. Material properties for the flange material have been specified, and material samples will be provided in process to ensure quality requirements are met.

The subscale nozzle chamber rework design and analysis and detail drawing release were completed. The rework design includes removing four each of the chamber aft end inlet and exit tubes, and cutting back all eight of the large water inlet manifolds.

The final chamber reoperation drawings have been completed and released to manufacturing for preparation of the manufacturing Master Planning Summaries and Operation Sheets.

The subscale nozzle design and analysis work was completed. All of the major nozzle components — the hydrogen inlet manifold, the nozzle liner assembly, and the injector rings — were structurally analyzed and meet all test program durability requirements. The heat transfer and aerodynamic performance analyses have been completed for the nominal operating points and the results incorporated into the mechanical design and used in the structural analysis. The updated subscale nozzle assembly is shown in Figure 5.1.1-7. As a result of NASA TS116 test personnel input at the Design Review, the water coolant tubes have been staggered and the hydrogen inlet manifold extended to allow for better installation and assembly access.

An enlarged view of the final film coolant injector configuration is shown in Figures 5.1.1-8 and 5.1.1-9. Analysis of the secondary film coolant has shown that the 72 rounded posts used to distribute the flow were a significant improvement compared to the original square post design based upon CFD analysis results in Figures 5.1.1-10 and 5.1.1-11. The 3-D model is a five-degree "pie-slice" of the cavity, and depicts one-half of one injector orifice along the top left symmetry plane. This orifice directs the flow axially into the top cavity, which then turns radially inward in between the posts. The flow is directed through another axially stepped cavity and into the hot gas path. The models show the pressure contours at the highest and lowest inlet pressure conditions, the two design limit cases for flow analysis. The results shown in Figures 5.1.1-12 through 5.1.1-15 indicate that although the distribution achieved in the 'rounded post' design is significantly improved over the 'square post' design, there is some concern about the incomplete flow distribution directly underneath the metering holes. Therefore, another scheme in which slots were machined in the posts was modeled. The most recent CFD model, shown in Figures 5.1.1-16 through 5.1.1-19, indicates that the slots machined in the posts do not significantly improve the flow maldistribution underneath the metering hole due to the high pressure differential across the cavity. The flow travels out of the orifice and through the slot in a supersonic jet which does not flare out and effectively cool that section of the injector ring lip. Currently, the nozzle team is brainstorming methods of smoothing out the flow to resolve the maldistribution problem.

The film injector slot geometries were designed to bracket the full-scale nozzle film injector operating conditions. Four primary film injectors will be used in the test program, two sonic and two supersonic injectors. All of the primary injectors are approximately 1/4-scale models of the full-scale nozzle candidate designs. The secondary film injectors are designed to provide effective film cooling of the injector ring itself, while minimizing impact on the nozzle core exhaust flow or downstream primary film cooling. The injector geometries were designed using the P&W slot film cooling code, the Two-Dimensional Kinetics code, and CFD codes.

The hydrogen supply manifold has been designed to minimize non uniform film coolant flow, with less than one percent variation in pressure. It is a constant diameter manifold, allowing simple machining and fabrication methods to be used.

The nozzle coolant liner heat transfer analysis was completed based upon coolant passage geometry (width, height, and wall thickness) designed for operation at a chamber pressure of 2250 psia and an overall O/F of 7.2 with no film cooling. The liner is cooled with approximately 25 lbm/sec of water at 300 psia and 540°R. The water coolant flow rate and water pressure was set to cool the liner wall with no boiling at the maximum design condition. A minimum safety factor of 2.0 was used to establish water flow per channel, resulting in a nominal liner hot wall thickness of 0.040 inch. At the maximum operating point using nominal and worst case film coolant conditions, the maximum liner hot wall temperature predictions are approximately 1130°R. At the maximum operating point and no film cooling, the maximum predicted hot wall temperature is approximately 1740°R. These temperatures and operating conditions were used in the structural calculations for life predictions.

The injector ring heat transfer model was completed to provide temperature data for use in structural life calculations. Maximum wall temperatures of approximately 1600°F occur in the injector ring at the maximum operating point.

As shown in Figure 5.1.1-20, the critical life locations of the nozzle assembly were identified early in the program to be those areas with large thermal gradients.

Based upon the temperature predictions of the nozzle liner heat transfer models, final calculations of liner fatigue life were completed using a MARC finite element model. The MARC model was used to model plastic deformations which occur during the thermal cycling of the component. The MARC plastic analysis included incremental pressures and temperatures for five full test cycles showing cyclic loading for each test cycle. The analysis results show the design exceeds life requirements, with a life prediction of 350 cycles at the minimum film cooling, 2250 P_c operating point. The nozzle liner test program calls for 25 tests, for a total safety factor of 14. Fracture life calculations to establish the maximum acceptable flaw size allowable in the nozzle liner weld location have shown that a flaw size no greater than 50 percent of the wall thickness is allowable to meet life requirements.

The injector ring was also modeled using the MARC finite element analysis tool. At the same minimum film cooling, 2250 P_c operating point the injector ring life prediction is 250 cycles at the hot wall and 70 cycles at the coolant wall side. Each injector ring usage is no more than 7 cycles for a total safety factor of more than 10. Fracture life calculations to establish the maximum acceptable flaw size allowable in the injector ring weld location have shown that a flaw size no greater than 50 percent of the wall thickness is allowable to meet life requirements.

A brief analysis of transient side loads which may occur at start-up and shutdown due to flow separation showed that the low loads and the stiff nozzle structure minimize the effect of side loads on test hardware. A full 180-degree separation was assumed at an area ratio of 7 extending to the nozzle exit. The resulting side load due to this worst case separation scenario is only 2400 pounds. The net effect of a 2400-pound additional load acting on the nozzle side wall is minimal, due to the extremely stiff structure of the liner with the nickel plating structural closeout. Additional stiffness is inherent due to the water inlet and exit tubes mounted to the nozzle and the test stand.

The structural analysis performed includes:

1. Initial calculations of nozzle liner fatigue life for screening of raw material between centrifugally cast or spun liner.
2. Preliminary finite element modeling of film coolant injector ring to understand deflections and predict fatigue life.
3. Preliminary calculations of spun nozzle liner fatigue life for final sizing of liner passages.

The initial calculations of liner fatigue life indicated that the significantly better properties of a spun liner were required, and that the centrifugally cast method of fabricating the liner raw material should not be pursued. First cut results of the finite element modeling for the film coolant injector ring indicate that although the ring has some slight plastic deformation due to high thermal loads, there will be sufficient life to meet all test goals. The preliminary nozzle liner fatigue life calculations are ongoing. The liner passages were sized for optimal heat transfer characteristics, and may be reduced in width to improve fatigue life if necessary.

The mechanical design work completed for the nozzle liner included:

1. Providing raw material definition for ordering liner, manifold, and injector ring raw material.
2. Determining fabrication sequences and reviewing preliminary tooling designs.
3. Determining assembly and disassembly sequences and coordinating assembly feature requirements on the components with the assembly engineers.
4. Selecting seals, fasteners, water coolant tube sizes, and other auxiliary hardware.
5. Packaging and arrangement of the chamber/nozzle components to best provide for assembly and disassembly of the components, including the regular changeout of the four different injector rings at TS116 during testing.
6. Defining fits, clearances, tolerances and other critical dimensions.
7. Identifying weld types.

A change in the hydrogen inlet manifold location is shown in Figure 5.1.1-7. The previous configuration used a "G-CON" inlet flange and extension pipe to duct in the gaseous hydrogen. NASA TS116 personnel contacted P&W in mid-November 1991 and requested a configuration change to a simple AN fitting in place of the G-CON flange. The detail drawings and the machining operation sheets were changed to reflect the new inlet configuration.

The secondary film cooling cavity configuration was finalized. As the results of the Computational Fluid Dynamics (CFD) analysis showed, the circumferential distribution in the secondary cavity was poor, which could result in local hot spots during test rig operation. The new configuration uses a distribution plate, wherein a piece of porous stainless steel (PSS) is attached to the cavity annulus just downstream of the metering orifices to allow the flow coming through the orifices to splash and turn before exiting the cavity. This configuration, shown in Figure 5.1.1-21, is intended to slow down and better distribute the flow so that uniform circumferential cooling of the injector ring is achieved.

A CFD model of this area was built for the secondary cavity and core gas stream flow at the low inlet flow condition, as shown in Figure 5.1.1-22. The assumptions made during the initial modeling are also shown, including the assumption that uniform flow conditions exist just downstream of the PSS ring. The core gas and secondary coolant flow interactions and resultant temperature contours are shown in Figures 5.1.1-23 and 5.1.1-24. Figure 5.1.1-23 is a view of the combustion chamber from upstream of the throat, including the secondary cavity and to approximately one-inch downstream of the secondary cavity exit into the core flow. Figure 5.1.1-24 is an enlarged view of the secondary cavity flow entering the core flow, showing the cooling effect of the coolant gas against the injector ring wall. Figure 5.1.1-25 shows the velocity vectors overlayed onto the hydrogen mass fraction contours, which shows that vortex mixing is occurring at the secondary cavity exit location. This vortex mixing causes a small amount of hot gas flow to entrain against the injector ring lip, thus reducing the cooling effectiveness. Figure 5.1.1-28 shows the pressure contours at the interaction which indicate a shock induced by the step in the nozzle wall contour. This shock will also be minimized by the increased radius on the injector ring lip. The final CFD analysis will be completed during the next reporting period, and will include all of the updated design details and operating conditions.

A scale model of the secondary cavity was designed and built to verify the effectiveness of the flow distribution in the secondary cavity, to verify the assumption of uniform flow just downstream of the PSS, and to examine an alternative design configuration. This flow rig is a two-dimensional, approximately 3X scale model of the secondary cavity, and is capable of both water and air testing. During water testing, colored dyes will be injected through the metering holes to visually examine circumferential flow distribution at the nozzle inlet. During the air testing, pressure probes will be used to obtain static pressure measurements in the secondary cavity. Measurements will be taken both with and without the PSS distribution plate to characterize its effectiveness in circumferential flow distribution. An alternative configuration will be included in the flow rig, which will use angled, slotted holes in the secondary cavity wall to force the flow to spread out circumferentially.

The primary and secondary film cooling configurations were analyzed using computational fluid dynamics (CFD). The results of the analysis are shown in Figures 5.1.1-26 through 5.1.1-39, and include results from design support for the secondary cavity, analysis of the core, secondary, and primary flow interactions, and analysis of the three-dimensional primary film coolant injector design. As shown in the previous bimonthly report, the film coolant distribution at the secondary cavity location was poor, which could result in local hot spots for the injector rings during hot-fire operation. The baseline configuration was analyzed using a distribution plate, wherein a piece of porous stainless steel (PSS) is attached to the cavity annulus just downstream of the metering orifices to allow the flow coming through the orifices to splash and turn before exiting the cavity. This configuration, shown in Figure 5.1.1-26, is intended to slow down and better distribute the flow so uniform circumferential cooling of the injector ring is achieved.

A CFD model of this area was built for the secondary cavity and core gas stream flow at the low inlet flow condition (Figure 5.1.1-27). The assumptions made during the initial modeling are also shown, including the assumption that uniform flow conditions exist just downstream of the PSS ring. Based upon the results discussed in the last bimonthly, the secondary cavity design was modified to provide a larger injector ring lip radius in order to reduce core gas mixing with the film flow. In addition, several gas inflow conditions were modified to understand and improve the film coolant properties and resulting wall temperatures. Table 5.1.1-2 summarizes the geometry and fluid conditions for the two secondary cavity analyses. The major changes were an increased lip radius, and an increased inlet pressure. The increased pressure represents the higher flow condition that will be run in the test matrix. Further analyses will study the impact of the low flow condition with the updated geometry changes included. The hydrogen mass fraction contours are compared in Figure 5.1.1-29, where significantly reduced vortex mixing of the film coolant with the core gas is evident. Figure 5.1.1-30 shows the gas temperature contours associated with the old and new designs. An adiabatic wall was used in all analyses, and no backside convective cooling of the injector lip was taken into account. The temperature contours for the first half of the injector ring (where backside cooling is not in effect) match closely with heat transfer temperature predictions used in the structural analysis. Figure 5.1.1-31 shows the penalty for the higher mass flowrate, which is the increased shock strength at the injection location on the pressure contour plots. This increased flowrate has a small impact on the pressure sensed by the primary lip, and will therefore have a small performance impact on the nozzle.

Figure 5.1.1-45 shows the film injector flow system with the porous stainless steel baseline design. Figure 5.1.1-46 shows a side view photograph of the flow model. Figure 5.1.1-47 shows the location of the side wall pressure taps, the slot exit pressure probe locations, and the dye injection ports on a schematic of the flow rig. Figures 5.1.1-48 through 5.1.1-50 show gage total pressure at the slot exit location for the baseline porous stainless steel design compared to the control configuration (no distribution plate), the 45 degree ramp design, and the double-perforated plate design. The pressure distribution on the outside of the first and third orifice locations can be ignored because of end wall effects. The pressure distribution of the baseline design is significantly better both at and between orifices than the other configurations. Figures 5.1.1-51 through 5.1.1-54 show the pressure distribution of the different configurations at the location of the pressure taps, just downstream of the metering orifice, as well as the slot exit measurements. In all of the cases, the porous stainless steel

design is an improved distribution between the first and the third orifices, when compared to the other design configurations. Based upon the flow rig data, the porous stainless steel design remains the baseline design and will be included in the hot fire testing.

The uncooled film injector ring design task is complete, and is intended to provide (for hot fire testing) a durable injector ring made from a high-temperature material so that primary film cooling can be blocked. By blocking the primary film cooling supply, the calorimeter nozzle can be run with essentially no film cooling to provide an anchor point for the code validation tasks and quantitatively examine the absolute effects of all film cooling configurations to be tested. The material for the uncooled ring will be chosen based upon availability and test durability concerns. A high-temperature capability graphite material is being considered to limit thermal stress. The secondary cavity flow, which provides some injector ring coolant, will still be used during the test to ensure a positive coolant outflow at the chamber/nozzle flange location and reduce injector ring wall temperatures. The primary coolant flow passages will not be machined into the part, thereby effectively blocking most of the primary coolant flow except that which *leaks* underneath the injector ring/nozzle mating fit (less than 5 percent of the total nominal film coolant flow).

Table 5.1.1-2. Comparison of Old and New Secondary Slot Model Geometry and Inflow Conditions

Parameter	Old Slot	New Slot
R _{lip}	0.005 in.	0.070 in.
m	0.210 lbm/sec	0.352 lbm/sec
P _O	70 psi	94.26 psi
T _O	530°R	535.5°R
M	0.20	0.05
P	68.06 psi	94.1 psi
T	525.8°R	535.25°R
ρ	7.536×10^{-4} slug/ft ³	1.023×10^{-3} slug/ft ³
γ	1.4	1.386

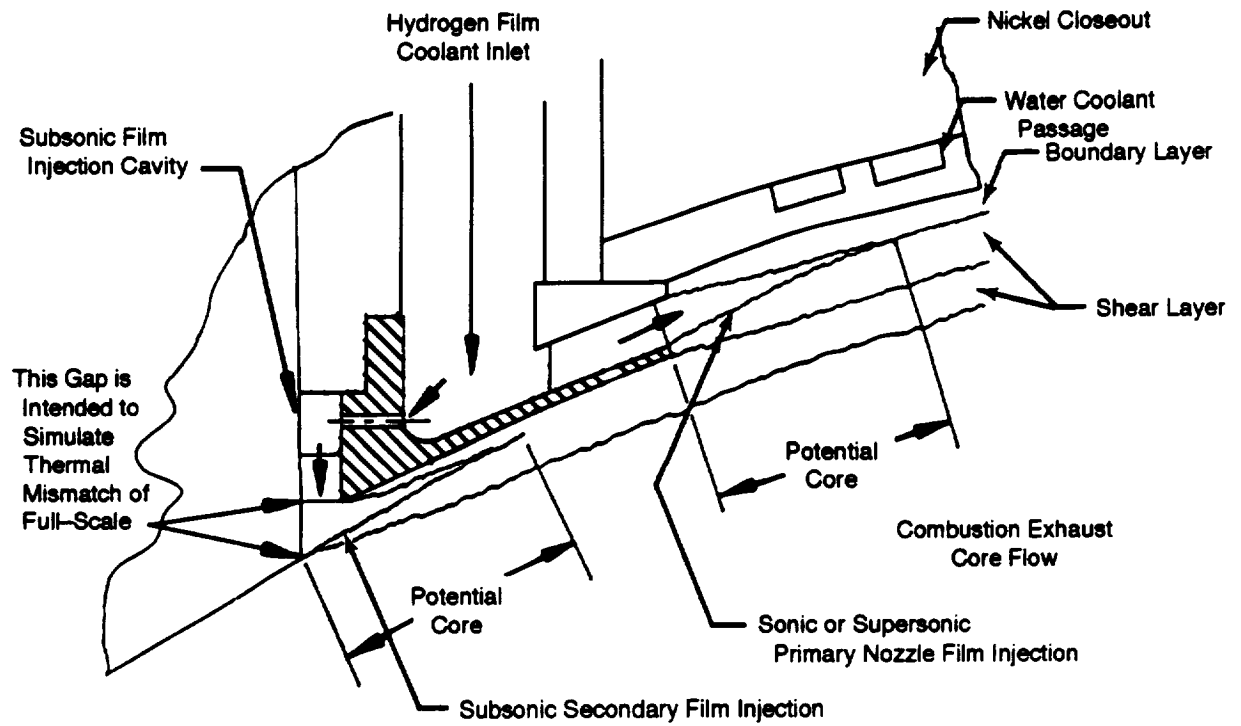
The next major CFD analysis was performed to understand the interaction of the core flow with the primary film coolant. Table 5.1.1-3 lists the boundary conditions used for the core flow, the secondary cavity inflow, and the primary cavity inflow in the CFD model. The hydrogen mass fraction contours shown in Figure 5.1.1-32 show that these conditions produce less mixing of secondary film and minimal impact of the secondary film on the primary film injection. The temperature contours shown in Figure 5.1.1-33 show that the secondary film layer provides adequate cooling for the injector ring when considering that the backside cooling is the primary cooling mechanism for the second one half of the injector ring length. The interaction of the normal and tangential film injection produces a complex shock and expansion wave, which is shown in Figure 5.1.1-34. These shocks are relatively weak and do not have a significant impact on the integrity of the primary film cooling jet, which is shown in Figure 5.1.1-35. The mixing of the film cooling jet and the core flow indicates that the exhaust film is approximately 50 percent hydrogen at the nozzle exit. The temperature contours, plotted in Figure 5.1.1-36, show that the primary film layer provides adequate cooling for the nozzle skirt. The hottest gas temperature at the nozzle wall is found near the exit and is approximately 1300°R. This model also assumes adiabatic wall for conservative temperature predictions. These temperature predictions are slightly lower than the temperatures used in the structural analysis, which indicates a conservative approach to the test hardware design. Figure 5.1.1-37 shows the pressure contours, revealing shock losses due to the throat expansion, the secondary, and primary film injection. These performance losses will be quantified and compared to performance predictions made with TDK analysis.

Table 5.1.1-3. Subscale Core/Film Coolant Interaction — Imposed Boundary Values for High-Flow Case

Property	Core Inflow	Subsonic Inflow	Primary Inflow
P ₀	2250 psi	94.26 psi	—
T ₀	6780°R	535.5°R	—
M	0.2233	0.05	1.456
P	2187.38 psi	94.1 psi	55.5 psi
T	6735.0°R	535.25°R	372.1°R
ρ	1.448×10^{-2} slug/ft ³	1.023×10^{-3} slug/ft ³	8.677×10^{-4} slug/ft ³
γ	1.134	1.386	1.386
\dot{m}	84.21 lbm/sec	0.352 lbm/sec	1.773 lbm/sec
Mesh Size: 75 × 61, 25 × 69, 59 × 81, 36 × 118, 36 × 118; 19,575 Grid Points			

Preliminary CFD analysis of the primary injector cavity included modeling the large supersonic injector to determine exit plane conditions. These results are shown in Figures 5.1.1-38 and 5.1.1-39. The pressure contours and Mach contours show that an excellent uniform exit profile achieved at the injection point into the nozzle. Further CFD analysis will include coupling the three-dimensional primary injector mesh with the core flow to determine the impact of the injector webs on the film integrity.

A scale model of the secondary cavity has been built and tested in the Aerothermal Design Lab facility at Pratt & Whitney (P&W). The purpose of this flow rig is to verify the effectiveness of the flow distribution in the secondary cavity, to verify the assumption of uniform flow just downstream of the porous stainless steel, and to examine several alternate design configurations. Figures 5.1.1-40, 5.1.1-41, and 5.1.1-42 show the top, front, and side views respectively, of the flow rig. Figure 5.1.1-43 can be compared with the secondary cavity design shown in Figure 7-2 to see the close match in geometry. The rig was used for both air and water testing. During water testing, colored dyes were injected through the metering holes to visually examine circumferential flow distribution at the nozzle inlet. During the air testing, pressure probes were used to obtain static pressure measurements in the secondary cavity. Measurements were taken both with the PSS distribution plate and other designs in order to characterize its effectiveness in circumferential flow distribution. The configurations run in the flow rig were various schemes to distribute the flow, and included Feltmetal, a screen, a simple plate with a row of holes drilled in it, the ramp design shown in Figure 5.1.1-44, and the PSS baseline design. Both the water and air testing results to date favor the PSS design over the next best configuration, the "ramp" design. Static pressure measurements taken at the cavity exit during air testing are shown in Figure 5.1.1-44. The PSS provides a more uniform pressure drop distribution across the cavity. One additional configuration is being built and tested in the flow rig during the next reporting period. All of the designs are interchangeable in the same secondary cavity annulus, so manifold and nozzle machining is not impacted.



4995

Figure 5.1.1-1. Subscale Nozzle Film Cooling Simulates Full-Scale Design

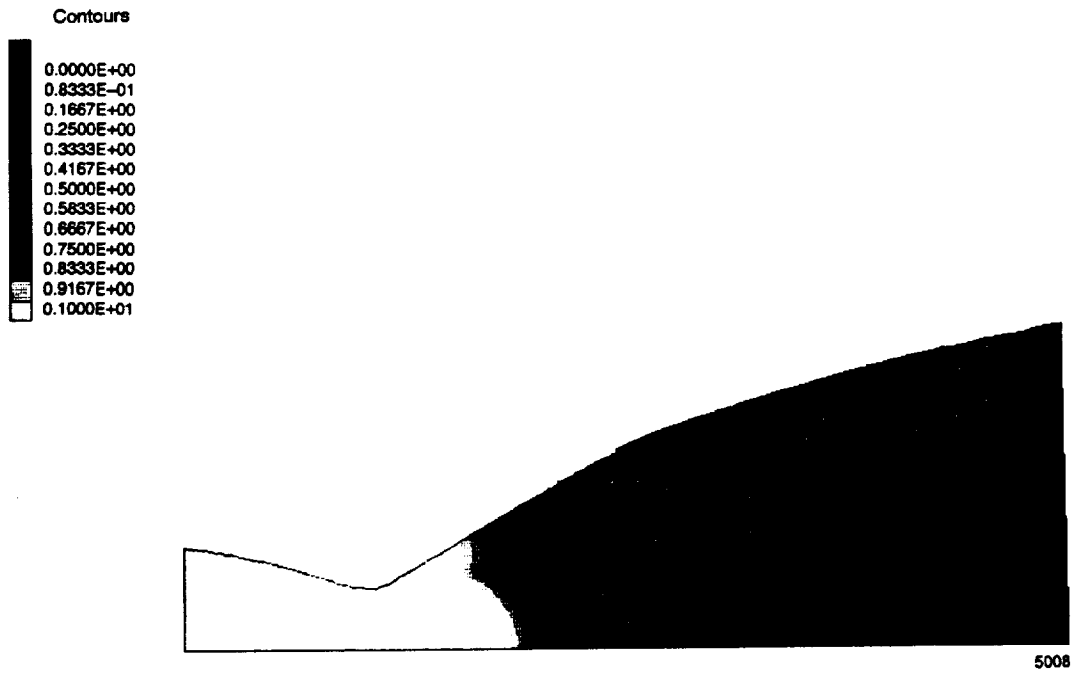


Figure 5.1.1-2. Subscale Nozzle Static Pressure Field

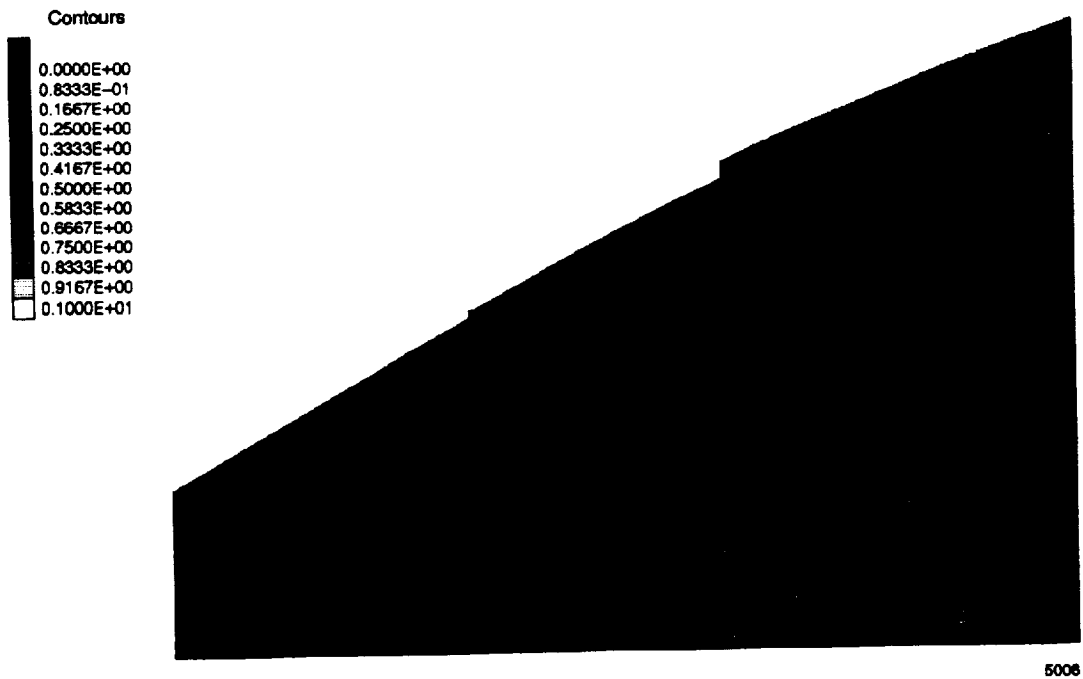


Figure 5.1.1-3. Film Coolant Injector Flow into Main Stream of Hot Gas Flow

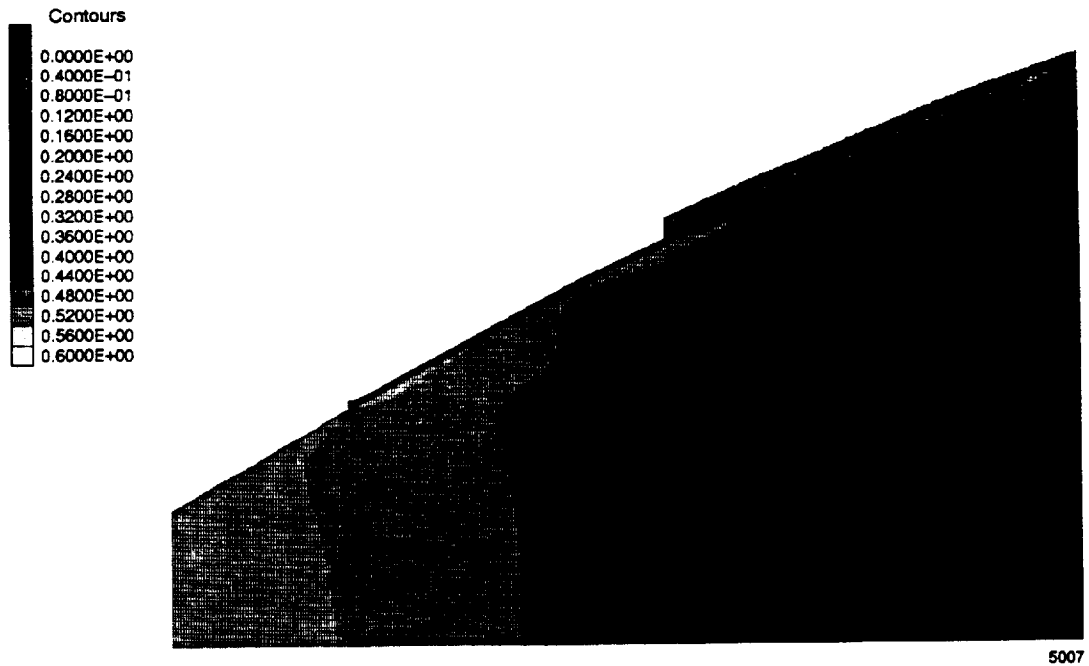


Figure 5.1.1-4. Subscale Nozzle Temperature Contours

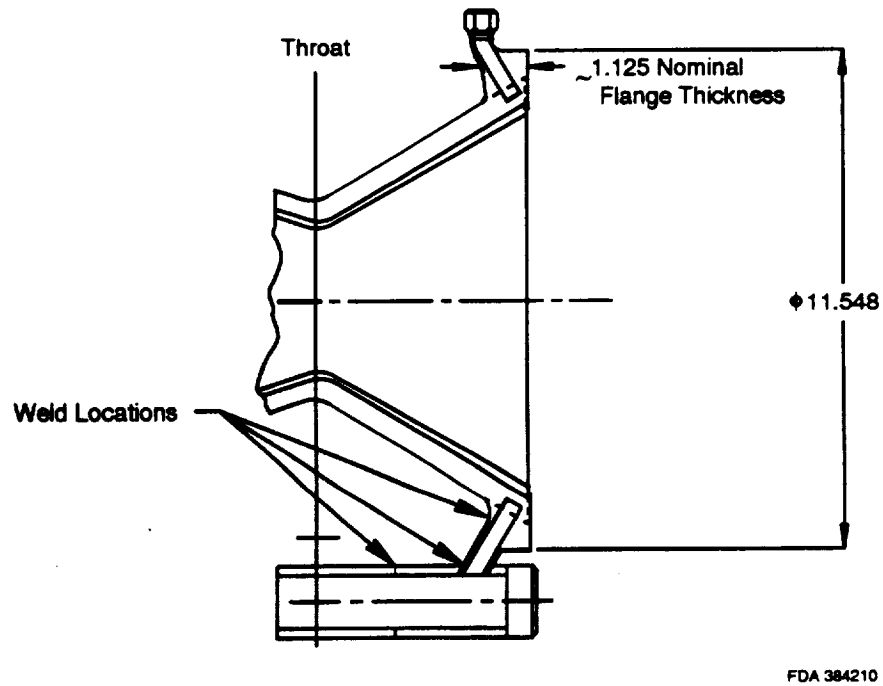
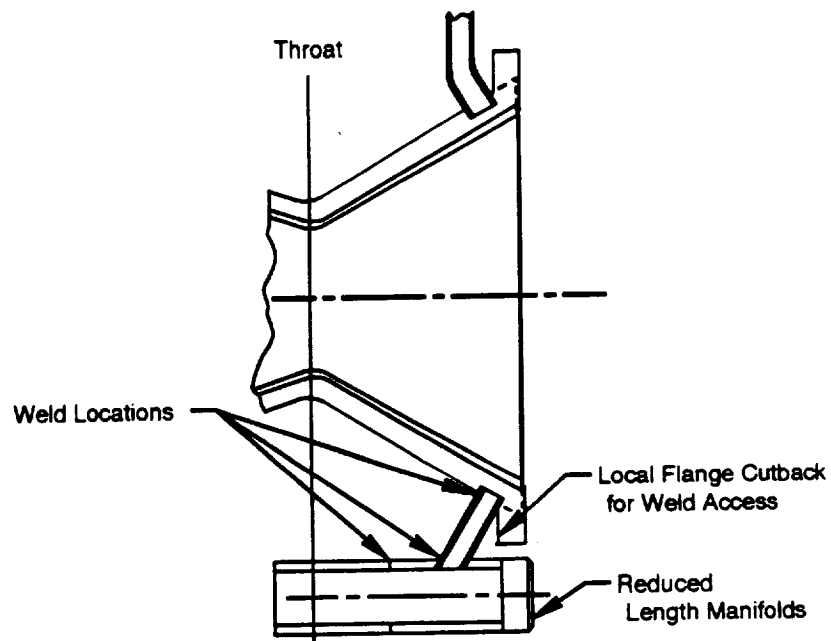
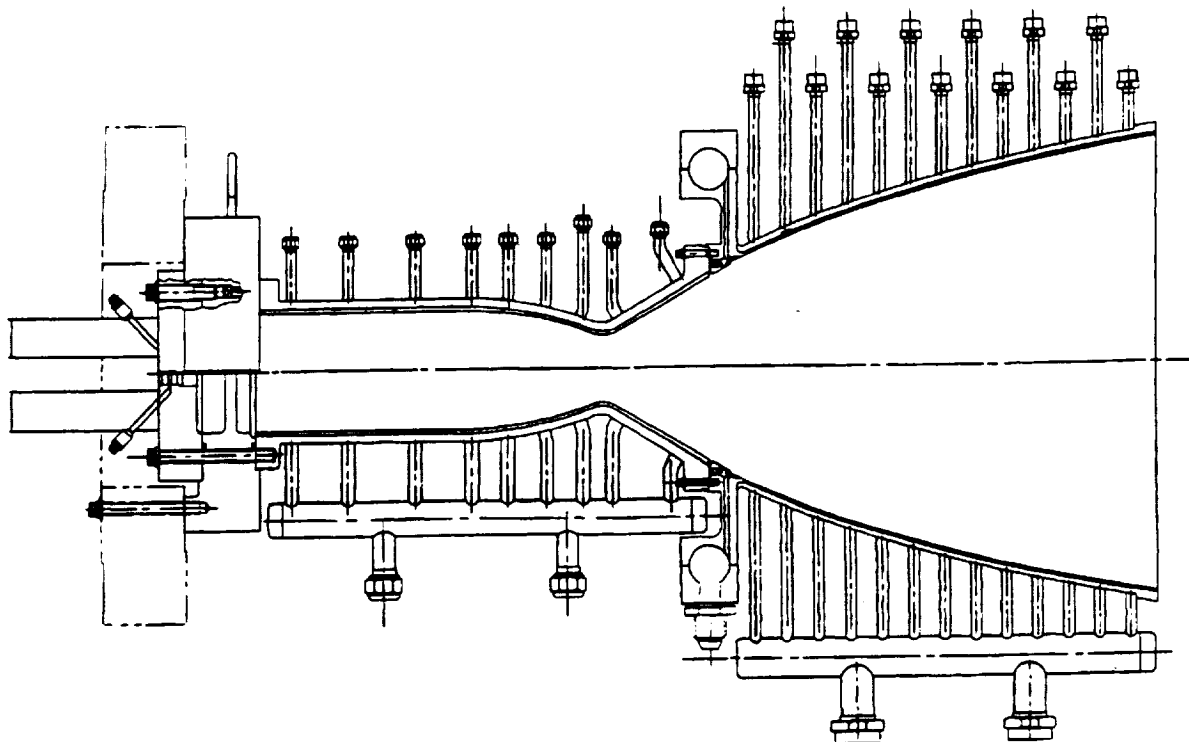


Figure 5.1.1-5. Chamber Rework Section at Port 72



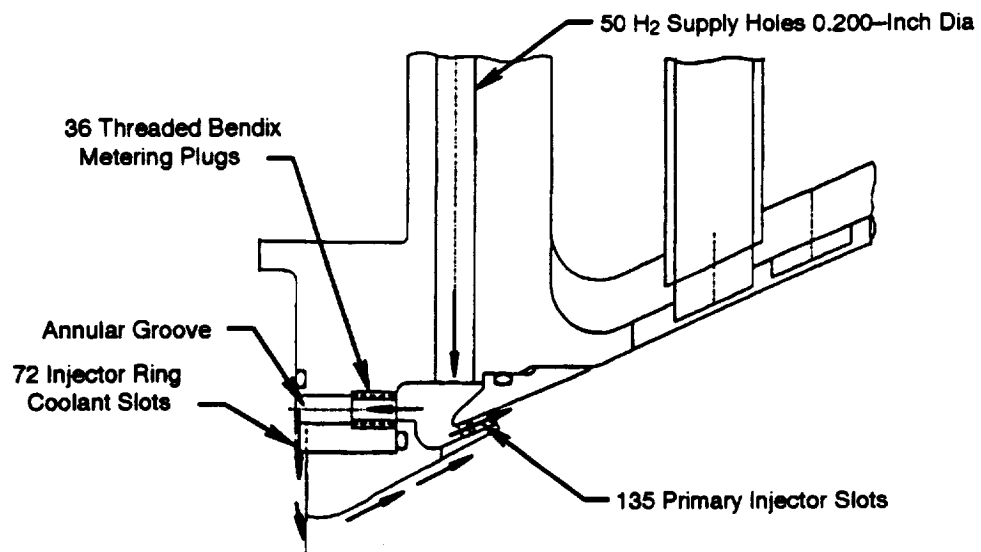
FDA 384211

Figure 5.1.1-6. Chamber Rework Section at Port 71



12243

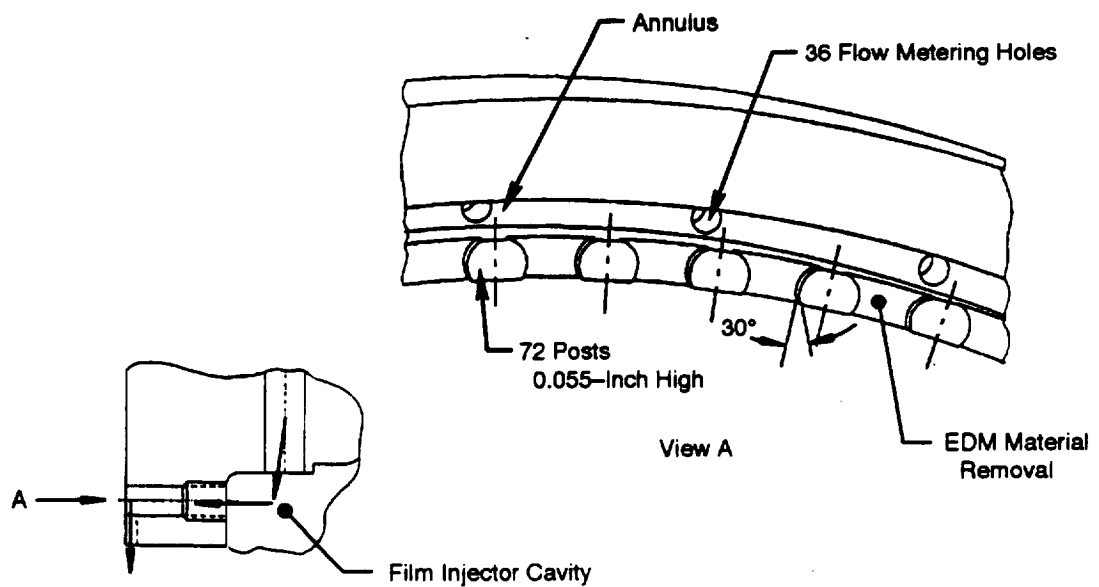
Figure 5.1.1-7. Subscale Thrust Chamber Assembly



9448

9448

Figure 5.1.1-8. Film Coolant Injector Configuration



9449

Figure 5.1.1-9. Subsonic Cavity Configuration

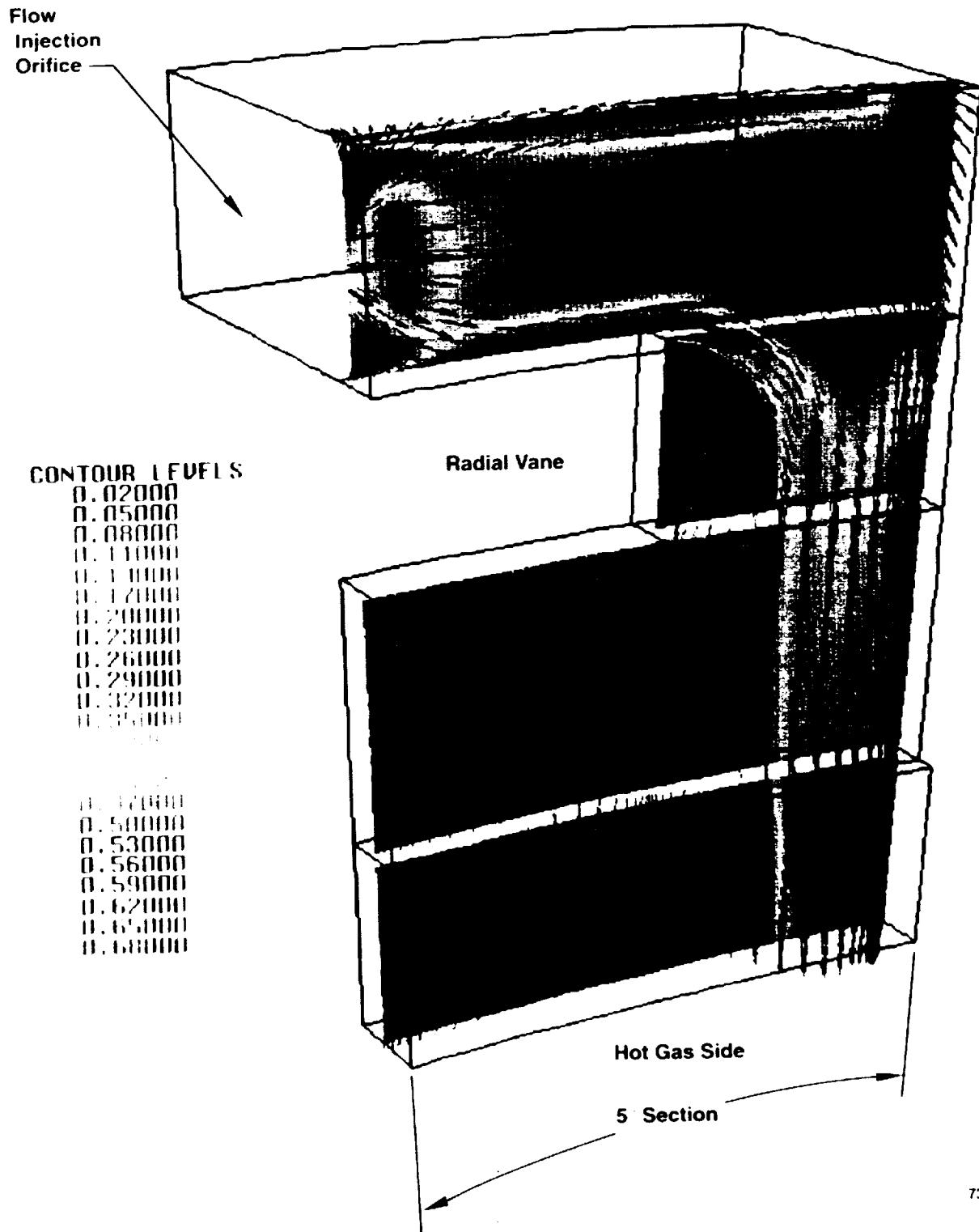


Figure 5.1.1-10. Flow Velocity Contours in Subsonic Cavity for Highest Inlet Pressure Case — Square Post Design

**CONTOUR LEVELS**

0.04000
0.10000
0.16000
0.22000
0.28000
0.34000
0.40000
0.46000
0.52000
0.58000
0.64000

0.82000
0.88000
0.94000
1.00000
1.06000
1.12000
1.18000

*Figure 5.1.1-11. Flow Velocity Field at Subsonic Cavity
Exit Plane for Highest Inlet Pressure Case — Square Post Design*

CONTOUR LEVELS

0.04000
0.10000
0.16000
0.22000
0.28000
0.34000
0.40000
0.46000
0.52000
0.58000
0.64000
0.70000
0.76000

DESIGN VELOCITY

1.00000
1.06000
1.12000
1.18000
1.24000
1.30000
1.36000

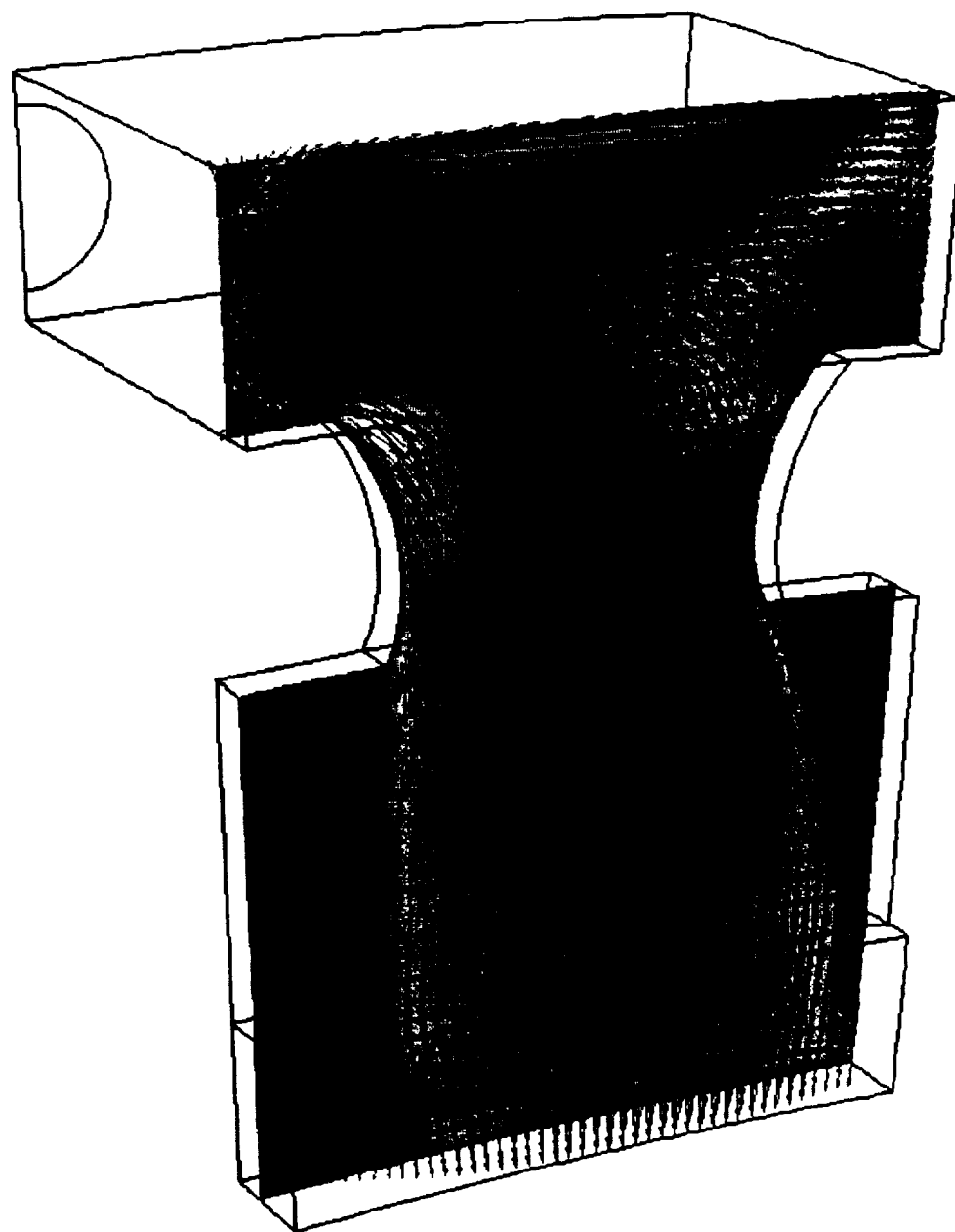
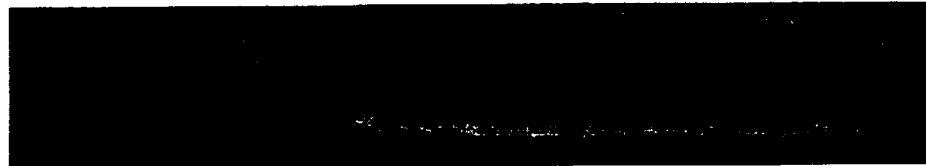


*Figure 5.1.1-12. Flow Velocity Contours in Subsonic Cavity
for Lowest Inlet Pressure Case — Rounded Post Design*



CONTOUR LEVELS

0.04000
0.10000
0.16000
0.22000
0.28000
0.34000
0.40000
0.46000
0.52000
0.58000
0.64000

0.82000
0.88000
0.94000
1.00000
1.06000
1.12000
1.18000

*Figure 5.1.1-13. Flow Velocity Field at Subsonic Cavity Exit
Plane for Lowest Inlet Pressure Case — Rounded Post Design*

CONTOUR LEVELS

0.04000
0.10000
0.16000
0.22000
0.28000
0.34000
0.40000
0.46000
0.52000
0.58000
0.64000
0.70000

0.76000
0.82000
0.88000
0.94000
1.00000
1.06000
1.12000
1.18000
1.24000
1.30000
1.36000

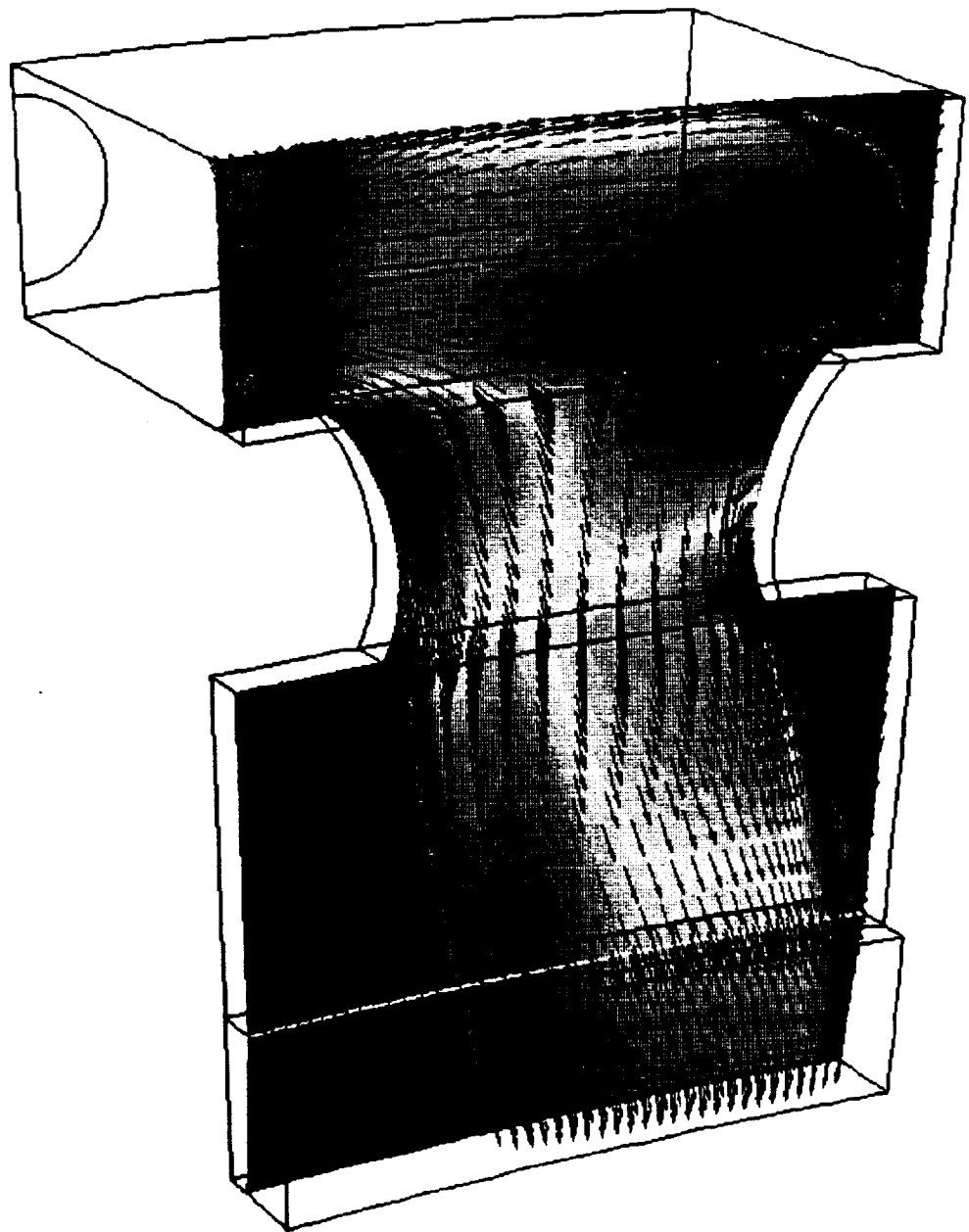


Figure 5.1.1-14. Flow Velocity Contours in Subsonic Cavity
for Highest Inlet Pressure Case — Rounded Post Design

ORIGINAL PAGE IS
OF POOR QUALITY



CONTOUR LEVELS

0.04000
0.10000
0.16000
0.22000
0.28000
0.34000
0.40000
0.46000
0.52000
0.58000
0.64000

0.82000
0.88000
0.94000
1.00000
1.06000
1.12000
1.18000

*Figure 5.1.1-15. Flow Velocity Field at Subsonic Cavity Exit
Plane for Highest Inlet Pressure Case — Rounded Post Design*

CONTOUR LEVELS

0.04000
0.10000
0.16000
0.22000
0.28000
0.34000
0.40000
0.46000
0.52000
0.58000
0.64000
0.70000

0.76000

CONTOUR LEVELS

1.00000
1.06000
1.12000
1.18000
1.24000
1.30000
1.36000

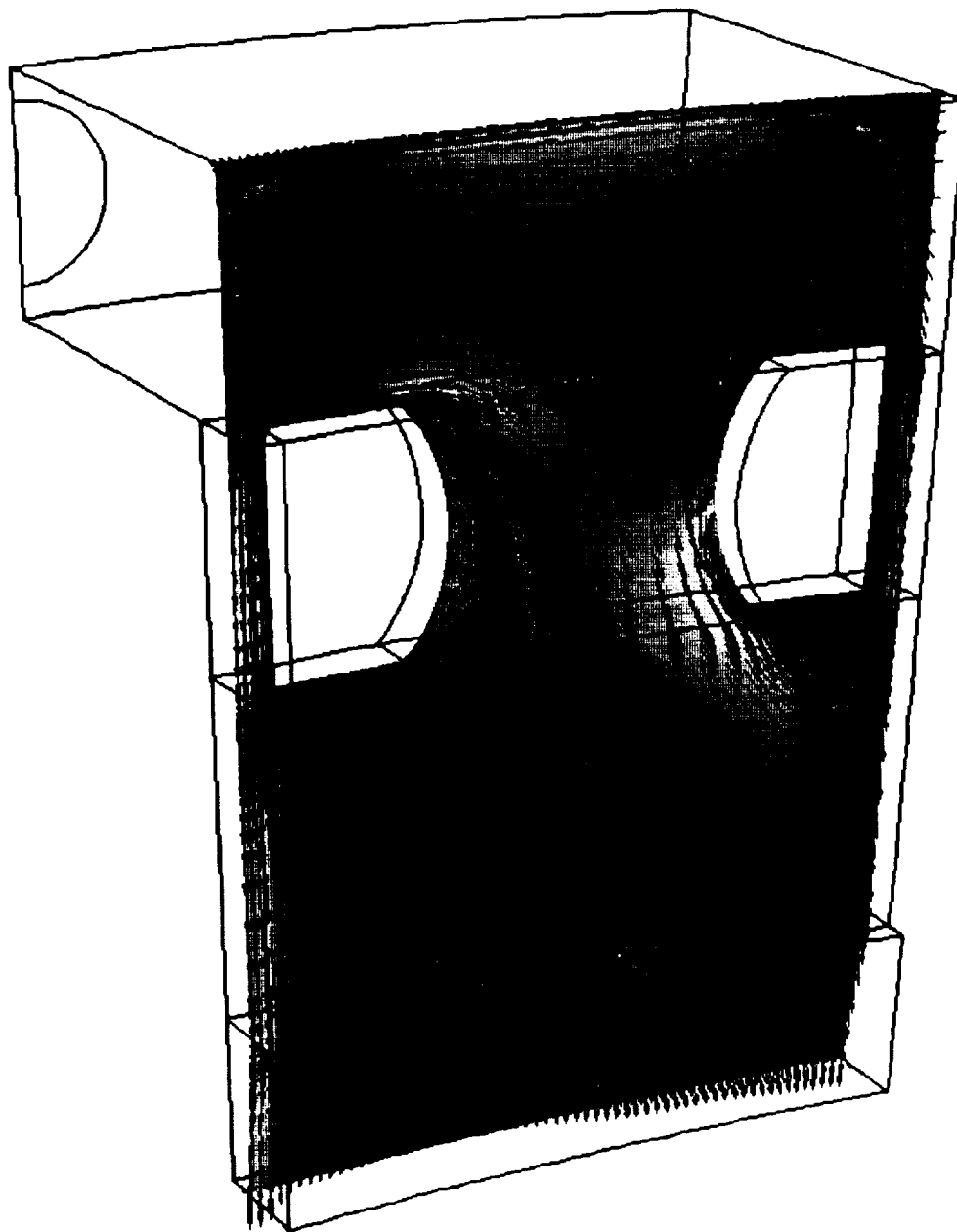


Figure 5.1.1-16. Flow Velocity Contours in Subsonic Cavity for Lowest Inlet Pressure Case — Rounded Post/Milled Slot Design



CONTOUR LEVELS

0.04000
0.10000
0.16000
0.22000
0.28000
0.34000
0.40000
0.46000
0.52000
0.58000
0.64000

0.82000
0.88000
0.94000
1.00000
1.06000
1.12000
1.18000

*Figure 5.1.1-17. Flow Velocity Field at Subsonic Cavity Exit Plane for
Lowest Inlet Pressure Case — Rounded Post/Milled Slot Design*

CONTOUR LEVELS

0.04000
0.10000
0.16000
0.22000
0.28000
0.34000
0.40000
0.46000
0.52000
0.58000
0.64000
0.70000
0.76000

0.82000
0.88000
0.94000
1.00000
1.06000
1.12000
1.18000
1.24000
1.30000
1.36000

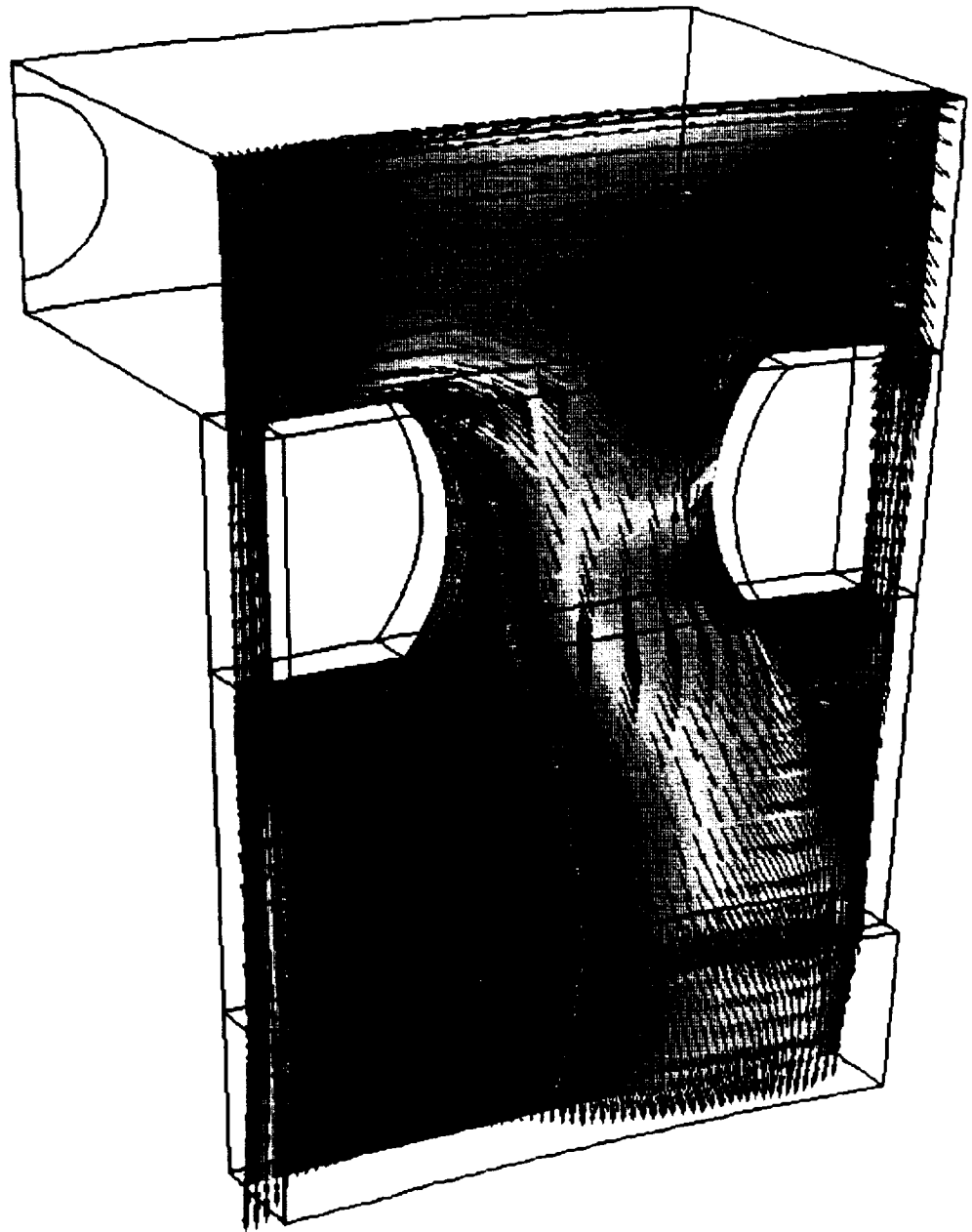


Figure 5.1.1-18. Flow Velocity Contours in Subsonic Cavity for Highest Inlet Pressure Case — Rounded Post/Milled Slot Design

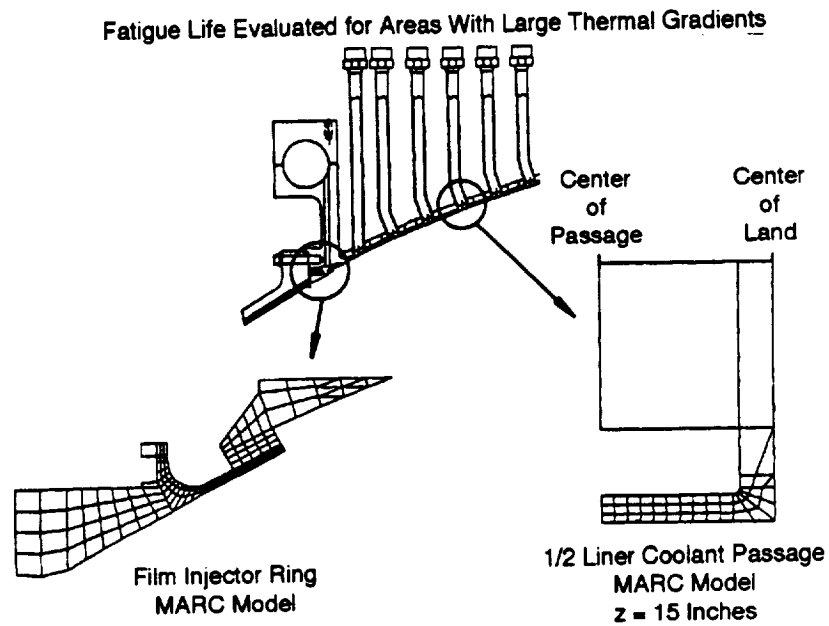


CONTOUR LEVELS

0.04000
0.10000
0.16000
0.22000
0.28000
0.34000
0.40000
0.46000
0.52000
0.58000
0.64000

0.70000
0.76000
0.82000
0.88000
0.94000
1.00000
1.06000
1.12000
1.18000

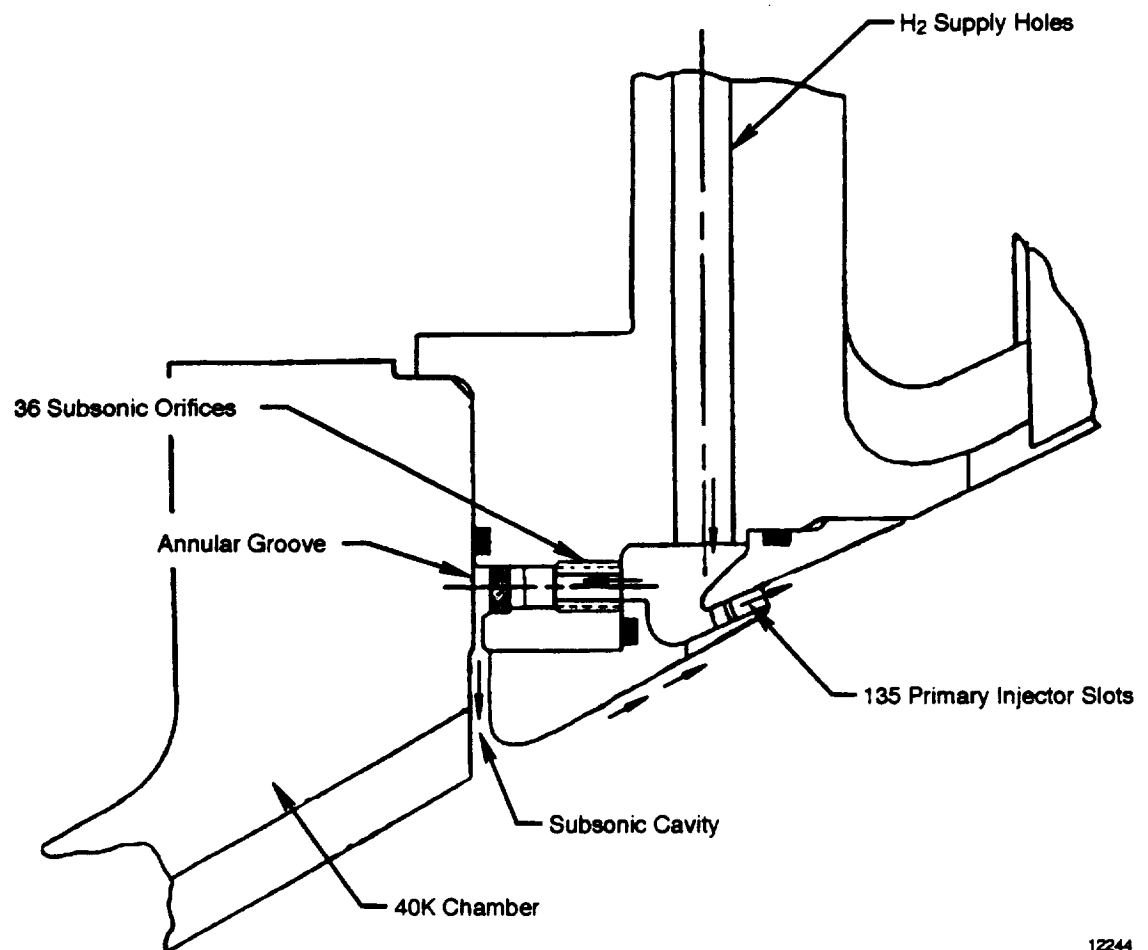
*Figure 5.1.1-19. Flow Velocity Field at Subsonic Cavity Exit Plane for
Highest Inlet Pressure Case — Rounded Post/Milled Slot Design*



9450

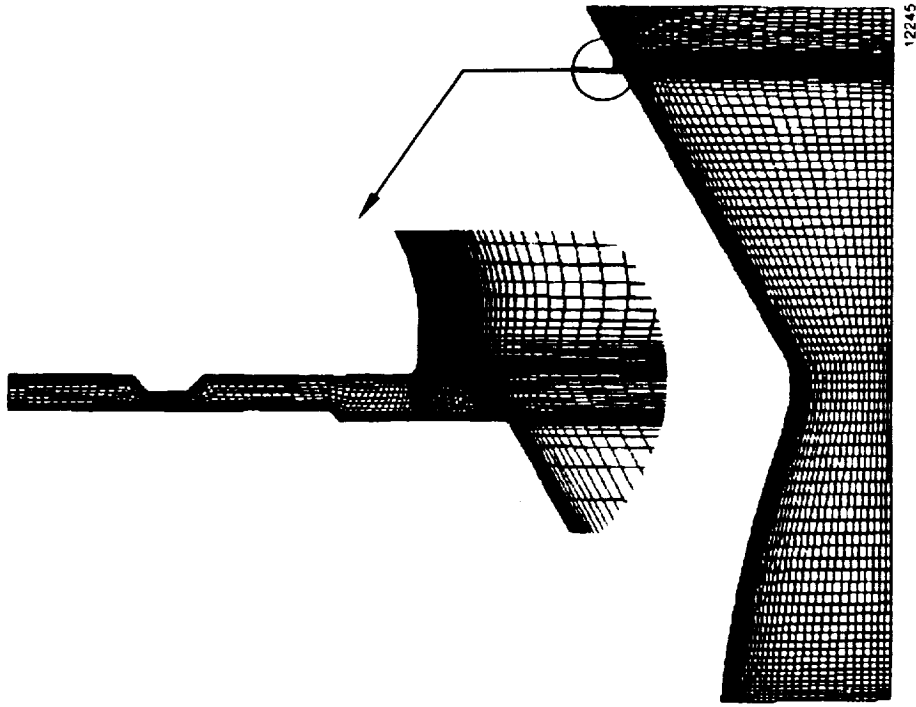
9450

Figure 5.1.1-20. Nozzle Assembly Critical Life Locations



12244

Figure 5.1.1-21. Analysis of Secondary Coolant Cavity — Design Solution: Porous Stainless Steel Filter



Assumptions:

- Algebraic Turbulence Model
- Equilibrium Chemistry in the Chamber
- Frozen Chemistry in the Interaction Region
- Chamber $P_o = 2250$ psi, $T_o = 6500^\circ\text{R}$
- Injector $P_o = 70$ psi, $T_o = 530^\circ\text{R}$
- Chamber Walls Fixed at $T = 1440^\circ\text{R}$
- Injector Walls are Adiabatic

Figure 5.1.1-22. CFD Flow Model of Secondary Cavity Flow Interaction

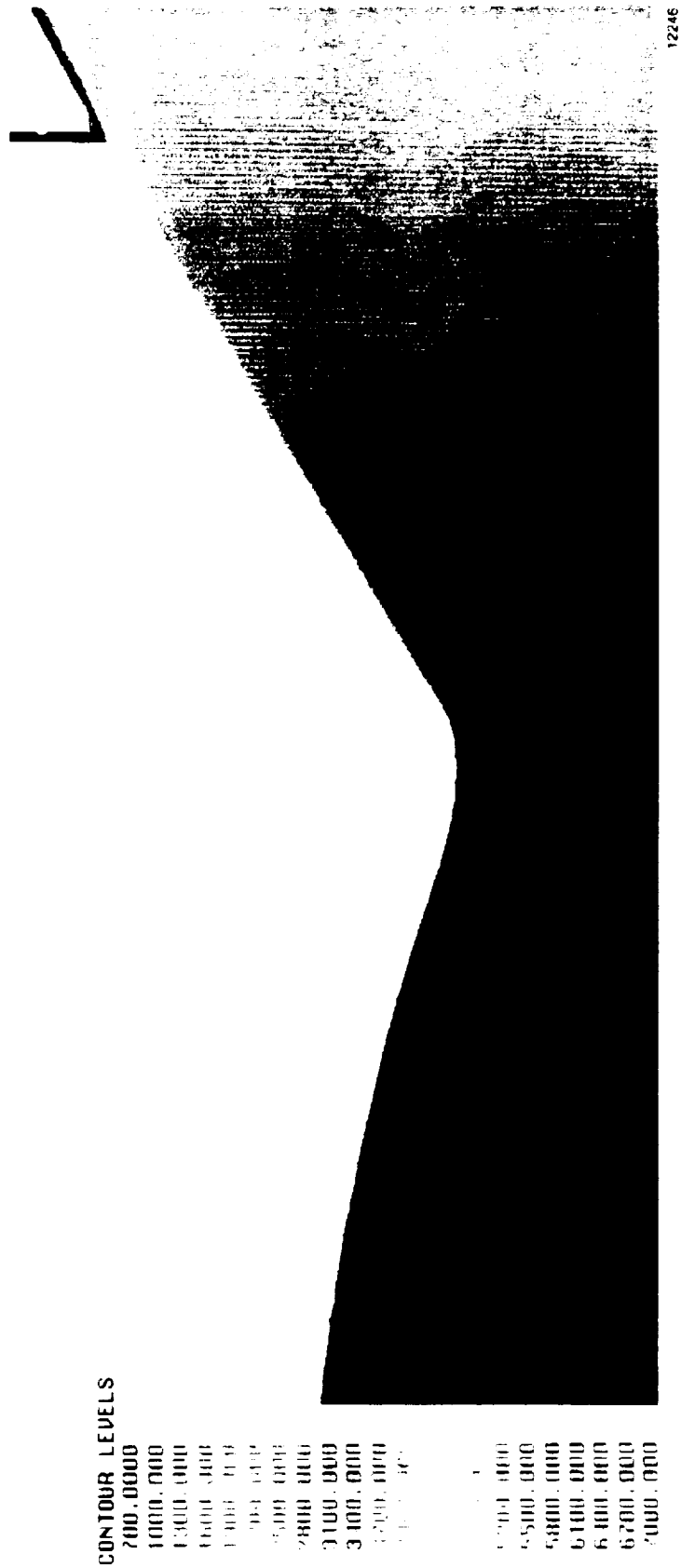


Figure 5.1.1-23. Core/Secondary Coolant Interaction — Nozzle Temperature Contours



Figure 5.1.1-24. Core/Secondary Coolant Flow Interaction — Temperature Contours Indicate Entrainment of Core Gases

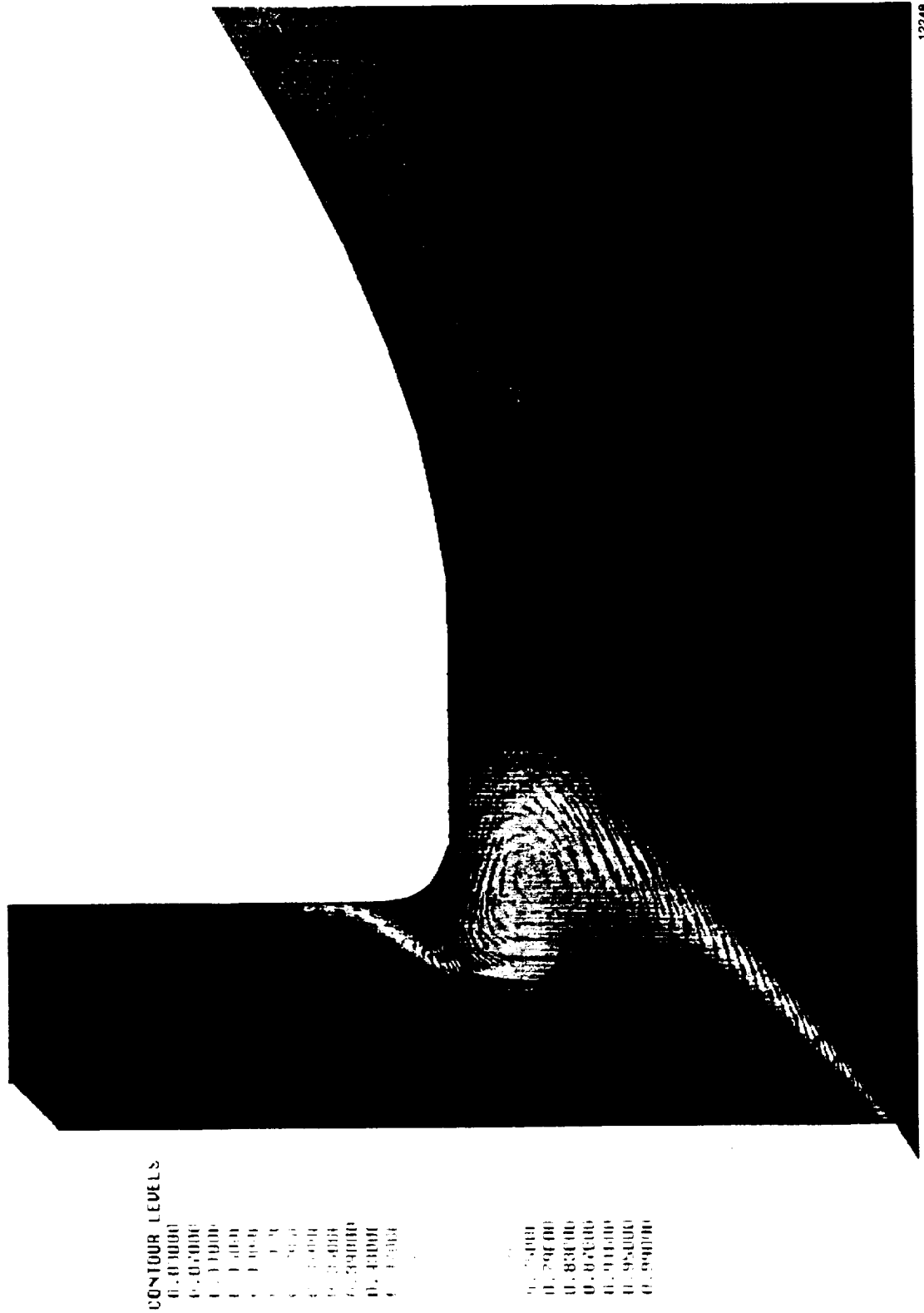


Figure 5.1.1-25. Core/Secondary Coolant Flow Interaction - Velocity Vectors/ H_2 Mass Fraction Contours Show Vortex Mixing

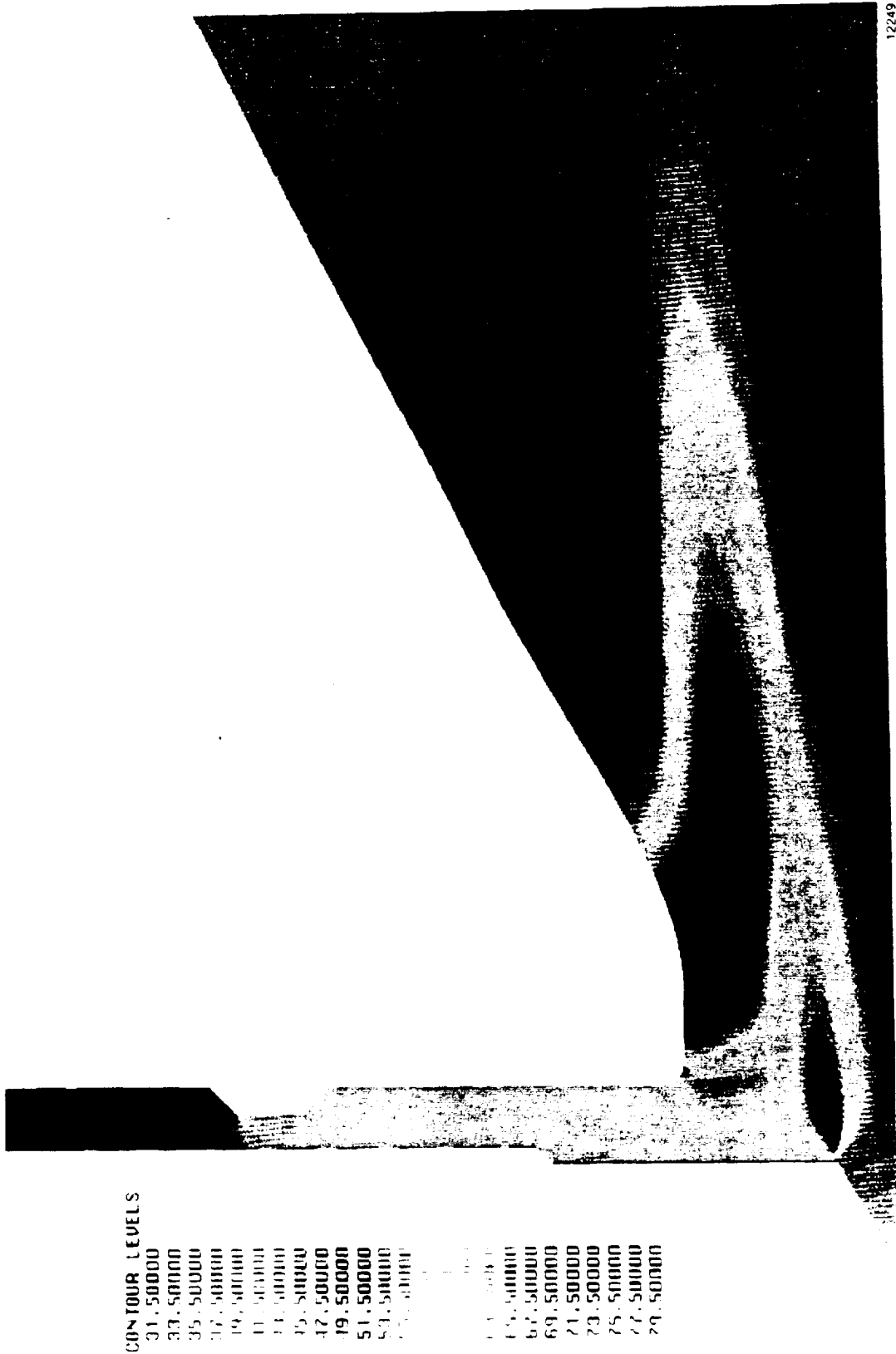
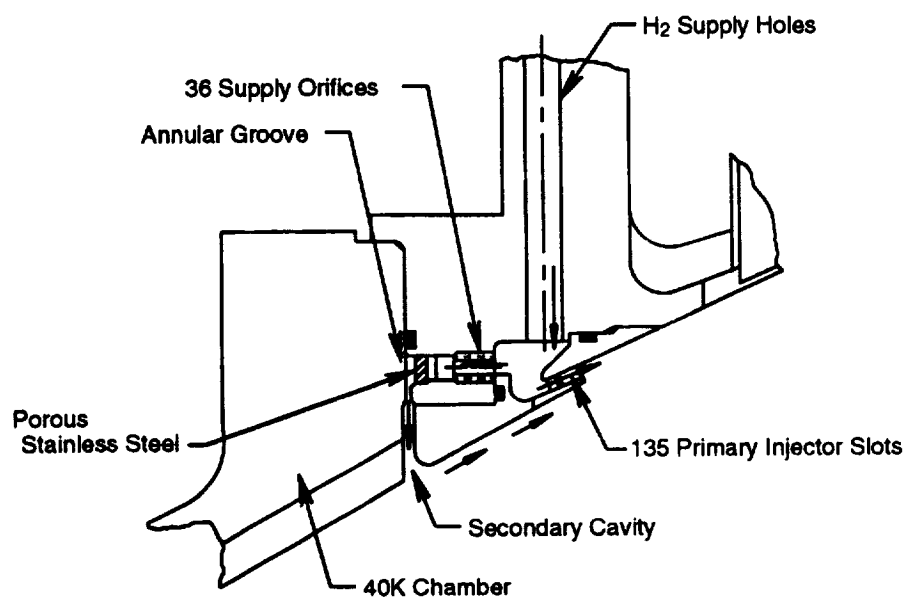


Figure 5.1.1-26. Core/Secondary Coolant Flow Interaction — Pressure Contours Indicate a Step-Induced Shock



14588

Figure 5.1.1-27. Secondary Cavity Design Using Porous Stainless Steel for Flow Distribution

Assumptions:

- Algebraic Turbulence Model
- Equilibrium Chemistry in the Chamber
- Frozen Chemistry in the Interaction Region
- Chamber $P_o = 2250$ psi, $T_o = 6500^\circ\text{R}$
- Injector $P_o = 70$ psi, $T_o = 530^\circ\text{R}$
- Chamber Walls Fixed at $T = 1440^\circ\text{R}$
- Injector Walls are Adiabatic

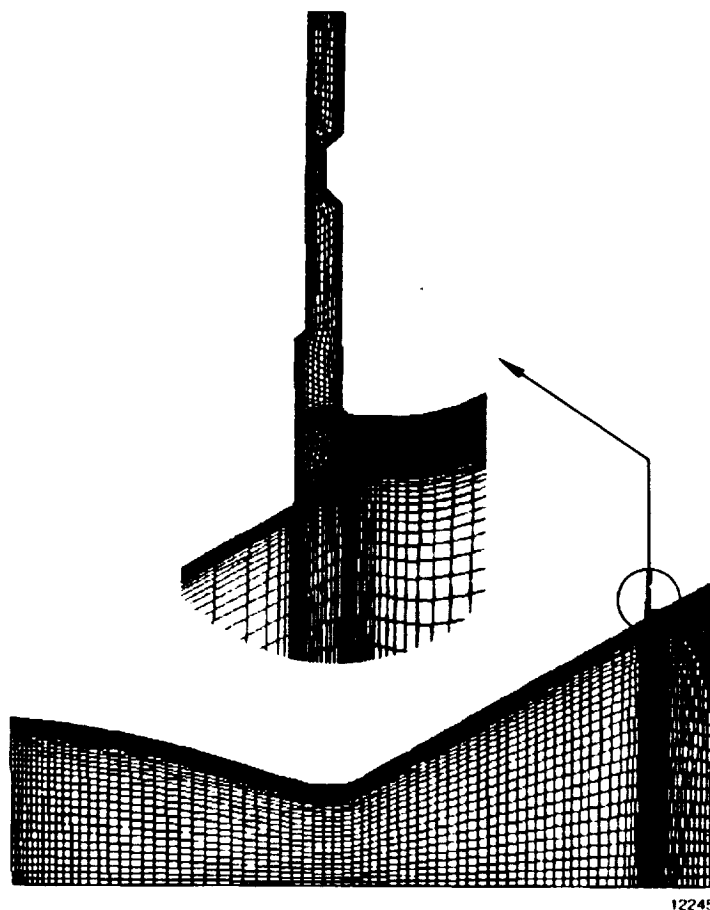
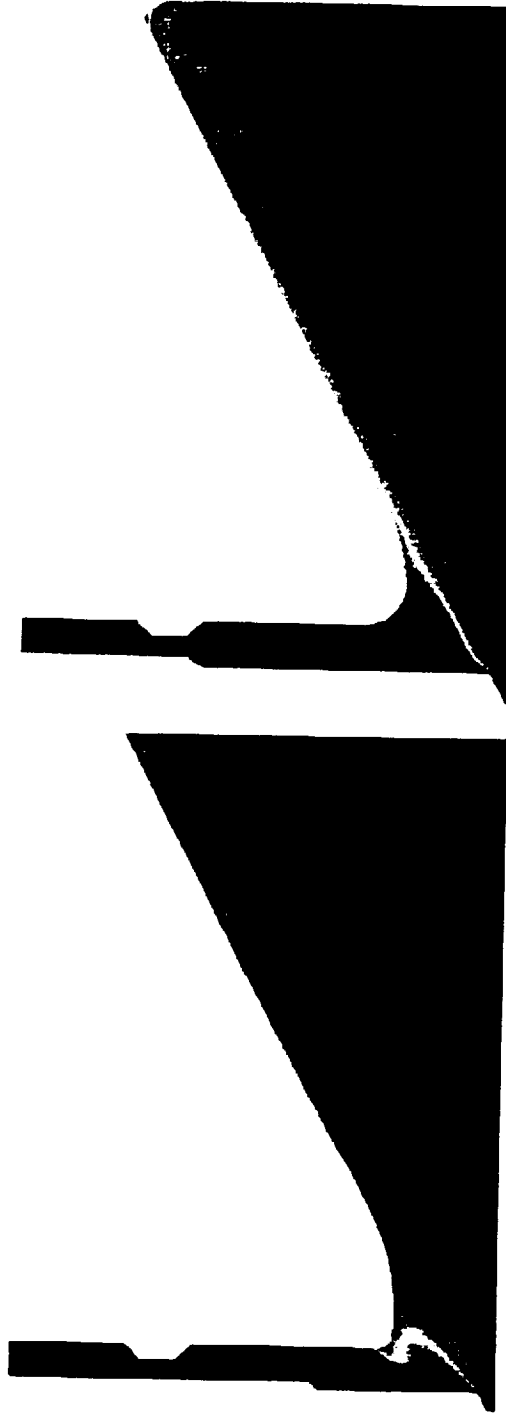


Figure 5.1.1-28. CFD Flow Model of Secondary Cavity Flow Interaction

0.03000
0.07000
0.11000
0.15000
0.19000
0.23000
0.27000
0.31000
0.35000
0.39000
0.43000
0.47000
0.51000
0.55000
0.59000
0.63000
0.67000
0.71000
0.75000
0.79000
0.83000
0.87000
0.91000
0.95000
0.99000



14618

Figure 5.1.1-29. Comparison of Old and New Subsonic Slot — New Conditions Result in Substantial Improvement in Film Effectiveness

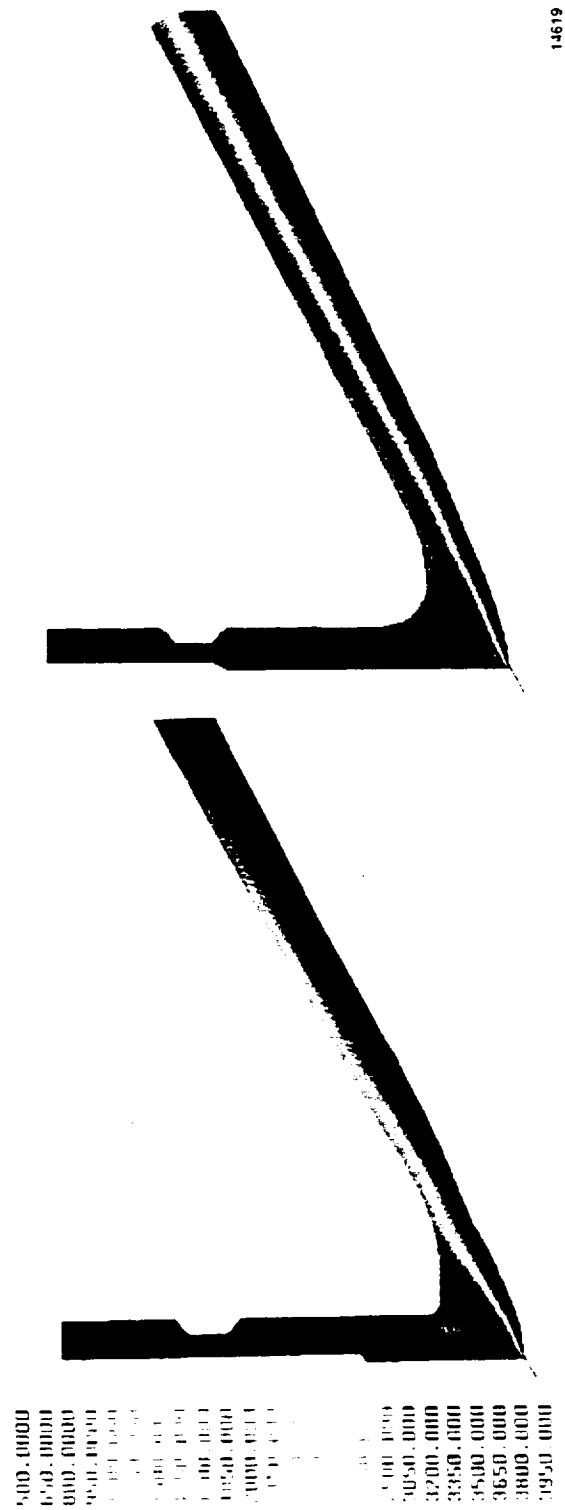


Figure 5.1.1-30. Comparison of Old and News Subsonic Slot — New Conditions Indicate Dramatic Improvement in Film Cooling

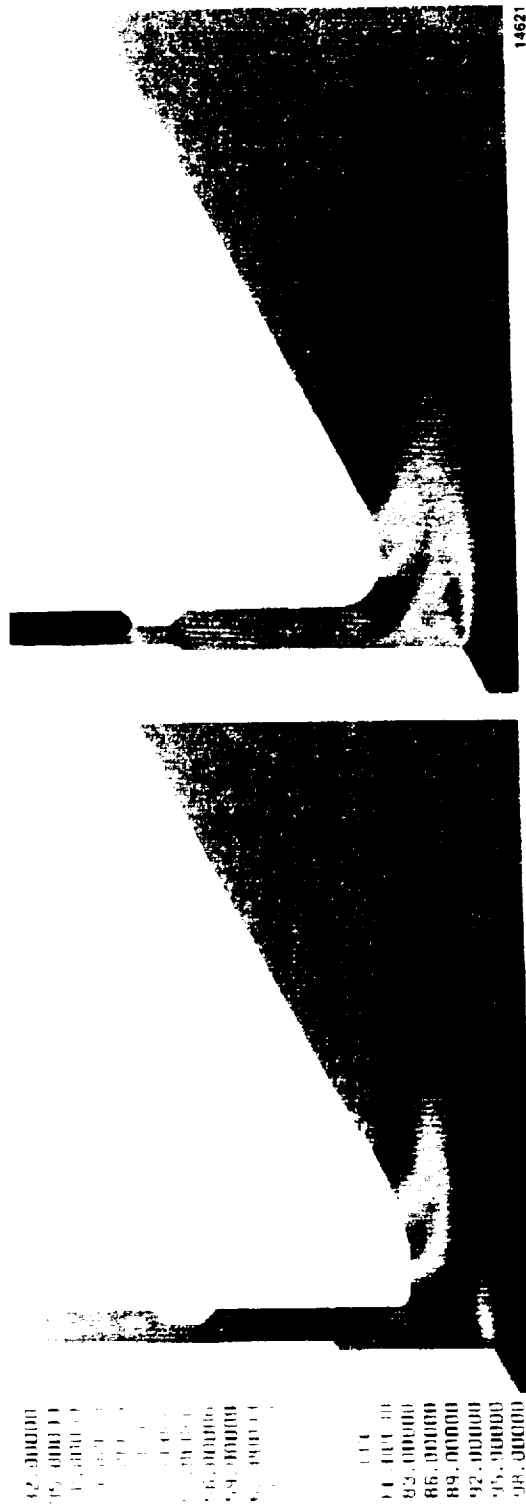


Figure 5.1.1-31. Comparison of Old and New Subsonic Slot — Penalty for High Mass Flow Rate is Increased Shock Strength

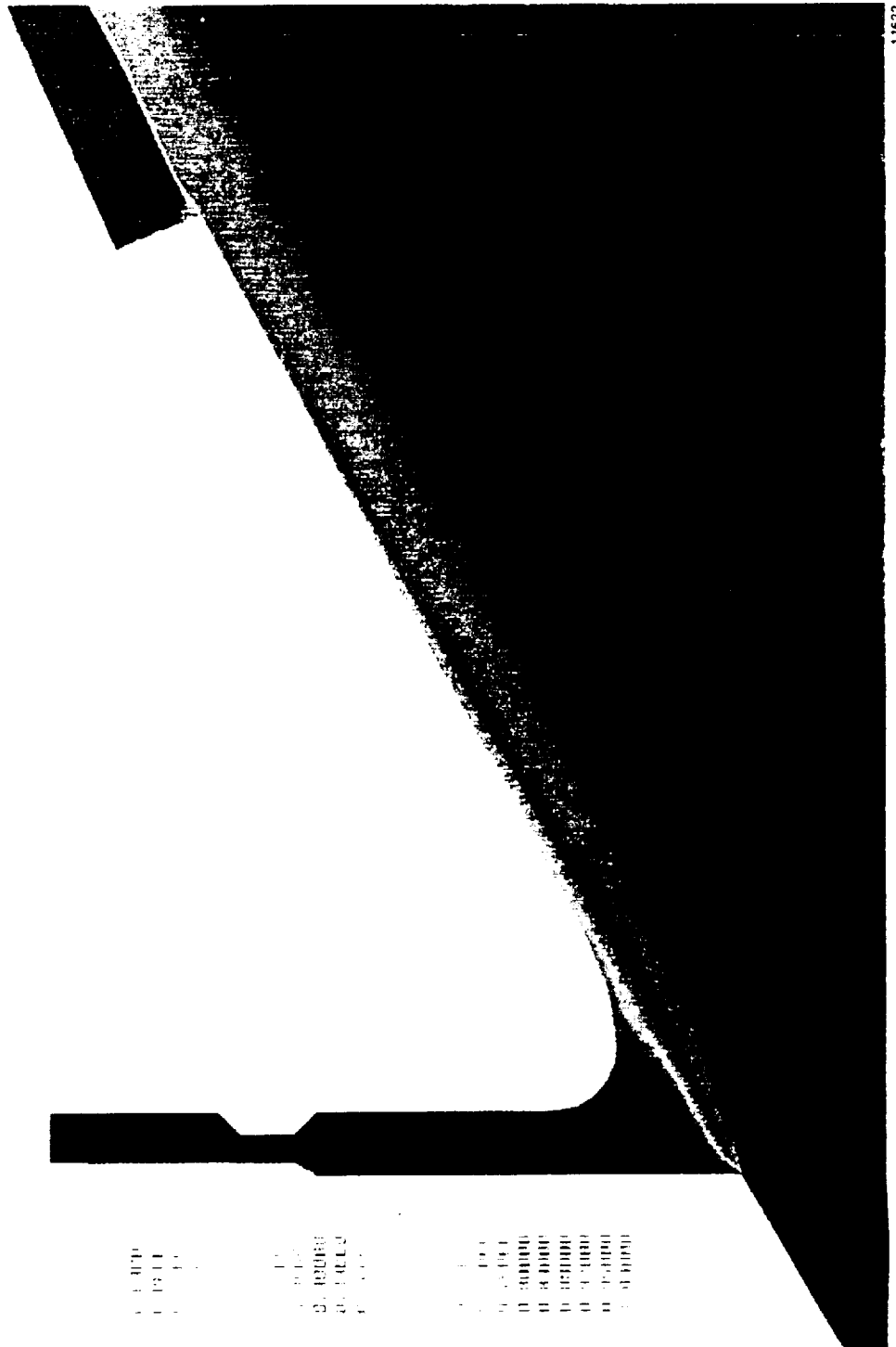


Figure 5.1.1-32. Subscale Core/Film Coolant Interaction — New Conditions Produce Less Mixing of Secondary Film

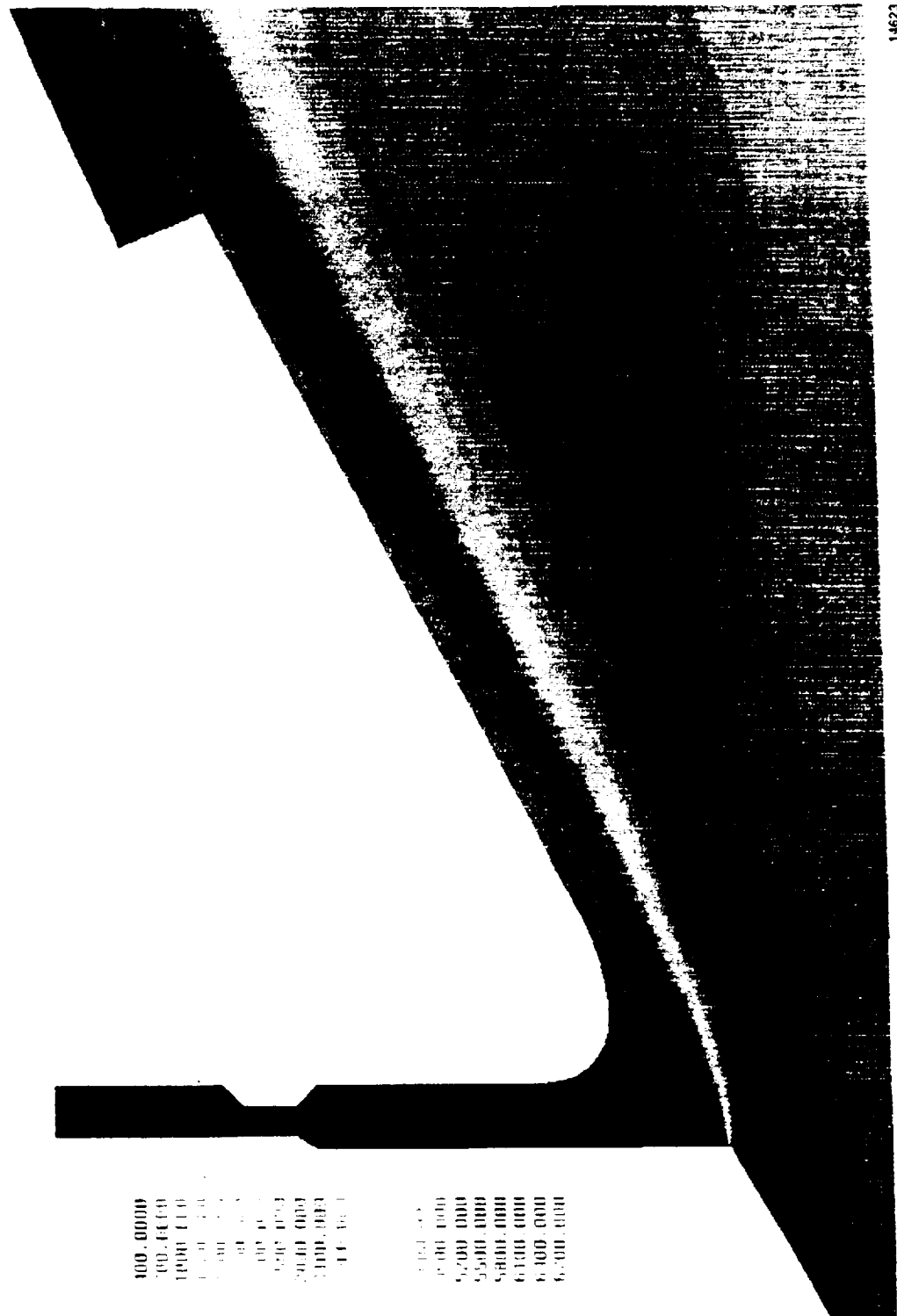


Figure 5.1.1-33. Subscale Core/Film Coolant Interaction — Boundary Film Layer Provides Adequate Cooling for Injector Ring



Figure 5.1.1-34. Subscale Core/Film Coolant Interaction — Normal and Tangential Injection Produce Complex Shock and Expansion

ORIGINAL PAGE IS
OF POOR QUALITY

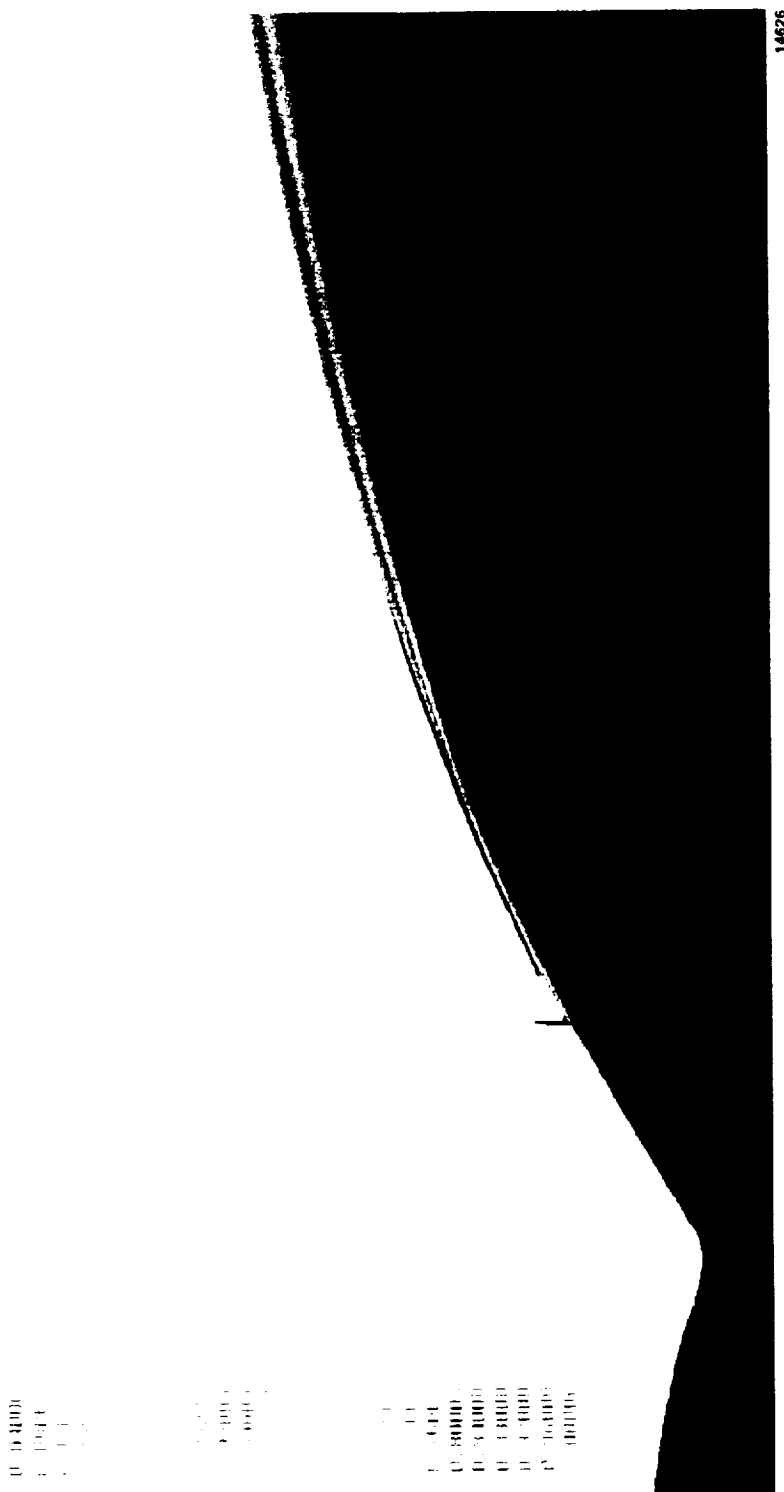


Figure 5.1.1-35. Subscale Core/Film Coolant Interaction — Integrity of Primary Jet Maintained

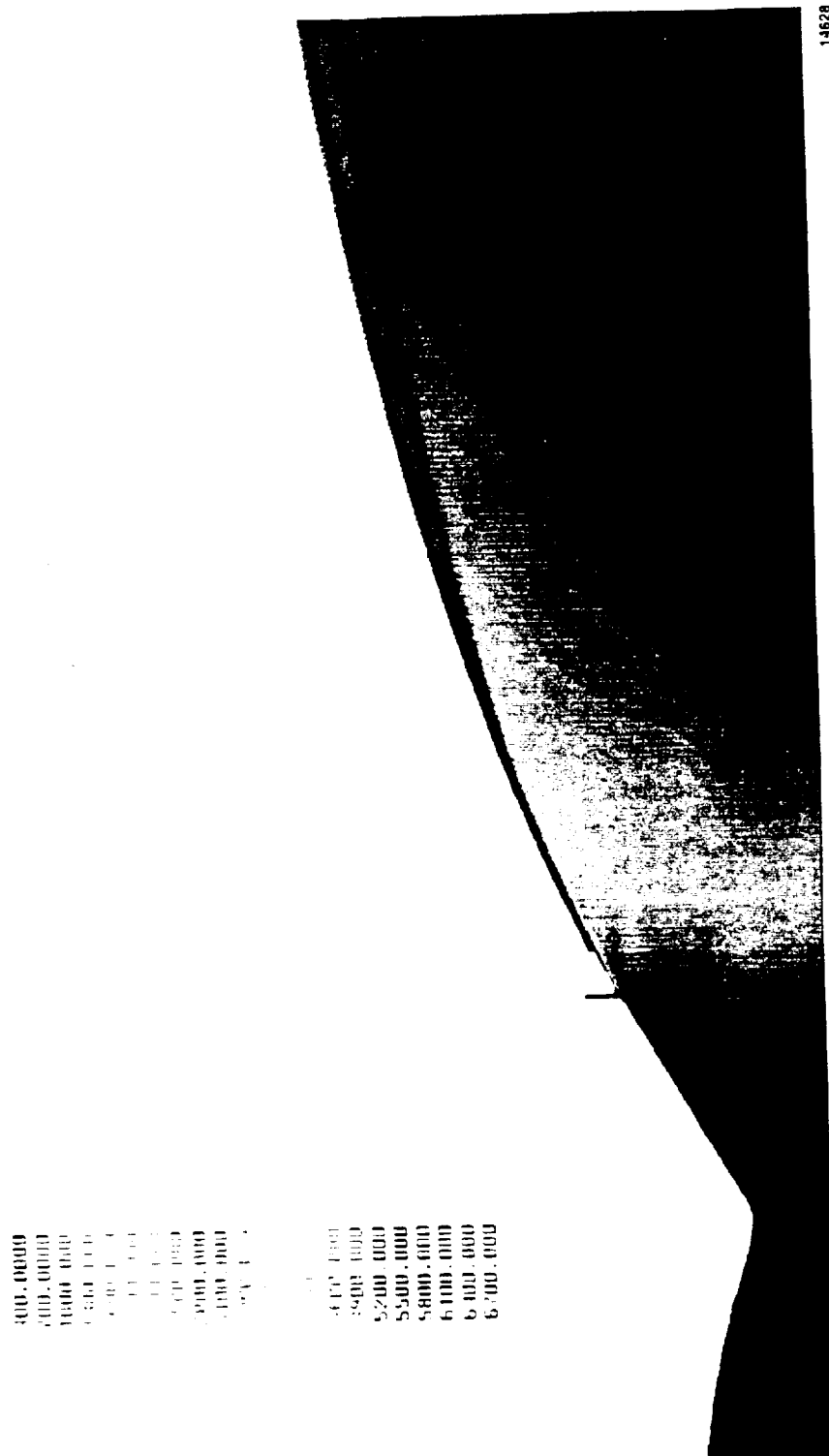


Figure 5.1.1-36. Subscale Core/Film Coolant Interaction — Primary Film Layer Provides Adequate Cooling for Nozzle Skirt

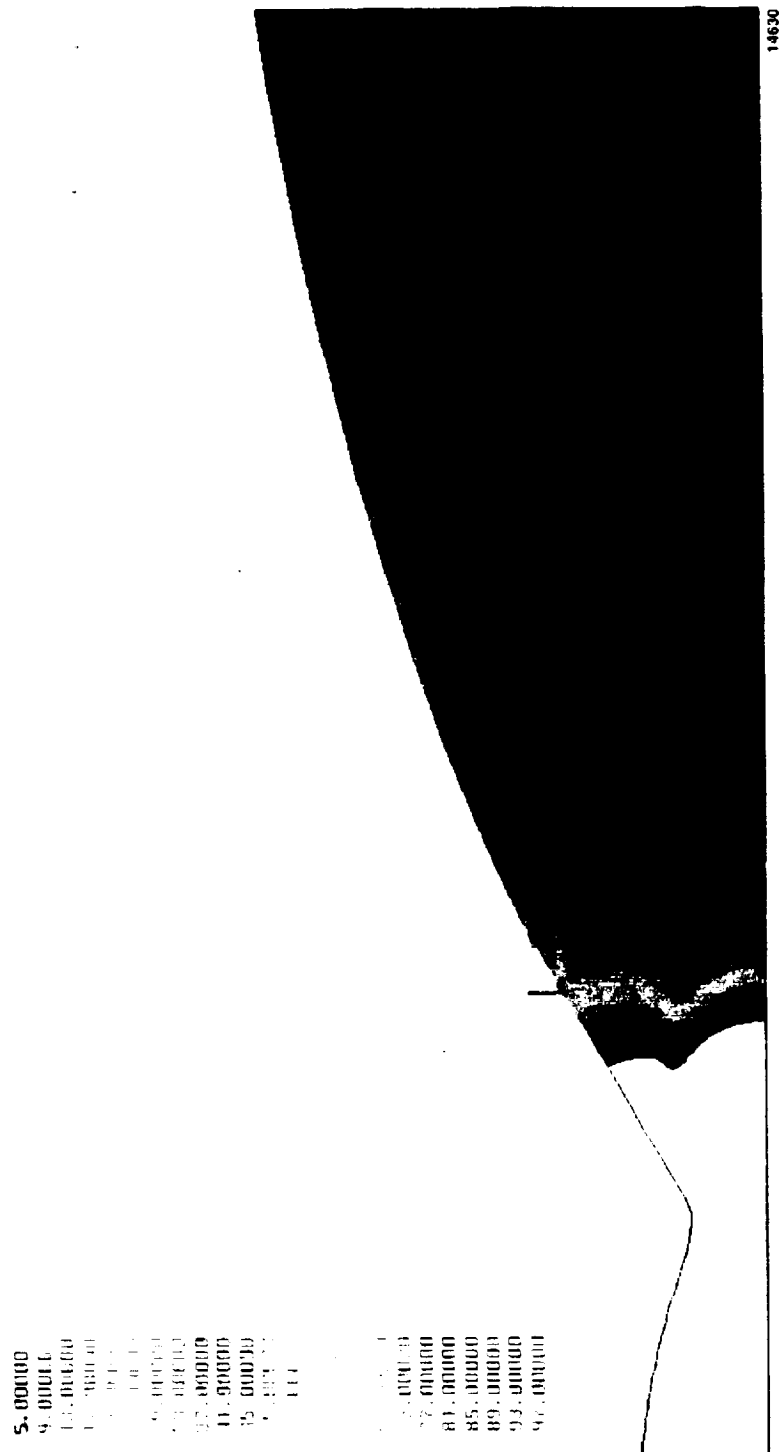


Figure 5.1.1-37. Subscale Core/Film Coolant Interaction Nozzle Geometry and Film Injection Produce Shock Losses

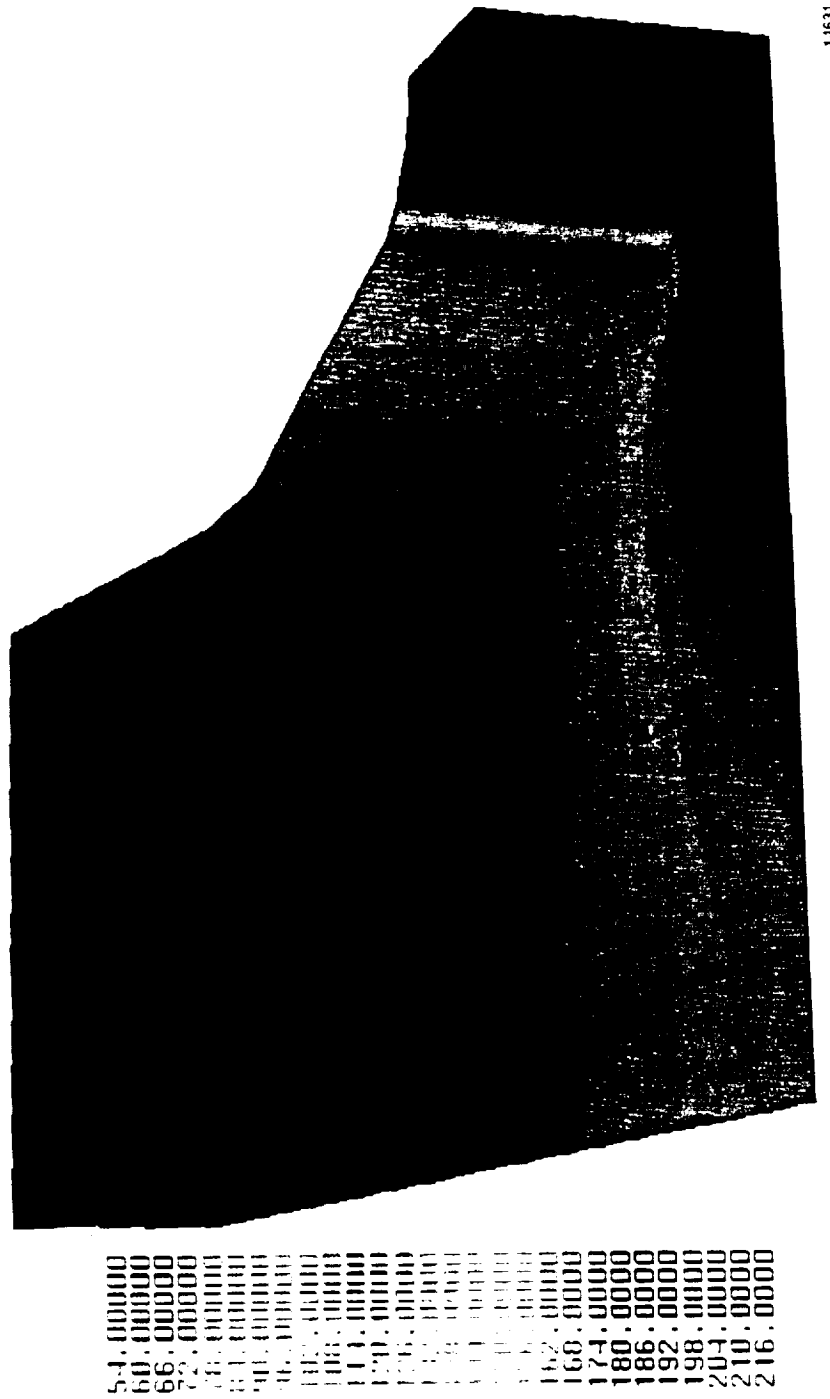


Figure 5.1.1-38. Subscale Three-Dimensional Primary Injector Analysis — Surface Pressures Indicate Uniform Exit Profiles

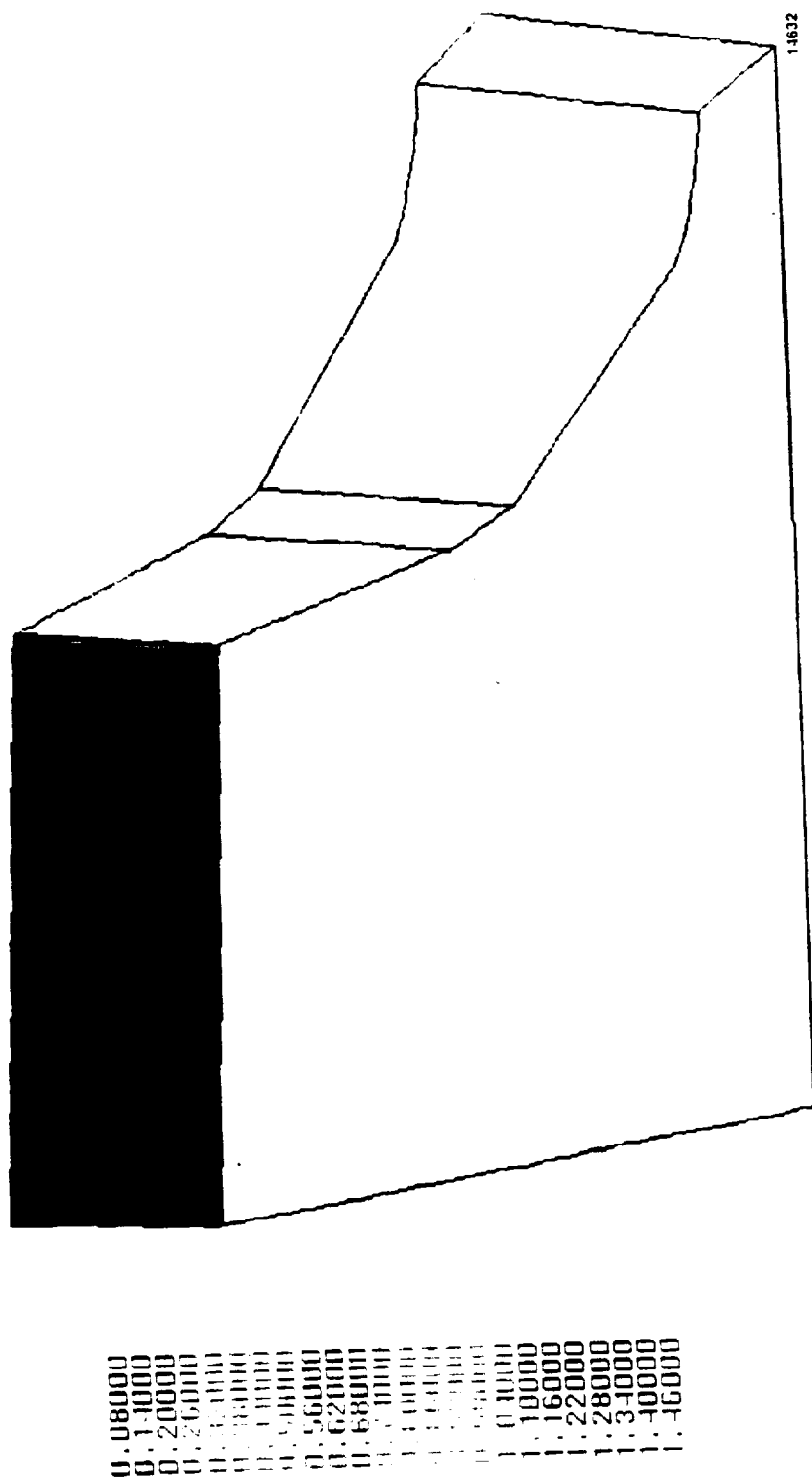
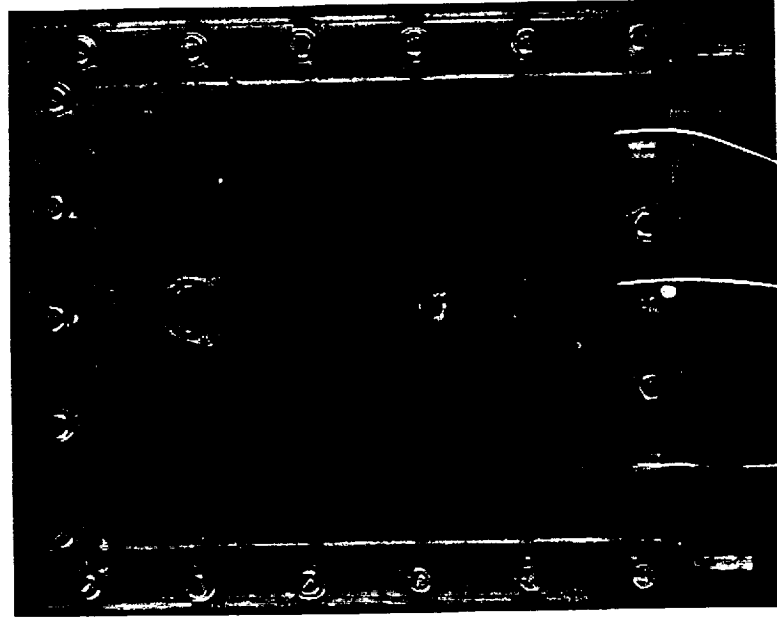
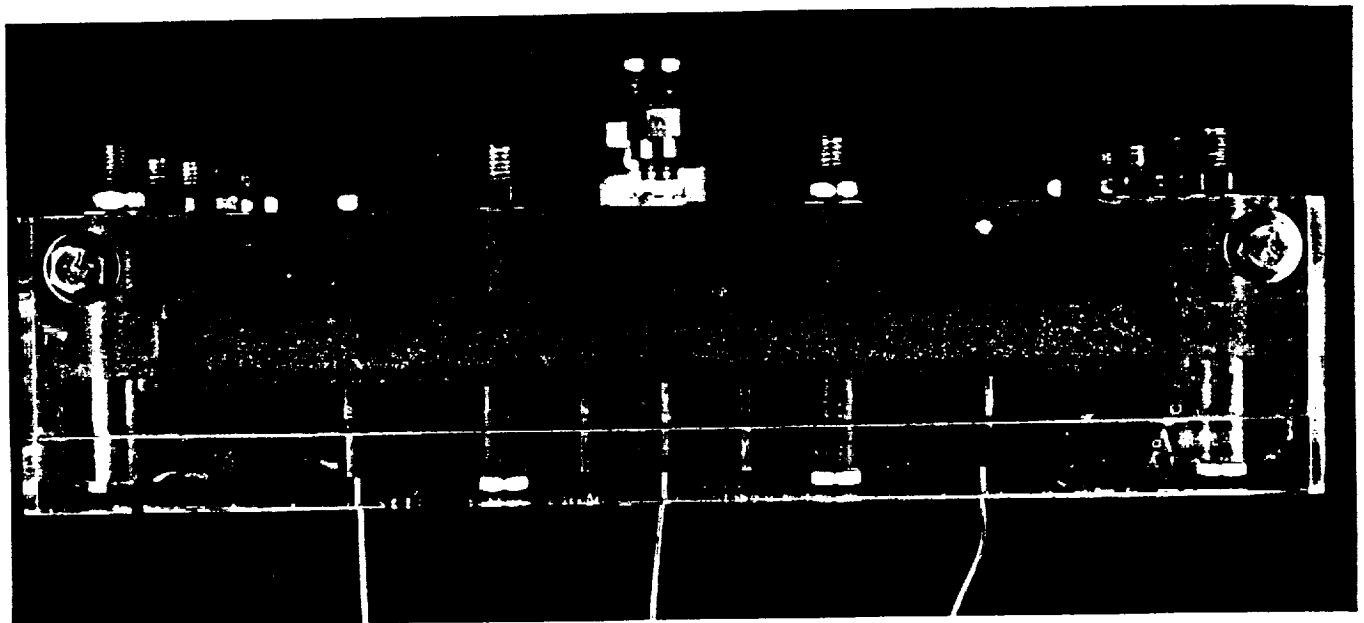


Figure 5.1.1–39. Subscale Three-Dimensional Primary Inflow Analysis — Exit Mach Contours Indicate Uniform Profile



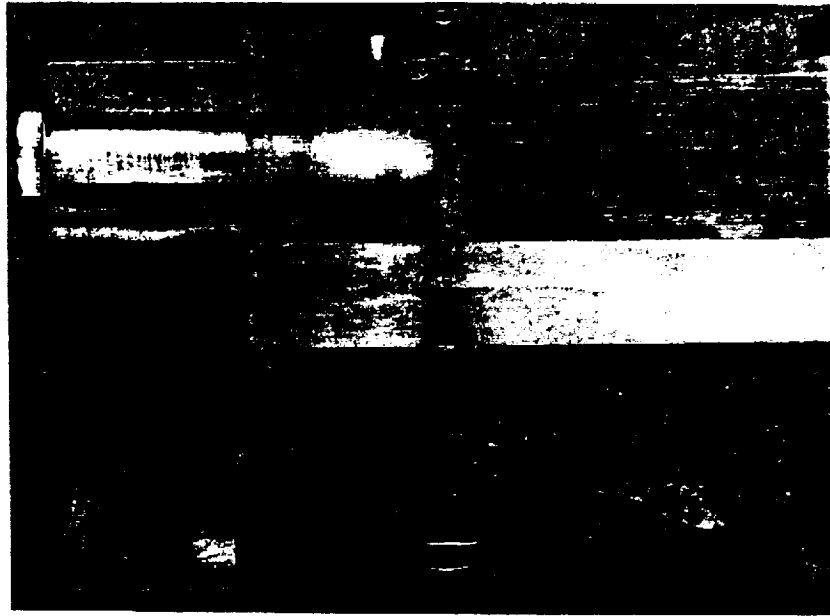
FE 625393

Figure 5.1.1-40. Subscale Nozzle Flow Rig



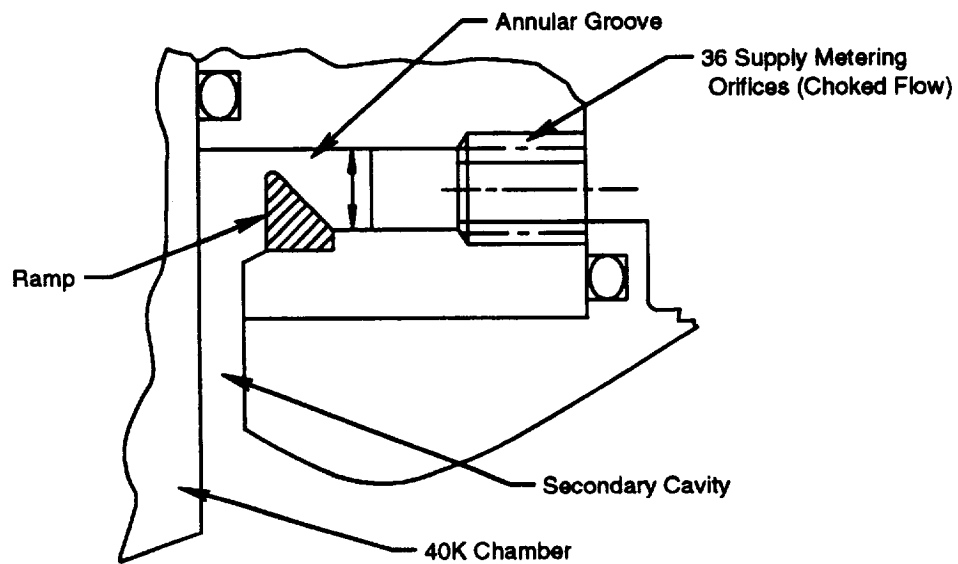
FE 625392

Figure 5.1.1-41. Subscale Nozzle Flow Rig



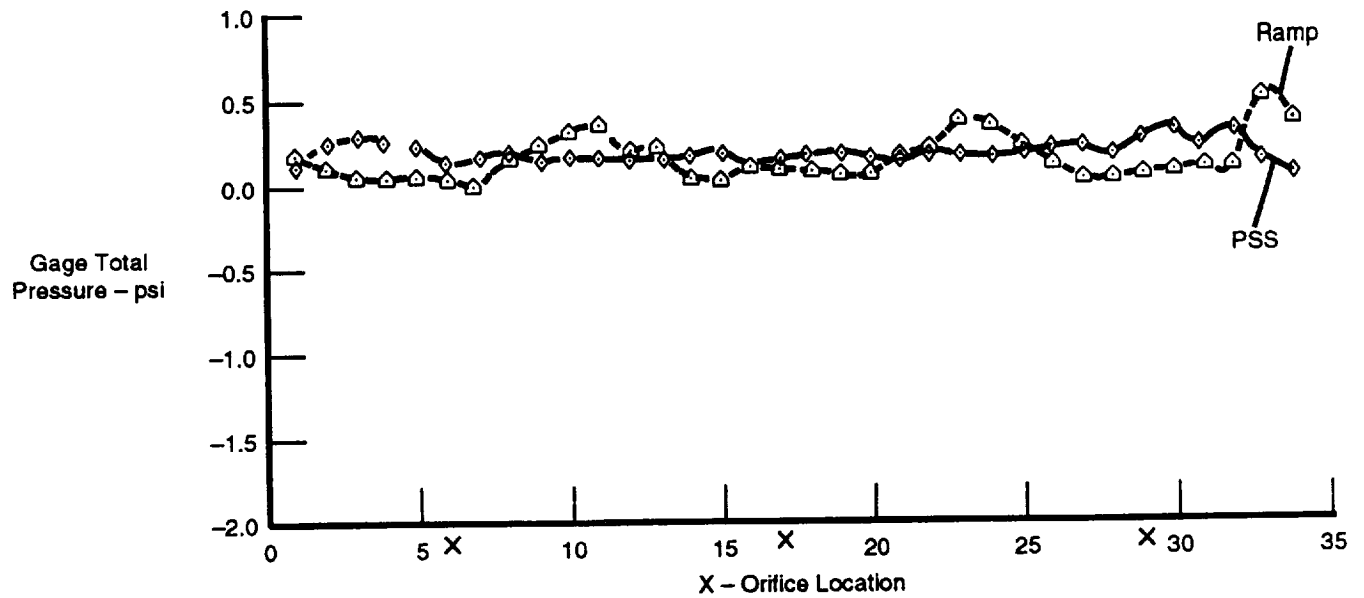
FE 625395

Figure 5.1.1-42. Subscale Nozzle Flow Rig



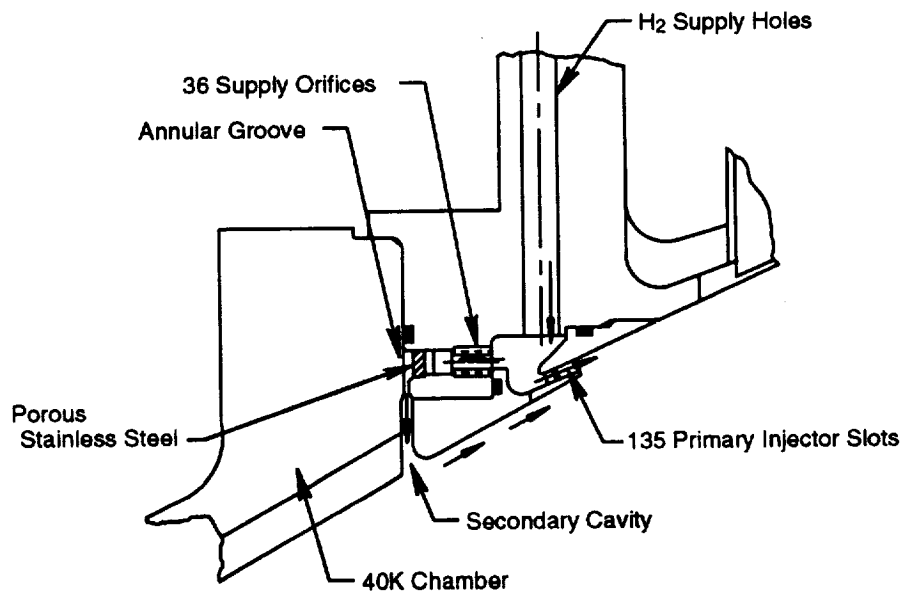
14590

Figure 5.1.1-43. Ramp Design for Secondary Cavity Flow Distribution



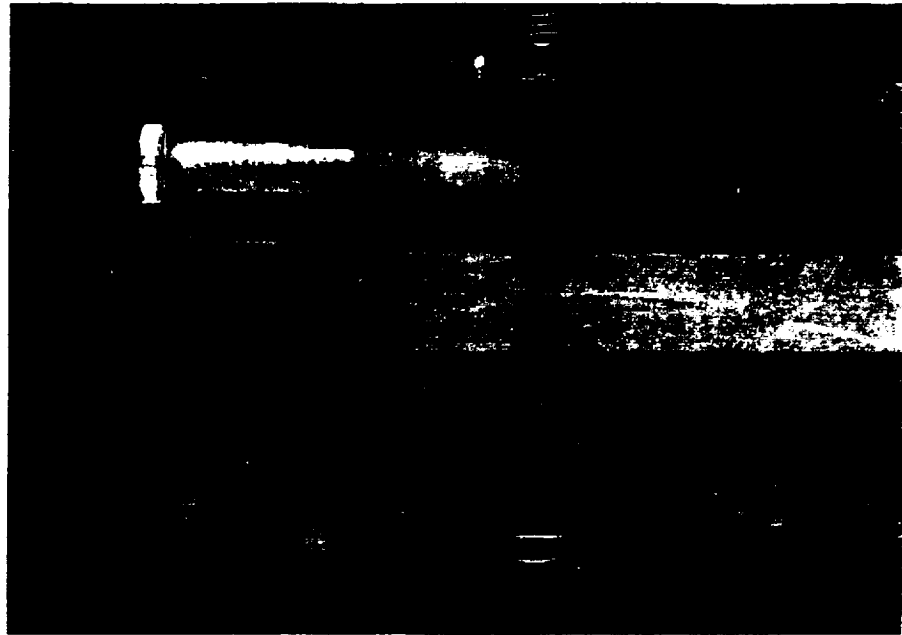
14591

Figure 5.1.1-44. Subscale Nozzle Flow Rig — Air Data: Ramp Versus Porous Metal Designs



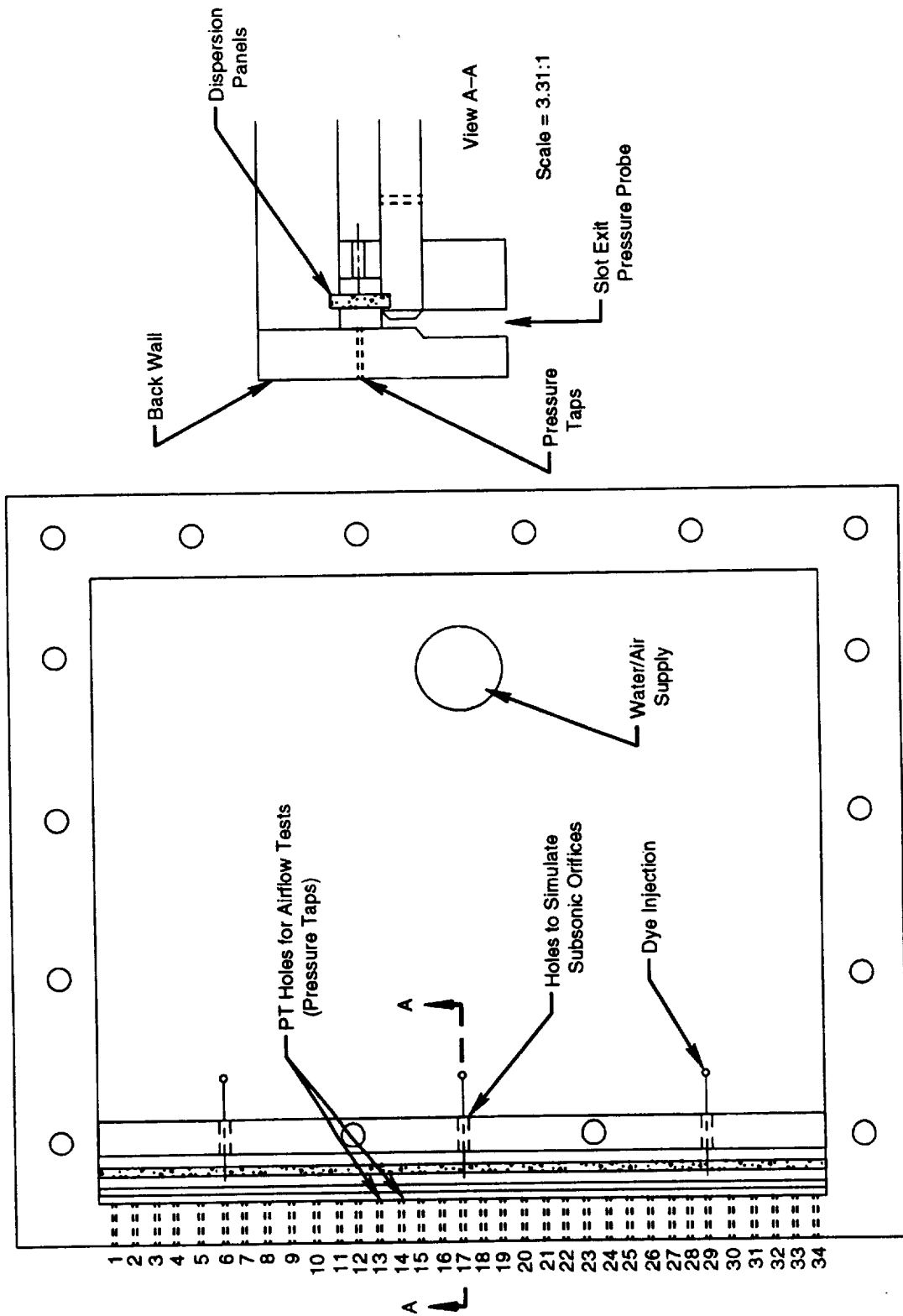
14588

Figure 5.1.1-45. Secondary Cavity Design Using Porous Stainless Steel for Flow Distribution



FE 625395

Figure 5.1.1-46. Subscale Nozzle Flow Rig



16540

Figure 5.1.1-47. Secondary Cavity Flow Rig

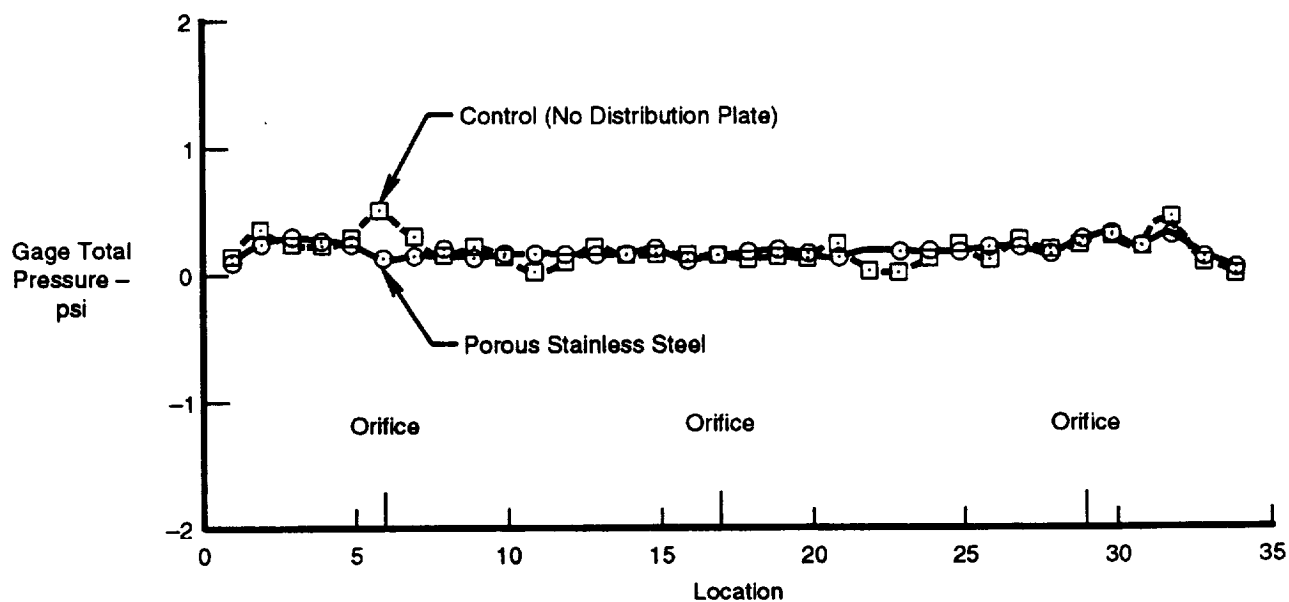


Figure 5.1.1-48. Gage Total Pressure Distributions At The Slot Exit

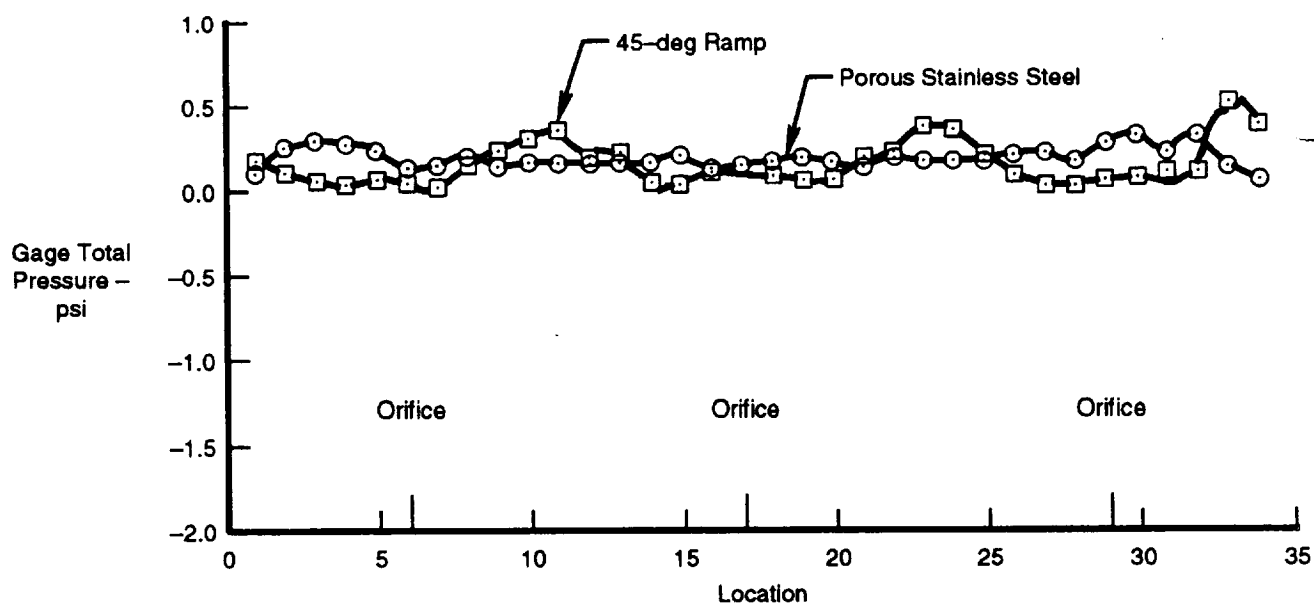


Figure 5.1.1-49. Gage Total Pressure Distributions At The Slot Exit

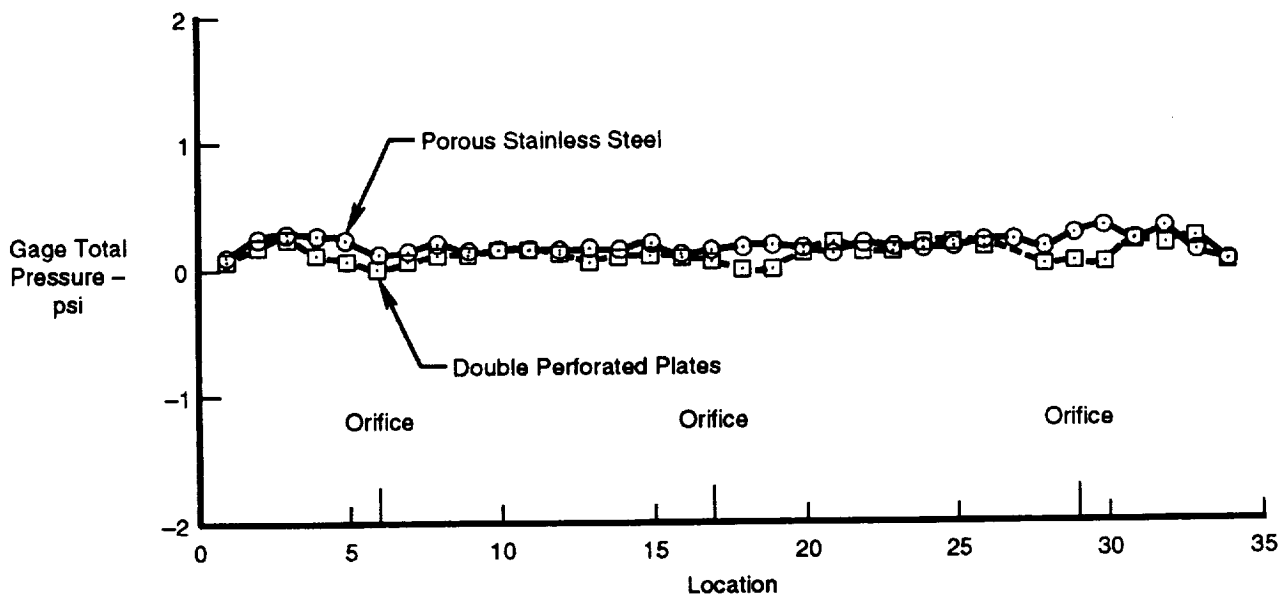


Figure 5.1.1-50. Gage Total Pressure Distributions At The Slot Exit

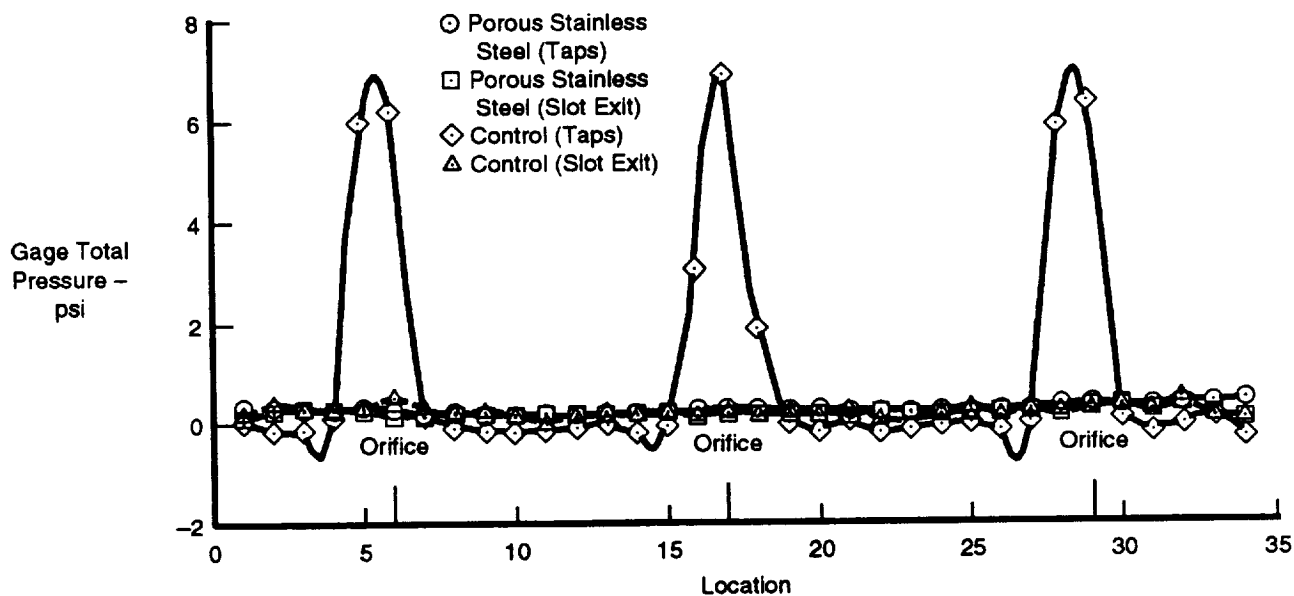


Figure 5.1.1-51. Pressure Distributions At Pressure Taps and Slot Exit

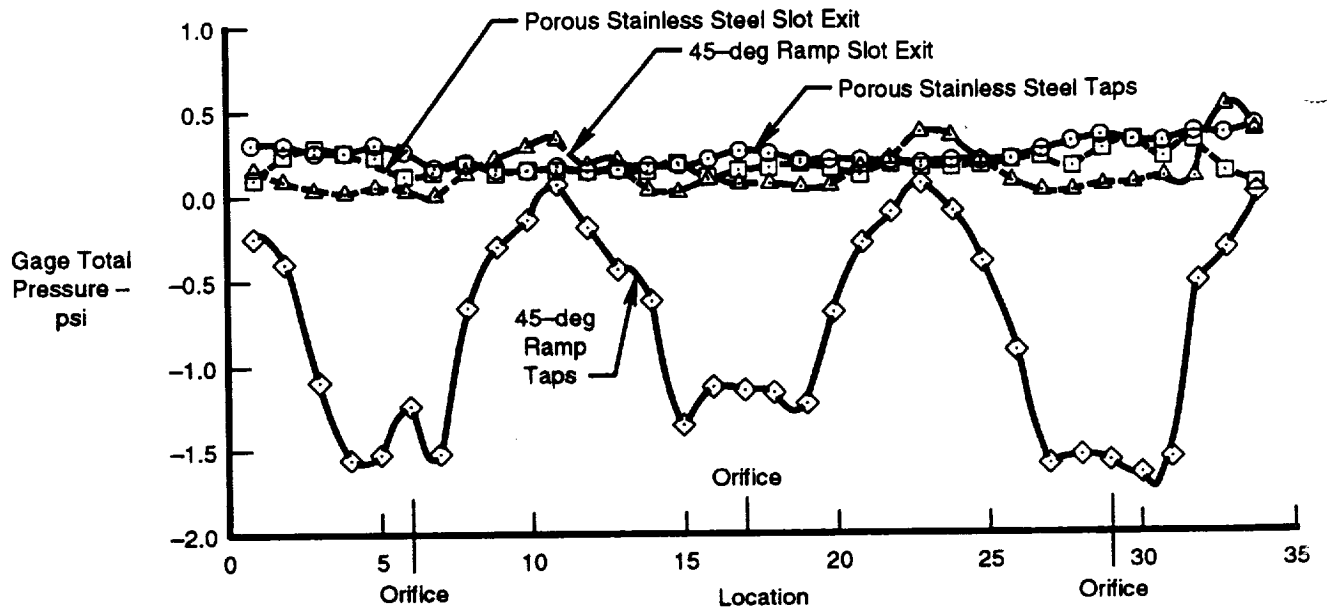


Figure 5.1.1-52. Pressure Distributions At Pressure Taps and Slot Exit

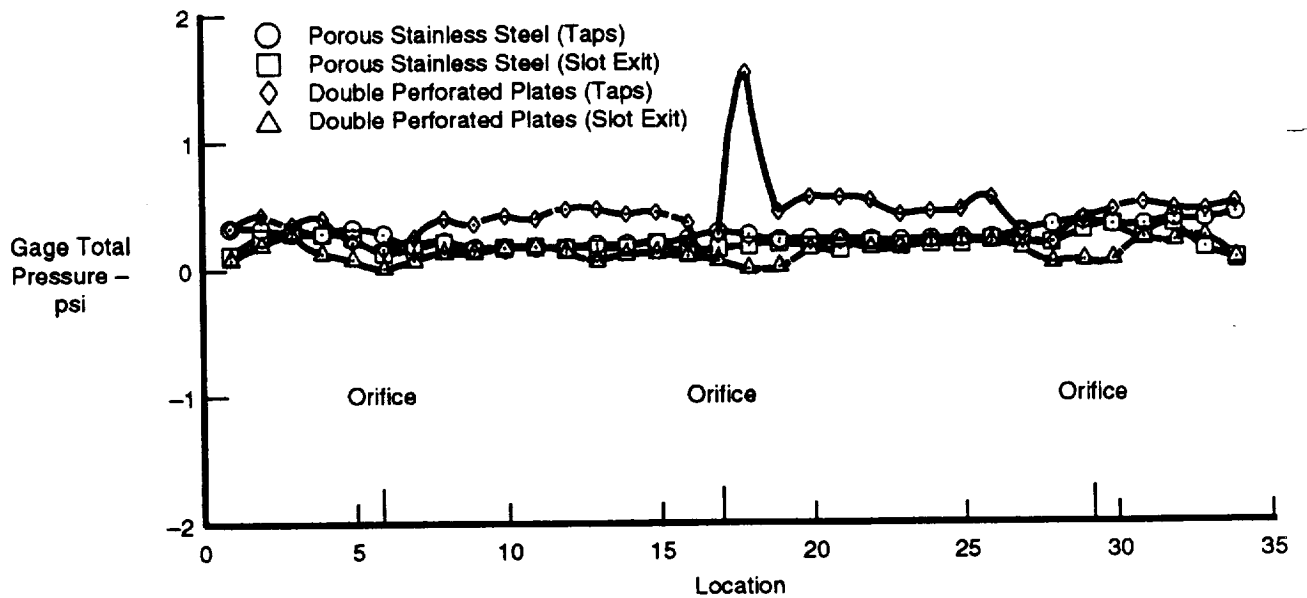


Figure 5.1.1-53. Pressure Distributions At Pressure Taps and Slot Exit



FE 626451

Figure 5.1.1-54. Nozzle Liner Installed On VTL For Rough Machining

5.1.2 Manufacturing and Assembly

A coordinated nozzle program manufacturing plan was developed, including a tool design plan. Assembly tooling requirements were established with the P&W assembly planners. As a result, the hardware designs included assembly and handling features to accommodate the assembly tooling.

The fabrication tool designs were completed and released for procurement and tool fabrication. The nine major tooling fixtures were completed in the shop. Figures 5.1.2-1 through 5.1.2-3 show the Chamber Rework Fixture, the Nozzle Assembly and Handling Fixture, and the Injector Ring EB Weld Fixture.

Inconel 625 plate samples were sent to the electroformed nickel supplier to conduct plating experiments. These experiments were designed to provide additional information on optimum plating conditions prior to shipping the actual nozzle liner.

Injector ring weld samples were completed in order to verify the cone-to-cone weld design of the two-piece ring assembly. Two cone-shaped rings of Inconel 625 were welded together, simulating the actual injector ring raw material geometry. Following EB welding, the rings were dimensionally inspected to check for movement or misalignment that may have occurred during welding. Results of the inspection indicate that minimal offset took place during the welding, with improved results expected on the actual parts using the welding fixture currently being fabricated.

The subscale nozzle manifold machining and welding, preparation of the liner raw material for use, and continuation of the chamber nickel plating to create the aft end flange were completed.

The Subscale calorimeter combustion chamber was successfully reoperated to remove the aft end tube manifold and nickel plating were completed. The reoperated chamber is shown in Figure 5.1.2-4.

The calorimeter nozzle manifold inner and outer rings were finished machined, welded together, and inspected. The assembly is shown in Figure 5.1.2-5 just before the electron beam (EB) tier weld. The tier weld was inspected using fluorescent penetrant and X-ray, and shows no indications or voids.

The nozzle spun liner was received from the spinning supplier Spincraft, was prepared for welding to the manifold. A machining flange was tack welded to the liner aft end, which has an additional 1 inch of stock left on until the final machining step, as shown in Figure 5.1.2-6. The liner was welded to the manifold using an EB weld, which was fully inspected and also shows no indications or voids. Figure 5.1.2-7 shows the manifold and liner tackwelded together, ready for the final weld in the EB weld chamber.

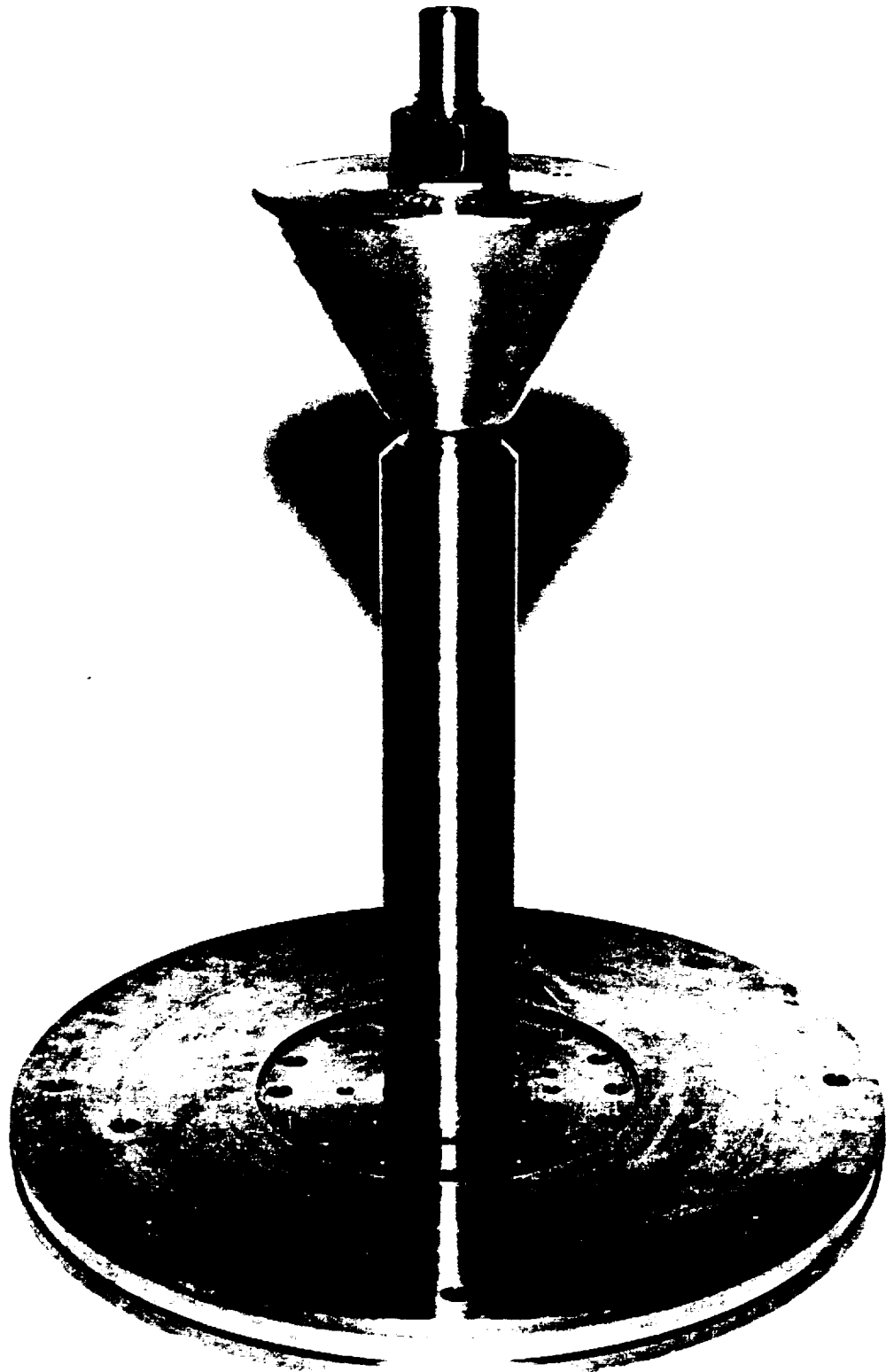
The liner/manifold assembly was mounted on a vertical turret lathe in preparation for the chamber/nozzle interface area machining. The initial machining steps include forming the seal grooves, the secondary cavity annulus, and the primary datums. The nozzle inner contour was finish machined in a separate machining fixture. The assembly was then placed in a machining fixture which provides an inner mandrel for structural support, and the outer diameter grooves will be machined. The machining of the inner contour and the grooves was then completed.

The nozzle liner and manifold assembly were electron beam welded together, and were then installed on the ID machining fixture to machine the final ID nozzle contour. The ID contour was then inspected using a coordinate measuring machine and the nozzle was installed on the OD machining fixture for machining the nozzle contour OD and the coolant grooves. The nozzle contour OD was finished down to a 0.145 in. thickness all over, which is the finished thickness at the top of the grooves to the nozzle hot wall ID. The grooves were then rough machined and then finished machined to achieve the 0.035 to 0.045 in. wall thickness. Sonic inspections

were conducted at each rough and finish machining step for each groove. The nozzle liner is shown in Figure 5.1.2-8 during groove rough machining on the NC vertical turret lathe in the P&W machine shop. After the ID contour, OD contour, and groove finish machining were completed, the nozzle was removed from the machining fixture and installed on the jig bore to machine the flange threaded holes, the orifice metering holes, and the four radial pin holes. The final machining process of installing the 0.067 in. instrumentation holes through the nozzle groove lands was then completed. The nozzle was fully inspected, cleaned, X-rayed, and installed on the shipping and handling fixture and shipped to the electroform nickel supplier for the liner closeout nickel plating. Various views of the finished machined nozzle liner are shown in Figures 5.1.2-9 through 5.1.2-11.

Nozzle liner machining was completed and the liner was sent to the plating supplier for electroformed nickel plating. The plating supplier experienced several problems fixturing and initiating the plating. These problems caused an additional 8-week delay in the fabrication schedule. The handling fixture, which was fabricated by P&W and shipped with the part, is made from anodized aluminum, as is standard tool design practice to prevent corrosion. The anodized surface treatment significantly limited the current flow into the part, which prevented plating. The fixture had to be disassembled, the anodizing treatment removed by chem-milling, the fixture and nozzle reassembled, and nonplated areas remasked. The overall size of the part also contributed to the schedule delays. The part was significantly larger than previous plated parts and required more complex fixturing and setup time for plating than was expected. After plating was completed, the outer contour nozzle was machined, and the assembly was cleaned and put in storage.

The preceding discussions defined the manufacturing activities involved with the calorimeter nozzle, calorimeter chamber, and assembly tooling up to early 1993. Based on direction from NASA-MSFC in late 1992 to put a hold on activities to minimize expenditures, all hardware was completed to a point at which it was stored for future disposition.



FE62274-41

Figure 5.1.2-1. Chamber Rework Fixture

FE622480

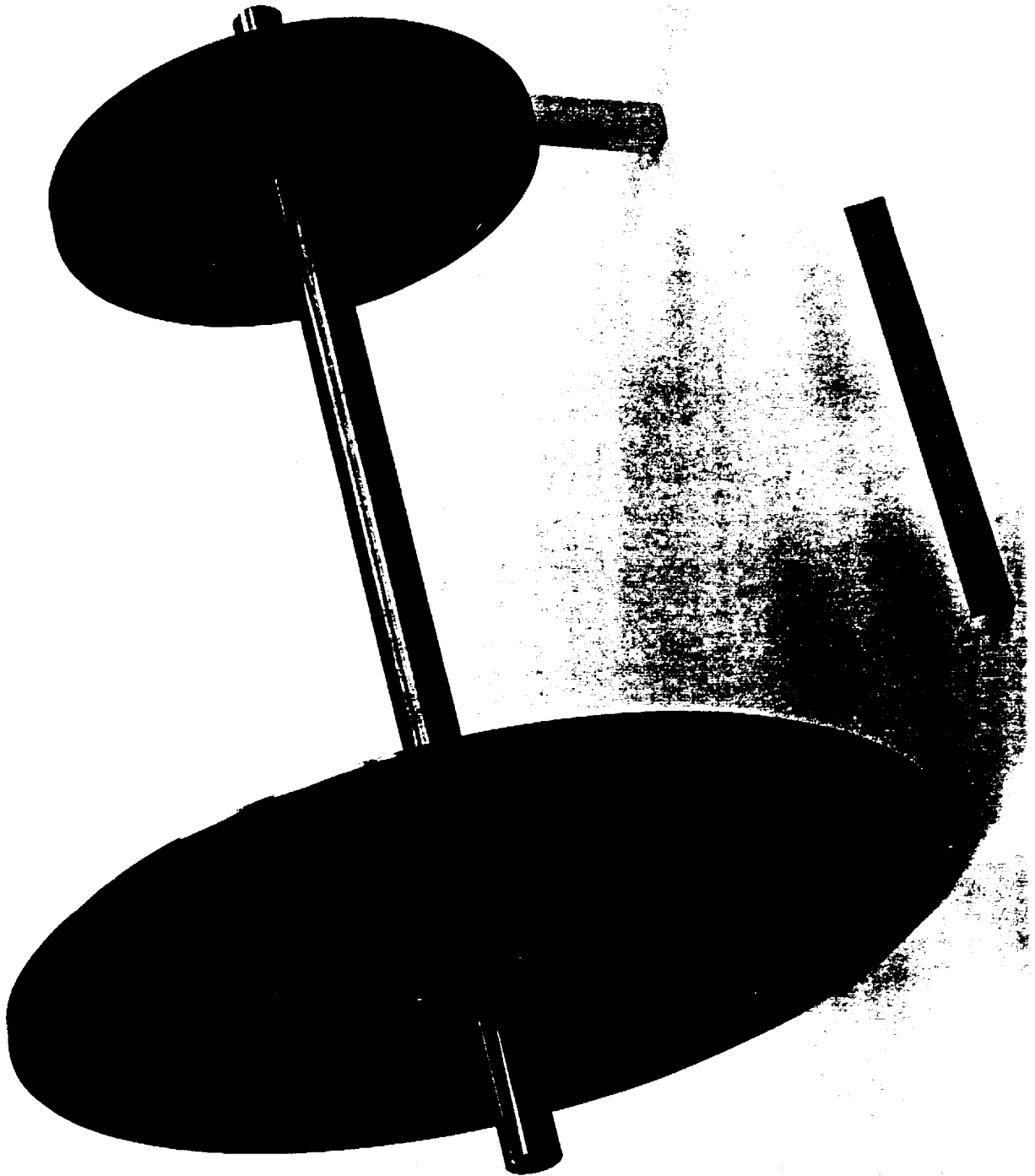


Figure 3.1.2-2. Subsonic Nozzle Snipping and Handling Fixture

FE62496

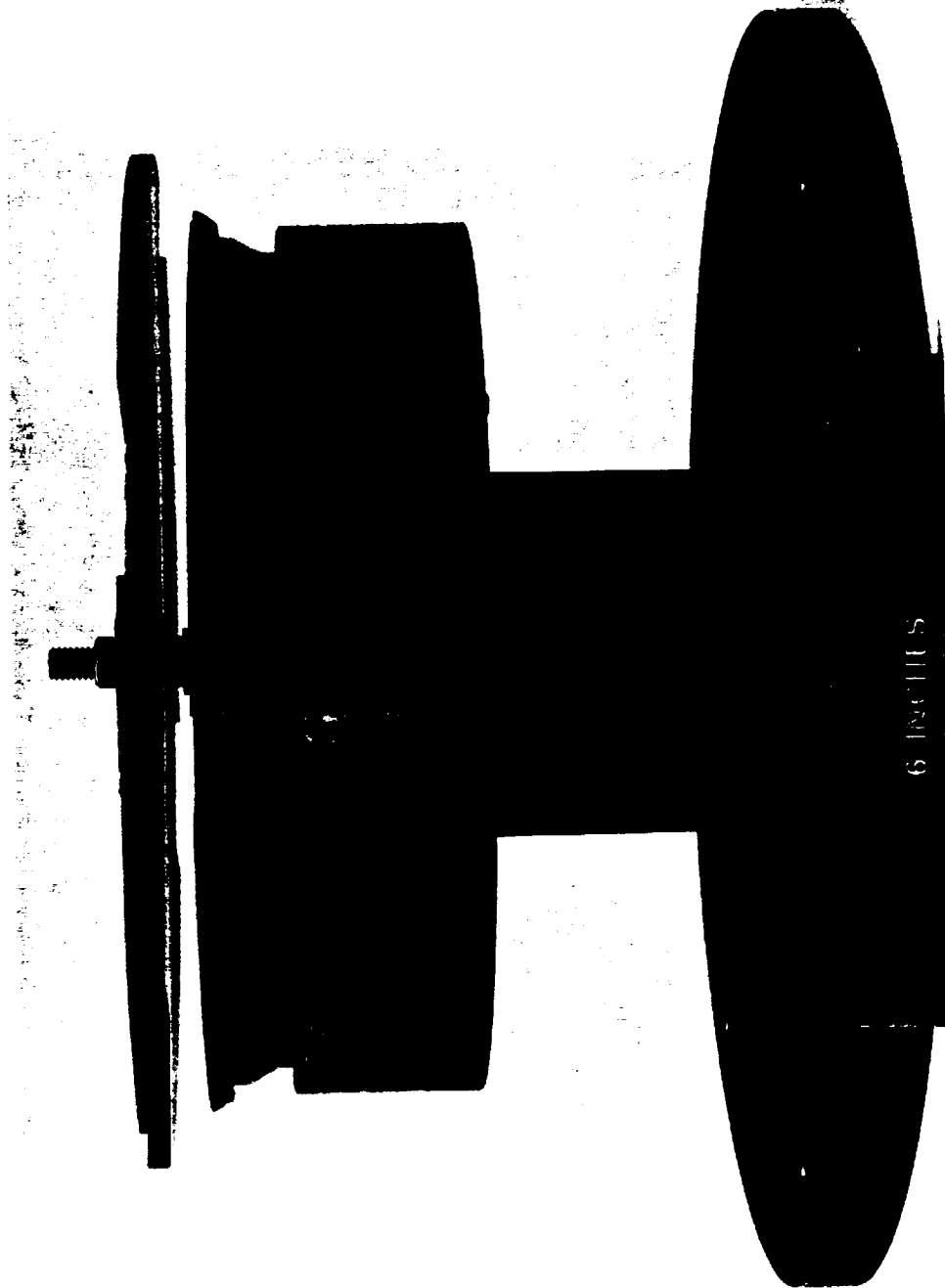
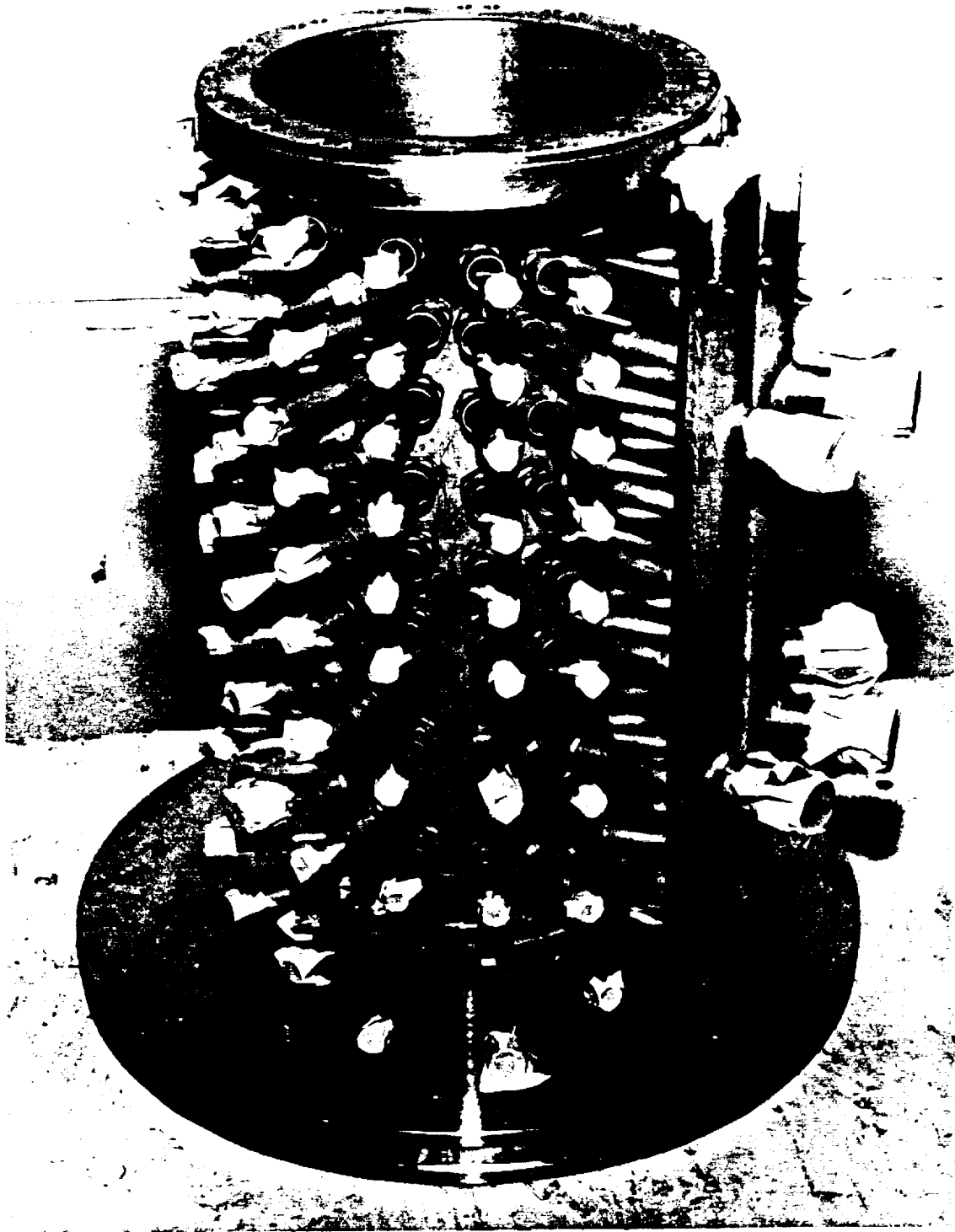
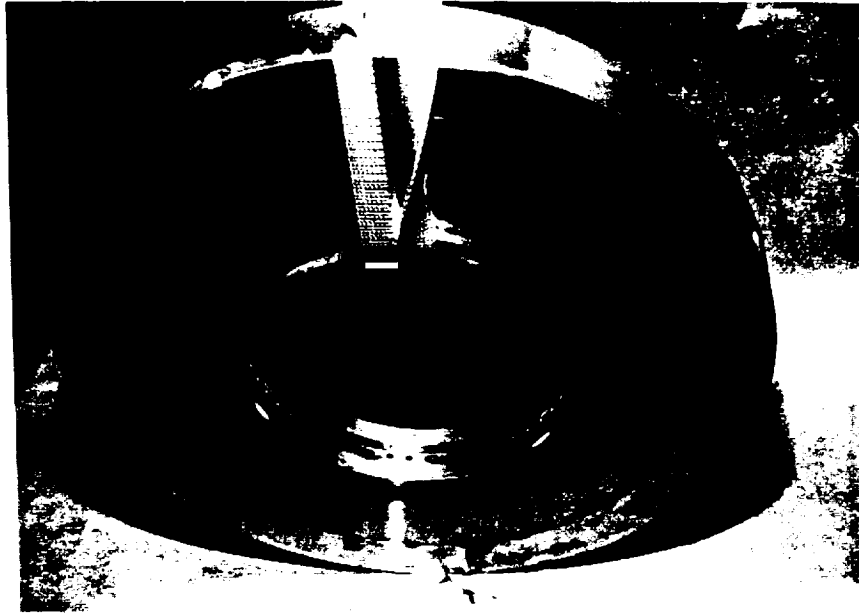


Figure 5.1.2-3. Injector Ring EB Weld Fixture



FE628546

Figure 5.1.2-4. Subscale Calorimeter Combustion Chamber



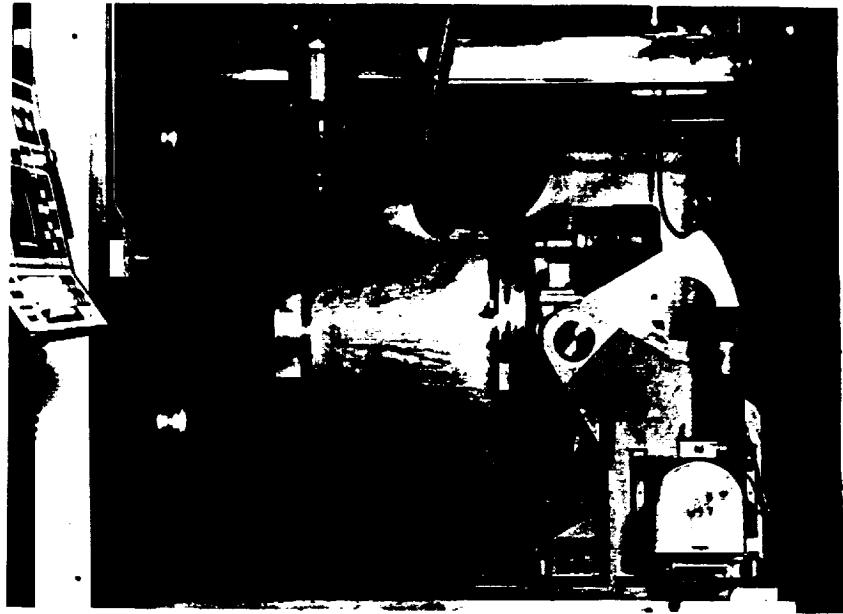
FE 625286

Figure 5.1.2-5. Calorimeter Nozzle Manifold Assembly Before EB Tier Weld



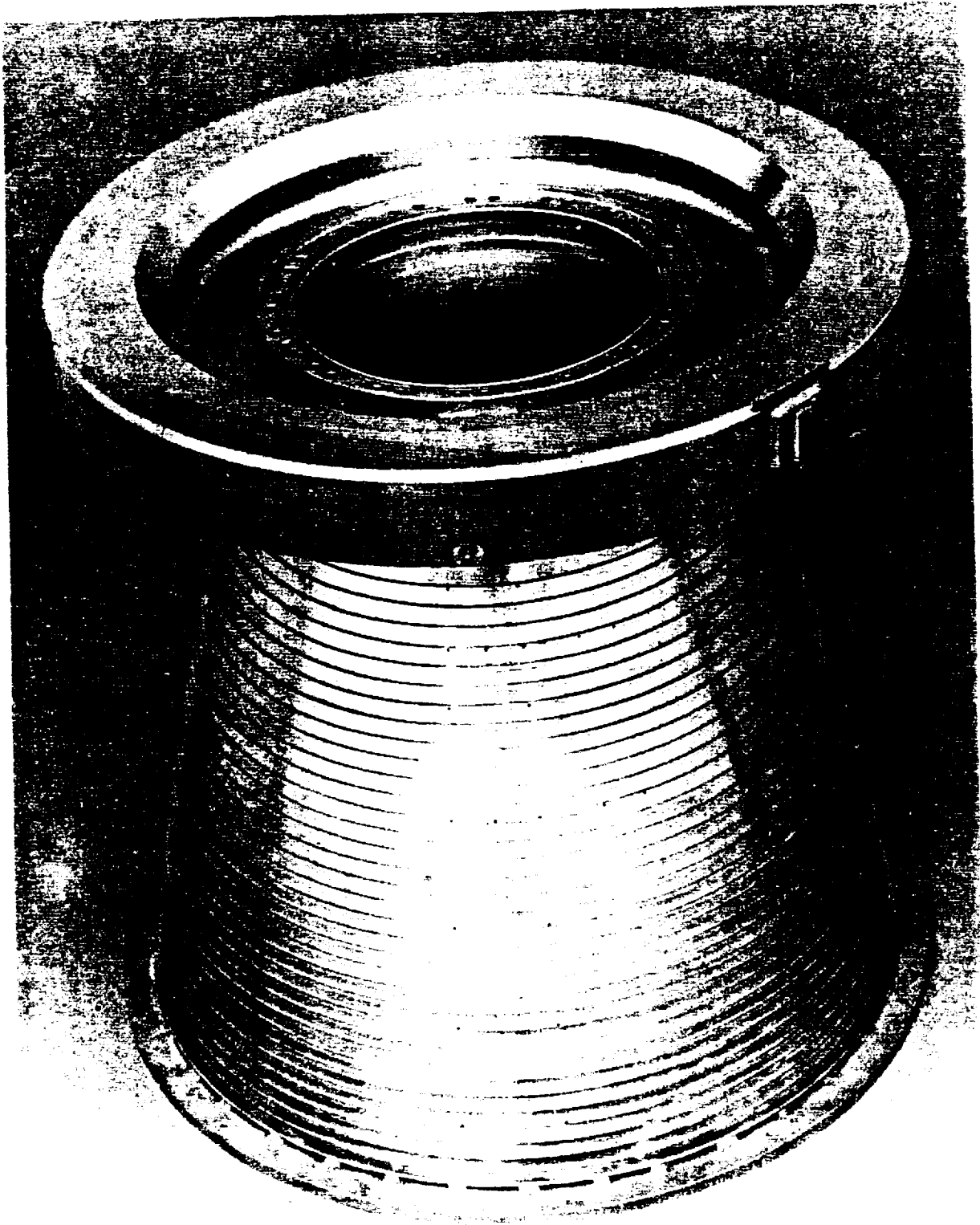
FE 625283

Figure 5.1.2-6. Calorimeter Nozzle Liner Raw Material Prepared for EB Welding



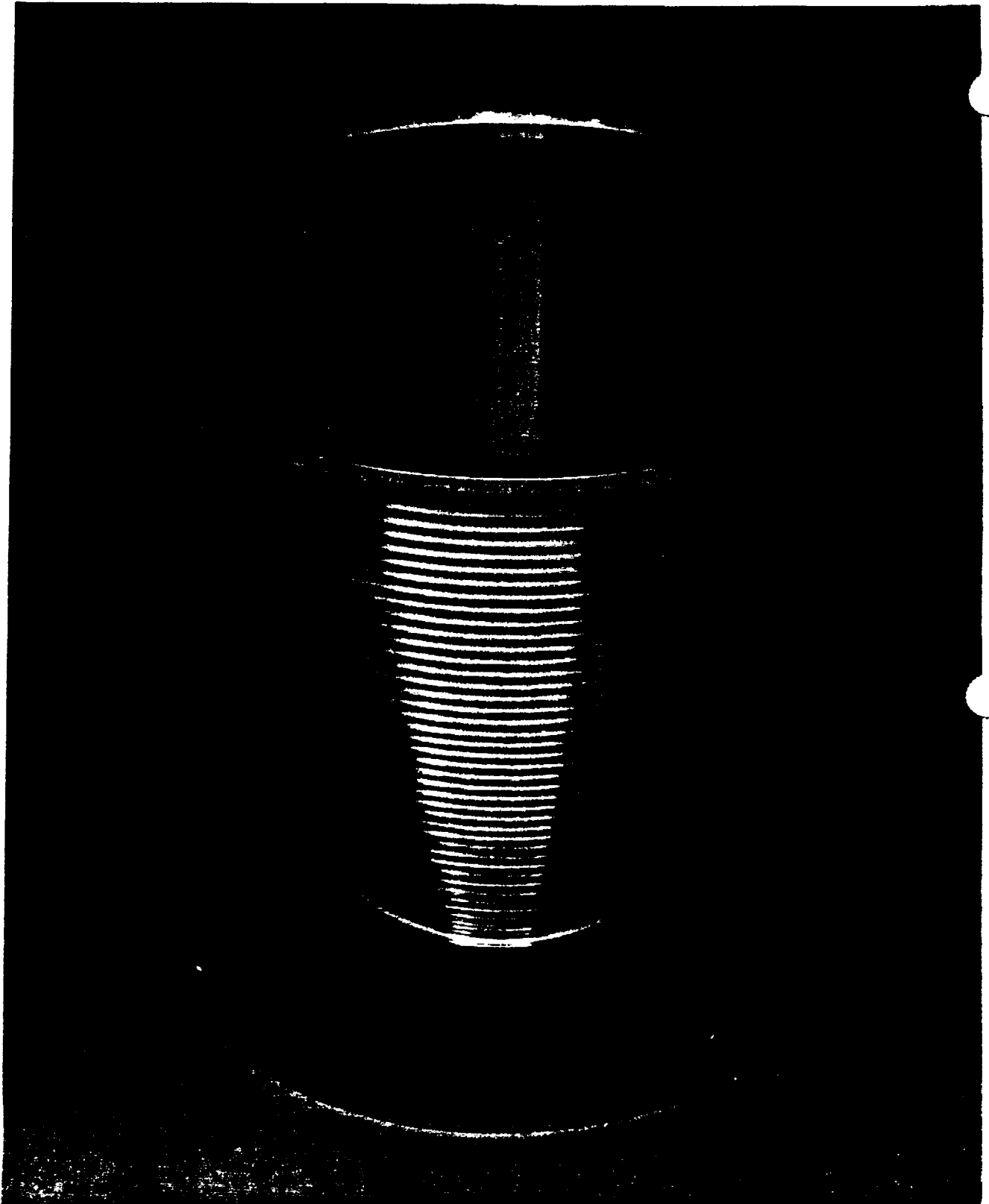
FE 625713

Figure 5.1.2-7. Calorimeter Nozzle and Manifold Assembly in EB Weld Chamber



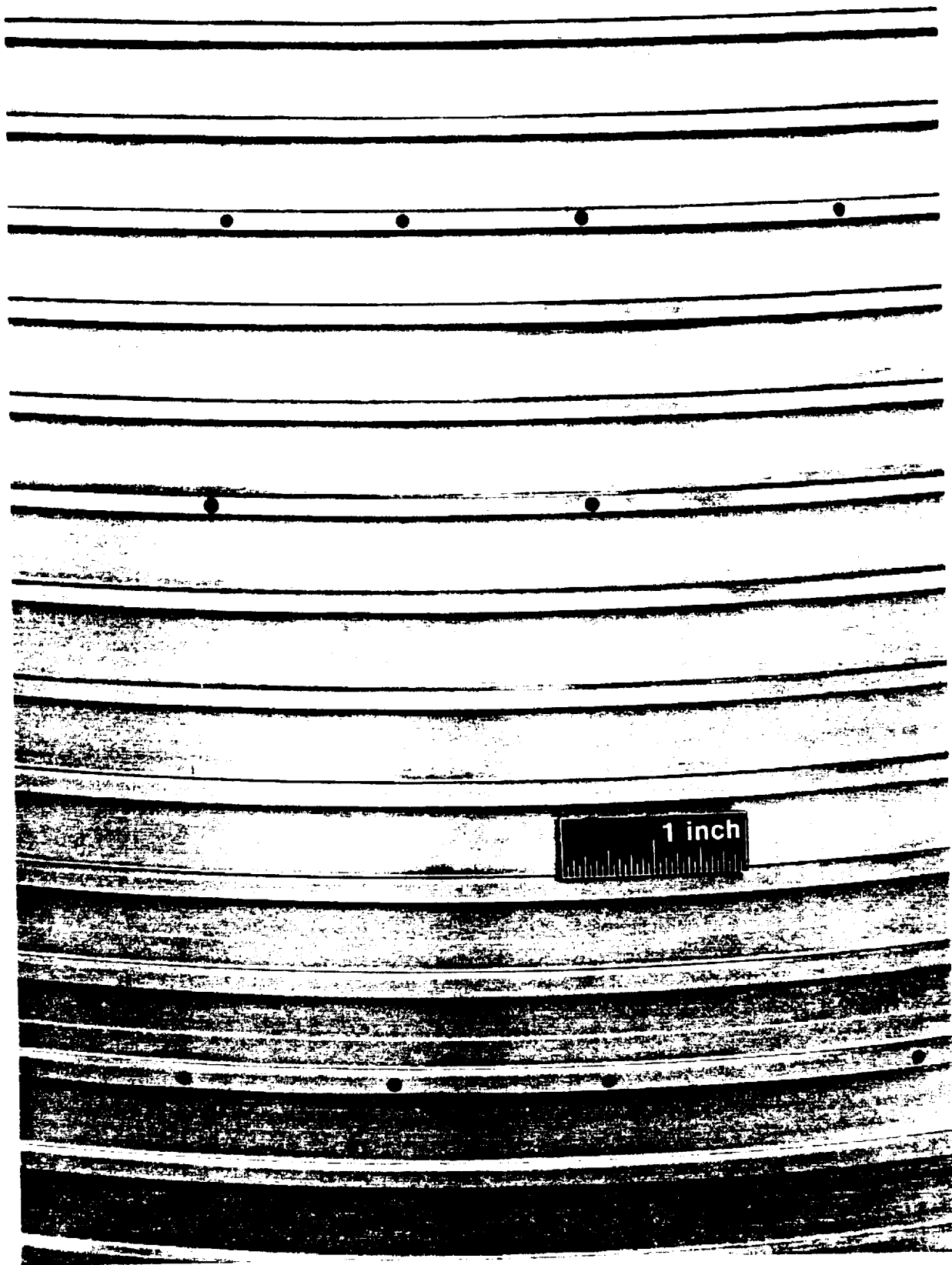
FE 627051

Figure 5.1.2-8. Fully Machined Calorimeter Nozzle Assembly



FE 627062

Figure 5.1.2-9. Fully Machined Calorimeter Nozzle Assembly



FE 627053

Figure 5.1.2-10. Calorimeter Nozzle Coolant Passages and Instrumentation Holes

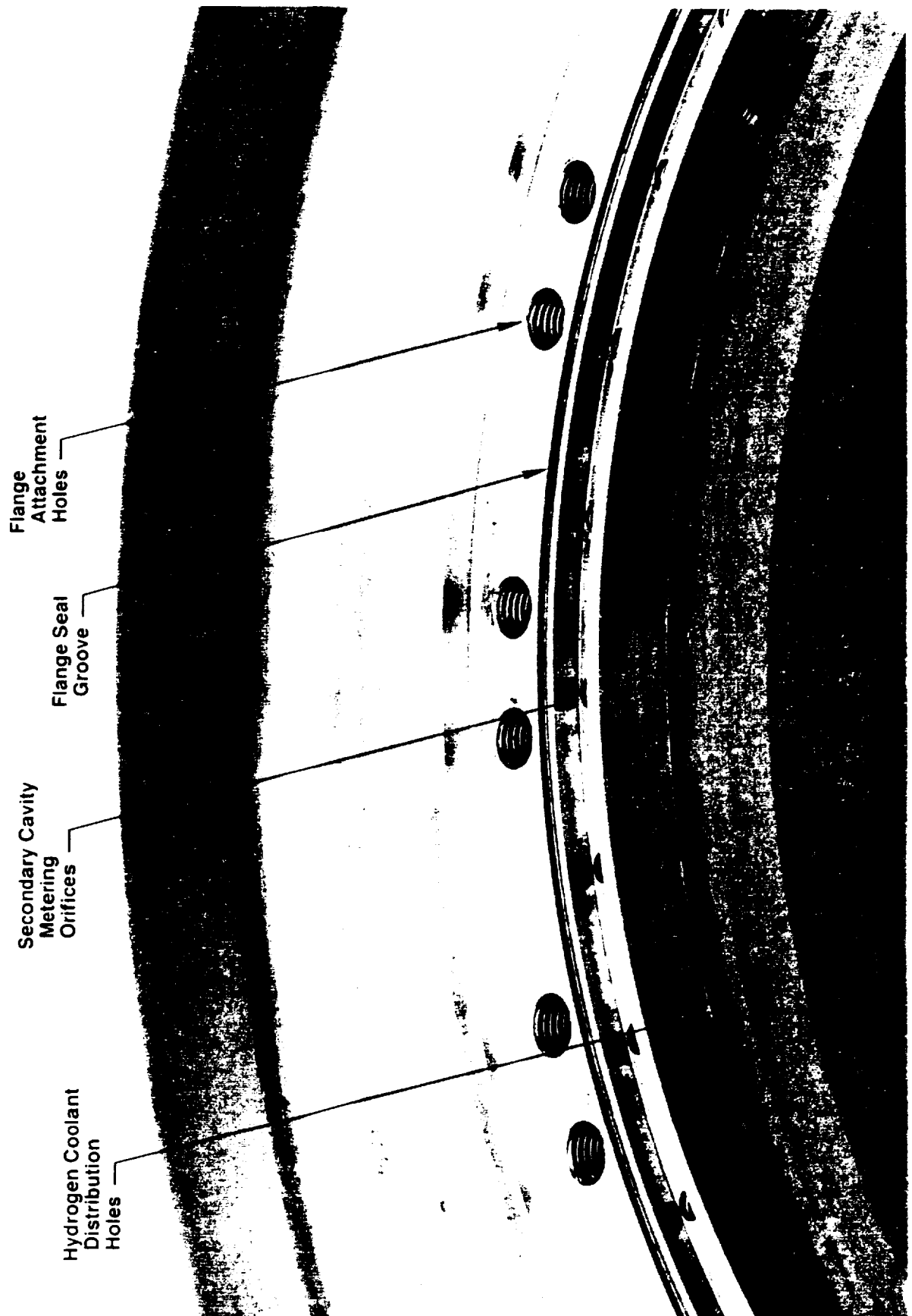


Figure 5.1.2-11. Calorimeter Nozzle Forward Flange

5.1.3 Integration and Test

The instrumentation plan originally presented in the proposal and at the Design Concept Review was revised to incorporate suggestions made during the DCR. The updated instrumentation schedule is shown in Figure 5.1.3-1.

The preliminary test matrix as discussed in the proposal was revisited based upon DCR comments. The suggestion was made to omit or significantly reduce the number of tests for the sonic injector configurations. Although there is significant engine system benefit for reducing nozzle coolant inlet pressures (which can be achieved by using sonic injector geometries rather than supersonic), the propulsion community has valid concerns regarding the repeatability, predictability, and overall film cooling effectiveness of the sonic configurations. However, due to the lack of applicable data and the significant incentive to investigate the sonic configurations in this test program, the sonic configuration should not be dropped from consideration at this time. The final test program test matrix is shown in Table 5.1.3-1.

The instrumentation plan has been updated as shown in Table 5.1.3-2 and Figure 5.1.3-2. Wall static pressure and metal temperature measurements will be taken at nine axial locations along the length of the nozzle, with three circumferential readings at each axial location. In addition, at six locations near the front end of the nozzle, gas temperature measurements will be taken using ceramic posts and high temperature thermocouples inserted through the nozzle liner wall. The gas temperature measurements are needed to assist in the transient data analysis for determining film cooling coefficients.

Based upon the recommendation of NASA TS116 test personnel, the hydrogen gas inlet manifold configuration has been changed from a G-CON flange to a simple AN fitting. Since a lower pressure supply system will now be used, the supply connections will be provided through standard tubing rather than the larger lines. All other test stand interface hardware features are unchanged from the August 1991 Design Review.

The original goal of the nozzle test program was to provide film cooling data at full-scale nozzle operating conditions. To be consistent with that goal, the main injector wall and core O/F ratio should be the same as the STME main injector configuration. The 40,000 lb thrust test hardware will match the STME main injector configurations where possible. However, durability concerns at wall O/F ratios higher than 4.0 for a chamber pressure of 2250 psi need to be investigated. The possible wall O/F ratios being considered for the STME main injector may be higher than 4.7, which would limit the chamber pressure to 2100 psi or significantly lower. A modification to the test matrix might include a series of tests at a significantly higher wall O/F than 4.0 (5.0 or higher) to obtain a wider range of data on the effects of wall O/F on film cooling. However, this data can only be obtained at lower chamber pressures, and the applicability of this data is currently being examined.

Table 5.1.3-1. Preliminary Nozzle Characterization Test Matrix - Taguchi DOX Technique

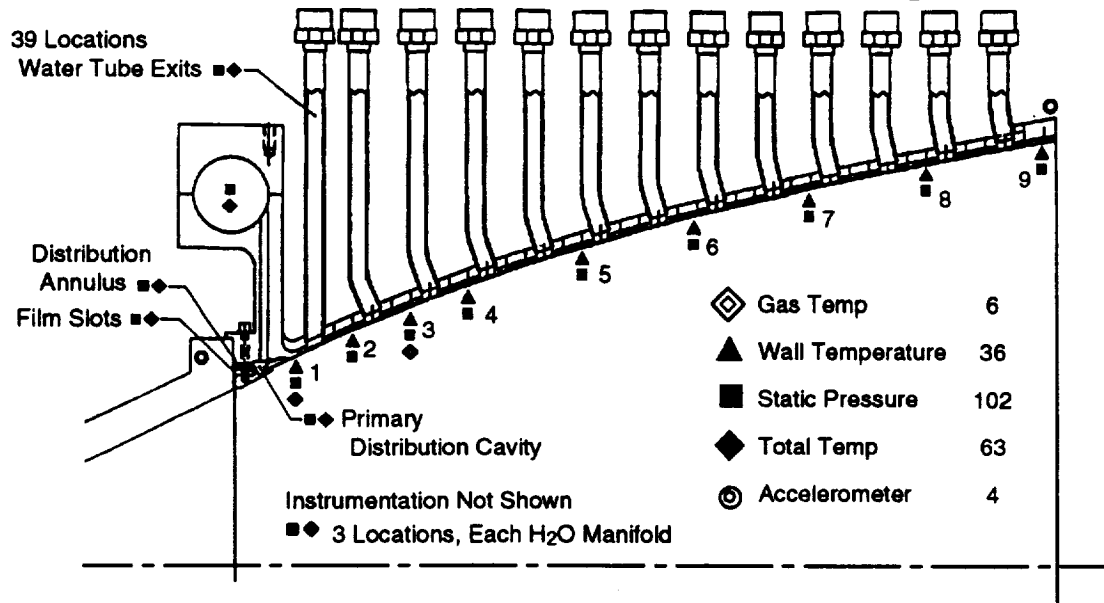
Variable Test Number	A Primary Slot Conf.	B Primary Orifice Size	D Subsonic Orifice Size	E Pc (psia)	F		
					Wall O/F	Core O/F	Overall O/F
3	Sonic	Small	Small	1200	4.0	7.5	5.5
4	Sonic	Large	Large	1200	4.0	7.5	5.5
5	Supersonic	Small	Large	1200	4.0	7.5	5.5
6	Supersonic	Large	Small	1200	4.0	7.5	5.5
7	Sonic	Small	Large	1750	4.0	7.5	5.5
8	Sonic	Large	Small	1750	4.0	7.5	5.5
9	Supersonic	Small	Small	1750	4.0	7.5	5.5
10	Supersonic	Large	Large	1750	4.0	7.5	5.5
11	Sonic	Small	Large	1200	5.0	7.5	6.2
12	Sonic	Large	Small	1200	5.0	7.5	6.2
13	Supersonic	Small	Small	1200	5.0	7.5	6.2
14	Supersonic	Large	Large	1200	5.0	7.5	6.2
15	Sonic	Small	Small	1750	5.0	7.5	6.2
16	Sonic	Large	Large	1750	5.0	7.5	6.2
17	Supersonic	Small	Large	1750	5.0	7.5	6.2
18	Supersonic	Large	Small	1750	5.0	7.5	6.2

* Two hydrogen flow rates (variable C) per run.

Table 5.1.3-2. Test Instrumentation Locations

Radial Location	Axial Location								
	1	2	3	4	5	6	7	8	9
0		Tg		Tg		Tg			
7.5		Tw	Tw	Tw	Tw	Tw	Tw	Tw	Tw
82.5	Ps	Ps	Ps	Ps	Ps	Ps	Ps	Ps	Ps
90		Tg		Tg		Tg			
97.5		Tw	Tw	Tw	Tw	Tw	Tw	Tw	Tw
108.75		Ps		Ps		Ps			
116.25		Tw		Tw		Tw			
131.25		Ps		Ps		Ps			
138.75		Tw		Tw		Tw			
148.75		Ps		Ps		Ps			
156.25		Tw		Tw		Tw			
172.5	Ps	Ps	Ps	Ps	Ps	Ps	Ps	Ps	Ps
180		Tg		Tg		Tg			
187.5		Tw	Tw	Tw	Tw	Tw	Tw	Tw	Tw
352.5	Ps	Ps	Ps	Ps	Ps	Ps	Ps	Ps	Ps

Tg = Gas Temperature, Tw = Hot Wall Temperature, Ps = Static Gas Pressure

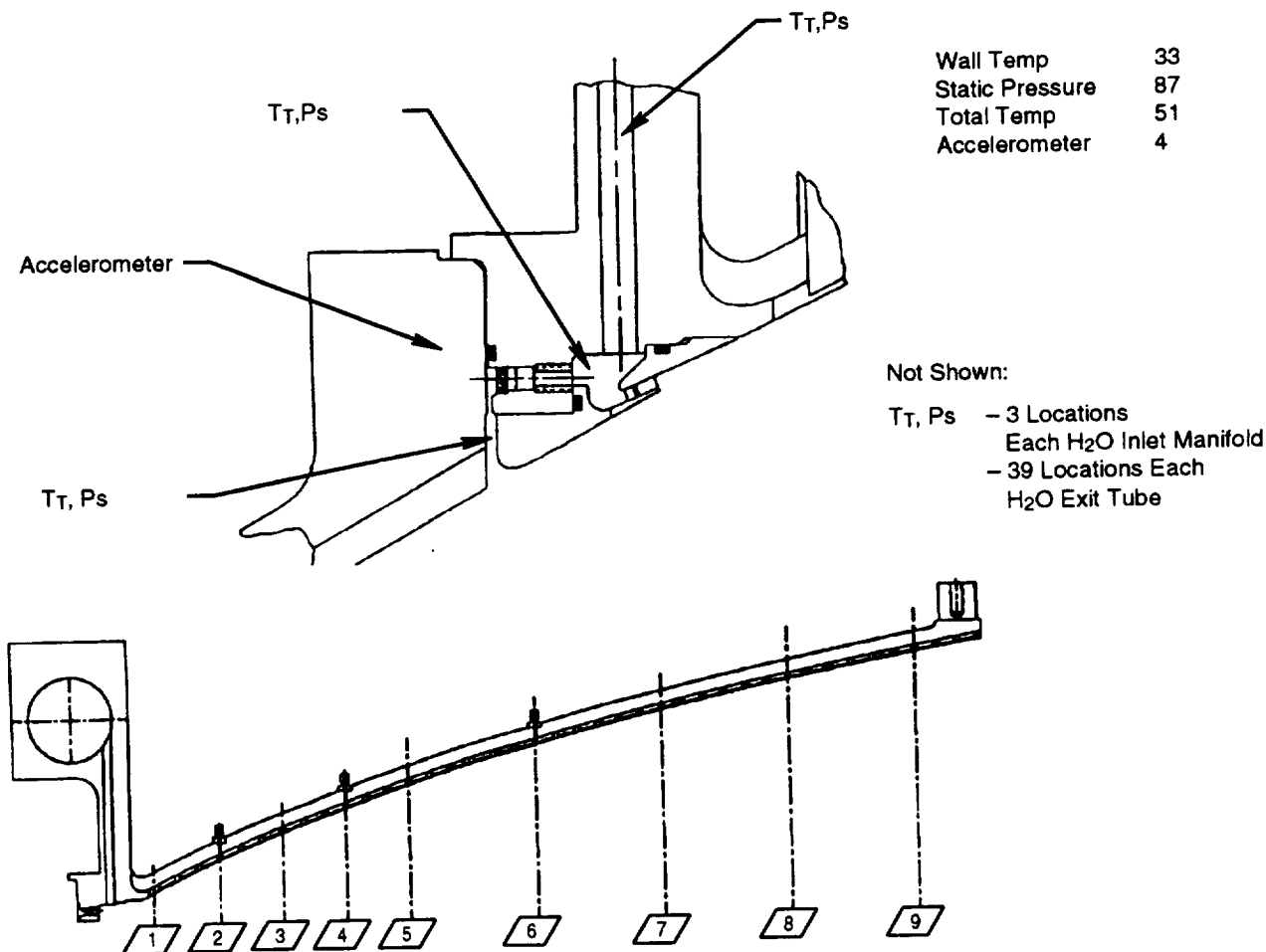


Hot Wall Circumferential Locations

0°									
22.5°									
45°									
67.5°									
90°									
-									
-									
-									
180°									
Axial Location	1	2	3	4	5	6	7	8	9

9534

Figure 5.1.3-1. Test Instrumentation Plan



12250

Figure 5.1.3-2. Test Instrumentation Plan

5.1.4 Subscale Injector Performance Enhancement

The 40K subscale injector was reworked and sent to NASA-MSFC. The rework consisted of the following:

- Repaired fuel sleeve threads
- Reworked to add seal removal access scallops to the injector-to-dome and injector-to-seal grooves; seal grooves lapped
- Machined larger instrumentation hole for an aspirated pressure tap
- Lapped injector liquid oxygen dome seal interface
- Calibrated dynamic pressure transducers
- Procured Rosemount temperature sensor
- Final cleaned and assembled.

The 40K subscale spoolpiece was also modified and sent to NASA-MSFC. The rework consisted of braze repair to eliminate a leak at the liner-to-flange interface, machine seal surfaces, and clean and ship.

The 40K subscale combustion was also shipped to NASA-MSFC.

References

1. Quentmeyer, R. J. "Experimental Fatigue Life Investigation Cylindrical Thrust Chambers," LeRC, NASA TM-X-73665 July 11-13, 1977.
2. Kazaroff, J. M. and Repas, G. A., "Conventionally Cast and Forged Copper Alloy for High-Heat Flux Thrust Chambers", LeRC, NASA Tech. Paper 2694, 1987.
3. NASA CR-168261, "Development of a Simplified Procedure for Rocket Engine Thrust Chamber Life Prediction with Creep", by O'Donnell & Associates, Inc., Oct. 1983.
4. Wieber, P. R.; Calculated Temperature Histories of Vaporizing Droplets to the Critical Point; AIAA Journal, Vol. 1, No. 12, pp. 2764-2770, December, 1970.
5. Lifshitz, A.; Scheller, K.; Burcat, A.; and Skinner, G. B.; "Shock-Tube Investigation of Ignition in Methane-Oxygen-Argon Mixtures" Combustion and Flame 16, 311-321 (1971).
6. Lewis, B., and Von Elbe, G.; Combustion, Flames and Explosions of Gases, Second Edition, Academic Press, Inc., New York and London, 1961.
7. Cowell, L. H. and Lefebvre, A. H.; "Influence of Pressure on Autoignition Characteristics of Gaseous Hydrocarbon-Air Mixtures", Paper No. 86-0068, SAE 1986 Transactions 95) (Section 6), 1-11. (1987).
8. Rosner, D. E.; On Liquid Droplet Combustion at High Pressures; AIAA Journal, Vol. 5, No. 1 pp. 163-166, January, 1967.
9. Faeth, G. M.; Dominicus, D. P.; Tulpinsky, J. F.; and Olson, D. R.; Supercritical Bipropellant Combustion; Twelfth Symposium (International) on Combustion, The Combustion Institute, 1969, pp. 9-18.
10. Carroll, R. G.; Connell, D. R.; and Limerick, C. D.; Performance Comparison of the Current SSME and a New Main Injector-Main Combustor Chamber Configuration Using the JANNAF Methodology; Twenty Second JANNAF Combustion Meeting, Jet Propulsion Laboratory, California Institute of Technology, Pasadena, California, October 7-10, 1985.
11. Crocco, L. and Cheng, S. I.; "Theory of Combustion Instability in Liquid Propellant Rocket Motors;" AGARDOGRAPH No. 8, Butterworths Scientific Pub., Ltd., London (1956).
12. Mitchell, C. E. and Eckert, K.; "A Simplified Computer Program for the Prediction of the Linear Stability Behavior of Liquid Propellant Combustors," NASA Contractor Report 3169, (1979).
13. Rouser, D. C., and Chen, F.F., "Cooling Height Pressure Combustion Chambers with Supercritical Pressure Water," AIAA-88-2845.
14. Dexter, C., "Burnout Heat Flux", MSFC Memorandum, for Record, August 29, 1984.
15. Svehla, R.A., and McBride, B.J. "Fortran IV Computer Program for Calculation of Thermodynamic and Transport Properties of Complex Chemical Systems," NASA TN kD-7056, January 1973.
16. Erland, K., "Statistical Methods Used in the Analysis of Rocket Engine Characterization Data," AIAA-91-2285, Paper Presented at the 27th Joint Propulsion conference, Sacramento, CA, June 24-26, 1991.
17. Valentine, R.S., Dean, L.E., and Pieper, J.L., "An Improved Method for Rocket Performance Prediction," J. Spacecraft, Vol. 3, No. 9, September 1966, pp. 1409-1414.
18. Pieper, J.L., Dean, L.E., and Valentine, R.S., "Mixture Ratio Distribution — Its Impact on Rocket Thrust Chamber Performance," J. Spacecraft, Vol. 4, No. 6, June 1967, pp. 786-789.
19. Bernstein, A., Heiser, W.H., and Hevenor, C., "Compound-Compressible Nozzle Flow." J. Applied Mechanics, September, 1967, pp. 548-554.
20. Carroll, R. G.; Connell, D. R.; and Limerick, C. D.; Performance Comparison of the Current SSME and a New Main Injector-Main Combustor Chamber Configuration Using the JANNAF Methodology; Twenty Second

JANNAF Combustion Meeting, Jet Propulsion Laboratory, California Institute of Technology, Pasadena, California, October 7-10, 1985.

21. Baily, R. and Weiss, A., Rocketdyne, Personal Correspondence with Connell, D. and Baker, J., P&W, May 1990.
22. Elam, Sandra K., "Subscale LOX-Hydrogen Testing With a Modular Chamber and a Swirl Coaxial Injector," AIAA-91-1874, Paper Presented at the 27th Joint Propulsion Conference, Sacramento, CA, June 24-26, 1991.

**APPENDIX A
HEAT TRANSFER MODELS**

*The following Appendix is reprinted from the first program
Bimonthly Progress Report (FR-20499-1, dated 10 October 1988).*

APPENDIX A HEAT TRANSFER MODELS

CHAMBER HEAT TRANSFER PREDICTION

Rocket combustion gas heat transfer levels and distributions are driven by complicated and interrelated thermodynamic, chemical and fluid flow mechanisms. These mechanisms are not only dependent on the propellant combination, the geometrical configuration, and operating conditions such as chamber pressure and mixture ratio, but also on the physical configuration as it relates to chemical efficiency and heat release characteristics.

The two major heat transfer contributors are generally grouped in terms of convective and combustion gas radiation components. For application within the STBE program, the convective heat transfer is predominant mode. The radiation heat flux is typically only 10 percent of the convective values in the subsonic portion of the chamber and diminishes further in the transonic and supersonic portions of the chamber as the static gas temperature drops throughout the expansion process. At the throat location where the convective heating is maximum, the radiation component represents an approximate level of only 2 percent of the local heat flux to the wall. Although gas radiation components must be adequately accounted for, it is no surprise that the prediction of the convective component captures the majority of the attention. Of course, when heat flux to the wall is determined empirically the measurements contain both the convective and radiant components. Poor combustion efficiency can substantially increase luminosity and therefore radiation heat load, with hydrocarbon fuel.

The convective process in its most simple representation expresses the heat flux to the wall in terms of the product between the driving temperature difference and a convective heat transfer coefficient that properly accounts for the fluid flow mechanism at the wall.

$$q = h_c(T_g - T_w) \quad (1)$$

where q = convective heat flux
 h_c = convective heat transfer coefficient
 T_g = adiabatic wall temperature of the gas
 T_w = heated surface temperature

The heat transfer coefficient in this simple relationship is normally described in terms of parameters that influence energy transfer across the boundary layer such as Reynolds No., boundary layer development length, boundary layer thickness, etc.

The actual heat transfer mechanism in the combustion chamber of a rocket rapidly becomes more complicated than the simple representation of Equation 1 implies when the actual process is more closely considered. The major contributors to this increase in complexity are the chemical reaction of the propellants, the high temperatures presents, the presence of high turbulence levels, possible combustion instabilities, abnormal boundary layer development triggered by recirculating propellant flows and chemical reaction, dissociation or re-combination within the boundary layer; large temperature differences between the gas stream and the heated wall can be also cause significant variations of fluid transport properties in and near the boundary layer. Despite the difficulty in accurately accounting for these mechanisms the most promising methods of reliably predicting combustion chamber heat transfer characteristics are derived from boundary layer theories.

In general, an attractive boundary layer analysis is initially selected for the basis of the prediction system. The influence of other mechanisms, such as dissociation, propellant heat

release and combustion efficiency are added to the analysis using appropriate theory or data for each added mechanism.

Various heat transfer coefficient prediction methods have been and are currently being used within the rocket community. They encompass the simple Bartz (Reference 3) closed form solution that correlates closely with fully developed pipe flow theory, incompressible boundary layer such as Sibulkin (Reference 4) and more rigorous boundary layer solutions such as the Bartz long form (Reference 5) or the Mayer Integral Method (Reference 6).

Since the mid 1960's Pratt & Whitney (P&W) has continuously developed its combustion chamber/nozzle thermal design analysis tools around the Mayer Integral Method. This boundary layer method was selected because of its combination of rigorous theory, ease and speed of computer application and applicability to wide variety of axisymmetric and free expansion surface nozzles. The method is based on the approximate solution of energy integral equation for boundary layers using Ambrok's method (Reference 7). The simplifying assumptions in the analysis correspond closely to those encountered in rocket nozzle flow. Semi-empirical data associated with the Blasius flat plate heat transfer coefficient, with modification for variable fluid properties based on Eckert's reference temperature method (Reference 8), are used within the analysis. The overall calculation procedure requires as input data the cooled wall temperature and the local free stream fluid data just outside the boundary layer.

Numerous improvements have been incorporated into the P&W system, not only to more accurately predict combustion chamber heat transfer characteristics, but also to increase its flexibility and ease of use. The prediction system is a finite portion of the P&W computer code 5160 Rocket Thermal Design System. Deck 5160 not only addresses the combustion side transfer, but has the capability to fully evaluate tubular/non-tubular coolant passage thermal and flow characteristics, properly accounting for the two-dimensional conduction effects, curvature enhancement and surface roughness effects within the wall. The coolant side capabilities of the program will not be addressed further in this section so that combustion gas prediction capabilities can be more fully delineated.

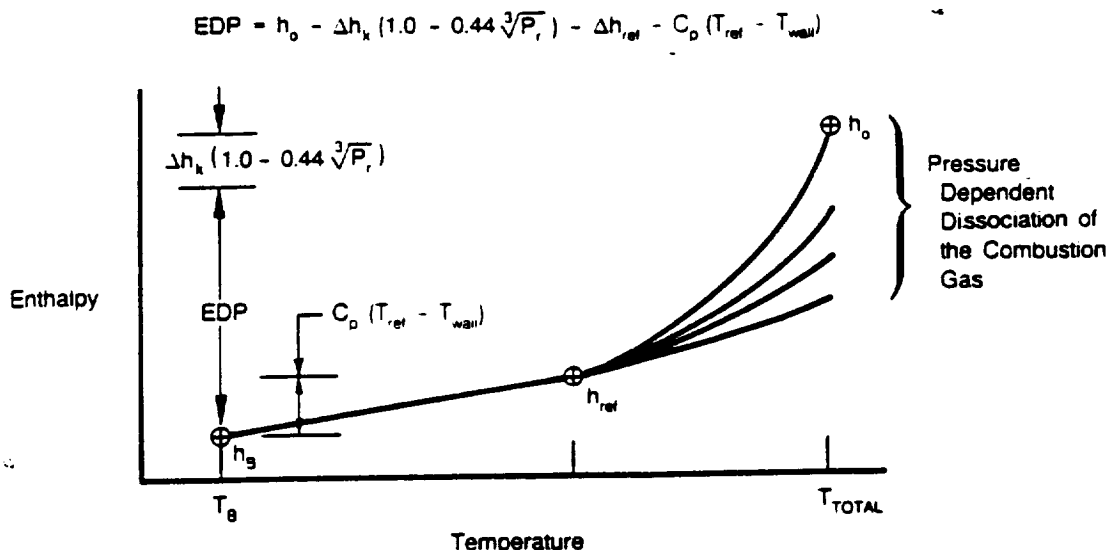
A large amount of combustion gas chemical dissociation is present in the combustion chamber. For this reason the combustion gas temperature does not provide the proper energy driving potential; combustion gas enthalpy level is more meaningful. This effect is accounted for in the P&W analysis by modifying the basic convective heat flow relationship (Equation 1) to the following.

$$q = h_g \times \text{EDP} / C_p \quad (2)$$

EDP = Enthalpy Driving Potential

C_p = specific heat evaluated at Eckert reference temperature.

Enthalpy driving potential, EDP, is the difference between the free stream stagnation enthalpy and the enthalpy level at the wall. Figure 12 is a graphic representation of the enthalpy driving potential. The stagnation enthalpy of the combustion gases is strongly dependent on chamber pressure due to dissociation of the combustion products. Dissociation of the combustion products occurs at temperature above 3000°R, which has been selected as the reference point. At temperatures below 3000°R the energy state of the gas can be represented adequately with specific heat.



FD 345583

Figure 12. Combustion Side Enthalpy Driving Potential

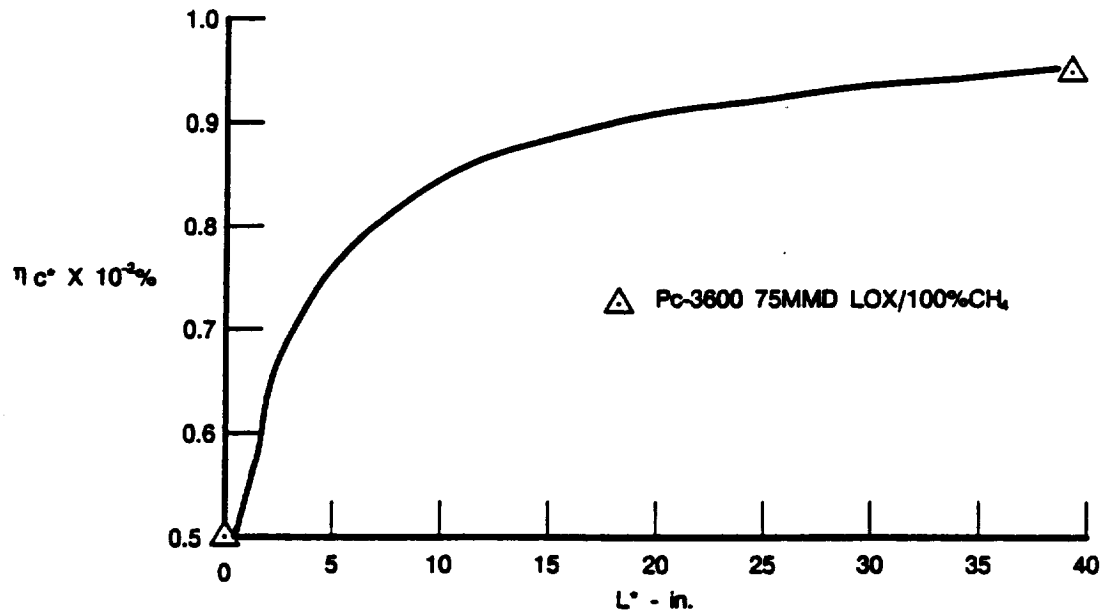
The combustion efficiency and the heat release of the chemical reaction defines the local hot gas energy state for heat transfer. The actual energy state of the gases at the throat plane, H_t , is related to the ideal value H_t' by the combustion efficiency ηc^* :

$$\frac{H_t - H_o}{H_t' - H_o} = (\eta c^*)^2 \quad (3)$$

where H_o = entering energy states of the propellants

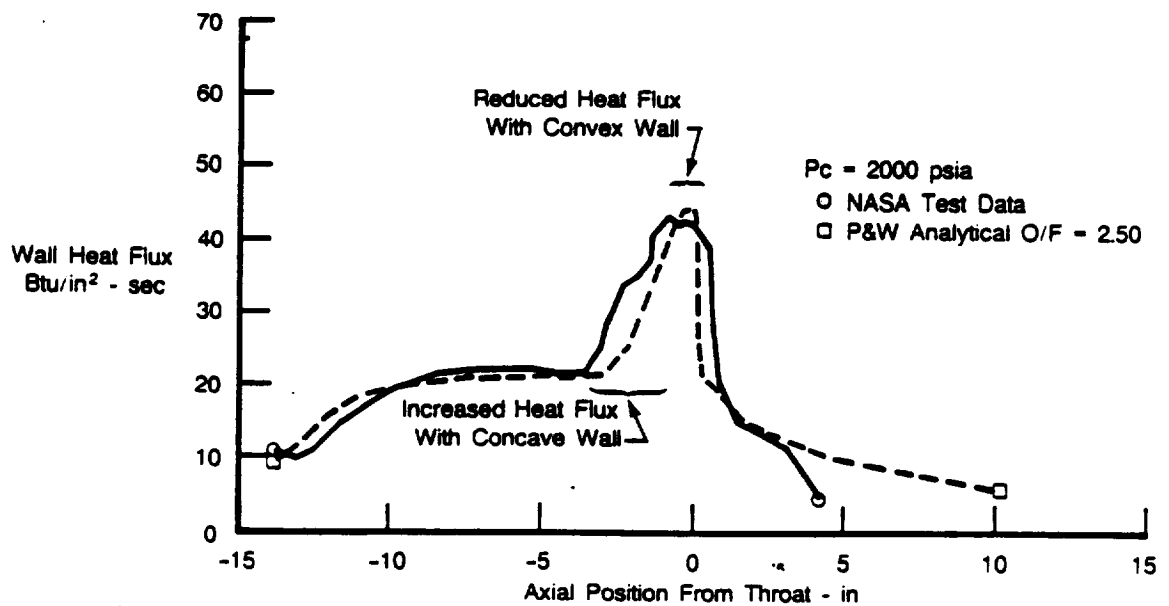
The energy intensity increases as the reaction process progresses through the chamber. The energy states and corresponding heat transfer driving potential are lower near the injector. The energy release profile can be generated within deck 5160, based on theoretical behavior, or it can be input specifically over the chamber length to better represent a particular injection/propellant combination. Figure 13 presents typical predicted values of combustion efficiency with chamber characteristic length.

Wall curvature within combustion chamber impacts the boundary layer and can therefore modify the anticipated local heat transfer levels. It has been observed and reported (e.g. Reference 9) that heat transfer within tubes can be altered by curving the tube. An enhancement in heat transfer coefficient results on the concave side of the tube and an attenuation occurs on the convex side. A similar effect occurs as a result of the necessary wall curvatures within a combustion chamber, even though the overall geometrical features differ somewhat. Heat transfer rates for the propellants of interest to the STBE program have been measured with cooled calorimeter chambers by References 2 and 10. Figures 14 and 15 present comparisons between the local measured heat flux levels and those predicted by the P&W Rocket Thermal Design System without accounting for any wall curvature effects. It should be noted that the measured heat transfer rates are higher than predicted immediately upstream of the throat where the chamber is concave and vice versa at the throat where the chamber is convex.



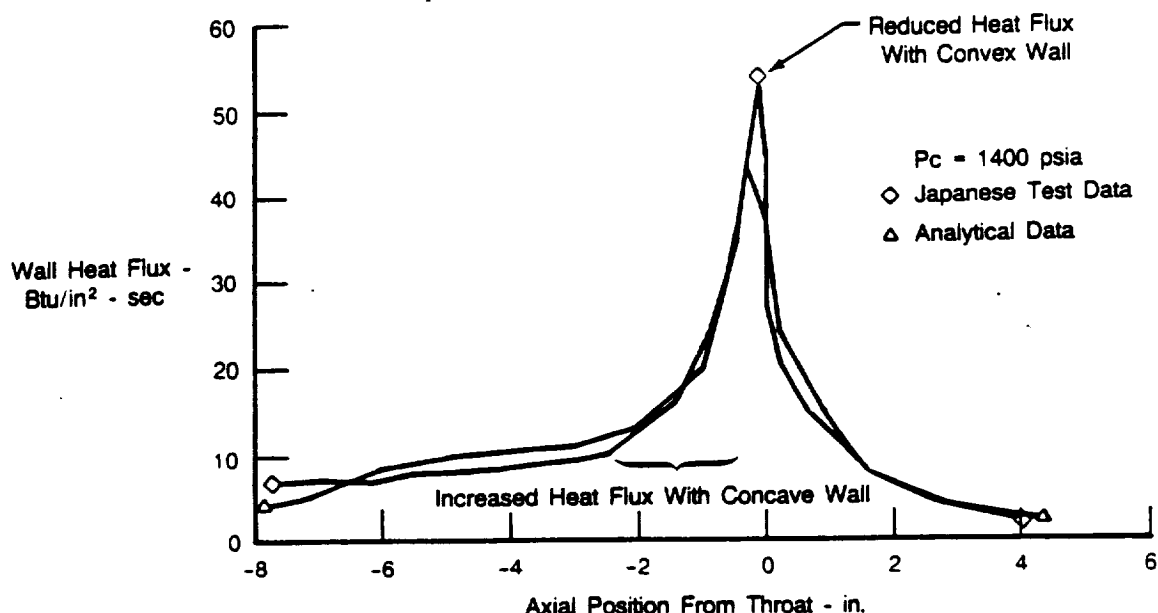
FDA 358534

Figure 13. Predicted Combustion Efficiency Versus Chamber Characteristic Length



FD 346027

Figure 14. LOX/Methane Chamber Heat Flux Comparison With Data From Reference 2



FD 348028

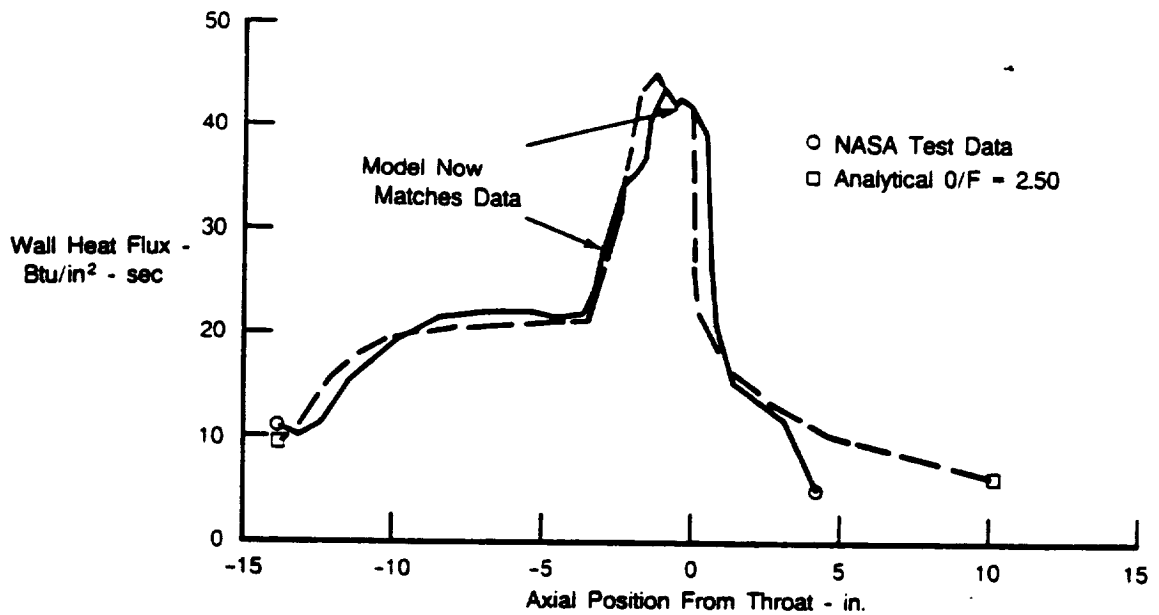
Figure 15. LOX/Methane Chamber Heat Flux Comparison With Data From Reference 10

The P&W Rocket Thermal Design System has been modified using wall curvature heat transfer enhancement factors obtained using regression techniques to the empirical data. Incorporation of these relationships allows the influence of chamber curvature to be properly addressed in the prediction of combustion gas convective heat transfer coefficients. Figures 16 and 17 compare the measured data to the P&W prediction system using the modifications for curvature enhancement effects. Significant improvement in the predictions is obvious for both sets of data.

Although the gas radiation component is generally small relative to the convective heat flux component, it is evaluated within the P&W Rocket Thermal Design System using a method formulated by Reference 11.

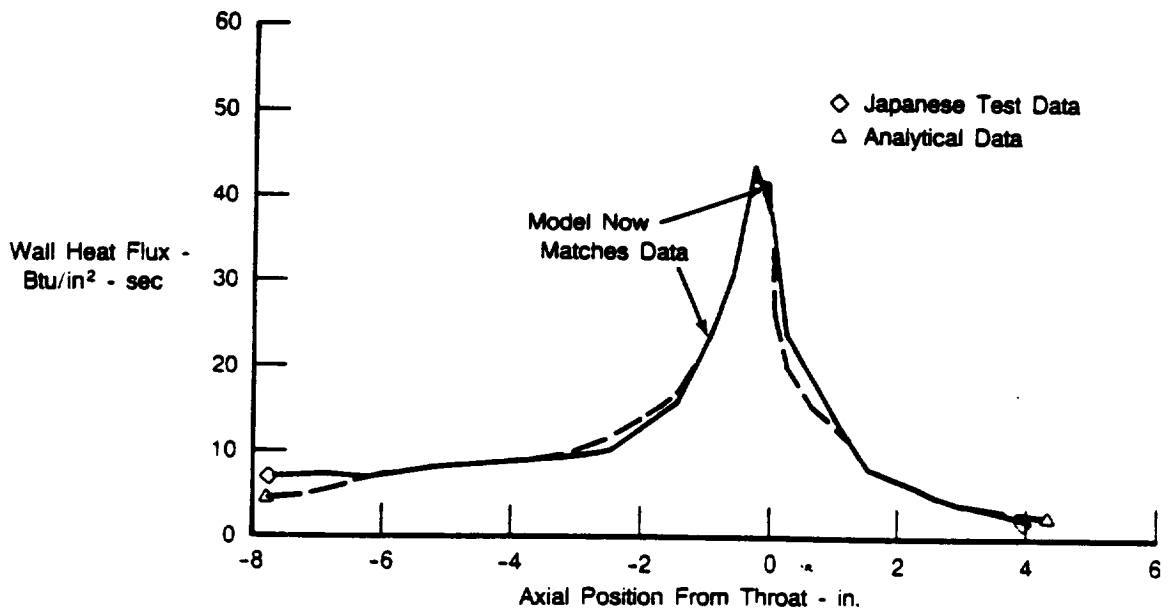
Predictions concerning the effects of O/F biasing on combustion chamber heat flux levels are obtained by assuming no mixing between the modified outer flow stream and the internal core of the main gas. In these cases the heat transfer to the wall is predicted based on the energy level and properties of this outer stream. In general this stream would be operating at a lower temperature level than the main core. The radiation heat flux to the wall, however, is based on core conditions since the majority of the radiating cloud is at the core conditions and the outer stream is essentially transparent to the radiation.

Another gas side phenomenon that could be encountered with a hydrocarbon fuel such as methane is carbon deposited at the wall. Significant deposition of solid carbon at the wall was not observed by either Reference 2 or 10. If large amounts are deposited, the carbon acts as an insulator and reduces the heat flow to the wall; whereas, small amounts of carbon being transiently deposited could disrupt the boundary layer and slightly increase the heat transfer rates. Based on the data presently available (Reference 2 and 10) any thermal impact of carbon coating on the wall is anticipated to be negligible.



FD 346029

Figure 16. LOX/Methane Chamber Heat Flux Comparison With Data From Reference 2 Using Curvature Enhancement



FD 346030

Figure 17. LOX/Methane Chamber Heat Flux Comparison With Data From Reference 10 Using Curvature Enhancement

As previously mentioned, the internal wall thermal analysis procedure accounts for passage curvature, surface roughness and large wall-to-coolant bulk temperature differences on the convective heat transfer coefficient of the coolant. Two-dimensional conduction effects are

automatically evaluated within the program and are applied to the combined conduction/convection mechanism in the determination of chamber wall temperature.

The coolant side heat transfer characteristics for hydrogen coolant are predicted using a modification of the Dittus-Boelter correlation (Reference 12). The basic correlation is modified for large wall-to-bulk coolant temperature differences by evaluating the fluid transport properties and density at a film temperature equal to the arithmetic mean of the coolant side wall temperature and the local coolant static temperature.

The effects of passage roughness on coolant heat transfer coefficient are based on the experimental work conducted by Dipprey and Sabersky (Reference 13). Heat transfer and fluid pressure drop data were acquired using water with selected values of sand grain roughness over a range of Prandtl and Reynolds Numbers.

Typical results presenting the ratio of roughened wall heat transfer-to-smooth wall heat transfer coefficient as a function of Reynolds Number and Prandtl Number are shown in Figure 18. Similar results for friction factor were also determined and are incorporated in the P&W Rocket Thermal Design Program.

The curvature enhancement factor used for the coolant passages were derived from the empirical data presented in Reference 9 through numerical regression techniques. The curvature results in an increase in coefficient on the concave side of the turn and reduction on the convex side. The level of enhancement depends on the ratio of the tube radius of curvature to the tube diameter and also the angular position through the turn, as shown in Figure 19.

Coolant entrance effects are also contained in the analysis to account for increased heat transfer coefficients within a developing boundary layer. The entrance effects from a variety of sources has been compiled within Reference 14. Figure 20 summarizes the results of this compilation and presents the enhancement, expressed as the ratio of local Nusselt to fully developed Nusselt Numbers, as a function of normalized length, X/D .

A forward marching, finite difference, iterative analysis is used within the program to determine wall temperature, heat flux, coolant temperature and coolant pressure throughout the chamber. The coolant pressure losses account for entrance and exit effects, friction loss, momentum loss, heat addition and local turning effects. Wall temperature at each calculation station is determined by iteratively varying the local heat flux.

Modified one-dimensional heat transfer analysis is used for the initial heat flux and wall temperature determination. The modification consists of a simplified fin analysis to account for the approximation of two-dimensional conduction characteristics of the passage webs and backwall. At specified intervals a nodal analysis is conducted to accurately evaluate the two-dimensional effects. Results of each nodal analysis are then used within the program to adjust the modified one-dimensional assumptions for subsequent calculation stations specified by the user. A sample of the output from a typical two-dimensional calculation station is shown in Figure 21.

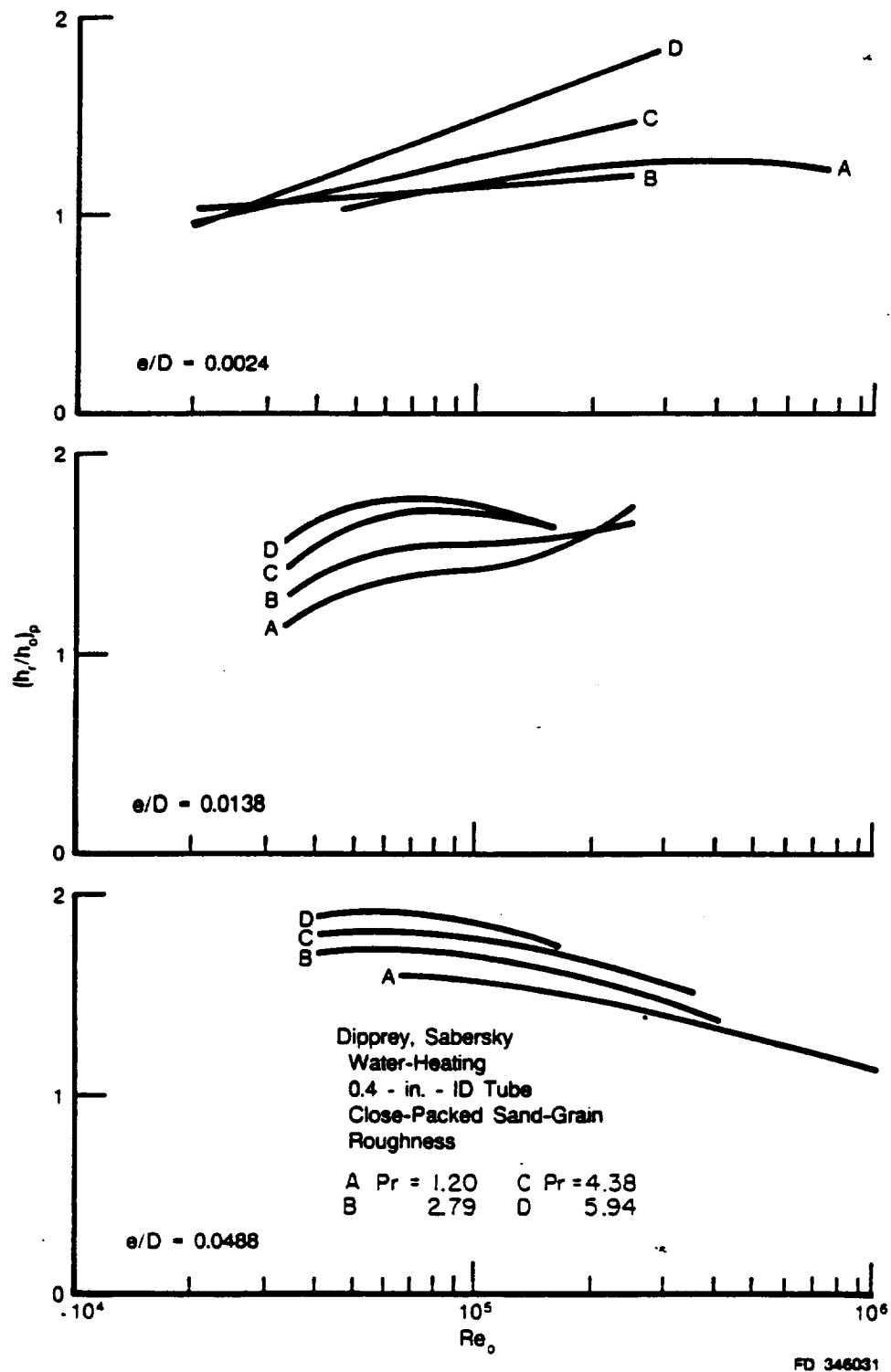
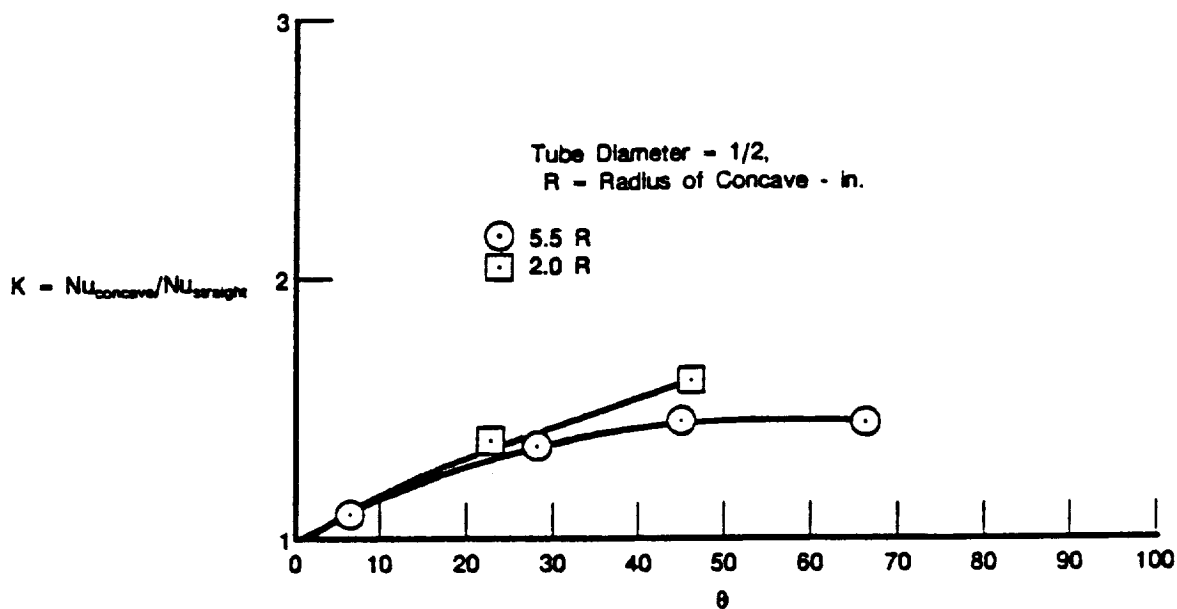
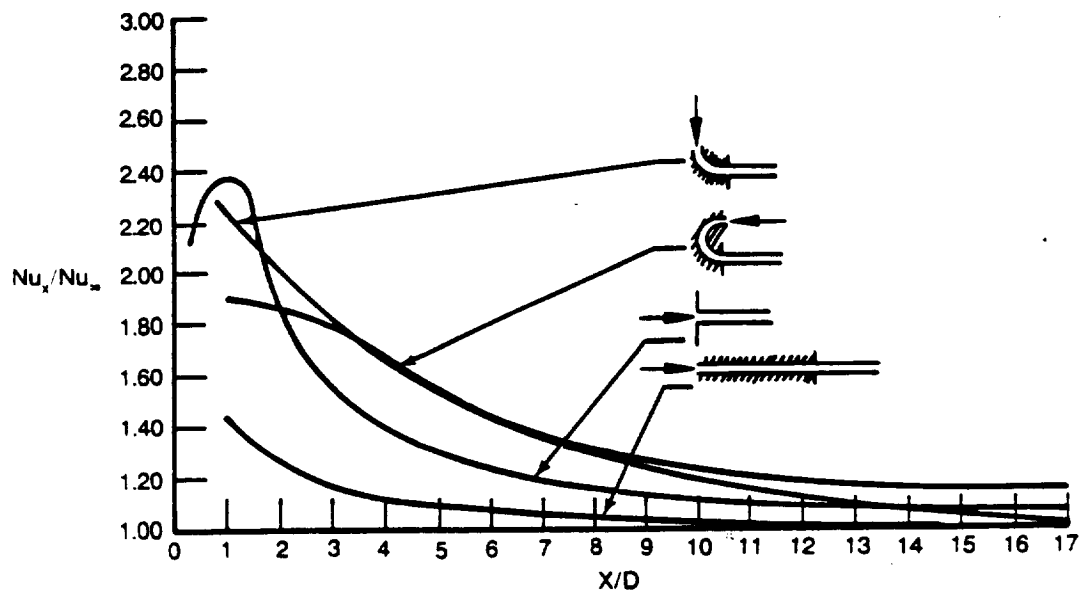


Figure 18. Performance of Tubes With Sand-Grain Roughness (From Reference 13)



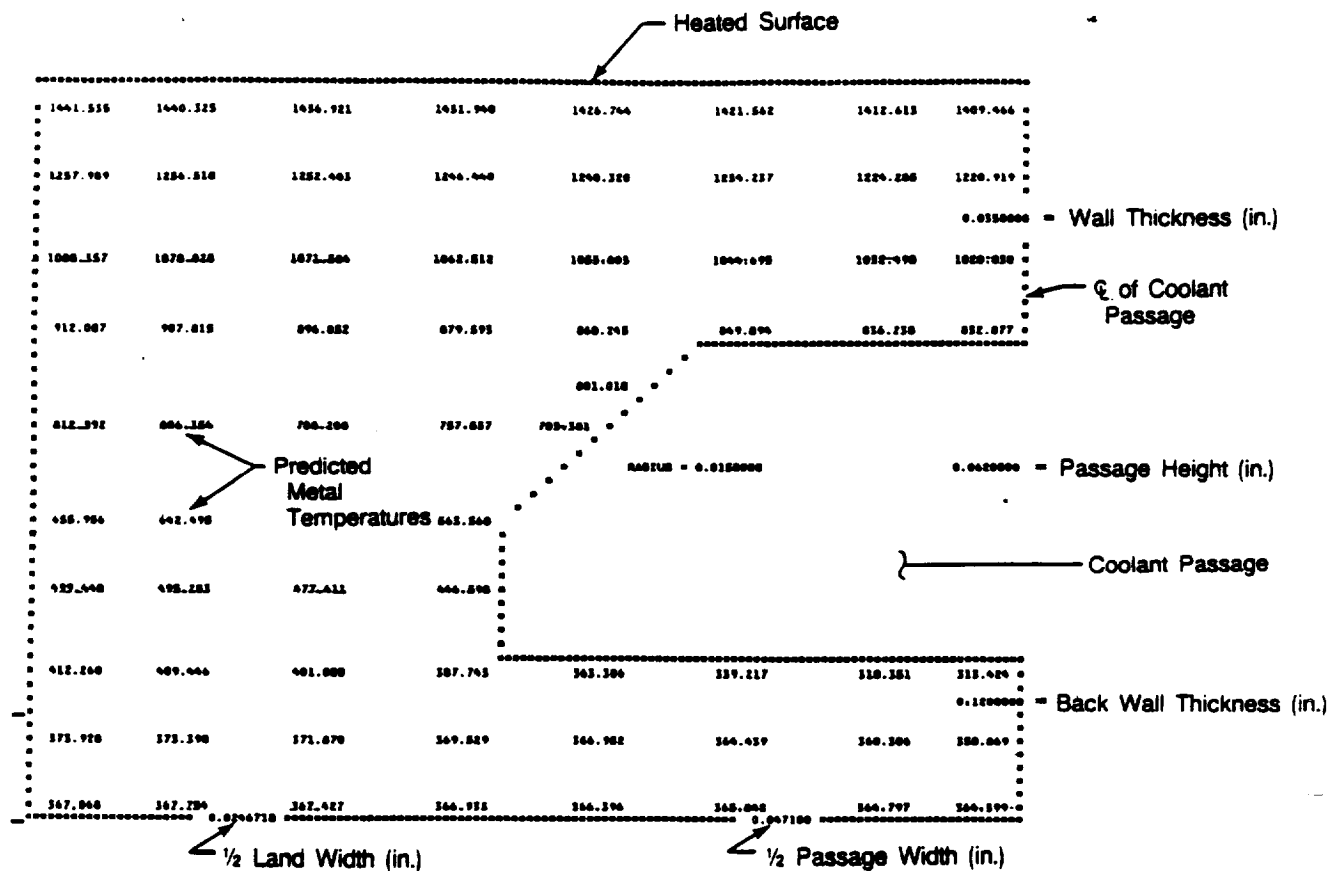
FDA 348032

Figure 19. Variation of Cooling Enhancement With Angular Position (Gaseous Hydrogen)



FD 348033

Figure 20. Measured Local Nusselt Numbers in the Entry Region of a Circular Tube for Various Entry Configurations, Air With Constant Surface Temperature



FD 348034

Figure 21. Sample Two-Dimensional Thermal Analysis Temperature Profile

APPENDIX A — REFERENCES

1. 3-Dimensional Thrust Chamber Life Prediction, Boeing Aerospace Company, March 1986 (NASA CR-134979).
2. Thrust Chamber Material Exploratory Technology Program Literature Review of Copper Base Alloys, prepared by Pratt & Whitney Government Products Division under Contract NAS3-23858, May 20, 1984 (FR-18383-1).
3. Bartz, D. R., "A Simple Equation for Rapid Estimation of Rocket Nozzle Convective Heat Transfer Coefficients," Jet Propulsion, January 1957.
4. Sibulkin, M., "Heat Transfer to an Incompressible Turbulent Boundary Layer and Estimation of Heat Transfer Coefficients at Supersonic Nozzle Throats" Journal of Aeronautical Sciences, February 1965.
5. Elliot, D. G., Bartz, D. R., and Silver, S., "Calculation of Turbulent Boundary-Layer Growth and Heat Transfer in Axi-Symmetric Nozzles," JPL TR No. 32-387, February 1983.
6. Mayer, E., "Analysis of Convective Heat Transfer in Rocket Nozzles," ARS Journal, July 1961.
7. Ambrok, G. S., "Approximate Solution of Equations for Thermal Boundary Layer with Variations in Boundary Layer Structure," Soviet Physics, Vol. 2, No. 9, 1957.
8. Eckert, E. R. G., "Engineering Relations for Heat Transfer and Friction," Transactions of ASME, Vol. 78, 1956.
9. Hendricks, R. C. and Simon, F. F., "Heat Transfer to Hydrogen Flowing in a Curved Tube," NASA, Lewis Research Center.
10. Tamura, H., Ono, F., Kumakawa, A. and Yatsuyangi, N., "LOX/Methane Staged Combustion Rocket Combustion Investigation," AIAA-87-1856, San Diego, July 1987.
11. Lefebvre, A. H. and Herbert, W. V., "Heat-Transfer Processes in Gas-Turbine Combustion Chambers," Proceedings of the Institute of Mechanical Engineers (London), 1960.
12. Dittus, F. and Boelter, L. M. K., Univ. Calif. Publications of Engineering 2:443, 1930.
13. Dipprey, D. F. and Sabersky, R. H., "Heat and Momentum Transfer in Smooth and Rough Tubes at Various Prandtl Number." JPL Tech. Rept. 32-269, 1962. Also, Int. J. Heat Mass Transfer, 6: 329, 1963.
14. Rohsenow, W. M. and Hartnet, J. P., Handbook of Heat Transfer, McGraw-Hill Inc., N. Y., 1973.

CN22

TURNER PUBLICATION

MARSHALL SPACE FLIGHT CENTER

HUNTSVILLE AL

DELETIONS OR CHANGES 544-4494

RETURN ADDRESS CN220

000002444